

STATE OF CALIFORNIA DEPARTMENT OF TRANSPORTATION
TECHNICAL REPORT DOCUMENTATION PAGE

TR0003 (REV. 10/98)

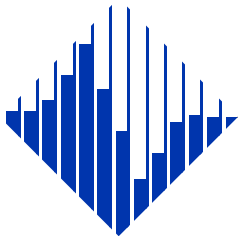
1. REPORT NUMBER CA15-2171		2. GOVERNMENT ASSOCIATION NUMBER		3. RECIPIENT'S CATALOG NUMBER	
4. TITLE AND SUBTITLE Structural Behavior of Column-Bent Cap Beam-Box Girder Systems in Reinforced Concrete Bridges Subjected to Gravity and Seismic Loads, Part I: Pre-Test Analysis and Quasi-Static Experiments				5. REPORT DATE November 2015	
				6. PERFORMING ORGANIZATION CODE UCB	
7. AUTHOR(S) Mohamed A. Moustafa, Khalid M. Mosalam				8. PERFORMING ORGANIZATION REPORT NO. UCB/CA15-2171 PEER Report 2015/10	
9. PERFORMING ORGANIZATION NAME AND ADDRESS Department of Civil and Environmental Engineering University of California, Berkeley 747 Davis Hall Berkeley, CA 94720-1792				10. WORK UNIT NUMBER	
				11. CONTRACT OR GRANT NUMBER 65A0391	
12. SPONSORING AGENCY AND ADDRESS California Department of Transportation Engineering Service Center 1801 30 th Street, MS 9-2/5i Sacramento, California 95816 California Department of Transportation Division of Research and Innovation, MS-83 1227 O Street Sacramento CA 95814				13. TYPE OF REPORT AND PERIOD COVERED Final Report 6/29/2011 – 6/15/2015	
				14. SPONSORING AGENCY CODE 913	
15. SUPPLEMENTAL NOTES Prepared in cooperation with the State of California Department of Transportation.					
16. ABSTRACT This report presents the second half of the mixed experimental-computational study that aimed at investigating the structural and seismic behavior of integral bent caps in reinforced concrete (RC) box-girder bridges. The main objective of the study was to accurately estimate the contributions of the deck and soffit slabs framing into the bent cap in as-built and retrofitted RC bridge systems under the combined effect of vertical and lateral loading. In particular, the study estimated the effective flange width of the bent cap beam due to the box-girder slabs contributions. Computational and experimental methods were utilized to investigate the problem at hand. The finite element (FE) computational part of the study consisted of two phases: pre-test and post-test analyses. The experimental program involved testing two 1/4-scale column-bent cap beam-box-girder sub-assemblies using quasi-static and hybrid simulation (HS) testing methods. This report presents the results of HS tests conducted on the second specimen and post-test analysis, which involved calibration of the FE model and parametric studies at the specimen and full prototype bridge levels. The pre-test analysis phase and the first part of the experimental program are discussed in Part I of the report (PEER 2015/09). To conduct the HS tests, this study developed a new practical approach that utilized readily available laboratory data acquisition system as a middleware for feasible HS communication. The proper communication among the HS components and verification of the HS system were first performed using tests conducted on standalone hydraulic actuators and the previously tested specimen. A carbon fiber reinforced polymer retrofit scheme was adopted for the second specimen to study the behavior of the bent cap at higher moment demands into its inelastic range of structural response. The retrofitted second specimen was then tested using multi-degree-of-freedom HS under gravity load using several scales of ground motions. The post-test analysis was the final stage of this study. The results from the as-built first-specimen cyclic tests were used to calibrate a detailed three-dimensional FE model. The calibrated model was used to explore the effect of reducing the bent cap reinforcement on the overall system behavior and to investigate the box-girder contribution at higher levels of bent cap seismic demand. The study revised the effective slab width for integral bent caps and concluded that the slab reinforcement within an effective width should be included for accurate bent cap capacity estimation. An illustrative design example to investigate the design implications of the revised effective slab width and bent cap capacity estimation on the optimization of the bent cap design for a prototype bridge is presented. To optimize the box-girder geometry for the most efficient slabs contribution to the bent cap structural behavior, another parametric study was conducted of the entire bridge level to investigate the effect of the box-girder geometry on the slab contributions and the bent cap effective width.					
17. KEY WORDS Bent Caps, Effective Slab Width, Seismic Behavior, Box-Girder Bridges, Cyclic Testing, Finite Element Modeling			18. DISTRIBUTION STATEMENT No restrictions. This document is available to the public through the National Technical Information Service, Springfield, VA 22161		
19. SECURITY CLASSIFICATION (of this report) Unclassified			20. NUMBER OF PAGES 381		21. PRICE

Reproduction of completed page authorized

DISCLAIMER STATEMENT

This document is disseminated in the interest of information exchange. The contents of this report reflect the views of the authors who are responsible for the facts and accuracy of the data presented herein. The contents do not necessarily reflect the official views or policies of the state of California or the Federal Highway Administration. This publication does not constitute a standard, specification, or regulation. This report does not constitute an endorsement by the Department of any product described herein.

For individuals with sensory disabilities, this document is available in Braille, large print, audiocassette, or compact disk. To obtain a copy of this document in one of these alternate formats, please contact: the Division of Research and Innovation, MS-83, California Department of Transportation, P.O. Box 942873, Sacramento, CA 94273-0001.



PACIFIC EARTHQUAKE ENGINEERING RESEARCH CENTER

Structural Behavior of Column-Bent Cap Beam- Box Girder Systems in Reinforced Concrete Bridges Subjected to Gravity and Seismic Loads

Part I: Pre-Test Analysis and Quasi-Static Experiments

Mohamed A. Moustafa

Khalid M. Mosalam

Department of Civil and Environmental Engineering
University of California, Berkeley

PEER Report No. 2015/09
Pacific Earthquake Engineering Research Center
Headquarters at the University of California, Berkeley

September 2015

Disclaimer

The opinions, findings, and conclusions or recommendations expressed in this publication are those of the author(s) and do not necessarily reflect the views of the study sponsor(s) or the Pacific Earthquake Engineering Research Center.

Structural Behavior of Column-Bent Cap Beam-Box Girder Systems in Reinforced Concrete Bridges Subjected to Gravity and Seismic Loads

Part I: Pre-test Analysis and Quasi-Static Experiments

Mohamed A. Moustafa

Khalid M. Mosalam

Department of Civil and Environmental Engineering
University of California, Berkeley

PEER Report 2015/09
Pacific Earthquake Engineering Research Center
Headquarters at the University of California, Berkeley
September 2015

ABSTRACT

This report presents a study for investigating the behavior of a column-bent cap beam-box girder bridge subassembly with special focus on the bent cap structural behavior. The main objective of this study was to accurately estimate the contributions of the deck and soffit slabs framing into the bent cap in reinforced concrete box-girder bridge systems under the combined effect of vertical and lateral loading. In particular, the study estimated the effective flange width of the bent cap beam due to the box-girder slabs contributions for more accurate and effective consideration of the stiffness and capacity of a bent cap. A mix of computational and experimental methods was utilized in this study to investigate the problem at hand. The study consisted of a large set of finite element (FE) analyses and two large-scale specimens were tested. The pre-test analysis, development of the test specimens, and quasi-static tests discussions and conclusions of the first test specimen comprise Part I of this report. The hybrid simulation development, second specimen tests, post-test analysis, and design implications are presented in Part II.

For the sake of the pre-test analysis, one-dimensional, two-dimensional, and three-dimensional FE models were developed for both the full prototype bridge and the test specimen. The different models were used to carry out several analyses that varied from linear elastic static analysis to nonlinear time history analysis. The pre-test analysis successfully verified the expected test specimen subassembly behavior, provided the input for the final loading protocol, delivered the test set-up design loads, and provided necessary information for instrumentation distribution. The first stage of the experimental program presented herein involved quasi-static cyclic loading tests of the first specimen in as-built and repaired conditions. Bi-directional cyclic loading tests in both transverse and longitudinal directions were conducted under constant gravity load. A rapid repair scheme was adopted for the tested specimen using a three-layer Carbon Fiber Reinforced Polymer (CFRP) column jacket. A similar quasi-static cyclic test to the as-built specimen was carried out for the repaired specimen for comparison purposes and to verify the essentially elastic status of the bent cap beam. The behavior of the bridge subassembly was investigated in light of the Caltrans Seismic Design Criteria (SDC) and the AASHTO design provisions. Test results showed that the system performed as desired and met all the seismic design objectives. Meanwhile, the effective slab width of the bent cap was extensively studied, and a revisited value for the slab contribution is provided at the conclusion of this report.

ACKNOWLEDGMENTS

This work was supported primarily by California Department of Transportation (Caltrans) under contract number 65A039. This Caltrans award and the administrative and practical support of Mr. Peter Lee and Dr. Ahmed Ibrahim of Caltrans are greatly appreciated. The Concrete Reinforcing Steel Institute (CRSI) is acknowledged for supporting the experimental program conducted in this study in part through donating the reinforcement steel used in the test specimens. The FRP Solutions Inc. provided and supported the repair and retrofit work required as part of the experimental program. The authors wish to thank all the staff at the Structures Laboratory at the University of California, Berkeley, nees@berkeley, and the Pacific Earthquake Engineering Research Center (PEER) for their help throughout the specimens' set-up and testing. Special thanks are due to Dr. Selim Günay for his technical input throughout the project. Any opinions, findings, and conclusions or recommendations expressed in this material are those of the authors and do not necessarily reflect those of Caltrans.

CONTENTS

ABSTRACT	iii
ACKNOWLEDGMENTS	v
TABLE OF CONTENTS	vii
LIST OF TABLES	xi
LIST OF FIGURES	xiii
1 INTRODUCTION.....	1
1.1 General.....	1
1.2 Problem Statement and Objectives	5
1.3 Experimental Framework	5
1.4 Computational Framework.....	7
1.5 Organization of the Report	8
2 BACKGROUND	11
2.1 Effective Width.....	11
2.1.1 Concept of Effective Flange Width	11
2.1.2 Effective Width of Flanged Beams in Building Codes.....	14
2.1.3 Effective Width of Flanged Beams in Bridge Codes.....	17
2.2 Review of Literature	21
2.2.1 Effective Width for Bridge Girders	22
2.2.2 Bridge Subassembly and Component Testing	24
2.2.3 Performance-Based Design of Bridges	29
3 DEVELOPMENT OF EXPERIMENTAL PROGRAM.....	31
3.1 Bridge Terminology	31
3.2 Prototype.....	33
3.3 Subassembly Development.....	35
3.3.1 Subassembly Geometry	35
3.3.2 Boundary Conditions	37
3.4 Specimen Design.....	39
3.5 Test Set-Up	42
3.6 Experimental Program	46

3.6.1	As-Built Specimen One: Quasi-Static Testing	46
3.6.2	Repaired Specimen No. 1: Quasi-Static Testing.....	47
3.6.3	Repaired Specimen No. 1: Hybrid Simulation Development Testing.....	47
3.6.4	Retrofitted Specimen No. 2: Hybrid Simulation Testing.....	47
3.7	Loading Protocol.....	48
3.7.1	Gravity Loads.....	48
3.7.2	Cyclic Load Pattern.....	49
3.8	Construction of Specimens.....	52
3.9	Material Properties.....	55
3.9.1	Concrete	55
3.9.2	Reinforcing Steel	64
3.9.3	Repair and Retrofit Materials.....	66
3.10	Instrumentation.....	67
3.10.1	Load Measurement.....	68
3.10.2	Displacement Measurement.....	68
3.10.3	Strain Measurement	71
3.10.4	Curvature Measurement.....	78
3.10.5	Cameras.....	79
4	PRE-TEST FINITE ELEMENT ANALYSIS.....	81
4.1	1D OpenSees Modeling.....	81
4.1.1	Subassembly Specimen Analysis.....	82
4.1.2	Prototype Bridge Analysis	86
4.2	2D SAP2000 Modeling.....	94
4.2.1	Subassembly Specimen Analysis.....	94
4.2.2	Prototype Bridge Analysis	96
4.3	3D Modeling of Reinforced Concrete.....	99
4.3.1	Modeling of Concrete	100
4.3.2	Modeling of Steel Reinforcement.....	104
4.3.3	Nonlinear Solution Strategy.....	107
4.4	DIANA Pre-Test Analysis	110
4.4.1	Mesh Development	110
4.4.2	Pushover Analysis.....	113
4.4.3	Time-History Analysis.....	119
4.4.4	Input for Test Set-Up and Instrumentation	127

5	QUASI-STATIC TESTS: AS-BUILT SPECIMEN ONE	131
5.1	Progression of Testing and Damage.....	132
5.2	Global Behavior	138
5.2.1	Force History	138
5.2.2	Displacement History.....	142
5.2.3	Force Displacement	146
5.2.4	Stiffness Determination	149
5.3	Column Local Behavior.....	155
5.3.1	Strain Behavior	155
5.3.2	Curvature Behavior.....	162
5.3.3	Moment-Curvature Relationships	166
5.4	Bent Cap Local Behavior	171
5.4.1	Strain Behavior	172
5.4.2	Curvature Behavior.....	177
5.4.3	Bending Moment Behavior.....	178
5.4.4	Moment-Curvature Relationships	181
5.5	Effective Slab Width (Tension Side)	185
5.5.1	Section B: Distribution	186
5.5.2	Section D: Distribution	189
5.5.3	Section B: Effective Slab Width	192
5.5.4	Section D: Effective Slab Width.....	197
5.5.5	Overall Effective Width in Tension Side.....	201
5.6	Effective Slab Width (Compression Side).....	205
5.6.1	Reinforcement Strain Distribution.....	206
5.6.2	Concrete Gauge Strain Distribution.....	211
5.7	Other Response Quantities.....	213
5.7.1	Longitudinal Slab Strain	213
5.7.2	Box-Girder Web Tie Strain.....	215
5.7.3	Joint Reinforcement Strain	215
5.7.4	Cap Beam Stirrups Strain.....	217
6	QUASI-STATIC TESTS: REPAIRED SPECIMEN ONE	219
6.1	Repair Procedure.....	219
6.2	Progression of Testing and Damage.....	225
6.3	Global Behavior	227

6.4	Column Local Behavior.....	234
6.5	Cap Beam Local Behavior.....	239
6.6	FRP Jacket Strain	245
7	CONCLUSIONS	247
7.1	Summary.....	247
7.2	Conclusions.....	248
7.3	Future Work.....	250
	REFERENCES.....	253
APPENDIX A	SPECIMEN DESIGN	257
APPENDIX B	STRUCTURAL AND SHOP DRAWINGS	277
APPENDIX C	CONSTRUCTION OF SPECIMENS	293
APPENDIX D:	TEST SET-UP PROCEDURE.....	303
APPENDIX E:	INSTRUMENTATIONS LIST	313
APPENDIX F	STRUTS FABRICATION AND CALIBRATION	321

LIST OF TABLES

Table 3.1	Differences between the modified prototype and Academy Bridge.....	34
Table 3.2	Summary of the reduced 1/4-scale specimen dimensions.	38
Table 3.3	Summary of the specimen cross-sections reinforcement.....	40
Table 3.4	Concrete mix design.....	56
Table 3.5	Compressive strength test results.....	57
Table 3.6	Stress-strain compressive test results using force control.....	58
Table 3.7	Stress-strain compressive test results using displacement control.....	60
Table 3.8	Splitting and modulus of rupture test results.	60
Table 3.9	Fracture energy from notched-beam test results (samples from individual lifts).	63
Table 3.10	Fracture energy from notched-beam test results (all samples together).	63
Table 3.11	Summary of mechanical properties of steel reinforcing bars.	65
Table 4.1	List of ground motions used in OpenSees bridge time history analysis.	89
Table 4.2	Short list of ground motions with most significant effect of vertical excitation on the considered bridge cap beam response.	91
Table 5.1	Summary of input displacement and corresponding drift ratio and ductility level.....	143
Table 5.2	Summary of displacement, force, stiffness, ductility, and drift ratio values for all runs in transverse direction (X).	151
Table 5.3	Summary of displacement, force, stiffness, ductility, and drift ratio values for all runs in in longitudinal direction (Y).	152
Table 5.4	Section B effective slab width at different load levels calculated using cap beam ϵ_{min}	196
Table 5.5	Section B effective slab width at different load levels calculated using cap beam ϵ_{mean}	197
Table 5.6	Section D effective slab width at different load levels calculated using cap beam ϵ_{min}	201
Table 5.7	Section D effective slab width at different load levels calculated using cap beam ϵ_{mean}	202
Table 5.8	Summary of overall effective slab width mean calculated using cap beam ϵ_{min}	204

Table 5.9	Summary of overall effective slab width mean calculated using cap beam ϵ_{mean}	205
Table 6.1	Repaired Specimen No. 1's improved force and stiffness relative to the as- built residuals.	232

LIST OF FIGURES

Figure 1.1	San Diego-Coronado box-girder bridge, California (photo courtesy of Brett Shoaf, Artistic Visuals).....	2
Figure 1.2	Typical California box-girder bridge: W80-E50 Connector Overcrossing, Yolo County, California (photo courtesy of Mark Yashinsky, Caltrans).	3
Figure 1.3	Damaged portion of the Golden State Freeway, part of CA Interstate-5, at Gavin Canyon after 1994 Northridge earthquake (courtesy of FEMA Photo Library).	3
Figure 2.1	Typical bending moment diagram in continuous beam with section flange in tension or compression identified [Moehle 2014].	12
Figure 2.2	Deformations and stresses in a beam flange loaded in tension [Moehle 2014].	13
Figure 2.3	Notion of effective flange width.	13
Figure 2.4	Eurocode 2 [EN-1992] definition of l_0 for calculation of effective flange width.	16
Figure 2.5	Eurocode 2 [EN-1992] effective flange width parameters.	16
Figure 2.6	Effective flange width in different cases of longitudinal girders and schematic linearized stress distribution along with corresponding effective width [AASHTO 2007].....	19
Figure 2.7	(a) Effective width of superstructure girders and (b) its distribution in the plan for one case of unskewed tangent bridges as given by Caltrans SDC [2013].	21
Figure 2.8	Effective width of bent cap beam as given by Caltrans SDC [2013].	21
Figure 3.1	Components of a RC box-girder bridge.....	31
Figure 3.2	Convention of the specimens' box-girder slab terminology.....	32
Figure 3.3	Different views of the modified Academy Bridge.....	34
Figure 3.4	Subassembly considered for testing, identified as the prototype bridge.....	36
Figure 3.5	Locations of zero moments along the longitudinal direction of the prototype bridge under vertical gravity loading.....	36
Figure 3.6	Locations of zero moments along the transverse direction of the prototype bridge under combined vertical and lateral loading.....	36
Figure 3.7	Different views of the 1/4-scale subassembly specimen.	39
Figure 3.8	Dimensions and reinforcement details for each of the specimen components: (A) column, (B) column head, (C) cap beam, (D) seat boundary beam, (E) joint reinforcement in transverse direction, (F) joint reinforcement in longitudinal direction, and (G) box-girder.	41

Figure 3.9	Schematic 3D view of the test set-up.....	43
Figure 3.10	Elevation view of the test set-up.	43
Figure 3.11	Side and plan view of the test set-up.	44
Figure 3.12	Vertical 1D calibrated strut used at the specimen's cap beam ends.	45
Figure 3.13	Test set-up for the bridge subassembly tests.....	46
Figure 3.14	Final loading protocol used for the first specimen cyclic loading test.	51
Figure 3.15	A view of first specimen test in progress under transverse cyclic loading.....	51
Figure 3.16	A view of first specimen test in progress under longitudinal cyclic loading.....	52
Figure 3.17	(a) Reinforcement steel mesh for the deck slab and (b) fabrication and setting up of the column and cap beam steel cages.	53
Figure 3.18	Seat beams and box-girder deck slab concrete placement (first lift).	53
Figure 3.19	(a) Installing custom-made cardboard boxes for box-section and (b) furnishing reinforcement steel mesh for the soffit slab.	54
Figure 3.20	(a) Finishing the surface of the second concrete lift and (b) curing of concrete surface using curing blankets.	54
Figure 3.21	(a) Column and column head formwork and (b) and (c) placing and vibrating the concrete of the column and column head.	54
Figure 3.22	(a) Removing the cardboard boxes used to create the box-girder cells and (b) final specimen configuration.	55
Figure 3.23	Slump test (left) and concrete sampling for material tests (top and bottom right).....	56
Figure 3.24	(a) Compressive strength test set-up and (b) typical mode of failure.	57
Figure 3.25	Strength gain for different concrete lifts up to 28 days (left) and up to final day of testing (right).....	57
Figure 3.26	Typical concrete stress–strain relationship using a force-controlled test (results shown are for samples from first concrete lift tested at 28 days).....	58
Figure 3.27	(a) Compressive test under displacement control at the University of California, Davis; (b), compressometer; and (c) typical mode of failure.	59
Figure 3.28	Typical concrete stress-strain relationship using a displacement-controlled test (results shown are for samples from second concrete lift at 298 days).....	59
Figure 3.29	Splitting tension test set-up (left) and typical mode of failure (right).	61
Figure 3.30	Close-up view of the concrete texture and aggregate size and distribution from a tested cylinder in splitting tension.....	61
Figure 3.31	Four point bending test set-up for estimating the concrete modulus of rupture (left) and typical mode of failure (right).	62
Figure 3.32	Notched-beam test set-up, instrumentation, and mode of failure.	63

Figure 3.33	Load-deformation relationships for notched-beam tests for all concrete lifts.	64
Figure 3.34	Test set-up and instrumentation for tensile testing of reinforcing bars.	65
Figure 3.35	Stress-strain relationships for the different reinforcing bars coupons: (a) #3 stirrups, (b) #3 longitudinal bars, (c) #5 bars, and (d) #6 bars.....	66
Figure 3.36	Different load cells used in testing: typical actuator load cell (left) and calibrated strut load cell (right).....	68
Figure 3.37	Wirepots set-up at the east instrumentation frame.....	69
Figure 3.38	Layout of the wirepots in plan view (east and south sides are identified).....	70
Figure 3.39	Layout of the wirepots in side view at east- and south-side frames.	70
Figure 3.40	LVDTs under the specimen monitoring the deformation of the cap beam and the box-girder.	71
Figure 3.41	Strain gauges used for reinforcing bars instrumentation where several chemical and mechanical protection layers were added to protect the gauges.	72
Figure 3.42	Instrumented specimen's beam and slab reinforcement bars.	73
Figure 3.43	(a) Embedded concrete strain gauges used in the soffit slab part of the box-girder; and (b) surface concrete strain gauges installed on top of the soffit slab of the second specimen only (some CFRP jacket strain gauges are shown as well).....	73
Figure 3.44	An example of strain distribution in the box-girder transverse reinforcement as obtained from DIANA pre-test analysis.	74
Figure 3.45	Layout of strain gauges used for the cap beam reinforcement.	74
Figure 3.46	Layout of strain gauges used for the box-girder soffit slab (top) and deck slab (bottom) transverse reinforcement.	75
Figure 3.47	Layout of strain gauges used for the box-girder soffit slab (top) and deck slab (bottom) longitudinal reinforcement.	76
Figure 3.48	Layout of strain gauges used for the column longitudinal and transverse reinforcement.	77
Figure 3.49	Schematic representation of parameters required to estimate column curvature using linear LVDTs.	78
Figure 3.50	(a) Distribution of LVDTs on the column and (b) photograph of installed LVDTs.	79
Figure 3.51	Overview of different types of cameras, their arrangement, and illumination system used during testing.	80
Figure 3.52	Example of strain distribution and crack pattern in the column-cap beam joint region obtained from the DIC technique during one of the cyclic loading tests.	80

Figure 4.1	Schematic representation of boundary conditions and geometry of the OpenSees model for the test subassembly specimen.	83
Figure 4.2	Force-displacement relationship for the OpenSees test subassembly under constant gravity load (three levels) and lateral pushover loading in the transverse direction.	84
Figure 4.3	Moment-curvature relationship for the subassembly's column section under constant gravity load (three levels) and lateral pushover loading in the transverse direction.	84
Figure 4.4	Moment-curvature relationship for the subassembly's cap beam section under constant gravity load (three levels) and lateral pushover loading in the transverse direction.	85
Figure 4.5	Schematic bending moment distribution along the column and bent cap beam in three load cases: (a) gravity load, (b) lateral load, and (c) combined gravity and lateral loads.	85
Figure 4.6	Stress-strain relationship for one of the cap beam tension side rebars under constant gravity load (three levels) and lateral pushover loading in the transverse direction.	85
Figure 4.7	Stress-strain relationship for the outermost west rebar of the column (refer to Figure 3.11 for definition of the north side) under constant gravity load (3 levels) and pushover loading towards east.	86
Figure 4.8	Schematic representation of OpenSees model of the modified Caltrans Academy Bridge.	87
Figure 4.9	Bridge bent with critical cross sections identified.	91
Figure 4.10	Moment-curvature relationships for bridge column (Section 1 in Figure 4.9) subjected to 30%-scale Kobe ground motion with and without vertical excitation component.	91
Figure 4.11	Moment-curvature relationships for bridge cap beam (Section 2 in Figure 4.9) subjected to 30%-scale Kobe ground motion with and without vertical excitation component.	92
Figure 4.12	Moment-curvature relationships for bridge cap beam (Section 3 in Figure 4.9) subjected to 30%-scale Kobe ground motion with and without vertical excitation component.	92
Figure 4.13	Axial load fluctuation in bridge interior column A (Figure 4.9) subjected to 100%-scale Northridge Sylmar ground motion with and without vertical excitation component.	93
Figure 4.14	Axial load fluctuation in bridge exterior column B (Figure 4.9) subjected to 100%-scale Northridge Sylmar ground motion with and without vertical excitation component.	93
Figure 4.15	Test subassembly SAP2000 model.	94
Figure 4.16	Investigated boundary conditions of the test subassembly.	95

Figure 4.17	Sample of linear analysis results of subassembly model due to lateral transverse loading: moment distribution in the cap beam and column (left); moment distribution in the subassembly deck in the transverse direction (right).	95
Figure 4.18	Stress distribution in the deck slab due to two different load cases.....	96
Figure 4.19	Three-dimensional view of the prototype SAP2000 model.....	97
Figure 4.20	Sample of linear analysis results of prototype model: moment distribution in bridge deck in the longitudinal direction (top), and moments in bent cap beam (bottom).	97
Figure 4.21	Three main modes of vibration and corresponding periods for the prototype bridge in the transverse, longitudinal, and vertical directions.	98
Figure 4.22	Used element types in the 3D DIANA models.	101
Figure 4.23	Rotating crack surface and unidirectional concrete material model in principal directions.....	103
Figure 4.24	Concrete stress-strain relationships.....	104
Figure 4.25	Reinforcement elements in FEA.	105
Figure 4.26	Reinforcing steel stress-strain relationships.....	107
Figure 4.27	Schematic representation of iterative nonlinear solvers [DIANA 2014].	108
Figure 4.28	Schematic representation of quasi-Newton iterations [DIANA 2014].	109
Figure 4.29	Schematic representation of linear stiffness iterations [DIANA 2014].	109
Figure 4.30	Load and displacement controls for the incremental procedure [DIANA 2014].	110
Figure 4.31	DIANA tetrahedron-element concrete mesh used for modeling the test specimen subassembly.	112
Figure 4.32	DIANA brick-element concrete mesh used for modeling the test specimen subassembly.	112
Figure 4.33	Embedded reinforcement mesh used for both DIANA 3D models of the test specimen subassembly.	113
Figure 4.34	Vertical force-displacement relationship due to vertical pushover and schematic representation of the resulting mode of failure; only the cap beam failed.....	115
Figure 4.35	Crack pattern (DIANA) in box-girder and bent cap due to vertical pushover.	115
Figure 4.36	Deformed shape (DIANA) of the subassembly due to vertical pushover.	116
Figure 4.37	Typical crack pattern and deformed shape (DIANA) due to lateral pushover.	116

Figure 4.38	Lateral force-displacement relationship at different axial load levels (0%, 6%, and 11% of column axial capacity) and schematic representation of the resulting mode of failure; only the column failed.....	117
Figure 4.39	Lateral force-displacement relationship at different axial load levels (17% and 19% of column axial capacity) and schematic representation of the resulting mode of failure; both the column and cap beam failed.....	117
Figure 4.40	Lateral force-displacement relationship at different axial load levels (21% and 23% of column axial capacity) and schematic representation of the resulting mode of failure; only the cap beam failed.	118
Figure 4.41	An envelope of the horizontal and vertical load values at failure, which summarizes the different pushover analysis cases and the corresponding modes of failure from DIANA specimen model.....	118
Figure 4.42	Schematic representation of the test specimen DIANA model with lumped mass at column top and tetrahedron elements for two different time history analysis cases.	120
Figure 4.43	Analysis results for the case of 25% Loma Prieta ground motion (transverse and vertical components) and 11% constant gravity load of column axial capacity: (a) lateral displacement history, (b) lateral force history, and (c) lateral force-displacement relationship.....	121
Figure 4.44	Analysis results for the case of 25% Loma Prieta ground motion (transverse and vertical components) and 11% constant gravity load of column axial capacity: (a) vertical displacement history, (b) vertical force history, and (c) vertical force-displacement relationship.....	122
Figure 4.45	Analysis results for the case of 50% Northridge ground motion (Sylmar record) with only horizontal excitation and 23% constant gravity load of column axial capacity: (a) lateral displacement history, (b) lateral force history, and (c) lateral force- displacement relationship.....	123
Figure 4.46	Analysis results for the case of 50% Northridge ground motion (Sylmar record) with only horizontal excitation and 23% constant gravity load of column axial capacity: (a) vertical displacement history, (b) vertical force history, and (c) vertical force-displacement relationship.....	124
Figure 4.47	Analysis results for the case of 50% Northridge ground motion (Sylmar record) with both vertical and horizontal excitations and 23% constant gravity load of column axial capacity: (a) lateral displacement history, (b) lateral force history, and (c) lateral force- displacement relationship.	125
Figure 4.48	Analysis results for the case of 50% Northridge ground motion (Sylmar record) with both vertical and horizontal excitations and 23% constant gravity load of column axial capacity(a) vertical displacement history, (b) vertical force history, and (c) vertical force-displacement relationship.	126
Figure 4.49	Strain distribution in the reinforcement along the cap beam and transverse slab cross-section for DIANA specimen model subjected to lateral pushover and constant gravity load.....	128

Figure 4.50	Strain distributions in the transverse slab reinforcement from the DIANA specimen model under two cases of loading: (a) vertical pushover, (b) lateral pushover with constant gravity load, (c) time history analysis using Kobe ground motion at 50%.	129
Figure 5.1	As-built Specimen No. 1 test set-up and progression of loading in the transverse direction.	133
Figure 5.2	As-built Specimen No. 1 set-up and progression of loading in the longitudinal direction.	134
Figure 5.3	Minor shear cracking in the column-bent cap joint region at transverse loading cycles that correspond to 1.0 (top) and 7.6 (bottom) ductility levels.	135
Figure 5.4	Minor flexural longitudinal cracks in the deck slab, i.e., bottom face of the inverted specimen, after all loading cycles. The horizontal line in the figure coincides with the box-girder centerline.	136
Figure 5.5	Propagation of the column cracking and spalling in the plastic hinge zone.	137
Figure 5.6	Final damaged state of the as-built Specimen No. 1 column: all the rebars were exposed and buckled, and six rebars ruptured.	137
Figure 5.7	History of the gravity load applied during the initial cyclic test runs of Specimen No. 1.	138
Figure 5.8	History of the force in both transverse and longitudinal directions (estimated from lateral actuators load cells) for all test runs of Specimen No. 1.	139
Figure 5.9	History of both of the north and south lateral actuators load cells measurements and the corresponding resultant forces in the transverse (f_x) and the longitudinal (f_y) directions for all cyclic loading groups.	140
Figure 5.10	Zoomed-in view of the history of both of the north and south lateral actuators load cells measurements and the corresponding resultant forces in the transverse (f_x) and the longitudinal (f_y) directions for one transverse and one longitudinal loading groups.	141
Figure 5.11	History of obtained displacements in both transverse (u_x) and longitudinal (u_y) directions for all cyclic loading groups.	143
Figure 5.12	Displacement orbit of the specimen's column head for all cyclic loading groups (transverse displacement u_x versus longitudinal displacement u_y).	143
Figure 5.13	History of the north and south lateral actuators temposonics measurements and the corresponding resultant displacement in the transverse (u_x) and the longitudinal (u_y) directions for all cyclic loading groups.	144
Figure 5.14	Zoomed-in view of the history of the north and south lateral actuators temposonics measurements and the corresponding resultant displacement in the transverse (u_x) and the longitudinal (u_y) directions for all cyclic loading groups.	145

Figure 5.15	Force-displacement relationship for all cycles groups in transverse direction (f_x versus u_x).....	147
Figure 5.16	Force-displacement relationship for all cycles groups in longitudinal direction (f_y versus u_y).....	147
Figure 5.17	Force-displacement envelope for all cycles groups in transverse direction.	148
Figure 5.18	Force-displacement envelope for all cycles groups in longitudinal direction.	148
Figure 5.19	Comparison of force-displacement envelopes (cycles 1 st peak) in both transverse and longitudinal directions.	149
Figure 5.20	Example of secant stiffness calculation in positive and negative loading directions for the 9.5 in. transverse displacement cyclic loading group.	150
Figure 5.21	Lateral secant stiffness degradation in transverse direction.	153
Figure 5.22	Lateral secant stiffness degradation in longitudinal direction.	153
Figure 5.23	Comparison of stiffness degradation in both transverse and longitudinal directions using the secant stiffness values.....	154
Figure 5.24	Comparison of stiffness degradation in both transverse and longitudinal directions using the stiffness values estimated from the small cycles that followed the main test loading groups.	154
Figure 5.25	Notation of loading direction and layout of instrumented column rebars.	155
Figure 5.26	History of the strain of the column rebars at lowest section in the plastic hinge where maximum strain is expected for all loading cycles.	156
Figure 5.27	Zoomed-in view of the history of strain of the column rebars at lowest section in the plastic hinge where maximum strain is expected for one group of transverse and one group of longitudinal loading cycles.	157
Figure 5.28	Strain distribution along east side rebar when loading is towards east.....	158
Figure 5.29	Strain distribution along east side rebar when loading is towards west.	158
Figure 5.30	Strain distribution along west side rebar when loading is towards east.	159
Figure 5.31	Strain distribution along west side rebar when loading is towards west.	159
Figure 5.32	Strain distribution along north side rebar when loading is towards north.	160
Figure 5.33	Strain distribution along north side rebar when loading is towards south.....	160
Figure 5.34	Strain distribution along south side rebar when loading is towards north.....	161
Figure 5.35	Strain distribution along south side rebar when loading is towards south.....	161
Figure 5.36	History of column curvature at the lowest section in the plastic hinge zone in both east-west (transverse) and north-south (longitudinal) directions for all loading cycles.....	163

Figure 5.37	Zoomed-in view of the history of the column curvature at the lowest section in the plastic hinge zone in both east-west (transverse) and north-south (longitudinal) directions for one group of transverse and one group of longitudinal loading cycles.	163
Figure 5.38	Curvature distribution along column height when loading is towards east.	164
Figure 5.39	Curvature distribution along column height when loading is towards west.	164
Figure 5.40	Curvature distribution along column height when loading is towards north.	165
Figure 5.41	Curvature distribution along column height when loading is towards south.	165
Figure 5.42	Comparison of LVDT-based and strain-based column moment-curvature relationship at Section 5 (mid-height, refer to Figure 3.50) due to all transverse loading cycles.	166
Figure 5.43	Comparison of LVDT-based and strain-based column moment-curvature relationship at Section 4 (22 in. from beam face, refer to Figure 3.50) due to all transverse loading cycles.	167
Figure 5.44	Comparison of LVDT-based and strain-based column moment-curvature relationship at Section 3 (16 in. from beam face, refer to Figure 3.50) due to all transverse loading cycles.	167
Figure 5.45	Comparison of LVDT-based and strain-based column moment-curvature relationship at Section 2 (10 in. from beam face, refer to Figure 3.50) due to all transverse loading cycles.	168
Figure 5.46	Comparison of LVDT-based and strain-based column moment-curvature relationship at Section 1 (4 in. from beam face, refer to Figure 3.50) due to all transverse loading cycles.	168
Figure 5.47	LVDT-based column moment-curvature relationship in N-S direction at Section 4 (22 in. from beam face, refer to Figure 3.50) due to all longitudinal loading cycles.	169
Figure 5.48	LVDT-based column moment-curvature relationship in N-S direction at Section 3 (16 in. from beam face, refer to Figure 3.50) due to all longitudinal loading cycles.	169
Figure 5.49	LVDT-based column moment-curvature relationship in N-S direction at Section 2 (10 in. from beam face, refer to Figure 3.50) due to all longitudinal loading cycles.	170
Figure 5.50	LVDT-based column moment-curvature relationship in N-S direction at Section 1 (4 in. from beam face, refer to Figure 3.50) due to all longitudinal loading cycles.	170
Figure 5.51	Comparison of column moment-curvature relationship in both transverse (E-W) and longitudinal (N-S) directions at Section 1 (4 in. from beam face, refer to Figure 3.50).	171

Figure 5.52	Schematic bending moment distribution along the bent cap beam center line in three cases of loading: (a) gravity load only (b) lateral load only (c) combined gravity and lateral loads, and (d) a more accurate distribution considering the column and beam actual cross-section width rather than center lines.	172
Figure 5.53	Strain profile along one of the cap beam tension side rebars due to combined gravity and one of the lateral transverse loading cycles in east direction.	173
Figure 5.54	Strain profile along one of the cap beam tension side rebars due to combined gravity and one of the lateral transverse loading cycles in west direction.	174
Figure 5.55	History of strain at bent cap beam maximum strain location at Section B for all loading cycles.	175
Figure 5.56	History of strain at bent cap beam maximum strain location at Section D for all loading cycles.	175
Figure 5.57	Lateral transverse force versus bent cap beam maximum strain at Section B for all loading cycles.	176
Figure 5.58	Lateral transverse force versus bent cap beam maximum strain at Section D for all loading cycles.	176
Figure 5.59	History of the curvature at cap beam Section B due to all lateral loading cycles.	177
Figure 5.60	History of the curvature at cap beam Section D due to all lateral loading cycles.	178
Figure 5.61	History of cap beam bending moment at Sections B and D due to lateral loading only and combined lateral and gravity loading for all loading cycles.	180
Figure 5.62	Comparison of column moment and sum of cap beam moments at Sections B and D ($M_{\text{beam}} = M_{\text{Section B}} + M_{\text{Section D}}$) due to lateral loading only.	181
Figure 5.63	Moment-curvature relationship for the bent cap at Section B for all the loading cycles in both transverse and longitudinal directions.	183
Figure 5.64	Moment-curvature relationship for the bent cap at Section D for all the loading cycles in both transverse and longitudinal directions.	183
Figure 5.65	Moment-curvature relationship for cap beam estimated from sectional analysis [XTRACT 2002] using the Caltrans SDC integral bent cap effective flanged section.	184
Figure 5.66	Degradation in the cap beam stiffness expressed in terms of normalized effective EI at different drift ratios and ductility levels calculated using curvatures from two different top and bottom rebar sets at Section B.	184

Figure 5.67	Degradation in cap beam stiffness expressed in terms of normalized effective EI at different drift ratios and ductility levels calculated using curvatures from two different top and bottom rebar sets at Section D.	185
Figure 5.68	Summary of the four main steps of the procedure used to estimate the bent cap effective slab width.	186
Figure 5.69	Strain distribution along cap beam and box-girder transverse deck slab reinforcement at Section B for different small-level loading cycles before yielding (loading is in positive east direction).	187
Figure 5.70	Strain distribution along cap beam and box-girder transverse deck slab reinforcement at Section B for different high-level loading cycles after yielding (loading is in positive east direction).	188
Figure 5.71	Strain distribution along cap beam and box-girder transverse deck slab reinforcement at Section B for different small-level loading cycles before yielding (loading is in negative west direction).	188
Figure 5.72	Strain distribution along cap beam and box-girder transverse deck slab reinforcement at Section B for different high-level loading cycles after yielding (loading is in negative west direction).	189
Figure 5.73	Strain distribution along cap beam and box-girder transverse deck slab reinforcement at Section D for different small-level loading cycles before yielding (loading is in positive east direction).	190
Figure 5.74	Strain distribution along cap beam and box-girder transverse deck slab reinforcement at Section D for different high-level loading cycles after yielding (loading is in positive east direction).	190
Figure 5.75	Strain distribution along cap beam and box-girder transverse deck slab reinforcement at Section D for different small-level loading cycles before yielding (loading is in negative west direction).	191
Figure 5.76	Strain distribution along cap beam and box-girder transverse deck slab reinforcement at Section D for different high-level loading cycles after yielding (loading is in negative west direction).	191
Figure 5.77	Generating effective width strain block using the strain distribution at Section B for a small- (top) and high-level (bottom) loading cycles using the observed cap beam minimum (ϵ_{min}) and mean (ϵ_{mean}) strain values.	193
Figure 5.78	Summary of the estimated cap beam effective width at Section B at different drift ratios (Group I: first positive peak of each transverse cyclic loading group).	194
Figure 5.79	Summary of the estimated cap beam effective width at Section B at different drift ratios (Group III: second positive peak of each transverse cyclic loading group).	194
Figure 5.80	Summary of the estimated cap beam effective width at Section B at different drift ratios (Group II: first negative peak of each transverse cyclic loading group).	195

Figure 5.81	Summary of the estimated cap beam effective width at Section B at different drift ratios (Group IV: second negative peak of each transverse cyclic loading group).	195
Figure 5.82	Generating effective width strain block using the strain distribution at Section D for a small- (top) and high-level (bottom) loading cycle using the observed cap beam minimum (ϵ_{min}) and mean (ϵ_{mean}) strain values.	198
Figure 5.83	Summary of the estimated cap beam effective width at Section D at different drift ratios (Group I: first positive peak of each transverse cyclic loading group).....	199
Figure 5.84	Summary of the estimated cap beam effective width at Section D at different drift ratios (Group III: second positive peak of each transverse cyclic loading group).	199
Figure 5.85	Summary of the estimated cap beam effective width at Section D at different drift ratios (Group II: first negative peak of each transverse cyclic loading group).....	200
Figure 5.86	Summary of the estimated cap beam effective width at Section D at different drift ratios (Group IV: second negative peak of each transverse cyclic loading group).	200
Figure 5.87	Mean effective width from all loading cycles in each group (bar chart) and overall average effective width from all loading cycles and groups (dashed lines) at Section B as compared to Caltrans SDC effective width value	203
Figure 5.88	Mean effective width from all loading cycles in each group (bar chart) and overall average effective width from all loading cycles and groups (dashed lines) at Section D as compared to Caltrans SDC effective width value.....	203
Figure 5.89	Strain distribution along cap beam and box-girder transverse soffit slab reinforcement (compression side) at Section B for different small-level loading cycles (strain values recorded at loading cycle peak when loading is in east direction).	207
Figure 5.90	Strain distribution along cap beam and box-girder transverse soffit slab reinforcement (compression side) at Section B for different high-level loading cycles (strain values recorded at loading cycle peak when loading is in east direction).	207
Figure 5.91	Strain distribution along cap beam and box-girder transverse soffit slab reinforcement (compression side) at Section B for different high-level loading cycles (strain values recorded at loading cycle peak when loading is in west direction).	208
Figure 5.92	Strain distribution along cap beam and box-girder transverse soffit slab reinforcement (compression side) at Section B for different high-level loading cycles (strain values recorded at loading cycle peak when loading is in west direction).	208

Figure 5.93	Strain distribution along cap beam and box-girder transverse soffit slab reinforcement (compression side) at Section D for different small-level loading cycles (strain values recorded at loading cycle peak when loading is in east direction).	209
Figure 5.94	Strain distribution along cap beam and box-girder transverse soffit slab reinforcement (compression side) at Section D for different high-level loading cycles (strain values recorded at loading cycle peak when loading is in east direction).	209
Figure 5.95	Strain distribution along cap beam and box-girder transverse soffit slab reinforcement (compression side) at Section D for different small-level loading cycles (strain values recorded at loading cycle peak when loading is in west direction).	210
Figure 5.96	Strain distribution along cap beam and box-girder transverse soffit slab reinforcement (compression side) at Section D for different high-level loading cycles (strain values recorded at loading cycle peak when loading is in west direction).	210
Figure 5.97	Sample of four concrete strain gauges history located at the compression zone from both sides of the bent cap beam at Section B.	212
Figure 5.98	History of box-girder deck longitudinal reinforcement strain measured in the rebar at the middle of the box-girder at north and south sides of the column for all cycles.	214
Figure 5.99	History of box-girder deck longitudinal reinforcement strain measured in a rebar aligned with a box-girder web at north and south sides of the column for all cycles.	214
Figure 5.100	History of box-girder web tie reinforcement strain measured at the first tie in an inner web from both the north and south sides of the column for all cycles.	215
Figure 5.101	History of box-girder web tie reinforcement strain measured at the first tie in an outer web from both the north and south sides of the column for all cycles.	216
Figure 5.102	Strain history of selected critical joint vertical and horizontal cross-ties.	216
Figure 5.103	Strain history of selected bent cap outer and inner transverse stirrups.	217
Figure 6.1	(a) Hammering loose concrete in the plastic hinge zone in the tested specimen; and (b) final damaged state of the tested specimen after removal of all loose chunks of concrete.	220
Figure 6.2	(a) Drilling holes along the cracks for epoxy injection; and (b) final pattern of injection sites for repair with epoxy.	220
Figure 6.3	(a) Installing the injection ports along the cracks and patching the concrete surface around the ports; and (b) exposed rebars coated with epoxy primer for better bond.	221

Figure 6.4	(a) Patching the column damaged core with high-strength mortar in the plastic hinge zone; and (b) 8-in.-deep vertical holes to add polymer reinforcing bars.	221
Figure 6.5	(a) Preparation of 20-in.-long CFRP bars using carbon fiber sheets coated with epoxy resin; (b) installing the wet CFRP bars in the holes drilled into the cap beam.	222
Figure 6.6	(a) Partially fixing the column-bent cap interface using a sand-epoxy mixture; and (b) overview of the partial repaired column after installing all injection ports, CFRP reinforcing bars, and patching the damaged parts in column core and at the column-bent cap interface.	223
Figure 6.7	(a) Installing the sonotube around the damaged zone to restore the column's circular shape; and (b) injecting fluid epoxy into the cracks using the installed injection ports.	223
Figure 6.8	(a) Pouring sand-epoxy mixture inside the sonotube formwork to restore the column shape; and (b) view of the partially repaired column after the sonotube was removed.	223
Figure 6.9	(a) A final layer of high strength mortar was applied to patch any remaining voids; and (b) applying a primer epoxy coat to the surface before applying the CFRP sheets.	224
Figure 6.10	(a) Applying the first epoxy-coated CFRP layer at the bottom section of the column; and (b) applying the last CFRP layer at the middle section of the column.	224
Figure 6.11	Final repaired column after it was wrapped by three CFRP layers.	225
Figure 6.12	Overview of repaired Specimen No. 1 cyclic loading test set-up when loading is in progress and applied in transverse direction.	226
Figure 6.13	Overview of repaired Specimen No. 1 cyclic loading test set-up when loading is in progress and applied in longitudinal direction.	226
Figure 6.14	Circumferencial tear in the CFRP jacket and cracking at the column-bent cap interface as lateral loading progressed.	227
Figure 6.15	Gravity load history at both vertical actuators and total applied gravity load throughout the repaired Specimen No. 1 transverse and longitudinal cyclic loading tests.	229
Figure 6.16	Total vertical reaction at the two bent cap end struts versus the total applied gravity load throughout the repaired Specimen No. 1 transverse and longitudinal cyclic loading tests.	229
Figure 6.17	Displacement orbit (plan view) of the lateral loading pattern applied to the repaired Specimen No. 1.	230
Figure 6.18	Displacement history of the lateral cyclic loading pattern applied during the repaired Specimen No. 1 tests in transverse and longitudinal directions.	230

Figure 6.19	Lateral force history measured during testing the repaired Specimen No. 1 under lateral cyclic loading in transverse and longitudinal directions.....	231
Figure 6.20	Comparison of force-displacement relationships for the as-built and repaired Specimen No. 1 cyclic loading tests in both transverse and longitudinal directions.	233
Figure 6.21	Comparison of secant stiffness degradation relative to the ductility levels for the as-built and repaired Specimen No. 1 cyclic tests in both transverse and longitudinal directions.....	234
Figure 6.22	Comparison of moment-curvature relationships at the base of the column from the as-built and repaired Specimen No. 1 cyclic loading tests in transverse and longitudinal directions.	236
Figure 6.23	Comparison of moment-curvature relationships at different levels of the column from the as-built and repaired Specimen No. 1 cyclic loading tests in transverse direction.	237
Figure 6.24	Comparison of moment-curvature relationships at different levels of the column from the as-built and repaired Specimen No. 1 cyclic loading tests in longitudinal direction.....	238
Figure 6.25	Calculation of the column head displacement for rocking as a rigid body around the base.	239
Figure 6.26	Column and total bent cap beam moment history for all repaired Specimen No. 1 cyclic loading tests in both transverse and longitudinal directions.....	241
Figure 6.27	Bent cap beam moment history at both Sections B and D for all repaired Specimen No. 1 cyclic loading tests in both transverse and longitudinal directions.....	242
Figure 6.28	Comparison of bent cap beam moment at Section B for all as-built and repaired Specimen No. 1 cyclic loading tests in both transverse and longitudinal directions.	242
Figure 6.29	Cap beam moment–curvature relationship comparison between Specimen No. 1 as-built and repaired tests at Section B.	243
Figure 6.30	Cap beam moment–curvature relationship comparison between Specimen No. 1 as-built and repaired tests at Section D.....	243
Figure 6.31	Sample of two of the six instrumented cap beam reinforcing bars strain history at Section B for all repaired Specimen No. 1 cyclic tests.....	244
Figure 6.32	Sample of two of the six instrumented cap beam reinforcing bars strain history at Section D for all repaired Specimen No. 1 cyclic tests.....	244
Figure 6.33	Circumferential CFRP jacket strain history in the column east and west sides for all repaired Specimen No. 1 cyclic loading tests in transverse and longitudinal directions.	246

Figure 6.34	Circumferential CFRP jacket strain history in the column north–east (top) and south–west (bottom) sides for all repaired Specimen No. 1 cyclic loading tests in transverse and longitudinal directions.	246
-------------	--	-----

1 Introduction

1.1 GENERAL

Bridges are key components of infrastructure systems that facilitate the traffic flow on all types of highways. There are several types of bridges that vary depending on the material used in their construction, namely, steel, reinforced concrete (RC), prestressed concrete (PC), or composite bridges. Moreover, bridge types vary depending on the load-carrying structural system, e.g., box-girder bridges, truss bridges, cable-stayed bridges, etc. In California, RC and PC box-girder bridges are the most common types of bridge systems. Two examples of box-girder bridges in California are the iconic San Diego–Coronado Bridge shown in Figure 1.1 and the overcrossing bridge shown in Figure 1.2. Vertical dead loads and live traffic loads are the usual loading scenarios experienced by the average bridge. Although lateral loads are less frequent, those lateral loading that result from extreme events, such as earthquakes, can be catastrophic. Major earthquakes, including the 1971 San Fernando, 1989 Loma Prieta, and 1994 Northridge, California, events, and the 1995 Kobe, Japan, and 1999 Chi-Chi, Taiwan, events, have demonstrated the vulnerability of bridges to seismic loads.

An example of one of the several bridge failures and damages reported after the 1994 Northridge earthquake is shown in Figure 1.3. It is crucial to understand the seismic response of bridge structures and improve their performance during seismic events. Considerable research efforts have been undertaken to better understand the structural behavior, improve the seismic performance, and optimize the design of bridges. An optimized design for the different components of bridges is beneficial, not only for economic reasons, but also for enhanced performance.

A central concept associated with seismic bridge design is the capacity design approach. Many research studies were conducted to improve the capacity design principles for bridges, especially after the Northridge earthquake. One of the world-leading authorities that sponsored and promoted many of those studies is the California Department of Transportation (Caltrans). Their bridge seismic design provisions are published in a special document—Caltrans *Seismic Design Criteria* (SDC)—that is being updated regularly. Recently, the Caltrans SDC was heavily utilized by the American Association of State Highway and Transportation Officials (AASHTO) to produce the national *AASHTO Guide Specifications for LRFD Seismic Bridge Design*, which was first published in 2009. The essence of the capacity design approach adopted by either the latest Caltrans SDC [2013] or *AASHTO Guide Specifications for LRFD Seismic Bridge Design*

[2011] is to direct all the damage during extreme events into the bridge columns, which are designed to be ductile to prevent overall brittle modes of failures and collapse. Although the desired column design and ductility can be defined by a performance-based earthquake engineering (PBEE) framework, it still has to satisfy the minimum requirements of Caltrans SDC or AASHTO LRFD seismic design provision. Designated as capacity-protected members, the bridge superstructure, joints, or bent cap beams are designed to remain elastic when the column reaches its over-strength capacity. Thus the accuracy of the capacity estimation of the integral bent cap beams in RC box-girder bridges is a critical part of the capacity design approach for bridges. The main goal of this study is to investigate how the contributions of the box-girder soffit and deck slabs to the stiffness and strength of the bent cap beams can be accurately estimated for the purpose of cap beam capacity calculations.

The motivation of this study and the mechanics of the sought framework was inspired by extensive similar research studies that were carried out for buildings. Unlike bridges, the common practice in capacity seismic design in buildings is the weak beam–strong column (WBSC) approach, where yielding and plastic hinging are desired in the beams rather than the columns. That is because columns are the main gravity load carrying elements, especially at elevated axial load levels (as in the lower stories of tall buildings). Accordingly, columns in buildings are required to stay elastic to avoid excessive deformations and possible progressive collapse due to formation of soft-story mechanisms. The essence of the WBSC, as suggested by ACI-318 [2008] for example, is to ensure that the capacity of the columns at a beam–column joint is at least 1.2 times the capacity of the beams connected at the same joint. Therefore, the ability to estimate accurately the capacity of the beam is required if the WBSC is to be adopted as a design strategy. Otherwise, unexpected failure or undesired mechanism can occur if the column is designed using an underestimated beam capacity.



Figure 1.1 San Diego-Coronado box-girder bridge, California (photo courtesy of Brett Shoaf, Artistic Visuals).



Figure 1.2 Typical California box-girder bridge: W80-E50 Connector Overcrossing, Yolo County, California (photo courtesy of Mark Yashinsky, Caltrans).



Figure 1.3 Damaged portion of the Golden State Freeway, part of CA Interstate-5, at Gavin Canyon after 1994 Northridge earthquake (courtesy of FEMA Photo Library).

Since moment frames in buildings are monolithically integrated with the floor systems and slabs, the slab contribution can strengthen and stiffen the beams. The contribution of the slab is accounted for in design by using a flanged section (T-beams are the most popular), where the flange width is the chosen effective width (b_{eff}) according to codes and standards. Based on the loading and the location of the flanged section along the beam, the flange can be located in the compression side of the beam (positive or sagging moment location), in tension (negative or hogging moments) at the top of the supports, or at a cantilever supported end. Previously, building code provisions were used to account for the effective width in the flanged section only in the compression side; however, in the last decade, new provisions were added to consider the slab contribution and slab transverse reinforcement in an equivalent effective width in the tension side as well. Again, this is to make sure the WBSC condition is satisfied if this is the desired mechanism. More details are provided in the background chapter that follows.

The same concept of the flanged effective width in compression and tension for building frames can be utilized in bridges but from a different perspective. As previously mentioned, the desired recent bridge seismic capacity design practice is to concentrate all the damage in the column while the beams remain elastic, i.e., the WCSB approach. Plastic hinges in the cap beams in bridges are undesirable due to limited access to the beam region within the box-girder, and uneconomical post-earthquake inspection and repair costs compared to the plastic hinging of the column. Also, bridge columns do not experience elevated axial load levels as in the case of tall buildings. As noted earlier, the Caltrans SDC and AASHTO LRFD seismic design provisions promote the WCSB capacity design framework. Accordingly, the superstructure, i.e., the bridge deck including the bent cap beam, is capacity protected by imposing the 1.2 times capacity check. In cast-in-place RC box-girders with integral bent caps, the contribution of the box-girder slabs results in a flanged bent cap beam section. Currently, the Caltrans SDC [2013] and AASHTO LRFD seismic design [2011] suggest an effective width of 12 times the soffit or deck slab thickness in tension or compression sides for the cap beam capacity check; however, the slab reinforcement is not considered in the capacity check. Evaluating the 12 times the slab thickness effective width along with the validity of considering the box girder slab reinforcement in the process of the bent cap beam design and capacity check is the main focus of this study.

Predicting the inelastic structural dynamic performance during a severe earthquake is challenging; however, several dynamic analysis techniques are now available and utilized frequently in quantifying seismic demands. In addition, experimental methods are more reliable in determining a structure's performance and validation of analytical and computational models. This study considered both experimental and computational methods to design a comprehensive mixed framework for evaluating the structural behavior of bent cap beams in RC box-girder bridges. A formal statement of the research problem, more details about the experimental and computational finite element (FE) analysis frameworks, and the organization of this report are presented in the next. Note: this report presents only the first part of the full study, which comprise the pre-test analysis and the first phase of the experimental program, and the reader is referred to the companion report for the second phase of the experimental program and the post-test analysis. Moreover, the reader is referred to Moustafa and Mosalam (2015) for a comprehensive summary of the full framework and key findings of this study.

1.2 PROBLEM STATEMENT AND OBJECTIVES

The study reported herein undertakes to develop a strategy for accurately estimating the stiffness and capacity of a bent cap, considering the contributions of the deck and soffit slabs framing into the bent cap in RC box-girder bridge systems under the combined effect of vertical and lateral loading. The three research objectives of this study included:

1. To investigate the behavior of bridge column-superstructure systems in light of the most recent AASHTO and Caltrans SDC provisions.
2. To investigate the system, particularly the integral cap beam, in different scenarios of as-built, repaired, and retrofitted bridge columns, i.e., to study whether strengthening bridge columns might migrate the mode of failure to the bridge superstructure because of possible amplified demands.
3. To determine what are the possible design implications and code recommendations, if any, dictated by accurate estimate of cap beam effective flange width and capacity calculation.

A mix of computational and experimental methods was utilized in this study. More details about the research methodology with a focus on the computational and experimental programs is discussed next. This study aimed to accomplish the following key goals:

- Revisit the effective width considered for bent cap beam design to account for the contributions from the box-girder soffit and deck slabs to its stiffness and strength
- Investigate the effectiveness of Carbon Fiber Reinforced Polymer (CFRP) repair and retrofit techniques mainly for altering the column structural behavior and evaluating the resulting subassembly performance
- Develop and successfully conduct multi-degree of freedom (MDOF) hybrid simulations (HS) tests as part of the conducted experimental program
- Calibrate a detailed FE model for the tested specimens and conduct a parametric study that complements the experimental observations for developing design recommendations of bent cap beams

The pre-test analysis, development of the test specimens, and main observations and conclusions drawn from the quasi-static tests of the first specimen of the experimental program are the core of the study reported herein. The discussion of the HS tests of the second specimen of the experimental program, post-test analysis, and design recommendations are presented in the part-two report of the study.

1.3 EXPERIMENTAL FRAMEWORK

The experimental program was devised to provide conclusive observations about the contribution of box-girder slabs to the bent cap beam behavior that served as the underlying

foundation for the computational model calibration and extended parametric study. Initially, the experimental program consisted of two identical 1/4-scale subassembly specimens to be tested using two different lateral loading schemes. A quasi-static test that uses cyclic lateral loading was the first chosen loading scheme. The second lateral loading scheme was composed of a HS method, using an online computational model subjected to selected earthquake excitation and interacting with the previously tested specimen. In light of the results from the first specimen quasi-static test, the experimental program was modified to include a total of four different tests. A similar test set-up was used for all tests: the 1/4-scale subassembly was placed in an inverted position, i.e., the box-girder was located closer to the strong floor of the laboratory, while the column pointed upward. This set-up was chosen for practical reasons and its ease in applying the combined gravity and the lateral loads at the column tip in its inverted position. A brief discussion of each of the four tests is presented next.

Specimen No. 1 was subjected to a quasi-static test in an as-built configuration under combined constant gravity load and bi-directional cyclic lateral loading. Two different levels of gravity load were used: (1) the first level corresponded to only the dead load; and (2) the second level considered additional loads due to live loads and the vertical component of the earthquake excitations. The bi-directional cyclic loading was applied independently in one direction at a time, i.e., a group of cycles was applied in the column-bent cap plane (transverse direction), which was then followed by a similar group of cycles in the box-girder longitudinal direction. The observed mode of failure was the desired Caltrans SDC WCSB, which motivated the expansion of the experimental program.

Before proceeding with further testing, a repair strategy was devised for Specimen No. 1, along with a retrofit decision for the as yet untested Specimen No. 2. The retrofit was aimed at strengthening the column using CFRP to amplify the moment demand on the cap beam to extend the capacity evaluation of the bent cap and explore different modes of failure—if any. Specimen No. 2 was planned to be tested using HS testing techniques, while Specimen No. 1 was to be repaired and reused for HS system development and trials before the final test occurred. However, a similar quasi-static test was also conducted first on repaired Specimen No. 1 to compare it with the test results from the as-built test to evaluate the efficacy of a rapid repair technique using CFRP. Thus, the sequence of the four tests was as follows: (1) Specimen No. 1 as-built was tested quasi-statically; (2) Specimen No. 1 was repaired and retested quasi-statically; (3) the repaired Specimen No. 1 was used in HS development and test trials; and (4) Specimen No. 2 was retrofitted and tested in a HS setting.

As mentioned, the second test in the four-test sequence was similar to the first quasi-static test but was applied to Specimen No. 1 after being repaired with CFRP. A constant gravity load that corresponds only to the second higher level used in the first test along with bi-directional cyclic lateral loading were used for the second test. A similar group of cycles used in the first test were reapplied to the repaired specimen in the second test. However, the test was intentionally stopped earlier than the corresponding first test so that the repaired Specimen No. 1 still retained some remaining force capacity so that it could undergo the third test regimen.

The main objective of the third test was to verify the accuracy of the HS system established particularly for this study but also intended to be a generic computational framework for future experimentation. Several test runs using the Northridge earthquake ground motions recorded at the Sylmar and Rinaldi stations were applied with and without the effect of gravity load. Although the gravity load had been part of the original test plan, the trials without gravity loads were introduced to check the stability of the developed HS system.

The fourth and final test in the experimental program was the HS testing of the second specimen that had been retrofitted before any testing. The HS tests involved several runs that included uni- and bi-directional loading, different scales for the lateral excitations, and three different levels of gravity load. Moreover, a new testing scheme was proposed and applied in few of the HS runs to account for the *P*-delta effect, which incorporated both the gravity load and the vertical component of the earthquake. This final test in the sequence had several objectives:

- Evaluate the bent cap beam behavior and quantify the effective slab width at higher moment demands than the design level
- Investigate the effectiveness of the CFRP retrofit technique
- Explore the consequences of a column retrofit or its over-design on the mode of failure of the bridge system under seismic loading
- Develop a generic and robust HS testing technique that utilizes readily available data acquisition and control systems, and combines them with a generic computational framework for a convenient and feasible HS system

1.4 COMPUTATIONAL FRAMEWORK

The computational framework adopted in this study was composed of two phases: (1) the pre-test analysis phase and (2) the post-test analysis phase. All the computational work conducted in this study was based on the FE analysis method. Several FE analysis software packages were utilized throughout this study in the pre- and post-test analysis phases, including OpenSees [McKenna et al. 2000], SAP2000 [Computers and Structures, Inc. 2012], and DIANA [2014]. Additional analyses included linear analysis under service dead and live loads, nonlinear pushover analysis, and nonlinear time history analysis.

The pre-test analysis primarily resolved several issues associated with the experimental work. Thus, several linear and nonlinear one-, two-, and three-dimensional (1D, 2D, and 3D) models were utilized in this study to conduct the pre-test analysis before the experimental test specimens were built or the test set-up was assembled. Three different types of models were used in the pre-test analysis. The first type used 1D elements for modeling either the full prototype bridge or the test subassembly specimen. OpenSees was used for analyzing the 1D models. The second type used 2D plane stress elements mainly for box-girder modeling. SAP2000 [2000] was used to analyze the 2D models. The most sophisticated level of modeling is the 3D solid element model. The general purpose FE analysis package DIANA [2014] (DIsplacement ANAlyzer) was used for creating and linearly and nonlinearly analyzing the 3D models. The pre-test analysis

phase had the following four main objectives; the corresponding FE analysis fulfilled one or more of these objectives:

- Verify expected subassembly behavior with respect to the mode of failure, and column and bent cap beam structural behavior
- Finalize the loading protocol especially for HS tests by ground motion selection and scaling
- Estimate the expected lateral forces during cyclic and HS tests for set-up design and checks
- Inform the decision making on the proper locations and distribution of the instrumentation where maximum and informative straining actions are expected

The post-test analysis used some of the pre-test analysis models to calibrate them against the experimental results and to carry out further analysis and a parametric study that complemented the experimental work. The main focus of the post-test analysis used the 3D DIANA solid model because of its accuracy and extended capabilities. The post-test analysis framework of this study consisted mainly of calibration of the model and a parametric study at the tested subassembly level. However, extensions to a full bridge model and parametric study are possible for future work. The calibration of the model calibration was intended to reproduce the experimental results from the 3D DIANA model by focusing on the RC constitutive model parameters. The calibrated model was subsequently utilized to investigate different bent cap beam reinforcement designs for optimal and cost-effective design. The same set of the calibrated nonlinear material model parameters are planned to be used in a full bridge model that is based on the prototype bridge used in this study. Global bridge geometrical parameters are planned to be varied to investigate how these parameters affect the bent cap effective width and design. Note: only the pre-test analysis phase is presented in this report. See a complete discussion of the post-test analysis part of the computational program along with the HS testing part of the experimental program in Part II.

1.5 ORGANIZATION OF THE REPORT

This report focuses on the development of the experimental program, pre-test analysis, and quasi-static testing of the as-built and repaired Specimen No. 1. The report consists of seven chapters and six appendices. Chapter 1 presents a general introduction of the problem statement, methodology, and main objectives of the undertaken study. Chapter 2 provides the necessary background related to the effective width of flanged beams in buildings and bridges. Previous studies that focused on evaluating the effective width and others that investigated bridge subassemblies and systems are reviewed and summarized as well. The development of the experimental program is present in Chapter 3 and includes the prototype bridge geometry, subassembly specimen geometry and design, construction of the test specimens, material properties, test set-up and loading protocol, and instrumentation protocol.

Chapter 4 briefly summarizes all the pre-test analyses carried out before beginning the experimental program. The pre-test analysis phase includes models and analyses for both the full prototype bridge and the subassembly specimens. Chapter 5 discusses all the experimental observations and results obtained from the quasi-static cyclic testing of as built Specimen No. 1. Much of the discussion is dedicated to the bent cap beam behavior and its effective slab width. The repair regimen for Specimen No. 1 is presented in Chapter 6. A similar quasi-static test to the first as-built specimen test was repeated for the repaired specimen, and key observations and response of the repaired specimen test are presented. The main conclusions and future avenues for research based on the results of this study are summarized in Chapter 7. Several appendices are included, which provide the additional details of specimen design, structural drawings, construction of the specimens, procedure of test set-up construction, a list of the instrumentation, and the calibration of the strut load cells used in the tests.

2 Background

The study presented herein is centered on the structural behavior of a box-girder bridge subassembly, focusing mainly on the effective slab width of the integral cap beam and the contribution of the box-girder slabs to the cap beam stiffness and strength. Relevant background associated with the flanged beam effective width in design codes and literature is presented below. Two main sections comprise the chapter. The first section presents the concept of the effective width and its importance as dictated by design philosophies. Because these philosophies can be different when considering buildings or bridges, a brief synopsis of building and bridge design along with code provisions for flanged beam effective width in both buildings and bridges is presented. The second section is dedicated to review the relevant previous studies that have focused on evaluating the effective width of bridge girders, testing bridge systems or subassemblies, and performance-based design of bridges.

2.1 EFFECTIVE WIDTH

The concept of the effective width in flanged RC beams is a key component of interest in this study. Its importance can vary from preventing collapse in buildings to possible reinforcement optimization in bridges. Therefore, different provisions for the effective width exist in building codes and bridge design standards, as discussed below.

2.1.1 Concept of Effective Flange Width

Two concepts are critical when designing flanged sections: the behavior of the flange and the effective portion of the flange (designated as effective flange width and commonly abbreviated as effective width). For RC beams cast monolithically with a flange, the flange increases the beam stiffness and strength. This flange can be a floor slab in a building or a soffit or deck slab in a box-girder bridge. Traditionally, the flange was assumed to be effective only in compression, but a flange also can act as a tension element [Pantazopoulou et al. 1988]. Whether the flange acts in tension or compression depends on the loading and location of the cross section. In a typical floor system comprising continuous beams with monolithic floor slab framing between columns, some sections will have negative and others will have positive bending moments; see Sections A-A and B-B in Figure 2.1, respectively. Different loading will result in a different bending moment distribution, which might change the flange in a given section from being in compression to be in tension or vice versa. In some cases the beam can

have flanges from both sides. For example, the integral monolithic bent cap beams in box-girder bridges are double-flanged (I-shape), where one flange will be in tension while the other side is in compression or vice versa.

Several sources are available in RC mechanics and design handbooks to better understand the behavior of flange and how it relates to shear lag. Figure 2.2 shows a cantilever flanged beam that is loaded so that the flange is in tension. Under this loading, elongation of the flexural tension region of the beam web is transferred to the flange along interface ad , including shear stress along that interface (Figure 2.2d). Equilibrium of forces in the direction of the beam span is achieved through tensile stresses acting on face ab of the flange. Moment equilibrium about point a requires tensile stresses along interface ad , which in turn requires shear stress along ab . Shear stresses acting within the flange panel $abcd$ cause cracks to bend away from the fixed edge (Figure 2.2c). Shear distortion, shown shaded in Figure 2.2d, relieves the tensile stresses with increasing distance along lines ab and ad , such that at sufficient distance the tensile stress drops essentially to zero. This action is known as *shear lag*. Note that equilibrium requires flange tension in both the longitudinal and transverse directions. Therefore, both longitudinal and transverse reinforcement are required in the flange. Several research studies have focused on understanding the shear lag phenomenon and the different factors that affect it, especially in box-girder bridges, such as Luo et al. [2001]. However, the study presented here and literature reviewed in the following section focus on the effective width, and for brevity's sake there is no further discussion of shear lag.

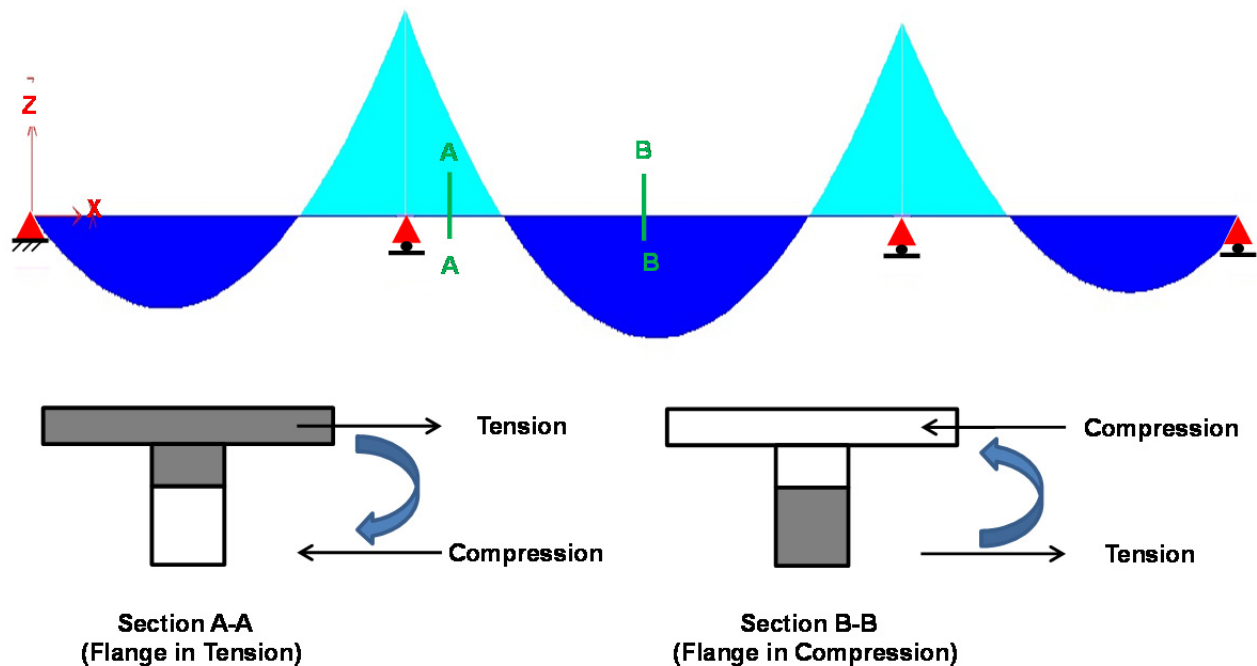


Figure 2.1 Typical bending moment diagram in continuous beam with section flange in tension or compression identified [Moehle 2014].

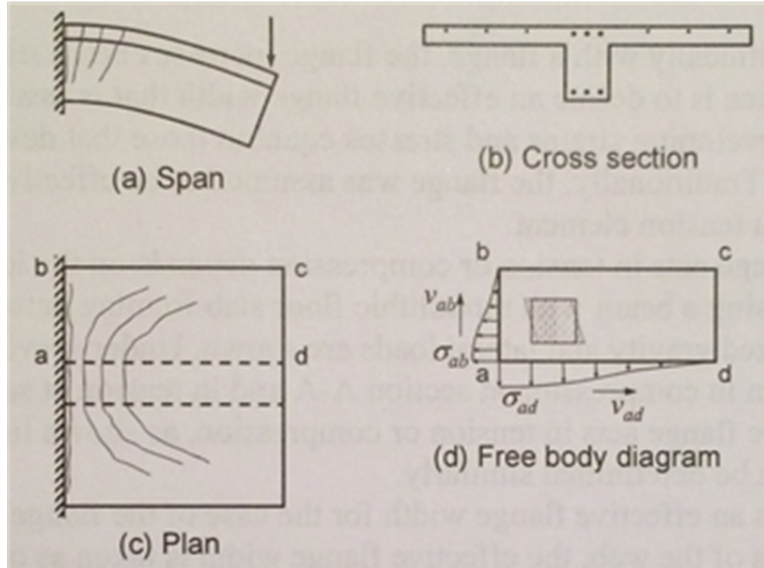


Figure 2.2 Deformations and stresses in a beam flange loaded in tension [Moehle 2014].

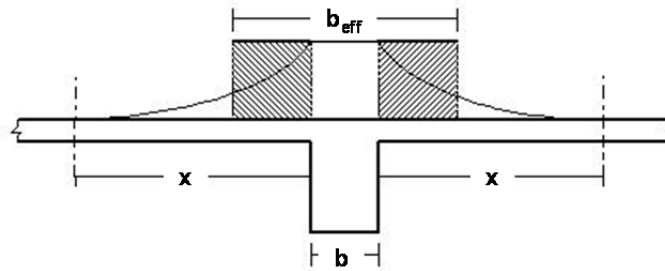


Figure 2.3 Notion of effective flange width.

The concept of the effective flange width is presented next. Common design practice is to define an effective flange width that is assumed to act monolithically with the beam. The choice of the effective width is typically based on an equivalent region of the slab, where strains and stresses are assumed to be equal to those that develop in the beam. The actual strain and stress distribution along both lateral sides of the beam resembles a flat bell-shape, where the largest values are developed in the beam and start decaying away from the beam. Figure 2.2d shows such distribution from one side of the beam along the edge ab . The strain bell-shape distribution is approximated with an equivalent rectangular strain block featuring similar strain in the beam and the adjacent flanges. The width of the equivalent strain block is known as the *effective width*, which is commonly referred to as b_{eff} . Figure 2.3 shows schematically the actual strain distribution in the beam and adjacent flange along with equivalent strain block used to define the effective width. This width is very advantageous in design since it provides a simple way of calculating the cross-section neutral axis and estimating the section properties. Design codes provide approximate formulas for estimating the effective width typically as a function of the slab thickness or beam span. The definition of the flange width as given by different building codes and bridge design standards is presented in following subsections.

2.1.2 Effective Width of Flanged Beams in Building Codes

The latest provisions related to the effective width of flanged beams in three different buildings codes that are widely used worldwide are presented below and include. The American Concrete Institute Standards ACI-318 [2011], the European Standards EN-1992 [2009], and the British Standards BS-8110 [2008].

2.1.2.1 ACI-318

The ACI-318 is the most popular building design code and is usually used as an underlying reference for various other international building codes. The ACI-318 provides extensive provisions that specify the effective flange width for T-beam (or L-beam) in the compression side. In addition, it includes special provisions that are associated with the capacity seismic design approach (discussed in more details in Section 2.1.4). The seismic provisions focus mainly on how the slab reinforcement within a T-beam tension effective width is considered and also special structural flanged-walls design provisions. Discussed first are the general compression side provisions and then followed by the special seismic provisions for beams and walls.

The general provisions for the T-beam effective flange width in compression are given in ACI-318, Section 8.12. These provisions are often recalled for effective flange width in tension, whenever applicable as seen in the seismic provisions, and are summarized as follows:

- In T-beam construction, the flange and web shall be built integrally or otherwise effectively bonded together.
- For beams with slab on both sides (T-beam flanges), the effective width shall not exceed one-quarter of the span length of the beam, and the effective overhanging flange width on each side of the web shall not exceed eight times the slab thickness, and one-half the clear distance to the next web.
- For beams with a slab on one side only, the effective overhanging flange width shall not exceed: one-twelfth the span length of the beam; six times the slab thickness; and one-half the clear distance to the next web.
- Isolated beams, in which the T-shape is used to provide a flange for additional compression area, shall have a flange thickness not less than one-half the width of web and an effective flange width not more than four times the width of web.
- Where primary flexural reinforcement in a slab that is considered as a T-beam flange (excluding joist construction) is parallel to the beam, reinforcement perpendicular to the beam shall be provided in the top of the slab in accordance with the following:
 - Transverse reinforcement shall be designed to carry the factored load on the overhanging slab width assumed to act as cantilever. For isolated beams, the full width of overhanging flange shall be considered. For other T-beams, only the effective overhanging slab width needs to be considered.

- Transverse reinforcement shall be spaced not farther apart than five times the slab thickness or 18 in.

The effective flange width is often recalled for recommended reinforcement distribution to control the cracks. The ACI-318 [2011] provides the following provision for reinforcement distribution in beams and one-way slabs (Section 10.6.6): where flanges of T-beam construction are in tension, part of the flexural tension reinforcement shall be distributed over an effective flange width as defined in ACI Section 8.12 (shown above), or a width equal to one-tenth the span, whichever is smaller. If the effective flange width exceeds one-tenth the span, some longitudinal reinforcement shall be provided in the outer portions of the flange.

The special seismic provisions that pertain to the effective flange width for beams and walls are presented. The reference to the tension effective flange width in beams was changed significantly from the ACI-318 2002 version to the 2012 version. In the older 2002 version, Section 21.4.2.2 specifies that the flange effective width for flange under tension should be taken as the smaller of: 25% of the beam span; center-to-center spacing of the beams; or sixteen times the slab thickness plus the beam width. In the ACI-318 2008 version, the reference to the tension effective flange width comes in the context of the beam capacity estimation as part of the capacity design approach requirement. The major change from the 2002 version is the requirement of considering the tension slab reinforcement within an effective width equals to the one in the compression side only for estimating the overstrength beam capacity. This change was based on research done by Wight and Sozen [1975] and French and Moehle [1991]; see commentary R21.6.2. These studies showed that using effective tension flange widths that comply with what is now the current ACI Section 8.12 provisions for compressive flange width gave reasonable estimates of girder negative bending strengths of interior connections at interstory displacement levels approaching 2% of story height.

In the case of walls, ACI-318 [2011] Section 21.9.5.2 specifies that unless a more detailed analysis is conducted, the overhanging effective flange width of flanged sections shall extend from the face of the web a distance equal to the smaller of one-half the distance to an adjacent wall web and 25% of the total wall height. The wall provisions are based primarily on data pertaining to the tension flange effective width, but the commentary R21.9.5.2 adds the following: where wall sections intersect to form L-, T-, C-, or other cross-sectional shapes, the influence of the flange on the behavior of the wall should be considered by selecting appropriate flange widths. Tests 21.48 [Wallace 1996] show that effective flange width increases with increasing drift level and the effectiveness of a flange in compression differs from that for a flange in tension. The value used for the effective compression flange width has little impact on the strength and deformation capacity of the wall; therefore, to simplify design, a single value of effective flange width based on an estimate of the effective tension flange width is used in both tension and compression.

2.1.2.2 EN-1992

EN-1992, also known as *Eurocode 2: Design of Concrete Structures* [2009], is the set of European Standards, known as Eurocodes, which specify technical rules for the design of

concrete, RC and PC structures. The EN 1992 provides the following provisions for the effective flange width for all limit states:

- In T-beams the effective flange width, over which uniform conditions of stress can be assumed, depends on the web and flange dimensions, the type of loading, the span, the support conditions and the transverse reinforcement. The effective width of flange should be based on the distance l_0 between points of zero moment, as defined in Figure 2.4 below.
- The effective flange width b_{eff} for a T-beam or L beam may be derived as given in Equation (2.1) where the parameters $b_{eff,i}$, b_w , and b are defined in Figure 2.5.

$$b_{eff} = \sum b_{eff,i} + b_w \leq b \quad (i=1,2)$$

$$b_{eff,i} = 0.2b_i + 0.1l_o \leq 0.2l_o \quad (2.1)$$

$$b_{eff,i} \leq b_i$$

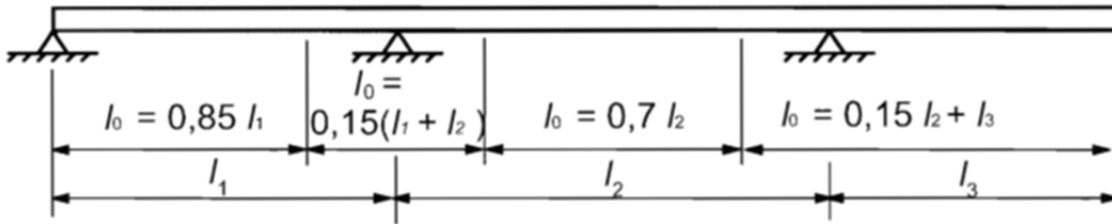


Figure 2.4 Eurocode 2 [EN-1992] definition of l_0 for calculation of effective flange width.

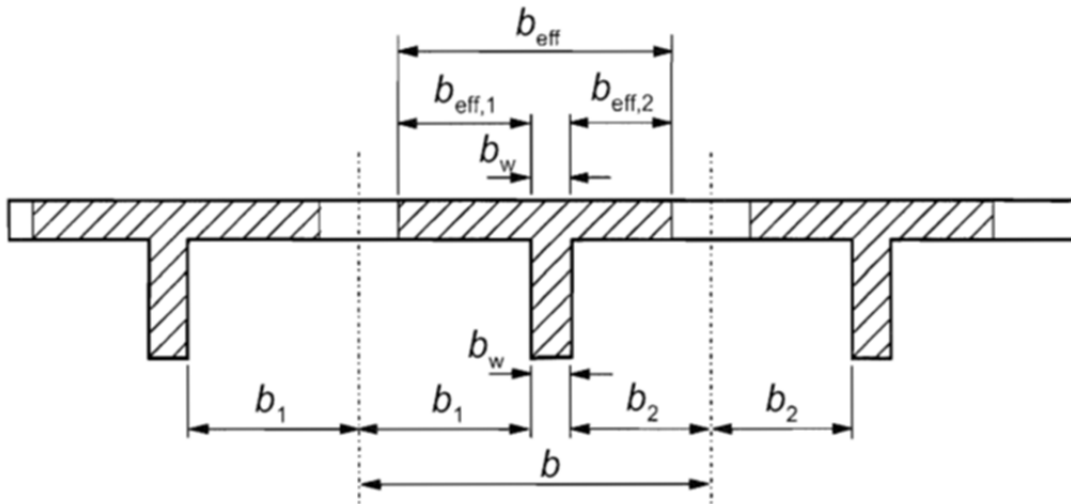


Figure 2.5 Eurocode 2 [EN-1992] effective flange width parameters.

2.1.2.3 BS-8110

The British Standards BS-8110 [2008] relates the effective flange width of flanged beams to the beam span only as opposed the slab thickness. Its provisions state that in the absence of a more accurate method for the determination of the effective flange width, it should be taken as: the web width + $L_z/5$ or the actual flange width if less in case of T-beams; and the web width + $L_z/10$ or actual flange width if less in case of L-beams; where L_z is the distance between points of zero moment; for a continuous beam, it may be taken as 0.7 times the effective beam span.

2.1.3 Effective Width of Flanged Beams in Bridge Codes

The effective width of flanged beams in the bridge design codes and specifications often refers to either the distribution under concentrated loads, such as truck wheels, or from slab contributions. Only the provisions related to the effective flange width from slab contributions are presented here. Meanwhile, the effective flange width itself can refer to either the slab flanges acting with longitudinal girders and box-girder webs or the effective flanges acting with integral bent cap beams. Here, longitudinal and transverse directions are with respect to the bridge axis. The integral bent cap effective width is associated usually with lateral, or in particular, seismic loading. In contrast, the longitudinal girders effective width is associated with both vertical and lateral loading. The *AASHTO LRFD Bridge Design Specifications* provides provisions only for longitudinal girders. However, special seismic design documents such as the Caltrans SDC or the recently published *AASHTO Guide Specifications for LRFD Seismic Bridge Design* discuss the integral bent cap beam effective flange width. Although is not the focus of this study, the AASHTO provisions for longitudinal girders are presented for completeness besides the integral bent cap beam seismic design provisions in the following subsections.

2.1.3.1 AASHTO LRFD Bridge Design Specifications

Section 4.6.2.6 of the *AASHTO LRFD Bridge Design Specification* [2007] contains provisions for the effective flange width of longitudinal superstructure girders or box-girder webs. The provisions given in clauses 4.6.2.6.1 and 4.6.2.6.3 for general effective width definition and in the case of cast-in-place multi-cell superstructures are presented below. The reader is referred to clauses 4.6.2.6.2 and 4.6.2.6.4 for additional information regarding effective flange width in cases of segmental concrete box beams and orthotropic composite steel decks.

A relevant part from the AASHTO Section 4.6.2.6 that is worth mentioning is the commentary that defines the effective flange width as follows: “Longitudinal stresses in the flanges are spread across the flange and the composite deck slab by in-plane shear stresses. Therefore, the longitudinal stresses are not uniform. The effective flange width is a reduced width over which the longitudinal stresses are assumed to be uniformly distributed and yet result in the same force as the non-uniform stress distribution would if integrated over the whole width.” In addition to the commentary definition, the key provisions that are related to the effective flange width are summarized in Figure 2.6 and extracted from AASHTO:

- In the absence of a more refined analysis and/or unless otherwise specified, limits of the width of a concrete slab, taken as effective in composite action

for determining resistance for all limit states, shall comply with Section 4.6.2.6 specifications.

- The calculation of deflections should be based on the full flange width.
- The effective span length used in calculating effective flange width may be taken as the actual span for simply supported spans and the distance between points of permanent load inflection for continuous spans, as appropriate for either positive or negative moments.
- The effective width for cast-in-place multi-web cellular superstructures may be taken to be as specified below in the following two bullets, with each web taken to be a beam. It may be also taken to be the full width of the deck slab if the effects of shear lag in the end zones are investigated.
- For interior beams, the effective flange width may be taken as the least of
 - One-quarter of the effective span length
 - 12.0 times the average depth of the slab, plus the greater of web thickness or one-half the width of the top flange of the girder
 - The average spacing of adjacent beams
- For exterior beams, the effective flange width may be taken as one-half the effective width of the adjacent interior beam, plus the least of
 - One-eighth of the effective span length
 - 6.0 times the average depth of the slab, plus the greater of one-half the web thickness or one-quarter of the width of the top flange of the basic girder
 - The width of the overhang

Section 5.7.3.4 touches briefly on the effective flange width and is concerned with the control of cracking by distribution of reinforcement. This section requires that where flanges of RC T-girders and box girders are in tension at the service limit state, the flexural tension reinforcement shall be distributed over the lesser of the effective flange width, specified in Section 4.6.2.6, or a width equal to $1/10$ of the average of adjacent spans between bearings. In addition, if the effective flange width exceeds $1/10$ the span, additional longitudinal reinforcement, with an area not less than 0.4% of the excess slab area, shall be provided in the outer portions of the flange as a requirement of crack control.

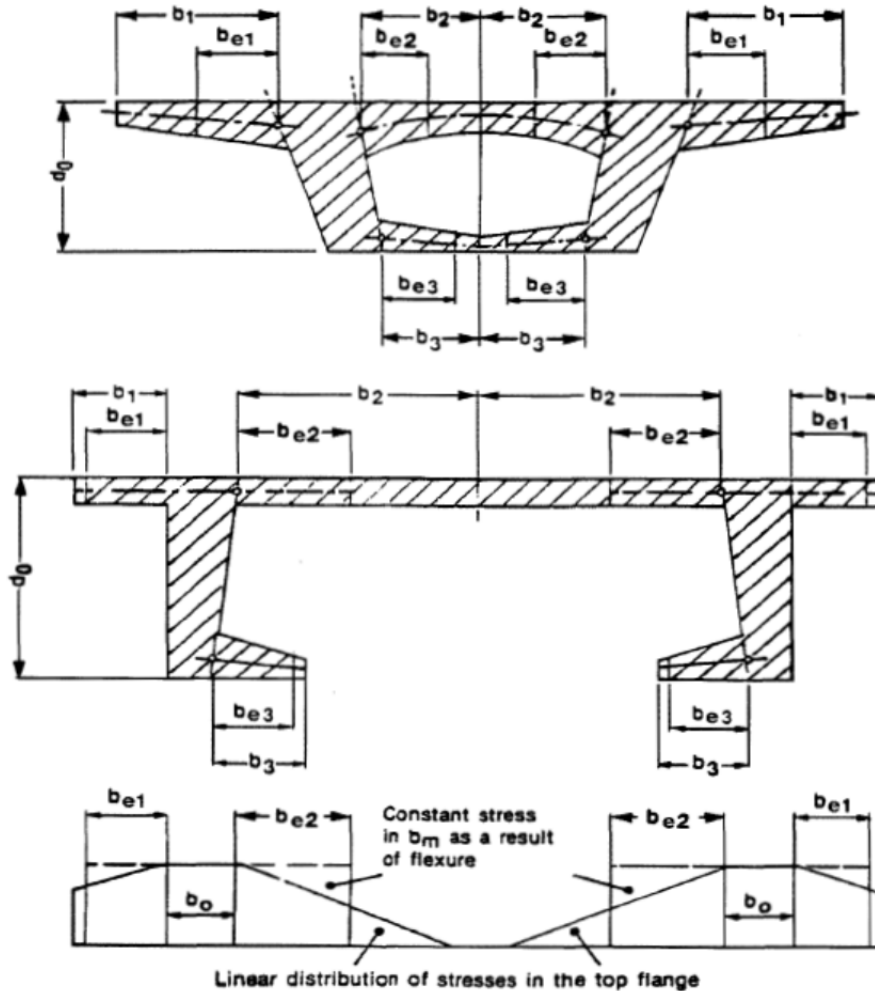


Figure 2.6 Effective flange width in different cases of longitudinal girders and schematic linearized stress distribution along with corresponding effective width [AASHTO 2007].

2.1.3.2 AASHTO Guide Specifications for LRFD Seismic Bridge Design (Caltrans SDC)

The AASHTO *Guide Specifications for LRFD Seismic Bridge Design* [2009] provides special provisions of bridge seismic design. These guide specifications differ from the current procedures in the LRFD specifications in the use of displacement-based design procedures instead of the traditional force-based “*R*-factor” method. The AASHTO seismic design provisions document appears to be inspired by the Caltrans SDC that has been used for more than two decades; the latest AASHTO seismic guidelines [2011] and Caltrans SDC version 1.7 [2013] are very similar. The provisions related to the effective flange of bridge superstructure and integral bent caps under seismic loading in the AASHTO guide specifications for LRFD seismic design [2011] and Caltrans SDC [2013] are identical. A summary of these provisions is presented in the following bullets:

- The effective width of superstructure resisting longitudinal seismic moments, B_{eff} is defined by Equations (2.2) and (2.3).

$$B_{eff} = D_c + 2 \times D_s \quad \text{Box girders \& solid superstructures} \quad (2.2)$$

$$B_{eff} = D_c + D_s \quad \text{Open soffit superstructures} \quad (2.3)$$

where D_c is the column diameter and D_s is the depth of the superstructure, as shown in Figure 2.7. The effective width for open soffit superstructures (e.g., T-beams and I-girders) is reduced because they offer less resistance to the torsional rotation of the bent cap.

- The effective superstructure width can be increased for cross sections away from the bent cap by using a spread from the cap face until the full section becomes effective (see Figure 2.7). On skewed bridges, the effective width shall be projected normal to the girders, with one end of the width intersecting the bent face such that one half of the width lays on either side of the column centerline (see Figure 2.7). Additional superstructure width can be considered effective if the designer verifies that the torsional capacity of the cap can distribute the rotational demands beyond the effective width stated in Equations (2.2) and (2.3).
- If the effective width cannot accommodate enough steel to satisfy the overstrength requirements, the following actions may be taken: thicken the soffit and/or deck slabs; increase the resisting section by widening the column; haunch the superstructure; or add additional columns.
- Bent caps are considered integral if they terminate at the outside of the exterior girder and respond monolithically with the girder system during dynamic excitation.
- The integral cap width considered effective for resisting flexural demands from plastic hinging in the columns shall be determined by Equation (2.4); see Figure 2.8:

$$B_{eff} = B_{cap} + (12 \times t) \quad (2.4)$$

where t is thickness of the top or bottom slab. Note that revisiting the 12-times slab-thickness used in the bent cap beam effective width estimation is a main focus of this study.

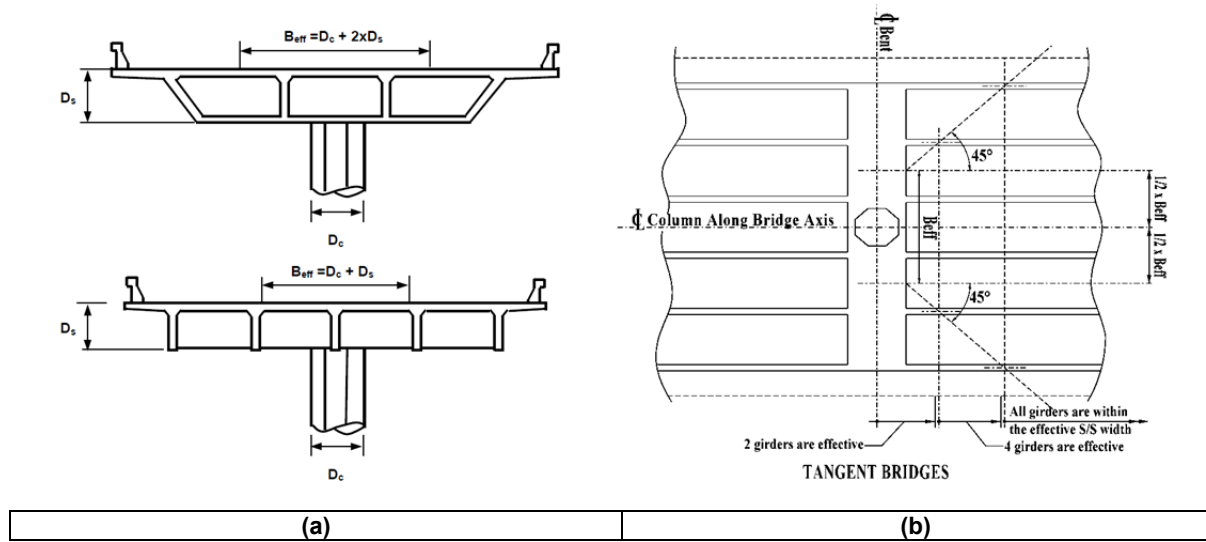


Figure 2.7 (a) Effective width of superstructure girders and (b) its distribution in the plan for one case of unskewed tangent bridges as given by Caltrans SDC [2013].

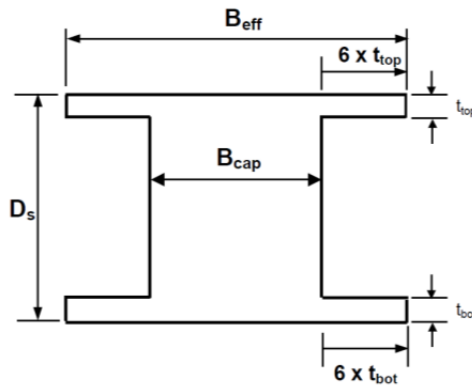


Figure 2.8 Effective width of bent cap beam as given by Caltrans SDC [2013].

2.2 REVIEW OF LITERATURE

The main focus of the study is the effective slab width in bridges, and accordingly, the experimental program conducted in this study consisted of testing two large-scale bridge subassemblies. The first specimen was tested in quasi-static cyclic loading. The second one was retrofitted with CFRP and tested using a hybrid simulation technique. The design of the testing protocol first involved reviewing previous research studies that focused on large-scale bridge components or subassembly testing. In addition, early studies that promoted bridge performance-based design and capacity design concepts were also reviewed. Next, some of those relevant studies are summarized below, broken down into three subsections: (1) a classic study that focused on the effective width for bridge girders, (2) bridge component and subassembly testing, and (3) performance-based bridge design. Note that the issue of the effective width in RC floors systems in building was extensively studied before and the reader is referred to the literature review by Moustafa [2014] for details. A review of the studies that utilized hybrid simulation

testing technique for investigating bridge components and systems behavior is included in the companion report.

2.2.1 Effective Width for Bridge Girders

2.2.1.1 *Cheung and Chan [1978]*

This study investigated the effective width in concrete and steel-concrete composite beam-slab type and box-girder bridges using the finite strip method. Only the effective width of the bridge longitudinal superstructure girders was considered; nothing related to an integral flanged cap beam in the bridge transverse direction was part of this study. The analytical method used was a variation of the FE method. Previous studies had determined the effective flange width of T-beams in the majority of cases investigated specific problems with specific geometric or loading configurations, such as a single T-beam with a flange of infinite width loaded by a concentrated force at mid-span, or multiple T-beams under uniformly distributed loads [Metzger 1929; Chwalla 1936]. Because irregularities as arbitrary girder arrangements, boundary conditions, and loading configurations were proven to be easily handled, to a certain extent, by using the finite strip method [Cheung 1969], Cheung and Chen [1978] to apply the finite strip method to determine the effective width in concrete and steel-concrete composite beam-slab type and box-girder for bridges. In this method, harmonic functions that mimic the boundary conditions longitudinally were used in conjunction with polynomials for the transverse direction. The stiffness matrix and load vector of the strip were derived in the usual manner of minimization of the total potential energy.

This study used the finite strip method to analyze simply supported concrete and steel-concrete composite beam-slab and box-girder bridges. The results obtained were used to determine the effective width of the compressive flange of the bridge girders. The finite strip selected for this study was derived by combining a plane stress strip with a bending strip, thereby making it suitable for the analysis of folded plate-type structures, which are subjected to membrane stresses as well as transverse bending forces. The strip had two nodal lines with four DOFs per nodal line (displacements in the x -, y -, and z -directions and rotation about the nodal line). In the analysis, the girder and deck were divided into a number of strips; thus any combinations of loadings and girder arrangements could be easily accommodated. After solving for the nodal displacements and rotations, the in-plane stresses and bending moments could be calculated at any point of a strip.

The effective compression flange width of a girder was determined by isolating the girder under consideration and required that the summation of the longitudinal in-plane stresses at any cross section in the isolated girder be zero. The longitudinal bending stresses arising from the local longitudinal bending moment were not included in the calculation since they would be cancelled out in the summation process. The effective width was defined as that portion of the flange over which the maximum compressive stress is assumed to act uniformly to produce a resultant equal to the compression force in the section. The effective width was thus calculated by dividing the total compression force by the deck thickness times the maximum compressive stress in the flange.

The effective flange widths of box girders were calculated in a similar manner. The study considered the AASHTO HS-25 truck load and extended the results for the AASHTO HS-20 truck load as well since both had identical axle configurations and axle loads that are linearly proportional to each other. The study focused only on the sections experiencing positive bending moment because the common design practice considered the negative moment sections noncomposite where the flange was ignored, and the calculation of effective flange width was therefore not required. The study used the obtained results of all the bridge types studied to conclude the following:

- The variables that had major effects on the effective flange width of bridge girders were girder spacing and span. Within the practical range of bridge member proportions, deck thickness and girder width and depth played a negligible role.
- Up to a span to one-half clear spacing ratio (L/B) of approximately 20, the effective overhanging flange width b_{eff} tended to increase with increasing span and spacing. For L/B ratios greater than 20, b_{eff} becomes more or less equal to the one-half of clear spacing between girders (B).
- The effective flange width of girders was independent of the number of traffic lanes of the bridge.
- Both box-girder bridges and beam–slab type bridges showed an identical trend where the effective width increases with longer span and larger spacing.
- For multi-cell box-girder bridges, the effective flange width of the interior webs was governed by the distance, center to center of webs, whereas the exterior webs follow a trend similar to that of beam–slab type bridges.
- The empirical results were in good agreement with the composite road bridge design code DIN 1078 of the Federal Republic of Germany (1955). Typical values of the calculated effective widths were also compared to the 1973 AASHTO provisions and the Canadian Standards Association CSA-S6 (1974) values. From the comparisons, it was found that the AASHTO and CSA-S6 values were quite conservative especially for beam-slab type bridges with small L/B ratios. For example, for an L/B ratio of 12, the effective width differences of about 56% for the concrete girder and 100% for the steel girder could result in compressive flexural stress differences of approximately 34% and 48% for the concrete girder and the steel girder, respectively.
- Variation of the effective width along the span was relatively uniform. Using this particular information, the authors attempted to establish an empirical relationship between the effective width, spacing, and span using a least squares curve fitting procedure. A non-dimensional relationship between b_{eff}/B and L/B was derived by fitting the calculated results to a curve described by the polynomial in Equation (2.11)

$$b_{eff}/B = \sum_{i=1}^{\infty} A_i (L/B)^i \quad (2.11)$$

where the first four terms were adopted in the polynomial and the constants A_i were determined as follows: $A_1 = 0.21237$, $A_2 = -0.01929$, $A_3 = 0.00078$, and $A_4 = -0.00001$.

- The resulted best-fit empirical curve was applicable to both concrete and steel-concrete composite girders and was in good agreement with the 1955 DIN-1078 values. The best-fit curve was compared against upper and lower bound values obtained by Metzger [1929] and Chwalla [1936] based on the theory of elasticity. It was shown that the fitted curve fell between the limiting curves.
- To apply the empirical design curve to continuous bridges, a number of multi-span continuous beam-slab and box-girder bridges were analyzed. In all cases, it was found that the design curve is applicable if the distance between the points of zero bending moment is adopted as the value L of the span. Therefore, it was recommended that the effective widths of continuous bridge girders be determined from the presented curve, assuming the distance between the points of contraflexure to be the equivalent simple span.
- The design curve developed from a complete folded plate-type analysis, using actual truck loads as was done in this study, was claimed to give more realistic values of the effective width of girders. Furthermore, the design curve incorporated two major variables, girder spacing and span, in the evaluation of the effective width while the corresponding AASHTO or CSA specifications provided discontinuous, one variable-dependent (girder spacing, slab thickness, or span) functions that, in general, led to conservative designs.

2.2.2 Bridge Subassembly and Component Testing

Investigations of bridges and infrastructure structural damage following severe earthquakes have been one of the main priorities of federal and different states' departments of transportation (such as Caltrans). For example, several research programs investigated the flexural and shear behavior of columns or cap beam-column joint regions that resulted in design guidelines and recommendations. Studies relevant to the program presented herein are briefly summarized below.

2.2.2.1 Seible et al. [1993, 1994]

In 1993 and 1994, Seible et al. conducted two full-scale tests at the Structures Laboratory in the University of California, San Diego. The results of the first test were used to determine the specimen design for the second test. The full-scale test specimens comprised a 5-ft-diameter column along with the cap beam and portion of the box-girder superstructure from a prototype PC bridge. The tests focused on the cap beam-column connection with #18 bars and under uni-

directional seismic-type loading. Of interest was: (1) the anchorage behavior of straight #18 bars based on the AASHTO design guidelines; (2) determining local distress levels and failure mechanisms in the cap beam-column connection; and (3) assessing local distress and failure behavior with respect to global seismic design principles of collapse prevention and damage control and reliability. The test in 1993 showed that the cap beam-column connection was capable of forcing initial plastic hinging into the column with ductility limited by the joint and cap beam deterioration; no premature bond slip or joint deterioration was noticed. It was observed that nominal maximum principal tensile stress levels of 6 to 8 $\sqrt{f'_c}$ contributed to the encountered cap beam-column joint distress. This led to horizontal cap dilation measured in the longitudinal bridge direction through the joint core and significant joint shear cracking. Such observed cracking and dilation did not cause brittle failure; however, it posed a problem for post-earthquake repair and a compromised serviceability design criteria.

Based on the observations from the first test, the design of the second specimen was slightly altered and the modified design verified by testing. The 1994 test addressed the observed issues through increasing the cap beam width, using additional vertical and horizontal joint shear reinforcement, and adopting a soffit flare. In the second test, most or nearly all the inelastic action had migrated to the column through a flexural hinge without joint shear cracking or bond slip. This is the classic weak-column-strong-beam design approach that allows damage repair without significant traffic interruption. The modified design also provided a high level of integrity to the cap beam-column region, which met serviceability requirements and functionality design limit state criteria. The proposed design changes also led to better constructability due to less reinforcement congestion as the cap beam was wider.

2.2.2.2 MacRae et al. [1994]

MacRae et al. conducted a three-quarters large-scale test of the Santa Monica Viaduct PC cap beam-column joint [1994]. The objective of the experiment was to determine the peak strength of the connection, the degradation of strength with lateral displacement, and the failure mode under reversed cyclic loading in-plane with the bent. No special shear reinforcement was provided in the cap beam-column joint. Thus, the sub-assembly specimen failed primarily due to joint shear failure. However, the strength degradation was gradual with the cycles of repeated loading. Moreover, no punching was observed in the vicinity of the cap beam-column region, even though the column axial load was increased during the test to 1.5 times the expected maximum column axial load. It was noted also that even when the full flexural strength at the base of the prototype column had been achieved, the overall bent behavior was still expected to respond reasonably. Only after a large amount of deformation would the top column connection be effectively pinned.

2.2.2.3 Mazzoni [1997]

Up to the late 1980s and early 1990s, unidirectional quasi-static testing was the most common loading technique. Only few bridge component or subassembly tests were conducted under bi-directional loading. The comprehensive study by Mazzoni [1997] considered both uni-directional and bi-directional loading. This study investigated the seismic design and response of the lower-

level beam-column connection in a RC double-deck bridge structure. Two 1/3-scale beam-column joints with different levels of joint shear stress demands were built according to the adopted design criteria and tested in the laboratory. The difference between the two specimens was related to the difference in capacity of the members framing into the joint. The nominal strength of the columns and beams of the second specimen were greater than those of the first specimen. This resulted in a higher joint shear stress demand imposed on the beam-column joint of the second specimen.

The study focused on several design issues and parameters besides the effect of bi-directional loading, including the yielding of columns versus beams, joint shear strength, detailing of transverse reinforcement in the joint, detailing of member longitudinal reinforcement in the joint, the effect of beams perpendicular to the loading direction, and the joint depth to bar diameter ratio. Only the conclusion related to the effect of bi-directional loading is presented herein. While bi-directional loading was applied first and then followed by uni-directional loading, the design strengths were reached only during the unidirectional response and not during bi-directional response. Although the bi-directional cycles dissipated a significant amount of hysteretic energy, they did not affect the uni-directional response envelope. The effects of bi-directional loading were determined to be important in the response of the structural system in terms of incorporating better load path and residual stresses, but did not affect the design strength of the test specimens.

In response to the importance of bi-directional loading in certain cases, FEMA introduced guidelines for conducting tests under bi-directional loading: FEMA 461 [2007]. These guidelines for the testing and loading protocols for determining the seismic performance characteristics of structural and nonstructural components was consulted to develop the loading protocol for the study presented in this report. The general FEMA-461 [2007] statement for bi-directional loading is as follows: “Imposed deformation or force will typically be applied in a single degree of freedom (unidirectional loading). Bidirectional loading (loading in two orthogonal horizontal directions) should be carried out whenever it is anticipated that such loading has a significant effect on any of the damage states and the associated fragility function. Written justification should be provided if it is decided in this case to apply only unidirectional loading.”

2.2.2.4 Naito et al. [2002]

The extensive study by Naito et al. [2002] investigated different designs for bridge beam-column joints. Motivated by the response of bridges to 1989 Loma Prieta, California, earthquake, this and subsequent studies resulted in higher design requirements for transverse reinforcement in bridge beam-column joints in California; however, the resulting reinforcement details were congested and hard to construct. The investigation examined four large-scale interior joints with details typical of those required in California. The experimental program included tied square cross-section columns and spirally reinforced circular cross-section columns. Both conventional and headed joint reinforcement configurations were investigated. A complementary study was conducted by Mosalam et al. [2002] to further investigate the beam-column joint behavior but within a larger bridge subassembly involving a representative portion of the box-girder. It is presented next.

The experimental results showed that the then-adopted design requirements produced joints that remain essentially elastic to relatively large drifts, whereas the columns developed inelastic rotations adjacent to the joints. The study showed also that the response of the square column subassemblies was not as stable as that of the circular column subassemblies, which was attributed to the linear (versus circular) arrangement of the column longitudinal reinforcement, resulting in simultaneous slip, buckling, and eventual simultaneous fracture of several longitudinal bars. The use of headed reinforcement within the joint regions was shown to be effective in reducing congestion and thereby improving constructability, while maintaining comparable structural behavior. In general, headed longitudinal column reinforcement exhibited less slip and underwent higher strain than conventional longitudinal reinforcement at similar levels of displacement demand. Finally, it was demonstrated that the lateral transverse joint reinforcement used in the tested joints was not significantly activated, reaching less than 25% of the yield strain. This suggested that less reinforcement could be used in connections with demands similar to those of the test specimens.

2.2.2.5 Mosalam et al. [2002]

The research by Mosalam et al. [2002] was an extension of the study by Natio et al. [2002] to investigate the results of two large-scale experiments conducted on RC bridge subassemblies. Each subassembly, which are very similar to the subassembly considered in the study reported herein, consisted of the middle column/cap-beam joint of a three-column bridge bent and a large part of the monolithically cast-in-place box-girder of a typical California highway bridge. The subassemblies were subjected to constant gravity load and gradually increasing bi-directional cyclic lateral loading. One subassembly represented common practice in California of the late 1990s, and the other subassembly considered a new design using headed reinforcing bars with reduced volume of transverse reinforcement to improve joint construction. Special attention was given to proper modeling of the boundary conditions and use of instrumented supports. The effect of bi-directional loading on global damage of the box-girder slabs was considered and was presented in the form of variation of the effective moment of inertia of the cap-beam cross-section with displacement ductility. Both subassemblies experienced excessive shear damage in the joint regions, with ultimate failure due to pullout of column longitudinal reinforcing bars. However, the use of headed bars led to better global and local performances due to improved confinement of the joint region with less volume of reinforcement. This study concluded that:

- Use of headed reinforcement was an efficient way to reduce reinforcement congestion within critical regions in RC bridges such as cap beam/column joints. The tested new design using headed reinforcement with less total amount of transverse steel was shown to lead to improved global response compared to the common design practice with conventional reinforcement. This was observed mainly from the more gradual strength degradation with cyclic loading, from the higher ultimate displacement ductilities in both of the longitudinal and transverse loading directions, and from the reduction of the average shear strain within the cap beam/column joint region.

- Caltrans' estimate of the effective slab width acting with the integral bent cap in resisting flexural demands as 12 times the slab thickness is conservative up to a displacement ductility level of five. For lower ductility levels, larger contribution of the soffit and deck slabs may be used in estimating the flexural stiffness of the effective cap beam. This may have significant design implications in the event that higher cap beam stiffness changes the seismic internal forces in the different bent sections.*
- The vertical and longitudinal horizontal headed reinforcements within the joint region were effective in confining these regions as supported by the strain measurements. This was reflected in delaying the pullout of the column longitudinal bars, i.e., requiring larger number of cycles for the column longitudinal bars to pullout compared to the case with conventional design. The conventional joint reinforcement in the form of vertical hooks and stirrups and horizontal hairpins was not as effective as the corresponding headed bars due to possible slippage of these bars in relation to the surrounding concrete.
- Based on the observed mode of failure, the study recommended further investigation of the use of headed bars as longitudinal column reinforcement as a possible way of preventing the observed pullout of these rebars. In this way, significant improvement of the seismic performance of the designed bridge system (ultimate drift ratios greater than 8.5% and ultimate displacement ductility greater than 6) can be obtained. Although more than 8% drift was achieved in the experimental study, this large drift was accompanied with excessive strength and stiffness degradation. The goal of investigating the use of headed bars as longitudinal reinforcement of the column is to eliminate the brittle mode of failure caused by bar pullout.

A general observation regarding the use of headed rebars based on the conclusions from Natio et al. [2002] and Mosalam et al. [2002] is that headed rebars are efficient in reducing joint congestion and lead to better constructability without compromising strength requirements. Earlier studies such as Ingham et al. [1995] and Thewalt and Stojadinovic [1995] came to the same conclusion, suggesting that using headed reinforcement usually results in a better performance because of enhanced anchorage. The same observation was the motivation for Hube and Mosalam's [2010; 2011] proposed new design for RC box-girder in-span hinges. Using headed rebars was shown to be effective in in-span hinges, as was the case for beam-column joints.

* Note that this particular observation is critical to the study presented herein to quantify better the cap beam effective slab width.

2.2.2.6 Other Relevant Studies

Most studies of the behavior of bridge columns in response to strong ground shaking has been restricted to columns rather than bridge subassemblies for two reasons: (1) plastic hinging in bridge columns is the desired mode of failure; and (2) uni- or bi-directional testing of single columns or even on a shaking table is more convenient and relatively easier than testing a bridge system or subassembly. Thus, numerous tests were conducted on columns to verify and ensure that desired ductility at failure had been achieved. Discussed below are a few examples of column tests found in the literature.

Lehman and Moehle [1998] investigated the lateral response of well-confined bridge columns with varying longitudinal reinforcement ratios and aspect ratios. The results were used to outline the performance-based seismic design framework for RC bridge columns. The behavior of RC bridge columns having varying aspect ratios and varying lengths for confinement extent was experimentally and analytically examined on four circular columns by Calderone et al. [2000]. Esmaily-Gh and Xiao [2002] conducted tests to evaluate the behavior of bridge columns subjected to variable axial load and various loading patterns and found that the axial load and loading pattern variation had a significant effect on the flexural strength capacity, mode of failure and damage pattern, and ductility and deformation of the columns.

Brown et al. [2007] studied the effect of bar buckling in RC columns. Eight circular columns, reinforced with longitudinal bars and circumferential spirals, were tested under constant axial load and cyclic lateral displacements. The goal was to further understand the phenomenon and generate data on bar-buckling mechanisms, with the aim of developing a numerical model. New modeling strategies for modern RC bridge columns were developed to accurately model column behavior under seismic loading, including global and local forces and deformations, as well as progression of damage [Berry and Eberhard 2007]. The models were calibrated using the observed cyclic force-deformation responses and damage progression observations of a 37-test database of spirally RC columns.

2.2.3 Performance-Based Design of Bridges

In response to the shift toward a performance-based design approach, research over the past couple of decades has focused on capacity design approach and nonlinear modeling and analysis procedures and techniques. According to ASCE-41 [2006], performance-based earthquake engineering (PBEE) is a methodology whereby a structure is designed to achieve predetermined performance levels or objectives in a specific hazard environment. Performance-based design is intended to allow structures to meet specific performance objectives with greater reliability than the traditional prescriptive code approach. The design of structural components for target performance levels requires an assessment of strength, stiffness, and deformation characteristics typically into the nonlinear range of elements and subassemblies that make up the seismic-force-resisting system as advised by ACI-374.2R [2013].

Hose and Seible [1999] conducted a study as a part of an early initiative by the Pacific Earthquake Engineering Research (PEER) Center to develop and demonstrate the parametric basis for performance-based bridge engineering. The study resulted in a bridge performance

database and catalog to evaluate the capacity of bridge systems and their subcomponents, allowing an accurate characterization and prediction of the structural behavior. The developed database was based on observations and results from various laboratory tests, as well as damage from past earthquakes.

Mackie and Stojadinovic [2003] defined the performance objectives in terms of annual probabilities of socio-economic decision variables being exceeded in a seismic hazard environment of the urban region and site under consideration. Further probabilistic seismic demand analysis was used to compute values of bridge-specific engineering demand parameters given ground motion intensity measures such as peak ground acceleration. An optimal probabilistic seismic demand model (PSDM) was developed and proposed for typical highway overpass bridges. Intensive efforts were undertaken to improve the performance, reliability, and economy of performance-based methods in extreme events. A cost-estimation approach of seismic performance was investigated in Ketchum et al. [2004]. The project focused mainly on providing revised and improved empirical rules for the influence of design ground-motions ensembles on bridge construction costs.

As previously mentioned, PBEE and probabilistic approaches require extensive nonlinear analyses. Aviram et al. [2008] developed practical guidelines for nonlinear analysis and modeling of bridge structures to assist practicing engineers in the implementation of nonlinear methods for bridge design subjected to seismic loading. This collection of practical and readily implementable recommendations is intended to assist in estimating the seismic demands on critical bridge components and systems. This Aviram et al. [2008] report also provides a comprehensive literature review of the current engineering practices in the U.S. and how they relate to desired analytical methods. Another factor that can significantly alter an entire bridge system response and is more feasible to tackle analytically is the bridge abutment response along with soil–structure interaction and backfill flexibility. Kramer et al. [2008] presented a performance-based evaluation of bridges on liquefiable soils with a focus on abutment modeling using nonlinear inelastic analysis. The report provides a detailed analytical model consisting of liquefiable and non-liquefiable soils, pile foundations, abutments, and the bridge superstructure along with the model validation. The study considered the computed response under various loading conditions and provided conclusions regarding the resulting damage and loss estimates. Further studies of RC bridge systems including soil-foundation-structure interaction are given in Dryden and Fenves [2009] and Mitoulis [2012].

3 Development of Experimental Program

This chapter discusses the development of the experimental program to investigate the structural behavior of integral bent cap beam in RC box-girder bridges subjected to earthquake loading. The determination of the prototype bridge configuration, the design of the experimental subassembly, the test set-up and boundary conditions, specimens' construction, material properties, and the instrumentation techniques used for the experiments are also presented.

3.1 BRIDGE TERMINOLOGY

Although several different types of steel and RC bridge types constitute the make-up of bridges up and down California, a typical bridge system is a RC integral box-girder bridge; see Figure 3.1. This system consists of a single-level elevated highway supported on multiple bents and abutments. Each bent consists of either single or multiple columns. These columns terminate in a solid RC beam, referred to as the bent cap beam, which spans the entire bridge width. The cap beam and columns make up the transverse bridge frames, which, in turn, support the highway bridge span.

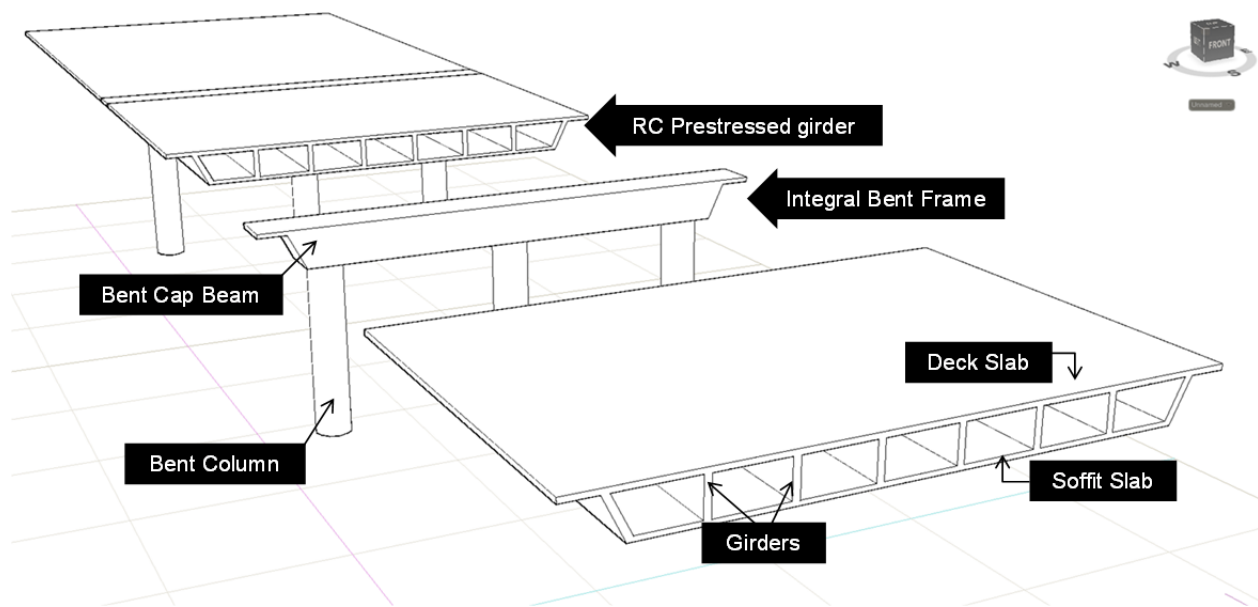


Figure 3.1 Components of a RC box-girder bridge.

Many different types of structural systems may be used to span the distance between bents. They range from composite steel plate girders that rest on top of the cap beam, to integral post-tensioned concrete box-girder systems constructed monolithically with the cap beam. A typical box-girder consists of a top deck slab, bottom soffit slab, and longitudinal webs, commonly referred to as girders. The different components of the bridge bents and longitudinal box-girder are shown in Figure 3.1. Long-span bridges are often divided into segments or frames to allow for shrinkage and expansion due to temperature variations. In monolithic construction, each frame typically consists of two to three bridge bents and their adjoining spans. Connection between adjacent longitudinal frames is accomplished through in-span hinges (seats) that are capable of transmitting vertical (and possibly transverse) forces while allowing for expansion and rotation.

Because of the nature of the test set-up utilized for the experimental program reported herein, the specimen bridge subassembly was tested in an inverted position (see Section 3.3.2) as illustrated in Figure 3.2. To avoid confusion, the slabs are referred to as the soffit slab and deck slab (see Figure 3.2) rather than top slab and bottom slab. The figure also shows the parts of the prototype bridge considered for the experimental subassembly, as discussed next.

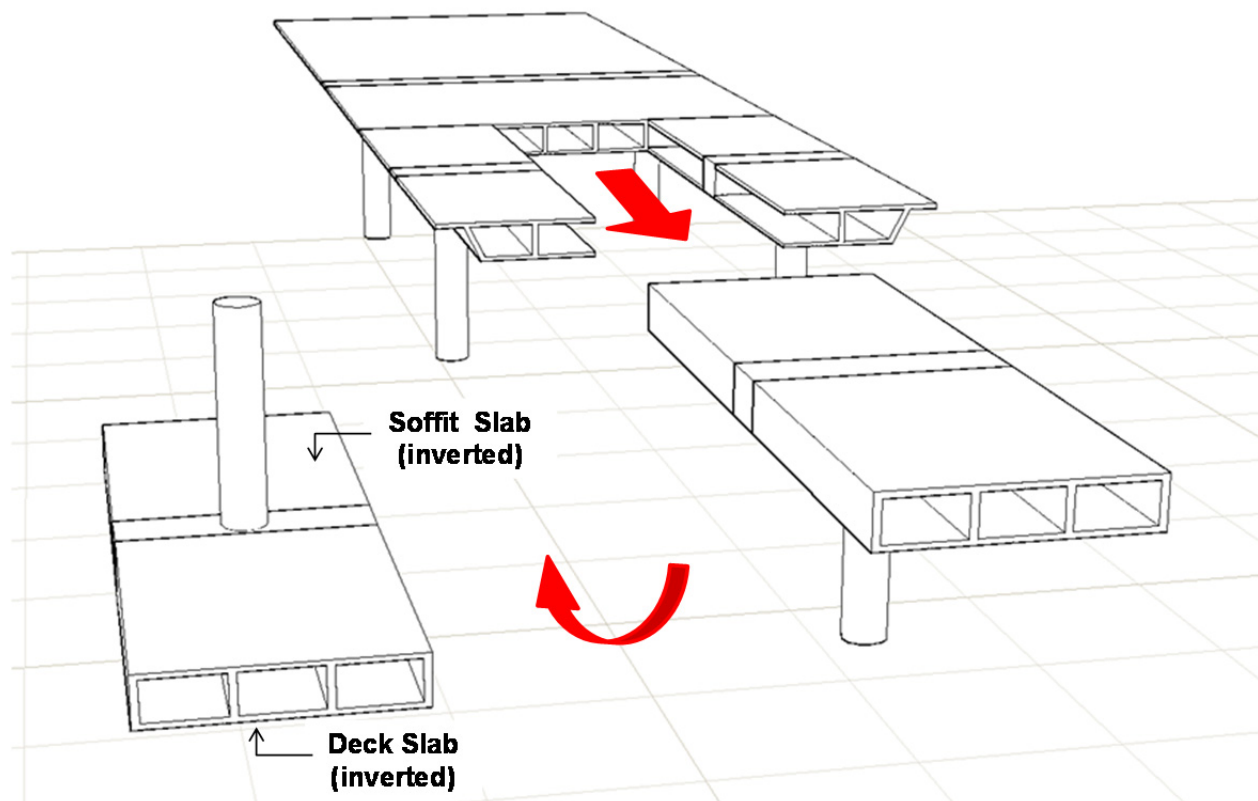


Figure 3.2 Convention of the specimens' box-girder slab terminology.

3.2 PROTOTYPE

To determine the geometry and structural configuration for the test specimens, a typical California bridge construction was used as the prototype. There are several methods for choosing a prototype bridge for research studies. One method involves conducting a survey of existing bridges and then averaging the spans and cross-section dimensions to generate a virtual prototype that is then considered a representative bridge. This method was adopted by Natio et al. [2001], where sixteen RC bridges built in California between 1985–1995 were evaluated. This study resulted in the selection of a representative prototype that consisted of a three-column bridge bent with an integral box girder and pinned column-to-footing connections. The prototype bridge considered average spans of 150 ft. between the bents, which consisted of circular columns and a cap beam depth that is comparable to the column diameter. Another method for choosing a prototype bridge is to use real existing bridges. This method is useful if a particular structural behavior is to be investigated or damage due to a specific loading case (e.g., specific earthquake) is analyzed. Lee and Mosalam [2014] used two existing bridges to investigate the behavior of RC columns in shear due to horizontal and vertical earthquake excitations. The two considered bridges were the Amador Creek Bridge and the Plumas-Arboga Overhead Bridge.

This study did not use either of the approaches described above because the goal was to investigate the structural behavior of integral bent cap beams and box-girder slab contribution in light of the AASHTO and Caltrans Seismic Design Criteria (SDC). For this project, a typical California bridge that is designed by the Caltrans Bridge Academy is utilized. This bridge—heretofore referred to as the Academy Bridge—is a representative of the most common RC box-girder bridge type with integral bent cap beams found in California. The Caltrans Bridge Academy used the Academy Bridge as a part of the complete hands-on design exercise for junior bridge engineers and professional bridge design workshops. The Academy Bridge was modified to allow generation of a symmetric and feasible subassembly specimen that could be accommodated at the Structures Laboratory at UCB.

The key features of the bridge, such as the main span, bent cap and box-girder geometry, and column diameter, were not changed or modified; the modifications were concerned only with the bent layout and elevation (height). The main modifications applied to the Academy Bridge prototype include: (1) a shorter column height, which still guaranteed a flexural governed behavior as intended for the original Academy bridge design; and (2) a symmetrical three-column bent that was unskewed. The differences between the original Academy Bridge and the modified prototype are summarized in Table 3.1. The detailed geometry and dimensions of the modified Academy Bridge prototype are shown in Figure 3.3.

Table 3.1 Differences between the modified prototype and Academy Bridge.

	Academy Bridge	Modified Prototype
Spans	3 spans: 124 ft, 168 ft, 112 ft	3 spans: 124 ft, 168 ft, 124 ft
Skewness	Skew at 15°	Orthogonal at 0°
Bent Height	44 ft (aspect ratio 7.33)	30 ft (aspect ratio 5)
Bent Layout	2 columns hinged at base	3 columns hinged as at base

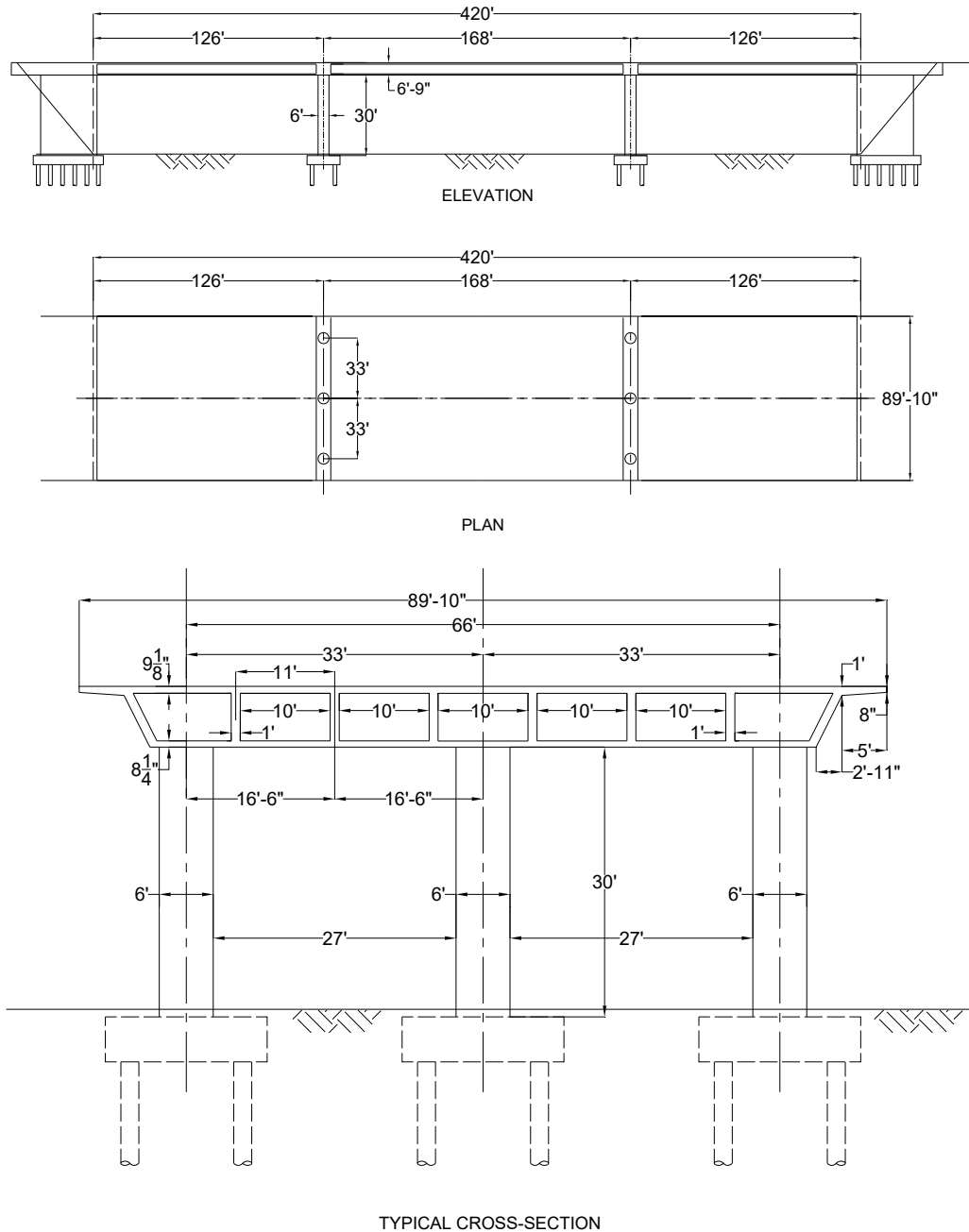


Figure 3.3 Different views of the modified Academy Bridge.

3.3 SUBASSEMBLY DEVELOPMENT

3.3.1 Subassembly Geometry

The experimental investigation focused on the behavior of integral bent cap beam and strain distribution in the box-girder slabs in a bridge system subjected to constant gravity loading and varying transverse (lateral) loading. Thus, a representative portion of the box-girder in the longitudinal direction of the bridge was considered at both sides of the bent cap beam and column to form the subassembly. The prototype bridge consists of multi-column bents where the transverse bridge frame consists of an integral bent cap supported on three columns. Only the middle column and part of the bent cap was considered in the subassembly. Figure 3.4 shows the representative portions of the bent cap beam in the transverse direction and box-girder in the longitudinal direction. The basis for choosing such a representative sample is described next.

Testing of a full-scale and a complete assembly of all the bridge components would be the ideal case scenario. Obviously, the largest possible scale is always favorable to mimic the actual behavior and avoid any scale effect bias; typically, however, a compromise between the subassembly scale versus the considered representative portions of the bent cap and box-girder is part of the test subassembly design decision. Given practical considerations and laboratory limitations, only a reduced-scale and a representative subassembly were used in this study. The most feasible physical boundary conditions for the test subassembly was the main criterion adopted in this study in addition to the laboratory space available for testing as dictated by the reaction frame and the actuators capacity.

Feasible boundary conditions are usually associated with minimal translational and rotational constraints i.e., provide least reactions, while also taking into account that laboratory hinged supports that allow free rotations—especially for massive RC components—are challenging and costly. Therefore, choosing the points of zero moments in the bridge under both vertical (gravity) and lateral cases of loading, in both transverse and longitudinal directions, leads to the most feasible boundary conditions. That is because partial fixations at zero moment locations are most likely to introduce the minimum secondary bending moments. For accurate estimation of zero moment locations in the prototype bridge, a SAP2000 [2009] elastic model for the prototype bridge was utilized. More details about the bridge model and boundary conditions verification are presented in Chapter 4.

For the bridge longitudinal direction, the bending moments and deflection inflection points are defined by gravity loads only because the lateral loads are resisted primarily by the bent cap and columns framing action. Based on the SAP2000 bridge model, the zero moment locations along the bridge box-girder longitudinal direction are shown in Figure 3.5. The zero moment location is at one-quarter of the spans continuous from both sides and one-third of the spans continuous only from one side. The prototype spans allow for a symmetric zero moment locations at both sides of a transverse bridge frame, which in turn results in symmetric test of the subassembly dimensions. For the transverse direction, the zero moment location along the bent cap beam is controlled mainly by the direction of the lateral load; see Figure 3.6. The beam zero moment location varies from approximately one-third to one-half of the span to either side of the

middle column as the lateral load direction is reversed. Meanwhile, the beam zero moment location varies from approximately one-half to two-thirds of the span adjacent to the outer columns. The test subassembly is considered for both earthquake cyclic loading and hybrid simulation with load reversals. Therefore, an approximate location of the zero moment is chosen to be at one-half of the beam span to account for the load reversals. The last component of the global geometry of test subassembly is the bent column. For a multi-column bent, a hinged pile cap is used as the column foundation. Therefore, the zero moment location along a hinged column is at a support location, i.e., the full column height is engaged and consequently considered in the resulting test subassembly.

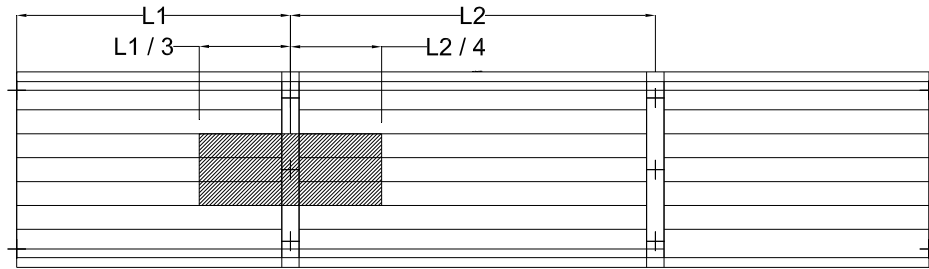


Figure 3.4 Subassembly considered for testing, identified as the prototype bridge.

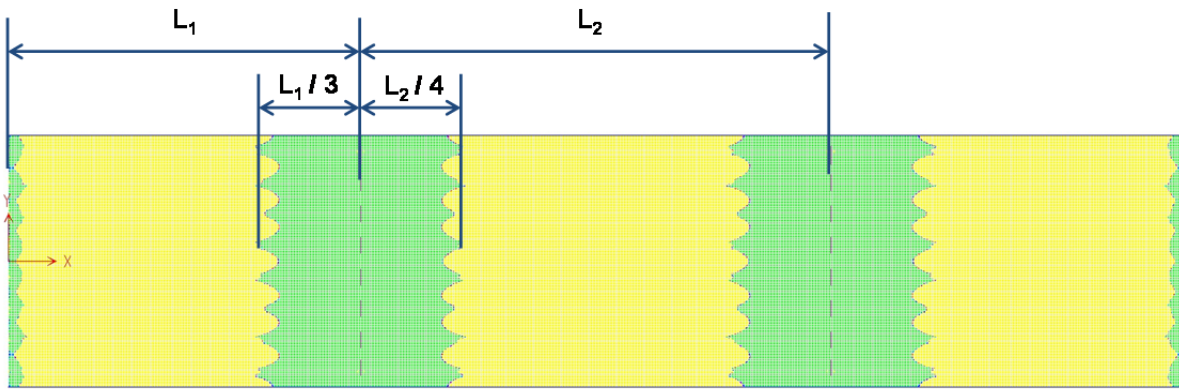


Figure 3.5 Locations of zero moments along the longitudinal direction of the prototype bridge under vertical gravity loading.

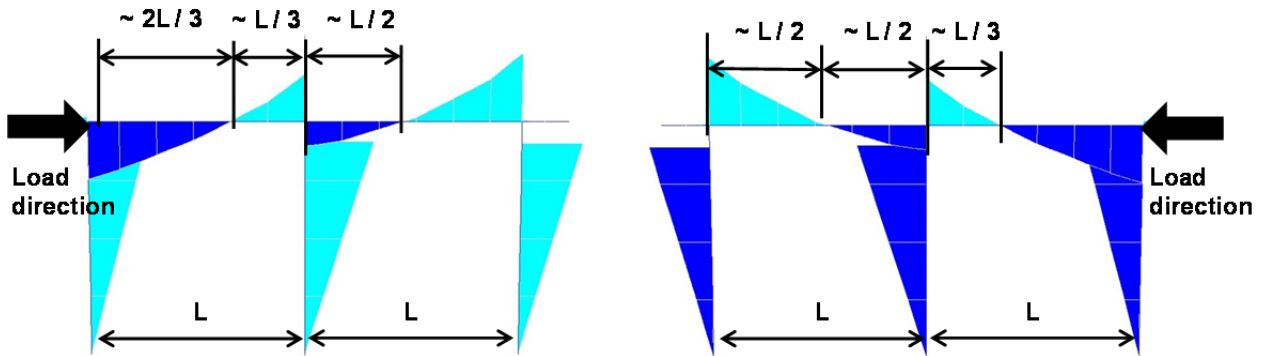


Figure 3.6 Locations of zero moments along the transverse direction of the prototype bridge under combined vertical and lateral loading.

As a result of the identified zero moment locations for each of the column, bent cap beam, and box-girder along with the available reaction frame height and laboratory space at the Structures Laboratory at UCB, a maximum scale of one-quarter is proposed for the test subassembly. The dimensions of the resulting test subassembly at one-quarter scale were found to be acceptable in light of the reaction frame dimensions and laboratory space. The expected forces required for the one-quarter-scale subassembly during either the quasi-static or hybrid simulation tests were found from pre-test analyses (see Chapter 4) to be accommodated within the available actuators capacities. In addition, the one-quarter scale allows for the use of normal concrete aggregate and standard reinforcement sizes. Therefore, a reduced one-quarter-scale test subassembly was finalized for the two test specimens considered in this study.

3.3.2 Boundary Conditions

To simplify the testing and the construction, the test specimen (the subassembly) was oriented upside-down with the box-girder and the cap beam against the floor and the column in the air. Given that the specimen was to be tested under combined vertical gravity and bi-directional lateral loading, a stable test set-up required proper boundary conditions for load application and resisting forces against the laboratory strong floor and reaction frame in the three global axes X , Y , and Z . How the boundary conditions affect the specimen geometry is presented below; details of the test set-up are presented in Section 3.5.

The inverted position required that the minimal physical boundary conditions relative to the regular orientation were required at five locations; the column end, namely (*action*), the two cap beam ends (*reaction*), and the two box-girder ends (*reaction*) as follows:

- The vertical and lateral actuators were connected directly at the inverted column top end at the anticipated zero moment location. Thus, no footing or pile cap was needed in this orientation; only a column head that facilitated the actuators' connection to the column was considered. A hexagonal shape column head was found to be the best geometry for accommodating the connections of the vertical and lateral loading systems.
- Two vertical struts were considered at the two cap beam ends. The vertical strut provided a vertical reaction only, while allowing for translation in the two horizontal directions, full rotations around the X - and Y -axes, and partial rotation around the Z -axis. This was intended to mimic the reactions at the chosen zero moment location for the symmetric subassembly.
- Two seat beams were considered at the box-girder ends. The seat beams were monolithically casted with the specimen at the box-girder ends. Such monolithic setting was expected to fully restrain the three translational DOFs, while partially restraining the rotations. Ideally, the rotations are required to be unrestrained to allow for the desired zero moments at such locations. This partial rotational fixation was necessary because the deck slab stiffness was much smaller relative to the seat beam and could have caused a cracking mechanism at the interface. It is assumed that such dynamic cracking

mechanism, i.e., opening and closing cracks, at that slab/seat beam interface will be able to accommodate the very small rotations at the box-girder ends without creating undesired large bending moments. This assumption was verified analytically using a SAP2000 [2012] model for the subassembly using different hinged and fixed end supports; see Chapter 4 for more details.

Based on the framework discussed above for the evolution of the test specimen geometry, scale and boundary conditions, the final specimen components and dimensions are summarized in Table 3.2 and presented in three different views in Figure 3.7.

Table 3.2 Summary of the reduced 1/4-scale specimen dimensions.

Column diameter	18 in.
Column height	90 in.
Cap beam/superstructure height	20-3/8 in.
Cap beam width	24 in.
Deck slab thickness	2-5/16 in.
Soffit slab thickness	2-1/16 in.
Box girder web thickness	3 in.
Clear width of box cell	30 in.
Clear height of box cell	16 in.
Subassembly overall length	264 in.
Subassembly overall width	102 in.

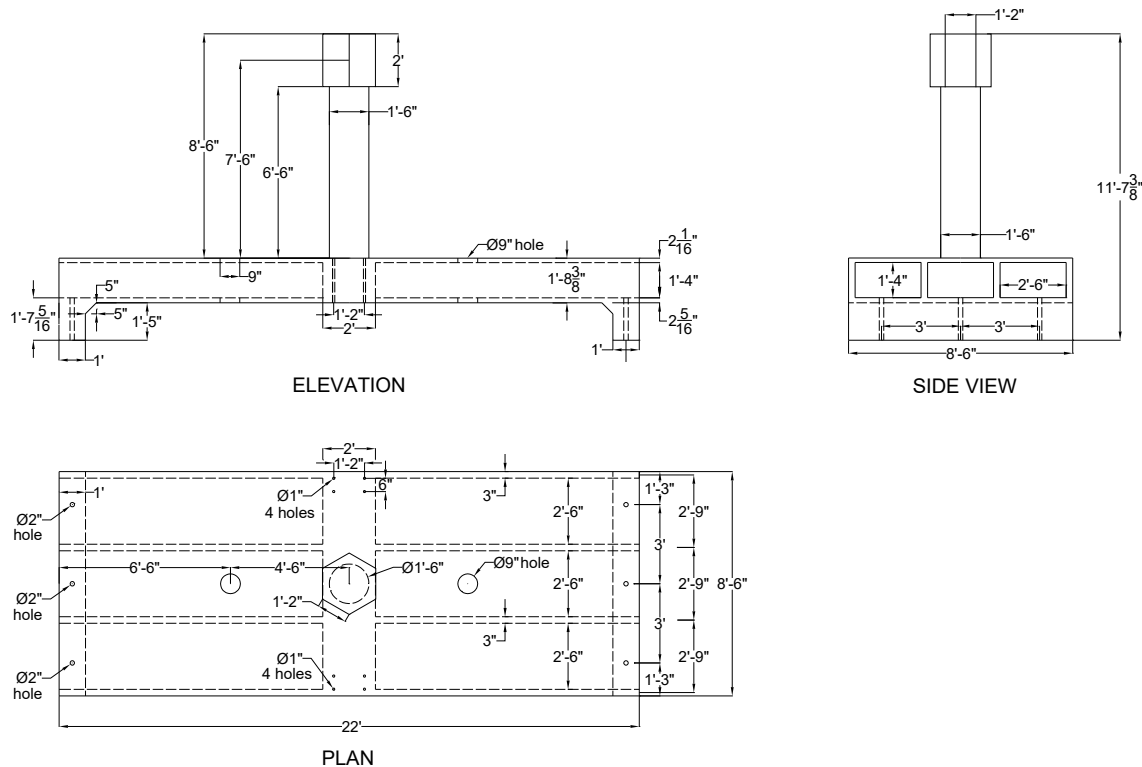


Figure 3.7 Different views of the 1/4-scale subassembly specimen.

3.4 SPECIMEN DESIGN

Two identical specimens were considered for this study; they were identical in design but subjected to different loading protocols. A brief summary of the specimen design and cross-section reinforcement is presented below; see Appendix A for details of the specimen design loads and calculations of required reinforcement.

To calculate the design loads for the reduced-scale specimen, first, the SAP2000 [2012] full prototype bridge model was used to estimate the loads and straining actions due to dead and live loads at the relevant structural element. Next, the element straining actions were scaled down according to the proper similitude relationships and used to design the different specimen sections. In addition, the provisions of the Caltrans SDC [2010] and the *AASHTO LRFD Bridge Design Specifications* [2007] were considered to estimate seismic design loads. The bent cap beam and box-girder superstructure were flexurally designated as capacity protected components to remain elastic when the column reached its overstrength capacity; see Appendix A for details of the utilized seismic capacity design approach.

The design of the specimen included flexural and shear design for each of the column, cap beam, beam-column joint, box girder deck and soffit slabs, box girder webs, and the seat beams required for the specimen attachment to the strong floor of the laboratory. The effect of prestressing was neglected in designing the box-girder. Although the prototype bridge comprises a longitudinally post-tensioned PC box-girder, this study focused only on the behavior of the cap

beam and box-girder slab contribution in the bridge transverse direction. Thus, no prestressing was needed for the specimen as long as the box-girder remained elastic in the longitudinal direction. The design was in accordance with *AASHTO LRFD Bridge Design Specifications* [2007], Caltrans SDC [2010], and ACI-318 [2008]. Reinforcement details of the main specimen's components are summarized in Table 3.3, and all of the specimen cross sections are shown in Figure 3.8.

Table 3.3 Summary of the specimen cross-sections reinforcement.

Column	16 #6 longitudinal bars
	#3 spiral at 2-1/2 in.
Cap beam	8 #5 negative reinforcement
	8 #5 positive reinforcement
	#3 stirrups with 4 branches at 5 in. spacing
Box-girder	#3 with standard hook in transverse direction at 4 in. spacing
	#3 straight bars in longitudinal direction at 2-1/2 in. spacing
	#3 single branch tie at 4 in. spacing

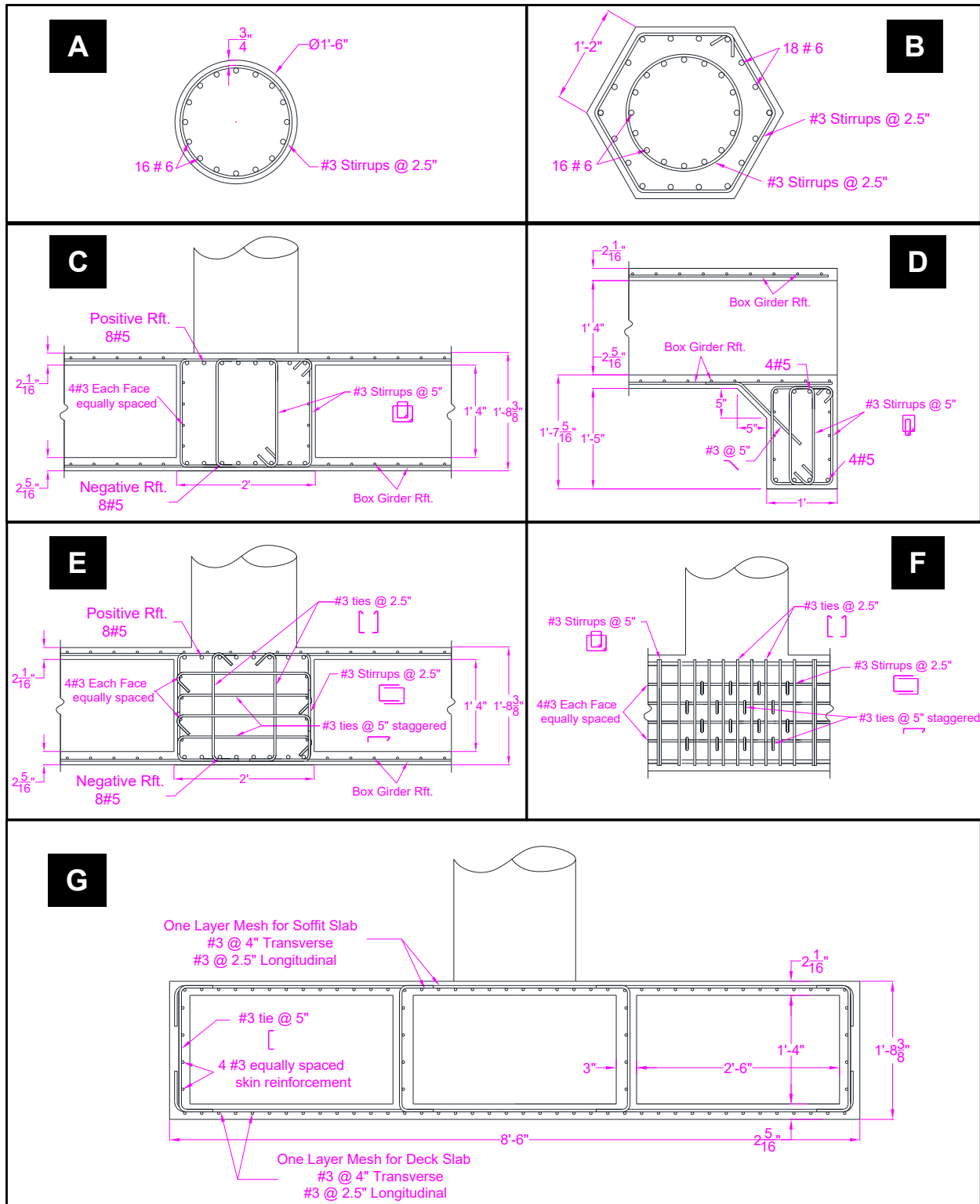


Figure 3.8 Dimensions and reinforcement details for each of the specimen components: (A) column, (B) column head, (C) cap beam, (D) seat boundary beam, (E) joint reinforcement in transverse direction, (F) joint reinforcement in longitudinal direction, and (G) box-girder.

3.5 TEST SET-UP

To facilitate the experimental program, the two specimens considered were constructed and tested upside down. Because the objective of the tests was to investigate the behavior of bent cap and slab contribution under combined vertical and lateral load, vertical and lateral loading systems were required. All loads were applied at the column end in its inverted position, while the specimen was line supported on two concrete beams at the box-girder ends and additionally point-supported by two vertical struts at the cap beam ends. A schematic representation of the test set-up, including the loading systems and boundary supports, is shown in Figure 3.9. The detailed test set-up and the relative locations of the loading actuators and supports are shown in different views in Figures 3.10 and 3.11.

The gravity load was applied at the column free end—with the top end in the inverted position—through two vertical hydraulic actuators and a steel spreader I-beam placed on top of the column head. The actuators pull downwards on the spreader beam through pinned connections from one end and react against the laboratory strong floor, also through pinned connections at the other end. All pinned connections were achieved through 3D ball-bearing clevises. Due to practical considerations, the spreader beam span had to be limited to avoid excessive flexibility, and to achieve constant and stable vertical load. Thus, the vertical actuators had to pass through both of the soffit and deck slabs of the specimen's box-girder to reach the strong floor. Two 9-in. holes were made in both slabs and at the two sides of the column for the actuator rods to pass through. Special 3-in.-diameter and 2-ft-long rods were fabricated to allow for the extension of the actuators. In addition, a 1-in. elastomeric rubber pad was used between the spreader beam and the concrete column top to avoid any stress concentration due to concrete surface imperfections and achieve a vertical uniform load application.

The lateral load was also applied at the column head, using two lateral hydraulic actuators that reacted against the laboratory steel reaction frame, as shown schematically in Figure 3.10. The lateral actuators setting allowed for applying both cyclic loading during the quasi-static testing of first specimen and the online computed earthquake displacement input during the hybrid simulation testing of the second specimen. To provide stability during both unidirectional and bi-directional loading, the actuators were located in one horizontal plane but connected to the column head at two inclined directions rather than two orthogonal directions; accordingly, two special considerations were required. First, geometric transformation was needed to transform the desired input displacements in X - and Y -directions that correspond to the bridge subassembly transverse and longitudinal directions, respectively, to the local actuators directions. Second, the column head geometry had to be designed to facilitate the two inclined lateral actuators connections. Based on the attachment points of the actuators to the reaction frame and the distance between the frame and the column head, a hexagonal shape was found to be the best choice, although more difficult to fabricate.

Similar to the vertical actuators end connections, the lateral actuators end connections were also 3D pins. The pinned nature of the actuator to the column head connection ensured the application of only lateral force without any vertical loads or bending moments. One-inch-thick steel plates were installed on the two opposite sides of the hexagonal column head and

prestressed together. The actuators were then bolted to the front plates. Thus, when the actuators extended, the force was transferred to the column as bearing on the front face directly. When the actuators retracted, the force was transferred through the prestressing to the other face of the column head and bearing was achieved from the back sides.

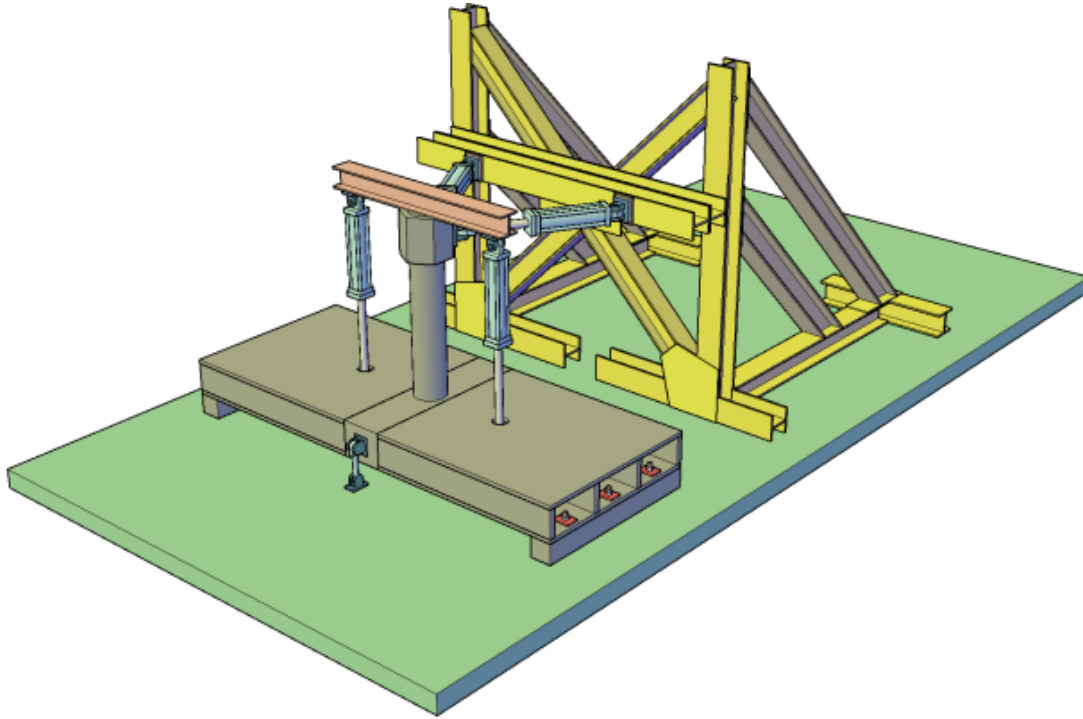


Figure 3.9 Schematic 3D view of the test set-up.

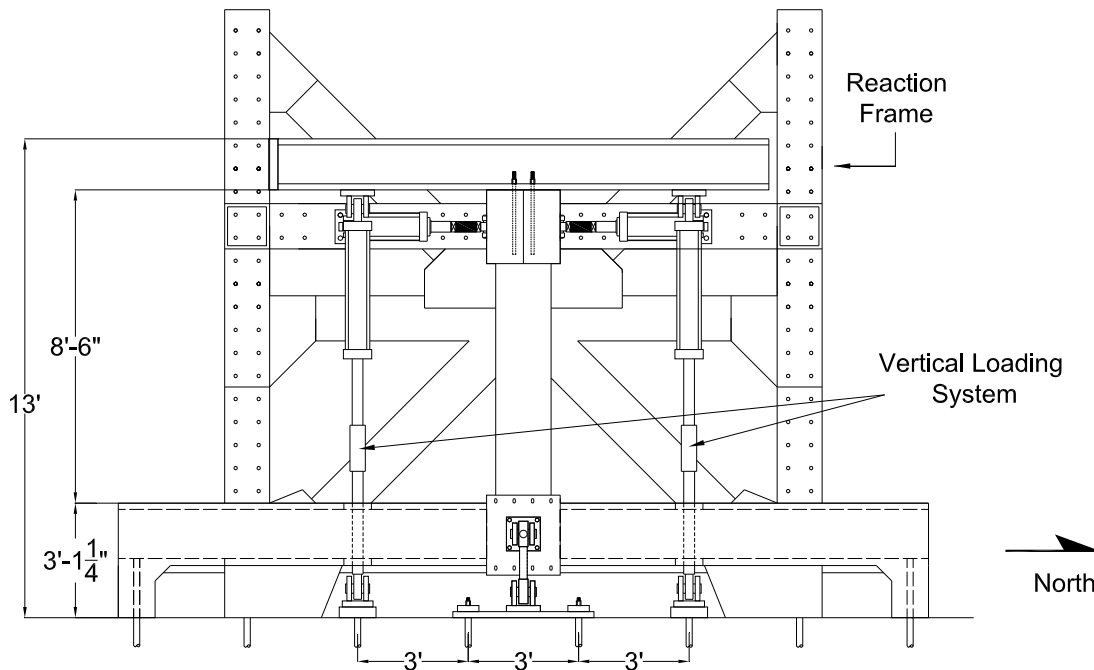
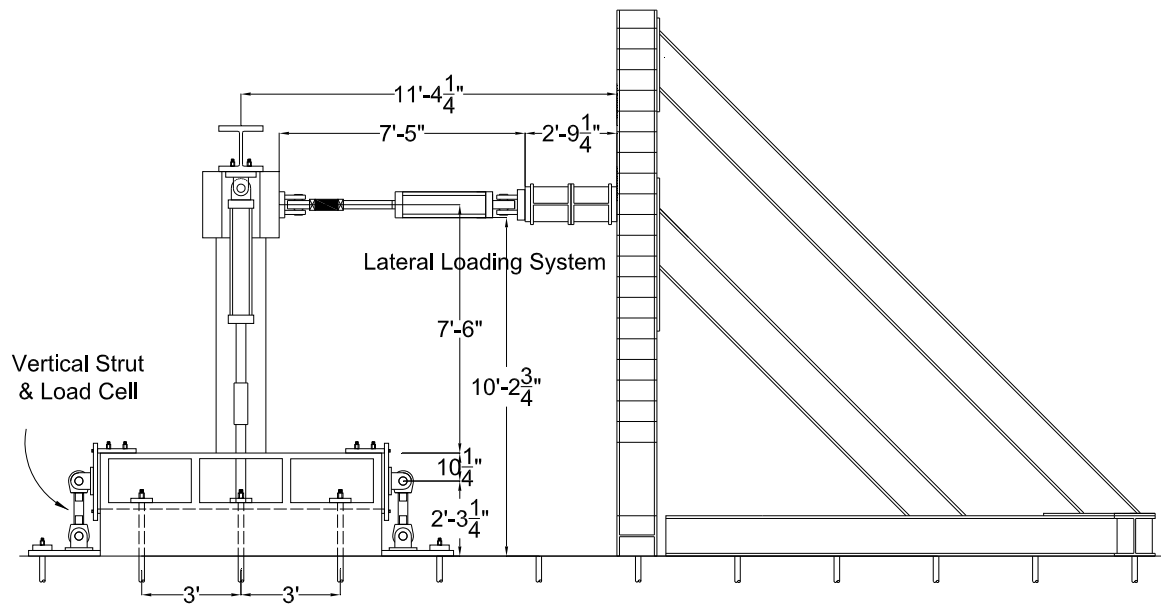
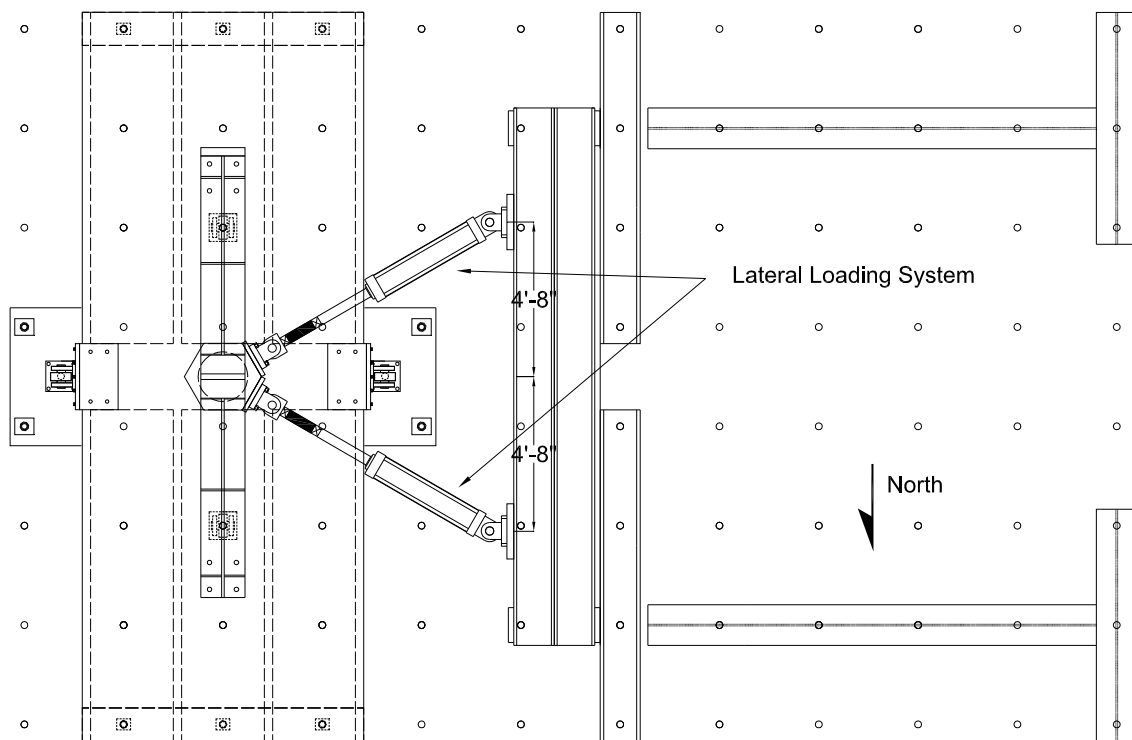


Figure 3.10 Elevation view of the test set-up.



SIDE VIEW



PLAN VIEW

Figure 3.11 Side and plan view of the test set-up.

As previously discussed, the specimen was attached to the laboratory strong floor through the seat beams and two vertical struts at the cap beam ends. The two RC seat boundary beams were cast monolithically with the specimen. Each beam had three through-pipes that were 3 ft apart and matched with the laboratory strong-floor hole pattern. The seat beams were hydrostoned to the strong floor, and then a total of six prestressing rods were used to prestress the specimen down to the strong floor. To provide the necessary horizontal and vertical reactions during lateral loading, the hydrostone and prestressing guaranteed enough friction resistance with the strong floor at the bottom faces of the seat beams bottom face.

To provide vertical reactions during application of the gravity and lateral loads, two vertical 1D struts, designed to mimic a roller support, were also used at the cap beam ends. The strut vertical reaction was designed to be transferred to the cap beam through the bearing to avoid any unnecessary shear or tensile stress states at the cap beam ends, and to achieve uniform stress distribution along the entire cap beam width. The load path at the cap beam end began with the vertical force in the strut reacting against the strong floor and transmitted to a side plate through four shear bolts and small bearing edge blocks around the clevis plate. The force was then transmitted from the side plate to the top and bottom plates through ten shear and friction bolts. The top and bottom plates were prestressed together to guarantee the only compression stresses exist at the cap beam end. Note that the top and bottom plates were hydrostoned to the cap beam surface to avoid any stress concentration resulting from the surface inconsistencies. Figure 3.12 is a schematic drawing of the vertical 1D strut along with the actual fabricated strut end connection; see Appendix D for a detailed photographic catalog of the test set-up procedure. The final assembled test set-up is shown in Figure 3.13.

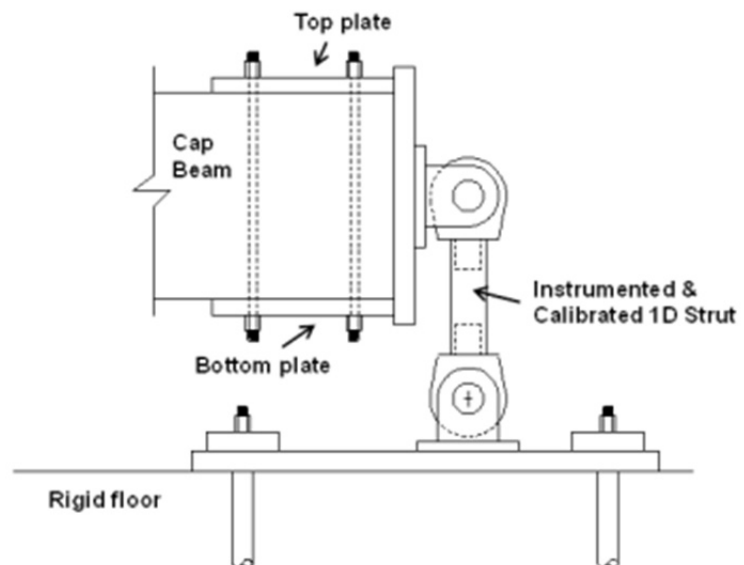


Figure 3.12 Vertical 1D calibrated strut used at the specimen's cap beam ends.

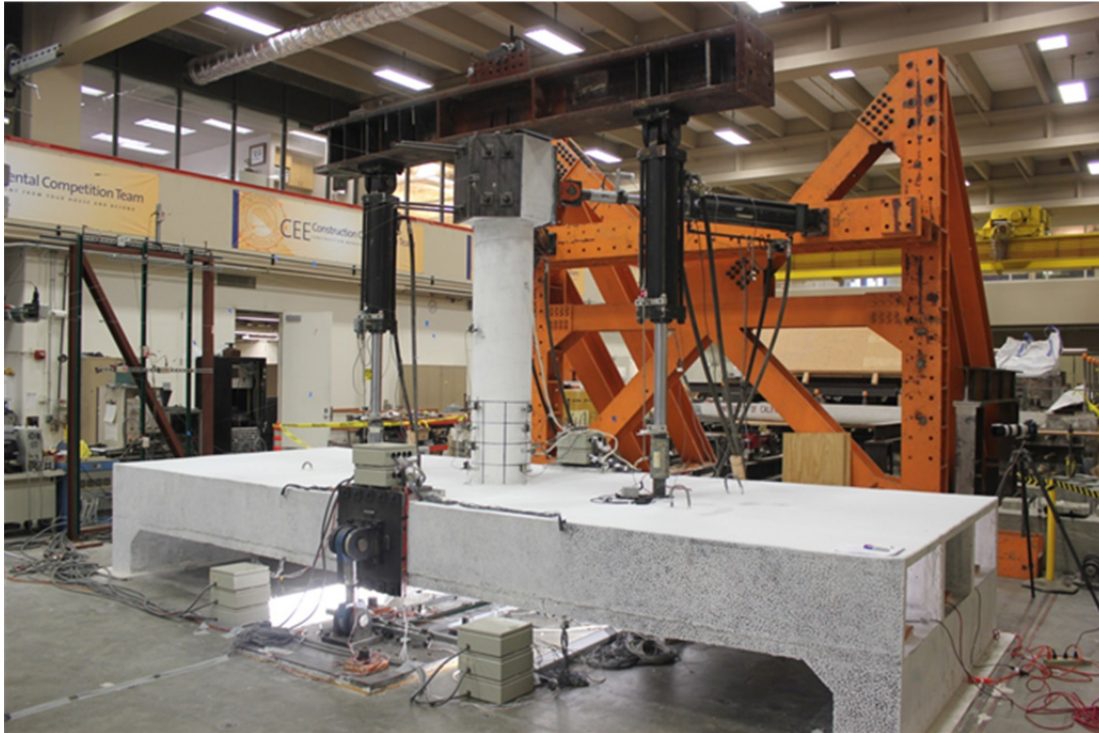


Figure 3.13 Test set-up for the bridge subassembly tests.

3.6 EXPERIMENTAL PROGRAM

The details of the testing sequencing and basis for the repair and retrofit decisions are presented below.

3.6.1 As-Built Specimen One: Quasi-Static Testing

The first test in the four-test series was a quasi-static test for Specimen No. 1, which was tested as-built under combined constant gravity load and bi-directional cyclic lateral loading. Two different levels for gravity load were used in the first cyclic loading test such that the first level corresponded to only the dead load, while the second level considered additional loads due to live loads and earthquake excitations. The bi-directional cyclic loading was applied independently in one direction at a time, i.e., a group of cycles was applied in the column-bent cap plane (transverse direction) then followed by a similar group of cycles in the box-girder longitudinal direction. The observed mode of failure was the desired Caltrans SDC weak-column–strong-beam mechanism (WCSB), which motivated expansion of the experimental program. Based on that observed behavior and test results of Specimen No. 1, it was decided to strengthen Specimen No. 2 before conducting any tests in an attempt to transfer higher moment demands to the bent cap beam. Meanwhile, Specimen No. 1 was repaired and re-tested twice. Description of each of these tests in the updated experimental testing program along with the objective behind the repair or retrofit decision are discussed in the following subsections.

3.6.2 Repaired Specimen No. 1: Quasi-Static Testing

Before proceeding with further testing, Specimen No. 1 was repaired, and Specimen No. 2 was retrofitted using Carbon Fiber Reinforced Polymer (CFRP). The first test left Specimen No. 1 completely damaged with several ruptured rebars. Thus, repair of the specimen was conducted to achieve a more stable system for the HS system development and trial tests before conducting HS test on Specimen No. 2. A quasi-static cyclic loading test was also conducted on repaired Specimen No. 1 before conducting the HS trial tests for comparison's sake with the test results of the original as-built specimen.

Accordingly, the second test in the four-test sequence was a similar quasi-static test compared to the first test but applied to repaired Specimen No. 1. A constant gravity load that corresponded only to the second level used in the first test along with bi-directional cyclic lateral loading was adopted for the second test. A similar group of cycles used in the first test were reapplied for the repaired specimen in the second test. However, the second test was intentionally stopped without applying the last group of cycles in both transverse and longitudinal directions group to ensure that the repaired specimen would retain sufficient remaining force capacity for the HS system development trials.

3.6.3 Repaired Specimen No. 1: Hybrid Simulation Development Testing

The third test used repaired Specimen No. 1. The main objective of this test was to provide a real HS test trial to verify the development of an HS system that would be applicable to future tests. Two main aspects of the development were verified through the third set of tests. The first was the back and forth communication between the computational and physical components of the hybrid system. It was necessary to ensure that the computed input displacements passed to the actuators and resulting forces measured at the actuators' load cells fed back to the computational platform through a robust communication loop. The second aspect of verification concerned the geometric transformation between global DOFs used in the computational model and the actuators' local DOFs. Both aspects were successfully verified through several test runs that used the Northridge earthquake excitations recorded at both of Sylmar and Rinaldi stations. The tests were conducted with and without the application of gravity loads. Note that the gravity load application was an essential part of the original test plan. Test trials that did not involve the gravity load were only intended to check the stability of the developed HS system.

3.6.4 Retrofitted Specimen No. 2: Hybrid Simulation Testing

The fourth and final test in the experimental program was HS testing of retrofitted Specimen No. 2. The retrofit was aimed at strengthening the column using CFRP to amplify the moment demand on the cap beam for further bent cap capacity evaluation and to explore different modes of failure. Another objective was to investigate whether or not an over-designed retrofit scheme could migrate the failure to different parts of the bridge; the effectiveness of CFRP confinement was also explored. The HS tests involved several runs that included uni- and bi-directional testing, different scales for the lateral excitations, and different levels of gravity load.

A new testing scheme was proposed and considered in a few of the HS test runs to account for the P -delta effect, which incorporated not only the gravity load but also the effect of the vertical component of the earthquake excitations. The HS runs mainly used the Rinaldi record from the Northridge earthquake at various scales up to 200% and three levels for the gravity load. Two of the gravity load levels were similar to the ones used in the first quasi-static test. The third level was used to further increase the moment demands in the bent cap beam and to be compatible with the higher excitation levels. More details regarding the loading protocol are presented next.

3.7 LOADING PROTOCOL

Two different types of lateral loading techniques were utilized in the experimental program: (1) a quasi-static cyclic loading with a prescribed load pattern; and (2) an online computed earthquake response input signal applied through HS test. While the lateral loading was applied either during a cyclic loading test or a HS test, through force control a constant gravity load was also applied during all tests. Meanwhile, lateral cyclic and HS input signals were applied using slow-rate displacement control. A rate of loading of 0.02 to 0.06 in./sec was used and varied based on the loading cycle or HS signal level. The higher the loading amplitude, the faster the loading rate became to ensure that the total testing time was reasonable.

For the cyclic tests, the lateral loading was an offline signal adopted from the FEMA 461 [2007] guidelines. The input signal for the lateral loading in the HS tests, however, was an online signal computed and updated based on a multi-DOF computational model subjected to the Rinaldi record from the Northridge earthquake. The gravity load levels for the HS tests were similar to those used in the quasi-static cyclic tests, except for an additional level that was used only in the last few HS tests.

3.7.1 Gravity Loads

As discussed earlier, a constant gravity load was applied through two vertical actuators and a spreader beam at the top of the inverted column. The total gravity load was split evenly between the two actuators. The vertical gravity load was applied first through force control before any lateral loading and remained almost constant during all tests. However, two levels of gravity load were used during cyclic tests, and a third level was used in the HS tests. The lowest gravity load level used was 82 kips (approximately 5% of the column axial capacity), which was used in small-level cycles before the first yield. The second level was double the value of the first level, i.e., 164 kips (approximately 10% of the column axial capacity). For the few HS tests that experienced a third higher level of gravity load, a total load of almost 240 kips (approximately 14.5% of the column axial capacity) was applied, which was the maximum load that could be applied by the vertical actuators.

The criteria for choosing the values and different levels of the gravity load considered the pre-test analysis results and practical considerations, and axial load values from bridge engineering practice. The first level of 82 kips load was chosen to obtain initial bending

moments in the bent cap beam that resembled the bending moments in the prototype bent cap under the distributed dead loads, with proper consideration of similitude relationships; however, the 82 kips value was not sufficient to mimic the prototype's corresponding value for the column axial load. Because the effects of additional live load and the vertical component of earthquake excitations may increase both the column's axial load and the bending moments in the bent cap beam, the second level of the gravity load at 164 kips was used for the higher levels of lateral cyclic and HS loading, where it was more crucial to model accurate column axial loads for correct confinement effects. It was decided to double the initial gravity load level to account for proper column axial load, consider additional live loads, and approximately account for axial force fluctuation due to the earthquake vertical excitations.

Expressing the gravity load level in a way that is more appealing to bridge engineers is to relate the gravity load value to the axial load capacity of the column. The axial capacity of the circular column can be approximated as the gross sectional area times the concrete compressive strength. The actual compressive strength was available from the material tests; see Section 3.9. The Caltrans SDC expected compressive strength was used rather than the actual strength for consistency because the different tests were conducted at different times where concrete properties varied. In addition, in engineering practice the axial load is related to the expected compressive strength rather than the nominal 28-day compressive strength due to the lack of actual material data during design. Accordingly, an expected compressive strength of 1.30 times the 5 ksi nominal 28-day strength was used. The resulting gravity load to column axial capacity ratio, referred to as axial load ratio (*ALR*) for brevity, for the 82 kips and 164 kips was 5% and 10%, respectively. The third level used in last set of HS tests corresponded, in turn, to approximately 14.5% axial load ratio. Equation (3.1) is an example of how the axial load ratio of 5% was calculated:

$$ALR (\%) = \frac{P}{A_c \times f'_{\text{expected}}} = \frac{82}{254 \times 6.5} = 5\% \quad (3.1)$$

where $P = 82$ kips is the gravity load (column axial load), $A_c = \pi/4 \times 18^2 = 254 \text{ in.}^2$ is the gross area of the circular column, and $f'_{\text{expected}} = 1.3 \times f'_c = 1.3 \times 5 = 6.5 \text{ ksi}$ is the expected compressive strength per the Caltrans SDC [2011].

3.7.2 Cyclic Load Pattern

To represent real lateral loading conditions in case of earthquake loading, a bi-directional cyclic loading scheme was optimal. Several options were considered for the bi-directional interaction: (1) a circular orbit per Hachem and Mahin [2000], (2) an elliptical orbit for bi-directional loading per Terzic and Stojadinović [2010]; and (3) a cross-shape orbit for bi-directional loading, i.e., alternating unidirectional cycles where a group of cycles is applied in one direction at a time. The third alternative was chosen for this study because it best served the investigation of the bent cap beam. Loading in the plane of the bent cap was indispensable to better understand the box-girder slab contribution and evaluate the effective slab width. Moreover, the torsional effects on the cap beam could be still considered when loading is pursued in the orthogonal direction to the

cap beam plane. Another reason for considering applying the load in one direction at a time is because it is more suitable for FE model calibrations and post-test analyses. Finally, some of the HS tests were planned to be bi-directional, with actual interaction considered through a computational model.

The second issue in finalizing cyclic loading patterns was the choice of the number and amplitude of the cycles in the different groups. Several past studies considered cyclic loading histories and patterns for quasi-static tests only, such as Leon and Deierlein [1996], Krawinkler [1996], and Clark et al. [1997], among others. Krawinkler [2009] compared several loading histories adopted from different standards and studies for seismic acceptance testing and performance-based design. Loading histories from ATC-24 Protocol [1992], SAC Protocol [Clark et al. 1997], SPD Protocol [Porter and Cherif 1987], CUREE [Krawinkler et al. 2000], ISO [1998], and FEMA 461 [2007] were compared. Based on Krawinkler's comparison, the authors' opinion is that the protocols are similar and are expected to produce similar performance assessments. Consequently, the FEMA 461 [2007] loading protocol was adopted in this study because it is the most current and was similar to other loading protocols.

According to FEMA 461, two cycles are applied at each ductility level, and the suggested ductility levels (μ) for testing are as follows: 0.25μ , 0.35μ , 0.50μ , 0.70μ , 1.0μ , 1.4μ , 2.0μ , 2.8μ , 4.0μ , 5.6μ , and 8.0μ . For control purposes, the amplitudes needed to be determined in displacement values. Based on hand calculations, a preliminary value of 1 in. was assumed for the column yield displacement to conduct the 0.25μ to the 1.0μ level tests. Next, the strain values in the column rebars were checked at the 1.0μ level test to verify if yielding took place or not. The strains were found to be less than the yield strain obtained from material tests. Therefore, another value of 1.25-in. yield displacement was used based on pre-test analysis results, which corresponded to when the first column yield actually did occur. The high-level cycles of 1.4μ , 2.0μ , 2.8μ , 4.0μ , 5.6μ , and 8.0μ were then related to the 1.25-in. yield transverse displacement, and the test was conducted accordingly. A plot summarizing both of the gravity load and all the lateral loading cycles that were applied during the full quasi-static test of the first specimen is shown in Figure 3.14. Photographs of the loaded specimen during the test in the transverse and longitudinal directions are shown in Figures 3.15 and 3.16, respectively.

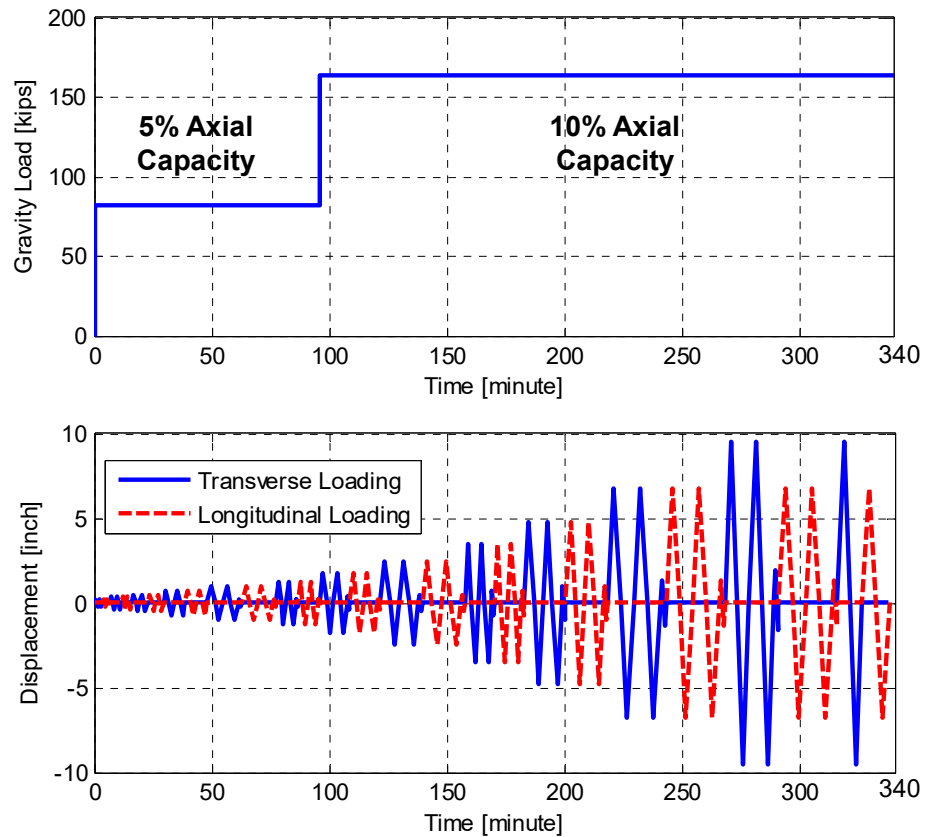


Figure 3.14 Final loading protocol used for the first specimen cyclic loading test.

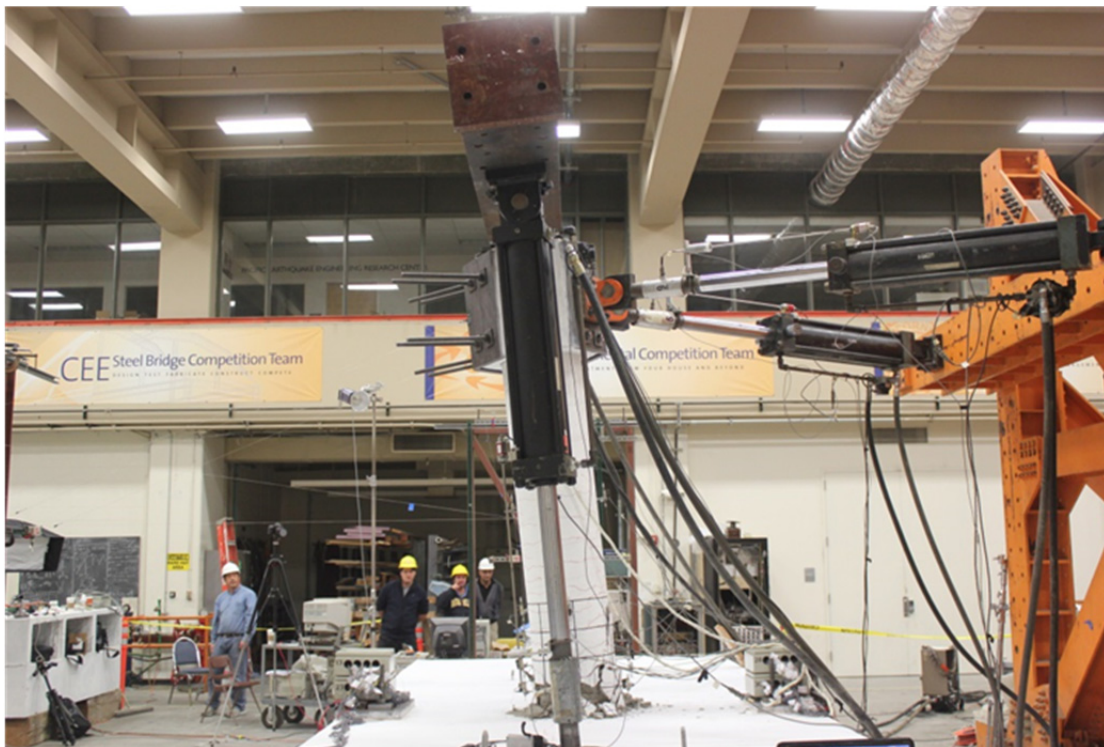


Figure 3.15 A view of first specimen test in progress under transverse cyclic loading.



Figure 3.16 A view of first specimen test in progress under longitudinal cyclic loading.

3.8 CONSTRUCTION OF SPECIMENS

Two identical specimens were constructed simultaneously at the Structures Laboratory at UCB. All phases of construction were conducted by a professional construction company, and ready concrete mix was delivered to the laboratory site in three different lifts. The specimens were constructed in three phases, and fresh concrete was cast at the end of each phase; this led to the existence of cold joints in the specimens. The construction phases and cold joints location were chosen to be as close as possible to real bridge construction. Similarly, the formwork and reinforcement fabrication adopted common practices in bridge construction to mimic actual construction conditions. Brief description of the different construction phases is presented below; see Appendix C for additional details of the construction process.

Phase 1 of the construction included laying out the formwork for the seat beams and the box girder deck slab, furnishing the deck slab transverse and longitudinal reinforcement, constructing the column and bent cap beam steel cages, placing all the steel cages in place, and casting the first concrete lift that included the seat beams and whole deck slab. Figures 3.17 and 3.18 show the deck slab reinforcement, column and cap beam cages, and casting of first concrete lift for the two specimens concurrently. Curing blankets in addition to the chemical E-CURE were used for curing during the first day after concrete casting to avoid shrinkage cracks.



Figure 3.17 (a) Reinforcement steel mesh for the deck slab and (b) fabrication and setting up of the column and cap beam steel cages.



Figure 3.18 Seat beams and box-girder deck slab concrete placement (first lift).

Phase 2 was the most complicated since it involved the construction of the rest of the box-girder, including its cells and cap beam. This phase started the following day after the deck slab was initially set by placing custom-made cardboard boxes (Figure 3.19) to create the inner cells of the box-girder section. Real bridge construction leaves the box-girder inner formwork in place; however, they were removed in this study to monitor response and facilitate crack observation, thus requiring use of the cardboard formworks. The box-girder web and soffit slab reinforcement was also laid out as part of this construction phase; see Figure 3.19. This phase was concluded with the second concrete lift, which included cap beam and all the box-girder webs and soffit slab. The concrete surface was smoothly finished (see Figure 3.20) and then cured using E-CURE and curing blankets to avoid shrinkage cracks in the thin soffit slab.

Phase 3 involved casting the specimens' columns and column heads. A sonotube was used for the circular column construction, and special timber formwork and platform was used for the hexagonal column head; see Figure 3.21. The last concrete lift was dedicated to casting the column and column head. The overhead crane at the laboratory was used to convey the hopper to the column top (see Figure 3.21). After construction was completed, three weeks after the last concrete lift was cast all formwork was removed. Figure 3.22 shows the cardboard formwork removal and the final specimen configuration before placement in the test set-up.



(a)

(b)

Figure 3.19 (a) Installing custom-made cardboard boxes for box-section and (b) furnishing reinforcement steel mesh for the soffit slab.



(a)

(b)

Figure 3.20 (a) Finishing the surface of the second concrete lift and (b) curing of concrete surface using curing blankets.



(a)

(b)

(c)

Figure 3.21 (a) Column and column head formwork and (b) and (c) placing and vibrating the concrete of the column and column head.



Figure 3.22 (a) Removing the cardboard boxes used to create the box-girder cells and (b) final specimen configuration.

3.9 MATERIAL PROPERTIES

Extensive material testing was conducted for concrete and reinforcing steel as part of the research program and is described below. A brief description of the materials used for the repair of the first tested specimen and the retrofit of the second specimen is included.

3.9.1 Concrete

Normal-weight concrete was used with a characteristic strength of 5 ksi and 3/8 in. maximum aggregate size because of the tight box-girder dimensions in the reduced-scale specimens. A similar concrete mix design was ordered for the three concrete lifts. A design water/cement (w/c) ratio of 0.411 was used, but each of the three lifts had a slightly different final w/c ratio, which varied between 0.385 and 0.413. Table 3.4 contains details of the mix design as provided by the vendor of the ready concrete mix vendor. A minimum slump of 7 in. was required to ensure proper workability and flowability of the concrete into the tight and congested box-girder and joint areas. A slump test was performed, and slump value was verified each time before accepting the concrete lift to avoid any construction problems; see Figure 3.23. The same figure also shows concrete cylinders, prisms, and notched-beams sampling for material testing.

Samples of the three concrete lifts used in the subassembly specimens were subjected to various compressive, tensile, and flexural tests. For determining the compressive characteristics, concrete cylinders were tested to determine the characteristic strength and strength gain, and compressive stress-strain relationships using load and displacement controls. For determining the tensile characteristics, the concrete was tested to determine splitting tensile strength and modulus of rupture. In addition, notched-beam samples were tested to determine the fracture energy.

Table 3.4 Concrete mix design.

Material	Description	ASTM	Specific Gravity	Admixtures (oz/yd)	Weight (lb)	Volume (ft ³)
Cement	Type I/II/V	C-150	3.15	-	752	3.82
Aggregate p gravel	Eliot 3/8"	C-33	2.68	-	1500	8.97
Natural Sand	Eliot Sand	C-33	2.65	-	1420.9	8.59
Type A Water Reducer	Wrda 64	C-494	1	2.0 - 4.0	-	-
Type F Hige Range Water	Adva 190	C-494	1	3.0 - 15.0	-	-
City Water	Water	C-94	1	37.0 gal	308.8	4.95
Air (2.5%)	-	-	-	-	-	0.67
TOTAL	-	-	-	-	3982	27.0

**Figure 3.23 Slump test (left) and concrete sampling for material tests (top and bottom right).****3.9.1.1 Compressive Strength Tests**

Compressive strength tests were conducted to monitor the strength gain of concrete with time at the standard ages: 7, 14, 21 and 28 days, and at each of the two main specimens test days (average age of 128 and 308 days for the cyclic test of Specimen No. 1 and the hybrid simulation test of Specimen No. 2, respectively). For this test, standard 6 in.×12 in. cylinders were used. The cylinders were cured next to the two subassembly specimens in same indoor laboratory conditions. The cylinders were capped with a sulfur compound and were tested in a Universal Testing Machine at the Concrete Laboratory of UCB in accordance with ASTM C39-05 [ASTM 2005]. The test set-up and a typical tested and crushed cylinder are shown in Figure 3.24. The test results for the concrete at all different ages are listed in Table 3.5. The strength gain of the concrete versus time (age) up to the standard 28 days characteristic strength, and actual strength on test days of the subassembly specimens is shown in Figure 3.25 for all three concrete lifts.

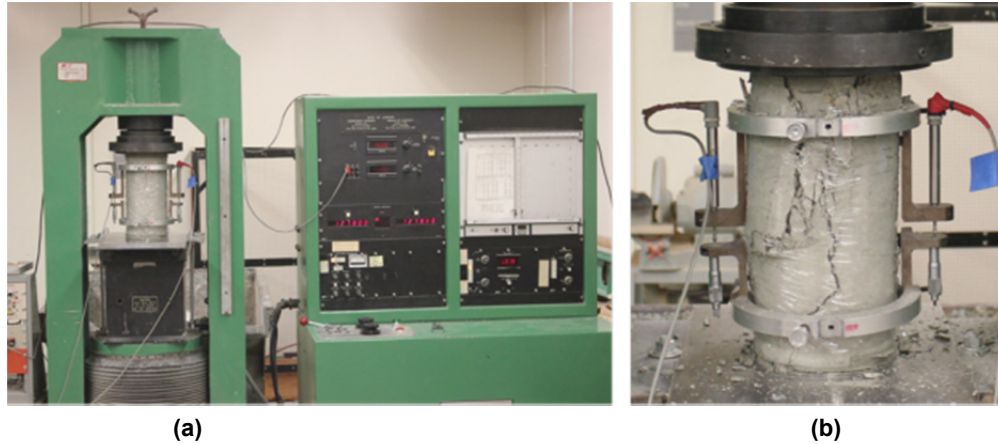


Figure 3.24 (a) Compressive strength test set-up and (b) typical mode of failure.

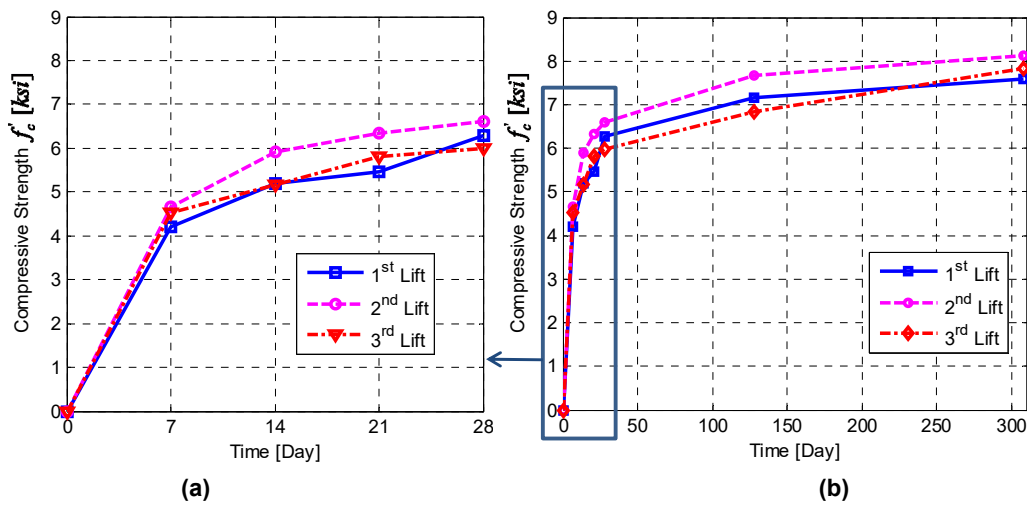


Figure 3.25 Strength gain for different concrete lifts up to 28 days (left) and up to final day of testing (right).

Table 3.5 Compressive strength test results.

	Age (days)	Stress at Peak (ksi)			Strain at Peak			Young's modulus (ksi)		
		Mean	St. Dev.	COV	Mean	St. Dev.	COV	Mean	St. Dev.	COV
Lift 1	28	6.27	0.18	0.028	0.0033	0.0002	0.074	3207.4	81.9	0.026
	128	7.15	1.03	0.144	0.0033	0.0009	0.264	3116.6	81.6	0.026
Lift 2	28	6.78	0.17	0.025	0.0033	0.0002	0.062	3215.7	66.3	0.020
	128	7.68	0.23	0.030	0.0029	0.0001	0.050	3565.9	84.7	0.024
Lift 3	28	5.30	0.73	0.138	0.0024	0.0006	0.237	3192.9	48.3	0.015
	128	6.85	0.36	0.053	0.0026	0.0001	0.042	3238.0	142.1	0.044

The same test set-up used for determining the compressive strength was used to obtain a compressive stress-strain test under force control to determine the constitutive behavior of concrete in the compression hardening region before the peak load. The only difference in protocol from regular compressive tests was the use of a compressometer around the cylinder to measure the strain (Figure 3.24). To estimate the stress-strain curve up to the failure point, a sample of three cylinders from each concrete lift was instrumented with the compressometer and tested at the age of 28 days and first specimen test day (128 days). The compressometer comprises two displacement transducers (LVDT) connected on the opposite sides of the cylinder to estimate average strain based on both transducers readings, as seen in Figure 3.24; see Table 3.6 for a summary of the test results (stress and strain at peak, and Young's modulus). From the stress-strain test, the modulus of elasticity E_c of concrete was computed using the secant stiffness at $0.4 f'_c$. A typical compressive stress-strain test results using force control from the 28 days test of the first concrete lift samples is shown in Figure 3.26.

Table 3.6 Stress-strain compressive test results using force control.

	Age (days)	Stress at Peak (ksi)			Strain at Peak			Young's modulus (ksi)		
		Mean	St. Dev.	COV	Mean	St. Dev.	COV	Mean	St. Dev.	COV
Lift 1	28	6.27	0.18	0.028	0.0033	0.0002	0.074	3207.4	81.9	0.026
	128	7.15	1.03	0.144	0.0033	0.0009	0.264	3116.6	81.6	0.026
Lift 2	28	6.78	0.17	0.025	0.0033	0.0002	0.062	3215.7	66.3	0.020
	128	7.68	0.23	0.030	0.0029	0.0001	0.050	3565.9	84.7	0.024
Lift 3	28	5.30	0.73	0.138	0.0024	0.0006	0.237	3192.9	48.3	0.015
	128	6.85	0.36	0.053	0.0026	0.0001	0.042	3238.0	142.1	0.044

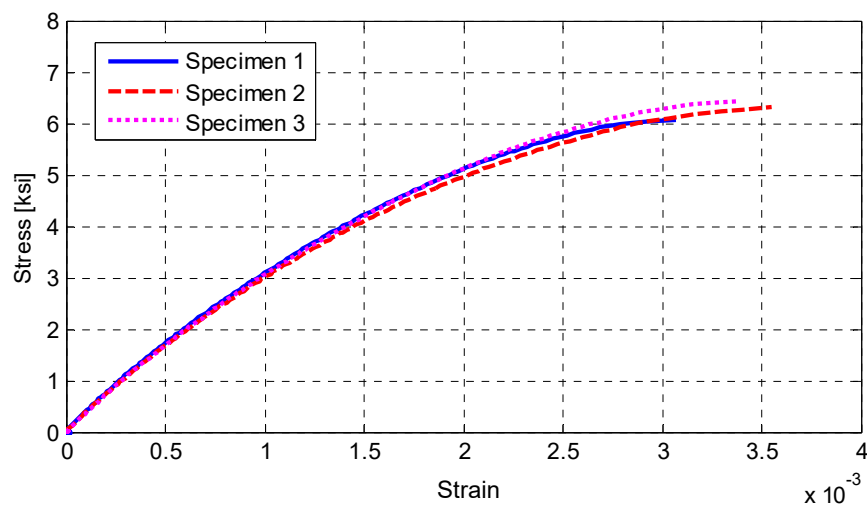


Figure 3.26 Typical concrete stress-strain relationship using a force-controlled test (results shown are for samples from first concrete lift tested at 28 days).

A compressive stress-strain test using displacement control was conducted to obtain a better estimate of the strain at peak and attempt to capture any post-peak constitutive behavior. A displacement-control testing machine and set-up at the University of California, Davis, was used for this purpose; see Figure 3.27. A total of nine cylinders (three from each concrete lift) were tested at age of 298 days, which was a few days before the HS test of Specimen No. 2. The summary of the test peak stress, strain at peak, and Young's modulus are shown in Table 3.7. Due to the nature of the loose compressometer used for such tests, the brittle failure of the cylinders displaced the compressometer significantly after failure. Thus, only a small portion of the immediate post-peak behavior and strain at peak were captured; see Figure 3.28.

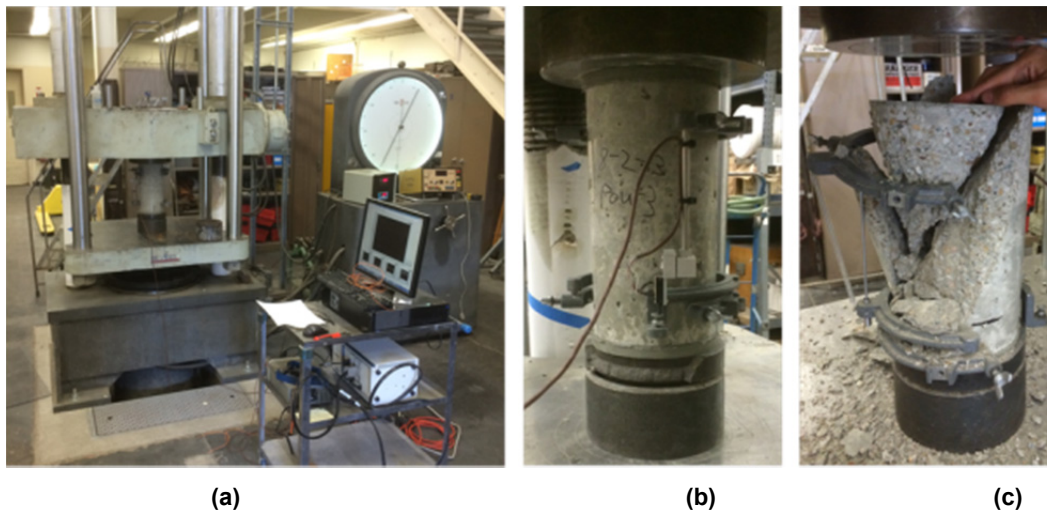


Figure 3.27 (a) Compressive test under displacement control at the University of California, Davis; (b), compressometer; and (c) typical mode of failure.

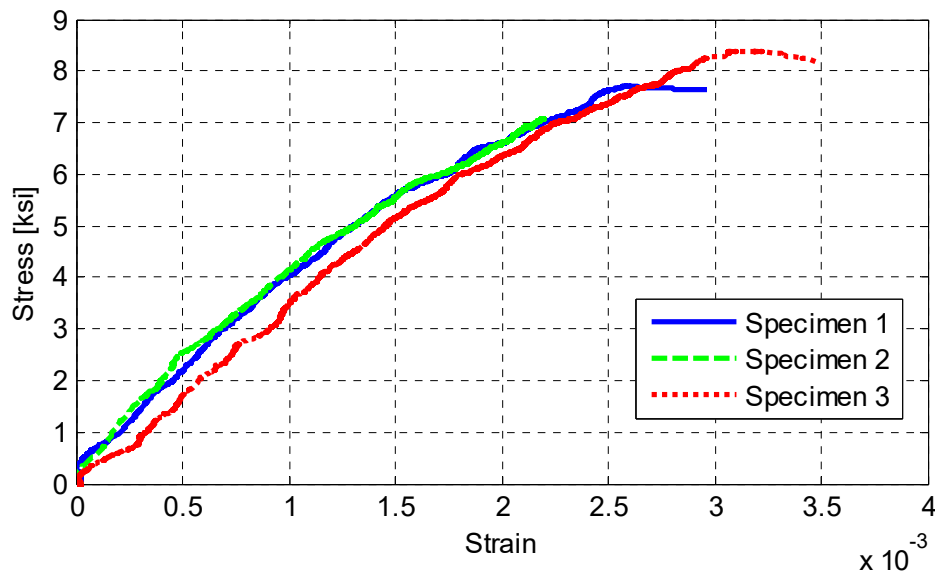


Figure 3.28 Typical concrete stress-strain relationship using a displacement-controlled test (results shown are for samples from second concrete lift at 298 days).

Table 3.7 Stress-strain compressive test results using displacement control.

	Age (days)	Stress at Peak (ksi)			Strain at Peak			Young's modulus (ksi)		
		Mean	St. Dev.	COV	Mean	St. Dev.	COV	Mean	St. Dev.	COV
Lift 1	298	6.84	0.31	0.045	0.0031	0.0002	0.064	3285.3	144.72	0.044
Lift 2		7.73	0.65	0.084	0.0027	0.0005	0.188	3823.3	565.40	0.148
Lift 3		7.16	0.22	0.030	0.0031	0.0002	0.071	3465.4	278.52	0.080

3.9.1.2 Tensile Tests

The splitting tensile strength represents a lower bound of the tensile strength of concrete. The test was conducted using standard 6 in.×12 in. concrete cylinders according to ASTM C496-04 [ASTM 2004a]. to capture actual concrete properties at the age of the subassembly specimens at day of testing, a sample of three cylinders from each concrete lift was tested at ages of 128 and 308 days For a splitting tension test, the concrete cylinder is placed on its side and loaded in compression; see Figure 3.29. The maximum load P was recorded, and the splitting tensile strength f_{ct} was estimated from Equation (3.2).

$$f_{ct} = \frac{2P}{\pi l d} \quad (3.2)$$

where l and d are the length and diameter of the standard cylinder, respectively. The test results are summarized in Table 3.8. A clear view of the concrete texture and aggregate distribution and size can be observed from the tested cylinders in splitting tension as shown in Figure 3.30.

Table 3.8 Splitting and modulus of rupture test results.

	Age (days)	Splitting tension f_{ct} (ksi)			Modulus of Rupture f_r (ksi)		
		Mean	St. Dev.	COV	Mean	St. Dev.	COV
Lift 1	128	0.50	0.012	0.025	0.79	0.043	0.054
	308	0.62	0.038	0.060	0.94	0.069	0.073
Lift 2	128	0.54	0.090	0.165	0.93	0.045	0.048
	308	0.58	0.033	0.057	1.02	0.097	0.095
Lift 3	128	0.48	0.059	0.125	0.96	0.046	0.048
	308	0.58	0.021	0.036	1.12	0.031	0.028

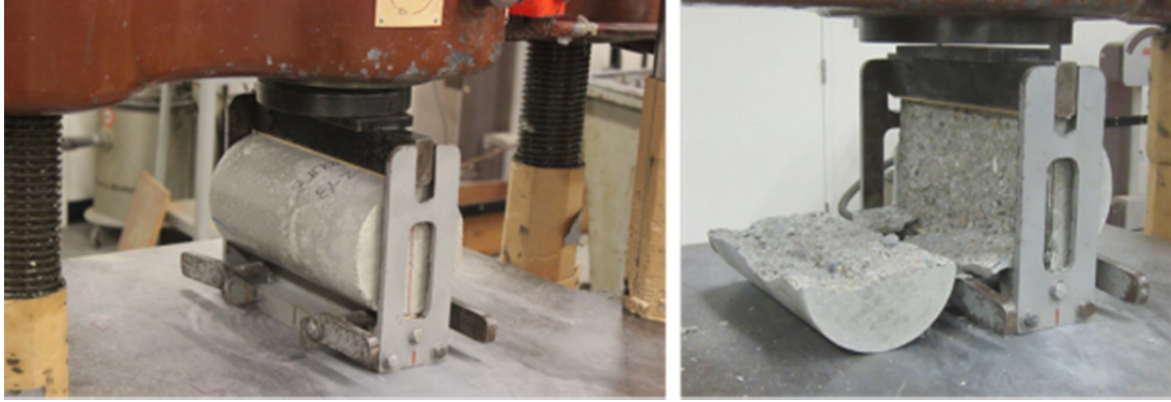


Figure 3.29 Splitting tension test set-up (left) and typical mode of failure (right).



Figure 3.30 Close-up view of the concrete texture and aggregate size and distribution from a tested cylinder in splitting tension.

The modulus of rupture test, or four-point flexural test, gives a higher estimate of the tensile capacity than the splitting strength test. The test was performed using 3 in.×3 in.×12 in. concrete beams according to ASTM C293-07 [ASTM 2007]. A sample of four beams from each concrete lift was tested at ages of 128 and 308 days, which was similar to the splitting tension test samples. The test required the beam to be simply supported with span $L = 9$ in. and subjected to four-point bending; see Figure 3.31. From the test, the maximum load P was recorded and the modulus of rupture f_r was computed from Equation (3.3)

$$f_r = \frac{PL}{bh^2} \quad (3.3)$$

where b and h are the width and height of the beam cross section, respectively. The test results are summarized, along with the splitting tension test results, in Table 3.7.

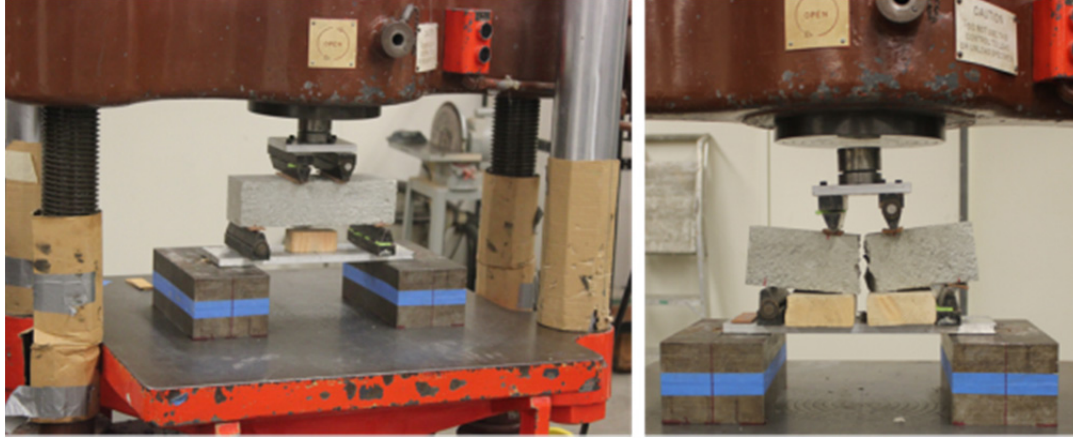


Figure 3.31 Four point bending test set-up for estimating the concrete modulus of rupture (left) and typical mode of failure (right).

3.9.1.3 Notched-Beam Tests

Fracture energy tests were conducted to evaluate the amount of energy released during tensile cracking of concrete. The fracture energy is defined as the amount of energy necessary to create one unit area of crack, and it has units of energy per unit area. The fracture energy is a key parameter in nonlinear concrete constitutive modeling and continuum FE analysis. Thus, the values obtained from these tests were utilized in the DIANA [2012] FE analysis subassembly model calibration and post-test analyses.

The test selected for this study was conducted according to the 1985 recommendation by Rilem. For this test, 4 in.×4 in.×36 in. concrete beams were cast to have a middle notch for crack initiation and propagation until failure. The notch is introduced in the beam using a wooden insert in the beam formwork, such that the area of ligament above the notch A_{lig} is half of the total cross-section height, i.e., 2 in.×4 in. The beams were simply supported at a span of 32 in. and loaded at the mid-point under displacement control. The test set-up and instrumentation used is shown in Figure 3.32. The deformation of the beam was measured at the mid-point with a displacement transducer. Because of the large scatter expected in fracture energy tests, many samples were tested for an accurate determination of the mean fracture energy.

A total of 15 beams were cast: three beams were casted from the first concrete lift and six beams from each of the second and third concrete lifts. From these 15 beams, only 12 beams were tested, at approximate age of 280 days; three beams were found broken when the formwork was removed. The load-deformation information was recorded until failure for all the tested notched-beams; see Figure 3.33. The area under the load-deformation relationship was estimated and used to calculate the fracture energy from Equation (3.4).

$$G_f = \frac{W_o + (m_1 + 2m_2)g\delta_0}{A_{lig}} \quad (3.4)$$

where W_o is the area under the load-deformation relationship, m_1 is the mass of the beam between the supports, m_2 is the mass of the loading support not attached to the machine, g is the acceleration of gravity, and δ_0 is the deformation at failure. The test results of samples of each

concrete lift individually and all beams together are summarized in Tables 3.9 and 3.10, respectively.

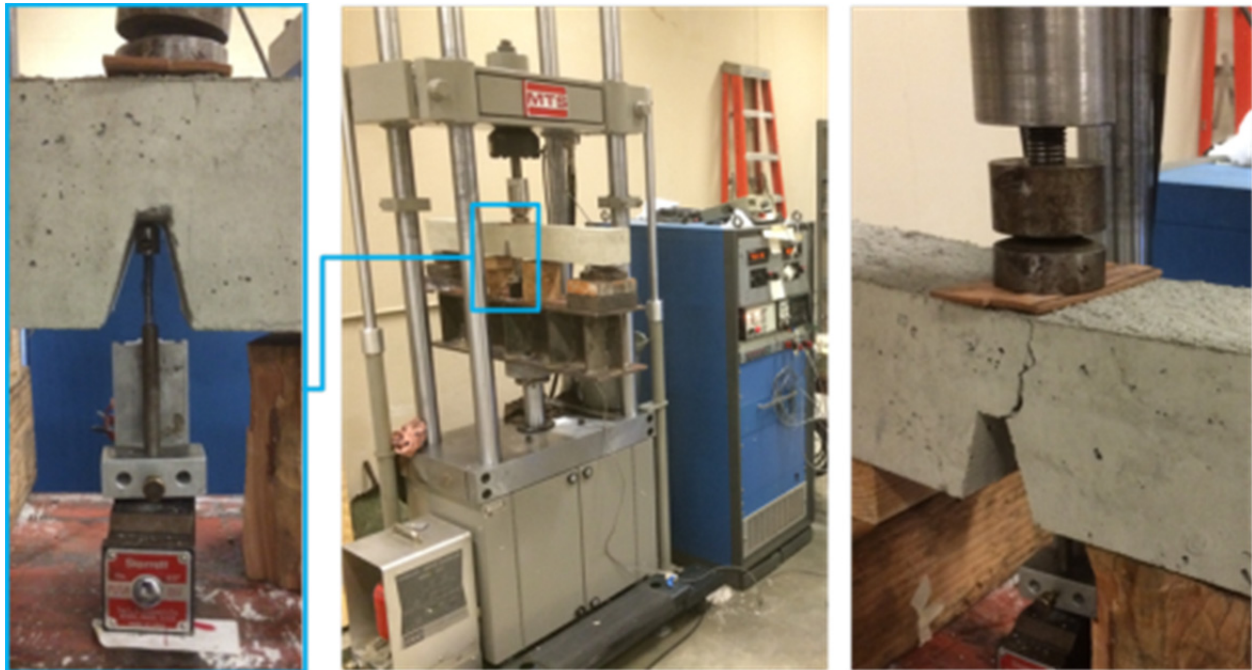


Figure 3.32 Notched-beam test set-up, instrumentation, and mode of failure.

Table 3.9 Fracture energy from notched-beam test results (samples from individual lifts).

	Test Response Quantity	Mean	St. Dev.	COV
Lift 1	Displacement at failure δ_o (in.)	0.083	0.019	0.230
	Peak Load P_o (lbf)	203.2	6.91	0.034
	Fracture Energy G_f (lbf/in.)	2.359	0.417	0.177
Lift 2	Displacement at failure δ_o (in.)	0.093	0.028	0.305
	Peak Load P_o (lbf)	197.9	109.2	0.552
	Fracture Energy G_f (lbf/in.)	2.289	0.734	0.321
Lift 3	Displacement at failure δ_o (in.)	0.074	0.010	0.135
	Peak Load P_o (lbf)	204.8	110.1	0.538
	Fracture Energy G_f (lbf/in.)	2.094	0.629	0.301

Table 3.10 Fracture energy from notched-beam test results (all samples together).

	Test Response Quantity	Mean	St. Dev.	COV
All Beams	Displacement at failure δ_o (in.)	0.083	0.021	0.253
	Peak Load P_o (lbf)	201.7	93.6	0.464
	Fracture Energy G_f (lbf/in.)	2.219	0.607	0.274

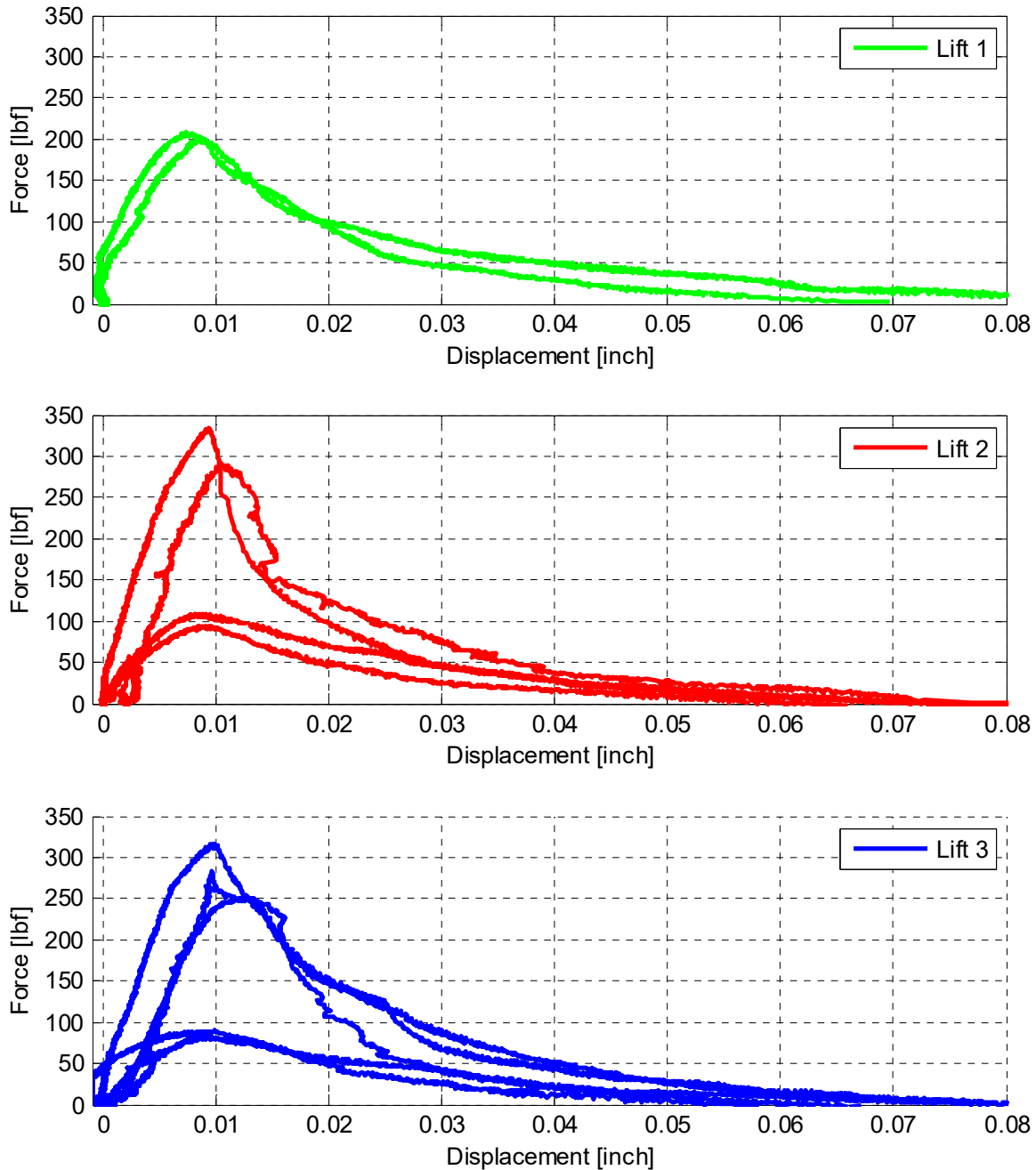


Figure 3.33 Load-deformation relationships for notched-beam tests for all concrete lifts.

3.9.2 Reinforcing Steel

The reinforcing steel used in the experimental program was Grade 60, meeting the requirements of ASTM A706-04 [ASTM 2004b]. Three different bar sizes were used in the specimen construction: #3, #5, and #6; however, the #3 bars were obtained from two different stocks such that all #3 longitudinal bars were from one stock, while all the #3 transverse steel used in column ties, beam stirrups, and box-girder ties were from the second stock. For each type of steel, three

coupons were tested using a Universal Testing Machine, as shown in Figure 3.34. The steel coupons were 32 in. long. To measure deformation, two displacement transducers were attached to the specimen as shown in Figure 3.34. This deformation was measured at 2 in. intervals. The bars were loaded according to ASTM E8-04 [ASTM 2004c]. All rebars were tested until rupture occurred. From the tests, the stress and strain were calculated by dividing the total force by the nominal cross-sectional area of the reinforcing bar and the deformation by the gauge length, i.e., 2 in., respectively. The test results of the reinforcing steel are summarized in Table 3.11. The stress–strain relationships obtained from all rebar tests are shown in Figure 3.35.

Table 3.11 Summary of mechanical properties of steel reinforcing bars.

	#3 longitudinal		#3 stirrups		#5 longitudinal		#6 longitudinal	
	Mean	St. Dev.	Mean	St. Dev.	Mean	St. Dev.	Mean	St. Dev.
Yield Stress f_y (ksi)	67.37	0.40	66.90	0.51	66.51	0.39	68.99	0.43
Yield Strain ϵ_y	0.0026	0.0001	0.0026	0.0	0.0026	0.0001	0.0026	0.0
Ultimate Stress f_u (ksi)	106.73	0.23	104.37	0.31	97.43	0.21	93.90	0.22
Ultimate Strain ϵ_u	0.1091	0.0089	0.1088	0.0048	0.0964	0.0103	0.1265	0.0059
Young's Modulus E_s (ksi)	27383	951	28000	369	25620	732	27173	329

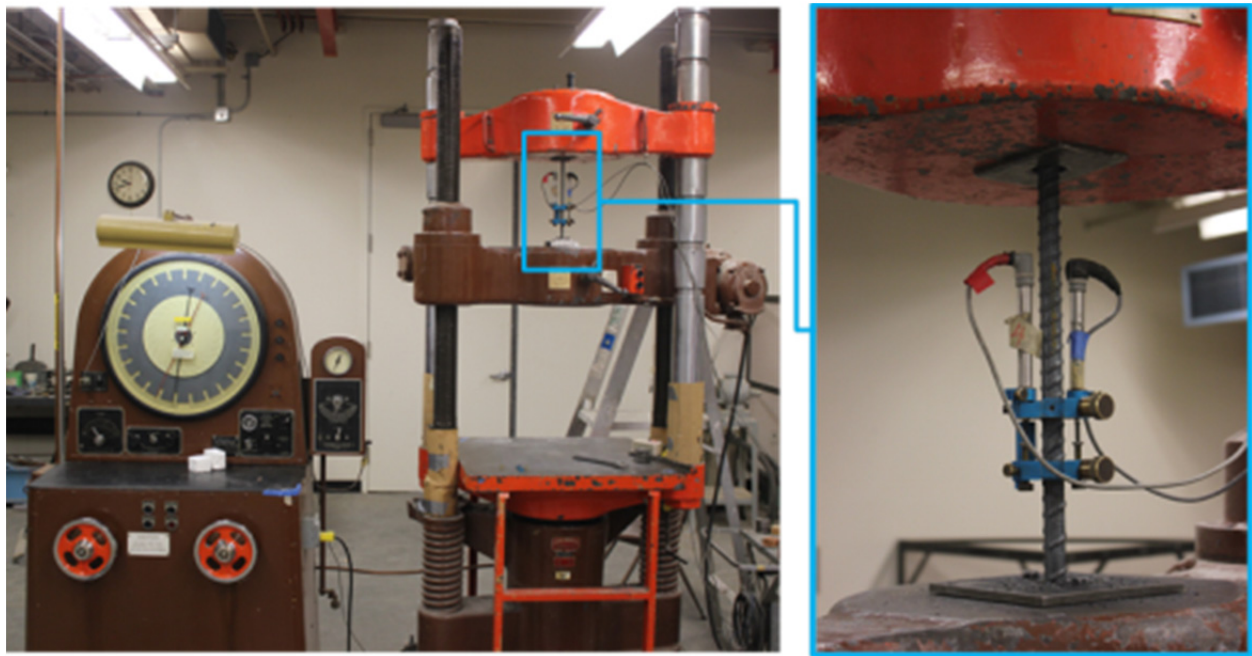


Figure 3.34 Test set-up and instrumentation for tensile testing of reinforcing bars.

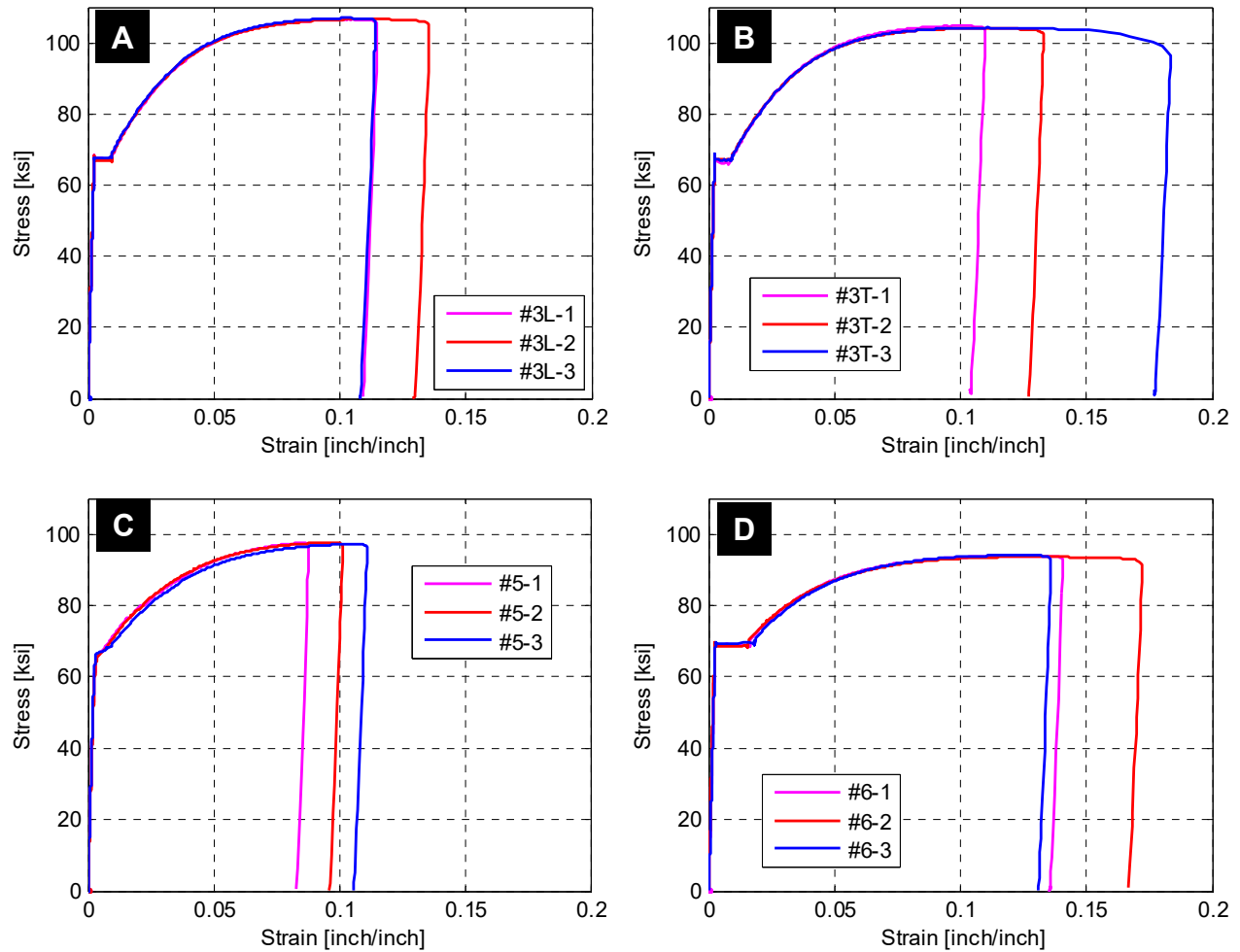


Figure 3.35 Stress-strain relationships for the different reinforcing bars coupons: (a) #3 stirrups, (b) #3 longitudinal bars, (c) #5 bars, and (d) #6 bars.

3.9.3 Repair and Retrofit Materials

Because the experimental program involved the repair of Specimen No. 1 and the retrofit of Specimen No. 2 before it was tested, it was useful to have a rough idea of the mechanical properties of the different materials used in both the repair and retrofit processes. Unlike concrete and reinforcing steel, testing representative material samples was not possible during the course of the study; however, nominal and characteristic properties as provided by the materials supplier are discussed below.

3.9.3.1 Unidirectional Carbon Fiber Fabric

Unidirectional carbon fiber fabric along with a two-component epoxy system comprised the Fiber Reinforced Polymer (FRP) system used for both of the repair and the retrofit processes. Three layers of FC061 unidirectional carbon fiber fabric were used for each of the repaired and retrofitted specimens. Note that FC061 Structural Fabric is a standard modulus continuous-fiber unidirectional carbon fiber fabric with superior tensile strength. FC061 Structural Fabric can be impregnated with RN075 Fiber Impregnation Resin to achieve a super-strong FRP composite

laminate for structural strengthening applications. The fiber fabric itself before resin application contains very high mechanical properties, with an average tensile strength of 700 ksi, an average tensile modulus of 34,000 ksi, and a rupture strain of 1.4%

3.9.3.2 Two-Component Epoxy System

Epoxy or any suitable resin is the second necessary component of FRP laminates used for structural purposes. A RN075 LPL Two Component Epoxy System was used along with the carbon fabrics to compose the FRP layers. The RN075 Fiber Impregnation Resin is a 100% solid, solvent-free, and two-component moisture tolerant epoxy. It is a low-viscosity epoxy for wetting and is used with carbon and glass fiber fabrics for structural strengthening. The mechanical properties reported for the resin itself are: 10.5 ksi compressive strength after 7 days curing, 6 ksi tensile strength after 14 days curing, and rupture strain that varies between 2–4%. The reported properties comply with the ASTM standards for epoxy and composites. The manufacturers reported an average laminate tensile strength for the FRP composite of 149 ksi with an average tensile modulus of 10,100 ksi and corresponding rupture strain of 1.2%. Note: a single ply thickness is 0.04 in.; the final thickness of the three-layer CFRP jacket was 0.12 in.

3.9.3.3 Patching Material and Structural Mortar

While only a composite jacket of carbon fabrics and epoxy resin was used to retrofit Specimen No 2, several other materials were used to repair the damaged plastic hinge region in Specimen No. 1. An overview of the mechanical properties of the patching material and structural mortar used during the repair is presented below; see Chapter 6 for more details about this repair procedure.

A Structural Mortar SM020 was used to fill the concrete cracks wider than 0.75 in. and patch the damaged surface for proper application of the CFRP composite layer. Based on the data provided by the manufacturer, the structural mortar had an average compressive and split tensile strength of 6.3 ksi and 595 psi, respectively, after 28 days. The modulus of elasticity based on the data from the elastic regime of the stress–strain plot was 2260 ksi. Bond and flexural strength of 0.5 ksi and 1.15 ksi, respectively, were measured after 28 days with failure noticed in the substrate.

Concrete cracks with width less than 0.75 in. were cap-sealed using the GS100 gel/paste epoxy system. Compressive and tensile strength of epoxy system was 10.5 ksi and 7.2 ksi, respectively. Rupture strain of the epoxy system was about 0.85%. The average flexural strength measured after 14 days was 5.6 ksi.

3.10 INSTRUMENTATION

Several parameters were measured during each test: force, displacement, and strain. In addition, curvatures were deduced from either strains or displacements. Cameras were also used extensively to capture cracks and damage propagation. A summary of the instrumentation and layout used for is presented next.

3.10.1 Load Measurement

Load was measured to assist in the control of both the vertical and lateral actuators and to measure the total forces applied to the specimen for capacity estimation. Several load cells were used to measure the actuator forces: two for the vertical actuators and another two for the lateral ones. In addition, the two struts used as part of the specimen physical boundary conditions were instrumented with strain gauges to work as load cells. The vertical load actuators were used to apply the gravity load under load control. Thus, the load cell measurements were indispensable to monitor the level of applied load. The lateral load actuators were run in displacement control. Load cell measurements were a crucial factor in estimating the total force applied to the specimen, base shear capacity, and in calculating the stiffness and its degradation during the experiment. The load cells were calibrated in compression using the universal testing machine at UCB. Special attention was paid to calibrating the fabricated strut load cells; see Appendix F. The two different types of load cells used for both the actuators and calibrated struts are shown in Figure 3.36.

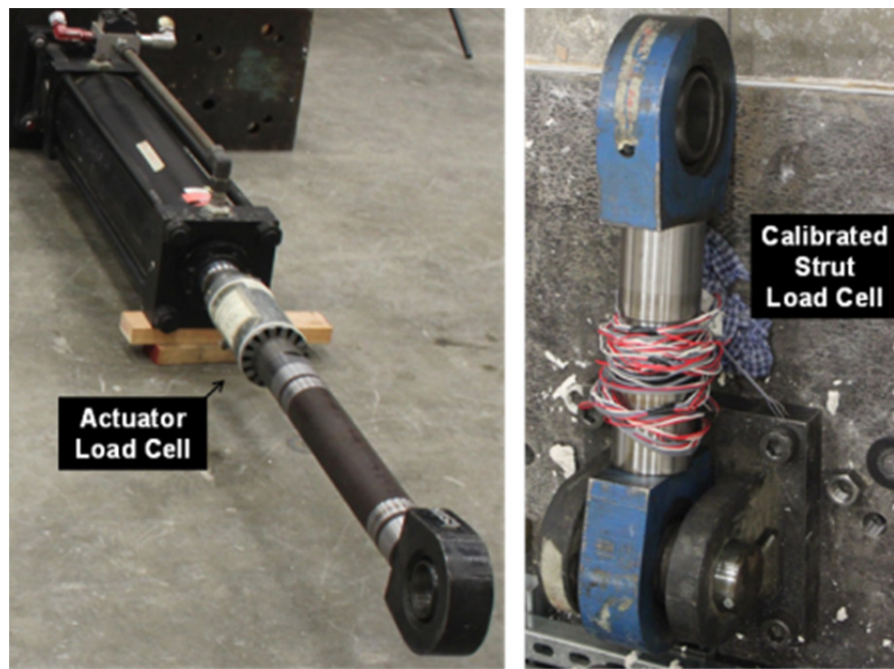


Figure 3.36 Different load cells used in testing: typical actuator load cell (left) and calibrated strut load cell (right).

3.10.2 Displacement Measurement

External deformations/displacements were measured using displacement transducers (wire potentiometers) and linear motion potentiometers. Three ranges of wire potentiometers (wirepots) were used to measure large column deformations: ± 5 in., ± 7.5 in., and ± 15 in. The ± 5 in. and ± 7.5 in. range transducers were used for measuring the column deformation at mid-height. The ± 15 in. range was used for larger displacements at the column's top in the inverted position where lateral load was applied. The wirepots have an accuracy of 0.10% of its full range, i.e., 0.03-in. resolution for a range of ± 15 in. Piano wires and strings were used to extend

the wire potentiometer ends to the column. At the column mid height, the wires were connected to the concrete face by an embedded hook. At the mid-height of the column's head where load was applied, the wires were attached to a steel ring that was welded to the plates used around the hexagonal column head for attaching actuators. Figure 3.37 shows the layout for the wire potentiometers mounted on the east-side instrumentation frame and wires attached to the column top. A total of 12 wirepots were used and were distributed in a 2D and 3D triangulation as identified; they are shown in plan and side views in Figures 3.38 and 3.39, respectively.

The other type of displacement transducers used were linear variable differential transformers (LVDTs) or more commonly known as linear motion potentiometers. The LVDTs were laid out underneath the specimen in its inverted position and used to measure the cap beam and box-girder displacements. Another set of LVDTs was used for column curvature measurements. For the LVDTs underneath the specimen, two ranges were used: ± 1 in. at the edges and ± 2 in. at the center. Steel hooks were used to attach the LVDTs to the concrete face. Tiny holes were drilled, filled with epoxy, and then the steel hooks were inserted in holes before the epoxy hardened to form the attachment points. Figure 3.40 shows the layout for the LVDTs underneath the specimen and how the wires were attached to the steel hooks implanted in the specimen deck slab and cap beam.

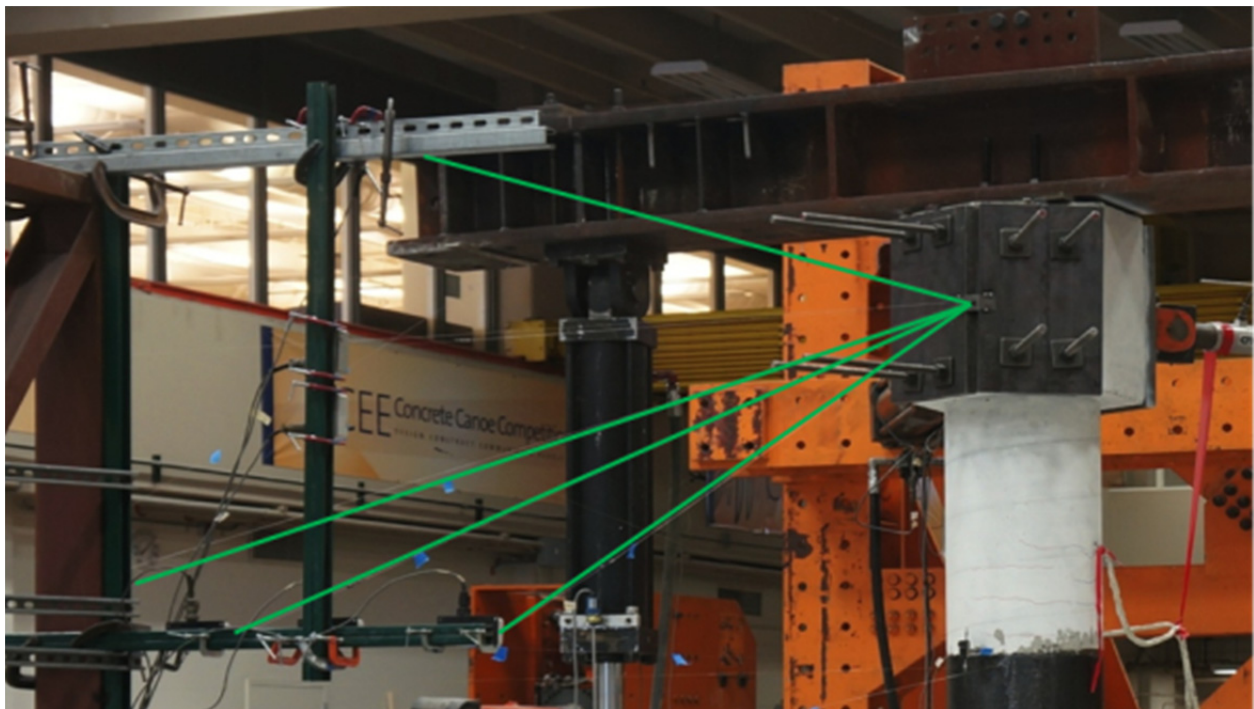


Figure 3.37 Wirepots set-up at the east instrumentation frame.

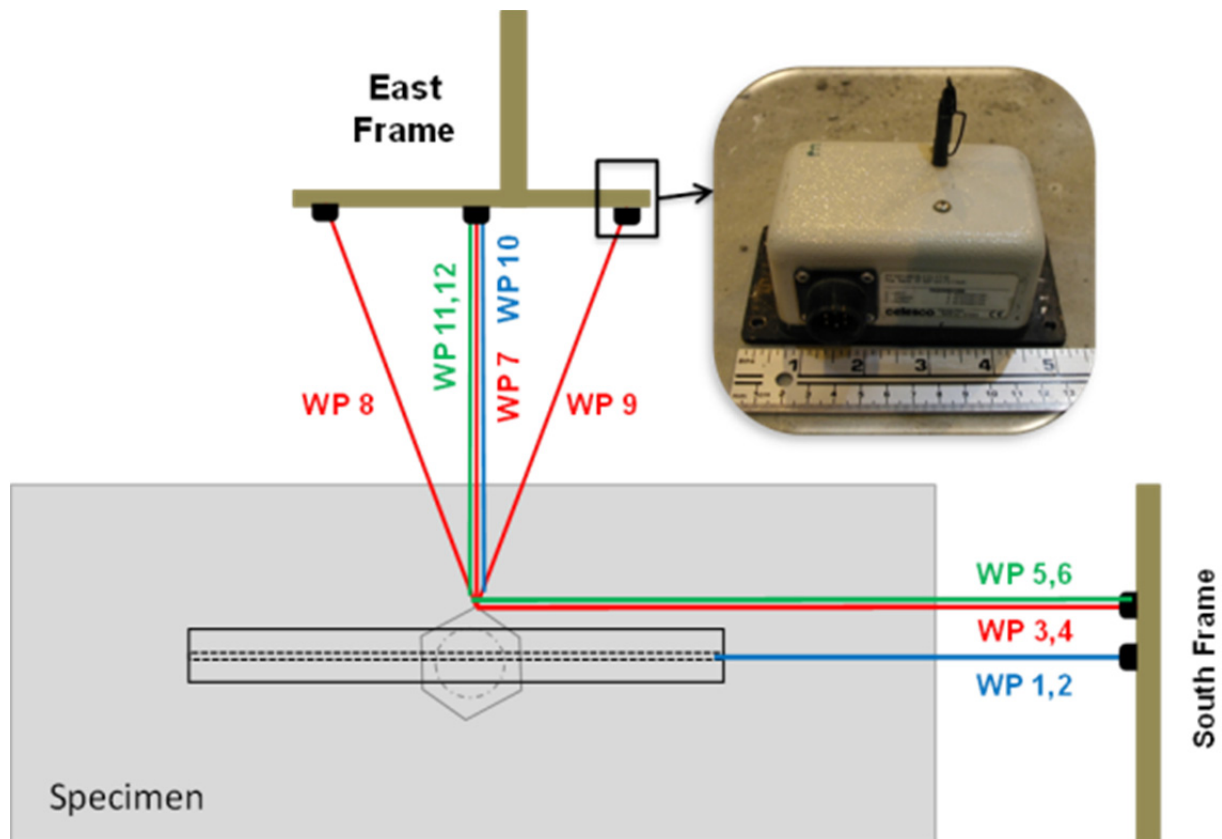


Figure 3.38 Layout of the wirepots in plan view (east and south sides are identified).

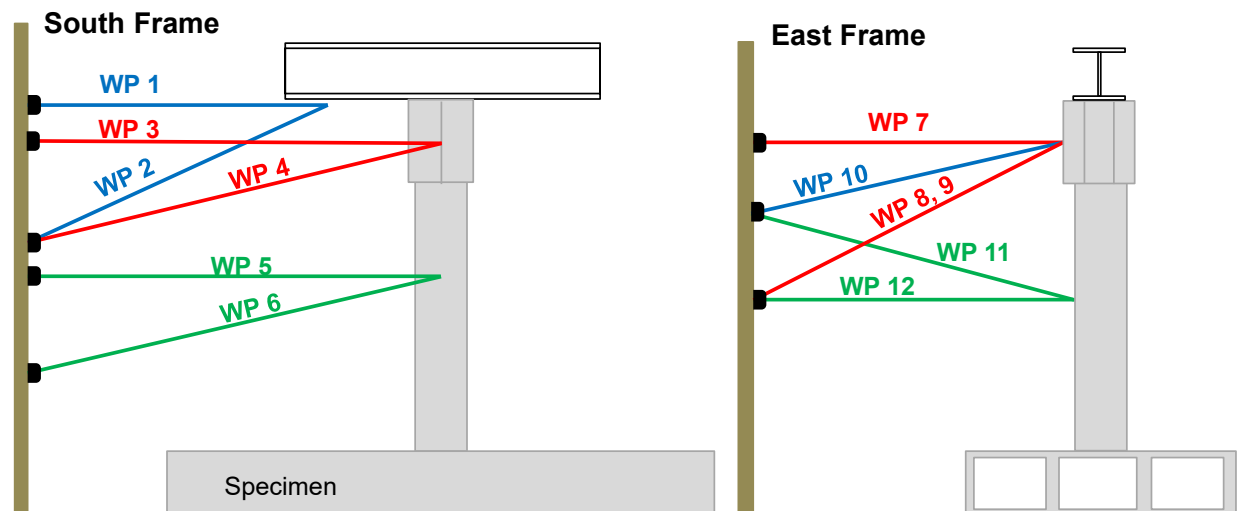


Figure 3.39 Layout of the wirepots in side view at east- and south-side frames.

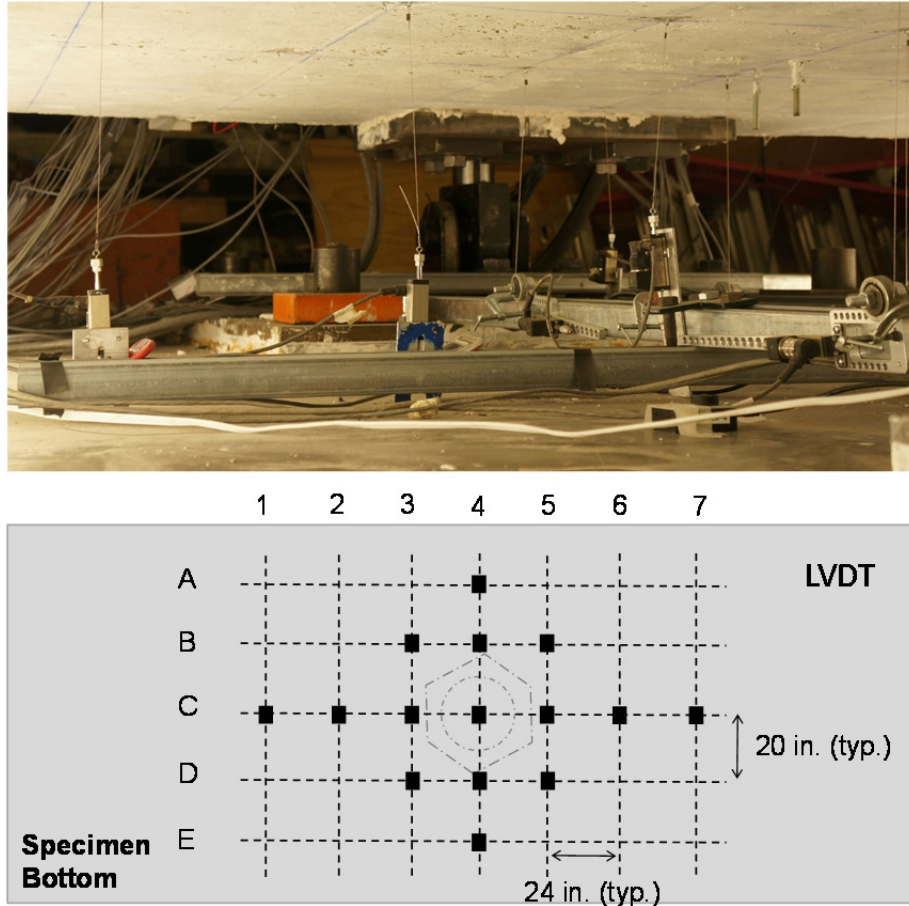


Figure 3.40 LVDTs under the specimen monitoring the deformation of the cap beam and the box-girder.

3.10.3 Strain Measurement

Strains were measured locally on the reinforcement and at some local points inside the concrete or on its surface. Although only reinforcement strain gauges are considered reliable and conclusive, concrete gauges can be useful in showing behavior trends rather than accurate strain readings. Reinforcement strains were measured using foil gauges mounted on the surface of the reinforcement. The utilized gauge size was 0.20 in.×0.08 in. and were post-yield gauges with a rated deformation capability of 15% strain. The bar surface deformations in the region surrounding the gauge location were removed, and the surface was polished. The strain gauge was glued to the surface and covered by four protective coatings: air-drying polyurethane, wax, polysulfide liquid polymer compound (providing a tough flexible barrier), and vinyl mastic tape. Figure 4.41 shows the process of installing strain gauges on the reinforcing bars. Note that instrumenting the rebars with strain gauges is critical in RC components or subassembly testing. Thus, proper attention is required to minimize the chances of losing strain gauges during construction. A picture of few stacks of the instrumented rebars stored in the laboratory before construction is shown in Figure 3.42.

Concrete strain was measured using embedded concrete gauges. As shown in Figure 3.43, 14 embedded concrete gauges were used and installed between the soffit slab transverse rebars, which was anticipated to be the compression side. Concrete gauges, 4.5 in. long, were also used. Other types of concrete gauge used in this study included surface concrete gauges, which were installed for Specimen No. 2 only. It was decided to use concrete surface gauges because the embedded gauges in the first test of Specimen No. 1 did not provide meaningful values. Figure 4.43 shows the layout of surface concrete gauges used in Specimen No. 2 on the compression side.

Finally, strain gauges were installed on the CFRP jacket to monitor the confinement strains in the jacket. Linear 0.20 in.×0.08 in. foil gauges, similar to the ones used for the steel reinforcement, were installed around the circumference of the CFRP jacket. These gauges were used to determine the effectiveness of the CFRP jacket and examine the resulting circumferential strains during either the repaired Specimen No. 1 or retrofitted Specimen No. 2. The FRP jacket strain gauges can be seen in Figure 4.43 as well.

The location of the strain gauges was determined based on the DIANA 3D pre-test model and analysis. The locations where maximum strain was expected—in the box-girder, column, or cap beam along with locations capturing the strain distribution in the transverse direction—were identified from the pre-test analysis. Figure 3.44 shows an example of the DIANA results for the strain distribution in a plan view inside the cap beam and box-girder under lateral loading. Accordingly, the strain gauge arrangements in the soffit and deck slabs transverse and longitudinal reinforcement are shown in Figures 3.46 and 3.47, respectively. The cap beam rebars were heavily instrumented as shown in Figure 3.45. The strain gauges used for the column longitudinal rebars and transverse hoops are shown in Figure 3.48.

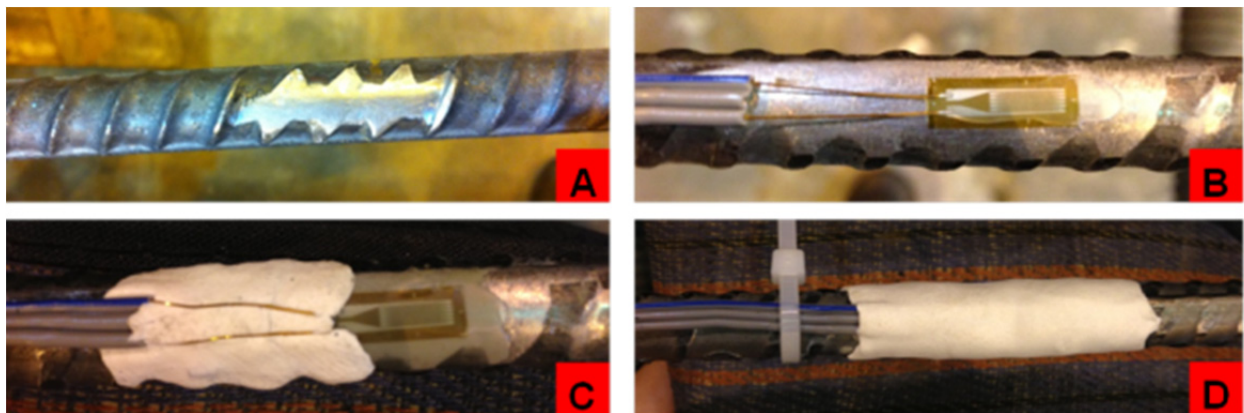
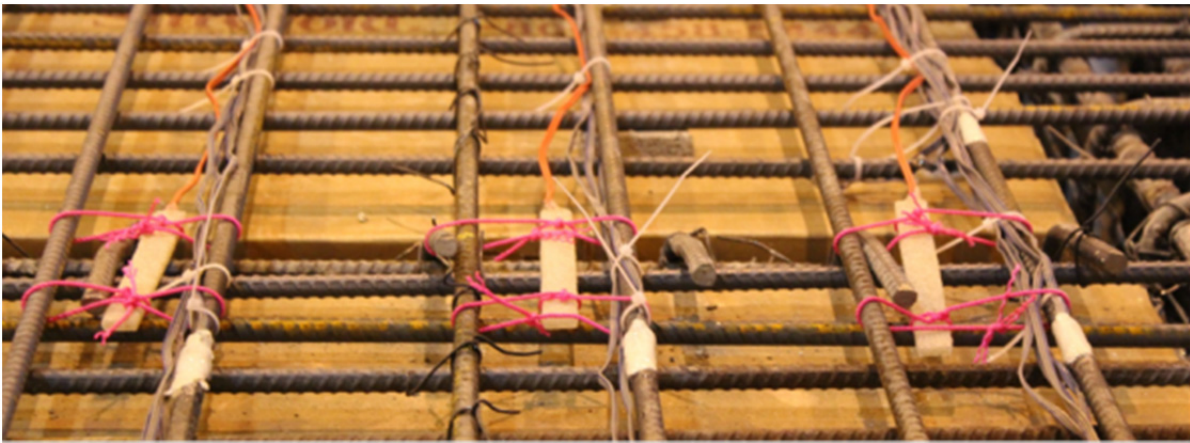


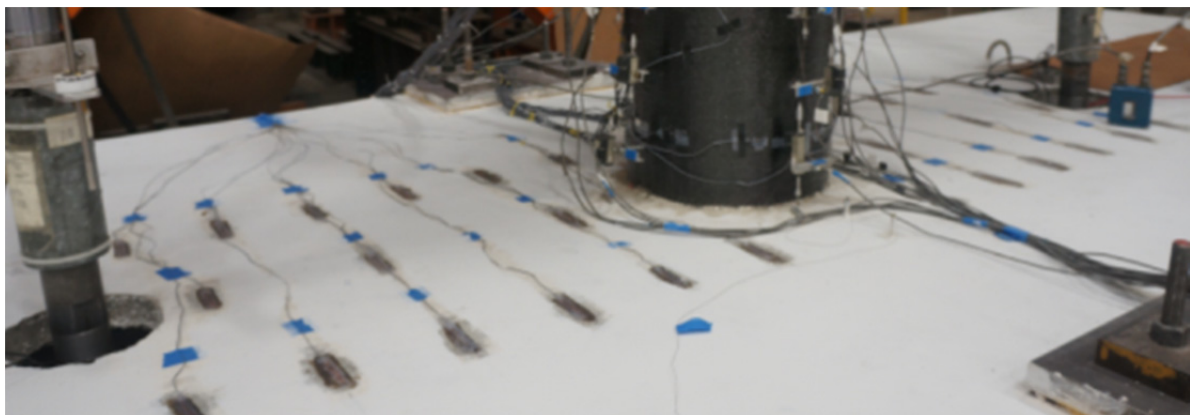
Figure 3.41 Strain gauges used for reinforcing bars instrumentation where several chemical and mechanical protection layers were added to protect the gauges.



Figure 3.42 Instrumented specimen's beam and slab reinforcement bars.



(a)



(b)

Figure 3.43 (a) Embedded concrete strain gauges used in the soffit slab part of the box-girder; and (b) surface concrete strain gauges installed on top of the soffit slab of the second specimen only (some CFRP jacket strain gauges are shown as well).

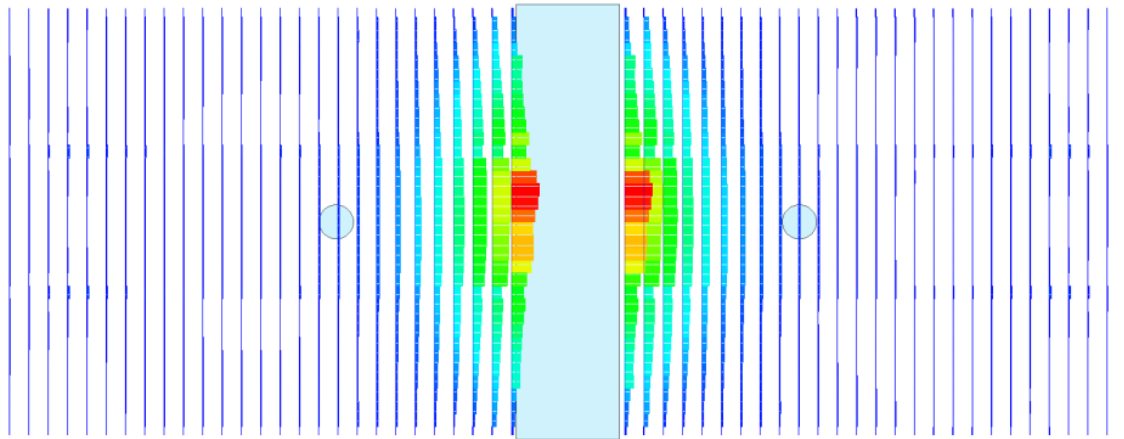


Figure 3.44 An example of strain distribution in the box-girder transverse reinforcement as obtained from DIANA pre-test analysis.

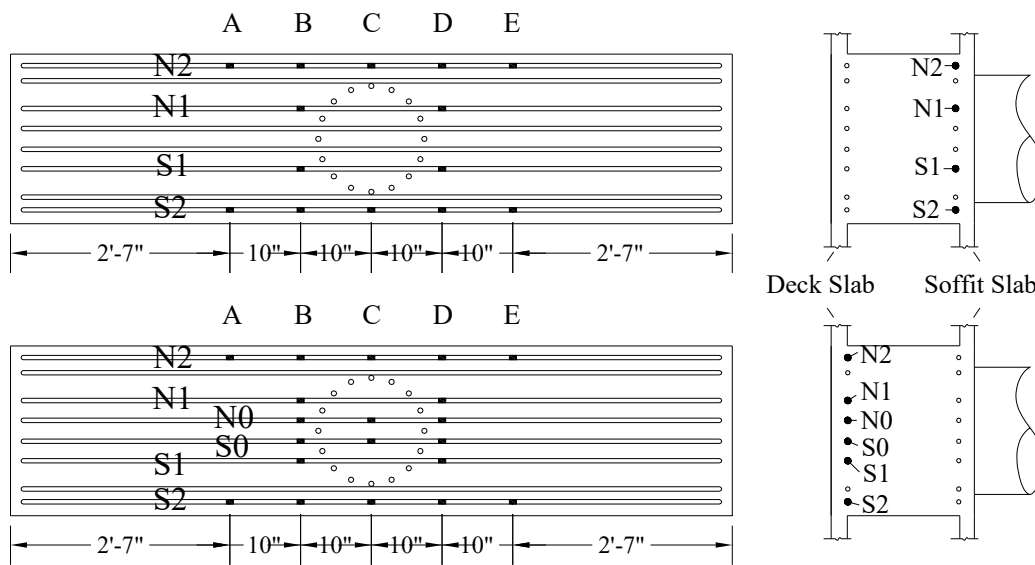


Figure 3.45 Layout of strain gauges used for the cap beam reinforcement.

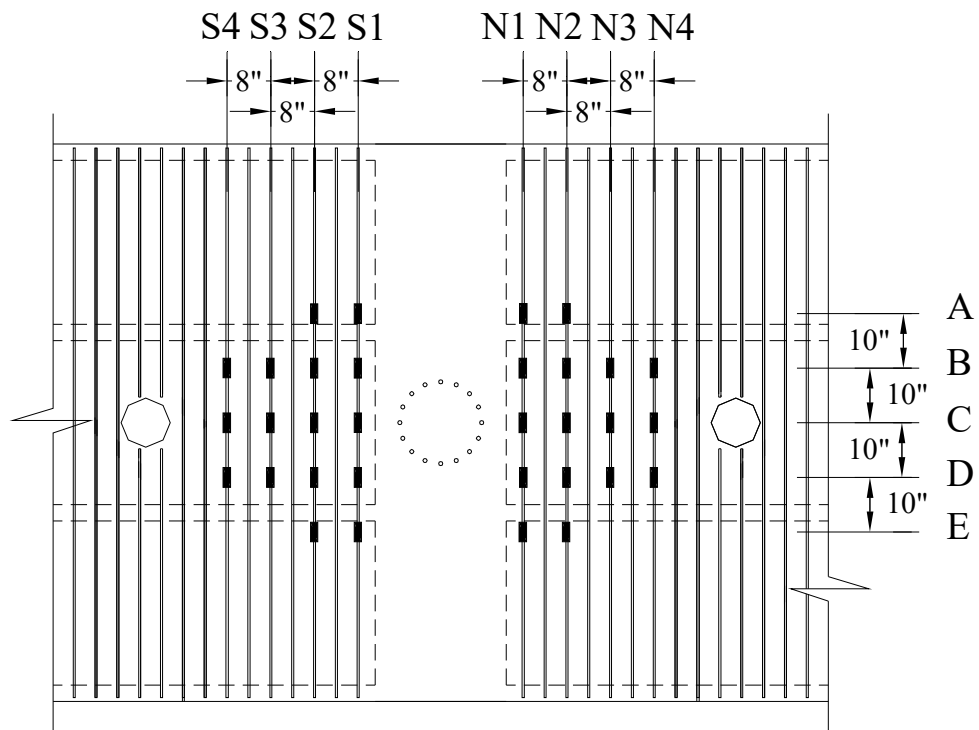
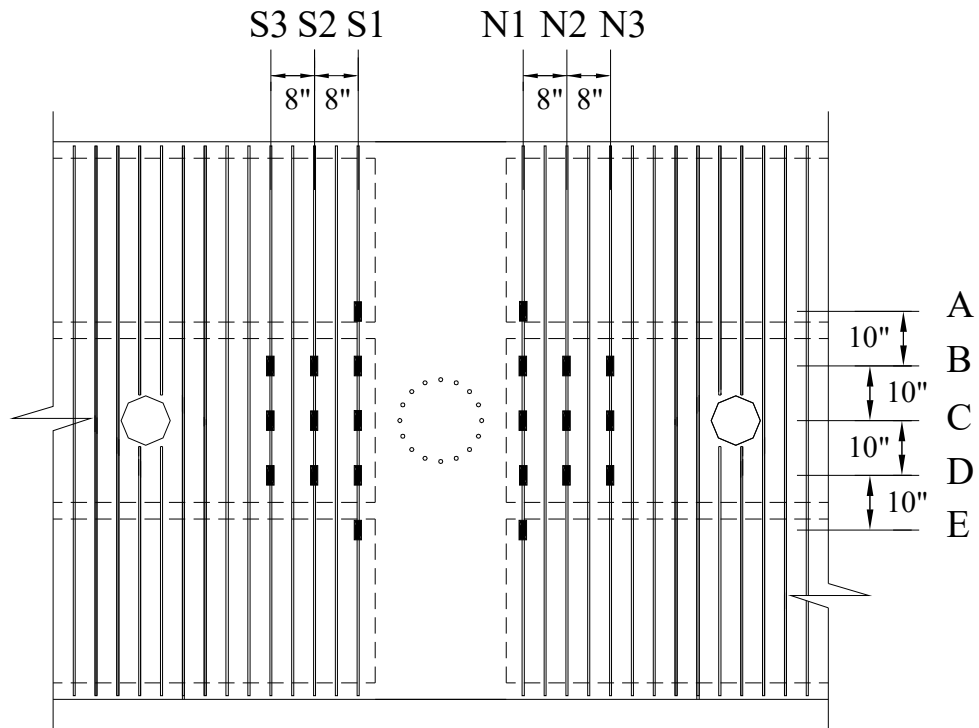


Figure 3.46 Layout of strain gauges used for the box-girder soffit slab (top) and deck slab (bottom) transverse reinforcement.

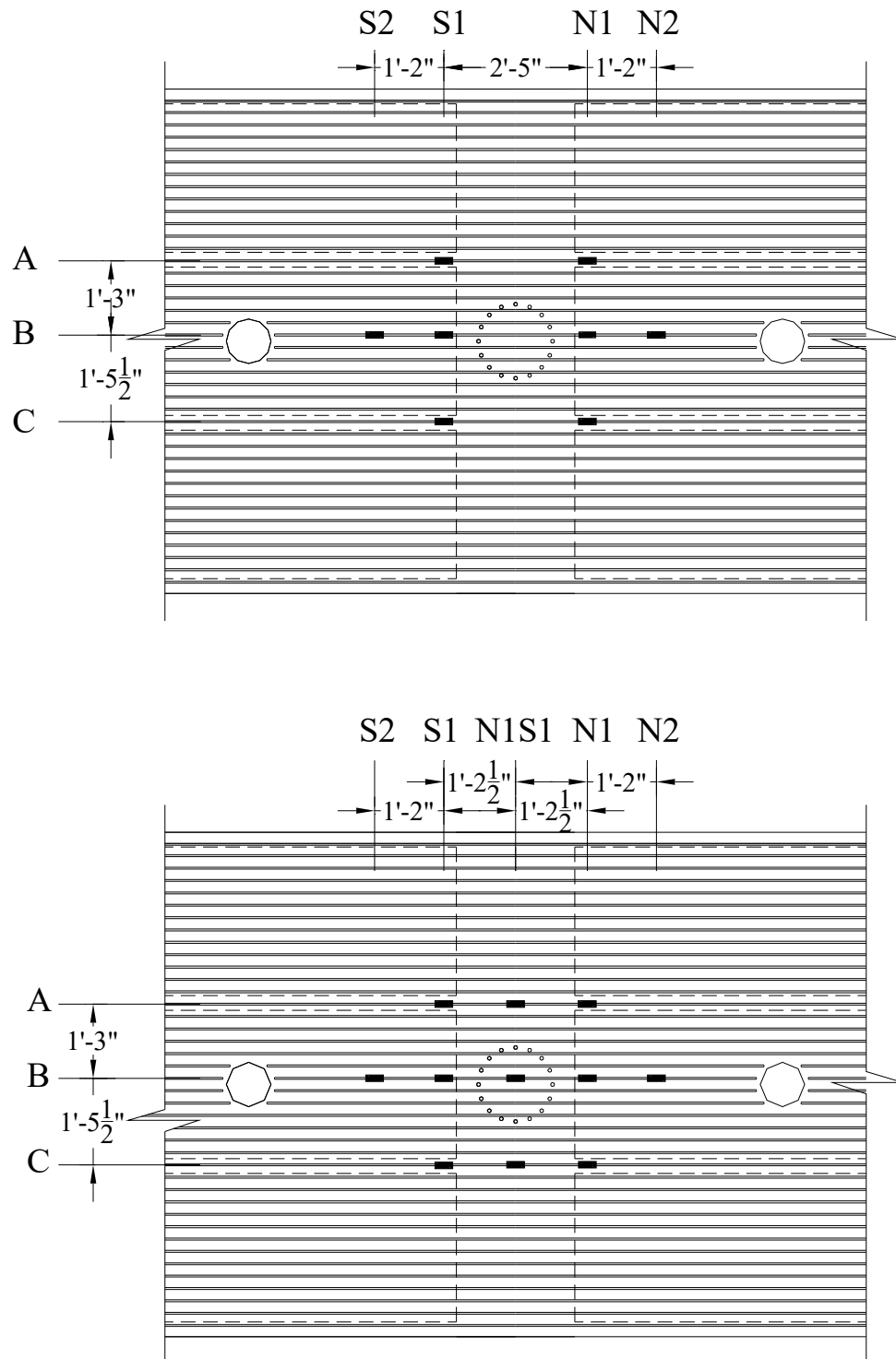


Figure 3.47 Layout of strain gauges used for the box-girder soffit slab (top) and deck slab (bottom) longitudinal reinforcement.

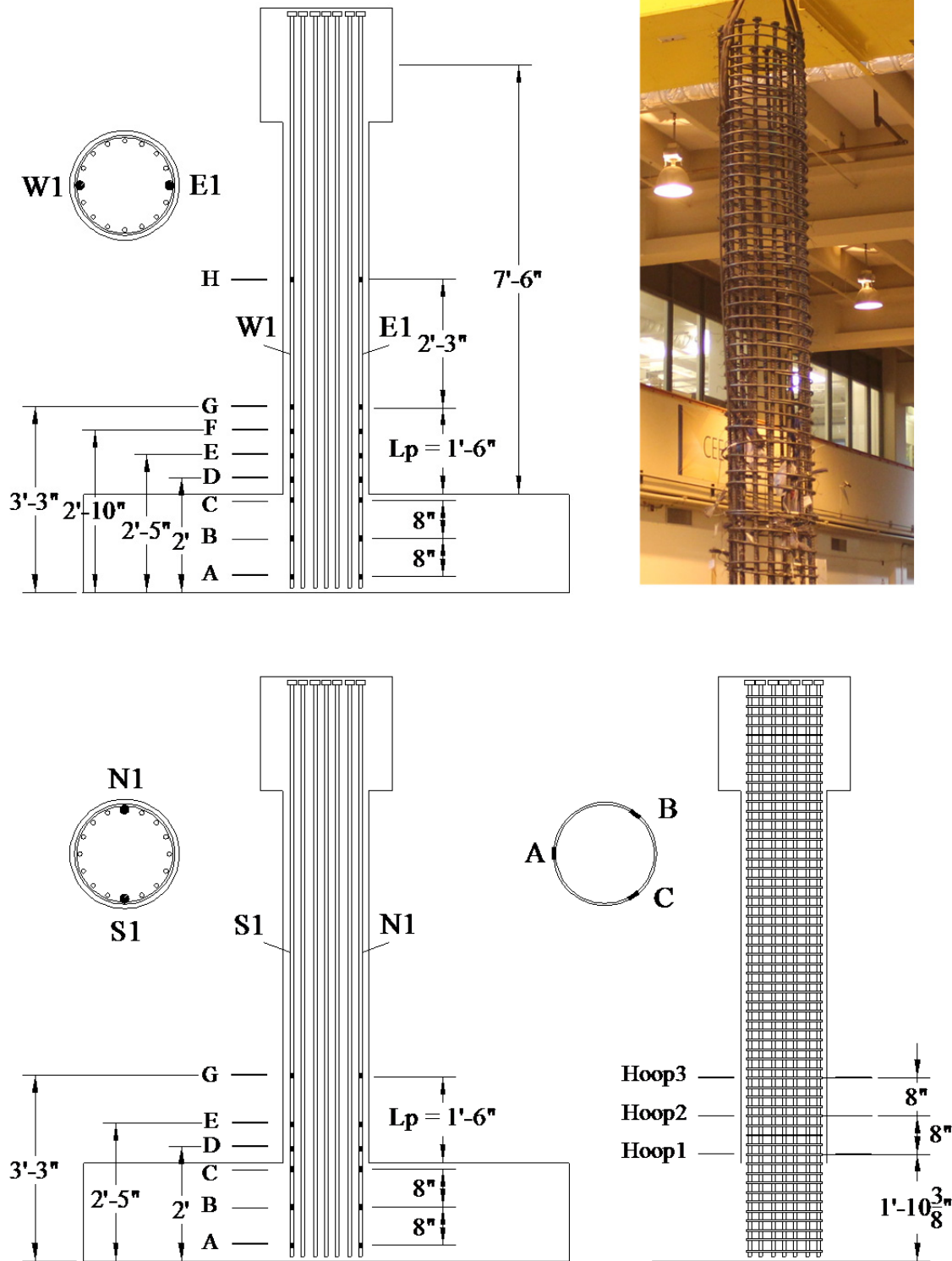


Figure 3.48 Layout of strain gauges used for the column longitudinal and transverse reinforcement.

3.10.4 Curvature Measurement

As previously mentioned, LVDTs were used for direct cap beam and box-girder displacement measurements under the specimen, and a different set was dedicated for column curvature estimation. The curvatures were not measured directly but estimated from the LVDTs relative displacement measurements; LVDTs are robust and reliable in calculating very small curvatures and rotation with high accuracy.

The subassembly column was instrumented with four levels of LVDTs in the north–south (longitudinal loading) direction and five levels in the east–west (transverse loading) direction. Each of the two opposite LVDTs at a certain level of measured displacements can be associated relatively to other levels. The relative displacements between each two measuring levels can be transformed to linear strains if the distance between the two levels is known. The linear strains at two opposite sides of the column can be then used to estimate the cross-section curvature at a given level using the horizontal distance between the two planes where the linear strains are calculated. This described process for estimating curvatures using LVDTs is illustrated in Equations (3.5) and (3.6), and Figure 3.49. The actual layout and set-up of the column's LVDTs dedicated to measuring curvature are shown in Figure 3.50.

$$\kappa = \frac{\varepsilon}{L} = \frac{\varepsilon_1 + \varepsilon_2}{D + \text{Offset}_1 + \text{Offset}_2} \quad (3.5)$$

$$\varepsilon_1 = \frac{\Delta h_1}{h_1}, \quad \varepsilon_2 = \frac{\Delta h_2}{h_2} \quad (3.6)$$

where $\Delta h_{1,2}$ is the : change in displacement at a given LVDT between two fixed points (direct reading of LVDT); $h_{1,2}$ is the distance between two fixed points set by the threaded rods projected out of the column; $\text{Offset}_{1,2}$ is the initial horizontal distance between the column face and a given LVDT center line, and D is the column diameter (in.).

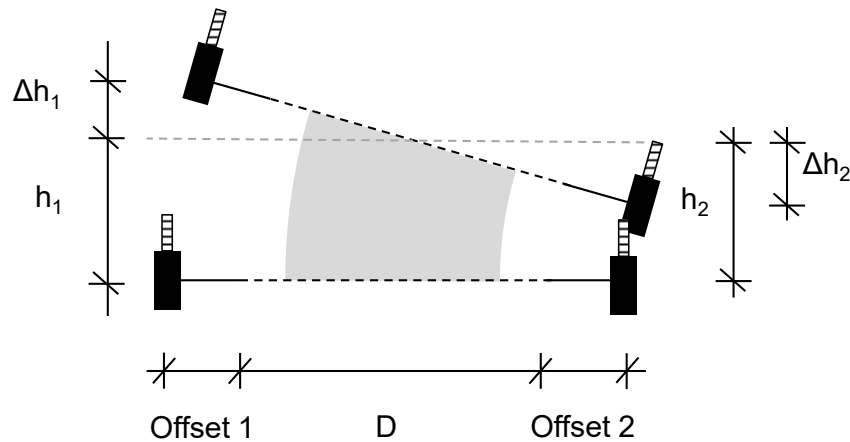


Figure 3.49 Schematic representation of parameters required to estimate column curvature using linear LVDTs.

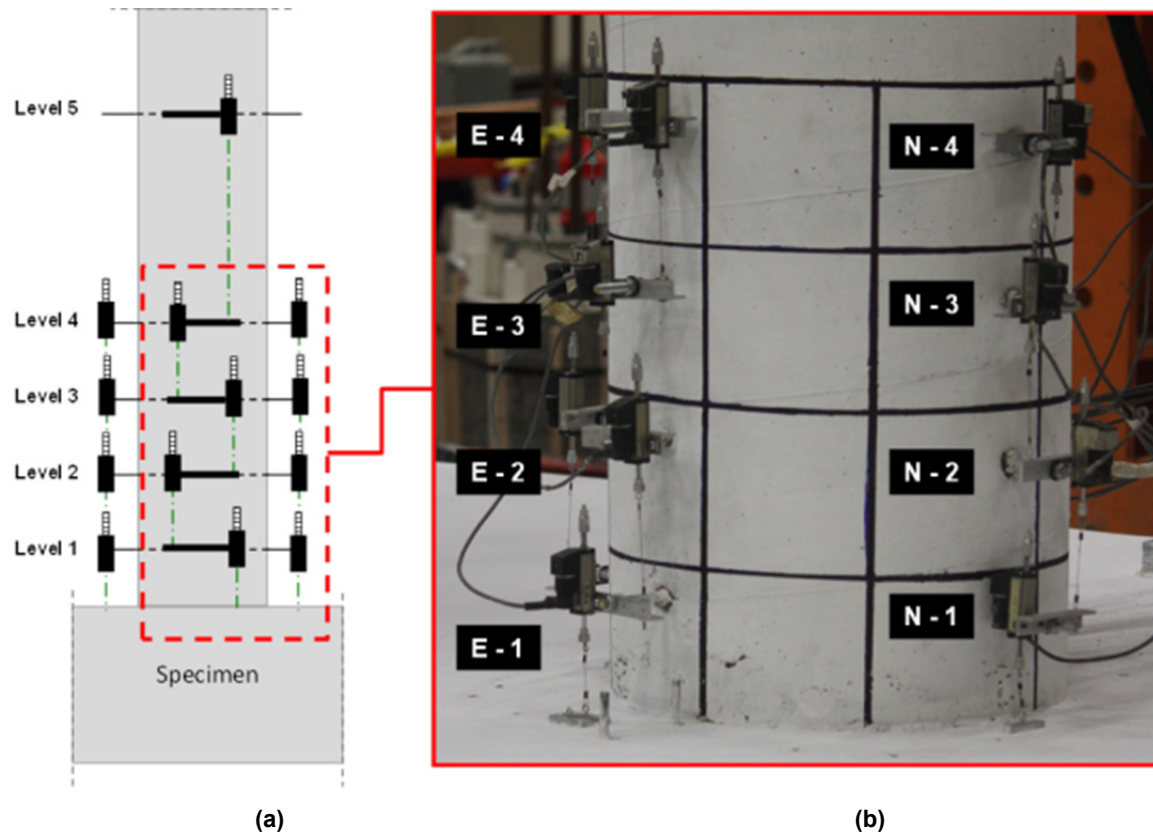


Figure 3.50 (a) Distribution of LVDTs on the column and (b) photograph of installed LVDTs.

3.10.5 Cameras

Cameras were used extensively throughout the experimental study. Figure 3.51 shows an overview of the arrangement of various cameras used during the tests. For all tests, several digital single-Lens reflex (DSLR) cameras were used to capture still pictures for crack and damage propagation. A monochrome DSLR camera was installed inside the north middle cell of the box-girder to capture joint region cracking. A random speckles pattern was applied to the north side of the column-cap beam joint region, which was exposed to the monochrome DSLR camera, for the purpose of adopting digital image correlation (DIC) measuring technique; this is a novel measuring technique that is undergoing extensive development for use in structural engineering applications at UCB. A random speckle pattern also was applied to the east side of the specimen; see Figure 3.13. In DIC, high resolution still pictures can be used to estimate surface displacement and strain distributions. An example of the strain distribution during one of the conducted quasi-static tests loading cycles obtained from DIC is shown in Figure 3.52.

In addition to the remote DSLR cameras, several other Gopro cameras were used underneath the specimen to capture crack pattern in the inverted box-girder's deck and the cap beam. Gopro cameras were also used in other box-girder cells to capture direct photographs of any cracks inside the cells, as seen in Figure 3.51. For better quality pictures of dark spots,

laboratory shop lights and flash lights were used inside the box-girder cells and under the specimen; see Figure 3.51.

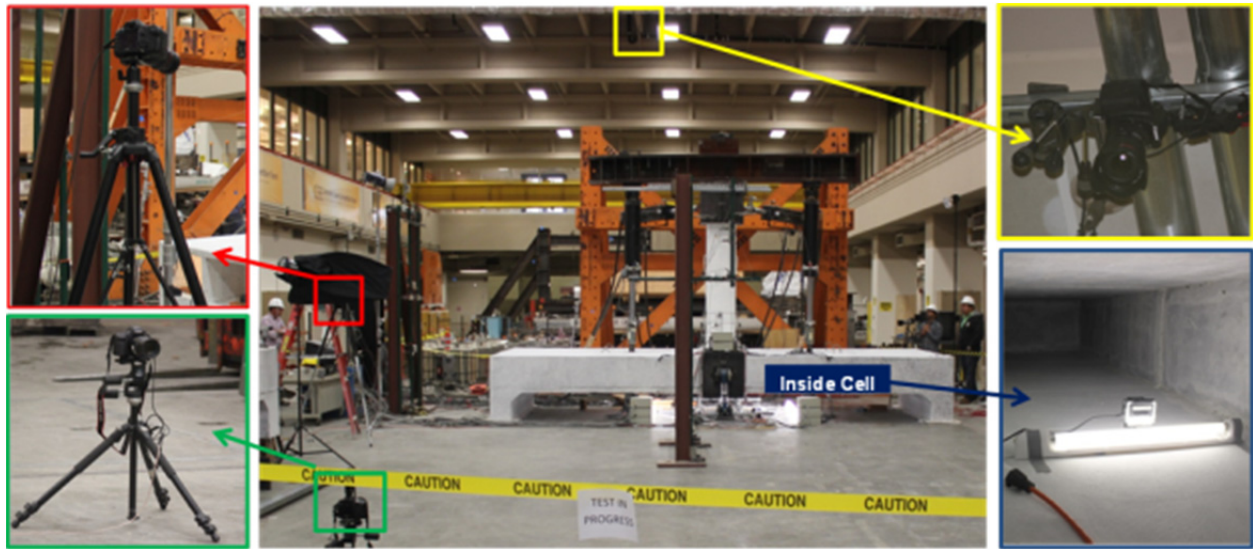


Figure 3.51 Overview of different types of cameras, their arrangement, and illumination system used during testing.

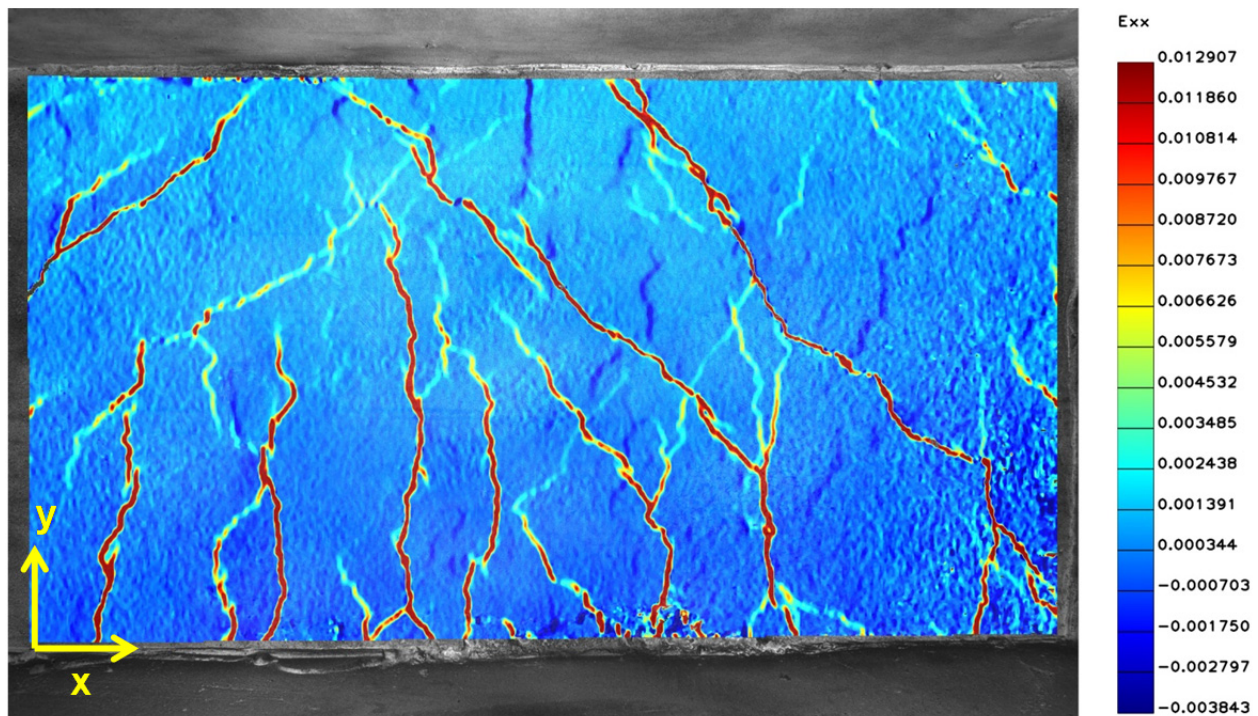


Figure 3.52 Example of strain distribution and crack pattern in the column-cap beam joint region obtained from the DIC technique during one of the cyclic loading tests.

4 Pre-Test Finite Element Analysis

This chapter presents all the different FE models developed and used in the pre-test analysis. The pilot studies conducted using these models are also discussed. Three different types of models were used. The first type of models utilized 1D elements for modeling either the full prototype bridge or the test subassembly specimen, which was OpenSees [McKenna et al 2000]. The second type of models used 2D elements mainly for box-girder modeling, which was SAP2000 [2012]. The most sophisticated level of modeling was the 3D solid element modeling, which was the general purpose FE analysis package DIANA [DIplacement ANalyzer 2011]; DIANA was also used to perform linear and nonlinear analyses. The pre-test analysis presented in this chapter is divided into four sections. The first section is dedicated to the 1D OpenSees models. The second section focuses on the SAP2000 models. The third section provides a very brief discussion of 3D modeling of RC. The last section presents the 3D DIANA models.

The pre-test analysis had several objectives: (1) verify expected subassembly behavior with respect to the mode of failure, column, and bent cap beam behavior; (2) finalize the loading protocol, especially for the HS test through ground motion selection and scaling; (3) estimate the expected lateral forces during cyclic and hybrid simulation loading for test set-up design and checks; and (4) determine the proper locations and distribution of the instrumentation where maximum straining actions are expected.

4.1 1D OPENSEES MODELING

Two simple 1D OpenSees models were used as the first part of the pre-test analysis. The first model was developed for the test specimen subassembly using the geometry and reinforcement design discussed in Chapter 3. Nonlinear pushover analysis was conducted for the test specimen model at different gravity load levels. The main objectives of the test specimen pushover analysis was to verify whether the cap beam failure is expected or not and how would the gravity load level affect the behavior of both the column and cap beam.

The second OpenSees model was developed for the prototype bridge adopted from the Caltrans Academy Bridge discussed in Chapter 3. The prototype bridge analysis was intended to investigate any possible effects of the vertical component of the earthquake excitations on the behavior of the bent cap beam. Nonlinear time history analysis was conducted under several ground motions that considered both bi-directional horizontal components only, and combined

vertical and bi-directional horizontal components. Details of the subassembly and prototype bridge analyses are discussed below.

4.1.1 Subassembly Specimen Analysis

The test subassembly is a simple OpenSees model that used three 1D beam-column elements with distributed plasticity. Each of the three elements represents one of the subassembly components: the column, the cap beam, and the box-girder. The boundary conditions used for the model and the dimensions of the idealized 1D elements of the subassembly, which coincide with the elements centerlines, are shown in Figure 4.1. The boundary conditions are roller supports at each of the cap beam ends and fixed-translation supports at each of the box-girder ends. In addition, one rotational DOF was restrained to provide the torsional stiffness of the box-girder section. Fiber sections were used for each of the three beam-column elements used in the model. All material properties used in this model are nominal material properties based on a concrete characteristic strength of 5 ksi and reinforcement steel yield of 68 ksi. The 68 ksi yield stress was used for the steel rather than the typical 60 ksi yield stress because of the sensitivity of the lateral force and column capacity to the steel yield stress. Two of the available material constitutive models in OpenSees were adopted for the model: *Concrete02* and *Steel02* for the concrete and reinforcement, respectively. The *Concrete02* models the nonlinear concrete behavior in both tension and compression. The *Steel02* model was calibrated to reflect elastic-perfectly plastic behavior since the model analysis is used only for preliminary behavior investigation.

Nonlinear pushover analysis was conducted at different levels of axial load in both transverse and longitudinal directions. Note that the transverse direction is always aligned with the cap beam, while the longitudinal direction is aligned with the box-girder. All loads were applied at the top of the column in the inverted position, as shown in Figure 4.1. The gravity vertical load was applied under load-control, i.e., using force increments, while the lateral pushover was applied under displacement control, i.e., using displacement increments. Although the modified Newton-Raphson algorithm was used most frequently for solving the nonlinear equilibrium equation, the linear stiffness method was also used when convergence was not obtained using the Newton-Raphson methods. More information about the incremental-iterative nonlinear solution strategy is presented in the 3D modeling of RC section. Note that a lumped mass was also added at the column top since this same model was also used as part of the HS computational model development and idealization. The discussion related to the use of this model as part of the HS test is included with the HS system components and development in the second part of this report. The three axial load levels considered were 5, 10, and 15%. An axial load level is the ratio between the applied gravity load to the expected axial capacity of the column based on the gross 18-in. column diameter and concrete nominal compressive strength of 5 ksi.

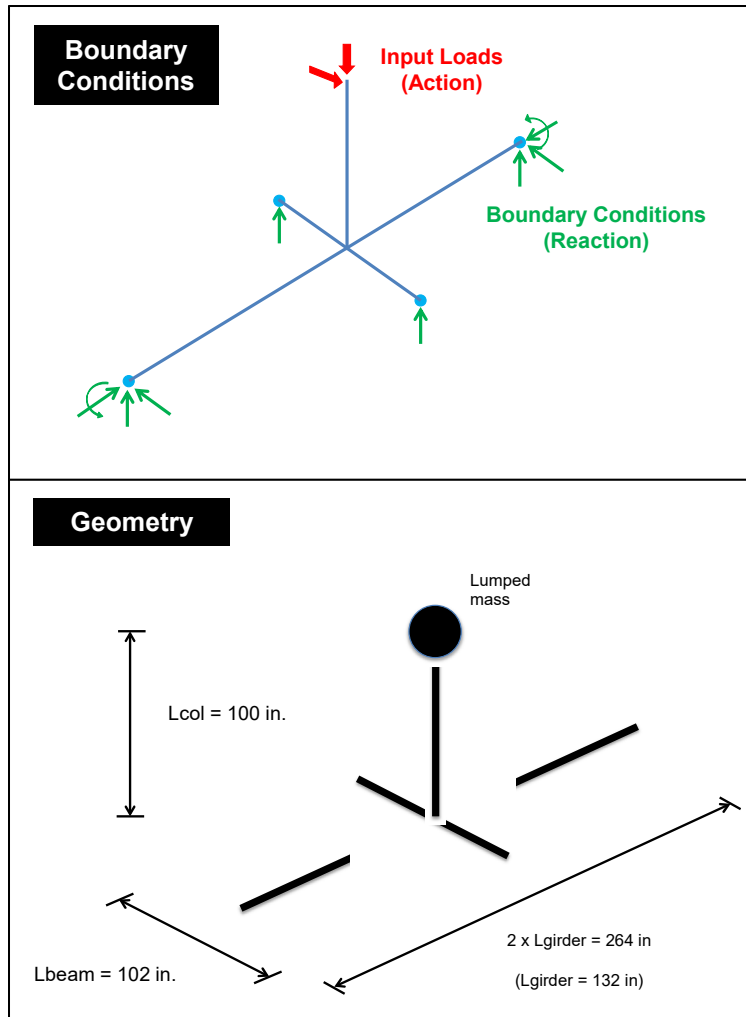


Figure 4.1 Schematic representation of boundary conditions and geometry of the OpenSees model for the test subassembly specimen.

Figure 4.2 shows the force-displacement relationship obtained from the lateral pushover analysis in the transverse direction under different gravity load levels, which shows a noticeable increase in the lateral force capacity as the axial load level is increased. The same observation is confirmed from the column moment–curvature relationship shown in Figure 4.3, where, as expected, the moment capacity of the column increases with the axial load level. The cap beam moment-curvature relationship shown in Figure 4.4 suggests that for the 5% and 10% cases, the cap beam did not yield. However, at 15% axial load, the cap beam failed; see curvature values in Figure 4.4.

Because of the nature of the set-up, there is a direct relation between the gravity load level and the cap beam moments, as evidenced by the bending moment distribution in the column-cap beam elements due to different load cases; see Figure 4.5. Another way of presenting the cap beam yield at the 15% axial load is to use the stress–strain relationship obtained for one of the rebars in the tension side of the cap beam; see Figure 4.6. This figure also confirms that no yielding in the cap beam took place at 5% or 10% axial load; however, as

shown in Figure 4.7, the column rebars yielded at all gravity load levels. The results suggest that varying the gravity load might delay plastic hinge formation in a column while pushing the cap beam further to higher moment demands.

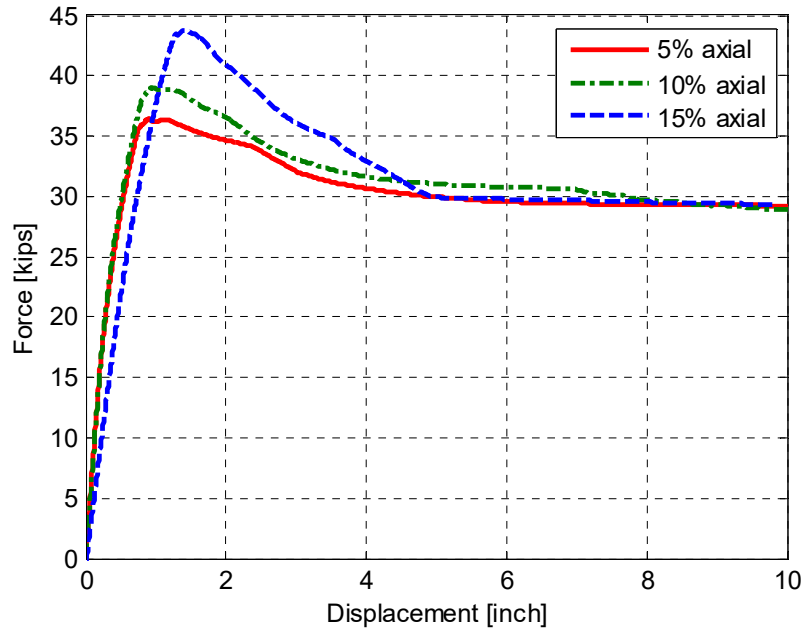


Figure 4.2 Force-displacement relationship for the OpenSees test subassembly under constant gravity load (three levels) and lateral pushover loading in the transverse direction.

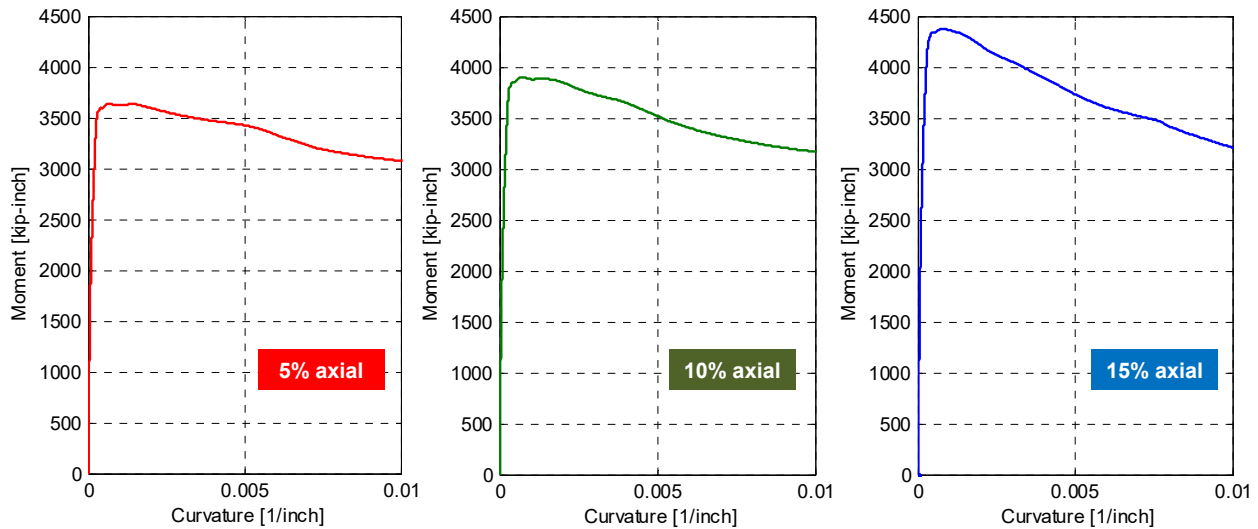


Figure 4.3 Moment-curvature relationship for the subassembly's column section under constant gravity load (three levels) and lateral pushover loading in the transverse direction.

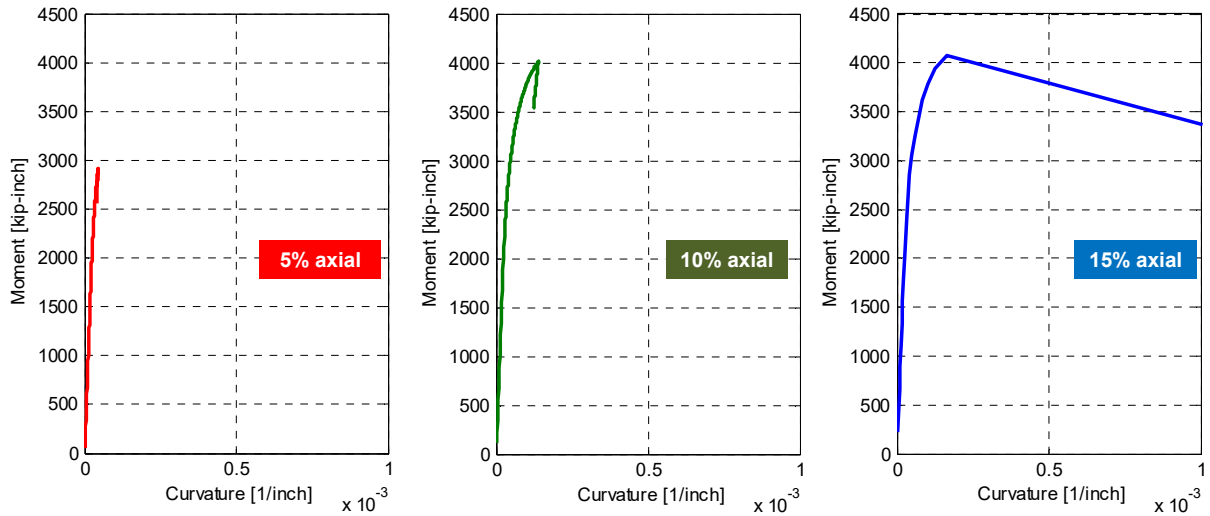


Figure 4.4 Moment-curvature relationship for the subassembly's cap beam section under constant gravity load (three levels) and lateral pushover loading in the transverse direction.

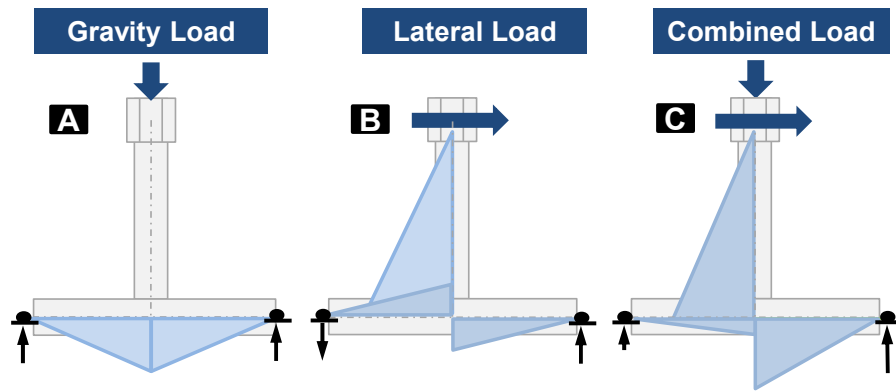


Figure 4.5 Schematic bending moment distribution along the column and bent cap beam in three load cases: (a) gravity load, (b) lateral load, and (c) combined gravity and lateral loads.

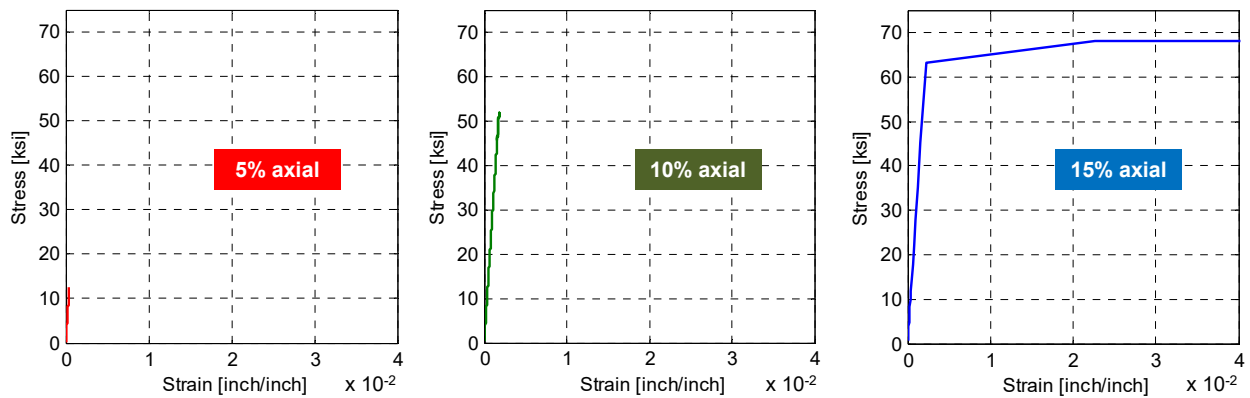


Figure 4.6 Stress-strain relationship for one of the cap beam tension side rebars under constant gravity load (three levels) and lateral pushover loading in the transverse direction.

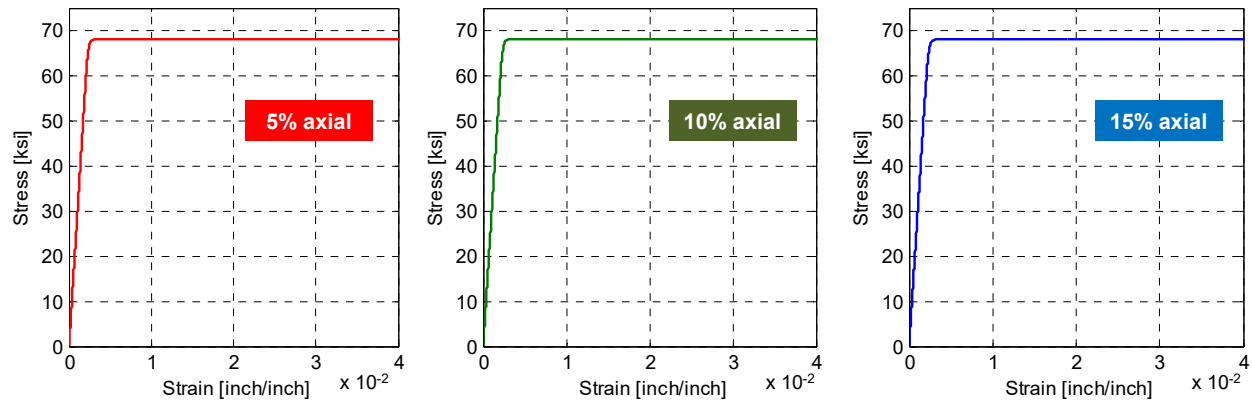


Figure 4.7 Stress–strain relationship for the outermost west rebar of the column (refer to Figure 3.11 for definition of the north side) under constant gravity load (3 levels) and pushover loading towards east.

4.1.2 Prototype Bridge Analysis

OpenSees was also used to perform a full prototype bridge nonlinear time history analysis. The full-scale prototype bridge—see Chapter 3 and in Figure 3.3—was modeled using 1D beam–column elements. A preliminary design was performed according to the AASHTO Guidelines [2007] and Caltrans SDC [2010] to estimate the reinforcement in the bent columns and cap beams. Based on practical recommendations from Caltrans engineers, approximate reinforcement for the box-girder was estimated as well and taken as a percentage of the box-girder area. Similar element types and model characteristics as the subassembly OpenSees model were utilized in the full bridge model. In summary, fiber sections were used for the columns, cap beams, and box-girder beam–column elements. In addition, the 5 ksi nominal concrete characteristic strength was used in the *Concrete02* model, and 68 ksi yield stress was used for *Steel02* model that was calibrated to resemble an elastic-perfectly plastic behavior. The total bridge mass was distributed along the full length of the box-girder and bent cap beams. This distribution was checked to ensure accurate distribution of the actual bending moments due to gravity loading. The periods and modes of vibrations obtained from the OpenSees model were compared against a more detailed SAP2000 bridge model (presented in the next subsection) to verify the mass distribution. The boundary conditions used for the bridge model were a hinged base for all columns with roller supports with additional torsional restraints at the two abutments locations. A schematic representation of the OpenSees bridge model showing the elements dimensions and mass distribution is shown in Figure 4.8.

Nonlinear time history analysis was the main type of analysis carried out for the bridge model, with the objective of investigating the possible effects of vertical component of ground motions on the bent cap beam behavior. This was done at an early stage of the study to decide if vertical excitations should be considered in the HS. Although it was decided that it was impractical to apply a vertical excitation during the HS test because of set-up limitations, the nonlinear time history analysis was very beneficial in choosing a short list of ground motions for further detailed pre-test analysis and final ground motion selection for the HS test.

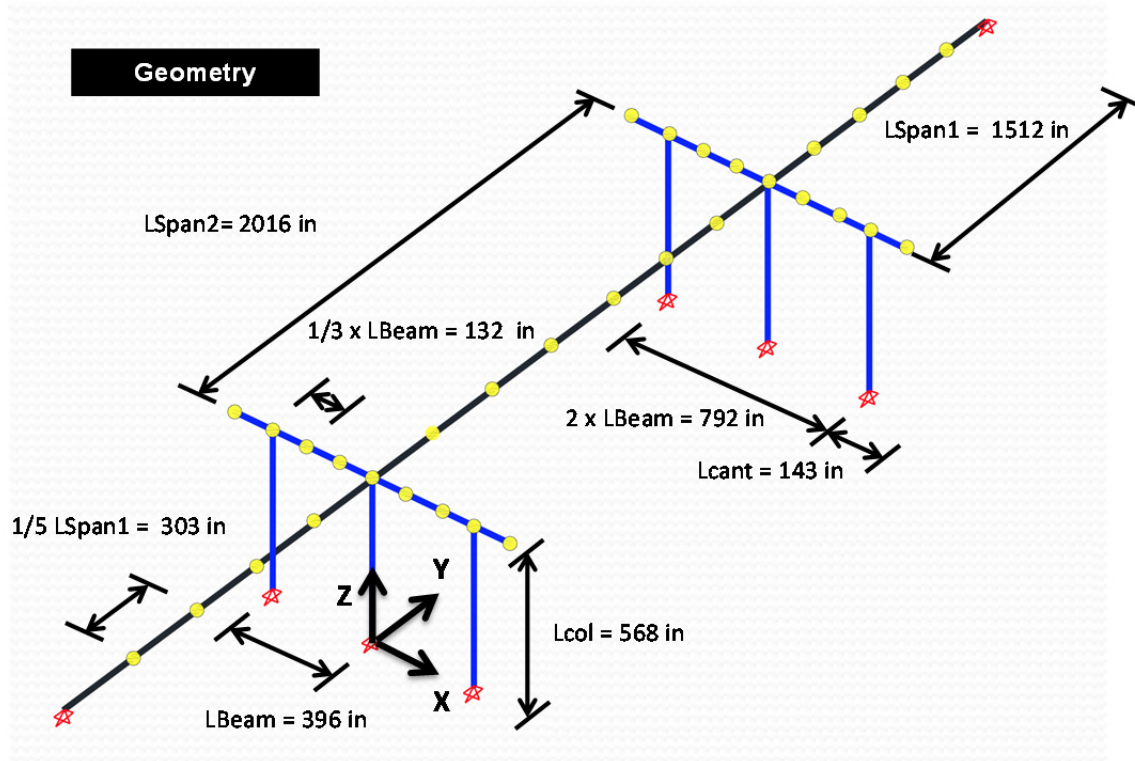


Figure 4.8 Schematic representation of OpenSees model of the modified Caltrans Academy Bridge.

The nonlinear time history analysis of the bridge was also used to estimate the axial load fluctuation in the bridge columns due to the vertical excitations. In summary, a large number of ground motions were selected and used to conduct two sets of nonlinear time history analysis on the OpenSees prototype bridge model. The first set used only the two horizontal components of the selected ground motions. The second set used both of the two horizontal components and the vertical component as well of the selected ground motions. Comparisons were made between the results of these two sets of ground motions to investigate whether the vertical component exerted significant additional demands in bending moment for the cap beam and in axial force for the column.

The PEER Next Generation Attenuation (NGA) strong ground motions database [2005] was used to select the ground motions for this study. The main criterion to select a pool of ground motions was the relative significance of the recorded vertical component. Several previous studies focused on the vertical-to-horizontal component scaling of ground motions and attenuation relationships for the vertical component response spectra, e.g., Campbell and Bozorgnia [2003] and Bozorgnia and Campbell [2004]. These studies suggest that only near-fault records for relatively large magnitude earthquakes would feature relatively large vertical accelerations. Accordingly, earthquakes of magnitude 6.50 or larger and stations that were within 10 km from the fault were selected to prepare the list of ground motions considered. The 6.5 magnitude and 10 km distance to fault were not a fixed value set by the literature, but rather the authors choose a reasonable list of ground motions that still included large recorded vertical

excitations. As summarized in Table 4.1, a total of 88 records, each comprising two horizontal and one vertical components, were selected from the PEER NGA database,. Note that Table 4.1 shows six highlighted ground motions where the vertical component was found to significantly increase the moment demands on the cap beam of this particular bridge model.

In the list of the 88 ground motions used to run two sets of nonlinear time history analysis, one set did not include the vertical component while the other included both horizontal and vertical components. This was done to compare the results obtained from a given ground motion record with (w/) and without (w/o) the vertical component. A total of six ground motions (highlighted in Table 4.1, and summarized in Table 4.2) were found to have the most significant effect on the bent cap beam due to the consideration of the vertical component of the ground motion. The considered significant effect means the occurrence of large curvatures at several sections in both of the bent column and cap beam. A large curvature in the bent cap beam was accompanied by the beam reaching its moment capacity, i.e., the forming of a cap beam plastic hinge. Selected sample results from two of the most severe six ground motions are shown here. Results from the Kobe ground motion runs (ID #5 in Table 4.2) are presented to show the effect of the vertical component on the cap beam moment and curvature demands. In addition, the results from Northridge Sylmar ground motion runs (ID #4 in Table 4.2) show the axial force fluctuation with and without vertical component inclusion. The cap beam and column critical sections used to plot the selected sample results are shown in Figure 4.9.

To investigate the effect of the vertical excitation on the cap beam demands, the results from 30% Kobe ground motion runs are presented. Figure 4.10 shows the comparison between the moment–curvature for the bent column section 1 (Figure 4.9) with and without the vertical excitation. Note that (1) the column failed in both cases whether the vertical excitation was considered or not; and (2) the column moment capacity in the case of the vertical component included was higher than that without vertical excitations. This can be attributed to the effect of the additional compression axial load that can lead to a higher moment capacity; see Figures 4.2 and 4.3.

Although the detailed effects of vertical excitations are not the focus of this analytical study, the reader is referred to other studies, e.g., Lee and Mosalam [2014], for a comprehensive investigation of the effect of vertical excitation on bridge columns axial and shear capacities. Of interest to this study is that the vertical excitation caused significantly larger curvature demands, which led to failure of the bent cap beam at Sections 2 and 3; see Figures 4.11 and 4.12.

Table 4.1 List of ground motions used in OpenSees bridge time history analysis.

ID	NGA Sequence	Earthquake				Station	
		Name	Magnitude	Year	Fault Type	Name	Distance (km)
1	77	San Fernando	6.61	1971	RV	Pacoima Dam (left abut)	1.81
2	126	Gazli, USSR	6.8	1976		Karakyr	5.46
3	143	Tabas, Iran	7.35	1978	RV	Tabas	2.05
4	158	Imperial Valley-06	6.53	1979	SS	Aeropuerto Mexicali	0.34
5	159	Imperial Valley-06	6.53	1979	SS	Agrarias	0.65
6	160	Imperial Valley-06	6.53	1979	SS	Bonds Corner	2.68
7	165	Imperial Valley-06	6.53	1979	SS	Chihuahua	7.29
8	170	Imperial Valley-06	6.53	1979	SS	EC County Center FF	7.31
9	171	Imperial Valley-06	6.53	1979	SS	EC Meloland Overpass	0.07
10	173	Imperial Valley-06	6.53	1979	SS	El Centro Array #10	6.17
11	179	Imperial Valley-06	6.53	1979	SS	El Centro Array #4	7.05
12	180	Imperial Valley-06	6.53	1979	SS	El Centro Array #5	3.95
13	181	Imperial Valley-06	6.53	1979	SS	El Centro Array #6	1.35
14	182	Imperial Valley-06	6.53	1979	SS	El Centro Array #7	0.56
15	183	Imperial Valley-06	6.53	1979	SS	El Centro Array #8	3.86
16	184	Imperial Valley-06	6.53	1979	SS	El Centro Differential	5.09
17	185	Imperial Valley-06	6.53	1979	SS	Holtville Post Office	7.65
18	189	Imperial Valley-06	6.53	1979	SS	SAHOP Casa Flores	9.64
19	284	Irpinia, Italy-01	6.9	1980	N	Auletta	9.55
20	285	Irpinia, Italy-01	6.9	1980	N	Bagnoli Irpinio	8.18
21	495	Nahanni, Canada	6.76	1985	RV	Site 1	9.6
22	497	Nahanni, Canada	6.76	1985	RV	Site 3	5.32
23	753	Loma Prieta	6.93	1989	RV-OBL	Corralitos	3.85
24	763	Loma Prieta	6.93	1989	RV-OBL	Gilroy - Gavilan Coll.	9.96
25	765	Loma Prieta	6.93	1989	RV-OBL	Gilroy Array #1	9.64
26	779	Loma Prieta	6.93	1989	RV-OBL	LGPC	3.88
27	802	Loma Prieta	6.93	1989	RV-OBL	Saratoga - Aloha Ave	8.5
28	821	Erzican, Turkey	6.69	1992	SS	Erzincan	4.38
29	825	Cape Mendocino	7.01	1992	RV	Cape Mendocino	6.96
30	828	Cape Mendocino	7.01	1992	RV	Petrolia	8.18
31	879	Landers	7.28	1992	SS	Lucerne	2.19
32	949	Northridge-01	6.69	1994	RV	Arleta - Nordhoff Fire	8.66
33	983	Northridge-01	6.69	1994	RV	Jensen Filter Plant	5.43
34	1004	Northridge-01	6.69	1994	RV	LA - Sepulveda VA	8.44
35	1013	Northridge-01	6.69	1994	RV	LA Dam	5.92
36	1044	Northridge-01	6.69	1994	RV	Newhall - Fire Sta	5.92
37	1045	Northridge-01	6.69	1994	RV	Newhall - W Pico Can	5.48
38	1050	Northridge-01	6.69	1994	RV	Pacoima Dam (downstr)	7.01
39	1051	Northridge-01	6.69	1994	RV	Pacoima Dam (upper)	7.01
40	1052	Northridge-01	6.69	1994	RV	Pacoima Kagel Canyon	7.26
41	1063	Northridge-01	6.69	1994	RV	Rinaldi Receiving Sta	6.5
42	1084	Northridge-01	6.69	1994	RV	Sylmar - Converter Sta	5.35

Table 4.1 Continued.

ID	NGA Sequence	Earthquake				Station	
		Name	Magnitude	Year	Fault Type	Name	Distance (km)
43	1085	Northridge-01	6.69	1994	RV	Sylmar - Converter east	5.19
44	1086	Northridge-01	6.69	1994	RV	Sylmar - Olive View	5.3
45	1106	Kobe, Japan	6.9	1995	SS	KJMA	0.96
46	1111	Kobe, Japan	6.9	1995	SS	Nishi-Akashi	7.08
47	1119	Kobe, Japan	6.9	1995	SS	Takarazuka	0.27
48	1120	Kobe, Japan	6.9	1995	SS	Takatori	1.47
49	1165	Kocaeli, Turkey	7.51	1999	SS	Izmit	7.21
50	1176	Kocaeli, Turkey	7.51	1999	SS	Yarimca	4.83
51	1182	Chi-Chi, Taiwan	7.62	1999	RV-OBL	CHY006	9.77
52	1193	Chi-Chi, Taiwan	7.62	1999	RV-OBL	CHY024	9.64
53	1197	Chi-Chi, Taiwan	7.62	1999	RV-OBL	CHY028	3.14
54	1231	Chi-Chi, Taiwan	7.62	1999	RV-OBL	CHY080	2.69
55	1244	Chi-Chi, Taiwan	7.62	1999	RV-OBL	CHY101	9.96
56	1489	Chi-Chi, Taiwan	7.62	1999	RV-OBL	TCU049	3.78
57	1490	Chi-Chi, Taiwan	7.62	1999	RV-OBL	TCU050	9.51
58	1491	Chi-Chi, Taiwan	7.62	1999	RV-OBL	TCU051	7.66
59	1492	Chi-Chi, Taiwan	7.62	1999	RV-OBL	TCU052	0.66
60	1493	Chi-Chi, Taiwan	7.62	1999	RV-OBL	TCU053	5.97
61	1494	Chi-Chi, Taiwan	7.62	1999	RV-OBL	TCU054	5.3
62	1495	Chi-Chi, Taiwan	7.62	1999	RV-OBL	TCU055	6.36
63	1499	Chi-Chi, Taiwan	7.62	1999	RV-OBL	TCU060	8.53
64	1501	Chi-Chi, Taiwan	7.62	1999	RV-OBL	TCU063	9.8
65	1503	Chi-Chi, Taiwan	7.62	1999	RV-OBL	TCU065	0.59
66	1504	Chi-Chi, Taiwan	7.62	1999	RV-OBL	TCU067	0.64
67	1505	Chi-Chi, Taiwan	7.62	1999	RV-OBL	TCU068	0.32
68	1507	Chi-Chi, Taiwan	7.62	1999	RV-OBL	TCU071	5.31
69	1508	Chi-Chi, Taiwan	7.62	1999	RV-OBL	TCU072	7.03
70	1510	Chi-Chi, Taiwan	7.62	1999	RV-OBL	TCU075	0.91
71	1511	Chi-Chi, Taiwan	7.62	1999	RV-OBL	TCU076	2.76
72	1512	Chi-Chi, Taiwan	7.62	1999	RV-OBL	TCU078	8.2
73	1515	Chi-Chi, Taiwan	7.62	1999	RV-OBL	TCU082	5.18
74	1519	Chi-Chi, Taiwan	7.62	1999	RV-OBL	TCU087	7
75	1521	Chi-Chi, Taiwan	7.62	1999	RV-OBL	TCU089	8.88
76	1528	Chi-Chi, Taiwan	7.62	1999	RV-OBL	TCU101	2.13
77	1529	Chi-Chi, Taiwan	7.62	1999	RV-OBL	TCU102	1.51
78	1530	Chi-Chi, Taiwan	7.62	1999	RV-OBL	TCU103	6.1
79	1545	Chi-Chi, Taiwan	7.62	1999	RV-OBL	TCU120	7.41
80	1546	Chi-Chi, Taiwan	7.62	1999	RV-OBL	TCU122	9.35
81	1550	Chi-Chi, Taiwan	7.62	1999	RV-OBL	TCU136	8.29
82	1551	Chi-Chi, Taiwan	7.62	1999	RV-OBL	TCU138	9.79
83	1605	Duzce, Turkey	7.14	1999	SS	Duzce	6.58
84	1611	Duzce, Turkey	7.14	1999	SS	Lamont 1058	0.21
85	1612	Duzce, Turkey	7.14	1999	SS	Lamont 1059	4.17
86	1615	Duzce, Turkey	7.14	1999	SS	Lamont 1062	9.15
87	1617	Duzce, Turkey	7.14	1999	SS	Lamont 375	3.93
88	1618	Duzce, Turkey	7.14	1999	SS	Lamont 531	8.03

Table 4.2 Short list of ground motions with most significant effect of vertical excitation on the considered bridge cap beam response.

ID	NGA Seq. #	Earthquake				Station	
		Name	Magn.	Year	Fault Type	Name	Distance-to-fault (km)
1	495	Nahanni, Canada	6.76	1985	Reverse	Site 1	9.60
2	779	Loma Prieta	6.93	1989	Reverse-Oblique	LGPC	3.88
3	1063	Northridge-01	6.69	1994	Reverse	Rinaldi	6.50
4	1084	Northridge-01	6.69	1994	Reverse	Sylmar	5.35
5	1119	Kobe, Japan	6.90	1995	Strike-Slip	Takarazuka	0.27
6	1505	Chi-Chi, Taiwan	7.62	1999	Reverse-Oblique	TCU068	0.32

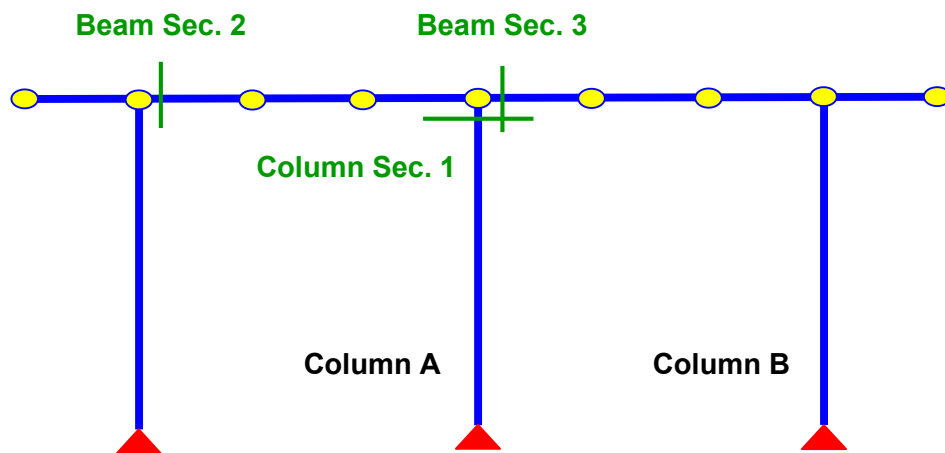


Figure 4.9 Bridge bent with critical cross sections identified.

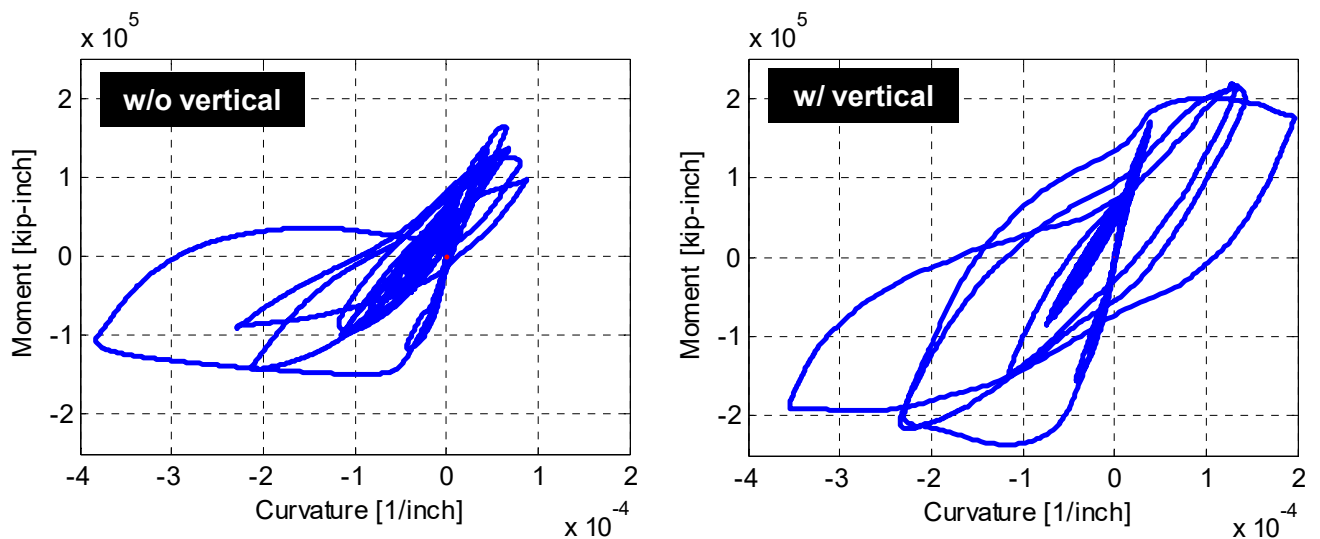


Figure 4.10 Moment–curvature relationships for bridge column (Section 1 in Figure 4.9) subjected to 30%-scale Kobe ground motion with and without vertical excitation component.

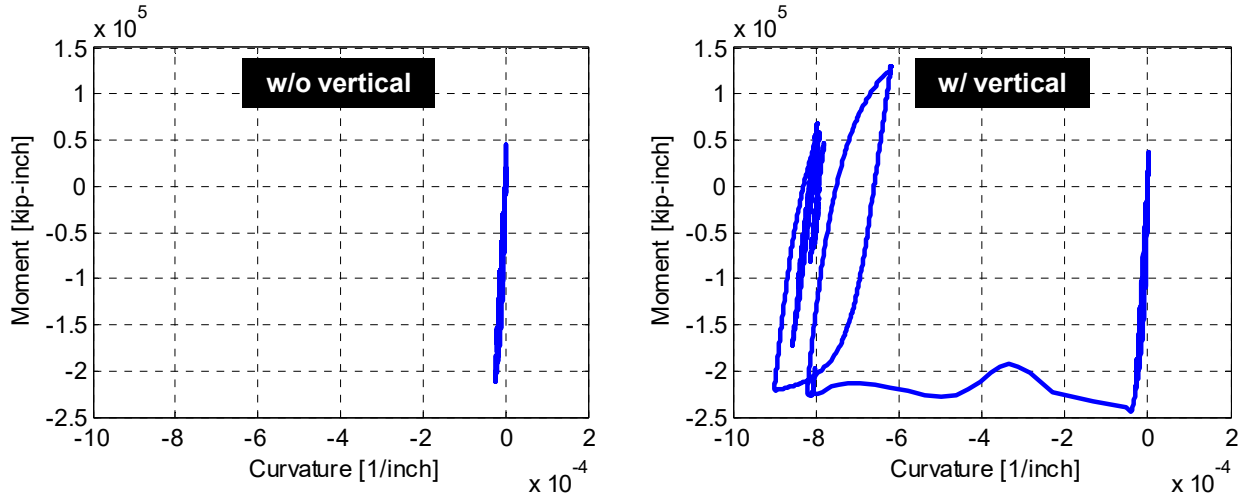


Figure 4.11 Moment-curvature relationships for bridge cap beam (Section 2 in Figure 4.9) subjected to 30%-scale Kobe ground motion with and without vertical excitation component.

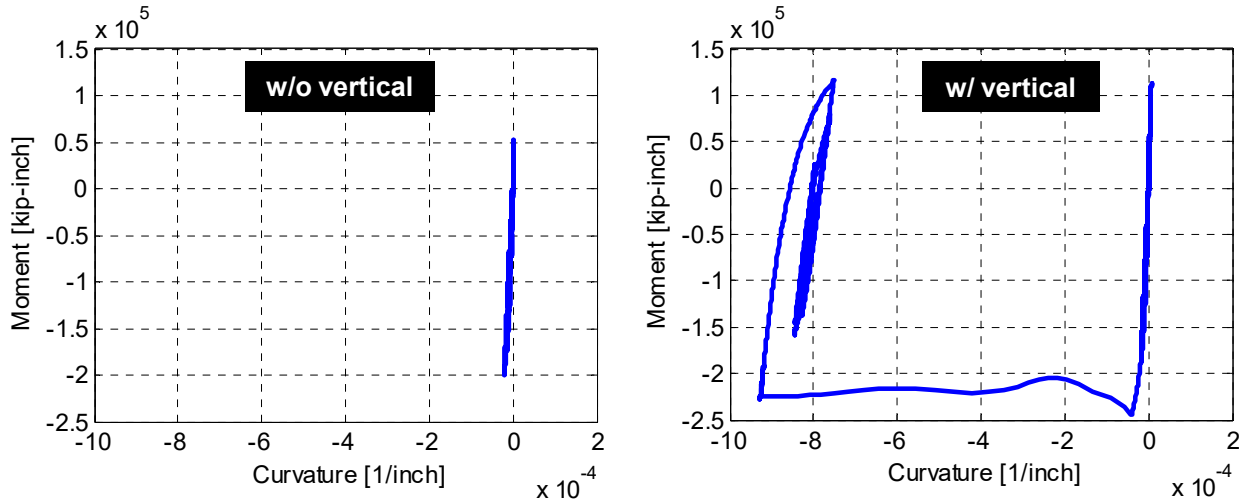


Figure 4.12 Moment-curvature relationships for bridge cap beam (Section 3 in Figure 4.9) subjected to 30%-scale Kobe ground motion with and without vertical excitation component.

Determining the effect of vertical excitations was useful in deciding which ground motion would have a more significant effect on the modified Academy Bridge prototype considered in this study. These results demonstrate that future studies are warranted that consider different bridge configurations for investigating the effects of vertical excitation on the cap beams and the resulting fluctuation in the columns axial load. However, this study does not aim at identifying the effects of vertical excitation on the axial or shear capacity of the columns. Only the fluctuation in axial load from a seismic demand perspective was considered as the basis for loading protocols.

Figures 4.13 and 4.14 show the axial load due to 100% Sylmar record of the Northridge ground motion in the bent interior column A and exterior column B, as identified in Figure 4.9,

respectively. Note that the axial load in the interior column fluctuated around an approximate value of 3200 kips versus a 1500 kips for the exterior column. This reflects directly the level of gravity load due to the bridge's own-weight and other superposed dead loads. When vertical excitation is included, the axial load was increased at some instances by almost 60% in case of interior column and 100% in case of exterior column. This was observed for most of the ground motions and not only the presented sample. Therefore, an increase of 50% to 100% in the gravity load during the course of the conducted experimental program was adopted to address the effect of vertical excitation not only on the column axial force, but the cap beam demands as well. This is because the additional gravity load due to the vertical excitation in the used test set-up also translates into additional moments in the cap beam and axial force in the column; see Figure 4.5.

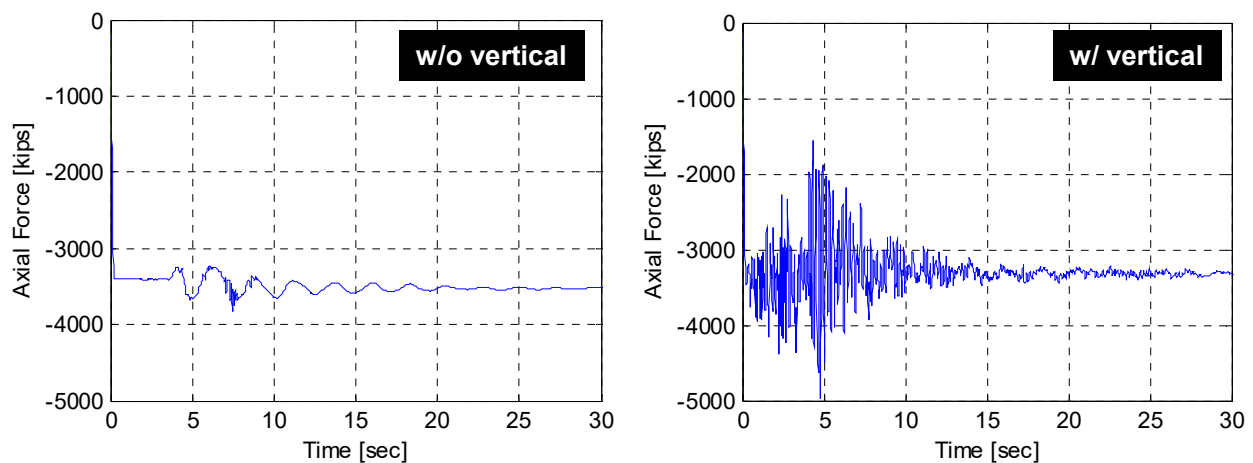


Figure 4.13 Axial load fluctuation in bridge interior column A (Figure 4.9) subjected to 100%-scale Northridge Sylmar ground motion with and without vertical excitation component.

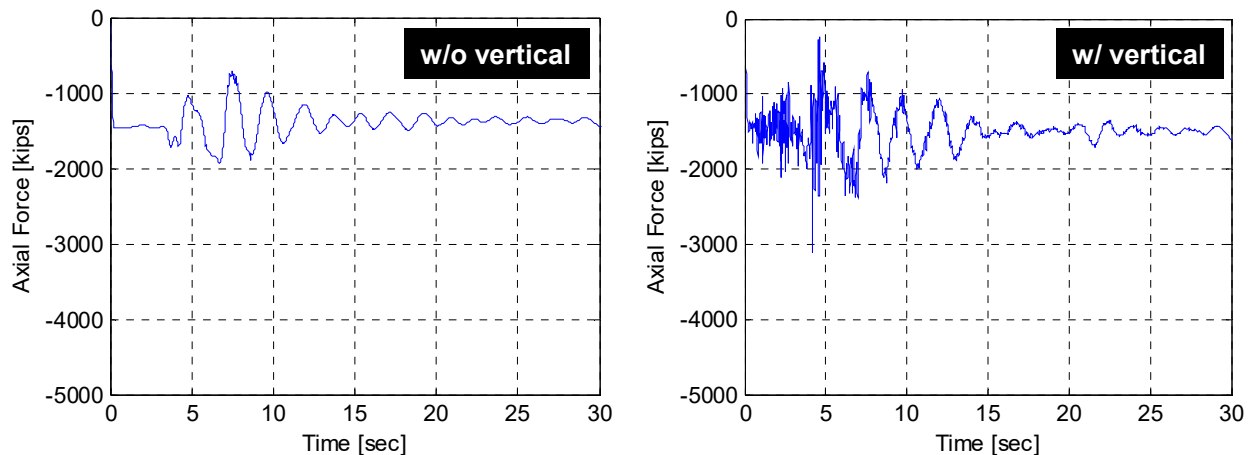


Figure 4.14 Axial load fluctuation in bridge exterior column B (Figure 4.9) subjected to 100%-scale Northridge Sylmar ground motion with and without vertical excitation component.

4.2 2D SAP2000 MODELING

A detailed bridge model for the prototype considered in this study was developed using the commercial software SAP2000 [2012] to provide several necessary response quantities. The prototype SAP2000 model was used to (1) determine the design forces and bending moments for the test specimen design, as previously discussed in Chapter 3; and (2) provide reference modes of vibration and periods of vibrations that were utilized for the calibration of the OpenSees full bridge model and HS computational model. The elastic SAP2000 bridge model was also used to determine the test specimen subassembly geometry and boundary conditions; see Chapter 3. Discussion of the specimen model is presented, which is then followed by a discussion of the full bridge elastic model.

4.2.1 Subassembly Specimen Analysis

A simple linear elastic model for the test subassembly was developed using SAP2000. The model used 1D beam-column elements for the bent cap beam and the column, and 2D plane stress shell elements for the box-girder. Figure 4.15 shows two different views of the developed subassembly model. Linear analysis under vertical and lateral concentrated loads at the column top in the inverted position of the test subassembly was carried out. The purpose of the linear analysis was to try different boundary conditions and compare the forces and bending moment distribution in the different subassembly components against the corresponding full bridge case. Four different cases of boundary conditions were investigated; see Figure 4.16. A sample of the analysis results for the third case of the boundary conditions is shown in Figures 4.17 and 4.18. When compared to the prototype bridge, it was found that either Case 3 or 4 provided a better match for the bent cap beam response. Also the effect of the whether using full fixation or hinges at the box-grader ends was minimal relative to bent cap beam response. It was concluded that whether the specimen boundary conditions for the seat beams were irrelevant because they did not alter the behavior in the vicinity of the bent cap beam.

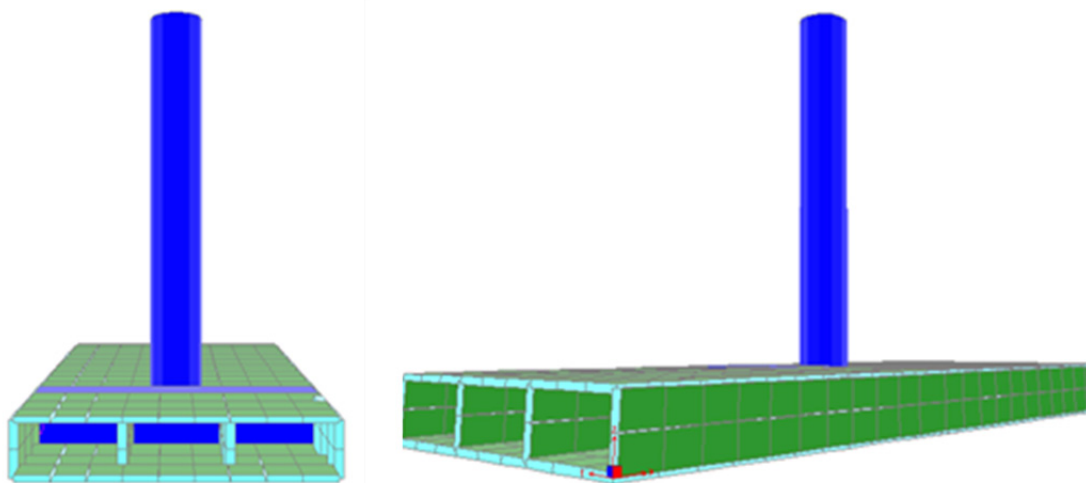


Figure 4.15 Test subassembly SAP2000 model.

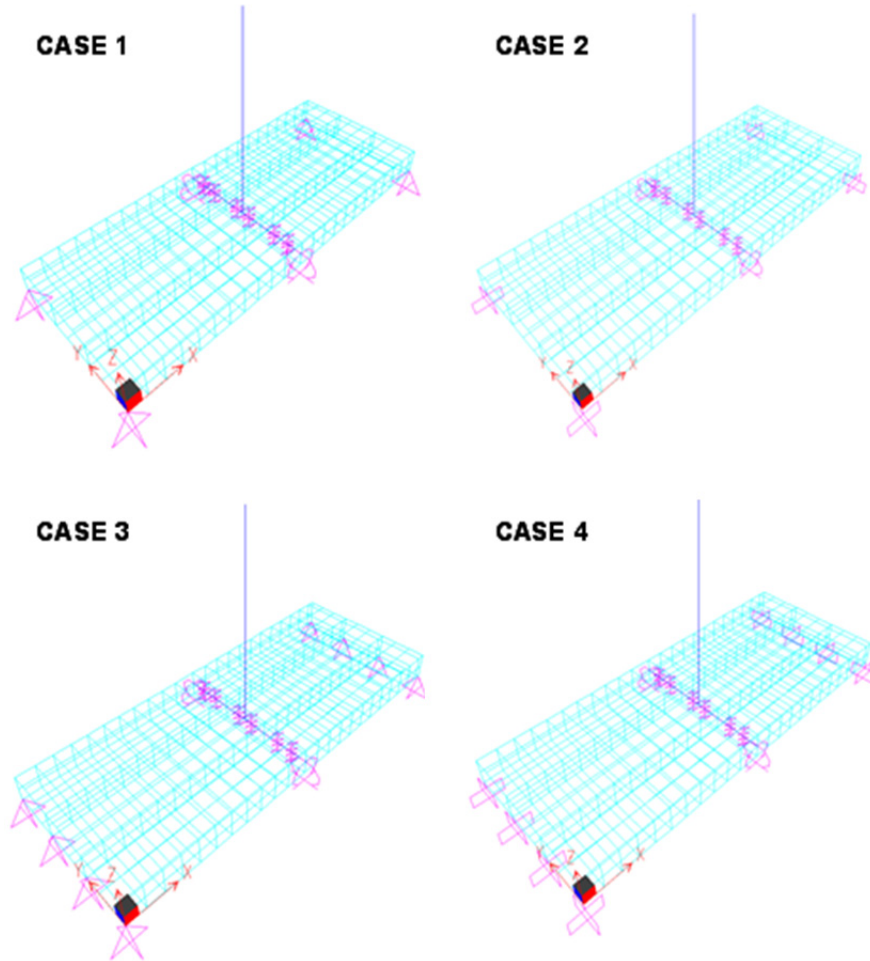


Figure 4.16 Investigated boundary conditions of the test subassembly.

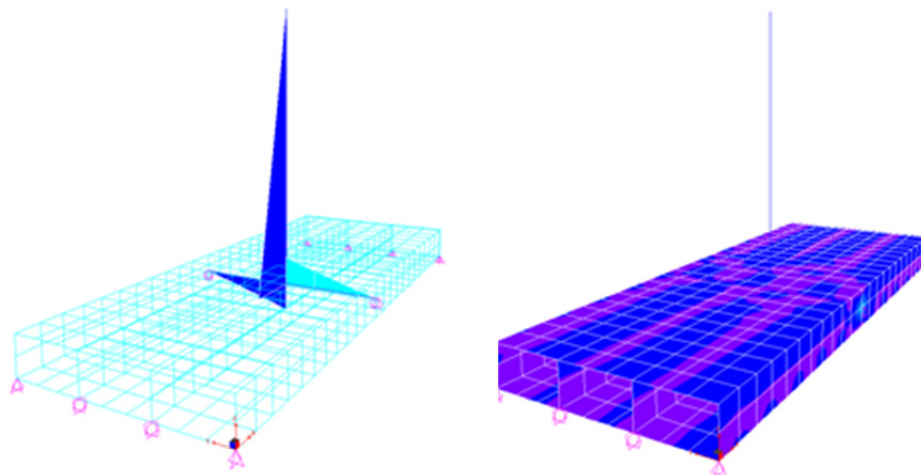


Figure 4.17 Sample of linear analysis results of subassembly model due to lateral transverse loading: moment distribution in the cap beam and column (left); moment distribution in the subassembly deck in the transverse direction (right).

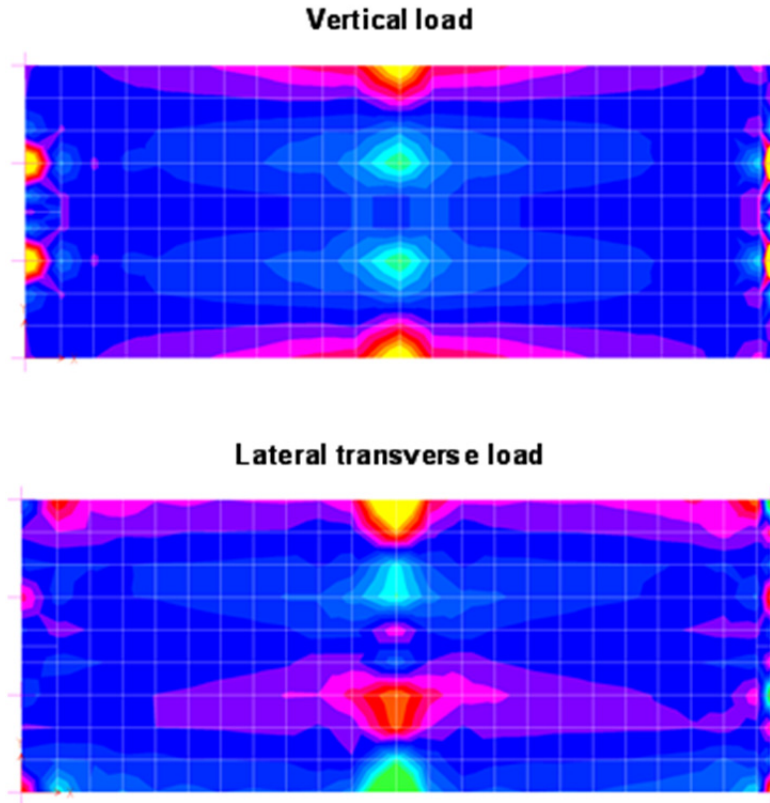


Figure 4.18 Stress distribution in the deck slab due to two different load cases.

4.2.2 Prototype Bridge Analysis

As previously mentioned, the prototype bridge SAP2000 model was used as the reference for designing the subassembly geometry, boundary conditions, and reinforcement. The bridge model used 2D shell elements for the box-girder superstructure and beam-column elements for the bent columns and cap beam; see Figure 4.19. The full prototype bridge was analyzed under gravity, i.e., dead weight and live traffic loads, and lateral loads to provide design forces and bending moments for the reduced-scale test specimen; see Appendix A for details. Note that proper similitude relationships were adopted for scaling the straining actions. The linear analysis of the prototype was used to also determine locations of zero-moments for choosing the subassembly geometry and dimensions. A sample of the bridge analysis under gravity and lateral transverse load is shown in Figure 4.20.

An eigensolution analysis was performed using the SAP2000 prototype bridge model in the interest of accurately defining the full superstructure mass and proper lateral stiffness of the bridge bents, the obtained periods and modes of vibration from this analysis were considered the reference for all dynamic aspects that followed throughout the study. The main three modes of vibrations and corresponding periods for the full prototype bridge in the transvers, longitudinal, and vertical directions are shown in Figure 4.21. The obtained periods were used in calibrating the lumped mass values for the OpenSees prototype bridge model and the DIANA test

subassembly model used to conduct dynamic time history analyses. These periods were used to calibrate the mass used in the computational part of the HS.

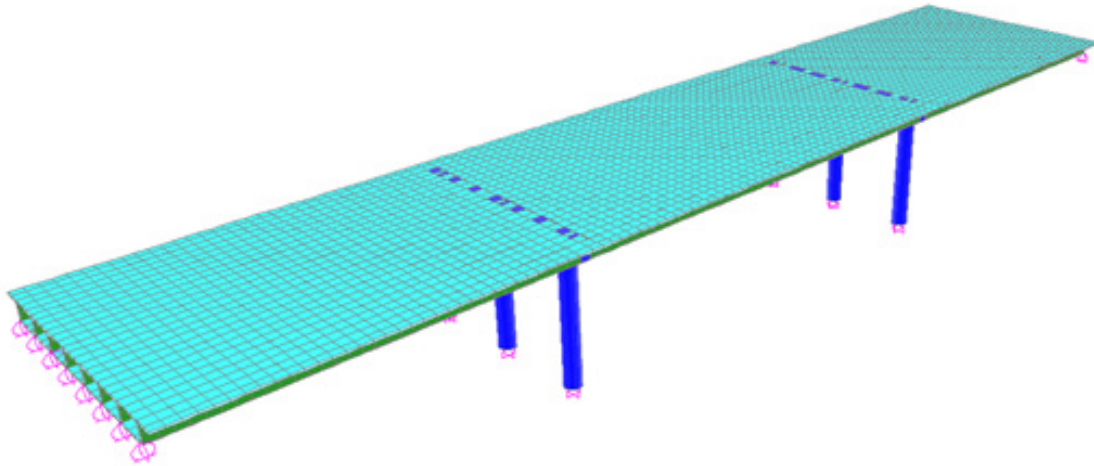
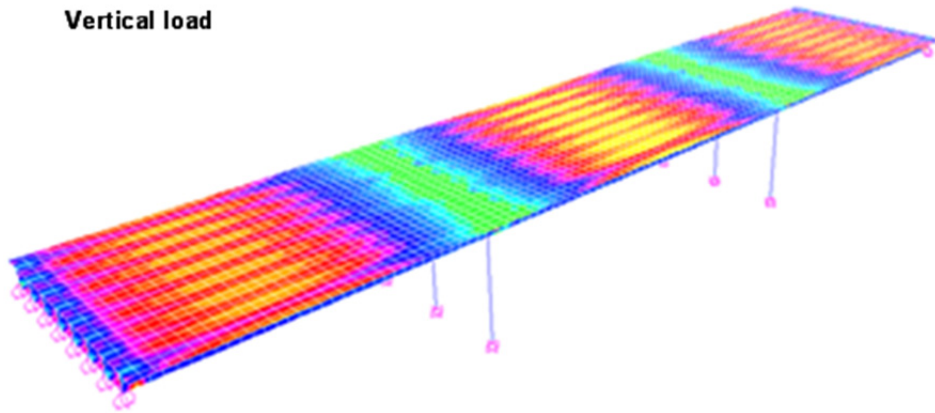


Figure 4.19 Three-dimensional view of the prototype SAP2000 model.

Vertical load



Lateral transverse load

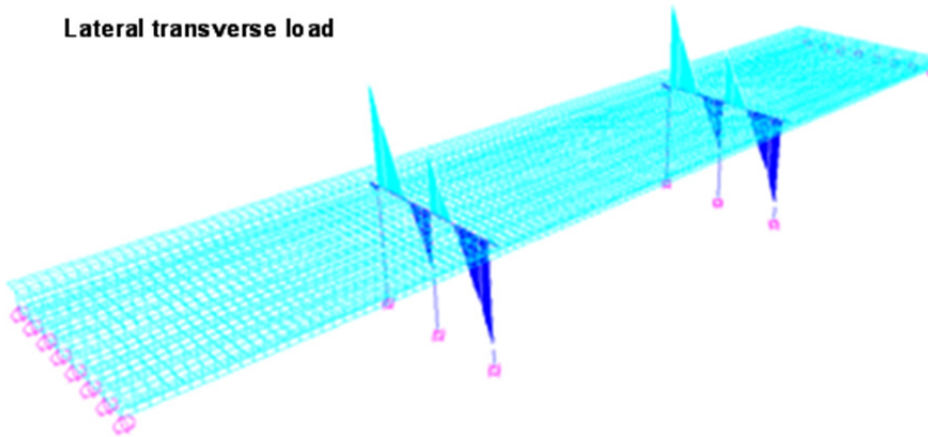
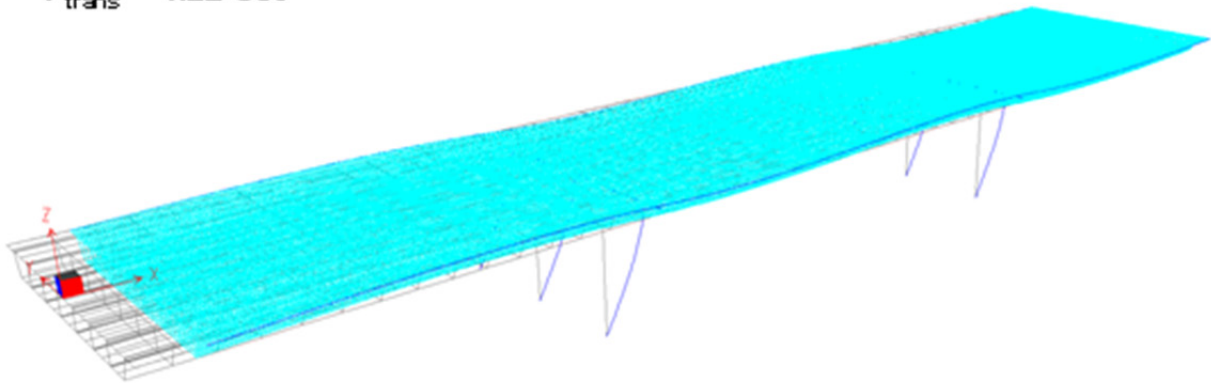
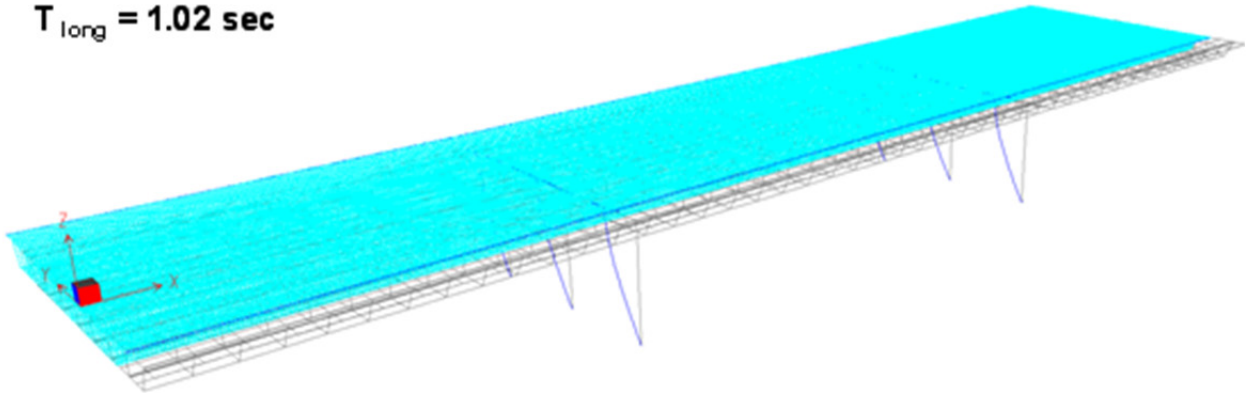


Figure 4.20 Sample of linear analysis results of prototype model: moment distribution in bridge deck in the longitudinal direction (top), and moments in bent cap beam (bottom).

$T_{\text{trans}} = 1.22 \text{ sec}$



$T_{\text{long}} = 1.02 \text{ sec}$



$T_{\text{vertical}} = 0.40 \text{ sec}$

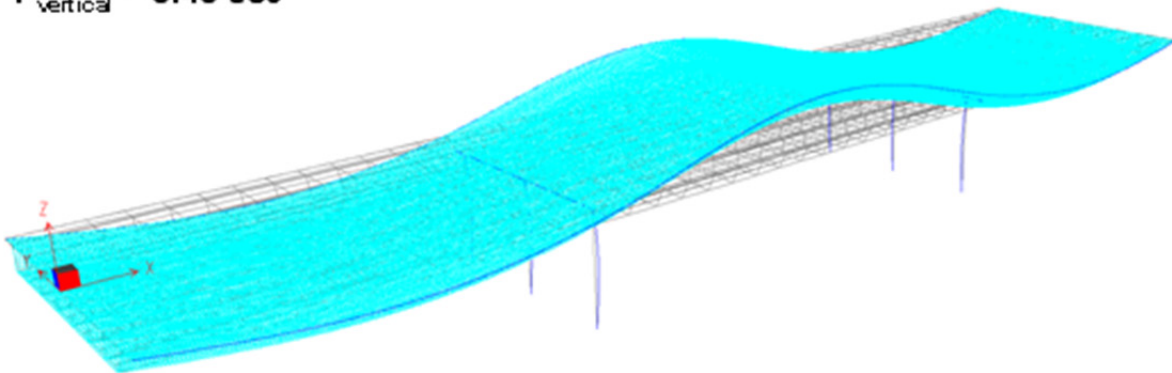


Figure 4.21 Three main modes of vibration and corresponding periods for the prototype bridge in the transverse, longitudinal, and vertical directions.

4.3 3D MODELING OF REINFORCED CONCRETE

Accurate modeling of the stress states and damage of a highly non-homogeneous material such as RC has always been challenging. It becomes more challenging when macro structural system models that feature different cases of static and dynamic loading are sought as a part of structural analysis and design procedures. Many computational methods exist for 3D modeling of the structural systems; how well these models reflect the actual behavior of RC bridges, particularly systems subjected to combined gravity and lateral loading, is not clear. Therefore, the third type of model developed in this study using 3D solid elements in DIANA [2014] was first utilized in the pre-test analysis phase, but calibrated later as part of the post-test analysis phase against the experimental results to gain confidence on how the actual behavior is reflected through computational modeling.

Advanced constitutive modeling of RC is the essence of the detailed 3D DIANA FE models. A discussion of the basics of 3D modeling of RC using FE formulation and using DIANA is below. The discussion is divided into three subsections that cover concrete modeling, reinforcing steel, and the nonlinear solution strategies used throughout this research. A short note on the FE formulation is presented first for completeness. A standard FE displacement formulation was adopted in this project. Displacement vector, $\{u\}$, within each element is interpolated from the vector of nodal degrees of freedom, $\{d\}$, using specific shape functions that depend on element type, $[N]$, as given in Equation (4.1)

$$\{u\} = [N]\{d\} \quad (4.1)$$

The strain vector within the element, $\{\varepsilon\}$, is obtained from the displacement by differentiation as in Equation (3.8)

$$\{\varepsilon\} = \partial\{u\} \quad (4.2)$$

where ∂ is the usual differential operator used in the case of small deformation. Combining Equations (4.1) and (4.2), the strain can be evaluated directly from the nodal displacements as given in Equation (4.3) using the strain shape function, $[B]$.

$$\{\varepsilon\} = \partial[N]\{d\} = [B]\{d\} \quad (4.3)$$

Using the principle of virtual work, the element stiffness matrix can be computed from Equation (4.4) such that:

$$\text{External Work} = \text{Internal Work} \rightarrow \delta\{u\}^T \{r\} = \int_V \delta\{\varepsilon\}^T \{\sigma\} dV \quad (4.4)$$

where $\{r\}$ is the vector of element external loads, δ indicates a virtual quantity, $\{\sigma\}$ is the stress vector within the element, and V represents the element volume. From Equations (4.3) and (4.4), the element stiffness matrix, $[k]$, can be derived as given by Equation (4.5)

$$[k] = \int_V [B]^T [E] [B] dV \quad (4.5)$$

where $[E]$ is the constitutive matrix. In this study, only the nonlinear behavior due to material damage is reflected in the matrix $[E]$; nonlinear geometry due to large displacements is not considered. Finally, using standard FE method, the global stiffness matrix of the structure, $[K]$, is assembled. Similarly, the global nodal loads vector, $\{R\}$, is assembled, leaving the global nodal displacements $\{D\}$ the only unknown in Equation (4.6).

$$[K]\{D\} = \{R\} \quad (4.6)$$

More details on the considered element types, the concrete and reinforcing steel material models, and the solution method of the above nonlinear system of equations are presented next.

4.3.1 Modeling of Concrete

4.3.1.1 Element Types

Two different types of meshing algorithms were used to develop the 3D DIANA models. Auto-meshing algorithms in DIANA generate only tetrahedron (pyramid) elements. Extruding quadrilateral faces or surface elements produce the brick elements. Auto-meshing was first used for the preliminary analysis and then a revised version of the model that utilized brick elements was developed. Only the brick element based-models were considered for model calibration and post-analysis phases. The first type of element used is the 12 DOFs pyramid TE12L element, see Figure 4.22(a), which comprises four nodes with three DOFs per node and three sides, and uses the isoparametric formulation. It is based on linear interpolation in terms of the natural coordinates ξ , η , and ζ given by Equation (4.7), and uses numerical Gauss integration. The linear polynomials yield a constant strain and stress distribution over the element volume. For numerical integration, DIANA by default applies a one-point integration scheme over the volume. However, four- and five-point integration schemes are also available for TE12L elements.

$$u_i(\xi, \eta, \zeta) = \alpha_0 + \alpha_1 \xi + \alpha_2 \eta + \alpha_3 \zeta \quad (4.7)$$

where $i = 1$ to 12 and α_0 to α_3 are constants determined by standard FE analysis.

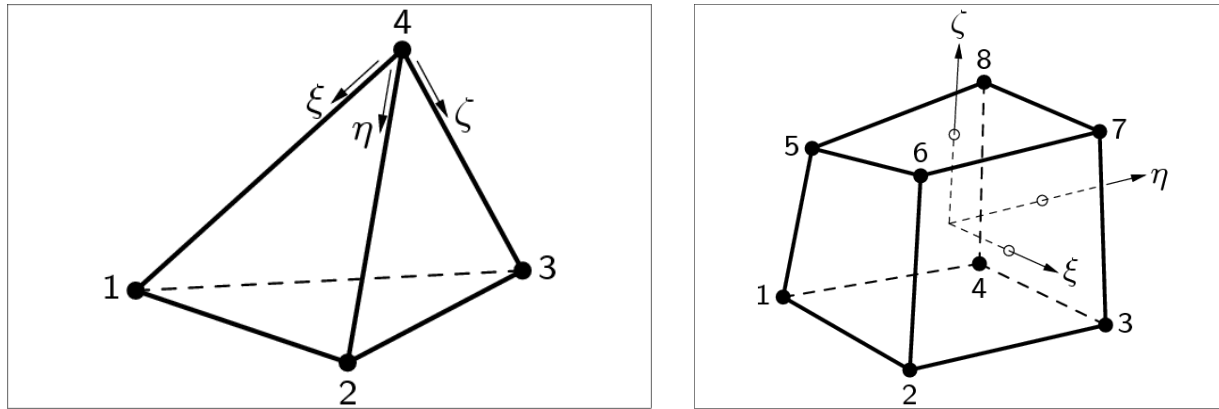
The second type of elements used in this study is the eight-node isoparametric 24 DOFs solid brick HX24L element shown in Figure 4.22(b). Similar to the TE12L, the brick element is based on linear interpolation and Gauss integration. The polynomials for the translation displacement field use tri-linear interpolation as expressed by Equation (4.8)

$$u_i(\xi, \eta, \zeta) = \alpha_0 + \alpha_1 \xi + \alpha_2 \eta + \alpha_3 \zeta + \alpha_4 \xi \eta + \alpha_5 \eta \zeta + \alpha_6 \zeta \xi + \alpha_7 \xi \eta \zeta \quad (4.8)$$

where $i = 1$ to 24 and α_0 to α_7 are constants determined by standard FEM.

Typically, a rectangular brick element approximates the strain and stress distribution over the element volume as follows. The strain ϵ_{xx} and stress σ_{xx} are constant in x -direction and vary linearly in y - and z -direction. The strain ϵ_{yy} and stress σ_{yy} are constant in y -direction and vary linearly in x - and z -direction. The strain ϵ_{zz} and stress σ_{zz} are constant in z -direction and vary linearly in x - and y -direction. By default DIANA applies a $2 \times 2 \times 2$ integration scheme. A $1 \times$

1 × 1 scheme is an available option. For either element type, the nonlinear material behavior of the concrete is incorporated using nonlinear constitutive model.



Tetra-hedron [pyramid] TL12L

Tri-linear brick HX24L

Figure 4.22 Used element types in the 3D DIANA models.

4.3.1.2 Constitutive Models

Concrete is a complex material with different tensile and compressive behavior, which depends on the confinement. When concrete reaches its tensile strength, it cracks with diminishing strength as the crack width increases. The cracks are geometrical discontinuities that separate the material. To model the cracking behavior of materials, there are two basic approaches, the discrete crack approach and the smeared crack approach [Rots 1991; Bažant and Planas 1998]. The discrete crack approach reflects the final damaged state most closely. It models the crack directly via a displacement-discontinuity in an interface element that separates two solid elements. The discrete approach does not fit the nature of the FE displacement method. In addition, it is computationally more convenient to employ a smeared crack approach. In this latter approach, a cracked solid element can be still considered a continuum but requires proper account of the stiffness change according to certain stress-strain relationships. This second approach is the one utilized throughout this research. Note that the underlying assumption of displacement continuity in smeared cracking contradicts the nature of the geometrical discontinuities that occurs across a crack. This assumption in some cases is known to cause stress locking [Rots 1991] and mesh bias.

The concrete behavior using the smeared crack approach can be modeled using either a multi-directional fixed-crack method or a total strain rotating-crack method. The multi-directional fixed-crack method considers that the orientation of the cracks remains constant, and, in turn, the stress-strain relationships are evaluated in a fixed coordinate system that is set once cracking initiates. The total strain rotating-crack method, however, considers that the orientation of the cracks rotates with the directions of the principal strains. Only the total strain method, which was developed along the lines of the 2D modified compression field theory [Vecchio and Collins 1986] and extended to 3D by Selby and Vecchio [1993], is utilized in this study. The total strain formulation follows the coaxial stress-strain concept, which is also known as the

rotating crack model, where the stress-strain relationships are evaluated in the principal directions of the strain vector. The basic concept of the total strain-based crack models is that the stress is evaluated in the directions given by the crack directions. The strain vector $\{\varepsilon\}_{xyz}$ in the element coordinate system xyz at iteration $i+1$ at time (or pseudo-time for nonlinear static loading) $t+\Delta t$ is updated with the strain increment $\{\Delta\varepsilon\}_{xyz}$ according to Equation (4.9)

$${}^{t+\Delta t}_{i+1}\{\varepsilon\}_{xyz} = {}^t\{\varepsilon\}_{xyz} + {}^{t+\Delta t}_{i+1}\{\Delta\varepsilon\}_{xyz} \quad (4.9)$$

This strain vector is subsequently transformed to the crack coordinate system nst (refer to the insert in Figure 4.23) with the continuously-varying strain transformation matrix ${}^{t+\Delta t}_{i+1}[T] = [T]({}^{t+\Delta t}_{i+1}\{\varepsilon\}_{xyz})$ according to Equation (4.10)

$${}^{t+\Delta t}_{i+1}\{\varepsilon\}_{nst} = {}^{t+\Delta t}_{i+1}[T] {}^{t+\Delta t}_{i+1}\{\varepsilon\}_{xyz} \quad (4.10)$$

The strain transformation matrix is determined by calculating the eigenvectors of the strain tensor. During loading, the concrete is subjected to both tensile and compressive stresses, which may result in cracking and crushing of the material. The deterioration of the material due to cracking and crushing in 3D structures is monitored with six internal damage variables $\alpha_k, k=1, \dots, 6$ (Figure 4.23). The loading-unloading-reloading conditions are monitored with unloading constraints $r_k, k=1, \dots, 6$ (Figure 4.23), which model the stiffness degradation in tension and compression separately. These constraints for tension and compression are expressed as given in Equations (4.11) and (4.12), respectively.

$$r_k = \begin{cases} 0 & \text{if } {}^{t+\Delta t}_{i+1}\varepsilon_k > \alpha_k \\ 1 & \text{if } {}^{t+\Delta t}_{i+1}\varepsilon_k \leq \alpha_k \end{cases}, \quad k=1,2,3 \quad (4.11)$$

$$r_k = \begin{cases} 0 & \text{if } {}^{t+\Delta t}_{i+1}\varepsilon_{k-3} < \alpha_k \\ 1 & \text{if } {}^{t+\Delta t}_{i+1}\varepsilon_{k-3} \geq \alpha_k \end{cases}, \quad k=4,5,6 \quad (4.12)$$

With the assumption of no damage recovery, the stress in direction j is given by Equation (4.13)

$$\sigma_j = f_j(\{\alpha\}, \{\varepsilon\}_{nst}) \times g_j(\{\alpha\}, \{\varepsilon\}_{nst}) \quad (4.13)$$

where f_j is the uniaxial stress-strain relationship, and g_j is the loading-unloading function. If unloading and reloading is modeled with a secant approach, g_j is given by Equation (4.14)

$$g_j = \begin{cases} 1 - \frac{\alpha_j - \varepsilon_j}{\alpha_j} & \text{if } \varepsilon_j > 0 \\ 1 - \frac{\alpha_{j+3} - \varepsilon_j}{\alpha_{j+3}} & \text{if } \varepsilon_j < 0 \end{cases} \quad (4.14)$$

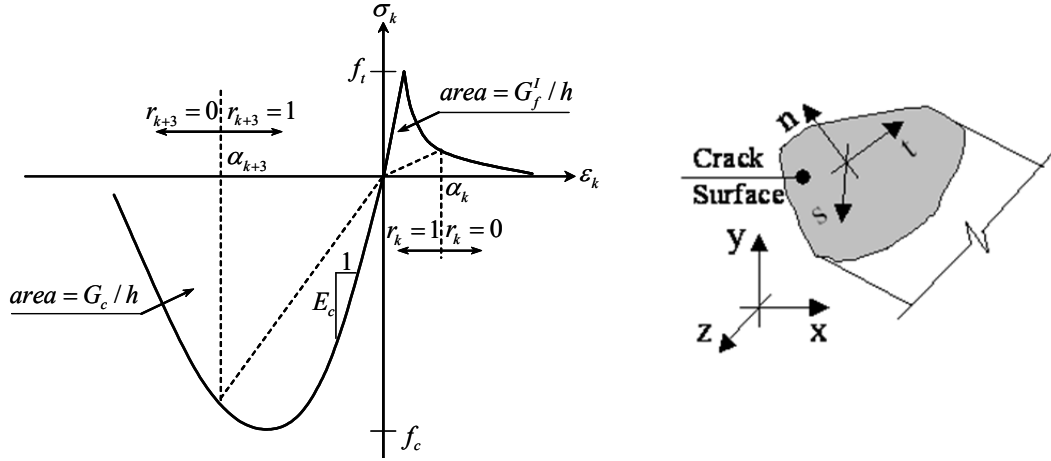


Figure 4.23 Rotating crack surface and unidirectional concrete material model in principal directions.

For the incremental-iterative solution scheme, the constitutive model should define the stiffness matrix, which is utilized to achieve equilibrium. In this study, a secant stiffness matrix approach was adopted. This approach has proven to be robust and stable in RC structures with extensive cracking. For this purpose, the secant stiffness terms in the j th direction are presented in Equations (4.15) and (4.16).

$$\bar{E}_j = f_j \left(\{\alpha\}, \{\varepsilon\}_{nst} \right) / \alpha_j \quad (\text{for tension regime}) \quad (4.15)$$

$$\bar{E}_j = f_j \left(\{\alpha\}, \{\varepsilon\}_{nst} \right) / \alpha_{j+3} \quad (\text{for compression regime}) \quad (4.16)$$

These secant stiffness terms can be geometrically interpreted as the slopes of the dashed inclined lines shown in Figure 4.23. The secant stiffness matrix in the nst coordinate system is given by Equation (4.17), which corresponds to the stiffness matrix of an orthotropic material with zero Poisson's ratio in all directions.

$$D_{secant} = \begin{bmatrix} \bar{E}_1 & 0 & 0 & 0 & 0 & 0 \\ 0 & \bar{E}_2 & 0 & 0 & 0 & 0 \\ 0 & 0 & \bar{E}_3 & 0 & 0 & 0 \\ 0 & 0 & 0 & \bar{G} & 0 & 0 \\ 0 & 0 & 0 & 0 & \bar{G} & 0 \\ 0 & 0 & 0 & 0 & 0 & \bar{G} \end{bmatrix} \quad (4.17)$$

where $\bar{G} = \beta_s G$, and the parameter β_s ($0 \leq \beta_s \leq 1$) is a non-dimensional shear retention factor that reduces the elastic shear modulus G of concrete after cracking to the constant value \bar{G} . For the full definition of all components and parameters of total strain crack model in DIANA, the basic properties, e.g., Young's modulus, are complemented with input for the compression, tension, and shear behavior. For behavior in compression, the uniaxial stress-strain relationship for the

concrete is based on elastic-perfectly-plastic behavior, shown in Figure 4.24(a), and governed by the concrete compressive strength f_c . The tensile relationship is based on linear tension softening, shown in Figure 4.24(b). The tensile behavior depends on the concrete tensile strength f_t and the fracture energy G_f^I from crack opening mode, i.e., mode I. The areas under the compressive and tensile stress-strain relationships control the ultimate compressive strain and the crack strain beyond which the concrete loses its entire respective capacities. These areas depend on the band-width (h), i.e., localization size, of plastification or damage due to cracking, which is expressed as $h = \sqrt[3]{V_e}$, where V_e is the volume of the FE. Note that for the pre-test analysis, expected material properties were used for f_c and f_t as defined by *Caltrans SDC* [2013] based on nominal concrete properties. Meanwhile, the fracture energy, G_f^I , was related to other concrete materials using the CEB-FIP Model Code recommendation [1993]. However, for the post-test analysis, actual material properties were used including that for the fracture energy.

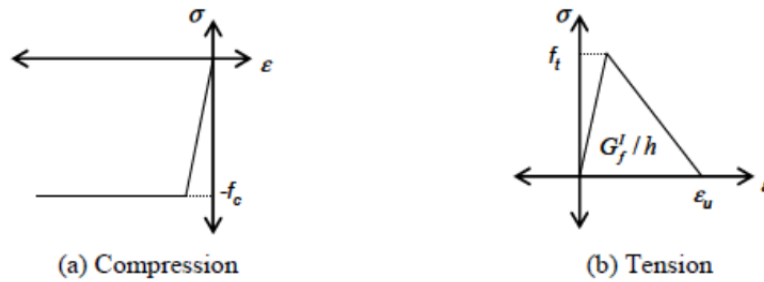


Figure 4.24 Concrete stress-strain relationships.

4.3.2 Modeling of Steel Reinforcement

Modeling of steel reinforcement, including any prestressing tendons, using FE is commonly performed by one of two different methods [DIANA 2014; Naito et al. 2001]. The first method, which is less computationally demanding, involves the use of embedded or smeared reinforcement within the concrete. The embedded reinforcement action is introduced in the concrete element through which it passes, and the stiffness of the concrete element is modified accordingly. The embedded reinforcement formulation implies perfect bond between the concrete and the reinforcement. However, bond-slip reinforcement could be used as well, which is the second method used for modeling reinforcement. The bond-slip reinforcement is more computationally demanding and involves separate discretization of the reinforcement from the surrounding concrete, i.e., the reinforcing bar is internally modeled using 1D discrete truss or beam elements, which are connected to the mother concrete elements by line-solid interface element. These interface elements between the concrete element edge and the reinforcement line element are what is needed to model the bond-slip effects. A schematic of both of the embedded and discrete reinforcement in a parent element is shown in Figure 4.25(a) and (b), respectively. One drawback of the discrete method is the additional nodes and DOF required. For example, Figure 4.25 suggests that when embedded reinforcement is adopted, two brick elements with total of 36 DOFs can be used. On the other hand, discrete representation of reinforcement requires the use of eight brick elements for concrete and two 1D elements for the reinforcement,

in addition to interface elements between the steel and the concrete to represent the slip and dowel actions. This latter modeling technique requires solving for 90 DOFs. Another drawback for discrete reinforcement is that the concrete mesh is restricted by the reinforcement locations. This restriction makes the concrete mesh difficult to generate, particularly in situations such as the soffit test specimen, which has high reinforcement ratios and tight box-girder dimensions. Therefore, only embedded reinforcement was considered for the pre-test analysis. Note that no bond-slip was observed from the experiments, so embedded reinforcement was used in post-test analysis as well. More details about embedded reinforcement formulation and constitutive modeling are presented next.

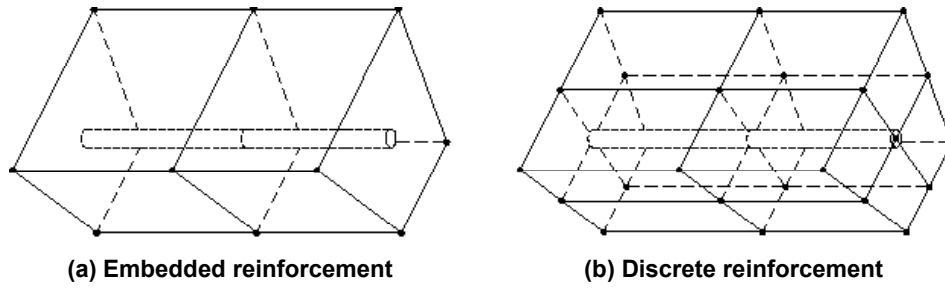


Figure 4.25 Reinforcement elements in FEA.

4.3.2.1 Embedded Reinforcement

Embedded reinforcement is introduced within the concrete element through which it passes, referred to as the parent element. The stiffness of this “parent element” is then modified based on the path of the reinforcement through the element. As a result, the assumption is made that there exists perfect bond between the concrete and the reinforcement. For the simple case where a uniform quantity of reinforcement is distributed across the element at a certain angle from the element natural coordinate system, the additional stiffness terms are easily computed. Given that the element displacements are computed from the nodal displacements, the reinforcement displacements, $\{u\}^r$, can be found using the same shape functions matrix, $[N]$ as those for the concrete elements as given by Equation (4.18):

$$\{u\}^r = [N]\{d\} \quad (4.18)$$

However, the reinforcement displacements are evaluated at the isoparametric coordinates of the reinforcement integration points, e.g., using a two-point Gauss integration scheme. The strain vector of the reinforcement can accordingly be evaluated by Equation (4.19)

$$\{\varepsilon\}^r = [B]^r \{d\} \quad (4.19)$$

where $[B]^r$ is the strain–displacement matrix evaluated at the reinforcement integration points. Standard transformation techniques are used to obtain the reinforcement strain vector in the same

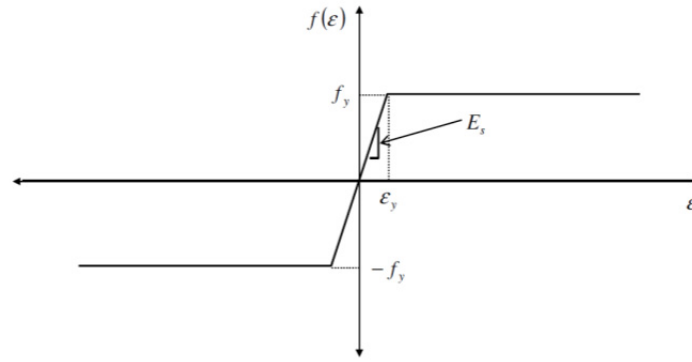
orientation as the parent element strain vector. Making use of transformation, reinforcement constitutive equations, and usual FE procedure, one can obtain the contribution of reinforcement to the stiffness of the parent element and the corresponding internal force vector of the reinforcement. Accordingly, the stiffness and internal force contributions of the reinforcement are accounted for in a similar manner as the concrete element stiffness and internal forces with only the exception that integration is performed at the reinforcement integration points rather than at the element integration points.

4.3.2.2 Constitutive Model

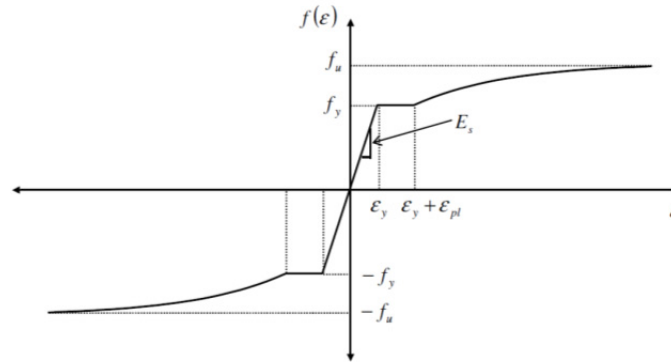
Reinforcing steel material is modeled assuming elasto-plastic behavior based on Von-Mises yield criterion with modulus of elasticity E_s and yield strength f_y . Two models were considered for hardening. The first is a simple uniaxial elastic-perfectly-plastic model with identical compression and tension behavior and no hardening, as shown in Figure 4.26(a). The simple model is a reasonable approximation for the pre-test analysis where generic behavior trends and approximate force capacity values are sought. However, for more accurate analysis during the post-test analysis phase, the hardening rule followed the Voce [1948] equation available in DIANA, which is schematically shown in Figure 4.26(b) and presented by Equation (4.20).

$$f(\varepsilon) = \begin{cases} \varepsilon E_s \leq f_y & \varepsilon \leq \varepsilon_y + \varepsilon_{pl} \\ f_y + (f_u - f_y) \left(1 - \exp \left[-\frac{\varepsilon - \varepsilon_y - \varepsilon_{pl}}{\varepsilon_{po}} \right] \right) & \varepsilon \geq \varepsilon_y + \varepsilon_{pl} \end{cases} \quad (4.20)$$

where f_y is the yield stress, f_u is the ultimate stress, E_s is the Young's modulus of the steel, ε_{pl} is the plateau strain, and ε_{po} is a parameter to adjust the strain-hardening regime. For post-test analysis, the Voce equation parameters (assumed to be the same for tension and compression) were calibrated against the actual reinforcing steel material properties presented in Chapter 3.



(a) Elastic-perfectly plastic



(b) Voce

Figure 4.26 Reinforcing steel stress-strain relationships

4.3.3 Nonlinear Solution Strategy

In nonlinear FE analysis, the relation between the force vector and displacement vector, in the weak-form of equilibrium or FE formulation, is no longer linear. Similar to the linear FE analysis, it is desirable to calculate a displacement vector that equilibrates the internal and external forces in nonlinear FE analysis. To determine the state of equilibrium in nonlinear cases, the problems are not discretized in space only (with finite elements), but also in time (with increments). The time increments used can be real time increments, for creep or dynamic analysis, or pseudo-time increments to describe sequence of events, i.e., provide a counter function. To achieve equilibrium at the end of a given event (increment), an iterative solution algorithm is used. When all the events (increments) are considered, the combination is called an “incremental-iterative” solution procedure. A brief discussion of the iterative and incremental procedures considered in this study is presented next.

4.3.3.1 Iterative Procedures

Several iterative methods are available in DIANA. Three pure iterative procedures are available: the Newton-Raphson method, the quasi-Newton method, and the linear stiffness method. DIANA offers two variations that can be used in combination with any of the pure iterative procedures, which are the *continuation method* and the *line search method*. Finally, several criteria to stop the iteration loop are discussed. Another variation of the iteration algorithm is the

Arc-length method. The idea behind all the iterative methods is to generate a sequence of approximations u_i for the solution, i.e., the displacement vector $\{u\}$ is determined through the recovered formula given by Equation (4.21).

$$\{u_{i+1}\} = \{u_i\} + \gamma_i (P_f - [K] \{u_i\}) \quad (4.21)$$

where P_f is the assembled load vector, and γ_i is an integration constant that defines the iterative solver such that eventually the residual, which is written as $(P_f - [K]\{u_i\})$, converges to zero. The three iterative procedures, mentioned above, were all used in this study and they are discussed in more detail next:

Newton-Raphson (regular and modified)

The regular and modified Newton-Raphson methods are illustrated schematically in Figure 4.27 (a) and (b), respectively. For the regular Newton-Raphson strategy, the tangent stiffness is calculated for every iteration within a given increment. This strategy yields a quadratic convergence, which means that the iteration process converges with a few iterations. The modified Newton-Raphson strategy computes the tangent stiffness at the start of the load increment and uses this same stiffness for all the iterations within this load increment. This method usually requires more iterations than the regular Newton-Raphson, but the computations are faster for each iterations since the tangent stiffness matrix is formulated, assembled, and decomposed only once at the beginning of each load increment. Generally, in FE analysis, regular Newton iteration can be used when minimal nonlinear behavior and damage (cracking or plasticity) in each increment is expected. For moderate levels of damage, the modified Newton iteration is better for convergence as it avoids calculating the stiffness of the moderately damaged elements at each iteration.

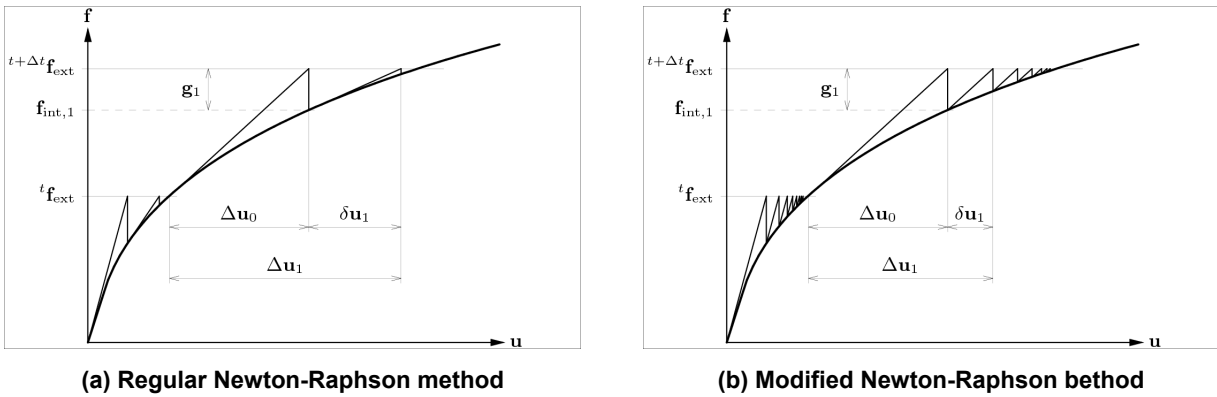


Figure 4.27 Schematic representation of iterative nonlinear solvers [DIANA 2014].

Quasi-Newton Method

The quasi-Newton method, also called “secant method,” essentially uses the information of previous solution vectors and out-of-balance force vectors during the increment to achieve a better approximation, as illustrated in Figure 4.28. Unlike Regular Newton-Raphson, the quasi-Newton method does not set up a completely new stiffness matrix at every iteration. The stiffness of the structure is rather determined from the known positions at the equilibrium path.

Three different methods are available in DIANA for assembling the quasi-Newton stiffness matrix: the Broyden, the Broyden-Fletcher-Goldfarb-Shanno (BFGS), and the Crisfield methods. Only the Broyden method was used in this study; it demonstrated the least rate of divergence in runs with large number of DOFs.

Linear and Constant Stiffness Iteration Methods

The linear and constant stiffness iteration methods can be used if the other methods become unstable, or if it is desirable to keep certain characteristics. The linear strategy uses the initial linear stiffness matrix for all the iterations in all the load increments, as illustrated in Figure 4.29. The linear stiffness method is usually very robust, especially in nonlinear dynamic analysis, but one drawback is that occasionally the system follows an unstable equilibrium path after bifurcations [DIANA 2014]. For situations where high nonlinearity is encountered, the linear solution strategy can be used. This procedure requires many iterations to reach a converged solution. However, the cost of each iteration is low since the tangent stiffness matrix is formulated, assembled, and decomposed only once at the beginning of the analysis.

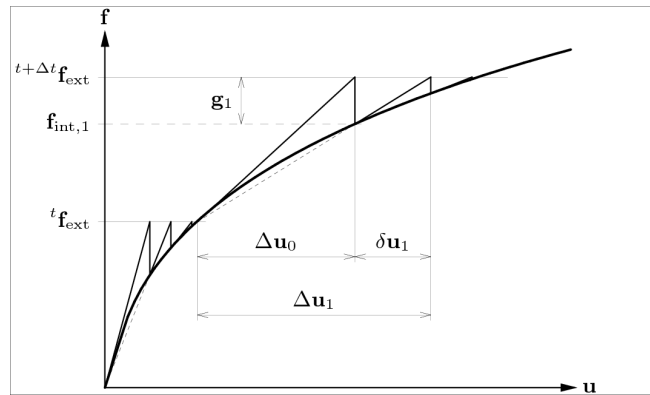


Figure 4.28 Schematic representation of quasi-Newton iterations [DIANA 2014].

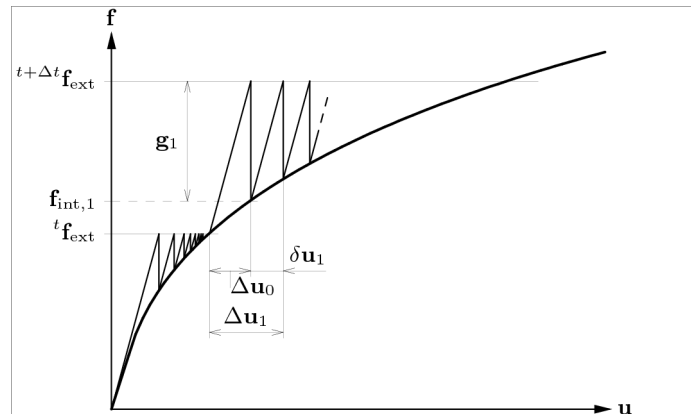


Figure 4.29 Schematic representation of linear stiffness iterations [DIANA 2014].

4.3.3.2 Incremental Procedures

The second part of the incremental-iterative solution procedure consisted of the incremental procedures. The initial choice of the step size for every increment is an important factor in the incremental-iterative process. Several methods can be used to determine step sizes. For instance, fixed increments, such as prescribed force increments, can be used versus adaptive increments, such as the Arc-length method where the step size is adapted based on the results of a current step. Only incremental methods that used fixed steps either in load control or displacement control were used in this study. When iterations are in process, the external force, f_{ext} , vector can be increased directly at the start of each increment. This is usually called “load control” and schematically represented in Figure 4.30(a). Another way to put an external load on a structure is to prescribe certain displacements at each increment, which is called “displacement control” and is shown in Figure 4.30(b).

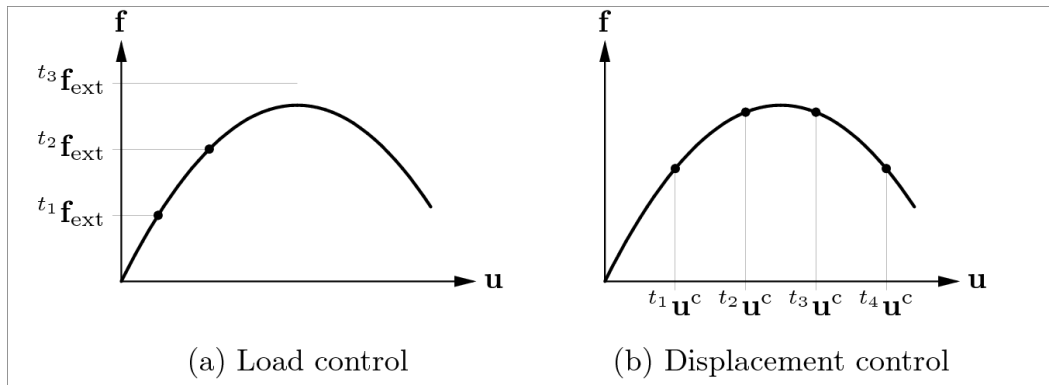


Figure 4.30 Load and displacement controls for the incremental procedure [DIANA 2014].

4.4 DIANA PRE-TEST ANALYSIS

The 3D modeling and analysis of the test specimen using DIANA [2014] was the most accurate and detailed model, satisfying most of the pre-test analysis objectives. The DIANA pre-test analysis aimed at: (a) estimating the subassembly column and bent cap behavior and mode of failure under different gravity and lateral load combinations; (b) estimating the expected lateral forces for accurate test set-up design; and (c) determining the location and distribution of the instrumentation. Two main types of nonlinear analyses were conducted, namely pushover and time history analysis.

4.4.1 Mesh Development

Two versions of the test specimen model that used different element types were developed in DIANA [2014]. The first model used the auto-meshing readily available algorithms in DIANA to create the mesh for the test specimen model. The resulting mesh composed of tetrahedron pyramid elements (TH12L). The auto-meshing resulted in a total of 7050 nodes that were

composed of 17526 TH12L elements for the concrete mesh elements only. An additional 392 bar elements were used for the embedded reinforcement. A better mesh was developed using manual 3D meshing that started with quadrilateral 2D surface mesh at different levels that was then carefully extruded at different levels to form the final 3D mesh. This meshing process resulted in a mesh that comprised of only brick elements (HX24L). Accordingly, a total of 14,347 nodes encompassing 8326 HX24L elements for the concrete mesh elements were obtained. In addition, the embedded reinforcement mesh created 348 bar elements. More details about the embedded reinforcement and the two element types used in concrete meshing were included in the previous section. A view of the two test specimen meshes that used tetrahedron and brick elements is shown in Figures 4.31 and 4.32, respectively. The embedded reinforcement mesh used for both models is shown in Figure 4.33.

The tetrahedron mesh was used to develop a preliminary model. Thus, the boundary conditions used in that model were mainly a full fixation at the bottom nodes of the two seat beams and two vertical roller supports at the two middle nodes in the ends of the bent cap beam portions of the model. Lateral displacement loading was applied in that model directly at the very top of the column in its inverted position.

The brick element model, however, was to be used for the post-test analysis calibration and parametric study. Accordingly, the bent cap beam side plates and clevises assemblages were modeled to better account for the physical boundary conditions. The seat beams were fixed in the three translational DOFs to reflect the lateral friction at the hydrostone interface between the seat beams and the strong laboratory floor. Loading in the brick elements model was applied at the correct locations at the column head to resemble the actual testing. Note that a rectangular column head was used to replace the actual hexagonal head for simplicity of modeling and load application. Both models used the total strain crack model and an idealized elastic-perfectly plastic constitutive model for modeling the concrete and the reinforcement, respectively. Nominal material properties that used the *Caltrans SDC* [2011] expected material properties definitions were used in defining the concrete and reinforcement material models parameters. In the case of the time history analysis, a lumped mass was defined at the column head portion of the model that was calibrated to maintain similar dynamic properties; namely the natural frequencies as determined for the prototype bridge, following the proper similitude relationships.

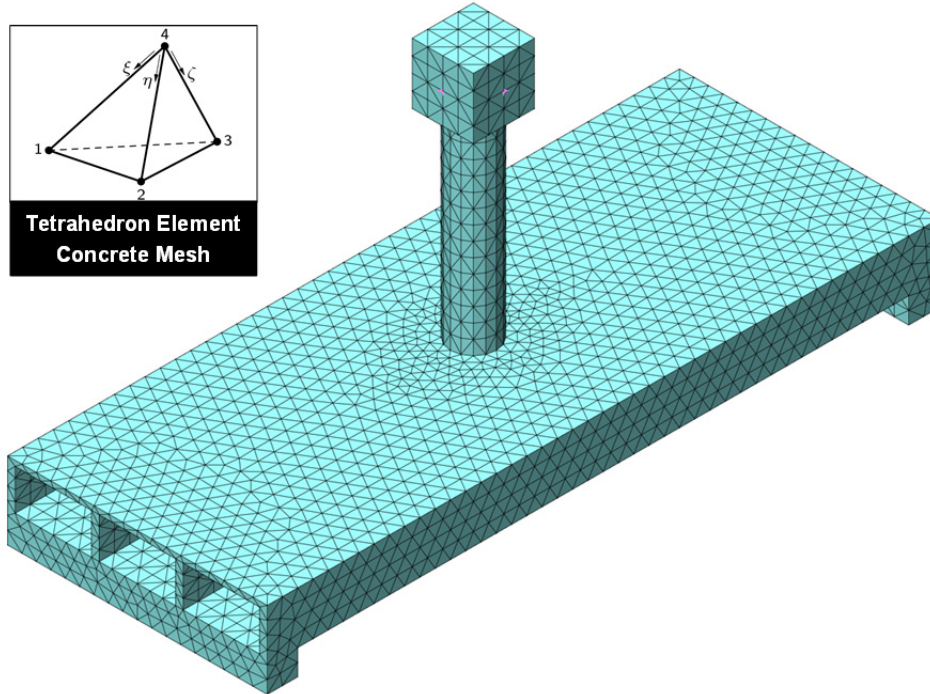


Figure 4.31 DIANA tetrahedron-element concrete mesh used for modeling the test specimen subassembly.

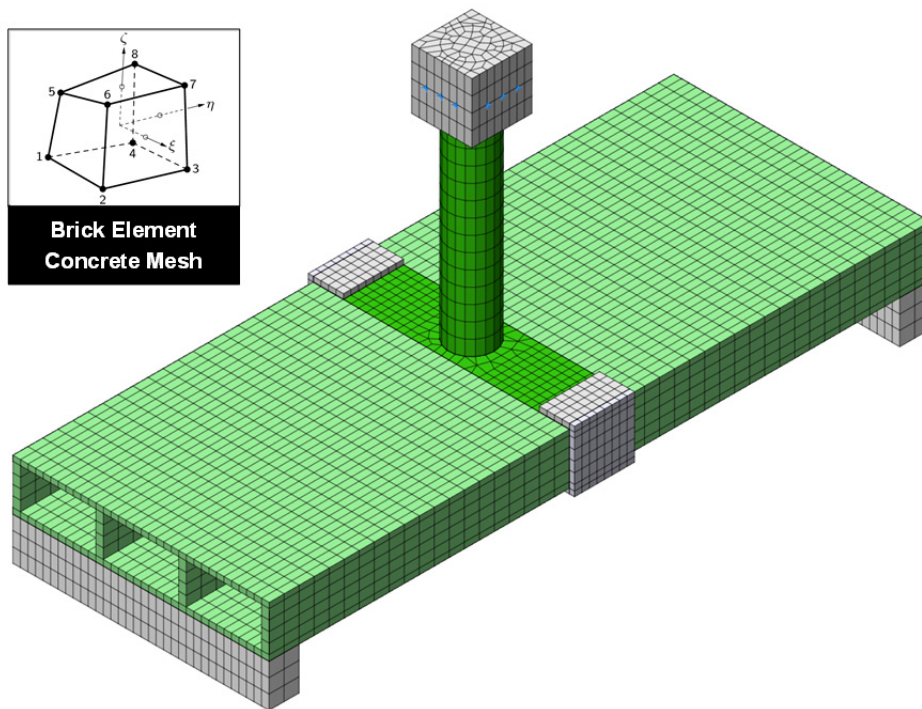


Figure 4.32 DIANA brick-element concrete mesh used for modeling the test specimen subassembly.

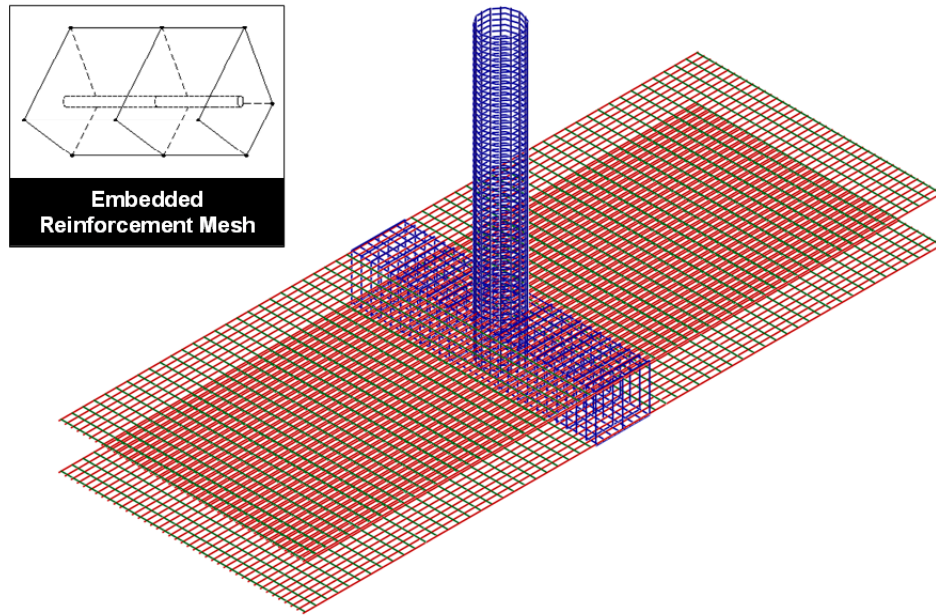


Figure 4.33 Embedded reinforcement mesh used for both DIANA 3D models of the test specimen subassembly.

4.4.2 Pushover Analysis

Different sets of lateral pushover analyses were conducted at different levels of gravity loads to determine how the subassembly force capacity and mode of failure changed. It is always beneficial to first explore the expected bending moment distribution in the specimen's column and bent cap using first principals. A schematic representation for that moment distribution was previously shown in Figure 4.5 in the OpenSees analysis discussion. This bending moment distribution was the basis for conducting a series of pushover analyses. First, a vertical displacement pushover was performed to identify the capacity of the specimen subassembly in the vertical direction. The vertical capacity is dictated by the lesser flexural capacity of either the box-girder or the bent cap beam. From the specimen design (Appendix A) and sectional analysis of both sections, the box-girder in the test subassembly is expected to have a much higher capacity than the bent cap beam. Therefore, the mode of failure obtained from the vertical pushover is expected to be only attributed to failure of the bent cap beam. The extensive yielding and elevated concrete crack strain values in the cap beam relative to the box-girder as obtained from the vertical pushover analysis confirm that the capacity is dictated by failure of the bent cap. The vertical force-displacement relationship from the vertical pushover analysis and schematic representation of the mode of failure are shown in Figure 4.33. Moreover, the crack pattern and deformed shape of the subassembly before yield and at the final damaged state as obtained from the DIANA vertical pushover analysis are shown in Figures 4.34 and 4.35, respectively.

A total of seven lateral pushover analysis sets under different constant gravity load were conducted. The seven levels of the gravity load were related to the nominal column axial capacity to obtain the following gravity load ratios (ALR): 0%, 6%, 11%, 17%, 19%, 21%, and

23%. These values were chosen based on convenient number of load steps and number of nodes to apply equal vertical forces to eventually apply the total gravity load under force control. The application of each of these seven gravity load cases was followed by a lateral displacement pushover in the transverse direction along the bent cap direction. According to the analyses, three different modes of failure were obtained: namely a failure in the column only (mode 1), failure in both of the column and the bent cap (mode 2), and failure in the bent cap only (mode 3). Mode 1 of failure was observed for three cases that experienced gravity load ratios of 0%, 6%, and 11%. The crack pattern and deformed shape due to a typical Mode 1 column failure is shown in Figure 4.36. The pushover force-displacement relationship for the three cases and the schematic mode of failure, Mode 1, are shown in Figure 4.37. Similarly, Figures 4.38 and 4.39 show the pushover curves and schematic mode of failure for the cases that experienced failure Modes 2 and 3, respectively.

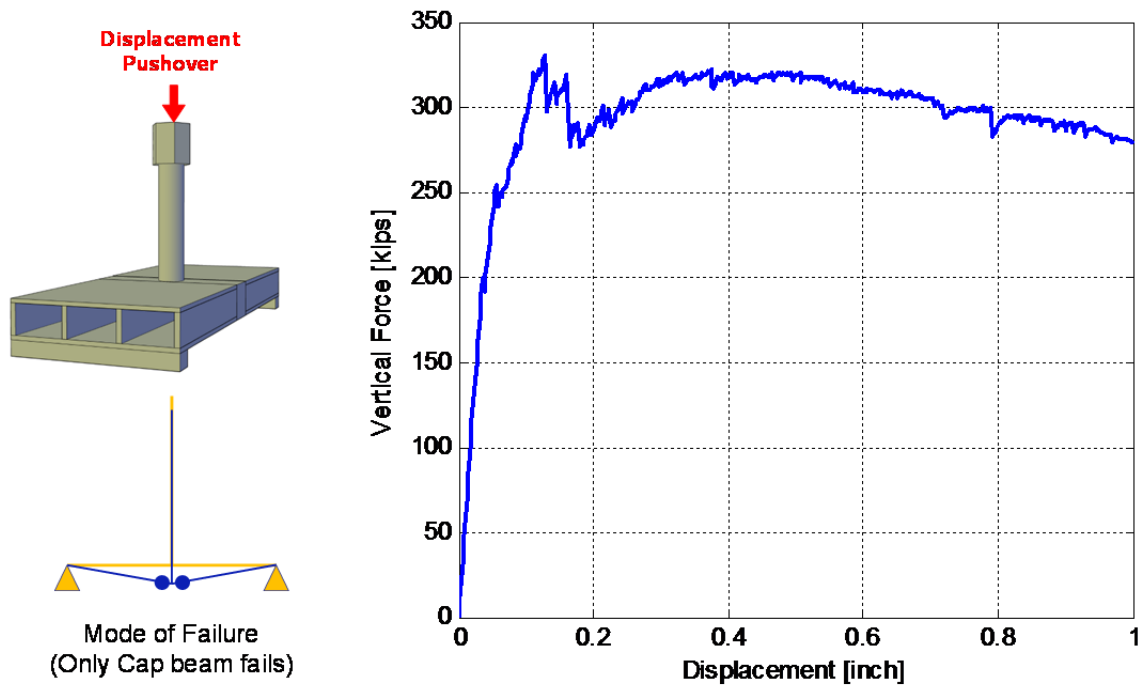


Figure 4.34 Vertical force-displacement relationship due to vertical pushover and schematic representation of the resulting mode of failure; only the cap beam failed.

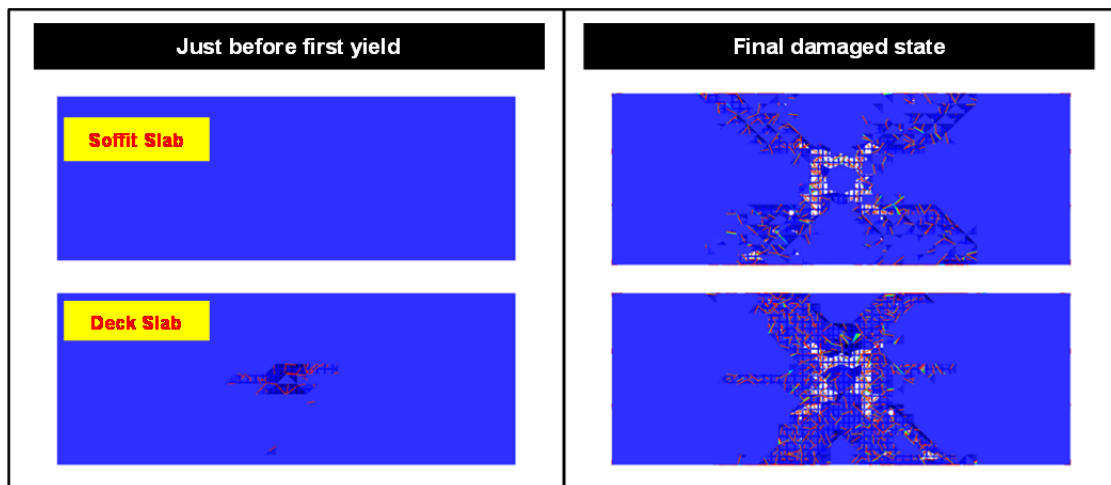


Figure 4.35 Crack pattern (DIANA) in box-girder and bent cap due to vertical pushover.

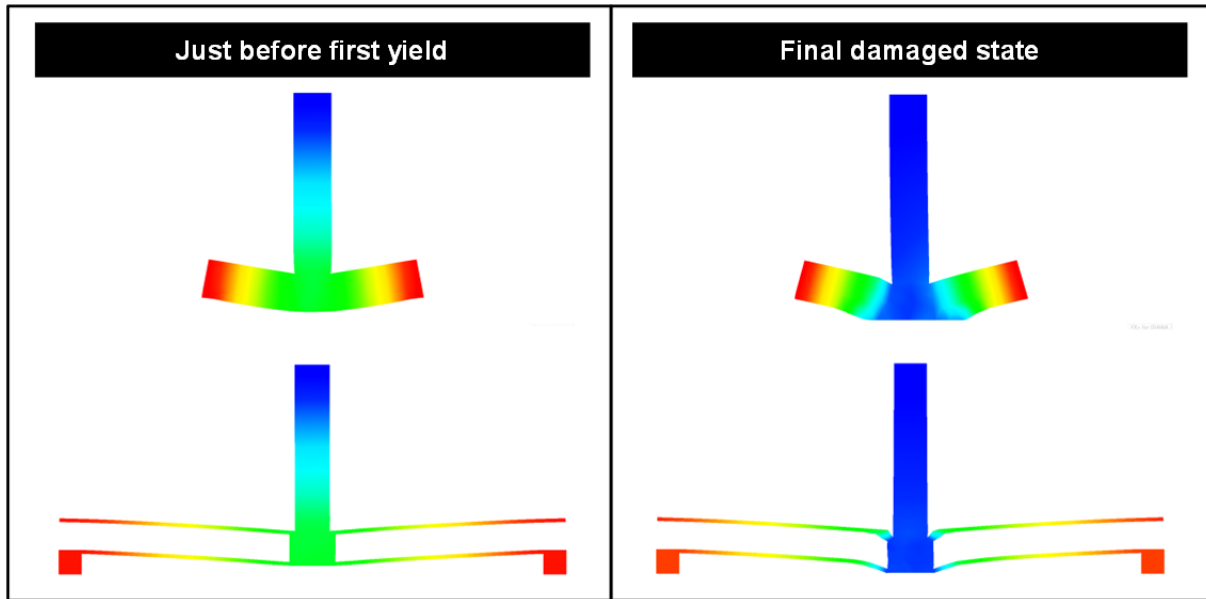


Figure 4.36 Deformed shape (DIANA) of the subassembly due to vertical pushover.

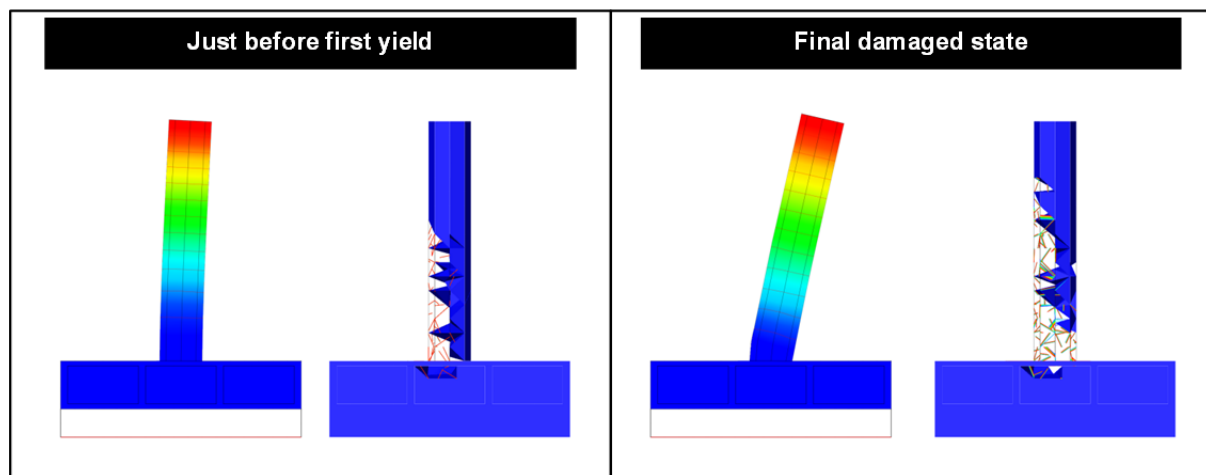


Figure 4.37 Typical crack pattern and deformed shape (DIANA) due to lateral pushover.

The analyses results from the vertical pushover and the seven lateral pushover analyses were compiled together in a gravity load-lateral (vertical–horizontal) capacity interaction diagram, as shown in Figure 4.40. The figure also identifies the three flexural modes of failure previously identified, i.e., plastic hinge in column only (mode 1); plastic hinge in both the column and bent cap (mode 2), and plastic hinge in bent cap only (mode 3). Note that only ductile flexural modes of failure are allowed in capacity design approach, and, specifically, the first mode of failure of plastic hinge in columns only is allowed by the bridge seismic design provisions, e.g., *Caltrans SDC* [2013]. The schematic moment distribution in Figure 4.5 and the envelope interaction diagram in Figure 4.40 demonstrate that the gravity load directly increases the moment demand in the bent cap in this test specimen setting and may cause its failure.

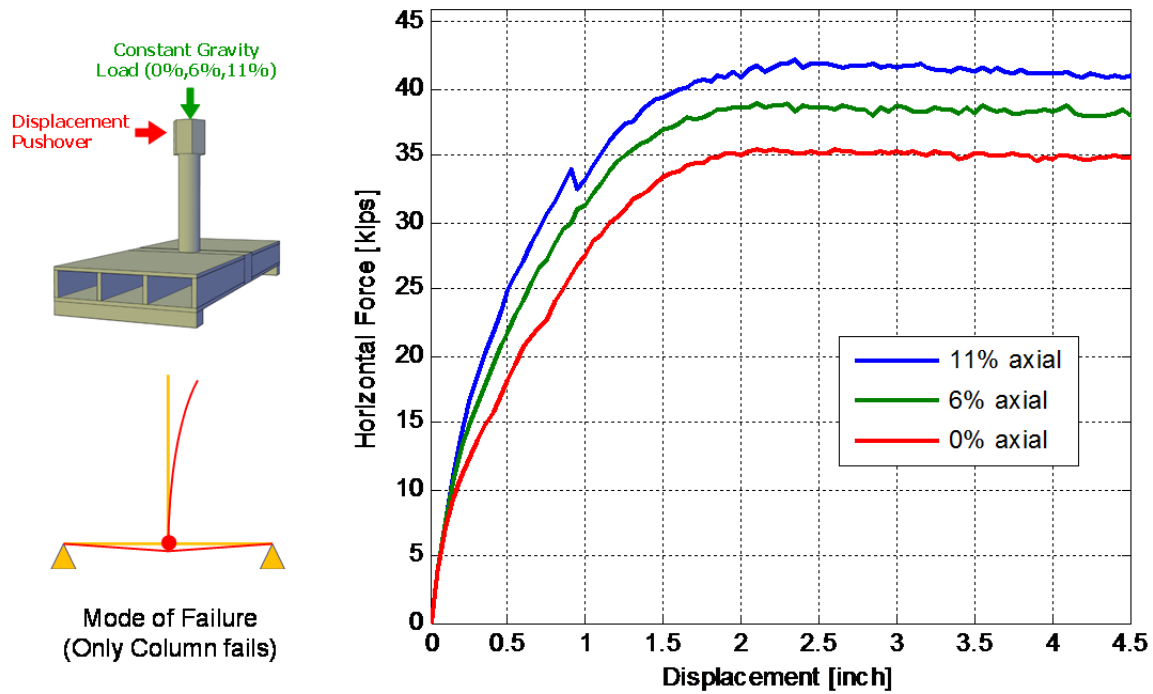


Figure 4.38 Lateral force-displacement relationship at different axial load levels (0%, 6%, and 11% of column axial capacity) and schematic representation of the resulting mode of failure; only the column failed.

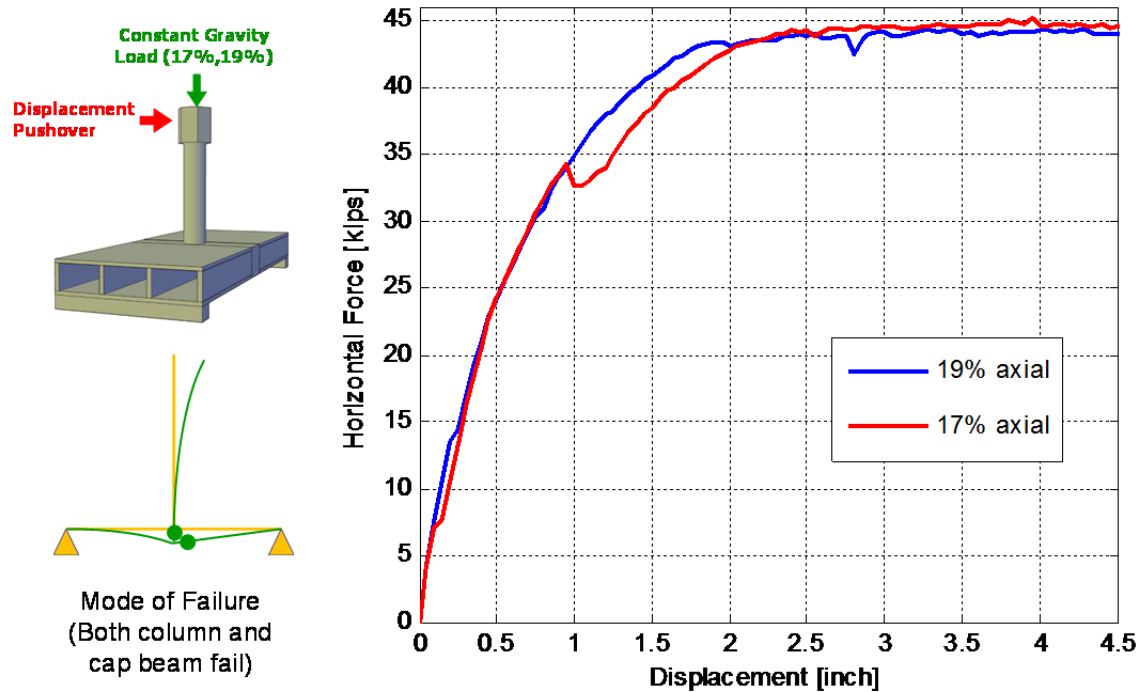


Figure 4.39 Lateral force-displacement relationship at different axial load levels (17% and 19% of column axial capacity) and schematic representation of the resulting mode of failure; both the column and cap beam failed.

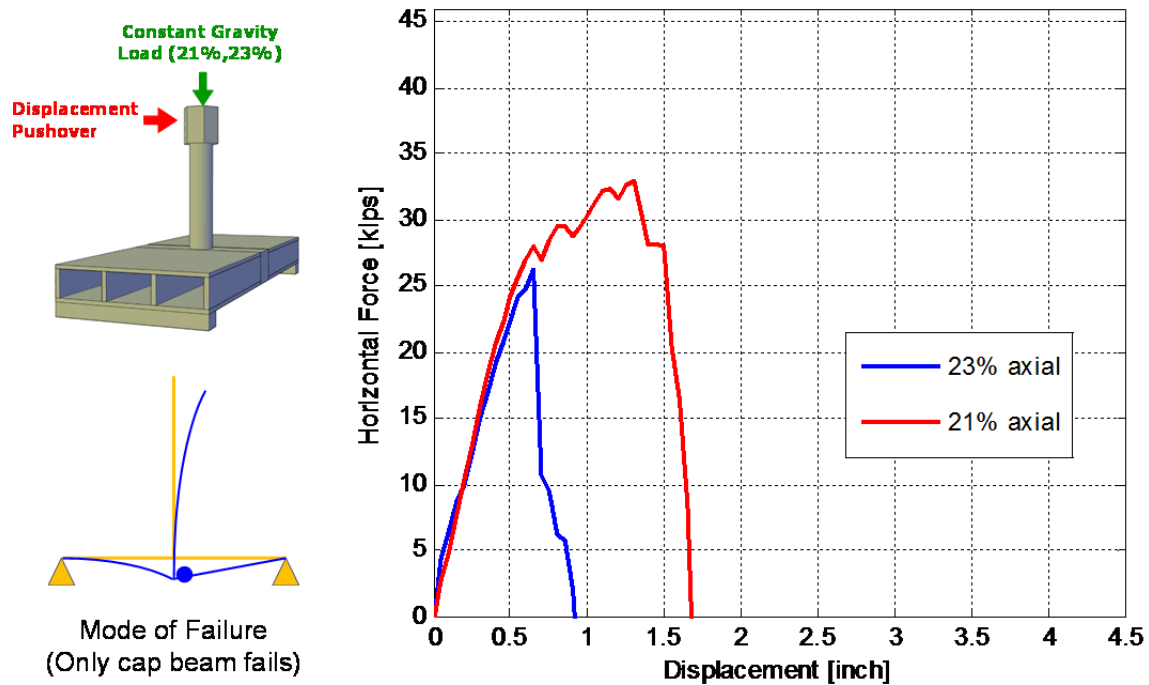


Figure 4.40 Lateral force-displacement relationship at different axial load levels (21% and 23% of column axial capacity) and schematic representation of the resulting mode of failure; only the cap beam failed.

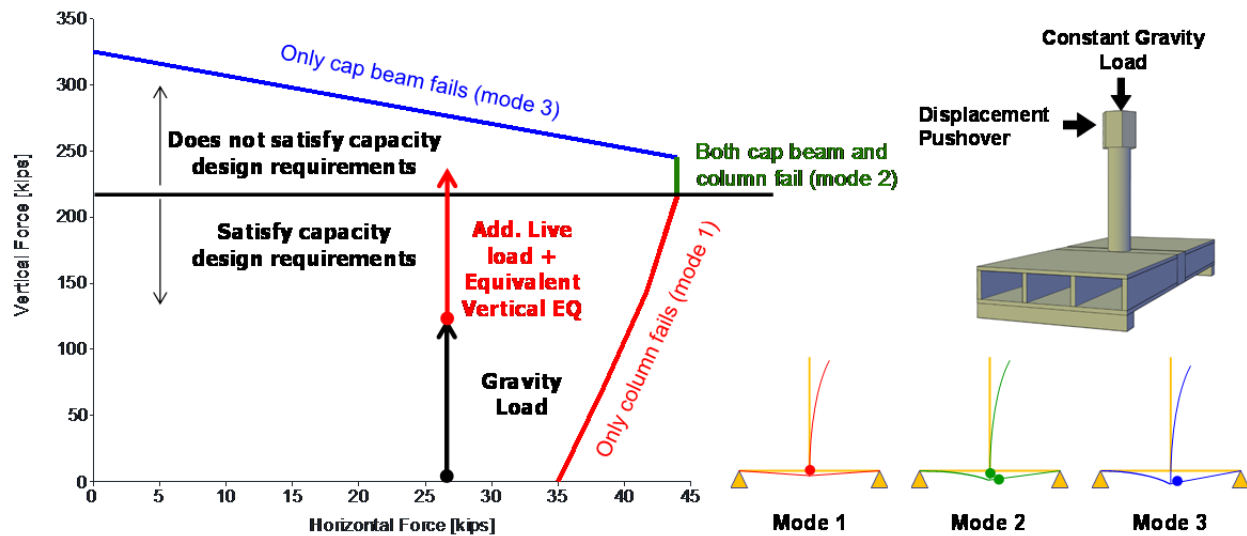


Figure 4.41 An envelope of the horizontal and vertical load values at failure, which summarizes the different pushover analysis cases and the corresponding modes of failure from DIANA specimen model.

Based on the insight provided by the detailed set of pushover analyses, it was decided to apply the gravity loading such that it represented as many of the above-mentioned modes of failure as possible. However, due to the capacity of the actuators used in the experimental testing, it was concluded that the 6% and 11% were appropriate for the test of as-built Specimen No. 1, which was meant to evaluate the bent cap behavior and modes of failure that followed from adopting the latest code provisions. For the test of retrofitted Specimen No. 2, to investigate the behavior of the bent cap into the inelastic range by increasing the demands on the bent cap was the main goal. Thus, an additional gravity load level that corresponded to the 17% gravity load ratio case discussed above was used. Note that in actual testing, the absolute gravity load values were related to the Caltrans axial column capacity that was based on the expected concrete strength rather than the actual one. Accordingly, the final three gravity load ratios (ALR) from the tests were 5%, 10%, and almost 15%, which corresponded to the 6%, 11%, and 17% from the analysis that used the expected concrete strength. These gravity load levels were tied to the vertical excitation resulted from the time history analysis as discussed next.

4.4.3 Time-History Analysis

The two detailed DIANA models were used to conduct different nonlinear time history analyses. Several gravity load levels were combined with different ground motions that were selected from the short list adopted from the OpenSees prototype bridge analysis (Table 4.2). Different components of the ground motions were used in the analysis. A preliminary set of analyses that used two horizontal components besides the vertical one were conducted first to understand the behavior of the test specimen subassembly under the effect of 3D ground motion. Additional analyses focused on using only one horizontal component in the transverse direction and compared it to the case when the same transverse horizontal component was used with the corresponding vertical component. The latter two cases are schematically shown in Figure 4.41. Only a sample of the several runs are shown here for brevity. First, the analysis under 25% Loma Prieta ground motion at 11% gravity load using the transverse horizontal and the vertical components is shown. Figures 4.42 and 4.43 show the displacement history, force history, and force-displacement relationship in the lateral transverse and vertical directions, respectively. Another example is the 50% Northridge ground motion recorded at Sylmar station at 23% gravity load when only transverse horizontal component is included, where Figures 4.44 and 4.45 show the lateral and vertical response of this other example, respectively. For comparison purposes, the response from 50% Northridge ground motion at 23% gravity load but using both horizontal and vertical components is presented in Figures 4.46 and 4.47 for the lateral and vertical response, respectively.

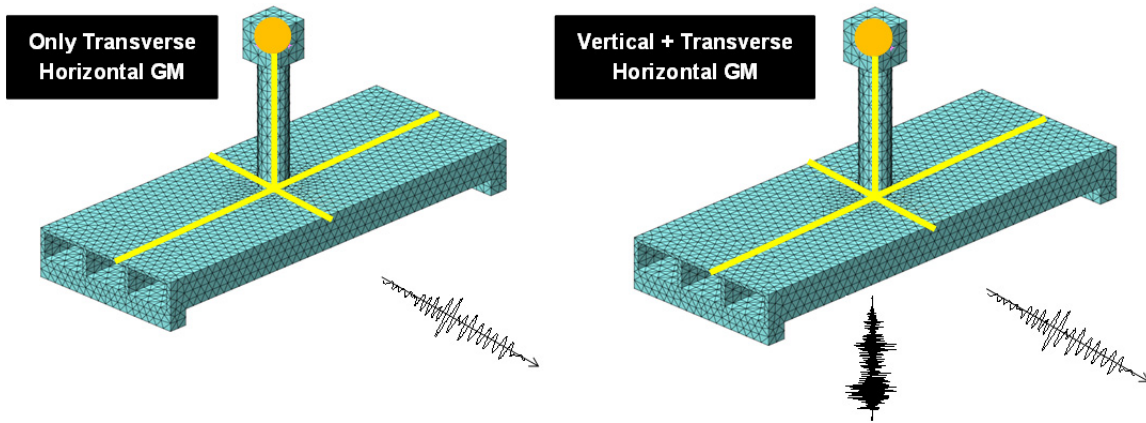
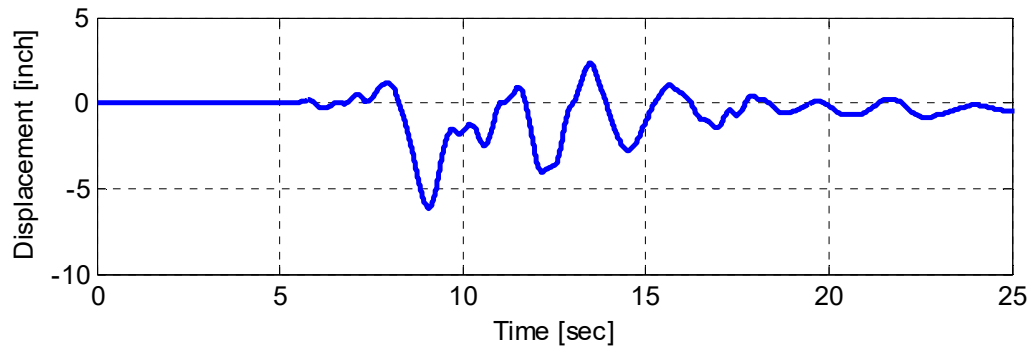
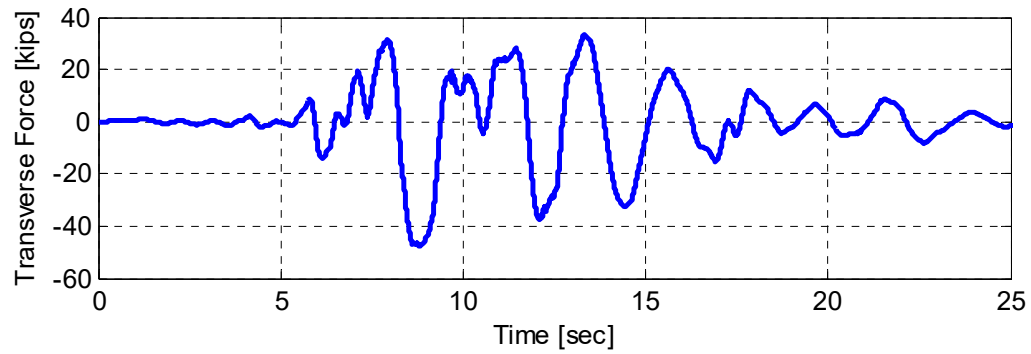


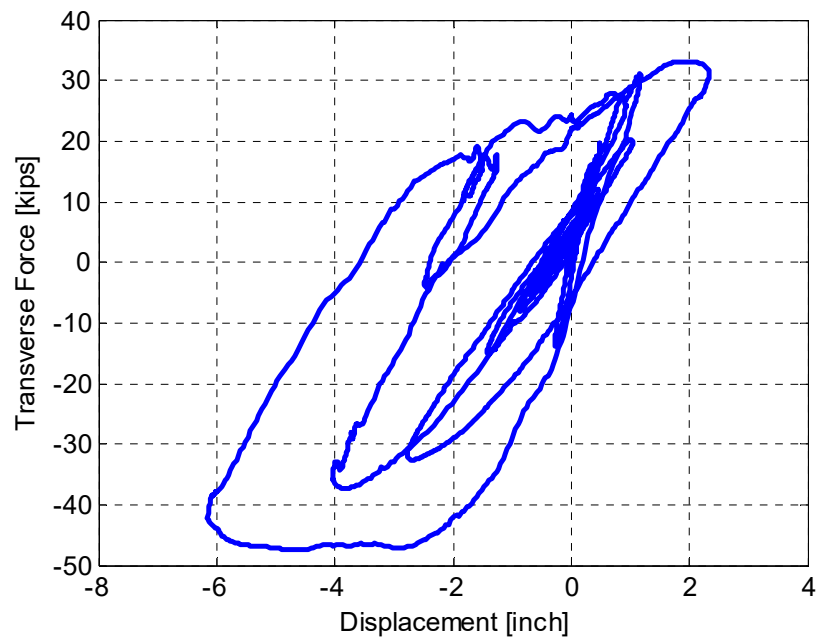
Figure 4.42 Schematic representation of the test specimen DIANA model with lumped mass at column top and tetrahedron elements for two different time history analysis cases.



(a)

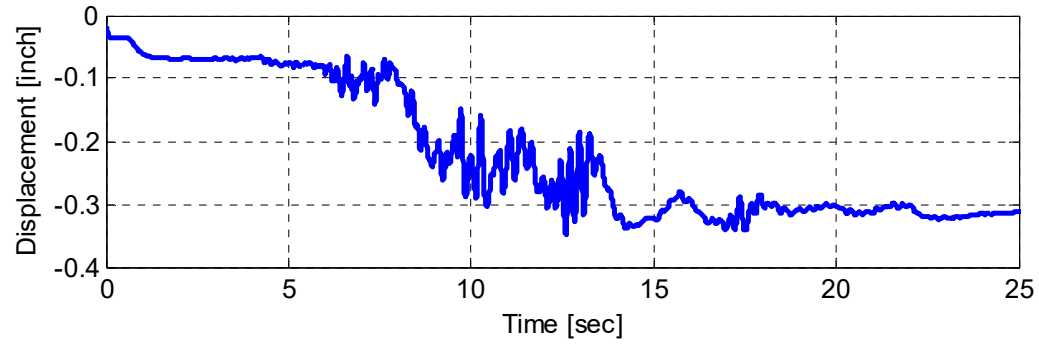


(b)

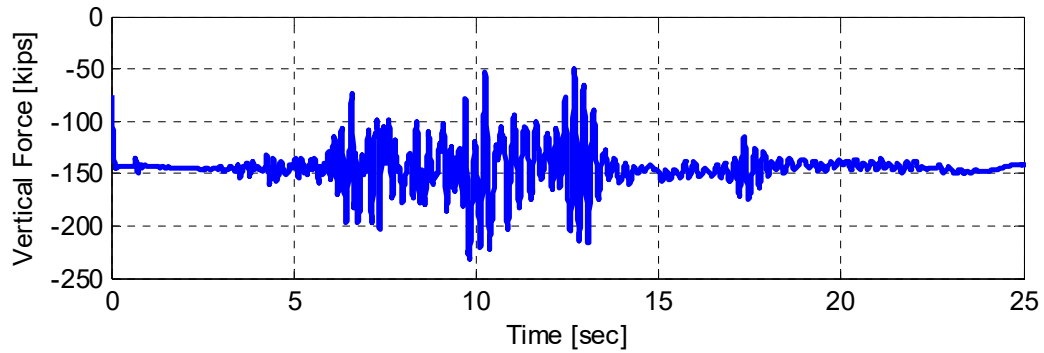


(c)

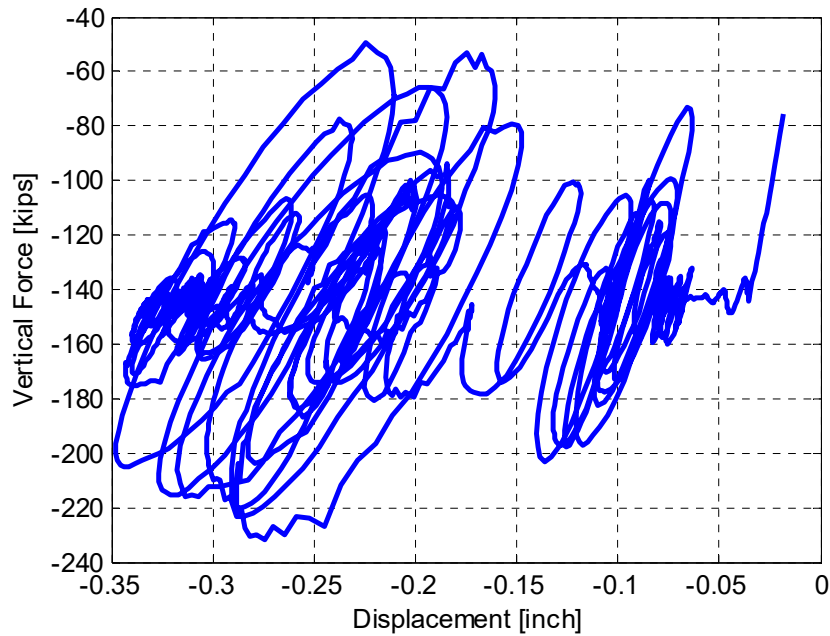
Figure 4.43 Analysis results for the case of 25% Loma Prieta ground motion (transverse and vertical components) and 11% constant gravity load of column axial capacity: (a) lateral displacement history, (b) lateral force history, and (c) lateral force-displacement relationship.



(a)

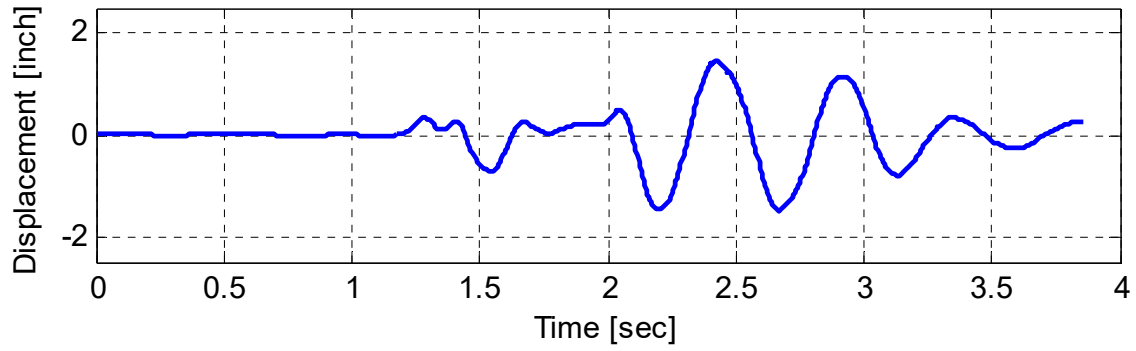


(b)

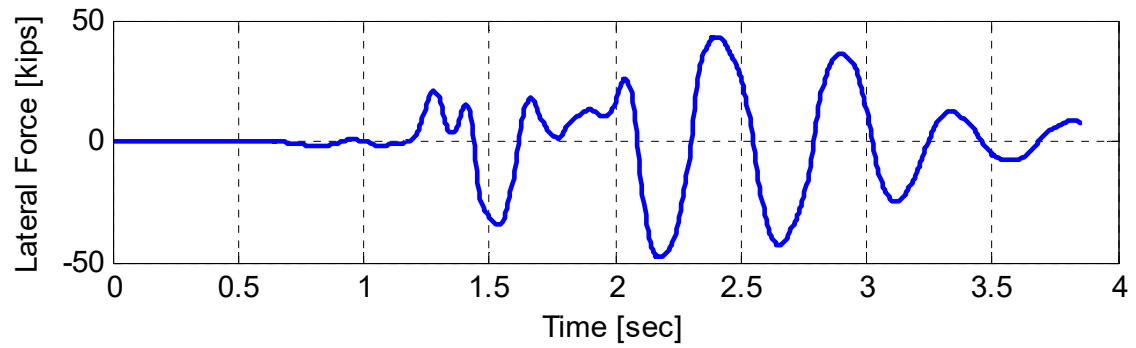


(c)

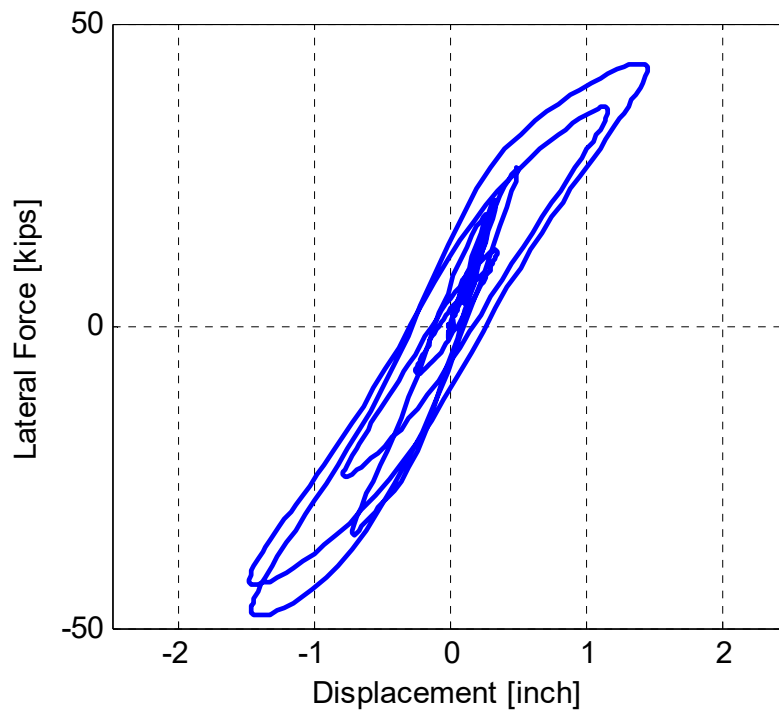
Figure 4.44 Analysis results for the case of 25% Loma Prieta ground motion (transverse and vertical components) and 11% constant gravity load of column axial capacity: (a) vertical displacement history, (b) vertical force history, and (c) vertical force-displacement relationship.



(a)

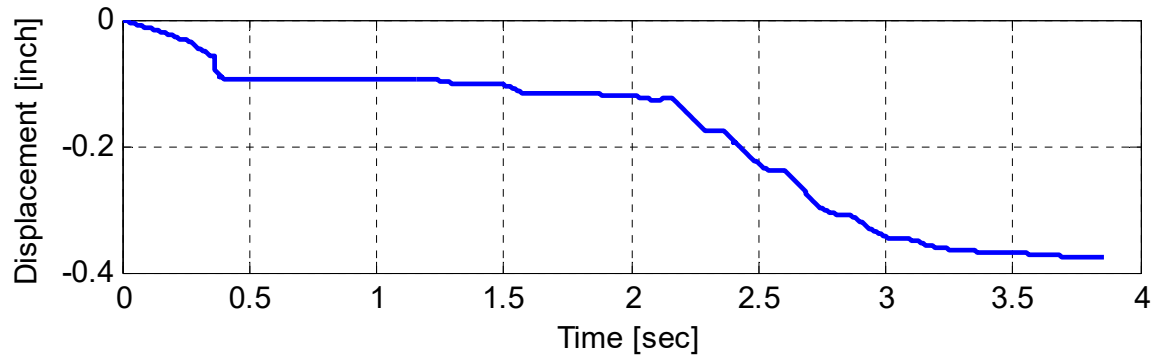


(b)

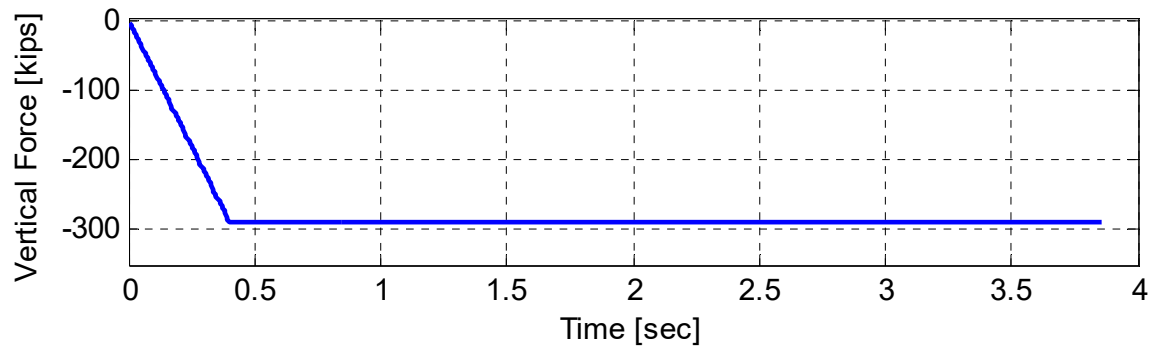


(c)

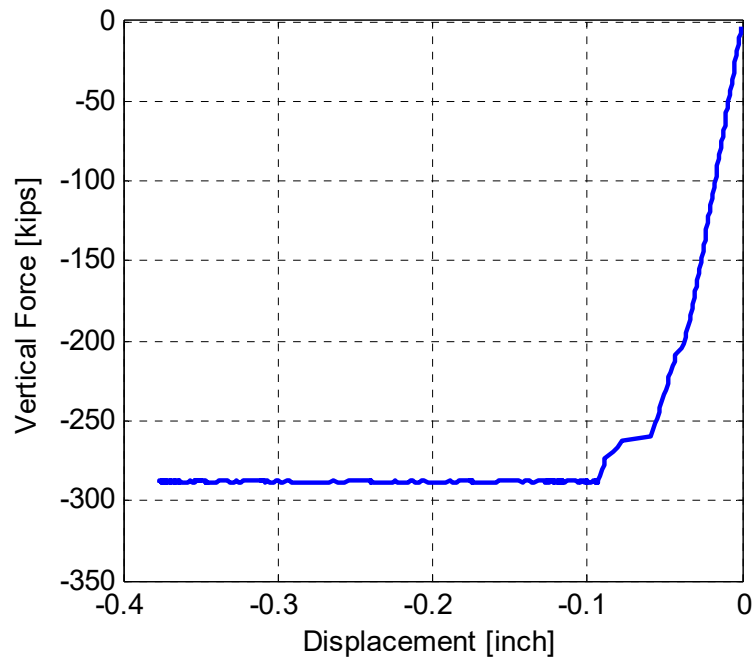
Figure 4.45 Analysis results for the case of 50% Northridge ground motion (Sylmar record) with only horizontal excitation and 23% constant gravity load of column axial capacity: (a) lateral displacement history, (b) lateral force history, and (c) lateral force- displacement relationship.



(a)

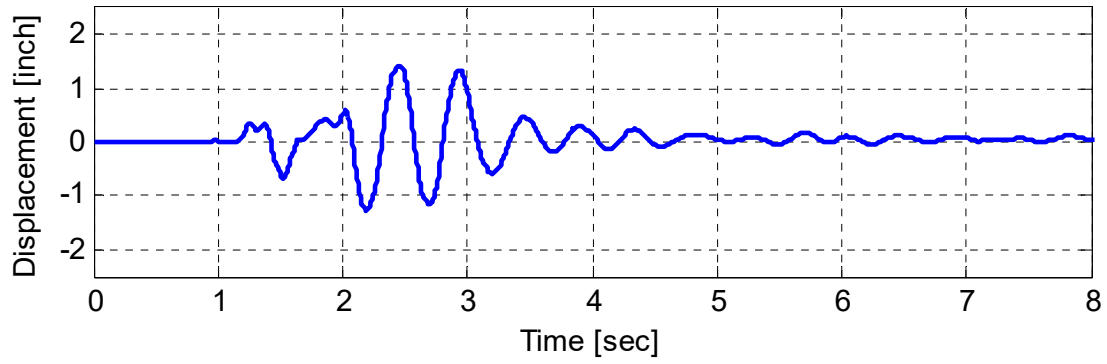


(b)

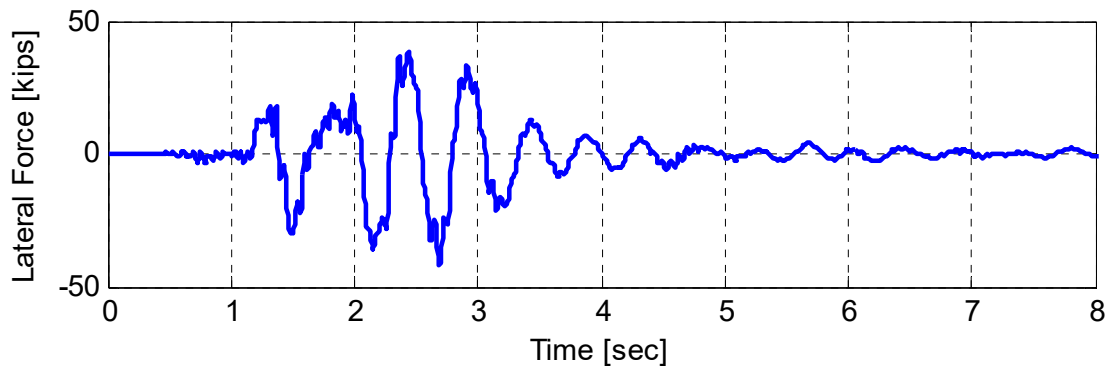


(c)

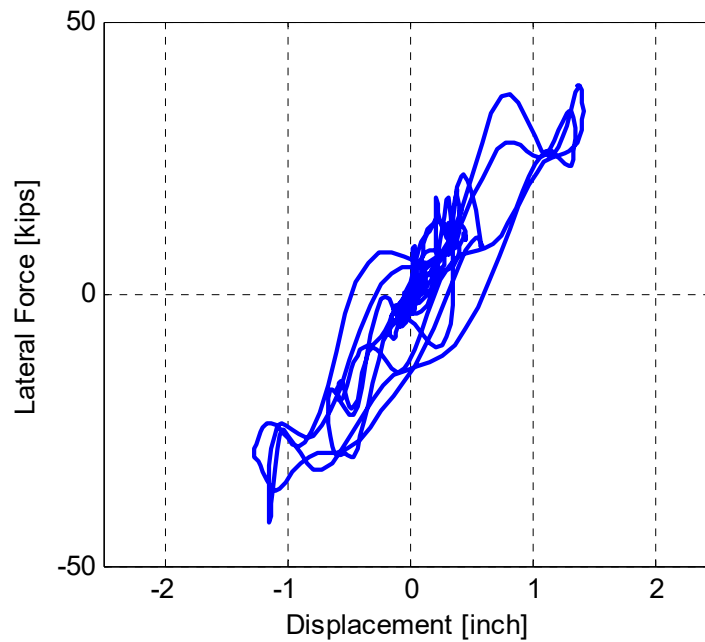
Figure 4.46 Analysis results for the case of 50% Northridge ground motion (Sylmar record) with only horizontal excitation and 23% constant gravity load of column axial capacity: (a) vertical displacement history, (b) vertical force history, and (c) vertical force-displacement relationship.



(a)

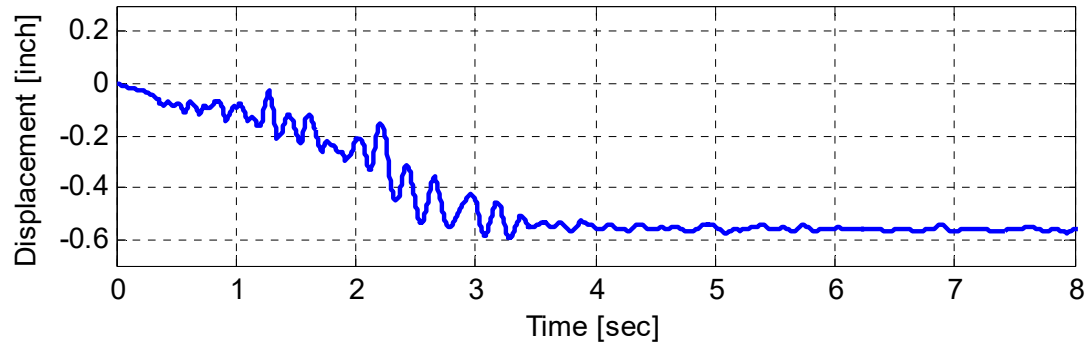


(b)

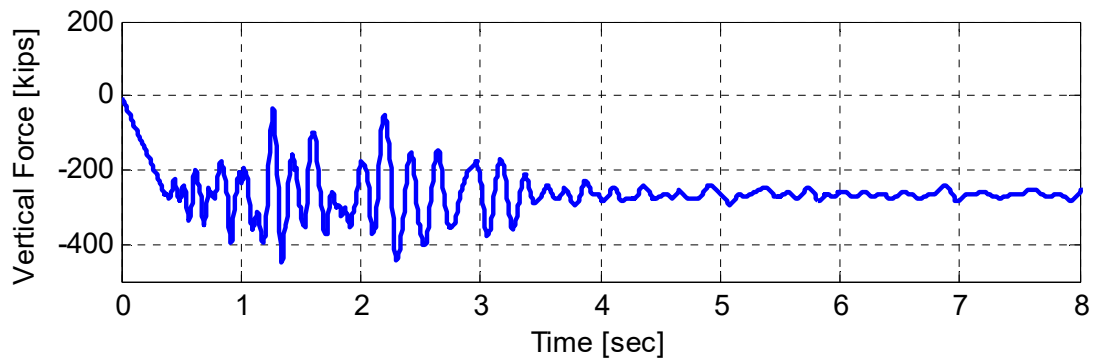


(c)

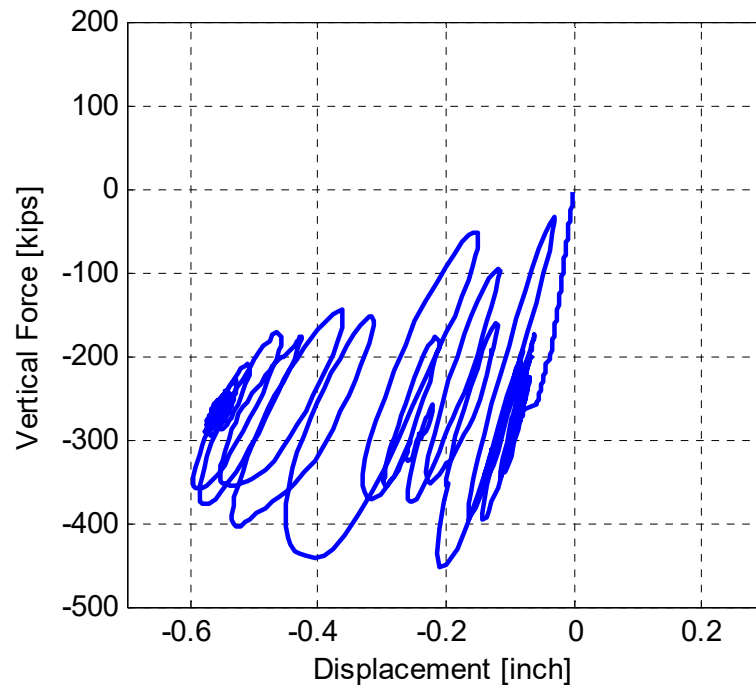
Figure 4.47 Analysis results for the case of 50% Northridge ground motion (Sylmar record) with both vertical and horizontal excitations and 23% constant gravity load of column axial capacity: (a) lateral displacement history, (b) lateral force history, and (c) lateral force- displacement relationship.



(a)



(b)



(c)

Figure 4.48 Analysis results for the case of 50% Northridge ground motion (Sylmar record) with both vertical and horizontal excitations and 23% constant gravity load of column axial capacity (a) vertical displacement history, (b) vertical force history, and (c) vertical force-displacement relationship.

The lateral behavior in the transverse direction, i.e., in the cap beam plane, and the vertical system behavior were shown for all the selected three time history analyses. The force values were capped when either the column or cap beam capacity was reached. The lateral force capacity from the different time history analysis runs agreed with the pushover analysis. A higher vertical force capacity was observed from the time history compared to the vertical pushover because of the effect of the lateral dynamic loading, which produced moments opposite in sign to those resulting from the vertical loading moments. The vertical force fluctuation shown in Figure 4.43 and Figure 4.47 implies that for cases that involved vertical excitation, the vertical excitation can increase the vertical load demand by almost 100% of the gravity load. This justifies to some extent the gravity load levels, which were selected to account for the effect of vertical excitations. The obtained displacement values from the dynamic analysis helped in identifying the mode of failure and overall system ductility, which was beneficial input for the second specimen HS testing.

In summary, the higher the initial gravity load, the less was the lateral ductility in case of when vertical excitation was included. That is because the vertical excitation along with higher gravity load caused the failure of the bent cap beam directly without causing significant damage in the column. Thus, it was concluded that 10% gravity is the most appropriate starting point for the case of HS tests to obtain higher ductility levels. The HS tests could accommodate an increase in the gravity load level up to 15% to account for higher vertical excitation effects, which would be compatible with higher ground motion scaled to obtain the expected simultaneous failure in both column and bent cap. Note that the 15% was a conservative estimate mainly because the conducted tests were all static tests where the gravity load was maintained for prolonged times. However, the actual increase in the gravity load due to vertical excitation obtained from the analysis showed that a dynamic effect took place only for a short period of time, i.e., the effect of the instantaneous increase in dynamic gravity loads should not be as excessive as the static load. Thus, the 15% axial load considered for the tests was conservative because it represented a more severe case.

4.4.4 Input for Test Set-Up and Instrumentation

The results of the detailed DIANA FE pre-test analysis was used to determine design forces of the test set-up and the instrumentation of the transverse slab reinforcement necessary to measure the strain distribution for effective width determination. First, the largest expected lateral force from the pushover analyses and maximum observed reaction in the cap beam end struts were determined for test set-up design. The maximum lateral force in the transverse direction was found to be almost 45 kips, as noted from the vertical-lateral force interaction diagram shown in Figure 4.40; a closer value was obtained for the capacity in the longitudinal direction from the preliminary analysis. This is mainly because the capacity was dictated by the column capacity, which was almost the same in both transverse and longitudinal directions. The 45-kips limit was verified to be much less than the combined horizontal actuators capacity and the lateral shear capacity of the prestressing rods used to hold down the specimen to the laboratory strong floor. Meanwhile, the maximum observed reaction in the cap beam end roller supports was found to be in the vicinity of 140 kips under combined lateral and gravity loads. The two vertical struts were

then designed to remain elastic up to 200 kips each, to provide accurate and meaningful strain readings for reaction calibration.

The pre-test analysis was used to determine the stress and strain distributions in the transverse slab reinforcement adjacent to the bent cap beam in both soffit and deck slabs so that decisions regarding instrumentation could be determined. A view of the strain profile in both soffit and deck slabs in elevation is shown in Figure 4.48 for a typical lateral pushover analysis case. In addition, the strain profile observed in the deck slab from more loading cases: vertical pushover analysis, a typical lateral pushover, and a typical time history analysis is shown in plan view in Figure 4.49 (a), (b), and (c), respectively. It was determined that the strain decays within about two feet from the cap beam face in case of deck slab and close to 1-1/2 foot in the soffit slab. Thus four bars were instrumented at each side of the cap beam in the deck slab, and three bars were instrumented at each side of the cap beam in soffit slab; see Chapter 3. The strain distribution was also assessed in respect to the two special holes that had to be constructed for vertical actuators rods; see Figures 4.49 and 4.48. Note that the strain decays and almost reaches zero away from the holes, providing confidence that the holes would not influence the stress/strain distributions. In summary, the pre-test FE analysis described in this chapter confirmed that the test set-up would obtain the desired behavior and mode of failure. Moreover, it confirmed that the experimental set-up was able to apply the required maximum loads and deformations to the test specimens. The FE analysis described in this chapter was improved using actual material properties to match the experimental results in the post-test analysis, as discussed in details in the companion report.

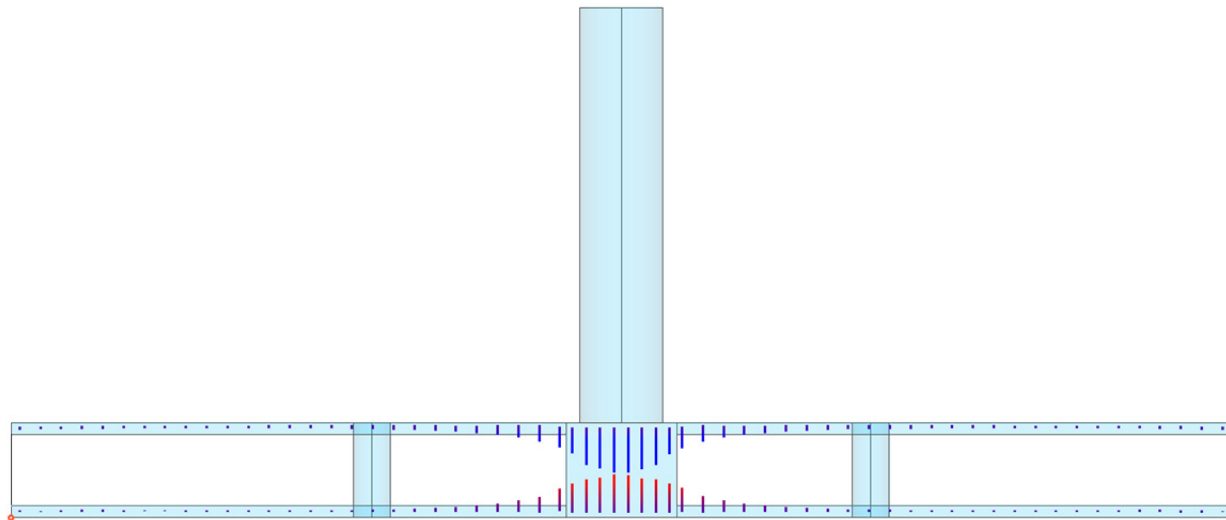


Figure 4.49 Strain distribution in the reinforcement along the cap beam and transverse slab cross-section for DIANA specimen model subjected to lateral pushover and constant gravity load.

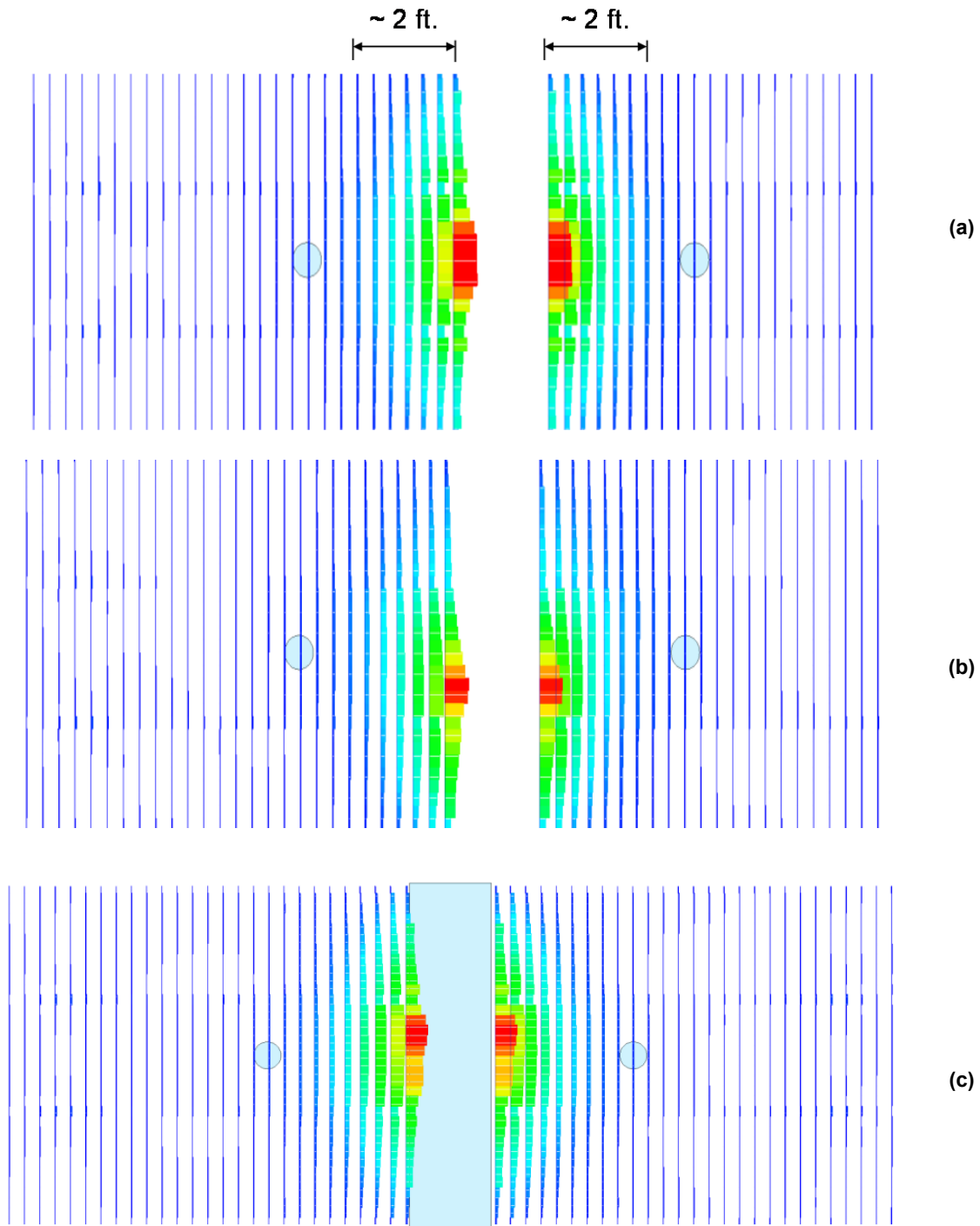


Figure 4.50 Strain distributions in the transverse slab reinforcement from the DIANA specimen model under two cases of loading: (a) vertical pushover, (b) lateral pushover with constant gravity load, (c) time history analysis using Kobe ground motion at 50%.

5 Quasi-Static Tests: As-Built Specimen One

Tests of Specimen No. 1 were a major part of the experimental program. It was first tested in the as-built condition under a quasi-static cyclic loading. After the cyclic test, the column was heavily damaged, losing both its force capacity and stiffness. It was decided to repair the column of Specimen No. 1 to restore partial capacity and stiffness for HS verification. The second set of tests on Specimen No. 1 subjected the repaired specimen to the same cyclic loading history for response comparison. The third set of tests comprised HS trial tests. The first set of tests is the focus of this chapter. The second set of tests is discussed in Chapter 6, and the HS trials are discussed in the companion report.

The experimental program's original objective was to (1) investigate the structural response of the bent cap beam and the bridge subassembly, and (2) determine the contribution of the box-girder slabs under lateral loading. The results from the as-built test provided data for a comparison of behavior of as-built Specimen No. 1 with the repaired Specimen No. 1, and the test results from retrofitted Specimen No. 2 that was tested using HS. Therefore, special attention was given to the post-processing results of Specimen No. 1. A comprehensive discussion of all key observations and results of first test are presented below.

As discussed in Chapter 3, the first test conducted was quasi-static cyclic loading test of as-built Specimen No. 1. The test was conducted under constant gravity load and 12 bi-directional lateral loading groups. The complete set of all loading groups was achieved in two full days of testing. All runs in both of the transverse and the longitudinal directions were compiled together. Thus, the time history used throughout this chapter presents the net time of actual testing, i.e., active loading. Note that the data acquisition was split between two DAQ systems: the Pacific Instruments¹ (PI), which records all channels readings continuously while the loading is active or paused; and the NEFF², which records data only during active loading. Therefore, presented below are two time scales from the different response histories. These are approximately a total time of 465 minutes for all data recorded by the PI, and 260 minutes for data recorded on the NEFF. The 200-minute difference reflects the total accumulated time of pauses during the tests when crack and damage propagation were documented.

¹ Pacific Instruments (www.pacificinstruments.com)

² NEFF Instruments, founded by Glyn Neff (www.neff.com)

The post-processing results for Specimen No. 1 consist of six main parts. Part one discusses the global behavior of the bridge subassembly specimen in terms of lateral forces, displacements, and stiffness in both transverse and longitudinal directions. Part two focuses on the local behavior of the column in terms of reinforcement strains, section curvatures, and bending moments. Part three presented a similar discussion for the local behavior of the bent cap beam strains, curvatures, and bending moments. Parts four and five discuss the effective width in tension and compression sides, respectively. Determination of the effective width is a key goal of the experimental study, which aims at revisiting the box-girder slabs contribution to the bent cap beam stiffness and moment capacity. Part six emphasizes other important response quantities that are of relevance to the final conclusions determined from the test.

5.1 PROGRESSION OF TESTING AND DAMAGE

The as-built Specimen No. 1 cyclic loading tests involved bi-directional loading in both transverse and longitudinal directions. Figures 5.1 and 5.2 show the test set-up and progression of the loading from a top view in the transverse and longitudinal directions, respectively. Throughout this study, the loading in the transverse direction refers to loading in the direction of the bent cap beam centerline, i.e., the east–west direction as defined in Figure 5.1. Whenever loading is pushing towards the east, it is designated as the positive transverse loading direction, and, in turn, the negative transverse loading direction is pulling towards the west. As shown in Figure 5.2, the longitudinal direction is loading in the north–south direction, i.e., along the box-girder centerline. Pushing towards the north defines the positive longitudinal loading, while pulling towards the south is the negative longitudinal direction. These different ways of defining the loading direction are used interchangeably throughout the discussion.

All damage incurred by Specimen No. 1 was concentrated in the column, which experienced a flexural plastic hinge mode of failure. No shear failure or extensive shear cracking was observed during the test. Note in Figure 5.3 that only minor shear cracking was observed in the column–bent cap joint region, which shows the joint region crack pattern at transverse loading cycles corresponding to 1.0 and 7.6 ductility levels. More information about the ductility levels obtained from the pursued cyclic loading pattern is presented below.

Minor flexural cracks were also observed in the side in tension of the box-girder and bent cap, which is the bottom face of the specimen in the inverted position, as shown in Figure 5.4. This figure was compiled from four fisheye-lens cameras that were installed underneath the specimen to observe the tension cracks. The longitudinal cracks are aligned with the box-girder centerline, and no permanent flexural cracks were observed along the bent cap beam; the longitudinal cracks were observed to open wider when lateral transverse loading was progressing and then reduced in width again after lateral loading was completed. This indicates that the final permanent crack pattern is mainly due to the applied concentrated gravity load rather than due to the application of any of the transverse or longitudinal lateral loading.

The main damage was observed in the column where a flexural plastic hinge developed. Figure 5.5 shows the progression of cracking, spalling, and concrete damage in the plastic hinge

region of the column. Figure 5.6 shows the final damaged state of the column and illustrates the buckled and ruptured reinforcing bars after all the spalled concrete parts were removed. All the column longitudinal rebars buckled, and six of them ruptured during cyclic tests of as-built Specimen No. 1, as shown in Figure 5.6.

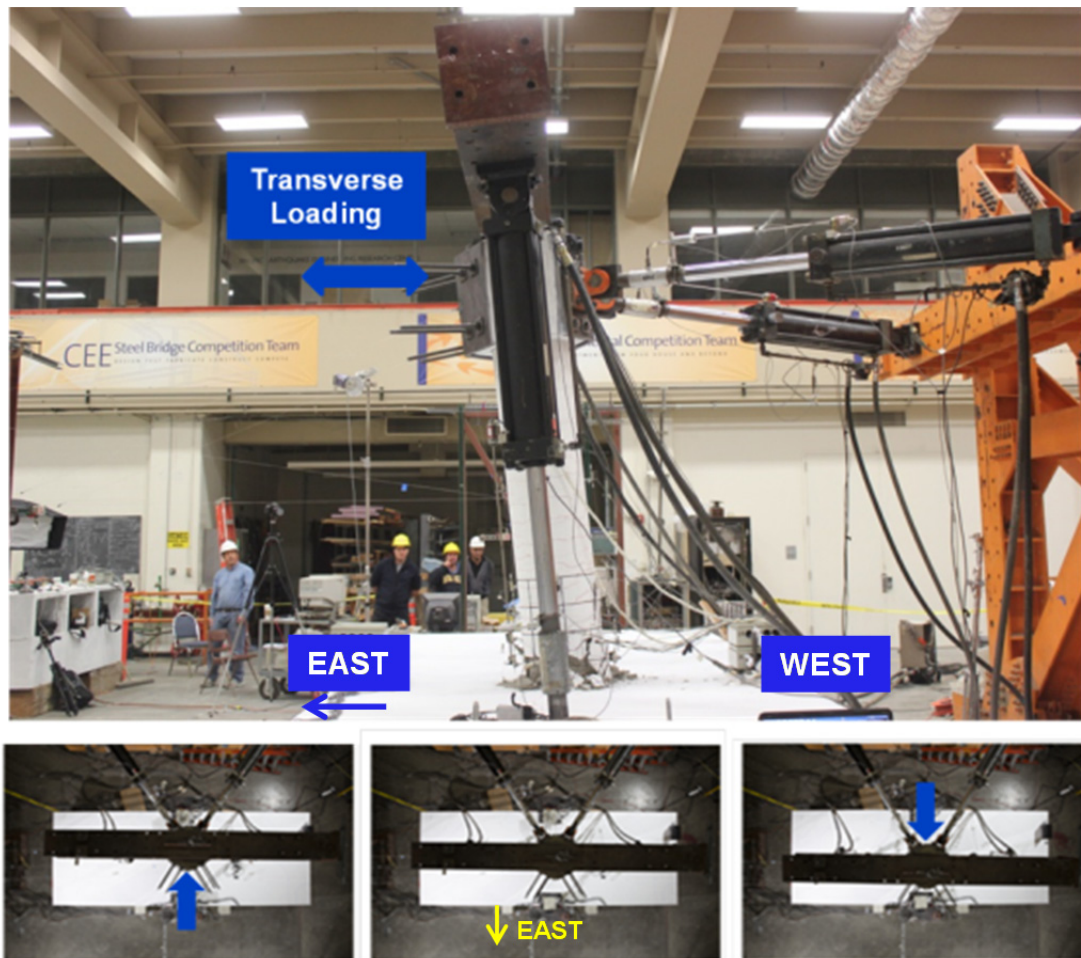


Figure 5.1 As-built Specimen No. 1 test set-up and progression of loading in the transverse direction.

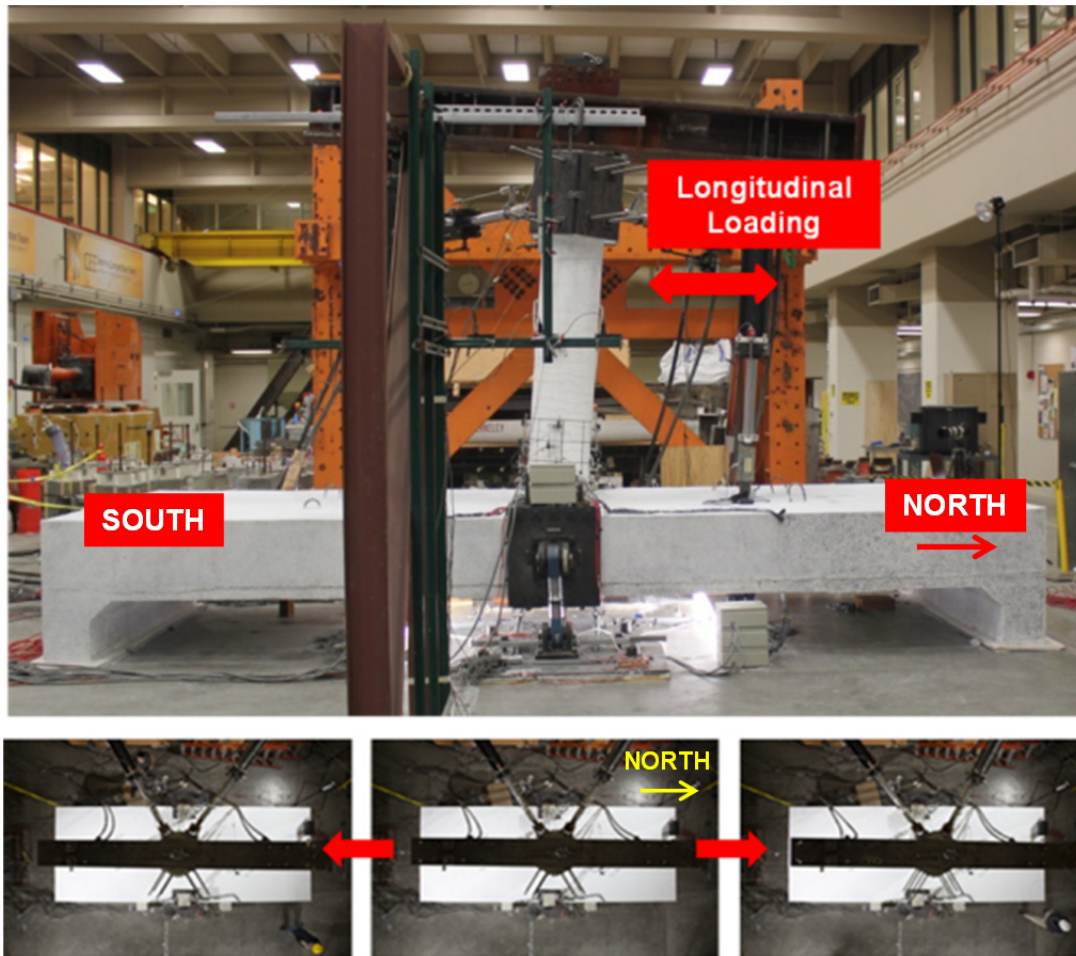


Figure 5.2 As-built Specimen No. 1 set-up and progression of loading in the longitudinal direction.

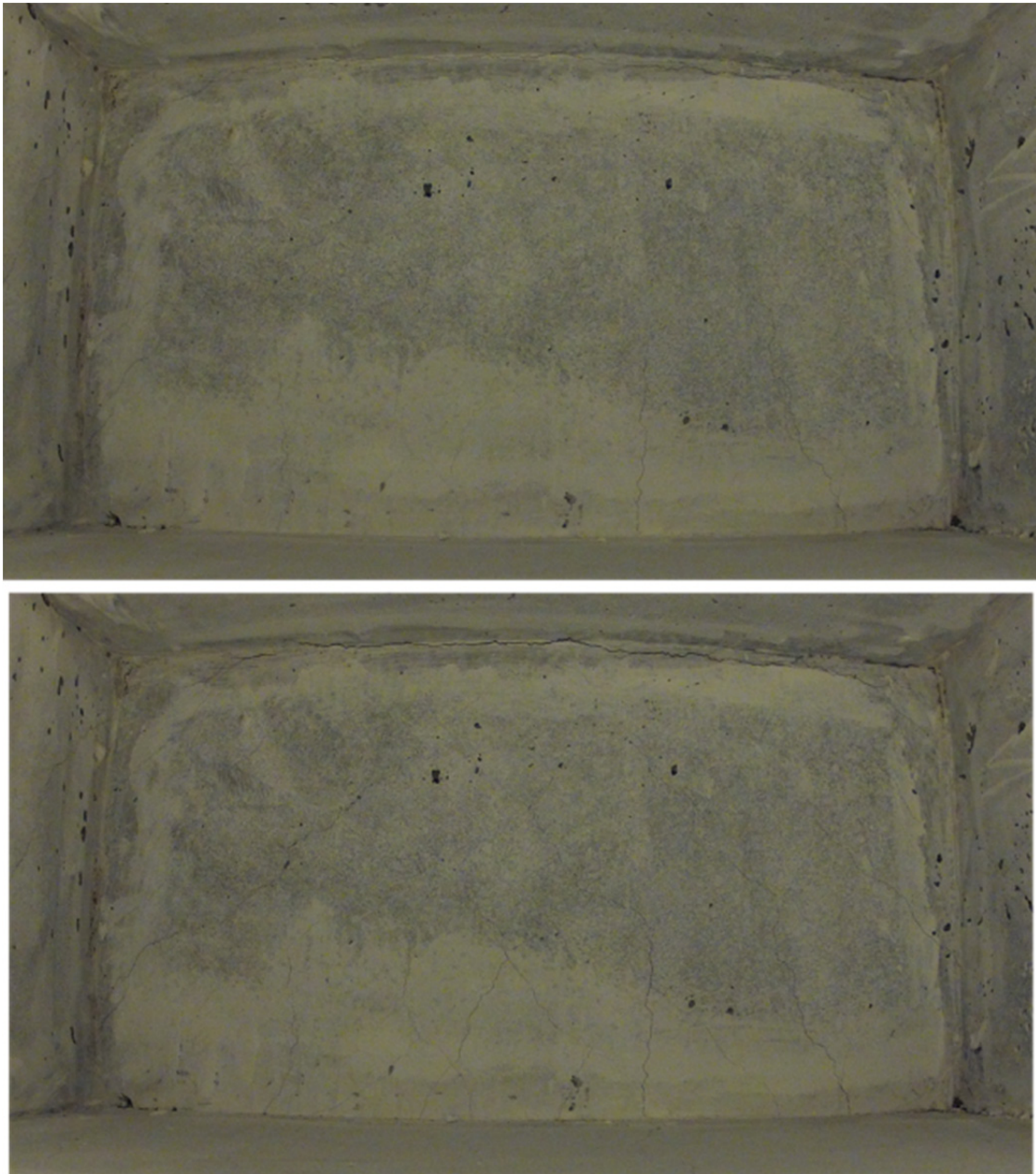


Figure 5.3 Minor shear cracking in the column-bent cap joint region at transverse loading cycles that correspond to 1.0 (top) and 7.6 (bottom) ductility levels.

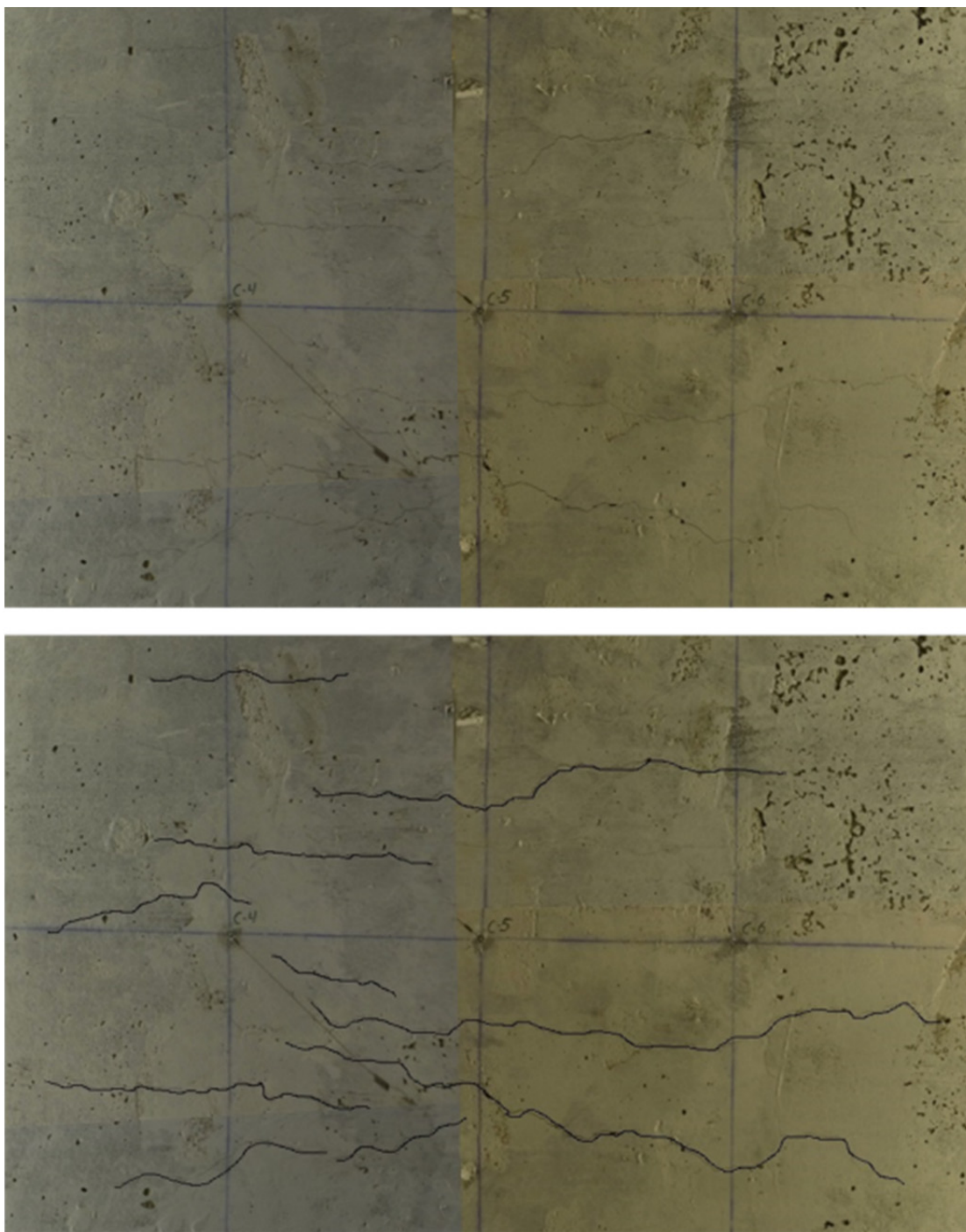


Figure 5.4 Minor flexural longitudinal cracks in the deck slab, i.e., bottom face of the inverted specimen, after all loading cycles. The horizontal line in the figure coincides with the box-girder centerline.

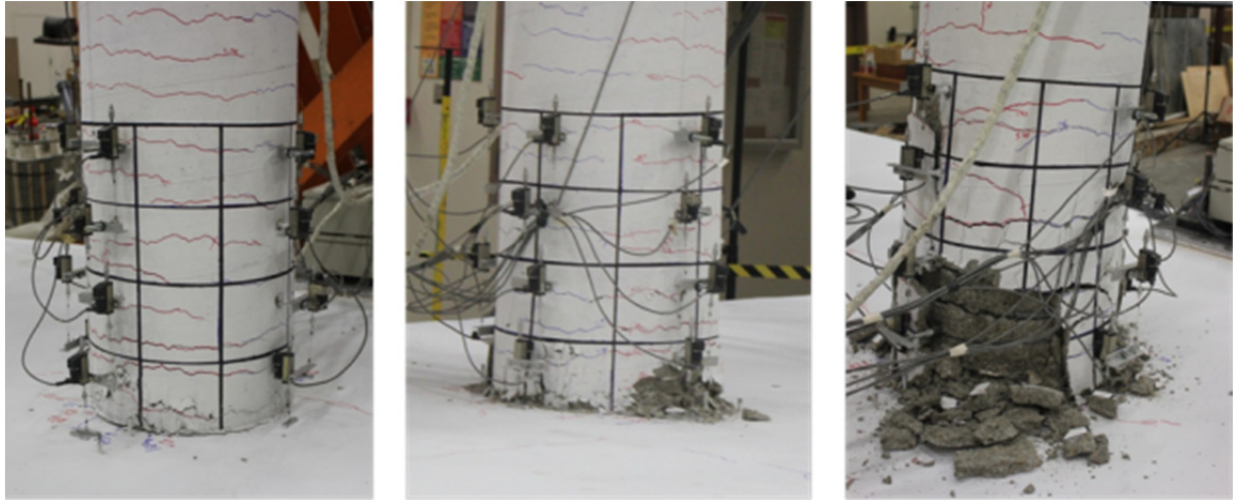


Figure 5.5 Propagation of the column cracking and spalling in the plastic hinge zone.



Figure 5.6 Final damaged state of the as-built Specimen No. 1 column: all the rebar were exposed and buckled, and six rebar ruptured.

5.2 GLOBAL BEHAVIOR

The global behavior of the tested specimen—the forces, displacements, and lateral stiffness—acquired from the test results is discussed in detail below.

5.2.1 Force History

The full loading cyclic history was applied over two days of testing. The reasons for splitting the test over two days are the slow nature of the load application and the need for experimentally revising the cyclic groups when yield of the first rebar occurred. The progressive cyclic loading groups are multiples of the yield displacement as recommended by FEMA 461 [2007]. It was decided to apply two different levels of the gravity load; see Chapter 3. The first level corresponded to approximately 5% of the column axial capacity for a total of 82 kips. This was maintained until the first yield was observed for the low-level lateral cycles: 0.25, 0.35, 0.5, 0.7, 1.0, and 1.25 in. top displacement in both transverse and longitudinal directions. The gravity load was then increased to 10% (164 kips) to account for additional live load and the possible effect of vertical excitations; see Chapter 4. That was the case for the larger loading groups of 1.75, 2.45, 3.5, 4.8, 6.8, and 9.5 in. in transverse direction, and 1.75, 2.45, 3.5, 4.8, and 6.8 in. (repeated twice) in the longitudinal direction. Before concluding the first test program, the gravity load was increased to 12% (190 kips), and one small displacement cycle was applied to see if the damaged column could still transfer moments to the bent cap beam. The actual full history of the gravity load and its three different levels applied during all the cyclic test runs is shown in Figure 5.7.

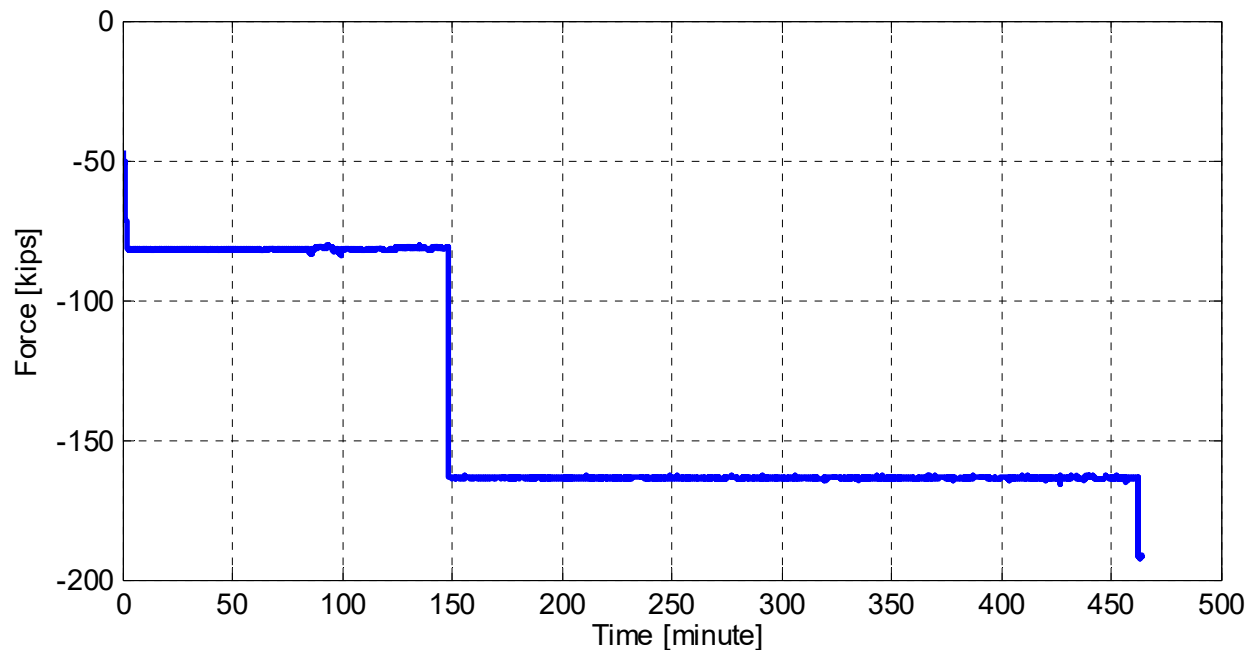


Figure 5.7 History of the gravity load applied during the initial cyclic test runs of Specimen No. 1.

The lateral force that develops in the actuator as a prescribed displacement was applied in one of the key response quantities that are monitored in a RC bridge subassembly test. The observed force—often recognized as the column base shear—is utilized to estimate the column bending moment. Therefore, as a cyclic test progresses, the forces are recorded to capture the base shear and bending moment capacities. In a flexural-controlled bridge column, the moment capacity is reached first, and the observed base shear is dictated by this moment capacity.

The resultant forces observed in transverse (f_x) and longitudinal (f_y) directions are shown in Figure 5.8. These are computed from the actual recorded actuators load cells forces. The exact geometry and configurations of the lateral actuators were used to compute the resultant f_x force during transverse loading cycles, and to compute the resultant f_y force during longitudinal loading cycles. Figure 5.9 shows the history of the two lateral actuators measured forces, designated as north and south actuators according to their location relative to the test set-up, and the resultant force in each of the transverse and longitudinal directions. Note that the actuators forces have approximately similar values and direction during a transverse loading cycle. On the other hand, during longitudinal loading cycles, the actuators forces have opposite directions and different values. A closer examination of all the forces for only one transverse and one longitudinal loading groups is shown in Figure 5.10.

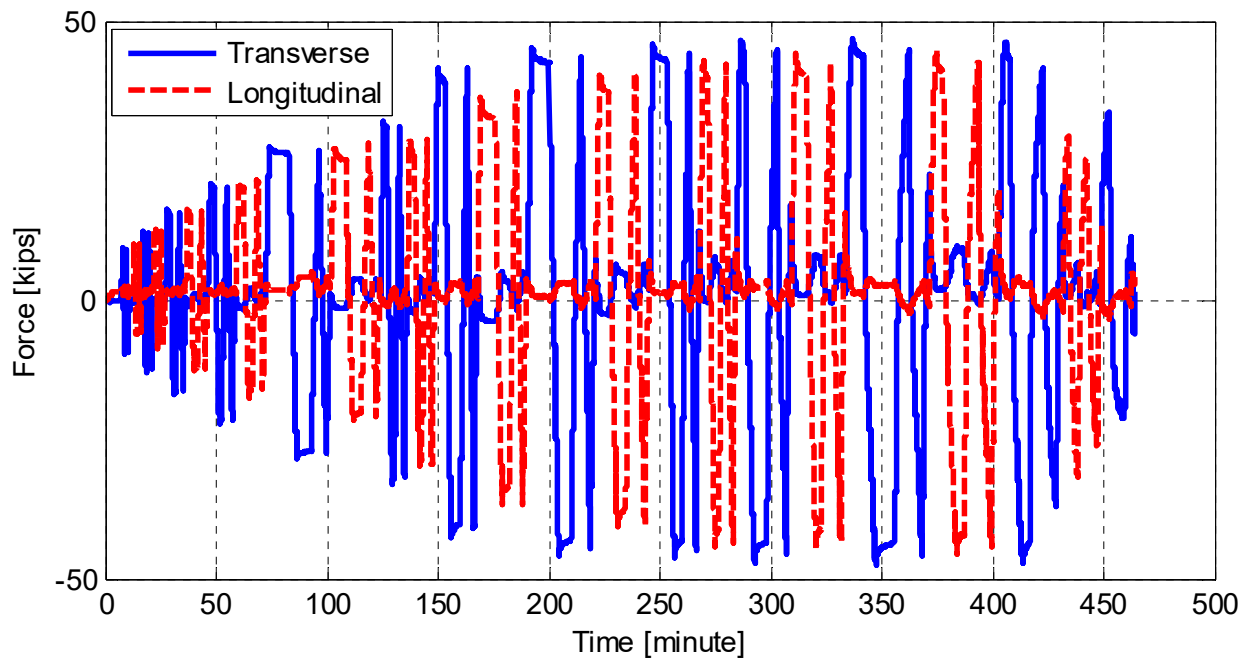


Figure 5.8 History of the force in both transverse and longitudinal directions (estimated from lateral actuators load cells) for all test runs of Specimen No. 1.

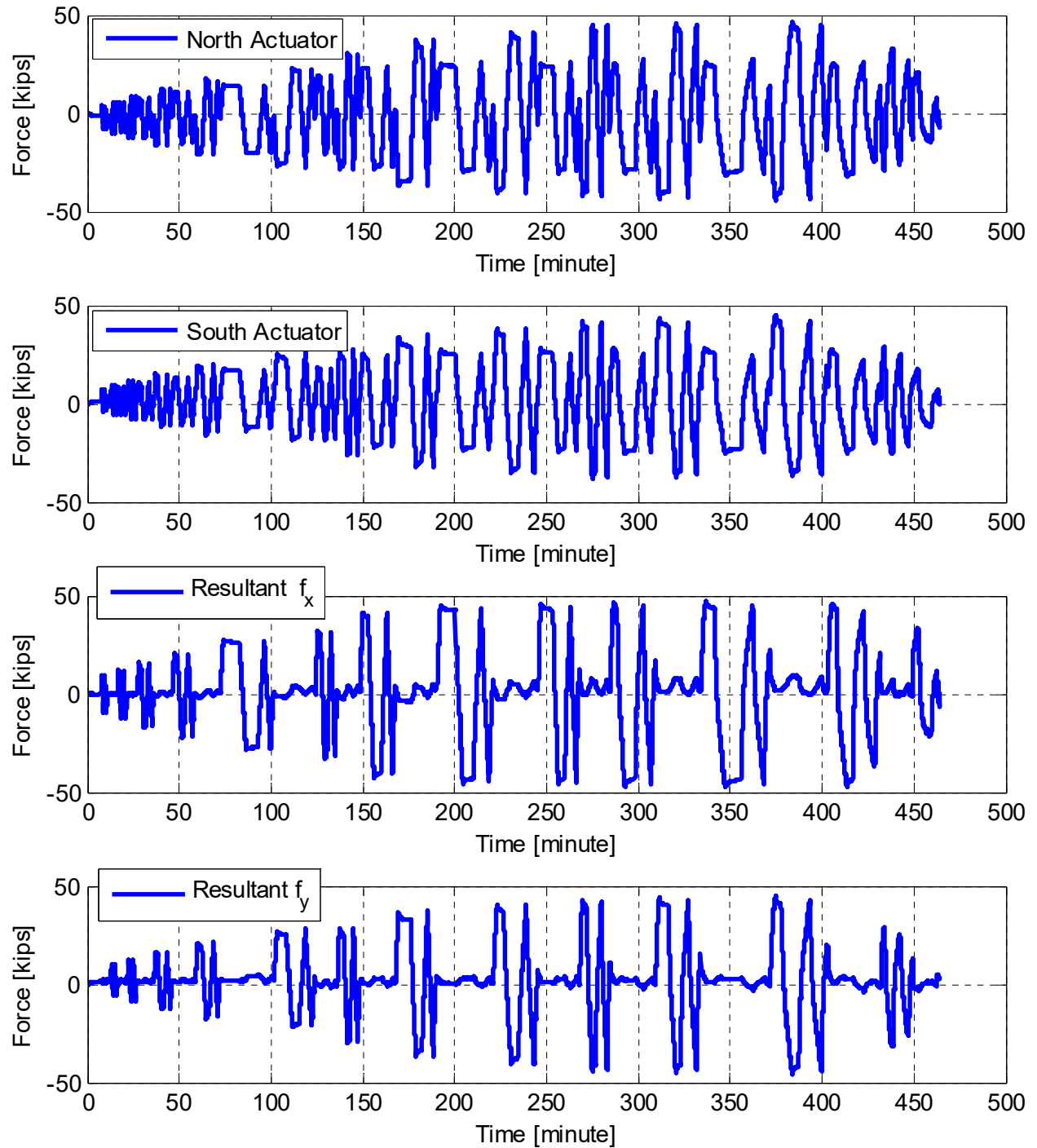


Figure 5.9 History of both of the north and south lateral actuators load cells measurements and the corresponding resultant forces in the transverse (f_x) and the longitudinal (f_y) directions for all cyclic loading groups.

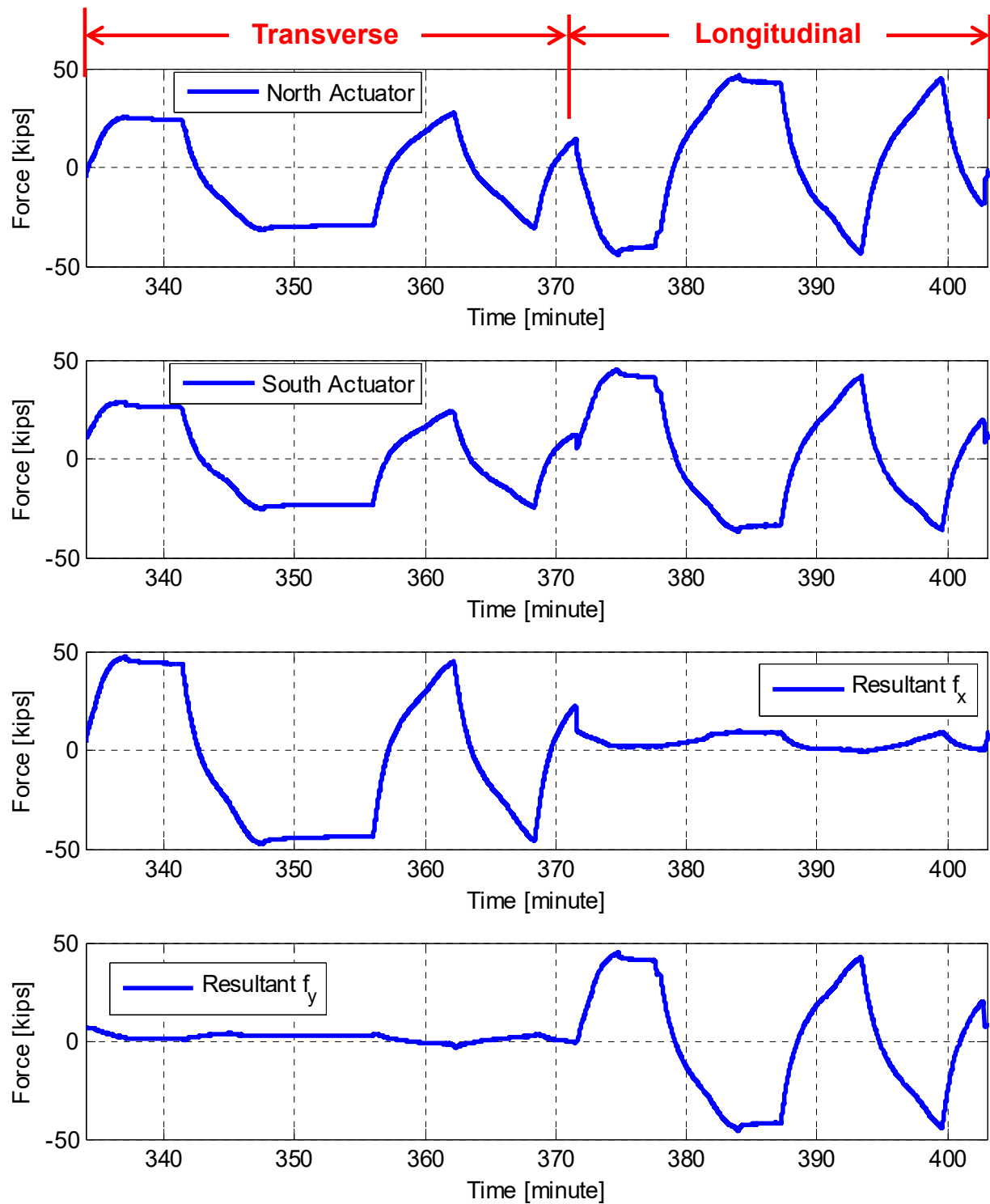


Figure 5.10 Zoomed-in view of the history of both of the north and south lateral actuators load cells measurements and the corresponding resultant forces in the transverse (f_x) and the longitudinal (f_y) directions for one transverse and one longitudinal loading groups.

5.2.2 Displacement History

For a cyclic loading test under displacement control, prescribed displacements are the primary input to the actuators, which in the case of the bridge subassembly described herein were directed in the transverse and longitudinal directions. For practical reasons, the actuators configuration was not aligned with the transverse and the longitudinal directions of the specimen (bridge subassembly). Accordingly, the actuators displacement input was transformed such that the resulting column head motion agreed with the desired transverse (u_x) or longitudinal (u_y) displacements. The actual obtained displacements during the test were tracked in the actuators' local direction through tempsonic transducers, and in the global transverse and longitudinal directions through wirepots. The geometry and configuration of the actuators were used to transform their local motion to the corresponding global transverse and longitudinal directions. The transformed actuators tempsonic measurements were compared to the wirepots displacements to check the quality of measurements and transformations. It was found that the displacements computed from the exact actuators' geometry and tempsonic measurements were the most accurate; therefore, only the displacement histories obtained from transformed tempsonic measurements are presented here.

Figure 5.11 shows the final obtained displacements in both transverse (u_x) and longitudinal (u_y) directions for all loading groups. The flat parts of the plot at given displacement peaks represent the pause in time as the research team investigated the specimen's crack and damage propagation. The column head displacement orbit during all the test runs is presented in Figure 5.12, which emphasizes that the displacement loading was obtained at only one direction at a time, i.e., either the transverse direction only or longitudinal direction only. The independent bi-directional loading tests are generally more useful in uncoupling and understanding the bridge system behavior in each direction separately. This is favorable for the case of this investigation of the bent cap beam effective width and box-girder slab contribution.

A realistic concurrent bi-directional loading is being more representative of earthquake loading, however. Therefore, the Specimen No. 2 was tested using both independent and concurrent bi-directional hybrid simulation loading schemes. Note that a larger displacement cycle at 9.5 in. column top displacement was only possible in the transverse direction because of the set-up limitations of the vertical loading system. Thus, the last displacement group at 6.8 in. was repeated again rather than applying the 9.5 in. cycles. It is also useful throughout this discussion to relate the applied displacements to the corresponding column drift ratio and/or displacement ductility level. The drift ratio is calculated by the ratio of the displacement at the column head (either u_x or u_y) to the 90-in. column height. The ductility level is calculated by the ratio of the column head displacement, either u_x or u_y , to the displacement at the first experimentally-determined yield (Δ_{yield}), which was found to be 1.25 in. The input displacements and corresponding drift ratio and ductility are shown in Table 5.1.

Figure 5.13 shows the history of the actual recorded tempsonic displacements of the north and south actuators along with the resulting displacements in both transverse and longitudinal directions. The two actuators move together in a similar direction and have similar values when u_x only is desired; the directions are reversed when only u_y is applied.

The zoomed-in view in Figure 5.14 shows clearly how the actuators' actual displacements relate to the desired (and observed) displacements: unlike the forces, the displacements are well-controlled. When only u_x is applied, the corresponding u_y value is almost zero and vice-versa. As shown in the force histories of Figures 5.9 and 5.10, some residual forces were still observed in one direction while loading was proceeding in the other orthogonal direction.

Table 5.1 Summary of input displacement and corresponding drift ratio and ductility level.

Displacement (in.)	0.25	0.35	0.50	0.70	1.00	1.25	1.75	2.45	3.50	4.80	6.80	9.50
Drift ratio (%)	0.28	0.39	0.56	0.78	1.11	1.39	1.94	2.72	3.89	5.33	7.56	10.56
Ductility level (μ)	0.20	0.28	0.40	0.56	0.80	1.00	1.40	1.96	2.80	3.84	5.44	7.60

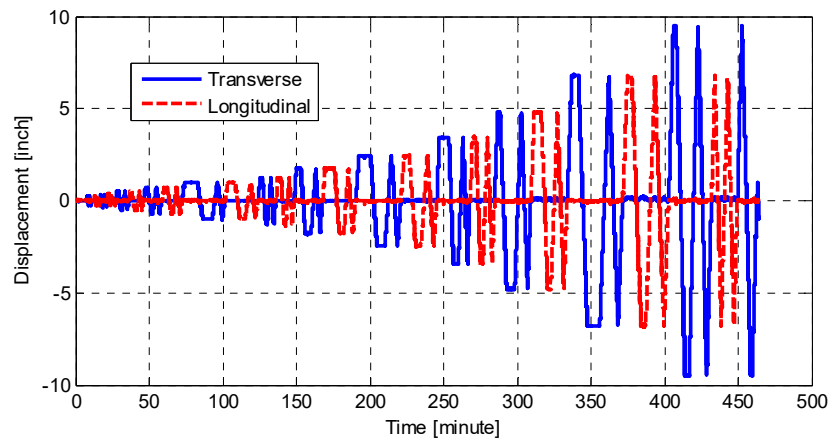


Figure 5.11 History of obtained displacements in both transverse (u_x) and longitudinal (u_y) directions for all cyclic loading groups.

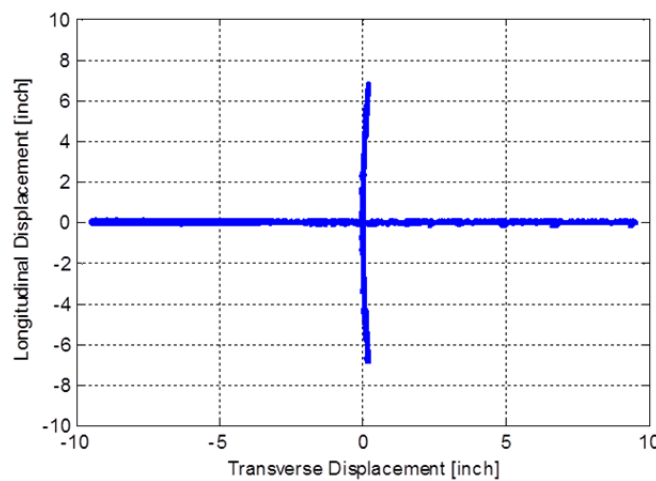


Figure 5.12 Displacement orbit of the specimen's column head for all cyclic loading groups (transverse displacement u_x versus longitudinal displacement u_y).

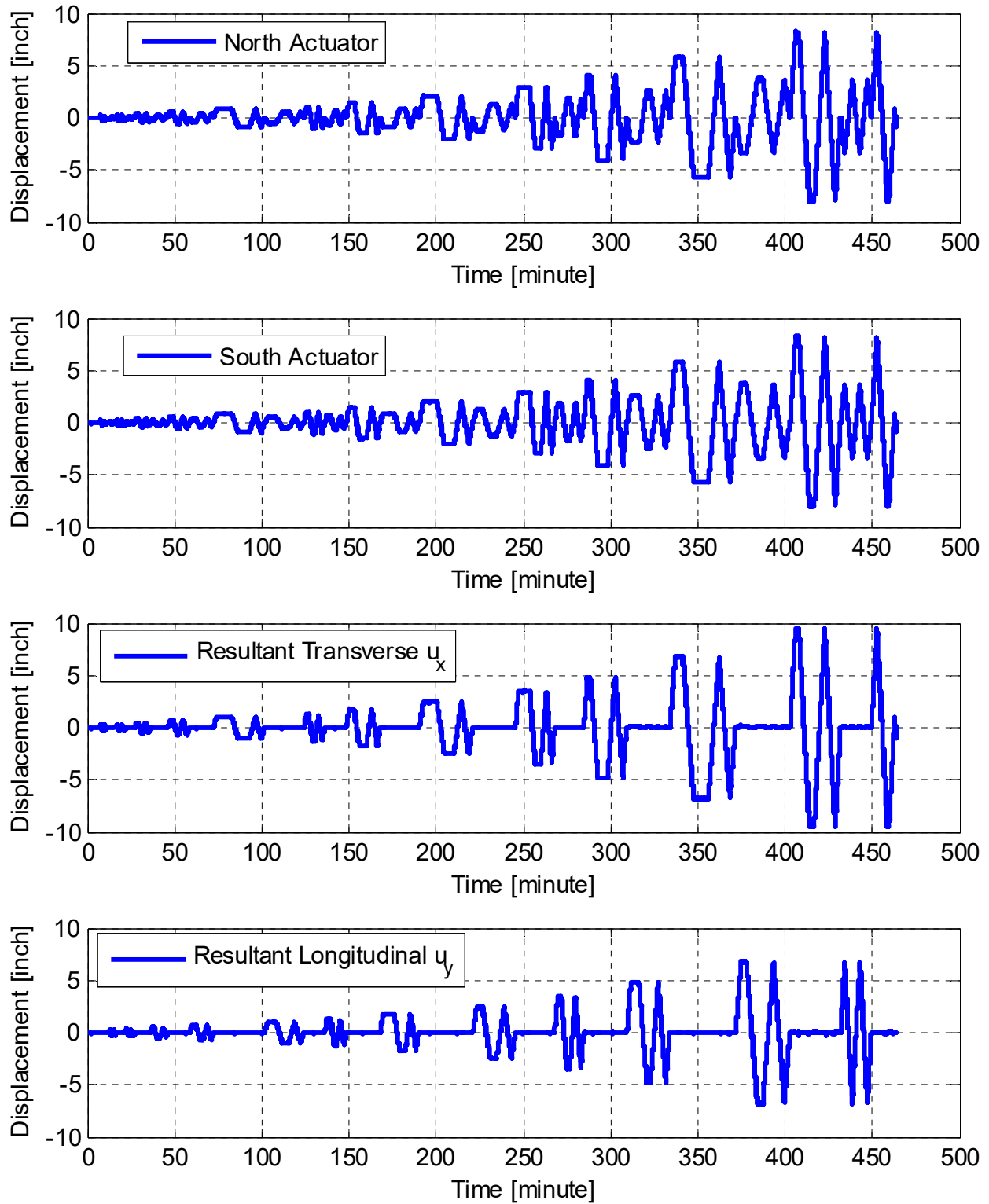


Figure 5.13 History of the north and south lateral actuators temposonics measurements and the corresponding resultant displacement in the transverse (u_x) and the longitudinal (u_y) directions for all cyclic loading groups.

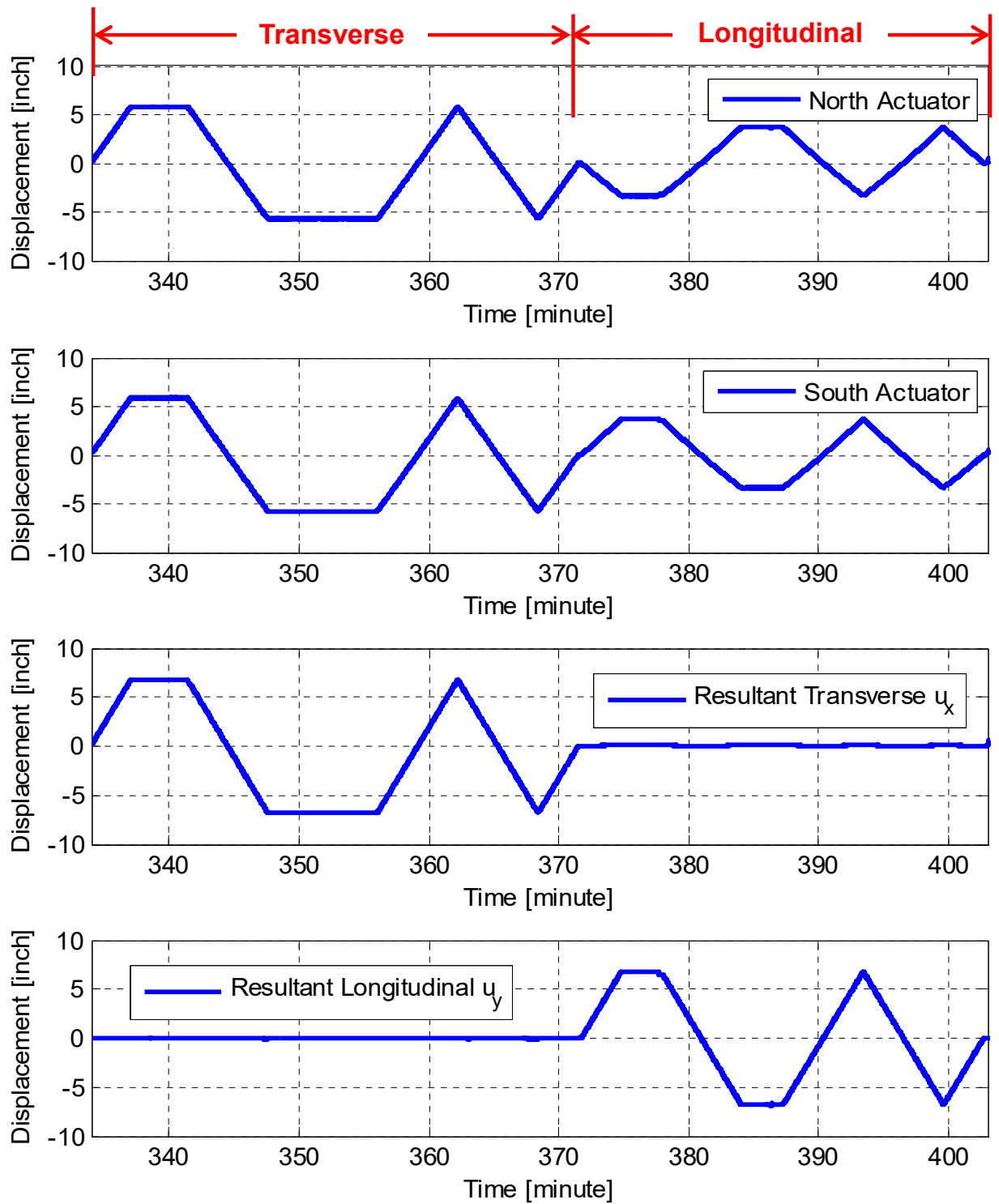


Figure 5.14 Zoomed-in view of the history of the north and south lateral actuators temposonics measurements and the corresponding resultant displacement in the transverse (u_x) and the longitudinal (u_y) directions for all cyclic loading groups.

5.2.3 Force Displacement

The final obtained forces and displacements in the specimen's transverse and longitudinal directions, designated as X and Y , respectively, were used to obtain the force-displacement relationships for the tested bridge subassembly as discussed in this subsection. The force-displacement response is considered a whole system response rather than a single column response because of the nature of the column-to-superstructure (bent cap and box-girder) connection. Note that a given cyclic loading group was applied first in the transverse direction and then in the longitudinal direction. It was expected that different behavior would be observed in the two directions.

The force-displacement relationships for all the cyclic loading groups in both transverse (f_x versus u_x) and longitudinal direction (f_y versus u_y) are shown in Figures 5.15 and 5.16, respectively. To capture the obtained force capacity and corresponding displacement, the envelopes of each of the force-displacement relationships in the transverse and the longitudinal directions are shown in Figures 5.17 and 5.18, respectively. The response obtained in both directions is compared in Figure 5.19. These figures show that the force capacity in the longitudinal direction is slightly less than the corresponding value in the transverse direction: 44.70 kips versus 47.00 kips for positive loading (i.e., actuators pushing the column head), and -45.55 kips versus -47.50 kips for negative loading (i.e., actuators pulling the column head) in the longitudinal and transverse directions, respectively. All the capacity or maximum recorded force values were obtained at the first peak of the eleventh loading cycle (6.8 in. applied displacement), corresponding to a drift ratio of 7.52% and a displacement ductility level of 5.42. The notation of the first peak of a given cyclic loading groups is shown in the inserts of Figure 5.17 or Figure 5.18. Note that each cyclic loading group consisted of two full cycles, which were individually recognized in two different envelope curves. The maximum obtained forces in each loading cycle in each of the transverse and longitudinal directions and the corresponding displacements are respectively summarized in Tables 5.2 and 5.3.

The force-displacement curves in Figures 5.17 and 5.18 show the ductile behavior of the column manifested in the strong beam–weak column design philosophy adopted for bridge designs. The column maintained almost full capacity up to a drift ratio of almost 10% and ductility level of seven. The capacity degradation occurred in the last loading cycle in each direction due to the rupture of the rebars. Each sudden drop in the force-displacement relationship indicates a rebar rupture, which typically occurred for the buckled rebars as the load was being reversed. A total of six rebars ruptured: four at the east side of the column and two at the west side. The east direction is the positive loading in the transverse direction, while the west is the negative loading direction. The rupture of the first and second rebars occurred during the second cycle of the 9.5 in. group in the transverse direction. Accordingly, the capacity of the column dropped significantly when loading was resumed in the longitudinal direction, as seen from the force-displacement relationships at the second set of 6.8 in. group. In addition, two additional rebars ruptured during the final longitudinal loading group. It was decided to proceed with another single-cycle 9.5 in. transverse loading cycle to see how the capacity degradation proceeded further. The last two rebars ruptured during that final transverse loading cycle, as observed from the force-displacement curve in the transverse direction.

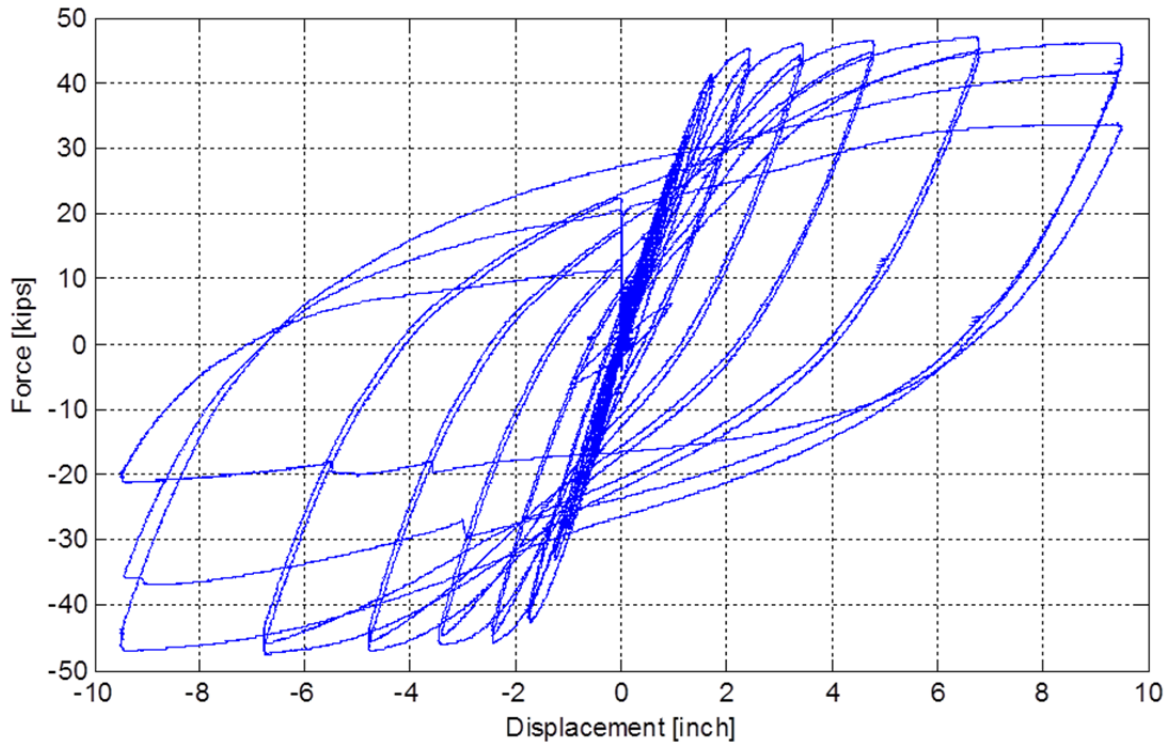


Figure 5.15 Force-displacement relationship for all cycles groups in transverse direction (f_x versus u_x).

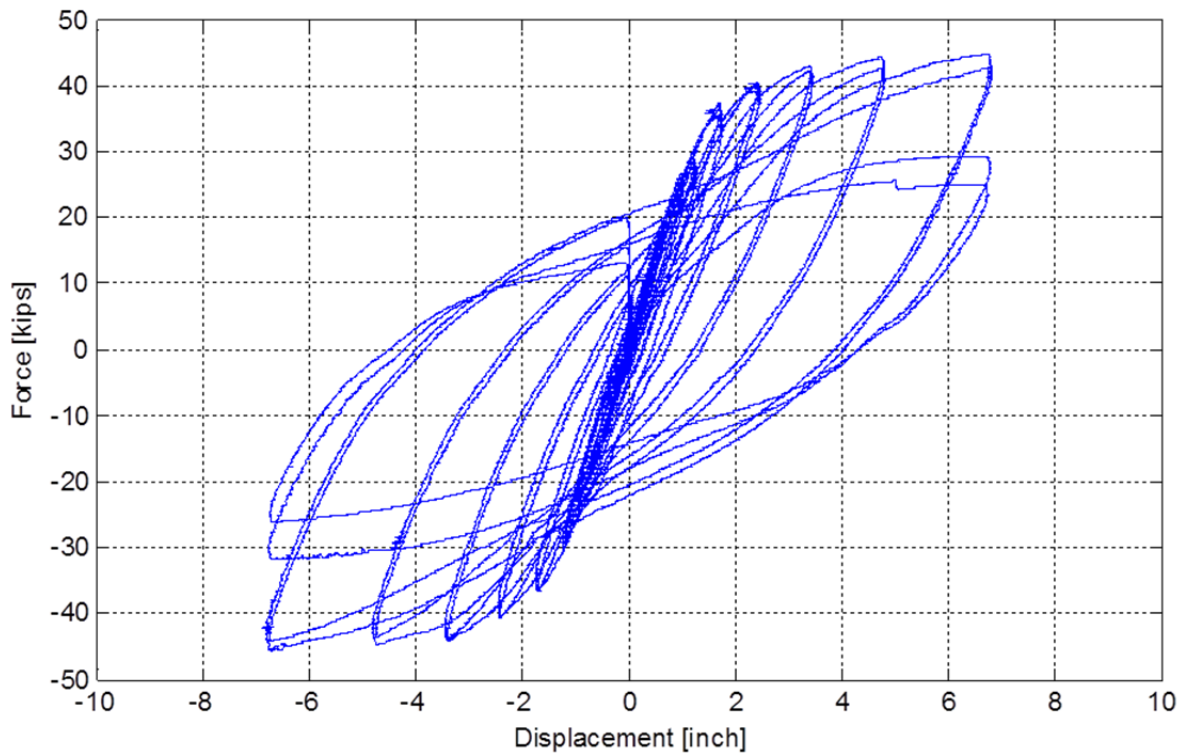


Figure 5.16 Force-displacement relationship for all cycles groups in longitudinal direction (f_y versus u_y).

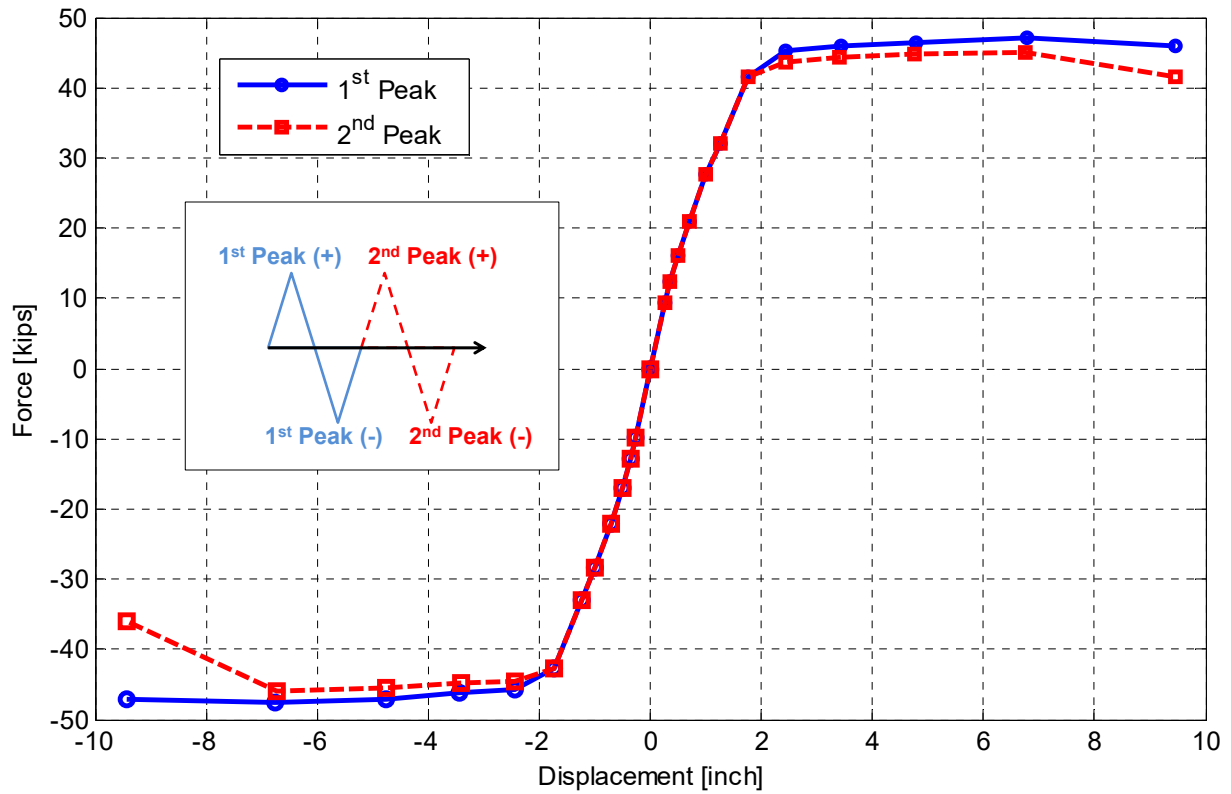


Figure 5.17 Force-displacement envelope for all cycles groups in transverse direction.

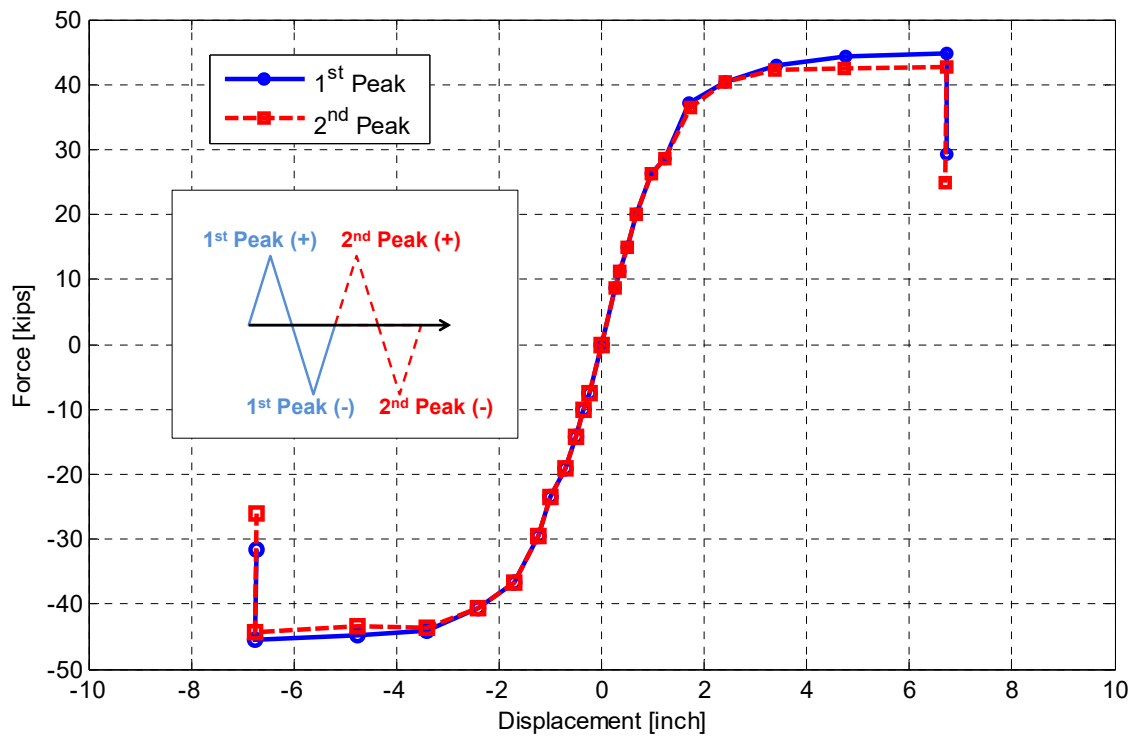


Figure 5.18 Force-displacement envelope for all cycles groups in longitudinal direction.

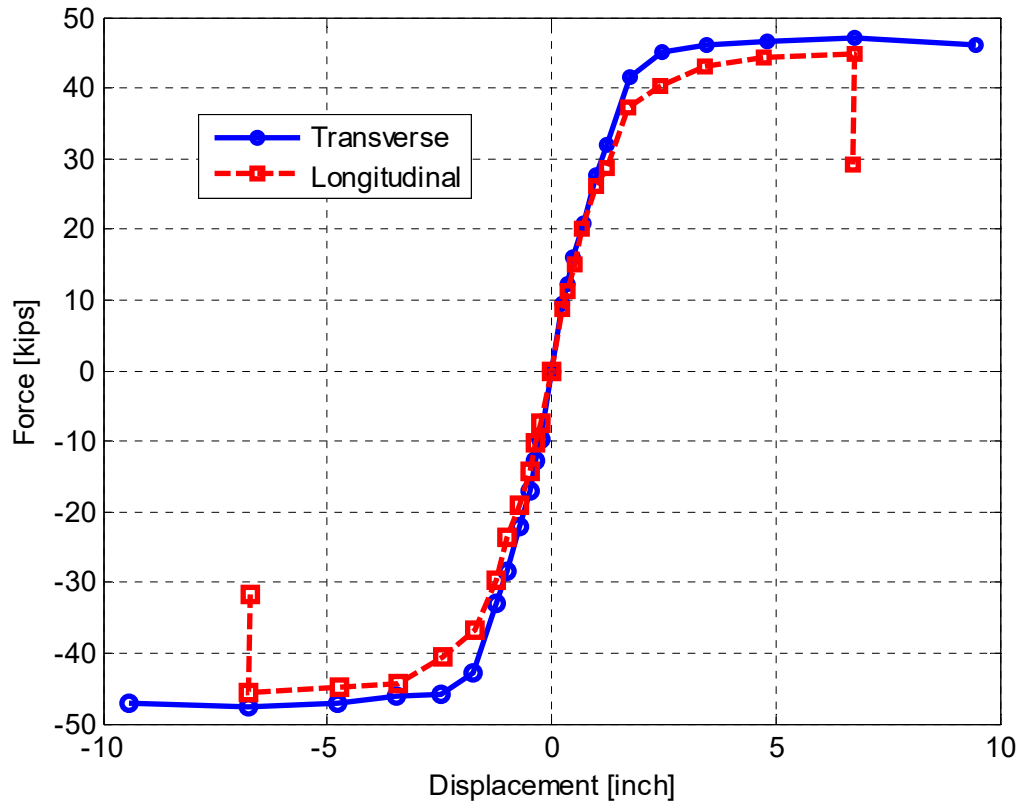


Figure 5.19 Comparison of force-displacement envelopes (cycles 1st peak) in both transverse and longitudinal directions.

5.2.4 Stiffness Determination

The lateral stiffness of the bridge subassembly was estimated using the recorded force and displacement values obtained from each of the loading cycles in both transverse and longitudinal directions; the stiffness after each loading cycle was estimated by several methods. A linear regression was determined to be the best fit to the force-displacement loop obtained from each cyclic loading group. The secant stiffness at the maximum recorded force and its corresponding displacement was estimated twice from positive and negative loading for each loading group. Figure 5.20 demonstrates how to compute the secant stiffness for one of the 9.5 in. transverse cycling loading groups. A summary of the estimated best fit for positive and negative stiffness values along with the observed maximum force and displacements are listed in Tables 5.2 and 5.3 for the transverse and longitudinal directions, respectively. The tables also list the corresponding drift ratio and ductility level for each loading group. The degradation of the secant stiffness, calculated from both positive and negative loading cases, is plotted against the drift ratio and ductility level in Figures 5.21 and 5.22 for the transverse and longitudinal directions, respectively.

To obtain another estimate of the stiffness, a small loading cycle (20% of the preceding cycle's amplitude) was applied after each of the main test loading groups in both directions. The initial stiffness was then obtained from those small cycles to judge the stiffness degradation as

loading progresses. A comparison between the stiffness degradation in both transverse and longitudinal directions using the previously mentioned secant stiffness and the stiffness values obtained from the small cycles is presented in Figures 5.23 and 5.24, respectively. The stiffness in the longitudinal direction is consistently less than that in the transverse direction at a given drift ratio or ductility level. This can be attributed to two factors: (1) the loading always began in the transverse direction first before it resumed in the longitudinal direction for a given group of loading cycles—accordingly, the cracking and nonlinearity happening during the transverse loading results in a relative reduction in the stiffness when the longitudinal loading takes place; and (2) the lower stiffness in the longitudinal direction may be a result of the relative flexibility of the column/box-girder static system in the longitudinal direction relative to the column/cap beam static system in the transverse direction.

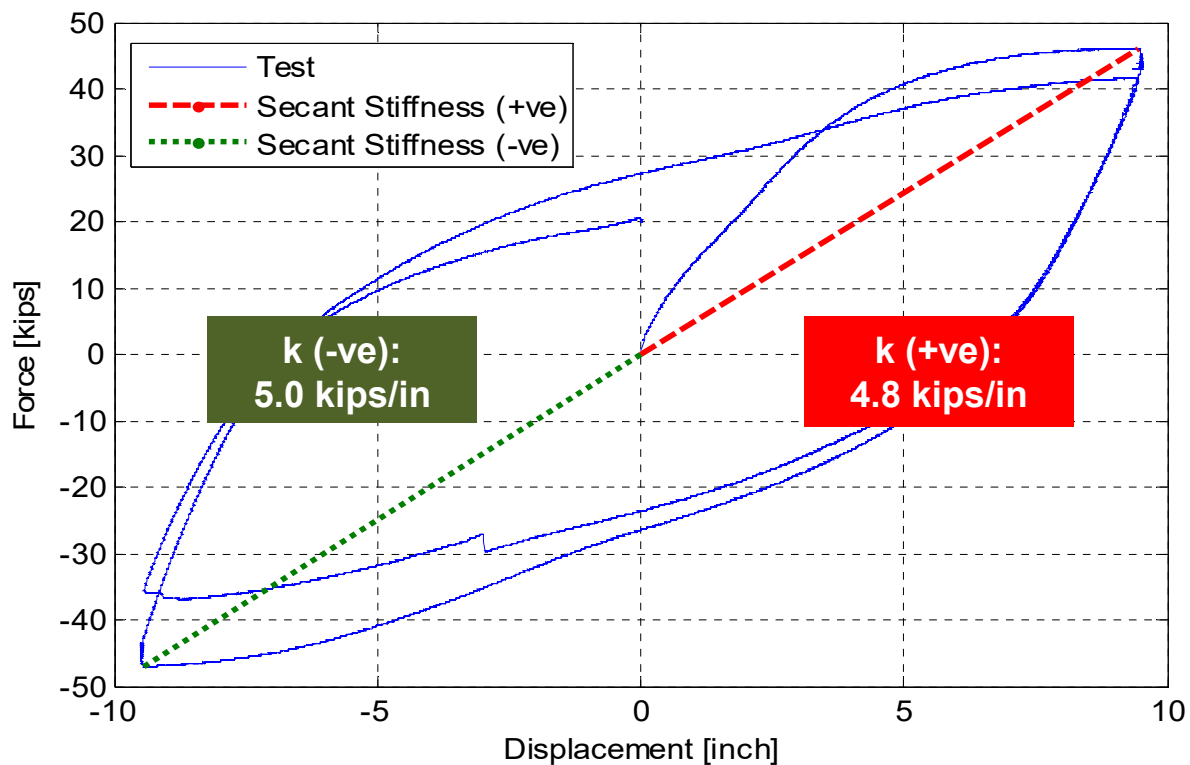


Figure 5.20 Example of secant stiffness calculation in positive and negative loading directions for the 9.5 in. transverse displacement cyclic loading group.

Table 5.2 Summary of displacement, force, stiffness, ductility, and drift ratio values for all runs in transverse direction (X).

Run #	Disp. u_x (in.)		Force f_x (kips)		Stiffness (kips/in.)			Drift Ratio (%)	Ductility (μ)
	+ve	-ve	+ve	-ve	Best Fit	Secant +ve	+ve	-ve	+ve
1	0.25	-0.25	9.35	-9.76	37.70	37.40	39.04	0.28	0.20
2	0.34	-0.35	12.30	-12.76	35.40	36.18	36.99	0.38	0.27
3	0.49	-0.49	16.12	-16.96	33.00	33.24	34.61	0.54	0.39
4	0.70	-0.70	20.86	-22.13	29.81	29.80	31.61	0.78	0.56
5	1.00	-1.00	27.60	-28.40	26.98	27.60	28.40	1.11	0.80
6	1.25	-1.24	32.00	-32.95	25.13	25.60	26.57	1.39	1.00
7	1.75	-1.74	41.50	-42.72	23.25	23.71	24.55	1.94	1.40
8a	2.45	-2.45	45.20	-45.80	17.71	18.45	18.69	2.72	1.96
8b	2.45	-2.45	43.60	-44.50	17.71	17.80	18.16	2.72	1.96
9a	3.45	-3.45	46.00	-46.18	12.48	13.33	13.39	3.83	2.76
9b	3.40	-3.42	44.30	-44.80	12.48	13.03	13.10	3.78	2.72
10a	4.80	-4.76	46.50	-47.10	8.80	9.69	9.89	5.33	3.84
10b	4.76	-4.76	44.70	-45.60	8.80	9.39	9.59	5.29	3.81
11a	6.77	-6.76	47.00	-47.50	6.12	6.94	7.03	7.52	5.42
11b	6.75	-6.74	45.00	-46.00	6.12	6.67	6.82	7.50	5.40
12a	9.46	-9.44	46.00	-47.10	3.86	4.86	4.99	10.51	7.57
12b	9.45	-9.42	41.60	-35.93	3.86	4.40	3.81	10.50	7.56
13	9.45	-9.40	33.72	-21.25	2.22	3.57	2.26	10.49	7.56

Table 5.3 Summary of displacement, force, stiffness, ductility, and drift ratio values for all runs in in longitudinal direction (Y).

Run #	Disp. u_x (in.)		Force f_x (kips)		Stiffness (kips/in.)			Drift Ratio (%)	Ductility (μ)
	+ve	-ve	+ve	-ve	Best Fit	Secant +ve	+ve	-ve	+ve
1	0.25	-0.24	8.59	-7.46	30.50	34.36	31.08	0.28	0.20
2	0.34	-0.34	11.33	-10.18	29.80	33.32	29.94	0.38	0.27
3	0.50	-0.49	14.90	-14.15	28.20	29.80	28.88	0.56	0.40
4	0.69	-0.70	20.00	-19.05	26.00	28.99	27.21	0.77	0.55
5	0.98	-0.99	26.20	-23.60	23.50	26.73	23.84	1.09	0.78
6	1.23	-1.24	28.70	-29.60	22.30	23.33	23.87	1.37	0.98
7a	1.71	-1.71	37.20	-36.70	19.70	21.75	21.46	1.90	1.37
7b	1.72	-1.71	36.40	-36.60	19.70	21.16	21.40	1.91	1.38
8a	2.42	-2.42	40.30	-40.60	15.60	16.65	16.78	2.69	1.94
8b	2.42	-2.42	40.30	-40.60	15.60	16.65	16.78	2.69	1.94
9a	3.40	-3.40	43.00	-44.20	11.60	12.65	13.00	3.78	2.72
9b	3.39	-3.40	42.20	-43.70	11.60	12.45	12.85	3.77	2.71
10a	4.75	-4.75	44.25	-44.77	8.23	9.32	8.97	5.28	3.80
10b	4.74	-4.75	42.50	-43.50	8.23	8.97	9.16	5.27	3.79
11a	6.74	-6.76	44.70	-45.55	5.62	6.63	6.33	7.49	5.39
11b	6.73	-6.75	42.60	-44.30	5.62	6.33	6.56	7.48	5.38
12a	6.72	-6.73	29.25	-31.70	3.30	4.35	4.71	7.47	5.38
12b	6.71	-6.73	25.00	-26.00	3.30	3.73	3.86	7.46	5.37

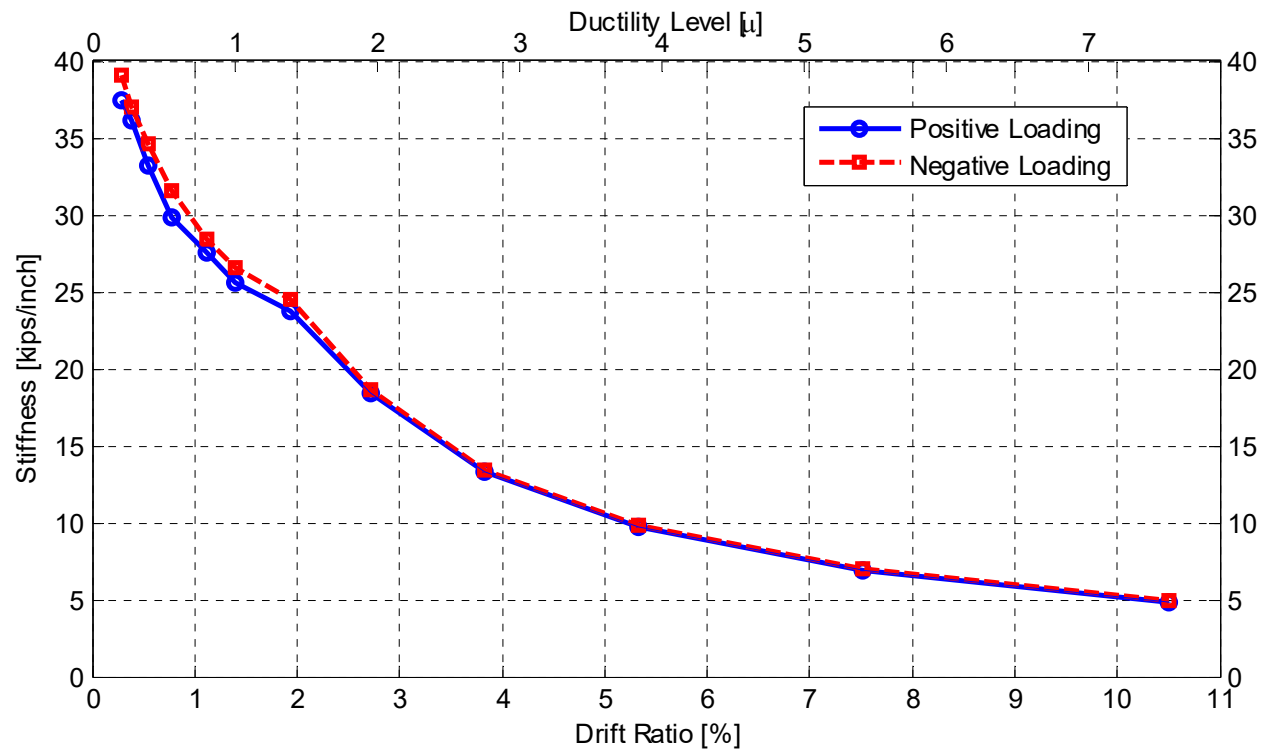


Figure 5.21 Lateral secant stiffness degradation in transverse direction.

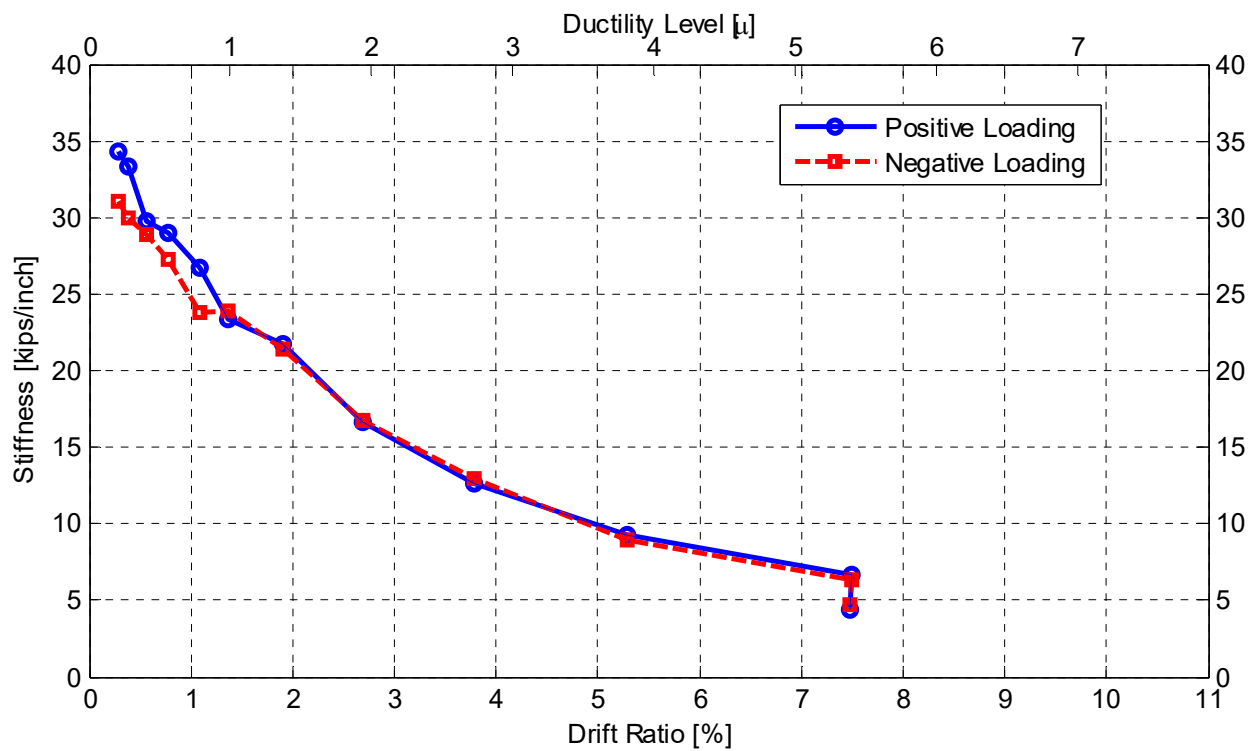


Figure 5.22 Lateral secant stiffness degradation in longitudinal direction.

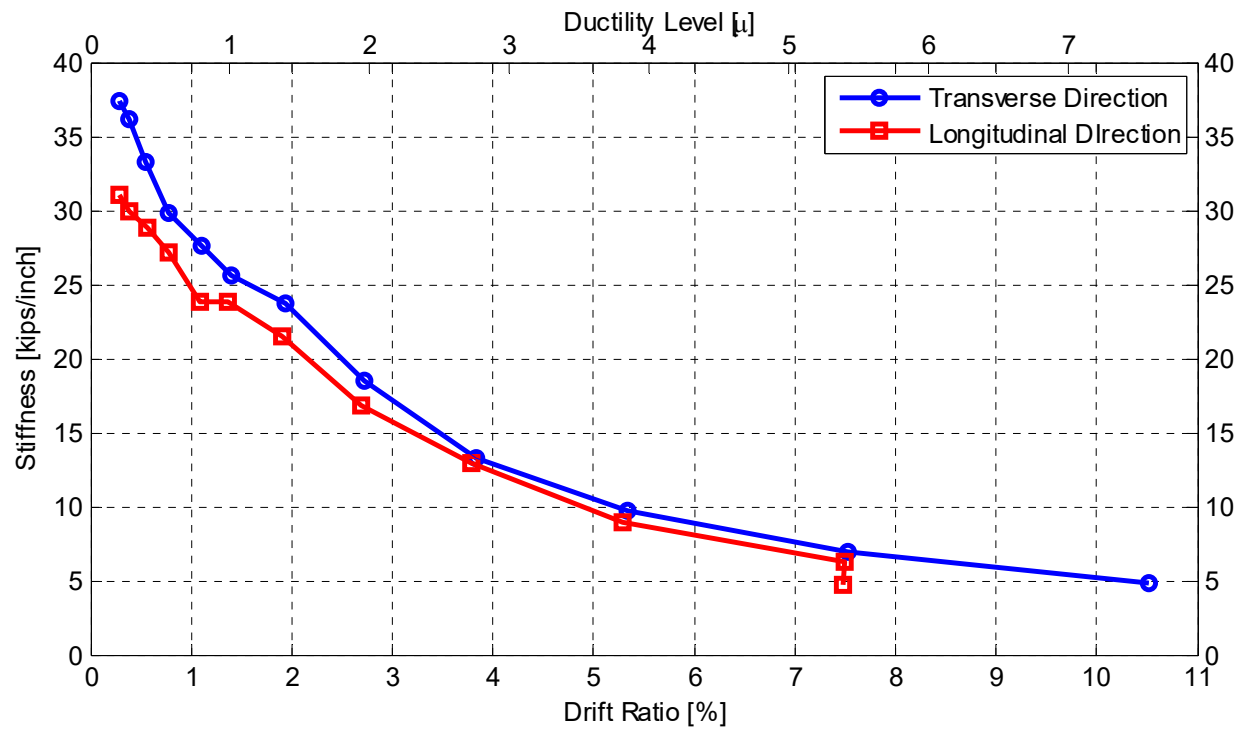


Figure 5.23 Comparison of stiffness degradation in both transverse and longitudinal directions using the secant stiffness values.

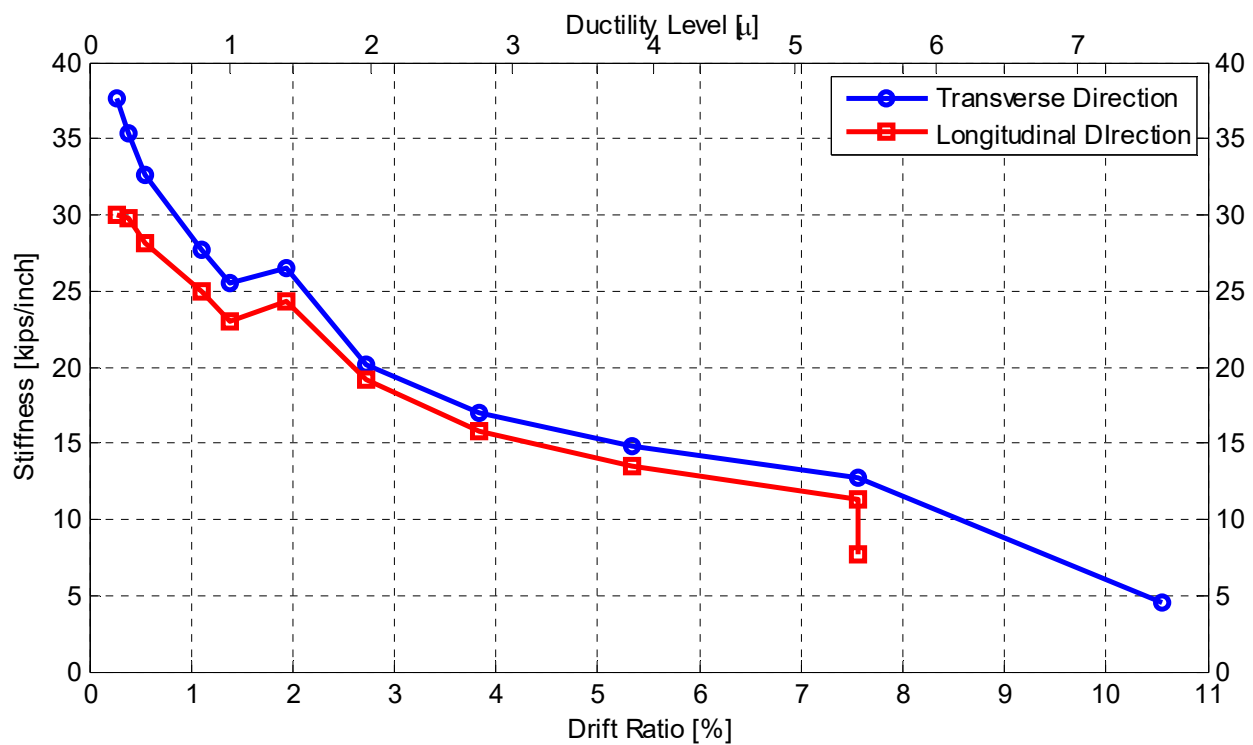


Figure 5.24 Comparison of stiffness degradation in both transverse and longitudinal directions using the stiffness values estimated from the small cycles that followed the main test loading groups.

5.3 COLUMN LOCAL BEHAVIOR

The discussion of the local column behavior presented in the following three subsections focuses on the strain and curvatures recorded at different levels in the column plastic hinge zone, and the column section's moment-curvature relationship in both transverse and longitudinal directions. The column data and observed response are also useful for populating the existing database of column tests and possible future studies that focus on analytical and FE modeling.

5.3.1 Strain Behavior

Strain gauges were installed at various levels along the four rebars that experienced the largest strains according to the adopted loading directions. The outermost north and south gauges experienced the largest strains during longitudinal (N-S) loading, while the outermost east and west gauges experienced the largest values during transverse (E-W) loading. The notation of loading direction is presented along with the four instrumented column rebars in Figure 5.25. The history of the strain measured in each of those four rebars is shown in Figure 5.26. The strain gauges were capable of recording the strain measurements almost throughout the test until a rebar ruptured, as seen from the east rebar strain history. A maximum strain of almost 8% (0.08) was recorded in the north rebar, which unlike the east and west rebars, did not rupture during the test. A close-up view of the different rebars strain history is shown in Figure 5.27, which shows how the strain developed only in east and west rebars during transverse loading, and north and south rebars during longitudinal loading. The shown strain histories were recorded at the strain gauges at the maximum column moment location in the plastic hinge zone, i.e., slightly above the beam face; the strain profile in each of the four instrumented rebars along the column height is also presented. Figures 5.28–5.35 show the strain profile for each of the four instrumented rebars captured at three different loading levels, 2.7%, 5.3% and 7.5% drift ratio, at both of the positive and negative amplitudes of the loading cycles. The strain profile agrees with the expected bending moment distribution along the column height. A nonlinear distribution is shown in the plastic hinge zone due to excessive yielding and damage.

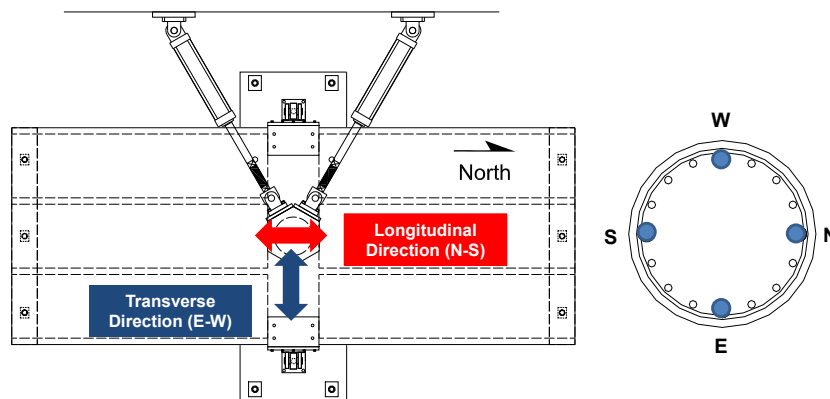


Figure 5.25 Notation of loading direction and layout of instrumented column rebars.

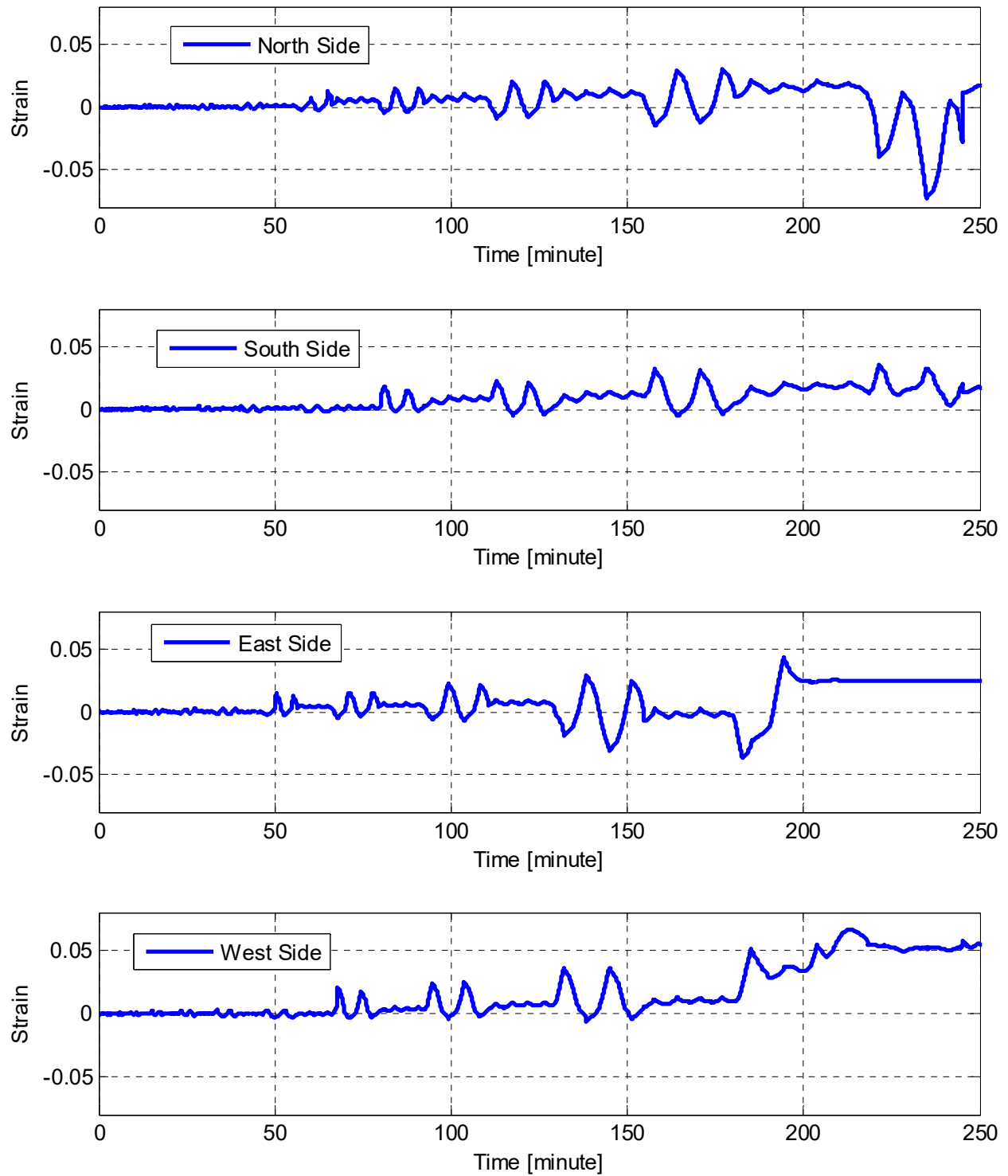


Figure 5.26 History of the strain of the column rebars at lowest section in the plastic hinge where maximum strain is expected for all loading cycles.

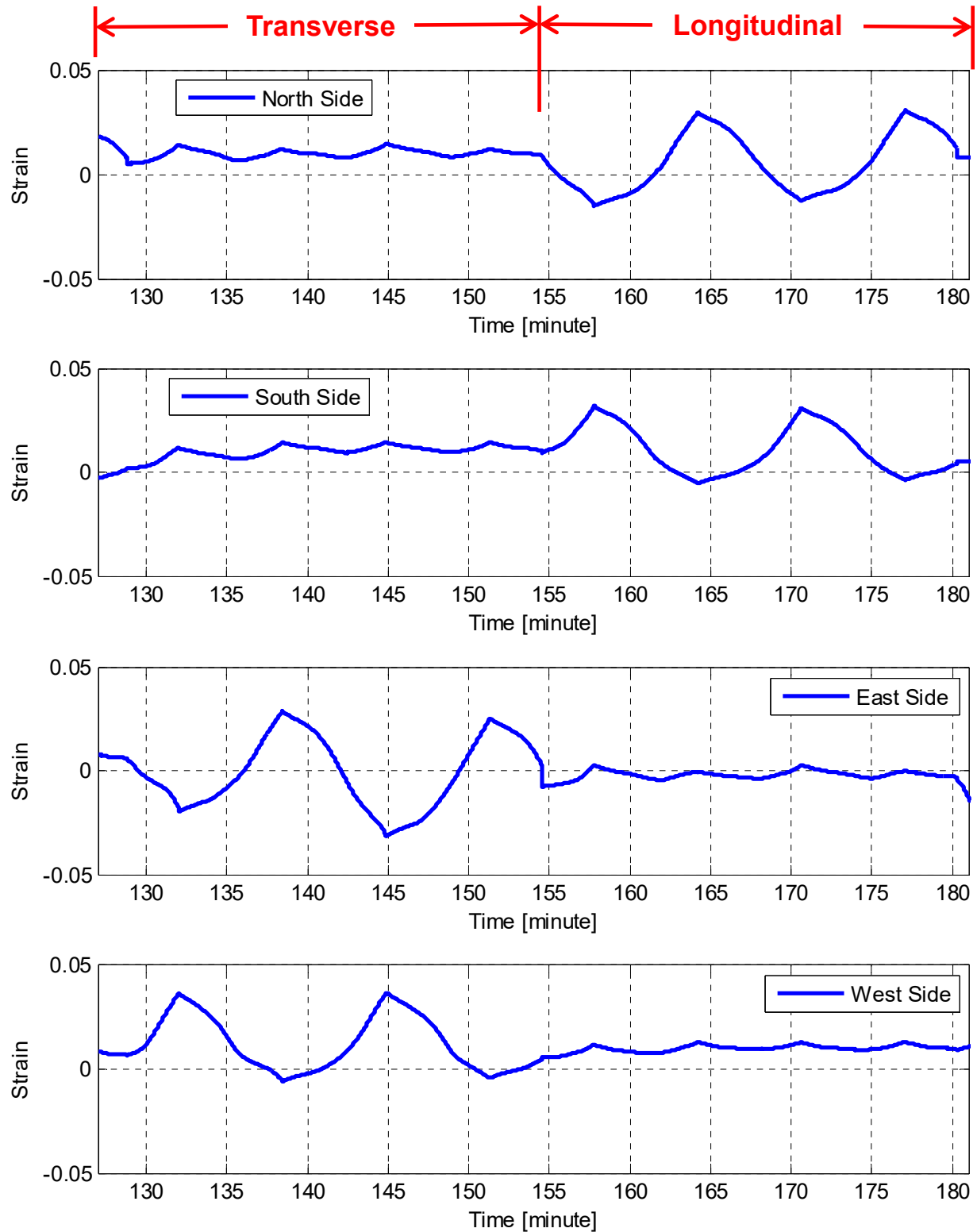


Figure 5.27 Zoomed-in view of the history of strain of the column rebars at lowest section in the plastic hinge where maximum strain is expected for one group of transverse and one group of longitudinal loading cycles.

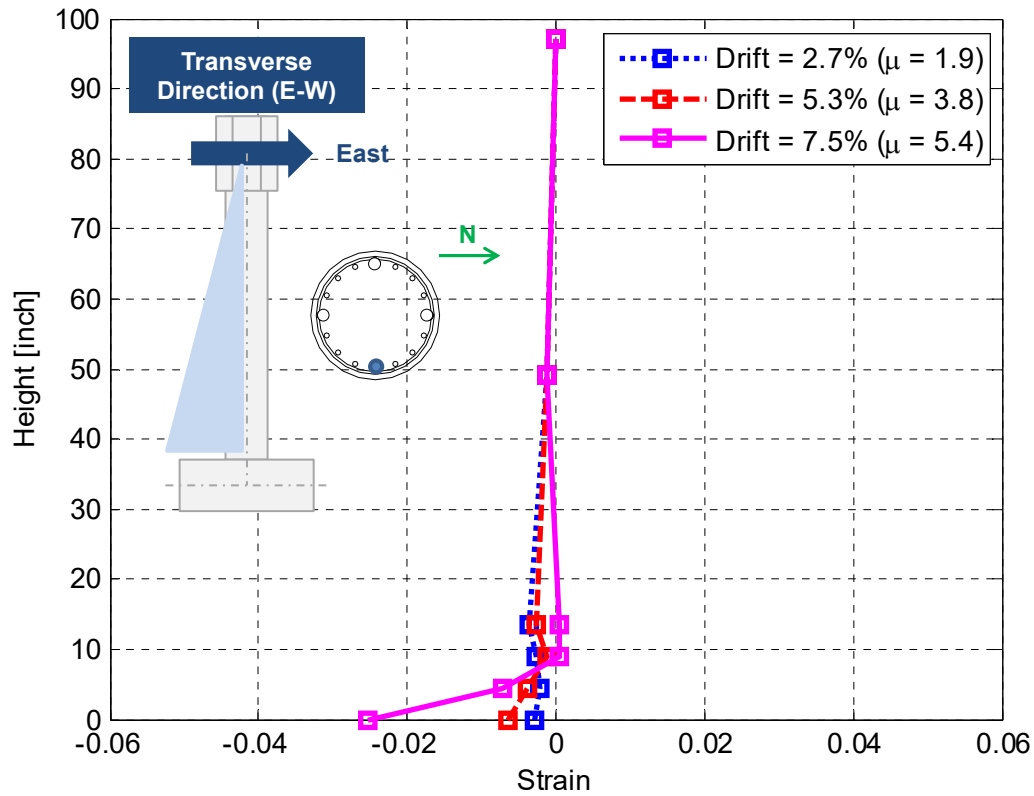


Figure 5.28 Strain distribution along east side rebar when loading is towards east.

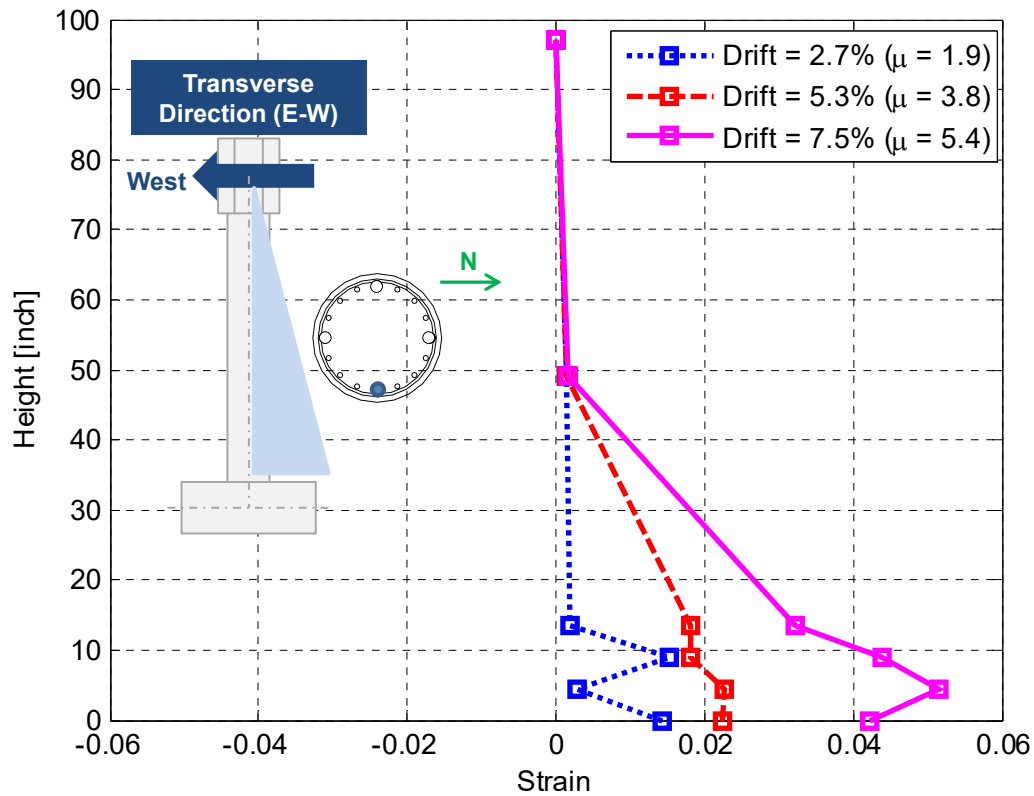


Figure 5.29 Strain distribution along east side rebar when loading is towards west.

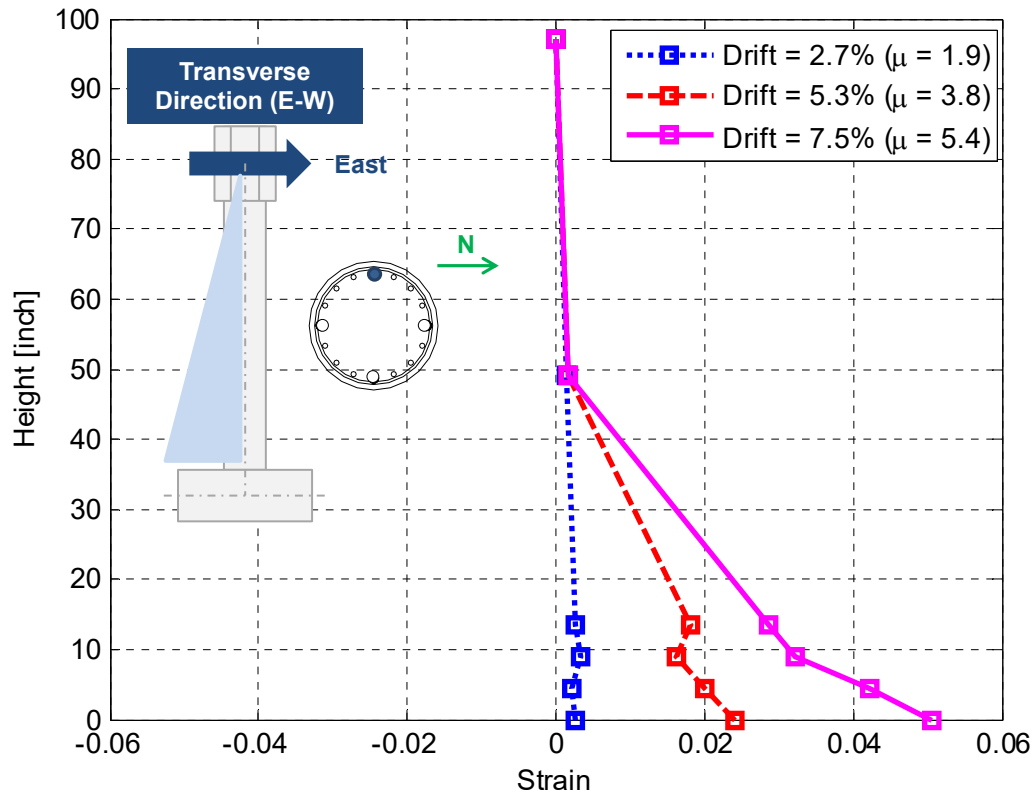


Figure 5.30 Strain distribution along west side rebar when loading is towards east.

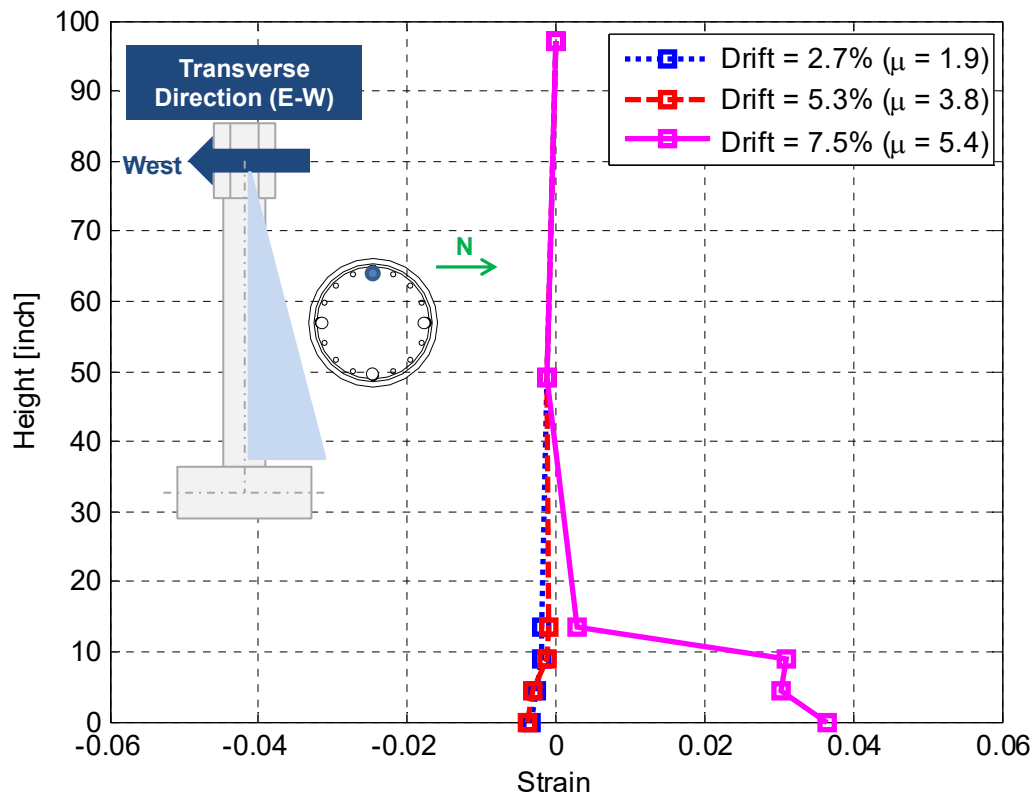


Figure 5.31 Strain distribution along west side rebar when loading is towards west.

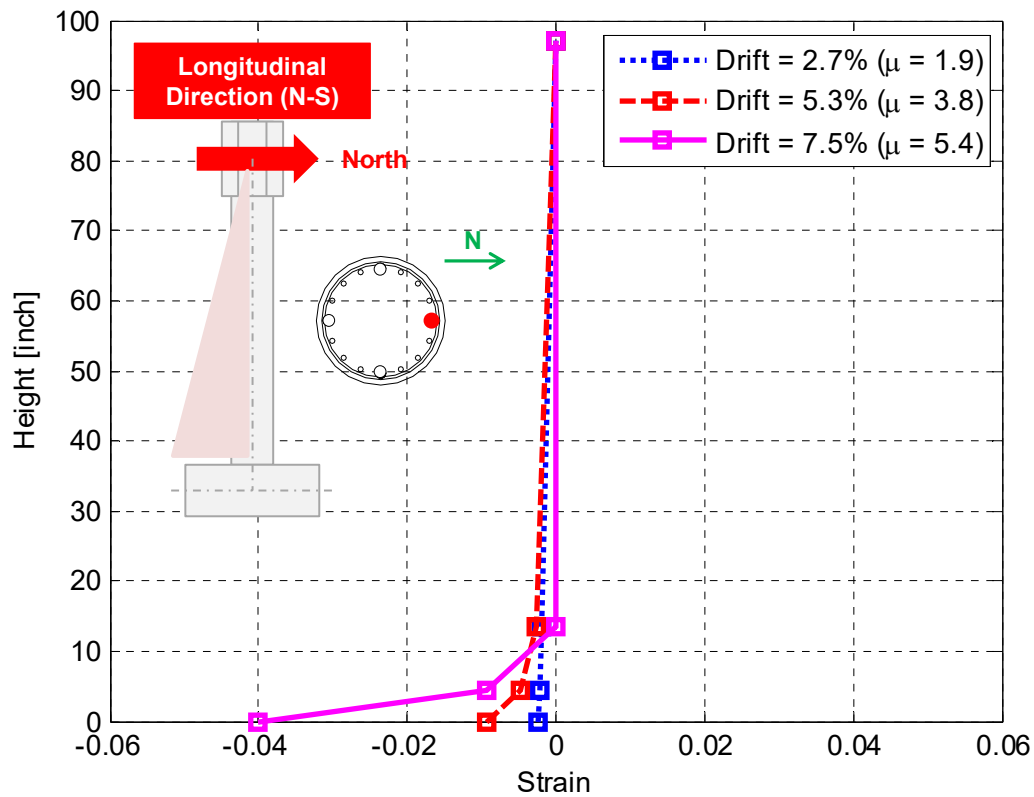


Figure 5.32 Strain distribution along north side rebar when loading is towards north.

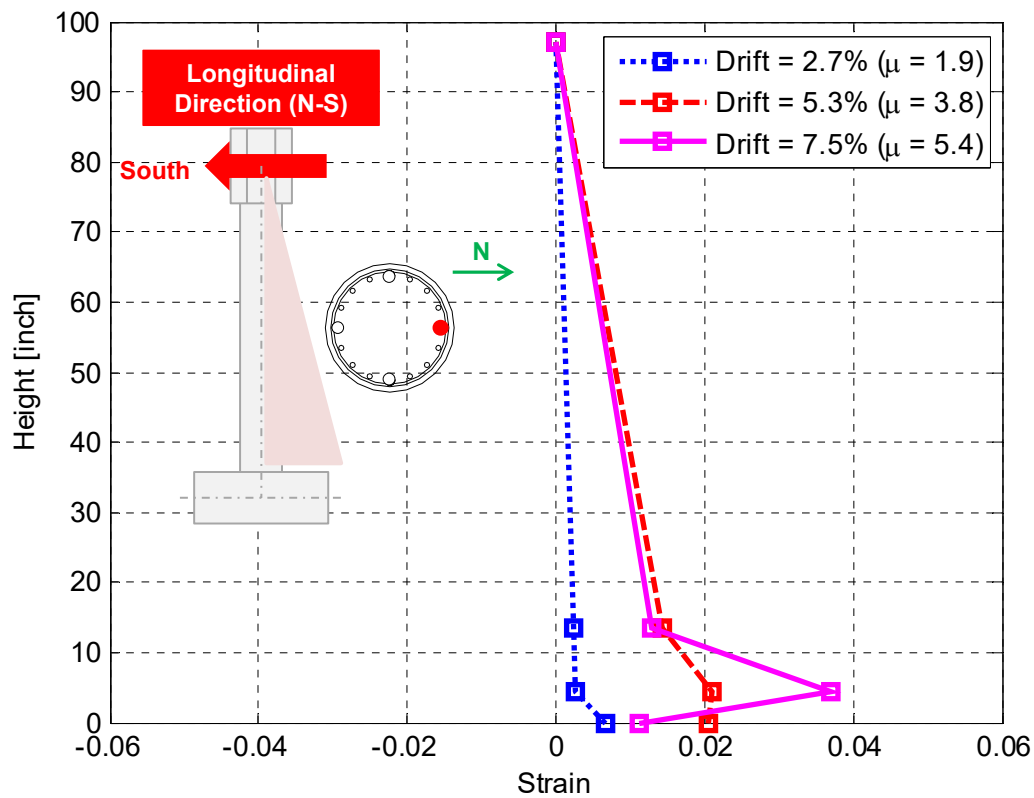


Figure 5.33 Strain distribution along north side rebar when loading is towards south.

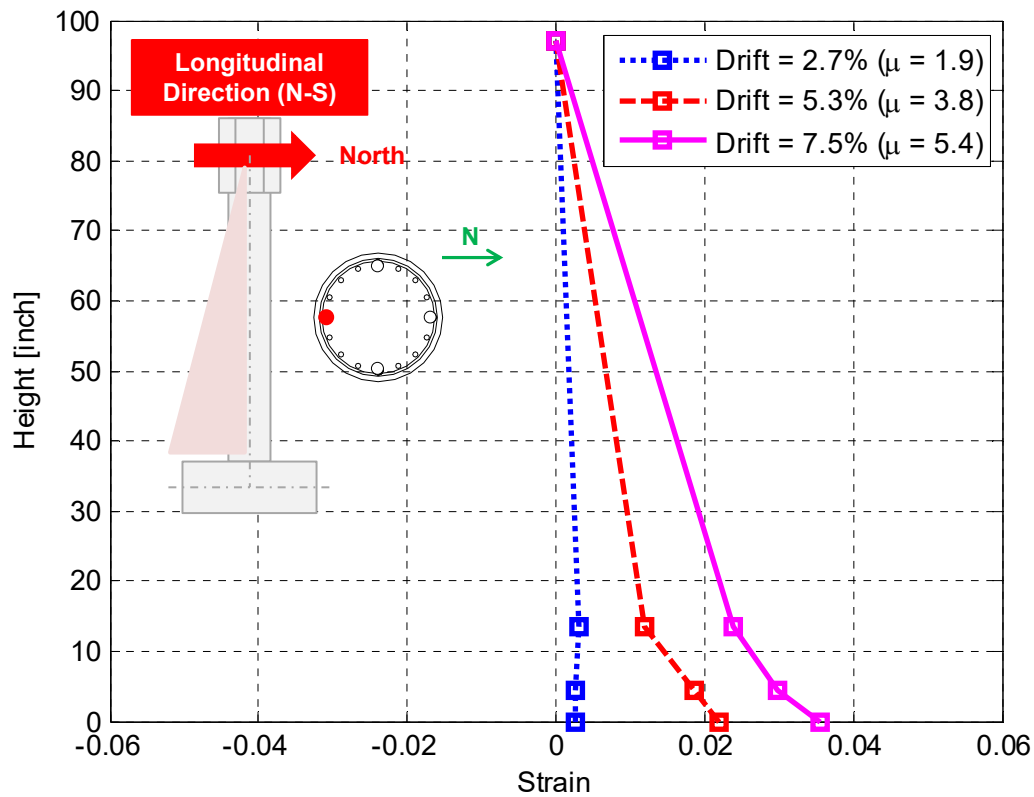


Figure 5.34 Strain distribution along south side rebar when loading is towards north.

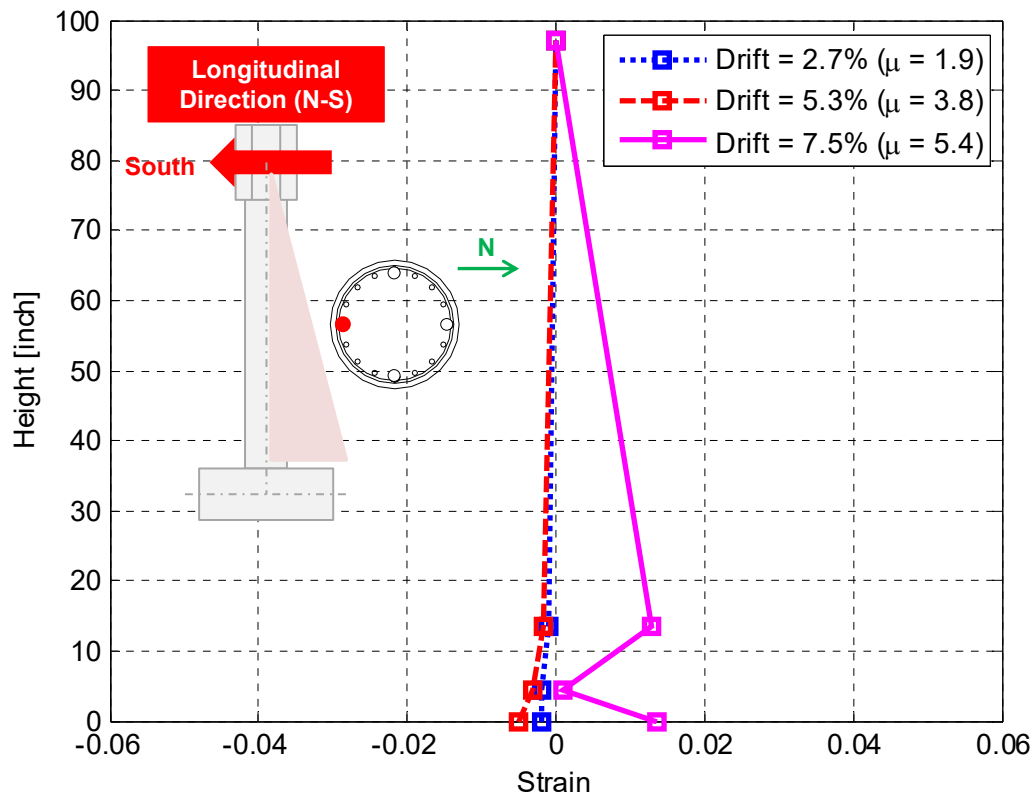


Figure 5.35 Strain distribution along south side rebar when loading is towards south.

5.3.2 Curvature Behavior

The history of the measured curvature at the lowest level in the column's plastic hinge zone, i.e., close to the beam face, is shown in Figure 5.36 for both of the transverse (E-W) and longitudinal (N-S) directions. A close-up view of the curvature history shown in Figure 5.37 emphasizes that most of the column rotations were planar with load, i.e., when loading was in the transverse direction, the column rotation and curvature was only in the E-W direction and vice versa in the longitudinal direction.

The distribution of curvatures along the column height is also of interest in terms of determining column behavior. As previously mentioned, optimally, the damage in a column should be concentrated in the plastic hinge zone so that it is ductile enough to accommodate large rotations and avoid any collapse at elevated lateral loading demands. The curvature profile along the column height is shown in Figures 5.38 and 5.39 for four levels of loading in the transverse direction when loaded in the east and west directions, respectively, i.e., the curvature recorded at the loading cycle positive and negative amplitudes. Similarly, the curvature distribution in the column's longitudinal direction for loading in north and south directions is shown in Figures 5.40 and 5.41, respectively. The four levels of loading included in these figures are drift ratios of 1.0%, 2.7%, 5.3%, and 7.5%, which correspond to ductility levels of 1.0, 1.9, 3.8, and 5.4, respectively. A maximum curvature value of almost 0.01 in.^{-1} was recorded before the LVDT instrumentation slipped because of the extensive concrete spalling. Considering a yield curvature of 0.00034 in.^{-1} as estimated from sectional analysis, the observed maximum curvature denotes a curvature ductility of 29.4. Meanwhile, the maximum curvature value corresponds to plastic rotation of approximately 0.15 radians (8.6°) using a 15-in.-plastic-hinge length as calculated by Caltrans SDC provisions. The plastic rotation and curvature ductility values show that the column designed according to the latest Caltrans SDC and AASHTO Guidelines is more ductile than the minimum code requirements.

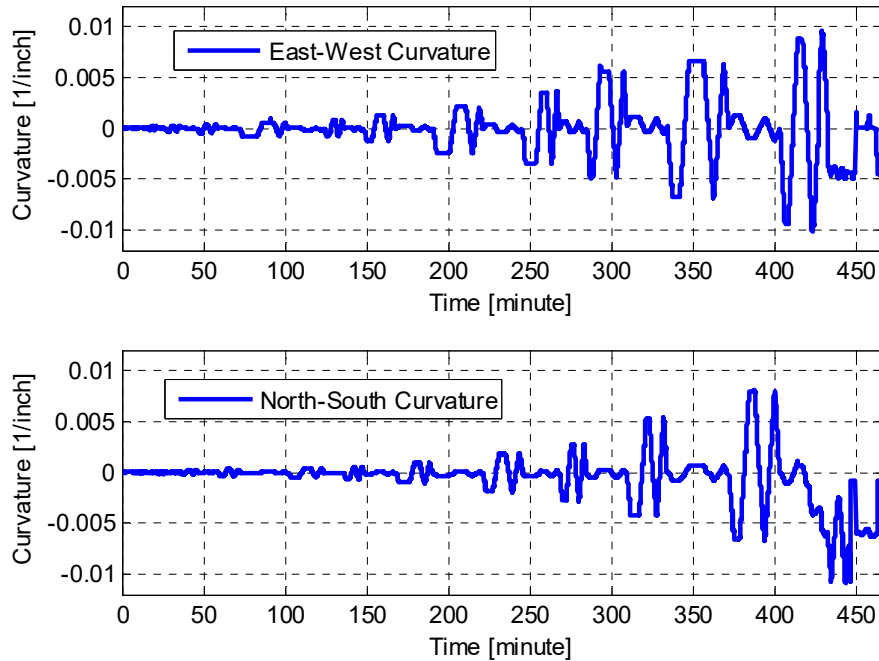


Figure 5.36 History of column curvature at the lowest section in the plastic hinge zone in both east-west (transverse) and north-south (longitudinal) directions for all loading cycles.

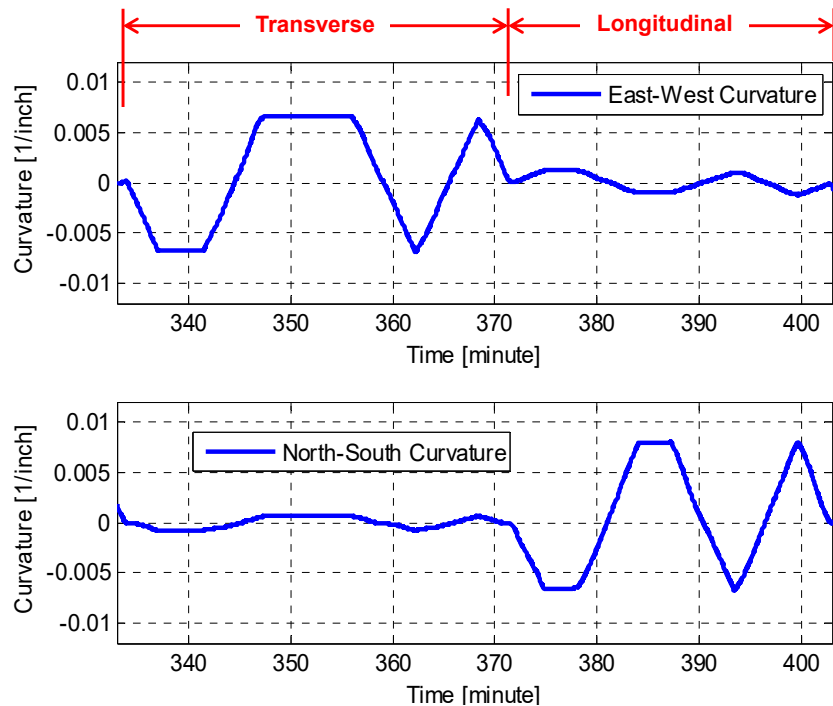


Figure 5.37 Zoomed-in view of the history of the column curvature at the lowest section in the plastic hinge zone in both east-west (transverse) and north-south (longitudinal) directions for one group of transverse and one group of longitudinal loading cycles.

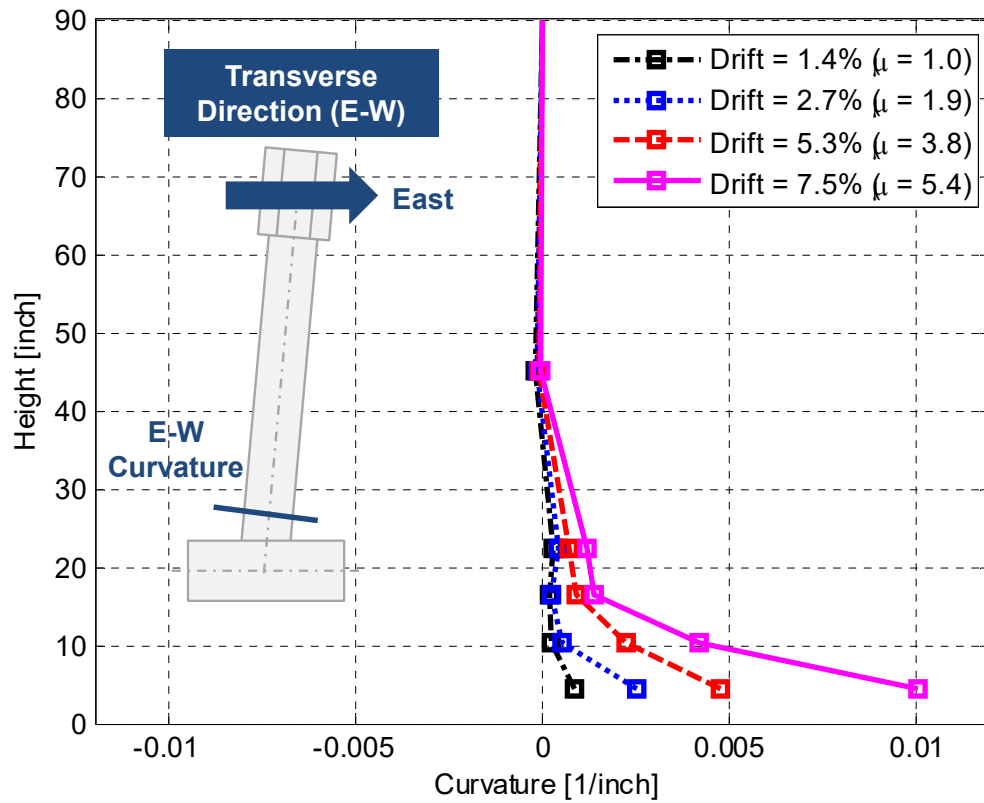


Figure 5.38 Curvature distribution along column height when loading is towards east.

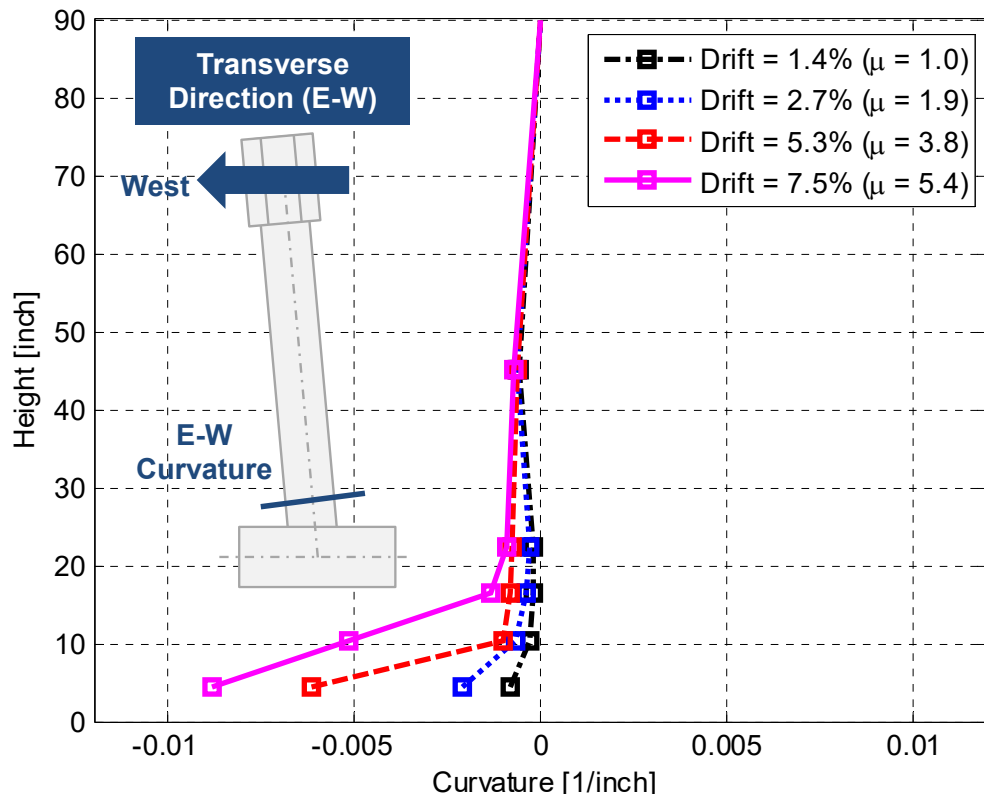


Figure 5.39 Curvature distribution along column height when loading is towards west.

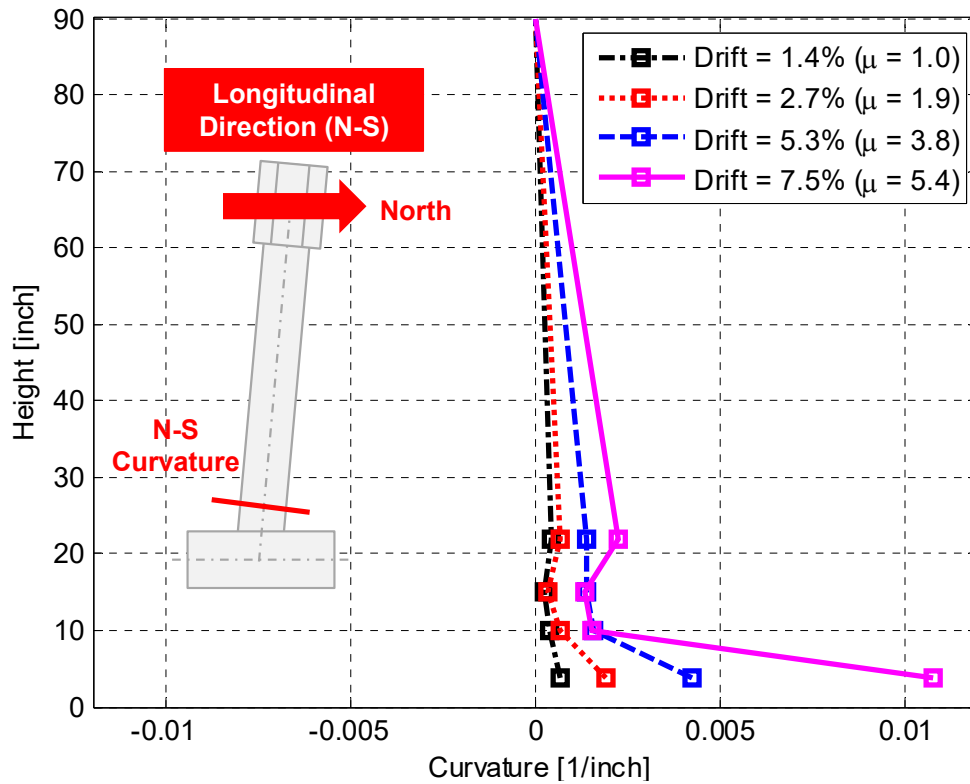


Figure 5.40 Curvature distribution along column height when loading is towards north.

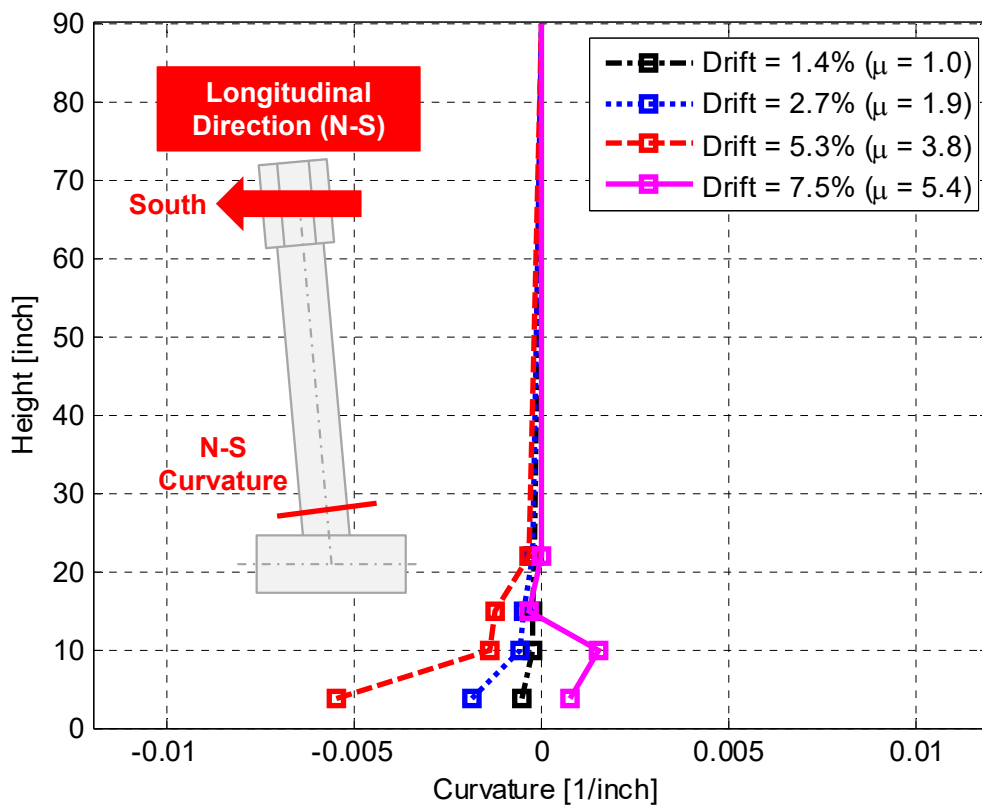


Figure 5.41 Curvature distribution along column height when loading is towards south.

5.3.3 Moment-Curvature Relationships

It is possible to obtain the moment-curvature relationships by relating the observed column curvatures to the corresponding bending moments. One way of estimating the column's curvature is to use the LVDTs dedicated to measure relative displacements to calculate strains and then the curvatures. Strains recorded in the column rebars can also be used to calculate curvatures as long as each two opposite strain gauges at a given level are used, and a linear strain distribution is assumed. Figures 5.42–5.46 compare LVDT-based and strain-gauge-based moment curvatures obtained at different sections in the transverse direction. At small-loading levels or linear elastic regime of the column, the curvature calculations from either the LVDTs or strain gauges compare well. However, at elevated loading levels and large plastic hinge rotations and deformations, the curvatures calculated from the LVDTs are more accurate and reliable. As shown in Figures 5.45 and 5.46 the strain-gauge-based curvatures are underestimated at the plastic hinge maximum rotation/curvature region. Therefore, only LVDT-based curvatures were used to plot the moment-curvature relationships in the longitudinal direction. Figures 5.47–5.50 show the moment-curvature at four different sections in the longitudinal direction. The moment-curvature relationships at the lowest section in the plastic hinge where the maximum curvatures were determined are compared for the transverse and longitudinal directions in Figure 5.51.

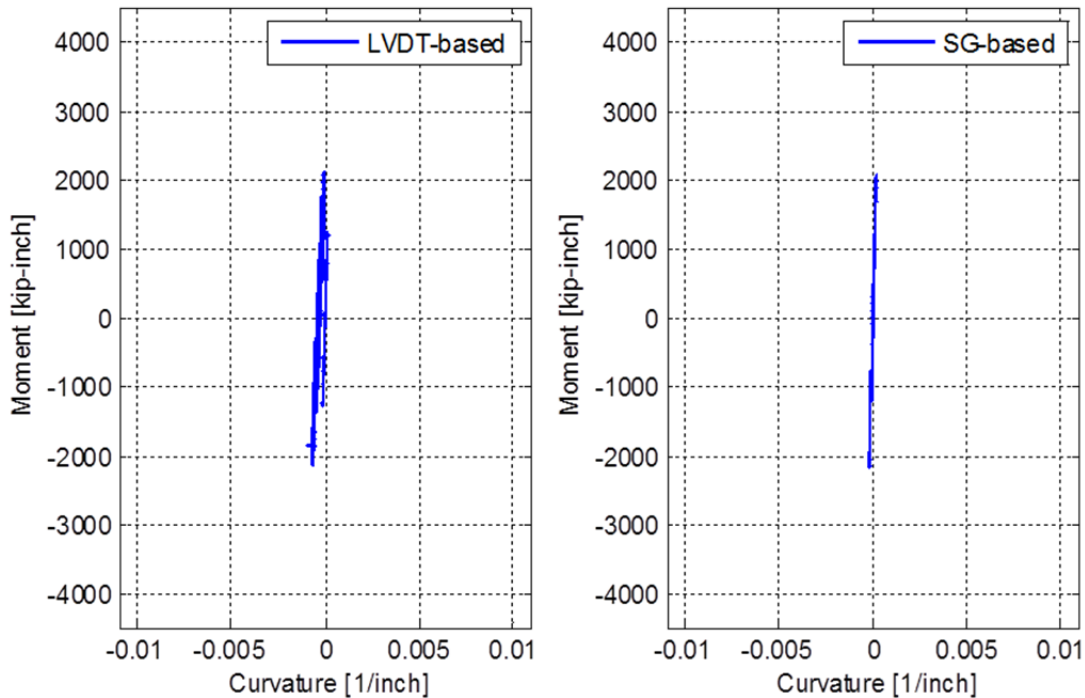


Figure 5.42 Comparison of LVDT-based and strain-based column moment-curvature relationship at Section 5 (mid-height, refer to Figure 3.50) due to all transverse loading cycles.

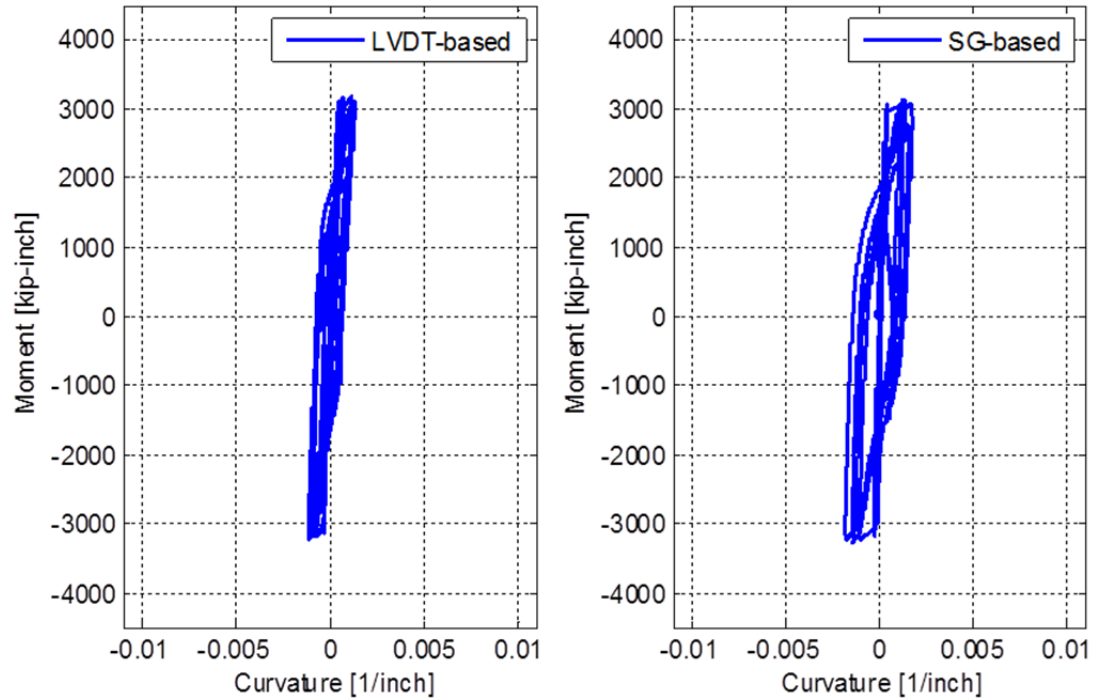


Figure 5.43 Comparison of LVDT-based and strain-based column moment-curvature relationship at Section 4 (22 in. from beam face, refer to Figure 3.50) due to all transverse loading cycles.

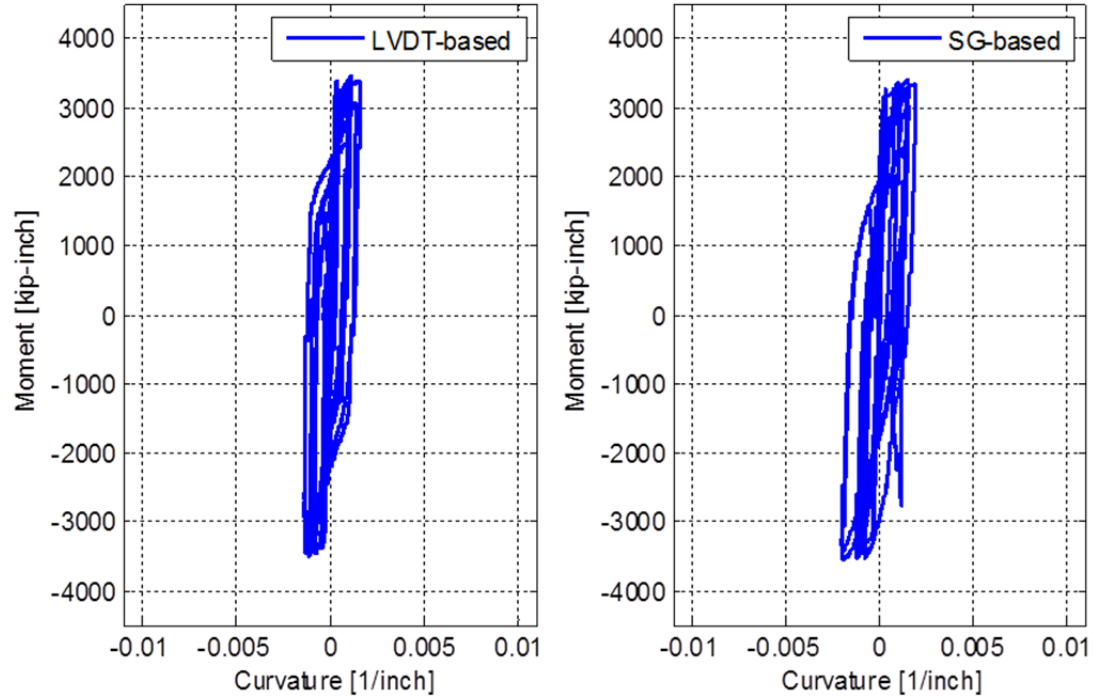


Figure 5.44 Comparison of LVDT-based and strain-based column moment-curvature relationship at Section 3 (16 in. from beam face, refer to Figure 3.50) due to all transverse loading cycles.

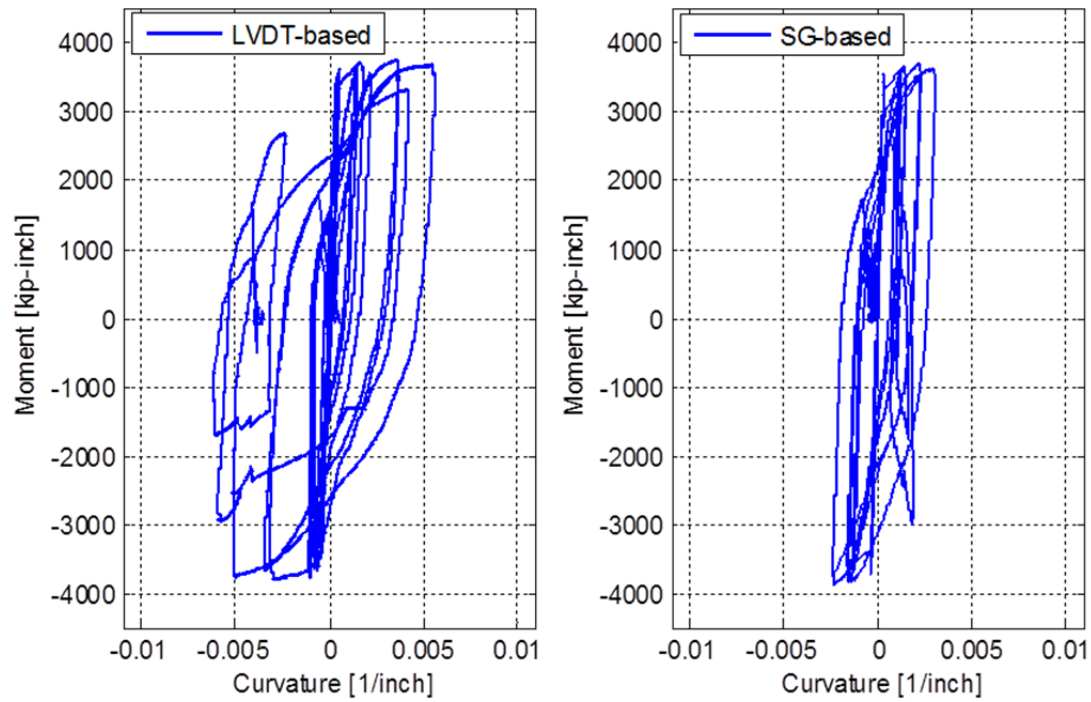


Figure 5.45 Comparison of LVDT-based and strain-based column moment-curvature relationship at Section 2 (10 in. from beam face, refer to Figure 3.50) due to all transverse loading cycles.

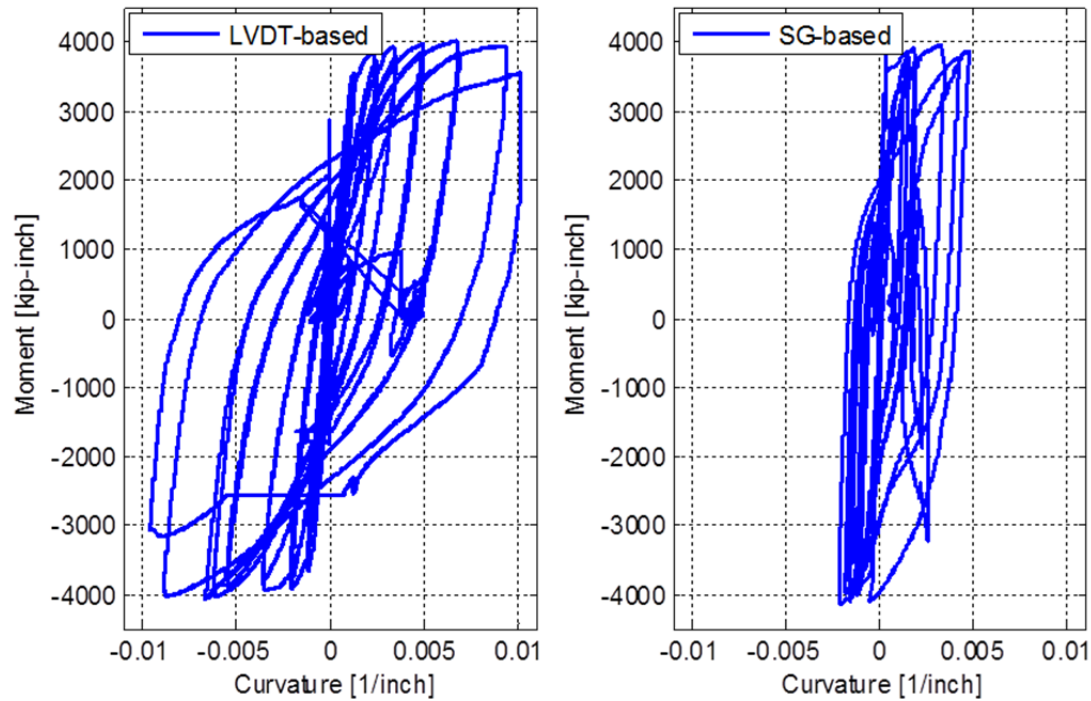


Figure 5.46 Comparison of LVDT-based and strain-based column moment-curvature relationship at Section 1 (4 in. from beam face, refer to Figure 3.50) due to all transverse loading cycles.

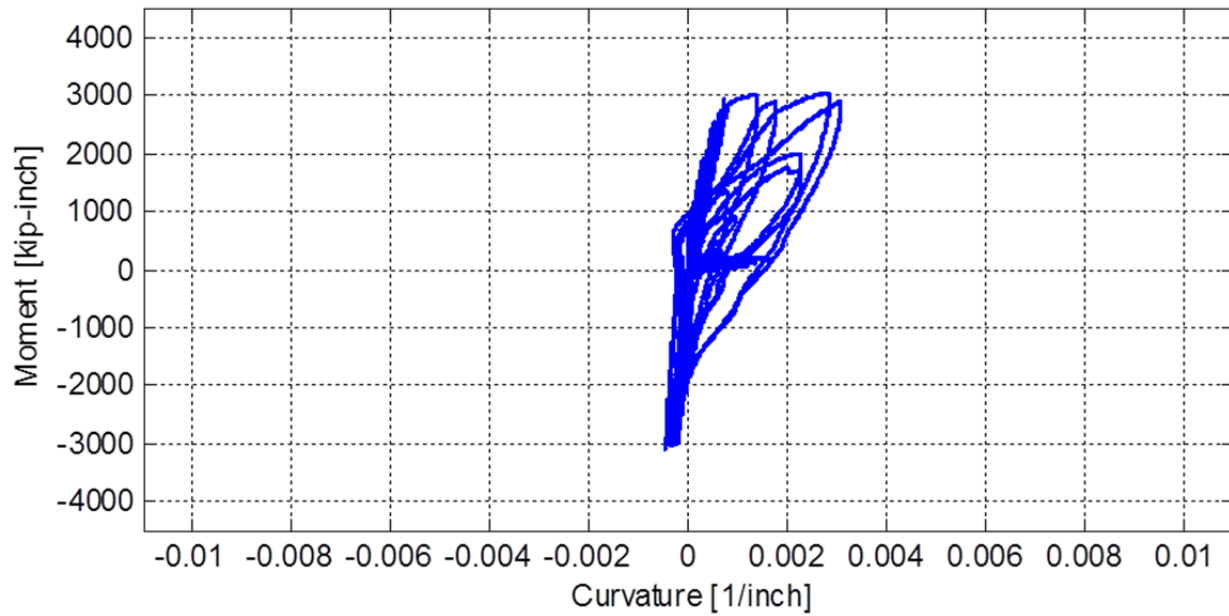


Figure 5.47 LVDT-based column moment-curvature relationship in N-S direction at Section 4 (22 in. from beam face, refer to Figure 3.50) due to all longitudinal loading cycles.

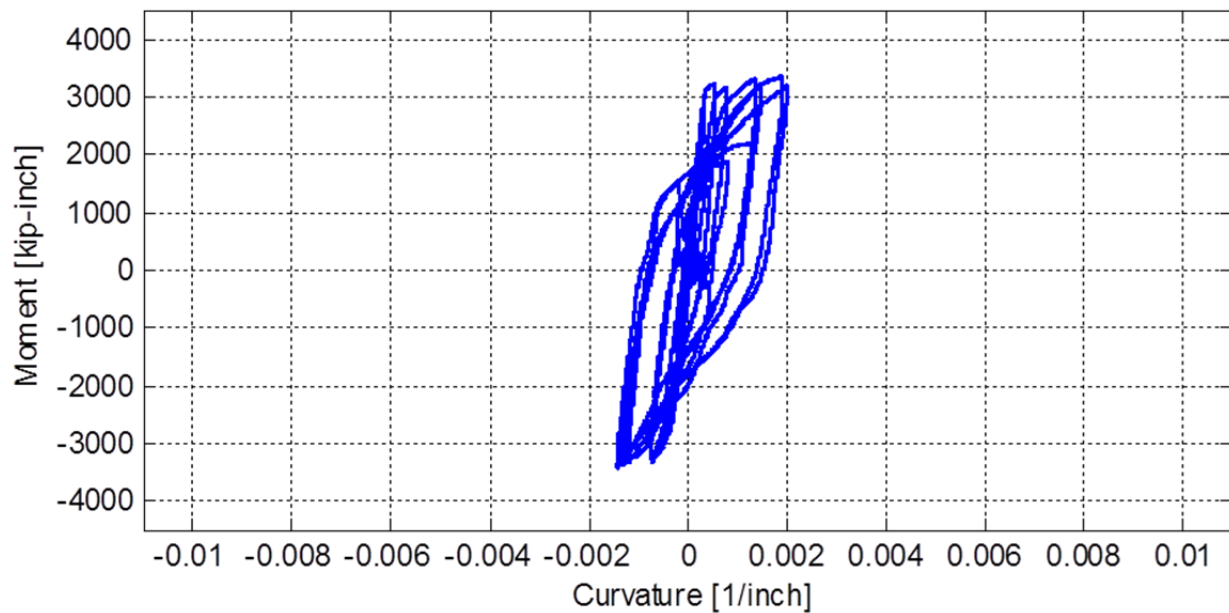


Figure 5.48 LVDT-based column moment-curvature relationship in N-S direction at Section 3 (16 in. from beam face, refer to Figure 3.50) due to all longitudinal loading cycles.

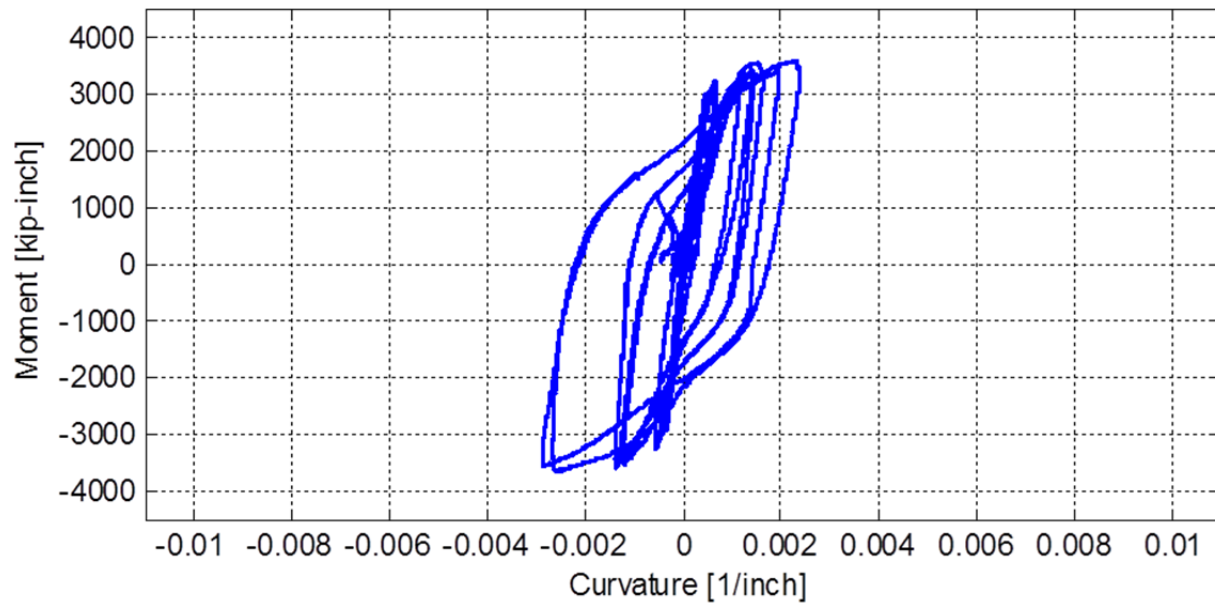


Figure 5.49 LVDT-based column moment-curvature relationship in N-S direction at Section 2 (10 in. from beam face, refer to Figure 3.50) due to all longitudinal loading cycles.

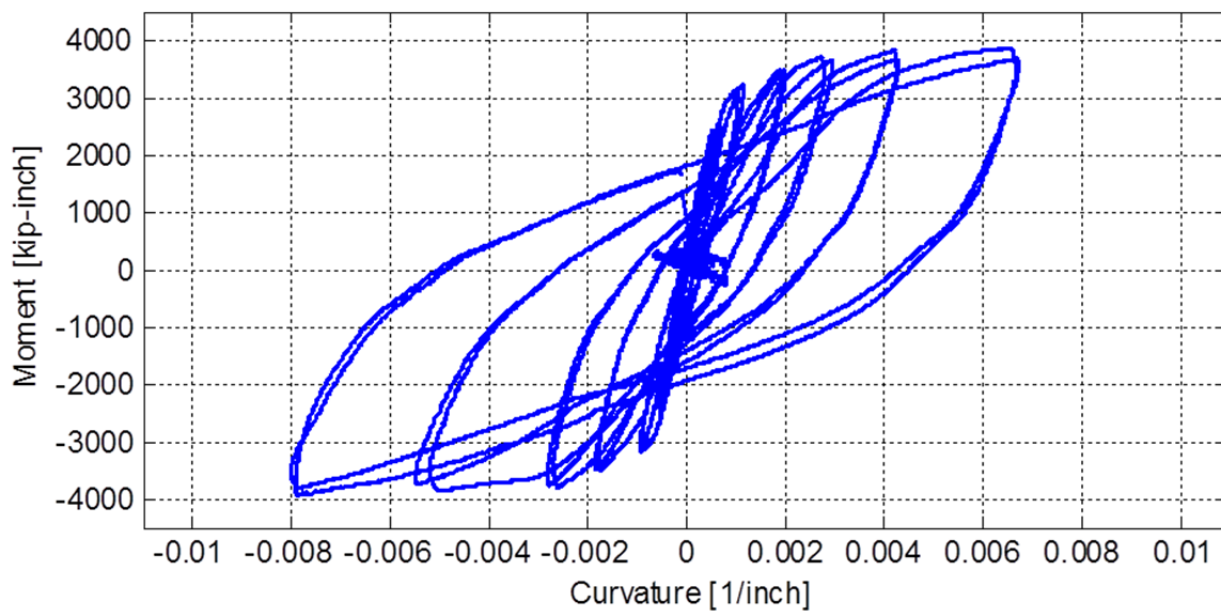


Figure 5.50 LVDT-based column moment-curvature relationship in N-S direction at Section 1 (4 in. from beam face, refer to Figure 3.50) due to all longitudinal loading cycles.

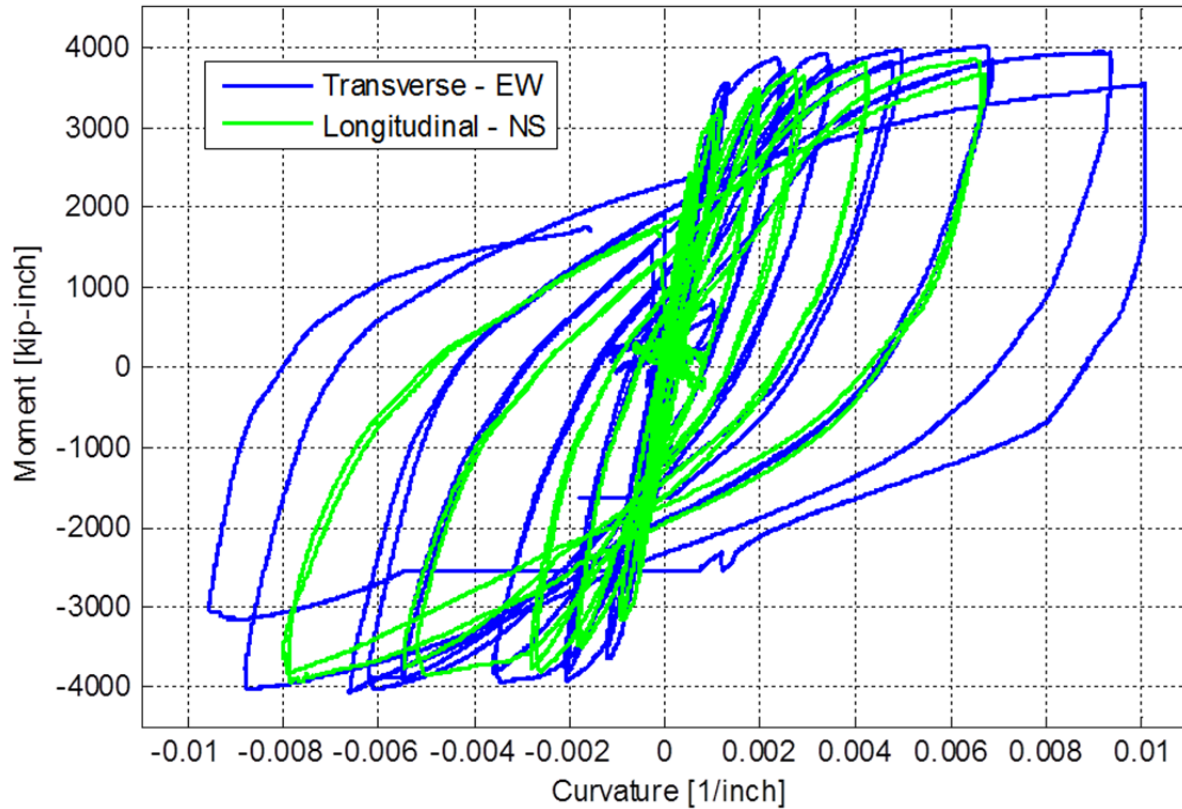


Figure 5.51 Comparison of column moment-curvature relationship in both transverse (E-W) and longitudinal (N-S) directions at Section 1 (4 in. from beam face, refer to Figure 3.50).

5.4 BENT CAP LOCAL BEHAVIOR

The main objective of this study was to evaluate the contribution of the box-girder slabs to the cap beam stiffness, the capacity of the cap beam and its mode of failure if any. To study the behavior of the cap beam, the strain at various locations in several rebars was measured and then used to estimate the section curvatures. In addition, the instrumented vertical struts used as part of the specimen boundary conditions were used to estimate the bending moments in the cap beam. As shown in Figure 5.52, Sections B and D were the specific locations where all the cap beam and box-girder slabs behavior was monitored. Figure 5.52 shows schematically the bending moment distribution along the cap beam in the tested subassembly specimen under different cases of loading. The figure shows a more exact sketch for the moment distribution considering the column and cap beam continuity and cross-section width rather than the center line. The strains, curvatures, bending moments, and moment-curvature relationships for the bent cap beam are discussed next.

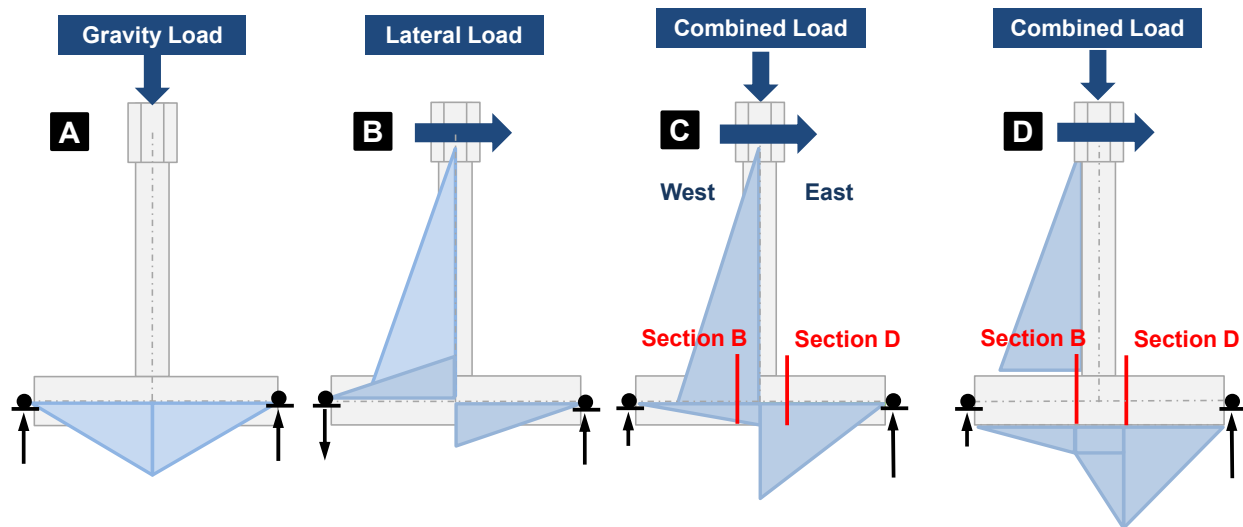


Figure 5.52 Schematic bending moment distribution along the bent cap beam center line in three cases of loading: (a) gravity load only (b) lateral load only (c) combined gravity and lateral loads, and (d) a more accurate distribution considering the column and beam actual cross-section width rather than center lines.

5.4.1 Strain Behavior

The subassembly Specimen No. 1 cap beam had eight longitudinal rebars for both positive and negative reinforcement. According to the inverted specimen orientation and moment distribution previously shown, the negative reinforcement (i.e., tension side) is at the bottom, while the top reinforcement is the positive reinforcement (i.e., compression side). Four of the top and six of the bottom rebars were instrumented with strain gauges at Sections B and D, as identified in Figure 5.52; strain gauges were installed along Sections A–E, for top and the bottom rebars; see Figure 3.45. The recorded maximum positive strain at each of those five sections in one of the beam bottom bars (tension side) at the positive (loading east) and negative (loading west) peaks of the 0.8μ transverse loading cycle are shown in Figures 5.53 and 5.54, respectively. The figures also show schematically the expected bending moment distribution according to the loading direction. The strain profile agrees with the moment distribution, which provides more confidence in the data obtained from strain gauges.

Once the strain profile along the cap beam length is verified, it is useful to check the history of the measured strains. Representative strain history plots in one of the cap beam bottom rebars (tension side) for all loading cycles at Sections B and D, where maximum strains along the beam length were recorded, are shown in Figures 5.55 and 5.56, respectively; note the almost invariable strain readings while loading in the longitudinal direction. Excessive progression in strain values was observed at the start of each transverse loading group of cycles. This is attributed to the fact that transverse loading directly altered the cap beam bending moment, while the longitudinal loading caused only torsion in the cap beam, which altered minimally the cap beam longitudinal strain values. While up to 8% strain was observed in the column rebars as the plastic hinge accumulated damage, only strains up to 1.3% were recorded and observed in the

bent cap beam. This is expected because the bridge design philosophy calls for an essentially elastic superstructure and bent cap beams.

Another way of looking at the measured strains in the cap beam is by plotting them against the progressing lateral load. The maximum strains measured at Sections B and D are plotted against the lateral transverse force in Figures 5.57 and 5.58, respectively. The strain increase at zero lateral force (marked with arrows) corresponded to the increase of strains resulting from gravity load application. As discussed previously, the gravity load was applied at two levels. The first gravity load level was followed by all the small-level lateral loading cycles, which resulted in almost linear elastic strain in the cap beam rebars; see Figures 5.57 and 5.58. The cap beam rebars started yielding after the second level of gravity load was applied, followed by the first high-level (1.4μ corresponding to 1.94% drift ratio) cycle. Once the rebars yielded, they became very sensitive to loading, and every new transverse loading cycle excessively increased the cap beam rebars strains, especially as loading was increasing towards the first peak in a given cycle. The longitudinal loading did not cause any significant increase in the rebars strain. The observed strain during longitudinal loading is shown in the figures in the form of small loops around the zero transverse force value at the end of each of the main loops after each transverse loading group of cycles.

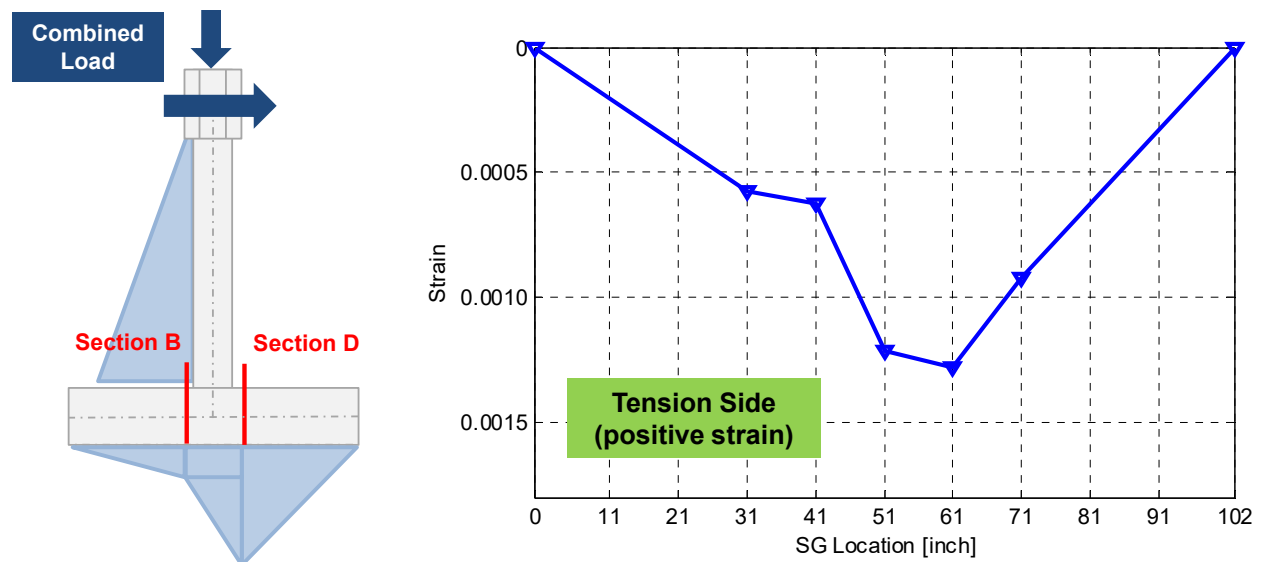


Figure 5.53 Strain profile along one of the cap beam tension side rebars due to combined gravity and one of the lateral transverse loading cycles in east direction.

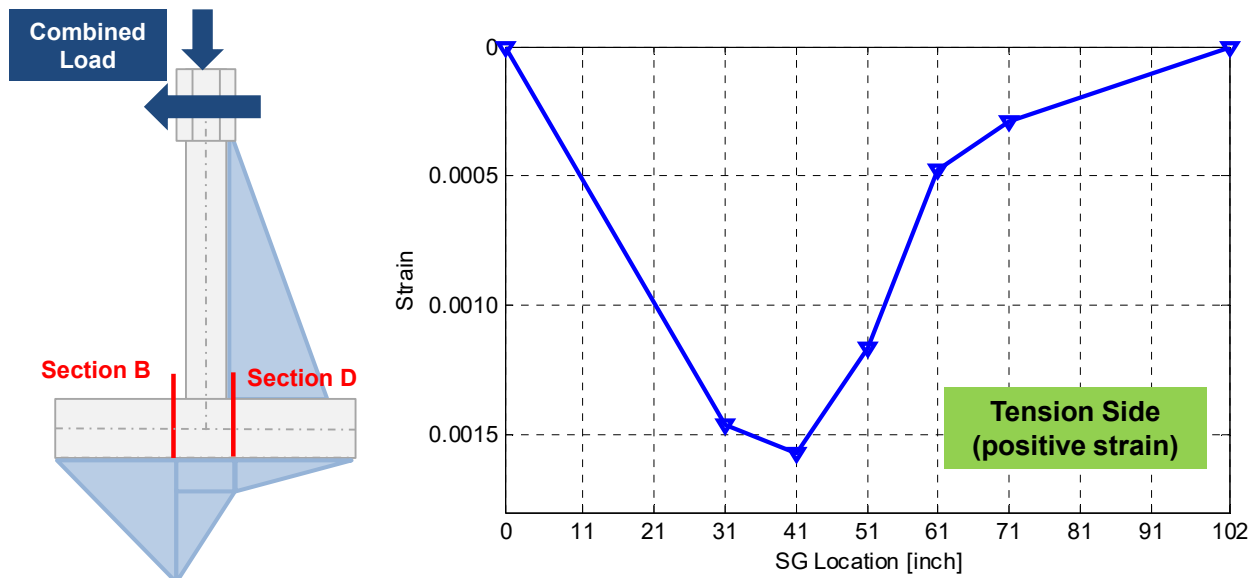


Figure 5.54 Strain profile along one of the cap beam tension side rebars due to combined gravity and one of the lateral transverse loading cycles in west direction.

Irrespective of the high post-yield recorded strain values, the bent cap beam can be still considered essentially elastic. This argument is supported by several factors. First, while all rebar yielding occurred only in the side in tension, no concrete spalling was observed or associated with the increased cap beam strain values. Only minor cracks at the bottom of the cap beam were observed. In addition, no concrete crushing or extensive cracking was observed in the side in compression of the cap beam.

Note that plastic behavior in a concrete element is associated with extensive concrete cracking and spalling because of either rebars buckling or concrete reaching crushing strain value being reached. In conclusion, the concrete in the cap beam was found to be almost elastic throughout the test, where no major cracking in the side in tension and not even minor cracking in the side in compression took place. Based on these results, it was decided to strengthen Specimen No. 2 and increase the column moment capacity and, accordingly, pass higher moment demands to the cap beam in an attempt to understand the plastic behavior of the cap beam. While column strengthening of the second specimen was pursued, Specimen No. 1 was partially repaired and retested again. The repaired specimen test demonstrated that the cap beam remained essentially elastic, even though the rebars had extensively yielded previously. When the specimen was unloaded and the repaired specimen test was conducted, linear elastic and much fewer strains were observed in the cap beam. See Chapter 6 for more details.

The onset of a plastic cap beam response was reported from the HS retrofitted Specimen No. 2 test. A conventional plastic hinge in the column was avoided and concrete crushing in the side in compression cap beam was observed before the test ended. See the companion report for the full discussion of the second specimen strengthening and HS tests. Note that cap beam plastic behavior is not a design objective in the recent performance-based or capacity bridge design philosophies; however, observing at least the onset of the cap beam plastic behavior is useful in

fully quantifying the effective slab width and for accurate capacity estimation. A more economic design of the cap beam can be consequently achieved when the contributions of the box-girder slabs and slab transverse reinforcement are fully utilized.

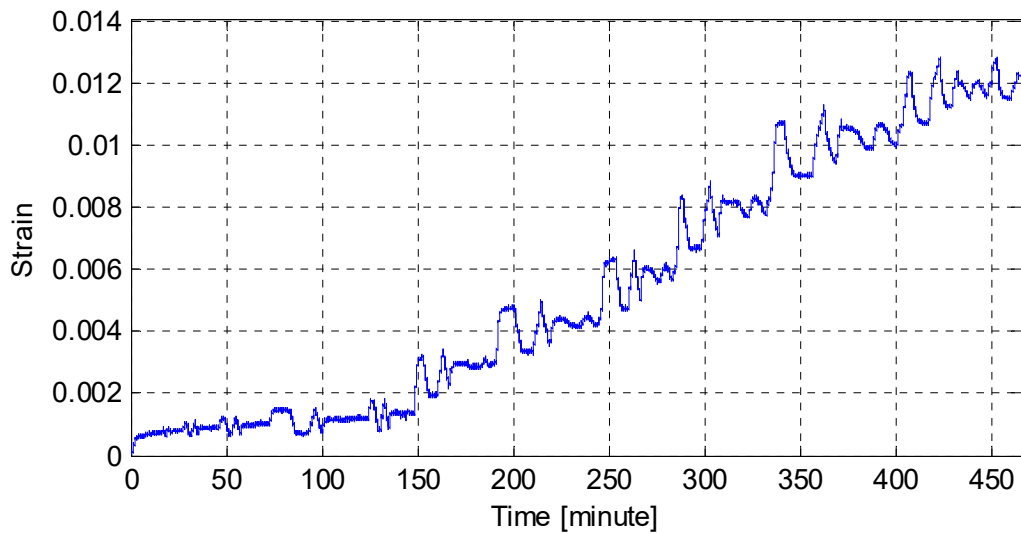


Figure 5.55 History of strain at bent cap beam maximum strain location at Section B for all loading cycles.

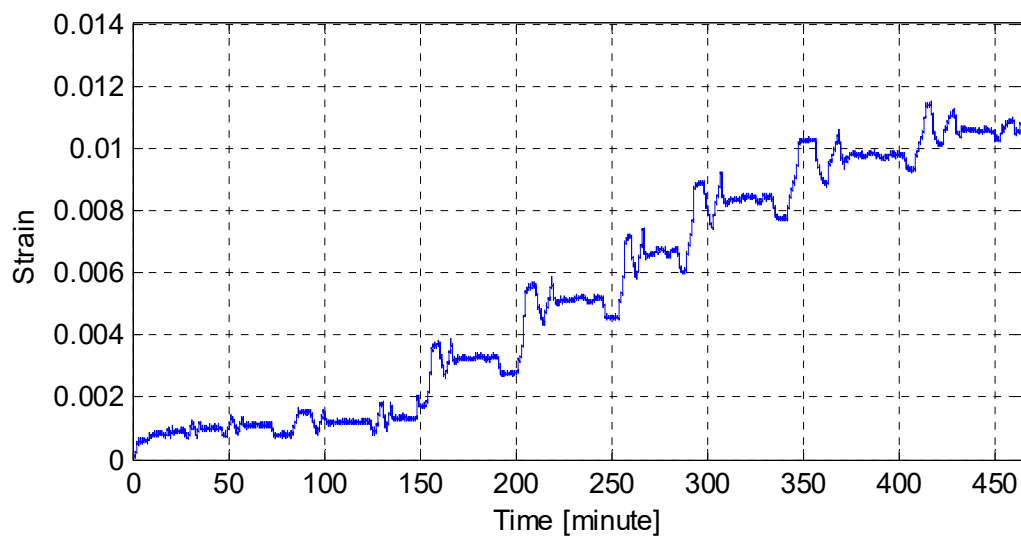


Figure 5.56 History of strain at bent cap beam maximum strain location at Section D for all loading cycles.

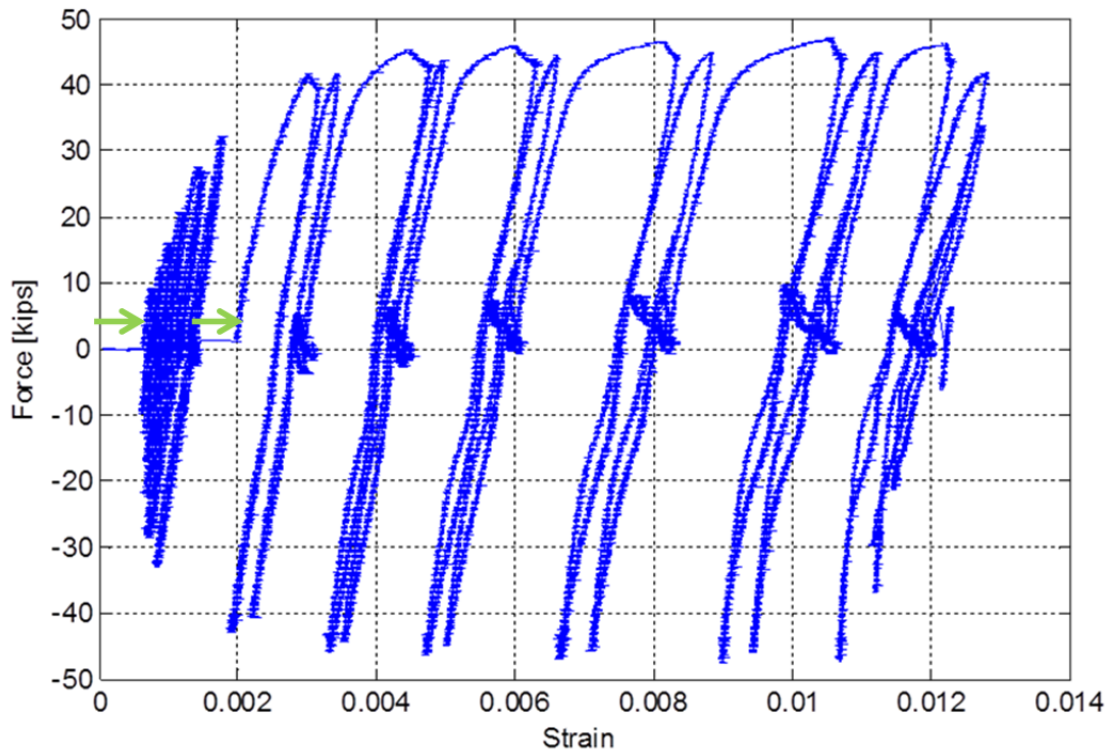


Figure 5.57 Lateral transverse force versus bent cap beam maximum strain at Section B for all loading cycles.

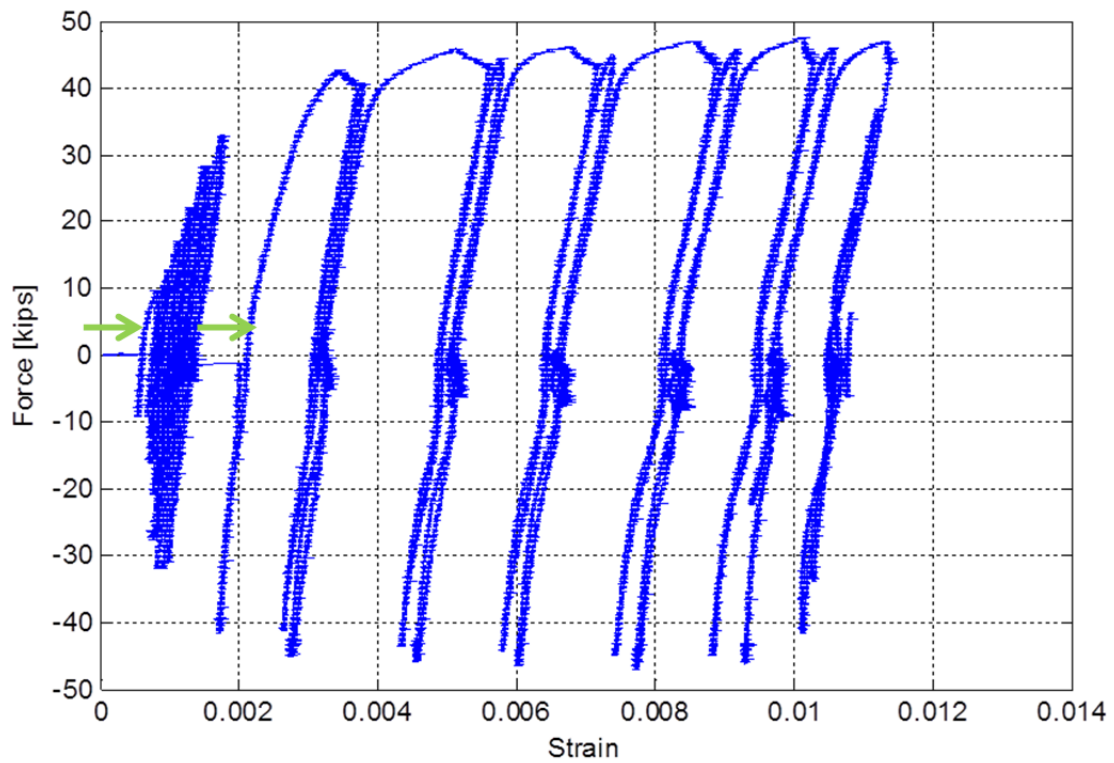


Figure 5.58 Lateral transverse force versus bent cap beam maximum strain at Section D for all loading cycles

5.4.2 Curvature Behavior

As previously noted, curvatures can be either estimated from a set of LVDTs properly aligned together or from the rebars strains at two opposite sides. In the case of the bent cap beam, using LVDTs was not practical. Thus, each two opposite strain gauges at a top and corresponding bottom cap beam rebar were used to estimate the cap beam curvature at both Sections B and D. The history of the estimated curvatures from using one set of rebars at Sections B or D are shown in Figures 5.59 and 5.60, respectively. Based on the sectional analysis results of the test specimen bent cap beam (shown in Figure 5.65), the yield curvature value was found to be 0.00017 in.^{-1} . Thus, it is possible to conclude from the experimentally-determined curvatures that the bent cap beam yielded during Specimen No. 1 cyclic loading tests, which was previously observed from the strain values at the bent cap tension side. However, based on the lack of visible damage, the yielded bent cap beam remained essentially elastic even when the strain in the side in tension; the cross-section curvatures reached almost six times their yield values.

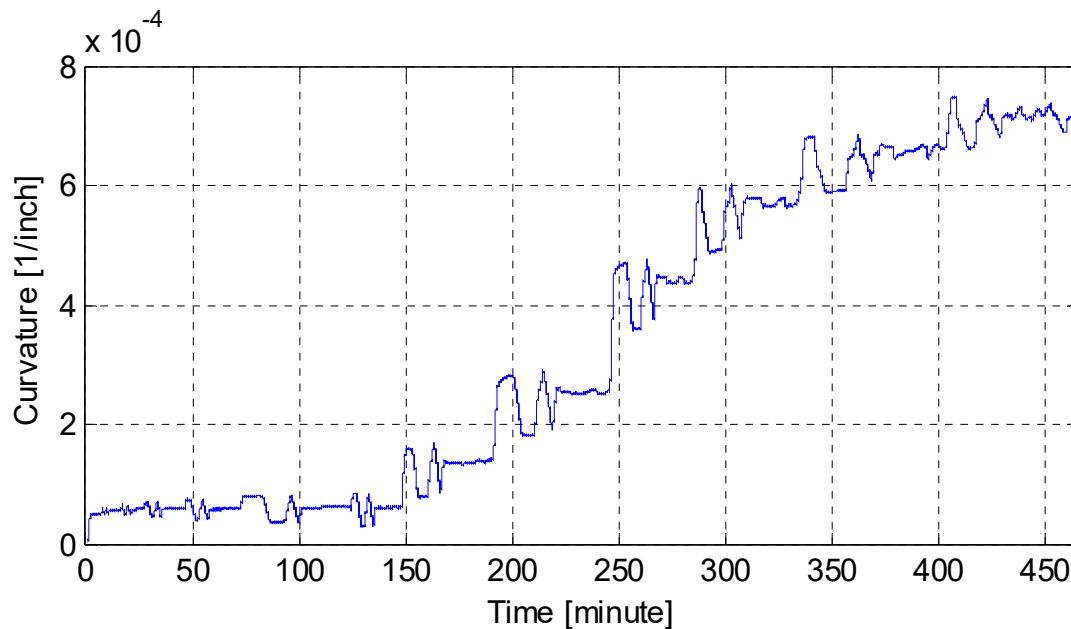


Figure 5.59 History of the curvature at cap beam Section B due to all lateral loading cycles.

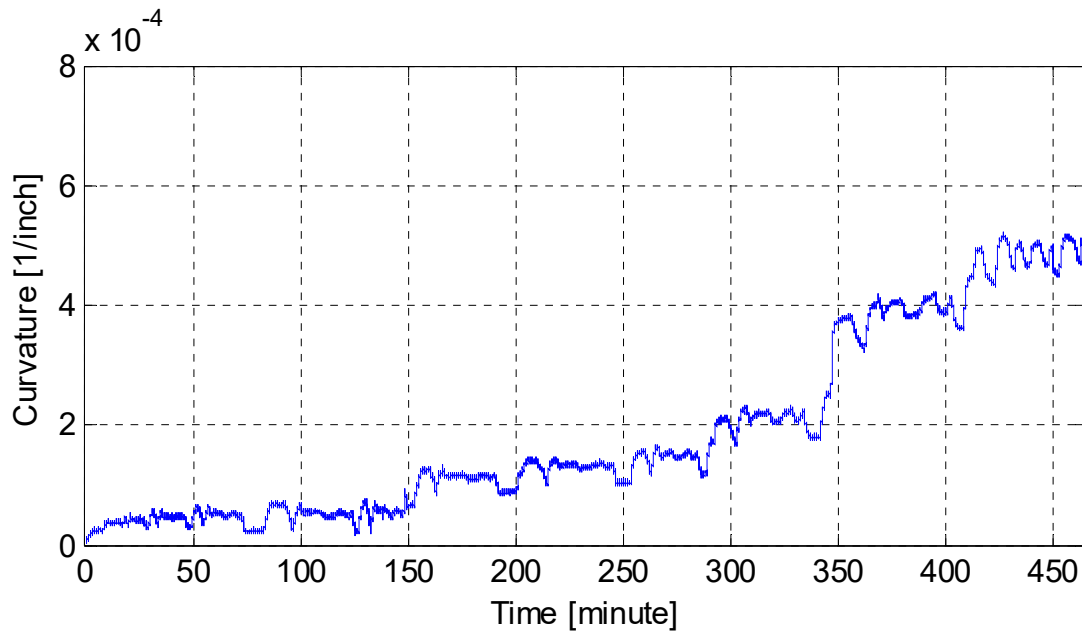


Figure 5.60 History of the curvature at cap beam Section D due to all lateral loading cycles.

5.4.3 Bending Moment Behavior

Investigating the bent cap beam bending moment behavior and capacity was a key objective of this study as it is tied to the box-girder slab contribution. To determine the bending moment in the cap beam where the maximum moments were expected at Sections B and D, two instrumented vertical struts were utilized. The moment history at both sections due to lateral loading only and to combined lateral and gravity loading is shown in Figure 5.61. Note that the vertical reactions at the beam end struts were always the total reactions due to both gravity and lateral loading. However, to isolate the beam moments due to the lateral load only, the reaction recorded at the end of the gravity load application was subtracted from the total reaction recorded during the lateral load cycles that followed.

The moments due to lateral loading only were of interest because they were used to verify the accuracy of the procedure, which used the vertical reaction at an end strut multiplied by its distance to the location of either Section B or D to estimate the moment directly. The verification relied on satisfying the moment equilibrium at the joint region due to the lateral loading case only. In this case, the bent cap beam moments at Sections B and D, the box-girder twist moment, and the column moment should sum up to zero. If the box-girder twist is relatively small and negligible, the total cap beam moment from Sections B and D due to lateral load only should approximately neutralize the column moment, designated as M_{col} , as verified in Figure 5.62. The figure shows that the sum of the moments at Sections B and D, designated as M_{beam} , is comparable to the column moment with difference that did not exceed 250 kip-in., i.e., less than 5% of the column moment value.

It was a critical element of this study to verify whether the bending moments calculated from the vertical struts were correct. As implied in Figure 5.62, the box-girder twist moment due

to loading in the bent cap plane is almost negligible; thus, the vertical struts provided correct moment values for the bent cap beam. A similar observation was also reported in a previous study by Mosalam et al. [2002]. A subassembly specimen, similar to the one tested in this study, was tested under bi-directional loading as well, but all the boundary conditions at both box-girder and cap beam ends were instrumented and calibrated. Accordingly, it was possible to quantify the load path in the subassembly components using the estimated reactions at all boundary conditions. They concluded that the bent cap beam moment can be directly calculated from the beam end struts vertical reactions. Moreover, they found that the effect of the reactions at the end of the box-girder resulting from the box-girder torsional stiffness have negligible effect on the bent cap beam moment value calculated directly from the cap beam end struts.

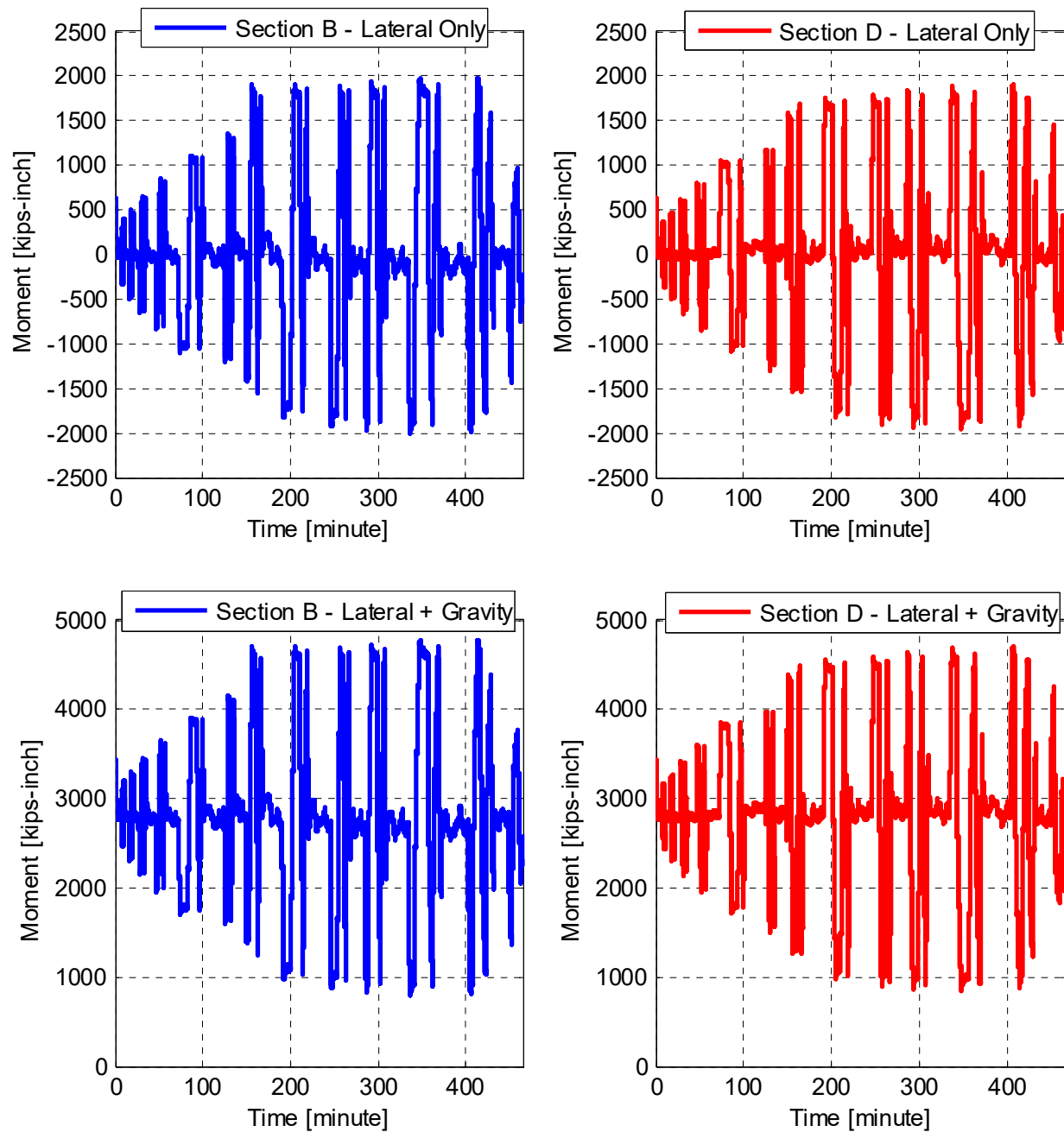


Figure 5.61 History of cap beam bending moment at Sections B and D due to lateral loading only and combined lateral and gravity loading for all loading cycles.

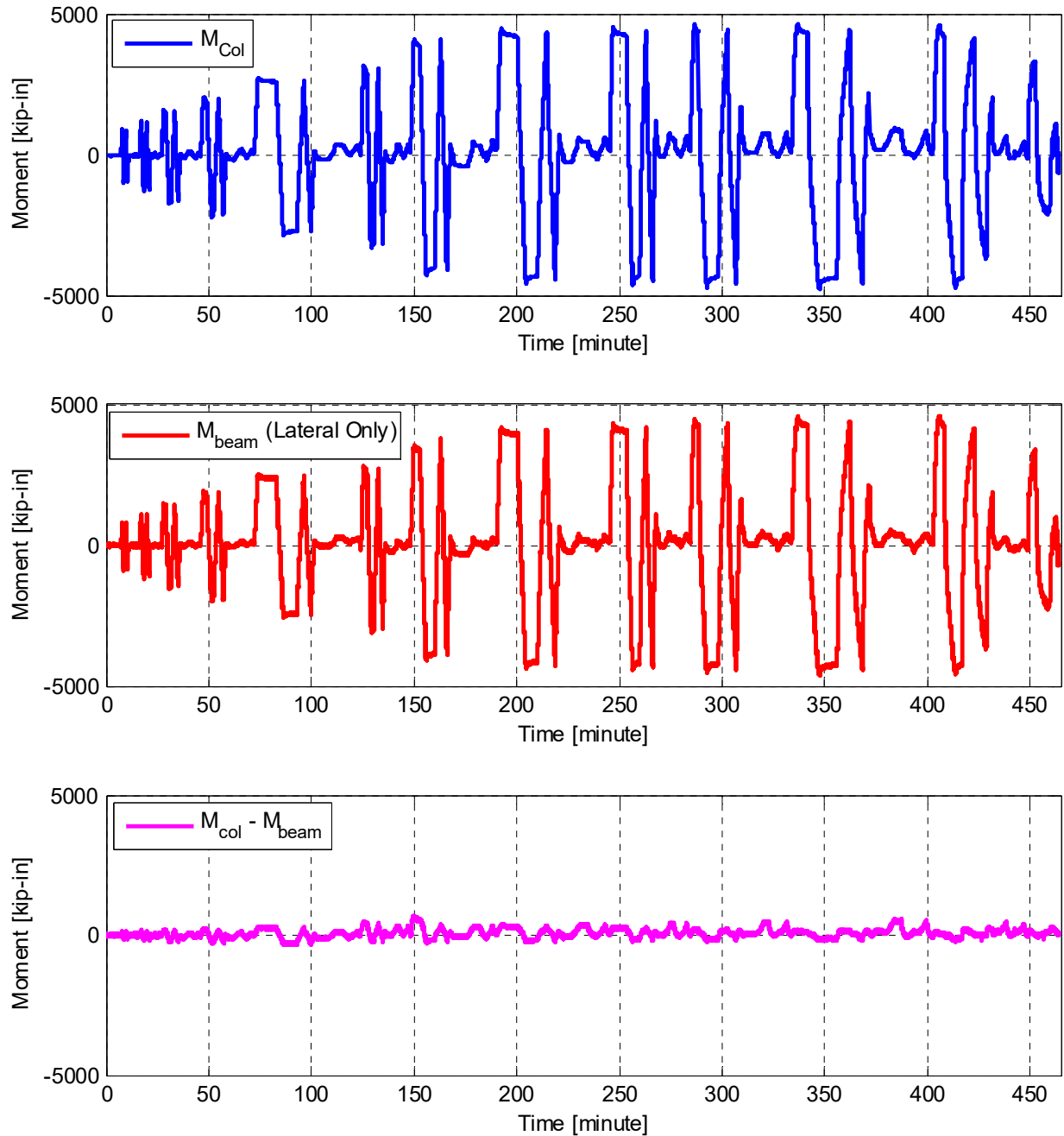


Figure 5.62 Comparison of column moment and sum of cap beam moments at Sections B and D ($M_{beam} = M_{Section B} + M_{Section D}$) due to lateral loading only.

5.4.4 Moment-Curvature Relationships

One way to use the bending moment to investigate the overall bent cap response is to plot it against the section curvatures, as presented earlier. Figures 5.63 and 5.64 show the moment-curvature relationships for the bent cap beam for all the cyclic loading cases at Sections B and D, respectively. The analytical nominal moment-curvature relationship obtained from classical

sectional analysis is shown in Figure 5.65 for comparison purposes. The results from the moment-curvature analysis, such as the yield moment, the ultimate moment, etc., are also shown in Figure 5.65.

It is observed from the experimentally determined moment-curvature relationships that the moment is capped in both Sections B and D at a value slightly higher than 4500 kip-in. When considered with the observed column behavior and damage, it is assumed that the bent cap moment was capped because the column had reached its capacity, which then capped the demand at the bent cap beam. However, the extensive curvature increase at this capped moment caused the yielding of the cap beam, as confirmed previously from the strain values. Note that the experimental value for the yield moment when curvature values began increasing significantly is about 4500 kip-in. As shown in Figure 5.65, the analytical value determined from sectional analysis is 3719 kip-in. The sectional analysis considered the Caltrans SDC effective flange width, but included the tension steel in the slab as well, although it is not part of the code requirement. The underestimated analytical value indicates that the tension steel within the effective slab width should be included, and larger effective width value might be needed for accurate cap beam moment capacity estimation. A more extensive discussion of the bent cap beam moment capacity is included in the HS test results and post-test analysis discussion in the companion report.

Another application of the moment-curvature relationship is to determine the effective EI for the bent cap cross section at different loading levels. The change in the effective EI reflects the change of the overall bent cap beam stiffness. Figures 5.66 and 5.67 demonstrate how the effective EI at the respective Sections B and D deteriorates with the loading level, expressed in terms of drift ratio and ductility level. The moment-curvature relationship from two different sets of top and bottom rebars were used for each section and shown in the figures. A normalized value for the effective EI was used where all the values are related to the effective EI determined from the slope of the moment-curvature relationship at first small cycle. The absolute values for the effective EI were found to be much less than the recommended Caltrans value, which is based on a 0.5–0.75 of the gross flanged section inertia. However, the relative change in the normalized effective EI still serves the purpose of investigating how the bent cap beam stiffness deteriorates at higher drift ratios and ductility levels.

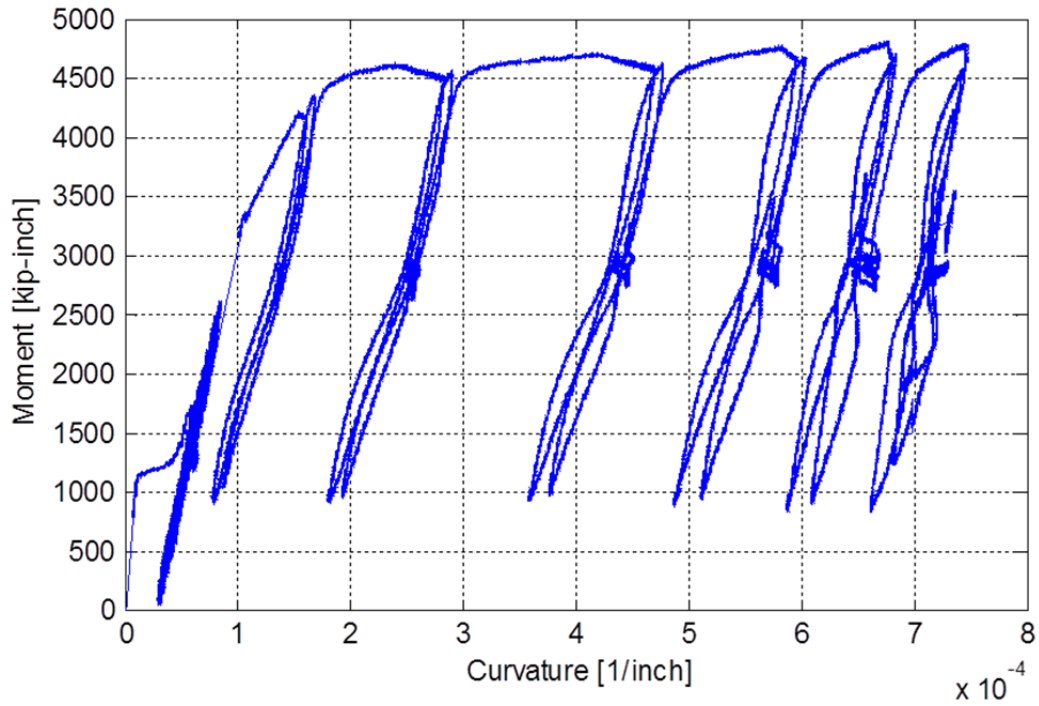


Figure 5.63 Moment-curvature relationship for the bent cap at Section B for all the loading cycles in both transverse and longitudinal directions.

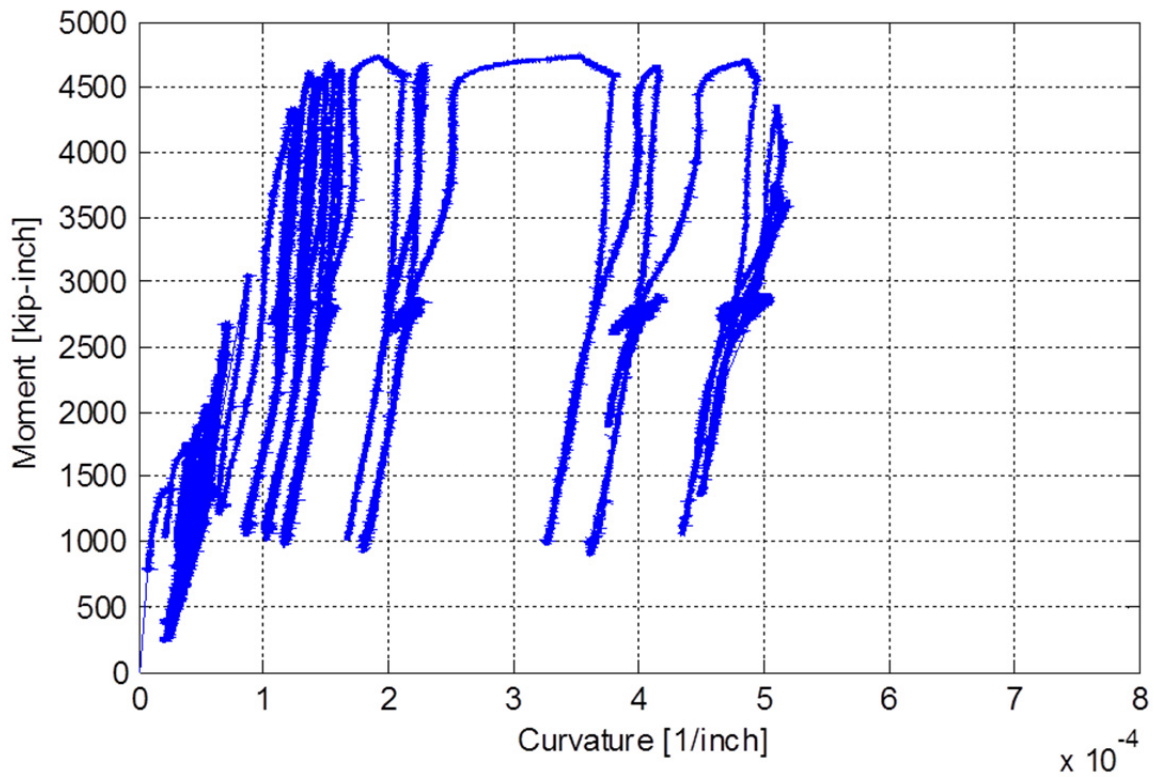


Figure 5.64 Moment-curvature relationship for the bent cap at Section D for all the loading cycles in both transverse and longitudinal directions.

Curvature at First Yield: $-1.618\text{E-}3$ 1/in
 Ultimate Curvature: $-4.539\text{E-}3$ 1/in
 Moment at First Yield: -3719 kip-in
 Ultimate Moment: -5024 kip-in
 Centroid Strain at Yield: $.9580\text{E-}3$ Ten
 Centroid Strain at Ultimate: $40.22\text{E-}3$ Ten
 N.A. at First Yield: -5.923 in
 N.A. at Ultimate: -8.862 in
 Energy per Length: 19.96 kips
 Effective Yield Curvature: $.1724\text{E-}3$ 1/in
 Effective Yield Moment: 3963 kip-in
 Over Strength Factor: -1.268
 EI Effective: $2.30\text{E+}7$ kip-in²
 Yield EI Effective: $243.0\text{E+}3$ kip-in²

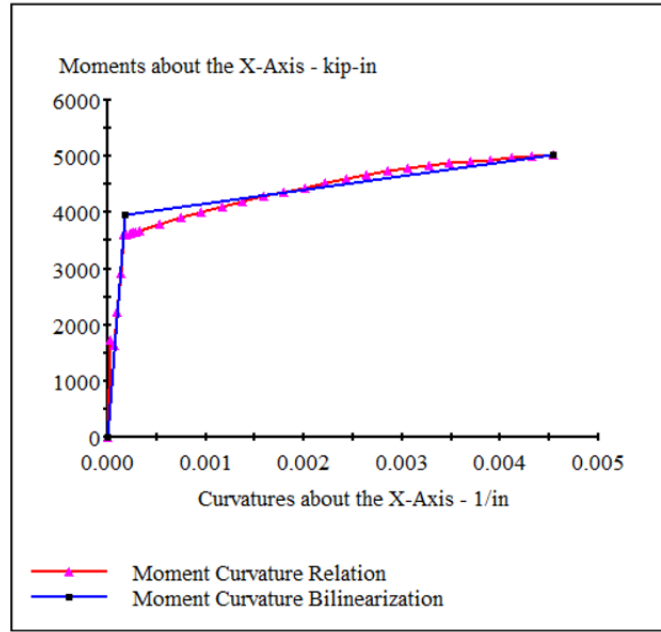


Figure 5.65 Moment-curvature relationship for cap beam estimated from sectional analysis [XTRACT 2002] using the Caltrans SDC integral bent cap effective flanged section.

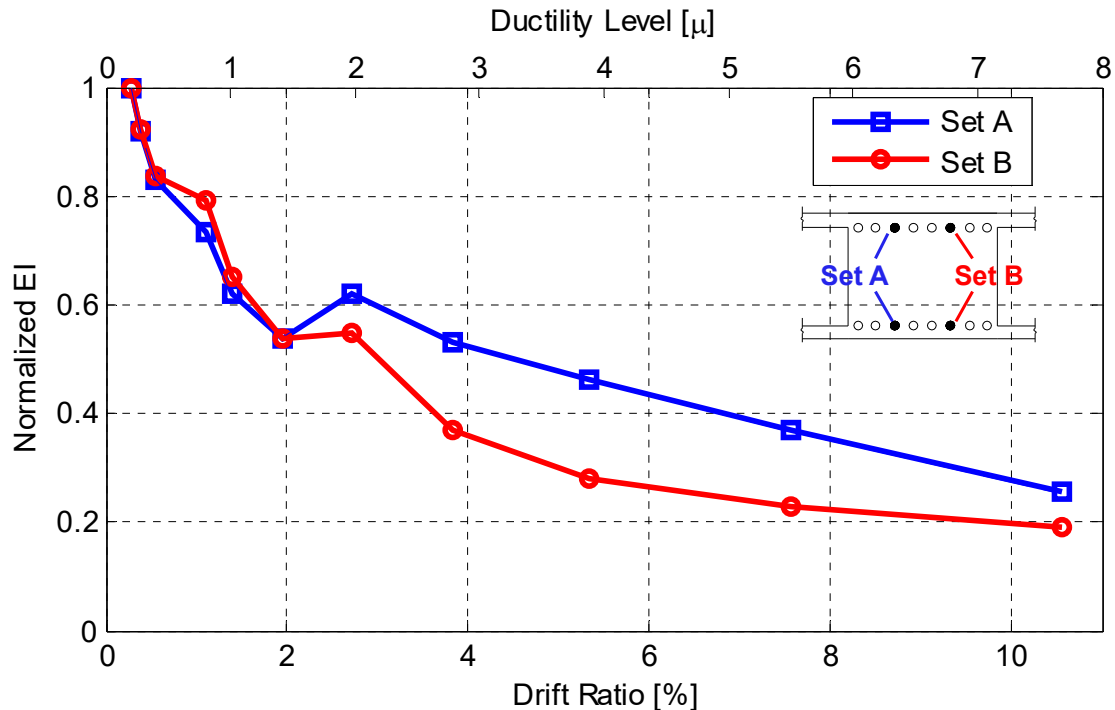


Figure 5.66 Degradation in the cap beam stiffness expressed in terms of normalized effective EI at different drift ratios and ductility levels calculated using curvatures from two different top and bottom rebar sets at Section B.

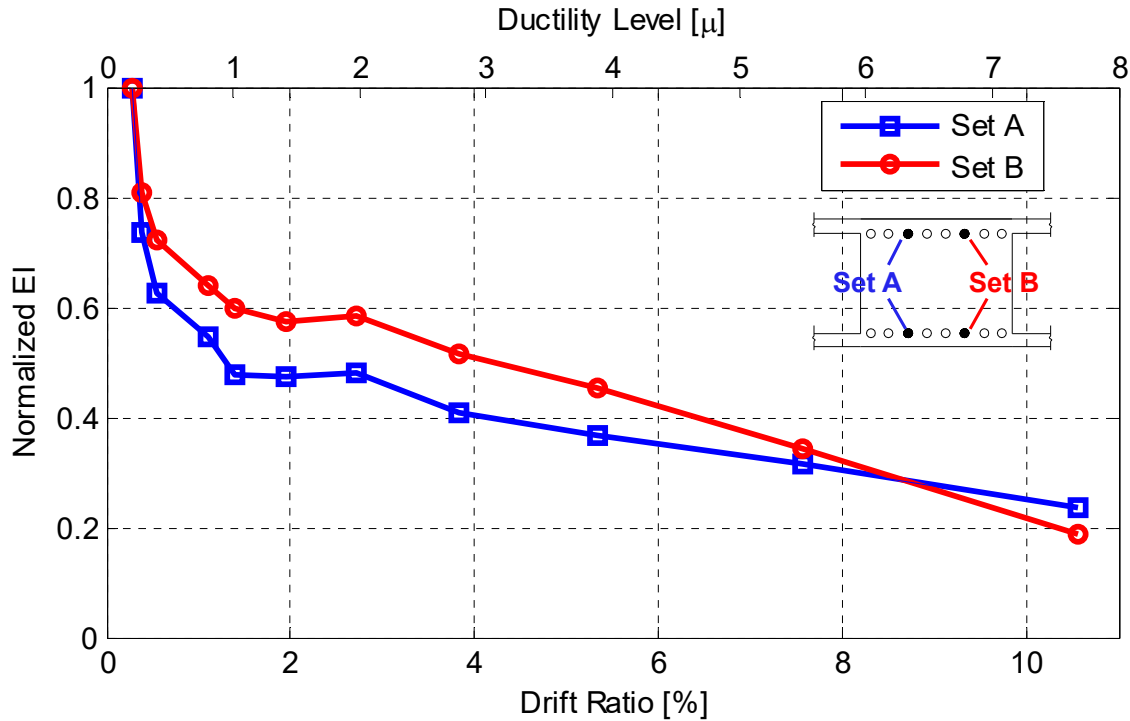


Figure 5.67 Degradation in cap beam stiffness expressed in terms of normalized effective EI at different drift ratios and ductility levels calculated using curvatures from two different top and bottom rebar sets at Section D.

5.5 EFFECTIVE SLAB WIDTH (TENSION SIDE)

The Caltrans SDC and AASHTO LRFD Guidelines for seismic design require considering a flanged section with an effective slab (thickness = t_s) width $12t_s$ for integral RC bent cap beams for balanced stiffness check and seismic capacity check. The effective slab width that is typically based on the equivalent strain block concept is revisited in this study. The strain distribution in the bent cap beam reinforcement and the adjacent transverse (with respect to bridge box-girder axis) slab reinforcement from both sides of the beam is determined for the cyclic tests of as-built Specimen No. 1 with both sides in tension and compression. For bent caps, the negative moment side that requires the tension reinforcement at the bent columns and supports is usually the top side, i.e., deck slab side in integral bent caps. This is the case in the prototype bridge and the specimen tested in this study. However, in the specimen's inverted position, the top of the cap beam faced the laboratory floor and so did the deck slab. Thus, the tension side was the lower side of the beam in the inverted position. The strain distribution in the side in tension was found to be more reliable than the compression side, which was very sensitive to the concentrated gravity load applied through the column. The results from the tension side strain distribution and revisited effective slab width are presented in this section. The compression side results are briefly discussed in the next section.

This section presents and discusses the strain distribution, equivalent strain block, and corresponding effective slab width at both Sections B and D, identified previously in Figure

5.52. A simple procedure to determine the effective slab width based on the concept of an equivalent strain block was devised; see Figure 5.68. The strain distribution was experimentally obtained and spatially extended at the two tails to determine the intercept at zero strain. The area under the strain distribution was computed and transformed to an equivalent strain block with an effective width where two strain values were used; namely, the minimum and the mean strain among the six gauges used at a given cross section in the cap beam reinforcement. The maximum strain was not used to avoid effects of the concentrated gravity load and scaling that caused highly localized strain values in the cap beam reinforcement.

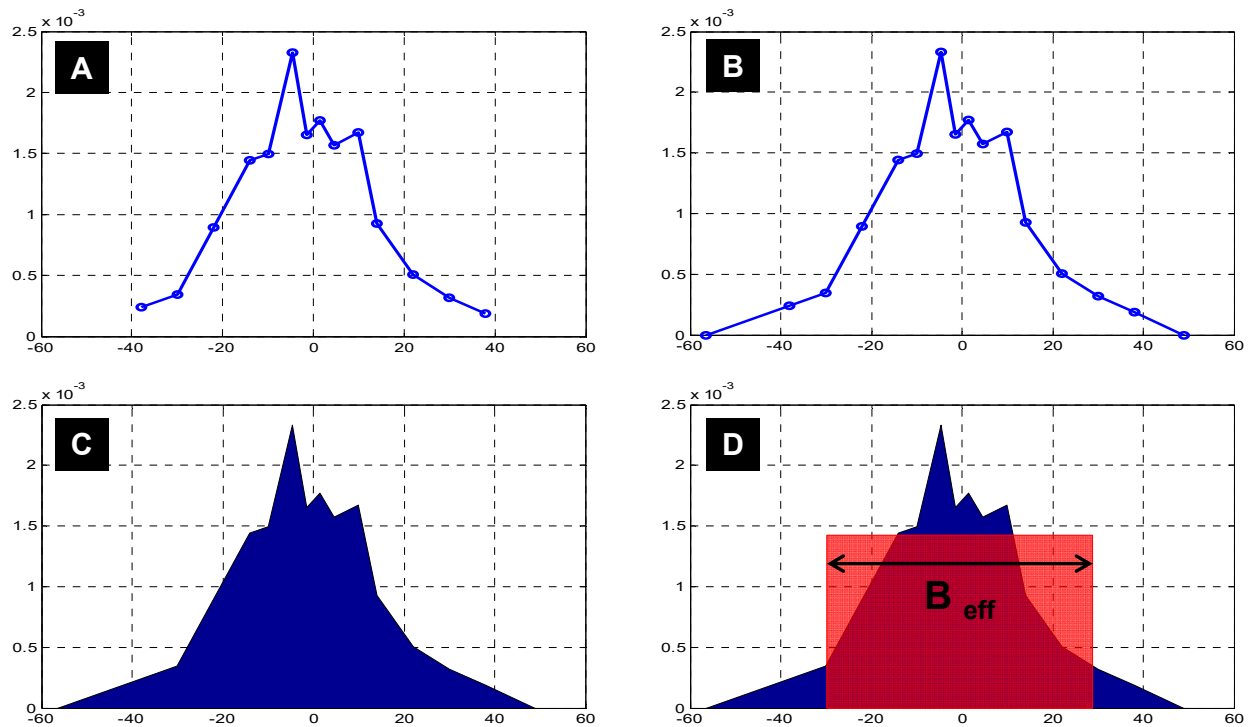


Figure 5.68 Summary of the four main steps of the procedure used to estimate the bent cap effective slab width.

5.5.1 Section B: Distribution

The strain distribution at different sections across the bent cap and transverse slab reinforcement based on different strain gauge readings was recorded continuously throughout all the loading cycles in both transverse and longitudinal directions. Only strain values acquired at peak of the loading cycles were considered. It is worth noting that each level of loading comprised two full cycles for a total of four peaks, identified previously in Figures 5.17 and 5.18 as first positive peak, first negative peak, second positive peak, and second negative peak. Only results obtained from second positive and second negative peaks are shown for brevity since the other two cases were found to be very similar. The most meaningful results were obtained when loading was in the transverse direction. That is because the longitudinal loading influenced mainly the box-girder flexural behavior rather than the bent cap beam. Therefore, all results shown in the reminder of this chapter were compiled from the strain readings at the second positive and

negative peaks of the transverse loading cycles, which were related to the drift ratio and ductility level (μ).

Figures 5.69 and 5.70 show the strain distribution at Section B at different loading levels when the transverse load was pushing towards the east side, which is designated as the positive loading direction. Figure 5.69 presents the distribution at the small-level cycles, i.e., before any of the reinforcing bars in the cap beam or even the column yielded, i.e., drift ratios 0.4%, 0.8%, 1.1%, and 1.4%; this corresponded to μ of 0.27, 0.56, 0.80, and 1.0, respectively. Figure 5.70 presents three high-level cycles along with the last small-level cycle to show how the distribution changed as yielding took place. Figure 5.70 considers four drift levels: 1.4%, 2.7%, 5.3%, and 10.5%, which corresponded to μ of 1.0, 1.96, 3.84, and 7.57, respectively. Figures 5.71 and 5.72 show the strain distribution at Section B for similar levels but for cases when loading was pushing towards the west side, i.e., reversed load in the negative direction.

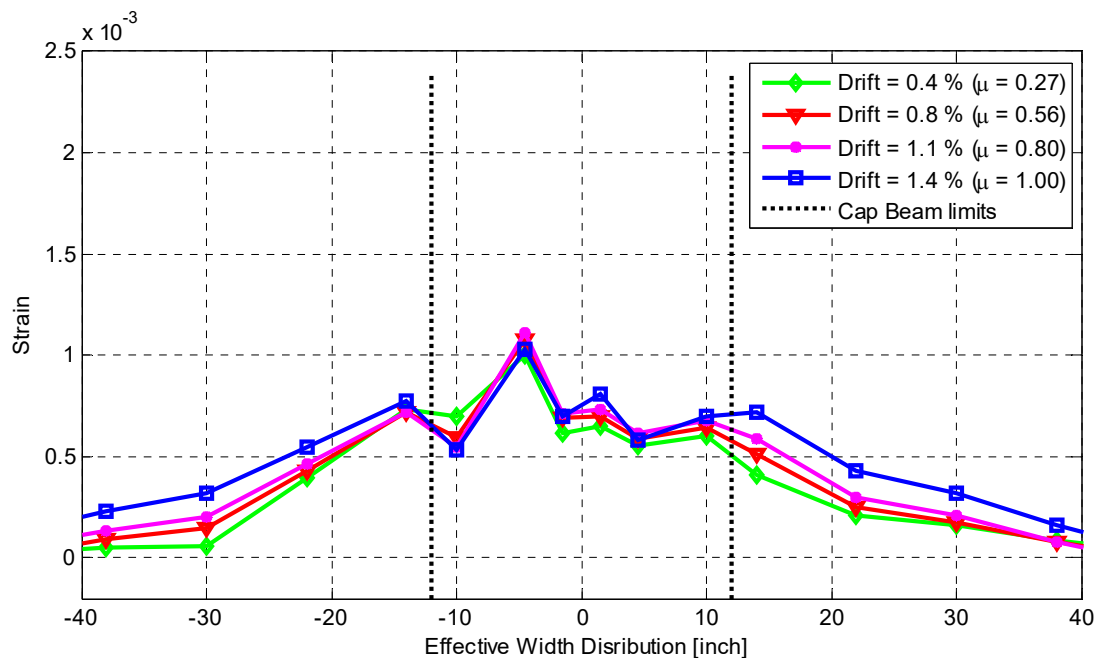


Figure 5.69 Strain distribution along cap beam and box-girder transverse deck slab reinforcement at Section B for different small-level loading cycles before yielding (loading is in positive east direction).

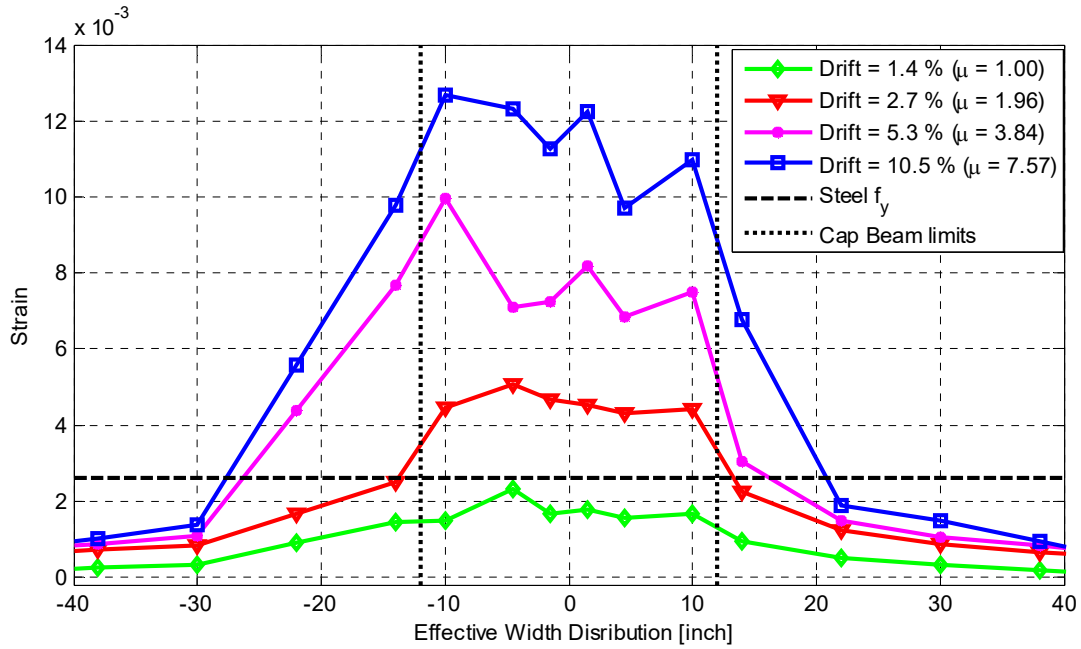


Figure 5.70 Strain distribution along cap beam and box-girder transverse deck slab reinforcement at Section B for different high-level loading cycles after yielding (loading is in positive east direction).

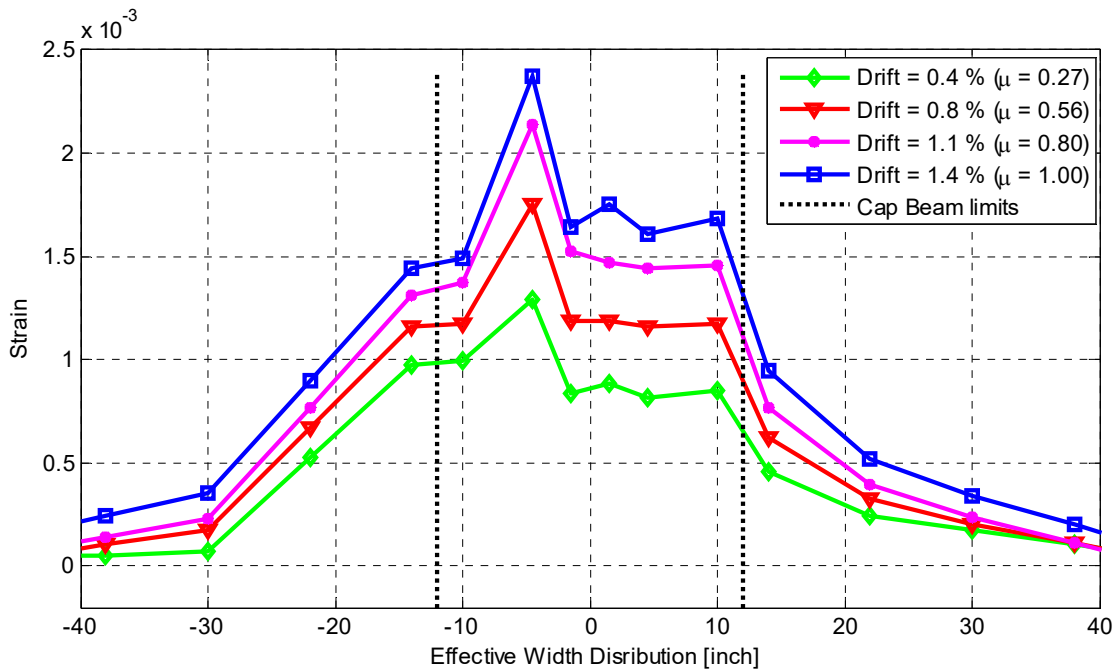


Figure 5.71 Strain distribution along cap beam and box-girder transverse deck slab reinforcement at Section B for different small-level loading cycles before yielding (loading is in negative west direction).

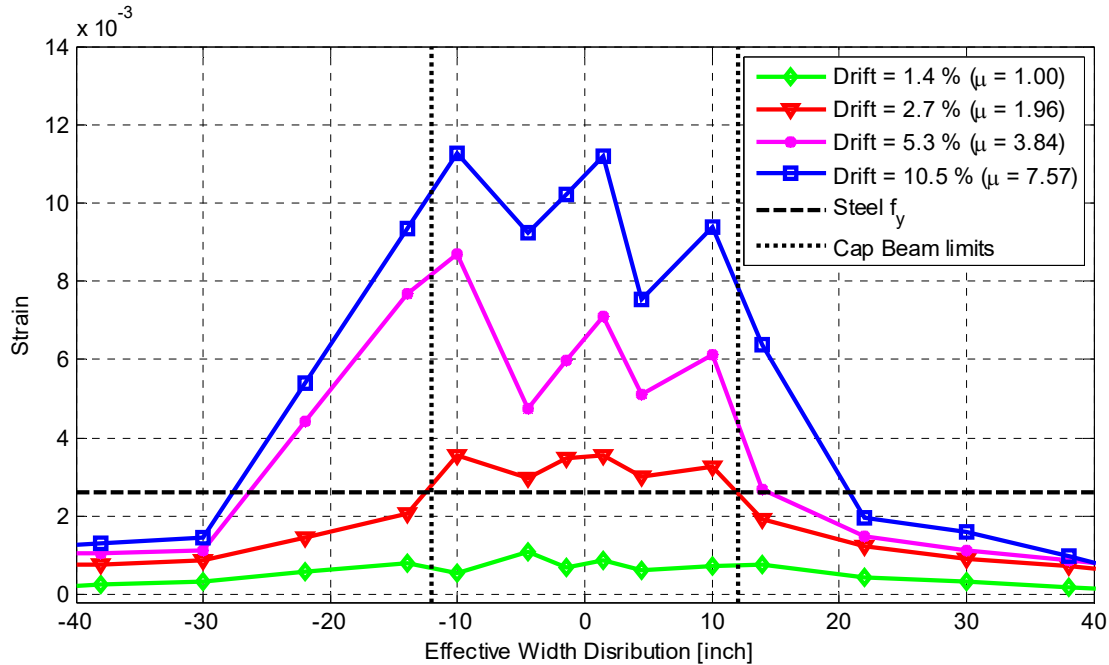


Figure 5.72 Strain distribution along cap beam and box-girder transverse deck slab reinforcement at Section B for different high-level loading cycles after yielding (loading is in negative west direction).

5.5.2 Section D: Distribution

Similar to the strain distribution shown at Section B, different loading levels and loading direction were considered to plot the strain distribution at Section D. Figures 5.73 and 5.74 show the distribution at different loading levels when the transverse load was pushing in positive direction towards the east side; Figures 5.75 and 5.76 show the distribution in case of loading in the negative direction towards the west. Strain distributions at Section D at small-level cycles before any yielding in any of the reinforcing bars at drift ratios 0.4%, 0.8%, 1.1%, and 1.4%, which corresponded to μ of 0.27, 0.56, 0.80, and 1.0, respectively, are shown in Figures 5.73 and 5.75 for loading in positive and negative directions, respectively. Distributions at larger loading levels at 1.4%, 2.7%, 5.3%, and 10.5%, which corresponded to a μ of 1.0, 1.96, 3.84, and 7.57, respectively, are shown in Figures 5.74 and 5.76 for loading in positive and negative directions, respectively.

Note that all plots in this subsection and the previous subsection show only the recorded strain values at locations that ranged between -40 and +40 in., according to the instrumented reinforcing bar location. The spatially extended tails that aimed at capturing the intercept at zero strain as part of determining the effective slab width, Figure 5.68(b), were not shown in the strain distribution presented in Figures 5.69–5.76. However, sample strain distribution that show the fully extended the distribution until the zero strain point are presented below.

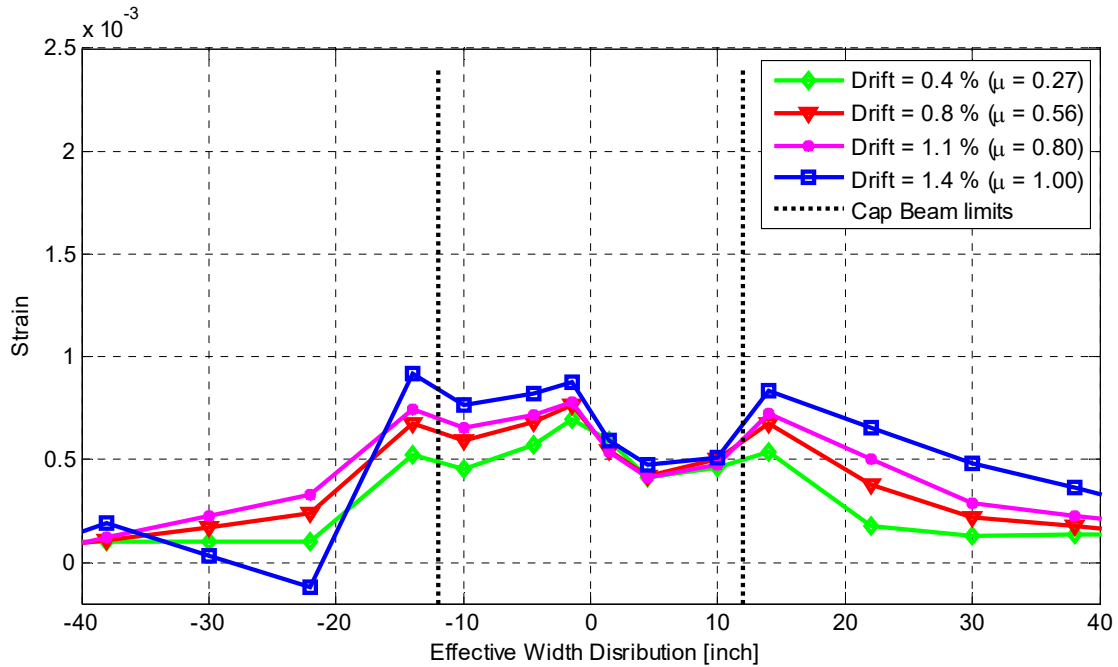


Figure 5.73 Strain distribution along cap beam and box-girder transverse deck slab reinforcement at Section D for different small-level loading cycles before yielding (loading is in positive east direction).

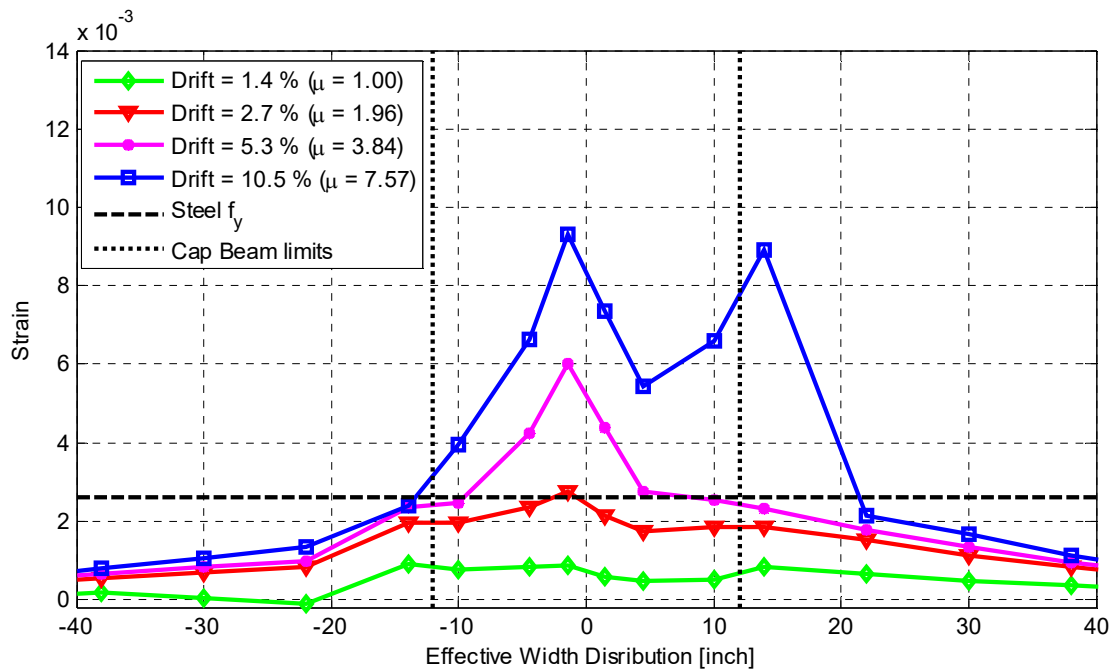


Figure 5.74 Strain distribution along cap beam and box-girder transverse deck slab reinforcement at Section D for different high-level loading cycles after yielding (loading is in positive east direction).

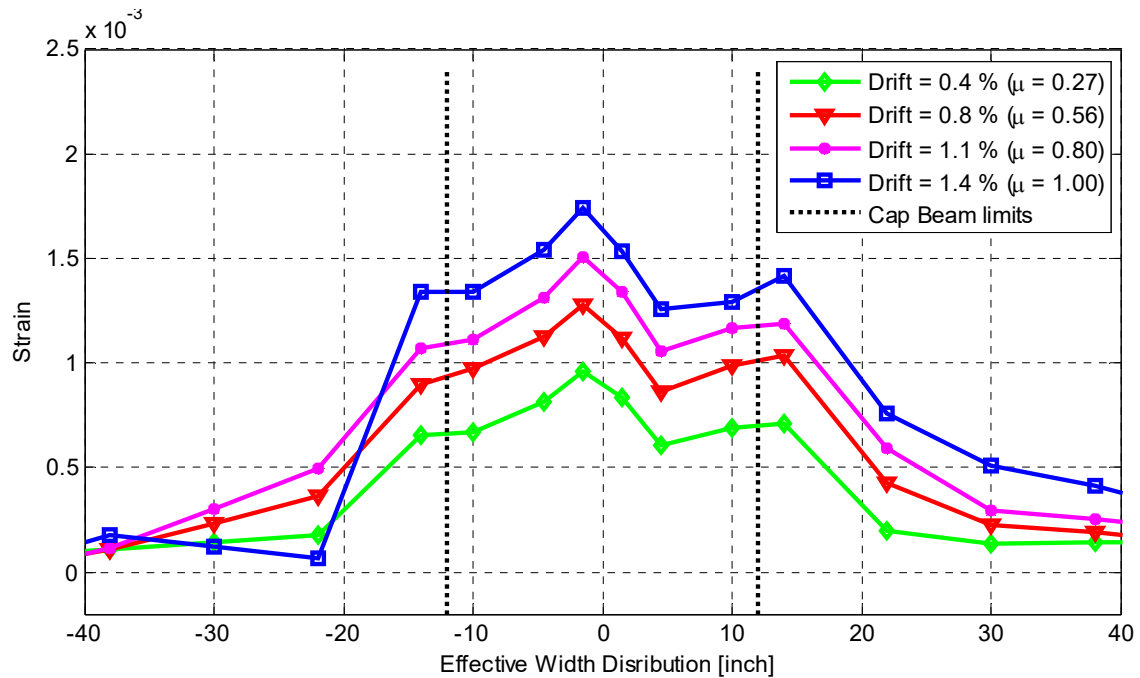


Figure 5.75 Strain distribution along cap beam and box-girder transverse deck slab reinforcement at Section D for different small-level loading cycles before yielding (loading is in negative west direction).

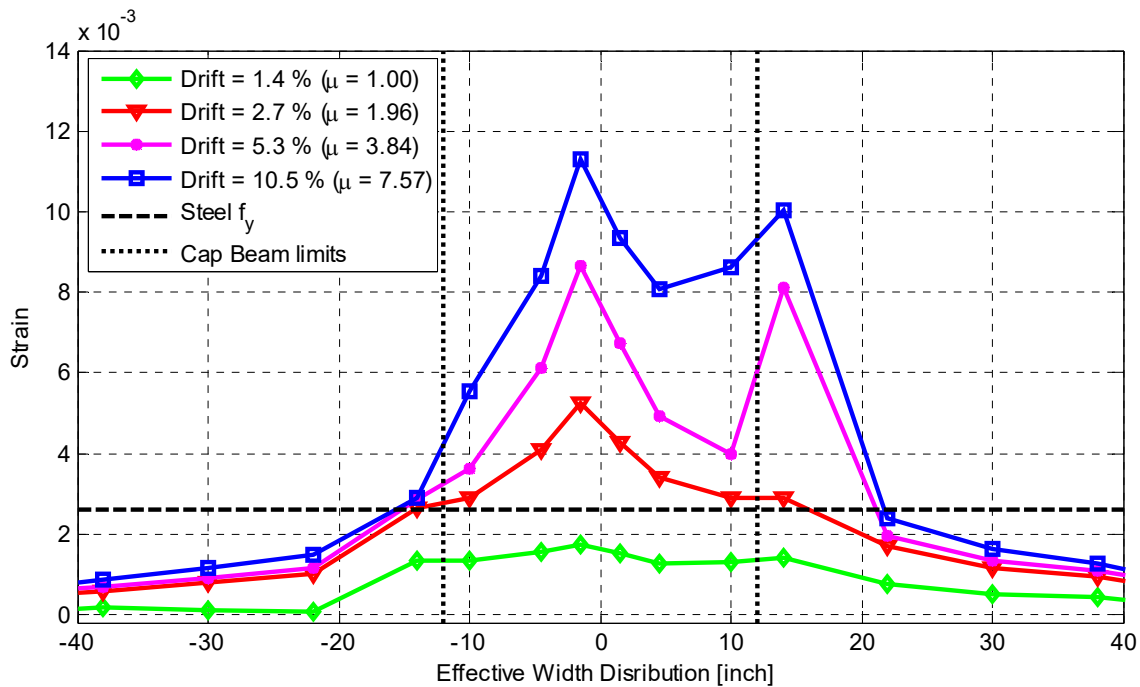


Figure 5.76 Strain distribution along cap beam and box-girder transverse deck slab reinforcement at Section D for different high-level loading cycles after yielding (loading is in negative west direction).

5.5.3 Section B: Effective Slab Width

As previously mentioned, the effective slab width is determined using the equivalent strain block concept; this simple procedure is shown in Figure 5.68. The strain distributions shown in a previous subsection are utilized to estimate the effective slab width at Section B at different loading levels and directions. Two values for the bent cap beam strain value were used to define the equivalent strain block (B_{eff}) throughout this study. These are the minimum and the mean of the six instrumented rebar strain gauge readings at a given cross section in the cap beam. In a prototype bridge, the full-scale bent cap beam reinforcement under distributed vertical loads experienced uniform strain. In this reduced-scale inverted specimen, the bent cap reinforcement did not experience uniform strain because of the concentrated gravity load and the scaling effect, which made the loading zone of almost comparable size to the beam cap beam. Therefore, both the minimum and mean values were considered to harmonize the cap beam strain. The maximum value was avoided because it represented localized unrealistic high strain values. An example of how the strain block was determined using the strain distribution at Section B and using the minimum and mean cap beam strain values is shown in Figure 5.77.

The total flange effective slab width, i.e., equivalent strain block width B_{eff} , was calculated for all loading cycles applied in the transverse direction at the peak of each loading cycle as mentioned before. This calculation process was repeated four times at the four peaks of each loading cycle group: first positive, first negative, second positive, and second negative peaks, which are referred to as Group I, II, III, and IV, respectively. A summary of the calculated B_{eff} at Section B using both cap beam minimum (ϵ_{min}) and mean (ϵ_{mean}) strain values is shown in Figures 5.78 and 5.79 for loading in the positive direction (Groups I and III), respectively. The calculated B_{eff} summary for loading in the negative direction (Groups II and IV) is shown in Figures 5.80 and 5.81, respectively. All figures show also the estimate value for B_{eff} in light of the Caltrans SDC provisions for the integral bent cap beam flanged section, which is directly referred to as the Caltrans value for brevity.

Another way of summarizing the same data presented in Figures 5.78–5.81 is given in Table 5.4 and 5.5 to conveniently read the calculated B_{eff} values directly. The tables relate the calculated B_{eff} values to the slab thickness (t_s) and bent cap beam width (b_{beam}) through a slab contribution constant (C), which quantifies the slab contribution as multiples of t_s given by Equation (5.1).

$$B_{eff} = b_{beam} + C \times t_s \quad (5.1)$$

Table 5.4 summarizes the B_{eff} and the slab contribution C for different loading levels and direction when the minimum cap beam strain value is used. Table 5.5 presents the case of using the mean cap beam strain value. The mean values for B_{eff} and slab contribution C for all loading cycles are listed in the same tables.

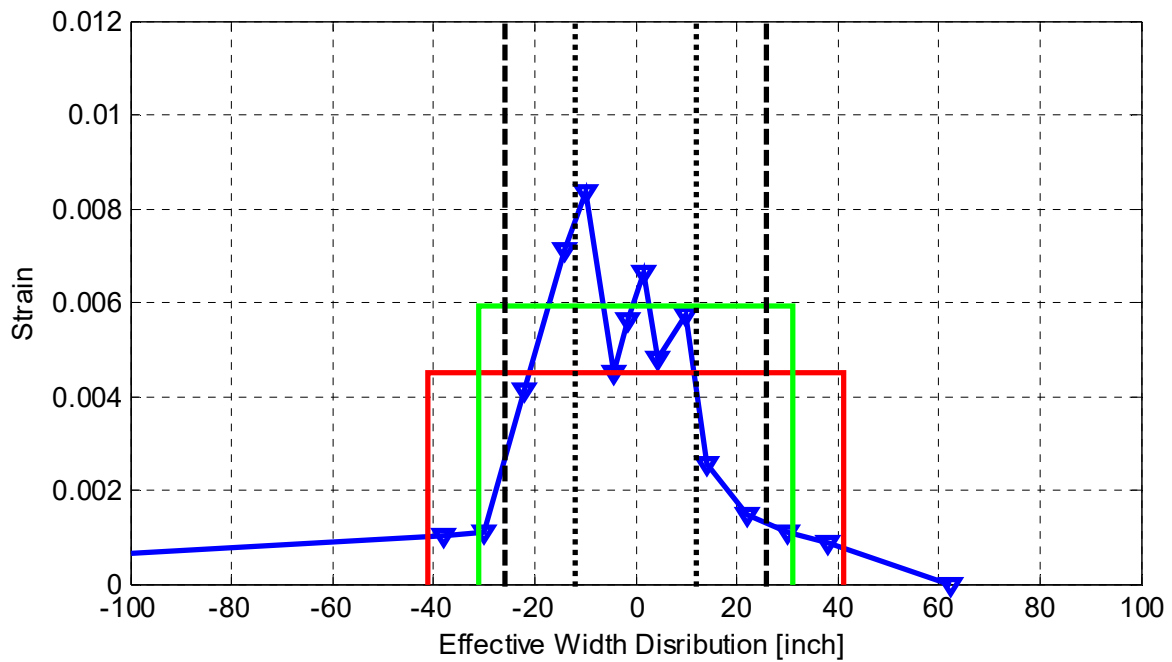
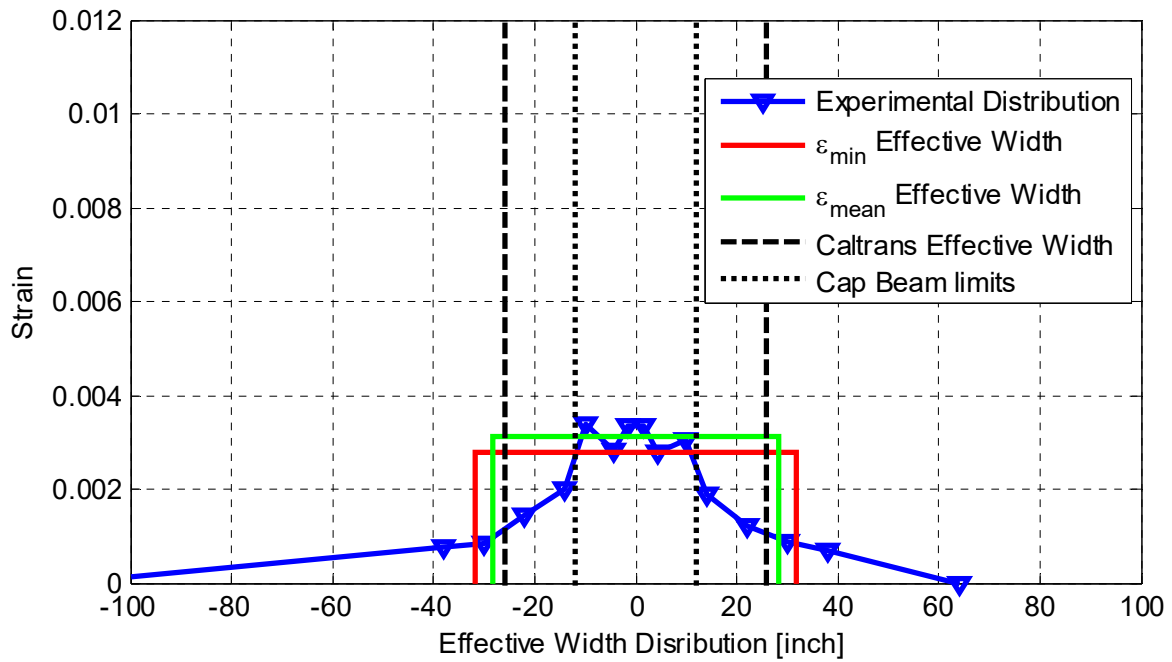


Figure 5.77 Generating effective width strain block using the strain distribution at Section B for a small- (top) and high-level (bottom) loading cycles using the observed cap beam minimum (ϵ_{min}) and mean (ϵ_{mean}) strain values.

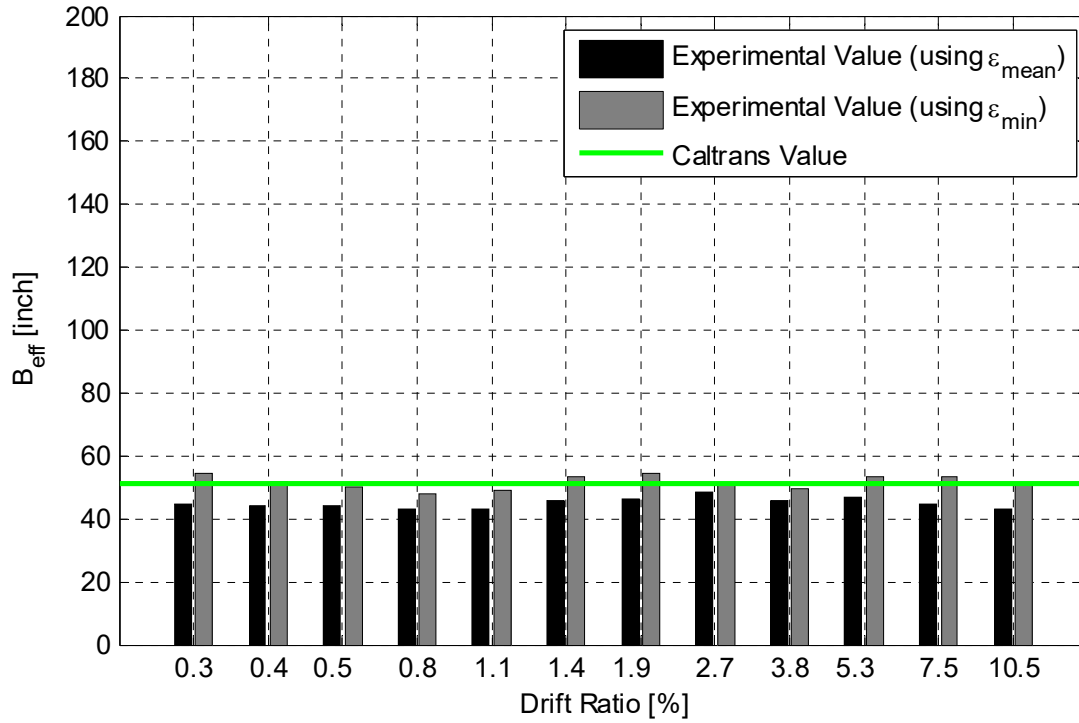


Figure 5.78 Summary of the estimated cap beam effective width at Section B at different drift ratios (Group I: first positive peak of each transverse cyclic loading group).

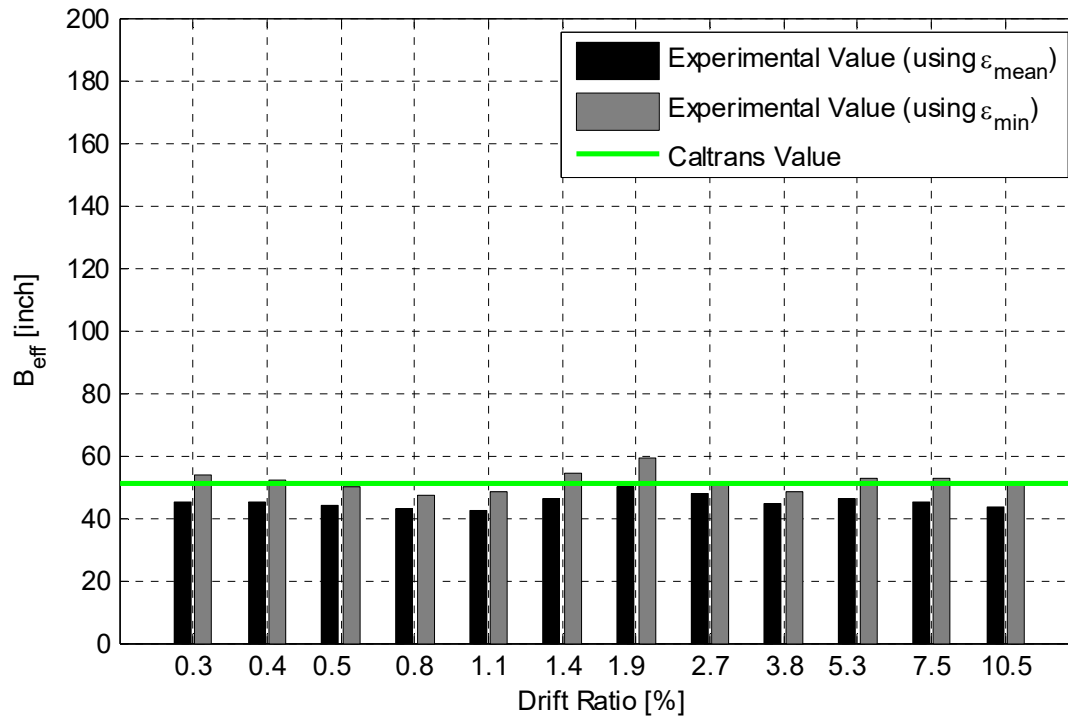


Figure 5.79 Summary of the estimated cap beam effective width at Section B at different drift ratios (Group III: second positive peak of each transverse cyclic loading group).

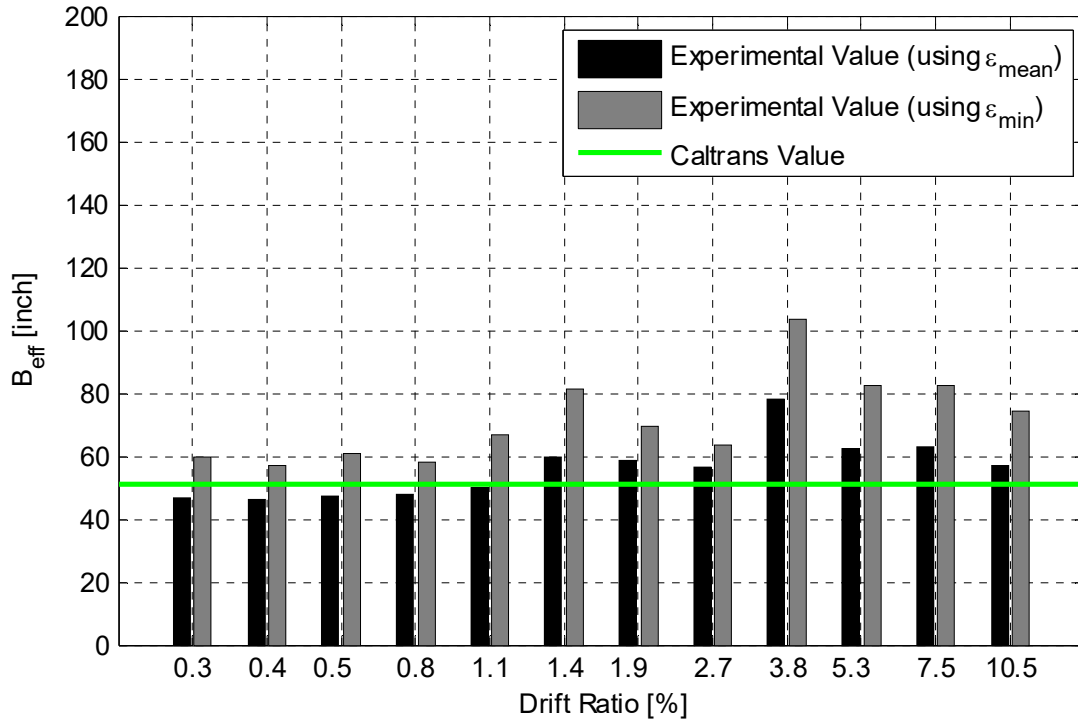


Figure 5.80 Summary of the estimated cap beam effective width at Section B at different drift ratios (Group II: first negative peak of each transverse cyclic loading group).

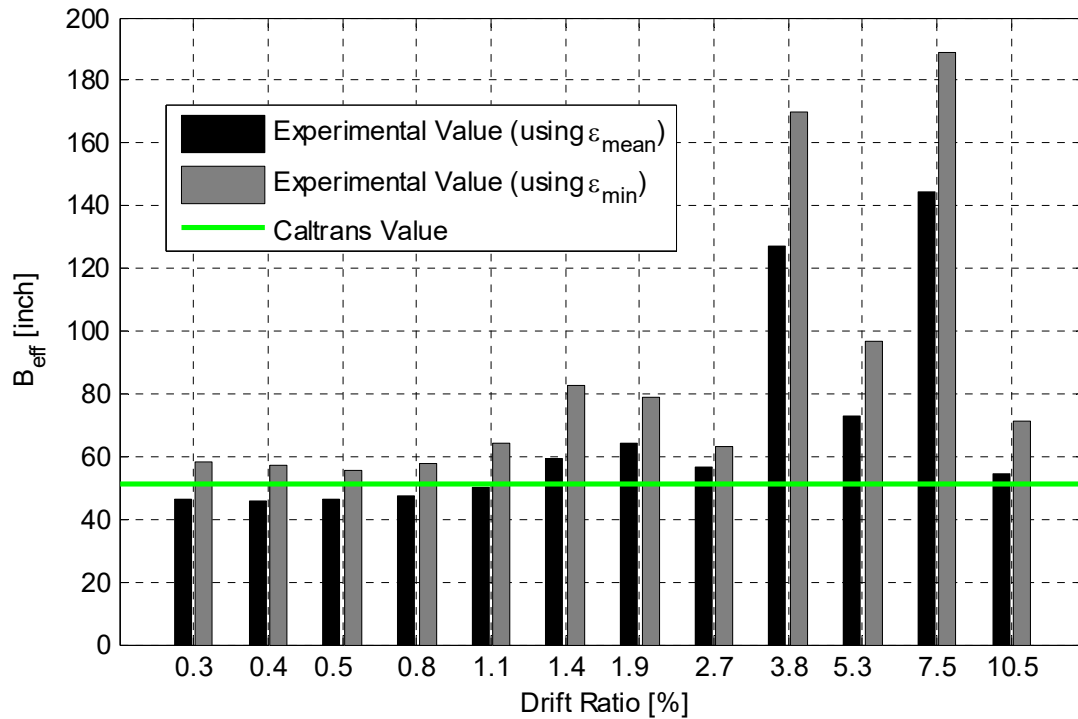


Figure 5.81 Summary of the estimated cap beam effective width at Section B at different drift ratios (Group IV: second negative peak of each transverse cyclic loading group).

Table 5.4 Section B effective slab width at different load levels calculated using cap beam ϵ_{min} .

Run	Drift ratio (5)	Ductility (μ)	Positive loading direction (Groups I and III)				Negative loading direction (Groups II and IV)			
			Strain block width, B_{eff} (in.)			Slab contribution (C)	Strain block width, B_{eff} (in.)			Slab contribution (C)
			1st cycle	2nd cycle	Mean		1st cycle	2nd cycle	Mean	
1	0.28	0.20	54.5	53.9	54.2	13.4	59.9	58.3	59.1	15.6
2	0.38	0.27	52.0	52.2	52.1	12.5	57.1	57.0	57.1	14.7
3	0.54	0.39	50.3	50.0	50.1	11.6	60.6	55.4	58.0	15.1
4	0.78	0.56	47.9	47.4	47.6	10.5	57.9	57.9	57.9	15.1
5	1.11	0.80	48.8	48.5	48.7	11.0	66.7	64.5	65.6	18.5
6	1.39	1.00	53.3	54.3	53.8	13.3	81.3	82.8	82.0	25.8
7	1.94	1.40	54.6	59.2	56.9	14.6	69.5	78.9	74.2	22.3
8	2.72	1.96	51.3	50.5	50.9	12.0	63.3	63.1	63.2	17.4
9	3.83	2.76	49.8	48.4	49.1	11.2	103.6	170.1	136.8	50.1
10	5.33	3.84	53.1	52.4	52.8	12.8	82.4	96.5	89.4	29.1
11	7.50	5.40	53.4	52.9	53.2	13.0	82.7	188.9	135.8	49.7
12	10.50	7.56	51.3	51.0	51.2	12.1	74.1	71.2	72.7	21.6
13	10.49	7.56	51.0	51.0	51.0	12.0	59.0	59.0	59.0	15.6
14	1.07	0.77	53.9	53.9	53.9	13.3	53.5	53.5	53.5	13.1
Mean for all loading cycles:					51.8	12.4			76.0	23.1

Table 5.5 Section B effective slab width at different load levels calculated using cap beam ϵ_{mean}

Run	Drift ratio (5)	Ductility (μ)	Positive loading direction (Groups I and III)				Negative loading direction (Groups II and IV)			
			Strain block width, B_{eff} (in.)			Slab contribution (C)	Strain block width, B_{eff} (in.)			Slab contribution (C)
			1st cycle	2nd cycle	Mean		1st cycle	2nd cycle	Mean	
1	0.28	0.20	44.6	45.1	44.9	9.3	46.6	46.2	46.4	10.0
2	0.38	0.27	44.2	45.0	44.6	9.1	46.0	46.0	46.0	9.8
3	0.54	0.39	44.0	44.2	44.1	8.9	47.2	46.5	46.9	10.2
4	0.78	0.56	43.1	43.2	43.1	8.5	47.7	47.6	47.7	10.5
5	1.11	0.80	43.0	42.4	42.7	8.3	50.0	50.2	50.1	11.6
6	1.39	1.00	45.6	46.1	45.8	9.7	59.7	59.2	59.5	15.8
7	1.94	1.40	46.3	50.1	48.2	10.7	58.6	64.4	61.5	16.7
8	2.72	1.96	48.3	47.7	48.0	10.7	56.5	56.8	56.6	14.5
9	3.83	2.76	45.8	44.3	45.1	9.4	77.9	127.1	102.5	34.9
10	5.33	3.84	46.6	46.4	46.5	10.0	62.3	72.8	67.5	19.3
11	7.50	5.40	44.7	44.9	44.8	9.2	62.8	144.3	103.5	35.3
12	10.50	7.56	43.2	43.3	43.3	8.6	56.8	54.7	55.7	14.1
13	10.49	7.56	43.2	43.2	43.2	8.5	46.1	46.1	46.1	9.8
14	1.07	0.77	44.9	44.9	44.9	9.3	44.0	44.0	44.0	8.9
Mean for all loading cycles:					44.9	9.3			59.6	15.8

5.5.4 Section D: Effective Slab Width

A similar framework as used before presents the effective slab width results at Section D. Figure 5.82 is one example of how strain block was determined using the minimum and mean cap beam strain values. at Section D. A summary of the calculated B_{eff} at Section D using both cap beam minimum and mean strain values is shown in Figures 5.83 and 5.84 for loading in the positive direction (Groups I and III), respectively. The calculated B_{eff} summary for loading in the negative direction (Groups II and IV) is shown in Figures 5.85 and 5.86, respectively. The Caltrans value for B_{eff} is shown in all figures as well. The same data are presented differently in Tables 5.7 and 5.8 to summarize B_{eff} and the slab contribution C for the different loading levels and direction when the minimum and mean cap beam strain values are used, respectively.

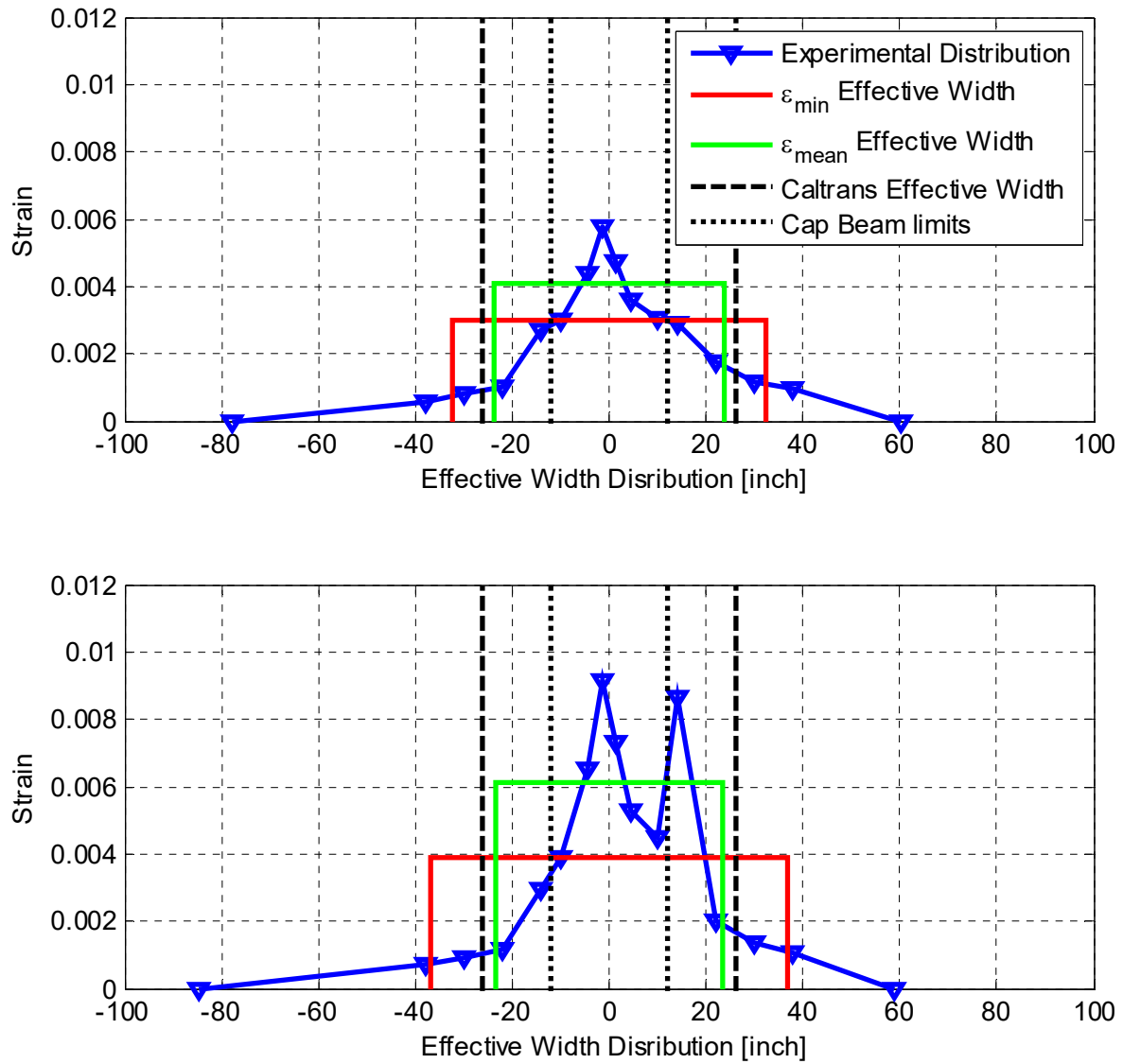


Figure 5.82 Generating effective width strain block using the strain distribution at Section D for a small- (top) and high-level (bottom) loading cycle using the observed cap beam minimum (ϵ_{\min}) and mean (ϵ_{mean}) strain values.

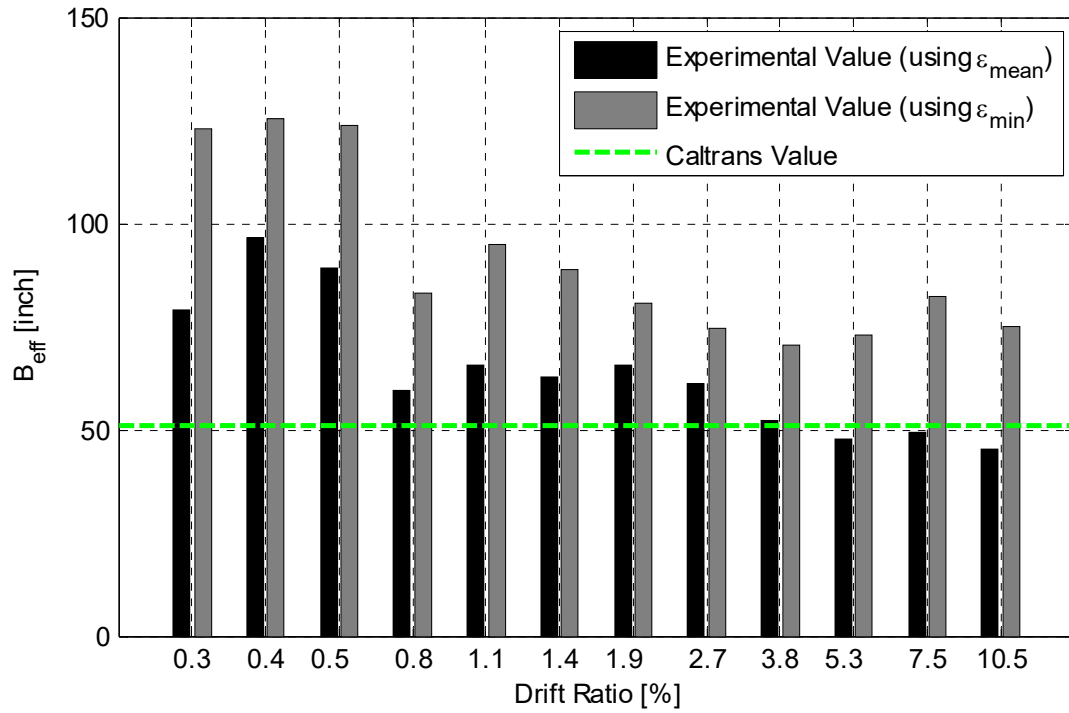


Figure 5.83 Summary of the estimated cap beam effective width at Section D at different drift ratios (Group I: first positive peak of each transverse cyclic loading group)

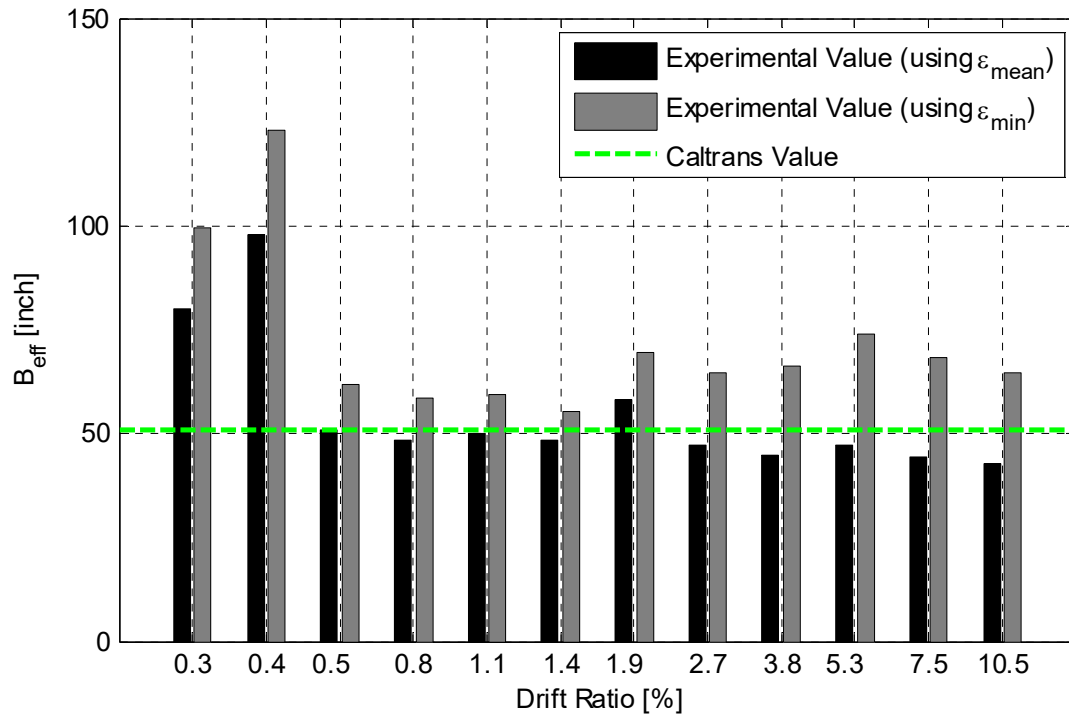


Figure 5.84 Summary of the estimated cap beam effective width at Section D at different drift ratios (Group III: second positive peak of each transverse cyclic loading group).

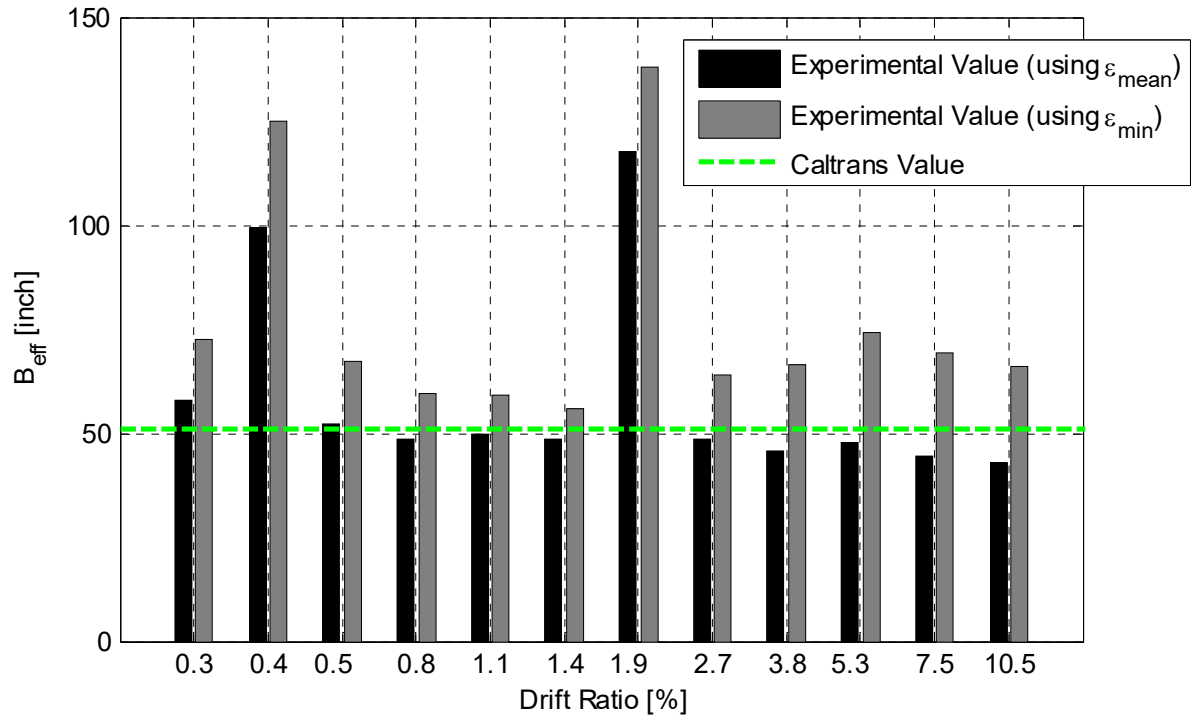


Figure 5.85 Summary of the estimated cap beam effective width at Section D at different drift ratios (Group II: first negative peak of each transverse cyclic loading group)

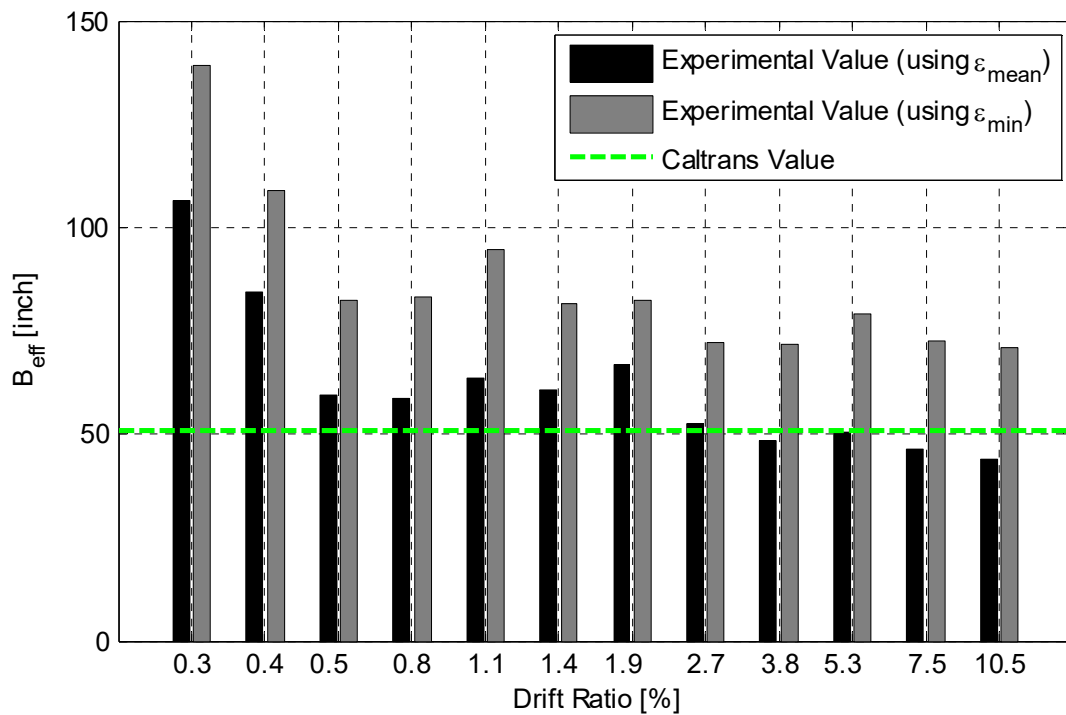


Figure 5.86 Summary of the estimated cap beam effective width at Section D at different drift ratios (Group IV: second negative peak of each transverse cyclic loading group).

Table 5.6 Section D effective slab width at different load levels calculated using cap beam ϵ_{min} .

Run	Drift ratio (5)	Ductility (μ)	Positive loading direction (Groups I and III)				Negative loading direction (Groups II and IV)			
			Strain block width, B_{eff} (in.)			Slab contribution (C)	Strain block width, B_{eff} (in.)			Slab contribution (C)
			1st cycle	2nd cycle	Mean		1st cycle	2nd cycle	Mean	
1	0.28	0.20	123.0	139.3	131.2	47.6	72.5	99.7	86.1	27.6
2	0.38	0.27	125.3	108.8	117.0	41.3	125.1	123.1	124.1	44.5
3	0.54	0.39	123.8	82.5	103.1	35.2	67.3	62.0	64.7	18.1
4	0.78	0.56	83.0	83.1	83.0	26.2	59.6	58.6	59.1	15.6
5	1.11	0.80	95.1	94.4	94.8	31.5	59.0	59.2	59.1	15.6
6	1.39	1.00	88.7	81.7	85.2	27.2	56.0	55.1	55.5	14.0
7	1.94	1.40	80.7	82.4	81.5	25.6	137.9	69.7	103.8	35.5
8	2.72	1.96	74.7	72.0	73.3	21.9	63.9	64.7	64.3	17.9
9	3.83	2.76	70.7	71.7	71.2	21.0	66.6	66.4	66.5	18.9
10	5.33	3.84	72.9	79.2	76.1	23.1	74.4	73.8	74.1	22.3
11	7.50	5.40	82.2	72.6	77.4	23.7	69.4	68.2	68.8	19.9
12	10.50	7.56	74.8	70.7	72.8	21.7	66.2	64.8	65.5	18.4
13	10.49	7.56	69.1	69.1	69.1	20.0	63.5	63.5	63.5	17.6
14	1.07	0.77	66.4	66.4	66.4	18.9	65.4	65.4	65.4	18.4
Mean for all loading cycles:					85.9	27.5			72.9	21.7

5.5.5 Overall Effective Width in Tension Side

To obtain more comprehensive conclusions, the calculated effective slab width is additionally averaged out from cases of loading in positive and negative directions together at both sections. Furthermore, the overall average for both sections together was calculated such that the mean value for all the loading cases renders a single number that summarizes all the experimentally determined effective slab width values. The average B_{eff} values for each group of loading and overall average for all groups combined is shown first for each of Sections B and D separately in Figure 5.87 and Figure 5.88, respectively. The averages for all the groups calculated using both the minimum (ϵ_{min}) and mean (ϵ_{mean}) cap beam strain values are also plotted against the Caltrans value for both sections in Figure 5.87 and Figure 5.88; note that the Caltrans value is conservative relative to what has been observed from the experiments.

The average values from all minimum and mean cap beam strain values are tabulated in Tables 5.8 and 5.9, respectively. Table 5.8 shows an average effective flange width, B_{eff} , of 63.9 in. and 79.4 in., respectively, for all loading groups Sections B and D versus an estimated value from the Caltrans SDC flanged section of 51 in. These values correspond to slab contributions $17.7t_s$ and $24.6t_s$ versus the well-known $12t_s$ Caltrans value. However, when the mean cap beam

strain value is used instead, Table 5.9 suggests that the former numbers drop to $12.6t_s$ and $14.9t_s$; the overall average of both Sections B and D is calculated and denoted in the tables. When all loading cases and Sections B and D were considered, a mean value for the slab contribution was determined to be $21.2t_s$ and $13.7t_s$ based on a minimum and mean cap beam strain values, respectively. It is concluded that the $12t_s$ is conservative, and a larger value is recommended to be considered for bent cap beam capacity estimation, which is discussed in more detail in the companion report.

Table 5.7 Section D effective slab width at different load levels calculated using cap beam ϵ_{mean} .

Run	Drift ratio (5)	Ductility (μ)	Positive loading direction (Groups I and III)				Negative loading direction (Groups II and IV)			
			Strain block width, B_{eff} (in.)			Slab contribution (C)	Strain block width, B_{eff} (in.)			Slab contribution (C)
			1st cycle	2nd cycle	Mean		1st cycle	2nd cycle	Mean	
1	0.28	0.20	78.9	106.5	92.7	30.5	57.9	80.0	69.0	20.0
2	0.38	0.27	96.7	84.6	90.6	29.6	99.3	98.0	98.7	33.2
3	0.54	0.39	89.2	59.4	74.3	22.4	52.4	50.9	51.6	12.3
4	0.78	0.56	59.5	58.5	59.0	15.5	48.6	48.4	48.5	10.9
5	1.11	0.80	65.5	63.6	64.5	18.0	49.8	49.9	49.8	11.5
6	1.39	1.00	62.8	60.6	61.7	16.8	48.5	48.3	48.4	10.8
7	1.94	1.40	65.5	66.8	66.2	18.7	117.8	58.4	88.1	28.5
8	2.72	1.96	61.0	52.4	56.7	14.5	48.8	47.4	48.1	10.7
9	3.83	2.76	52.3	48.5	50.4	11.7	45.9	44.8	45.3	9.5
10	5.33	3.84	47.9	50.3	49.1	11.1	47.6	47.1	47.3	10.4
11	7.50	5.40	49.4	46.4	47.9	10.6	44.6	44.3	44.5	9.1
12	10.50	7.56	45.2	43.9	44.6	9.1	42.8	42.8	42.8	8.3
13	10.49	7.56	43.0	43.0	43.0	8.4	42.0	42.0	42.0	8.0
14	1.07	0.77	42.3	42.3	42.3	8.1	42.4	42.4	42.4	8.2
Mean for all loading cycles					60.2	16.1			54.7	13.7

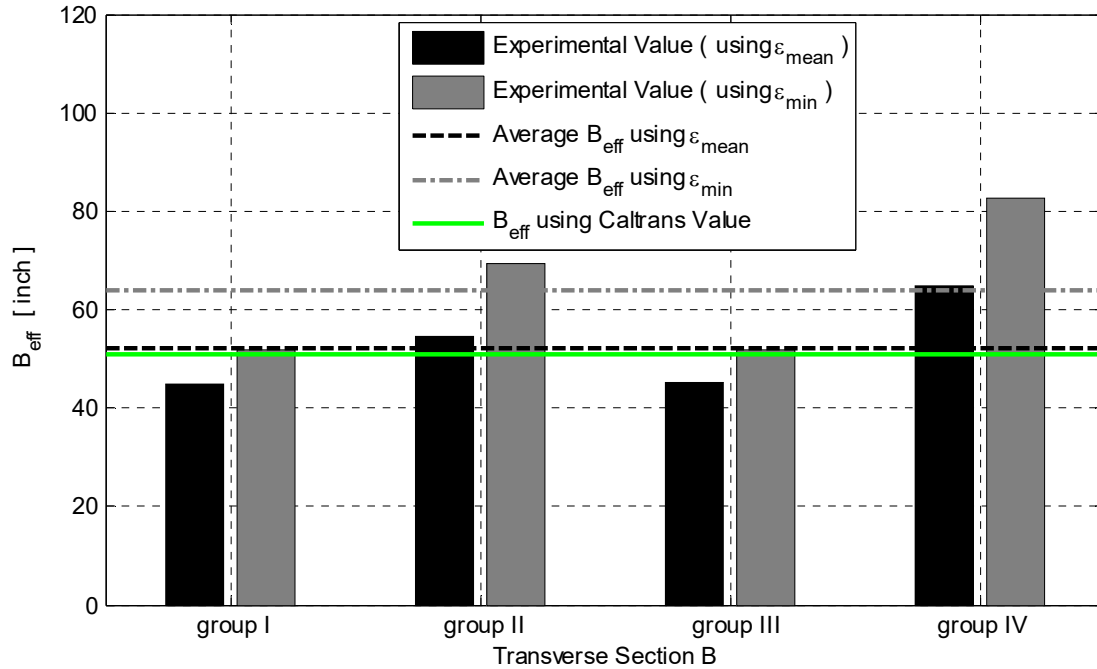


Figure 5.87 Mean effective width from all loading cycles in each group (bar chart) and overall average effective width from all loading cycles and groups (dashed lines) at Section B as compared to Caltrans SDC effective width value

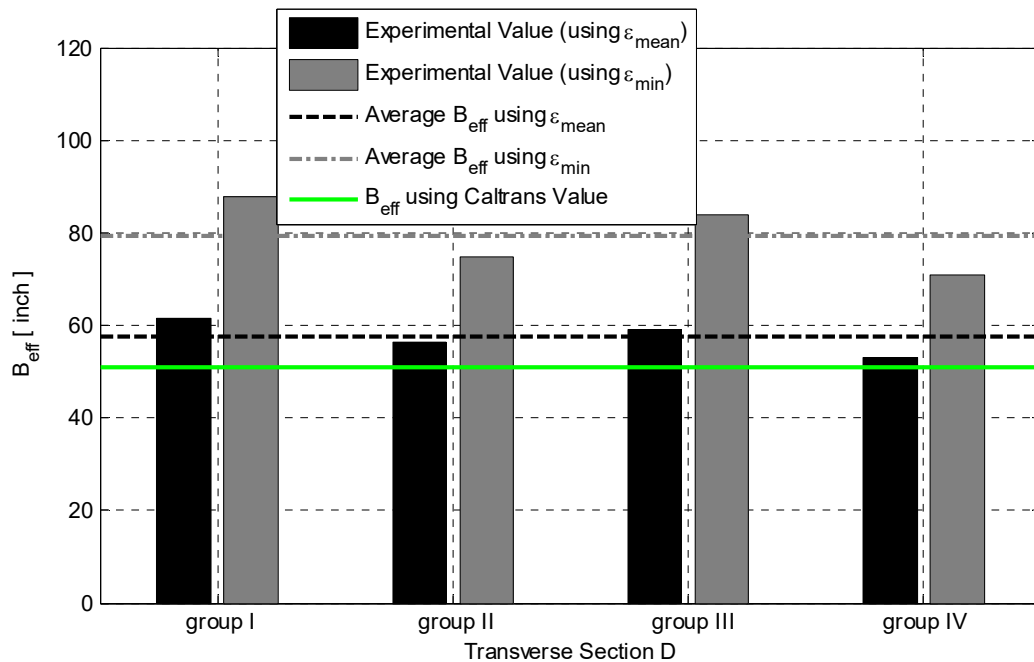


Figure 5.88 Mean effective width from all loading cycles in each group (bar chart) and overall average effective width from all loading cycles and groups (dashed lines) at Section D as compared to Caltrans SDC effective width value

Table 5.8 Summary of overall effective slab width mean calculated using cap beam ϵ_{min} .

Run #	Drift (%)	Ductility (μ)	All groups I, II, III, IV mean (Section B)		All groups I, II, III, IV mean (Section D)		Overall mean for both sections	
			B_{eff} (in.)	Slab contribution (C)	B_{eff} (in.)	Slab contribution (C)	B_{eff} (in.)	Slab contribution (C)
1	0.28	0.2	56.6	14.5	108.6	37.6	82.6	26.1
2	0.38	0.27	54.6	13.6	120.6	42.9	87.6	28.3
3	0.54	0.39	54.1	13.4	83.9	26.6	69	20
4	0.78	0.56	52.8	12.8	71.1	20.9	61.9	16.9
5	1.11	0.8	57.1	14.7	76.9	23.5	67	19.1
6	1.39	1	67.9	19.5	70.4	20.6	69.2	20.1
7	1.94	1.4	65.5	18.5	92.7	30.5	79.1	24.5
8	2.72	1.96	57.1	14.7	68.8	19.9	62.9	17.3
9	3.83	2.76	93	30.7	68.8	19.9	80.9	25.3
10	5.33	3.84	71.1	20.9	75.1	22.7	73.1	21.8
11	7.5	5.4	94.5	31.3	73.1	21.8	83.8	26.6
12	10.5	7.56	61.9	16.9	69.1	20.1	65.5	18.5
13	10.49	7.56	55	13.8	66.3	18.8	60.6	16.3
14	1.07	0.77	53.7	13.2	65.9	18.6	59.8	15.9
Mean for all loading cycles			63.9	17.7	79.4	24.6	71.7	21.2

Table 5.9 Summary of overall effective slab width mean calculated using cap beam ϵ_{mean}

Run #	Drift (%)	Ductility (μ)	All groups I, II, III, IV mean (Section B)		All groups I, II, III, IV mean (Section D)		Overall mean for both sections	
			B_{eff} (in.)	Slab contribution (C)	B_{eff} (in.)	Slab contribution (C)	B_{eff} (in.)	Slab contribution (C)
1	0.28	0.2	45.6	9.6	80.8	25.3	63.2	17.4
2	0.38	0.27	45.3	9.5	94.7	31.4	70	20.4
3	0.54	0.39	45.5	9.6	63	17.3	54.2	13.4
4	0.78	0.56	45.4	9.5	53.8	13.2	49.6	11.4
5	1.11	0.8	46.4	10	57.2	14.7	51.8	12.4
6	1.39	1	52.7	12.7	55	13.8	53.9	13.3
7	1.94	1.4	54.8	13.7	77.1	23.6	66	18.7
8	2.72	1.96	52.3	12.6	52.4	12.6	52.4	12.6
9	3.83	2.76	73.8	22.1	47.9	10.6	60.8	16.4
10	5.33	3.84	57	14.7	48.2	10.8	52.6	12.7
11	7.5	5.4	74.2	22.3	46.2	9.9	60.2	16.1
12	10.5	7.56	49.5	11.3	43.7	8.7	46.6	10
13	10.49	7.56	44.7	9.2	42.5	8.2	43.6	8.7
14	1.07	0.77	44.5	9.1	42.4	8.2	43.4	8.6
Mean for all loading cycles			52.3	12.6	57.5	14.9	54.9	13.7

5.6 EFFECTIVE SLAB WIDTH (COMPRESSION SIDE)

The behavior of the reinforcing steel bars in the tension side in RC flanged sections under flexure is more representative of the effective slab width and slab contribution than the side in compression. That is because all of concrete in tension cracked at both service and limit states, and it is assumed that only the steel was effective in carrying the loads. However, in the side in compression, the concrete contributed significantly to the flexural capacity. Thus, if possible, it is useful to acquire the strain or stress distribution in the compression zone, especially if the contribution of the slabs is required. Unfortunately, using embedded concrete gauges to measure concrete strain directly is not very reliable. Therefore, the compression steel was instrumented such that the strain of the surrounding concrete can be assumed to be the same as the steel as long as a perfect bond between the steel and concrete is maintained. The sections that have been used for exploring strain distributions, namely, Sections B and D, are far away from the beam end, and it is safe to assume that no bond slip took place at those sections.

Both embedded concrete strain gauges and compression steel strain gauges were used to acquire the strain distribution at the side in compression. However, the data recorded at the compression side was noisy and extremely sensitive to the applied concentrated gravity load. Accordingly, the data obtained from the side in compression, from both the concrete and steel gauge, were not conclusive; however, they are shown here for completeness. Moreover, for

investigating the bent cap beam capacity in the post-test analysis, a similar effective width to that obtained from the tension side was considered for the compression side.

5.6.1 Reinforcement Strain Distribution

Several reinforcing bars in the bent cap beam compression side and adjacent transverse soffit slab bars were instrumented to obtain a strain distribution similar to that obtained for the side in tension. The strain distribution from the different strain gauge readings was recorded continuously throughout all the loading cycles in both transverse and longitudinal directions. Only results obtained from second positive and second negative peaks of each group of transverse loading cycles are shown for brevity. The results were selected for small-level cycles of drift ratios 0.4%, 0.8%, 1.1%, and 1.4%, which corresponded to μ of 0.27, 0.56, 0.80, and 1.0, respectively. Meanwhile, the 1.0 ductility level (1.5% drift ratio) results along with 1.96, 3.84, and 7.57 ductility levels (2.7%, 5.3%, and 10.5% drift ratio) comprised the selected high-level cycles.

Figures 5.89 and 5.90 show the distribution in the compression side at Section B at the small-levels and high-levels of loading, respectively, when the transverse load was pushing towards the east, i.e., the positive loading direction side. Figures 5.91 and 5.92 show the strain distribution at Section B for similar levels when loading was pushing towards the west side, i.e., reversed load in the negative direction. Figure 5.93–5.96 show the distribution in the compression side for different levels and loading direction for Section D. Note that the strain values in the soffit slab transverse reinforcement barely changed with the increased lateral loading levels. Only the cap beam reinforcement strain varied with lateral loading and in certain loading directions; e.g., the negative loading direction for Section B and positive loading for Section D. Accordingly, the area under the distribution could not be accurately calculated because some strain values were negative due to compression, and others were positive due to overriding tension.

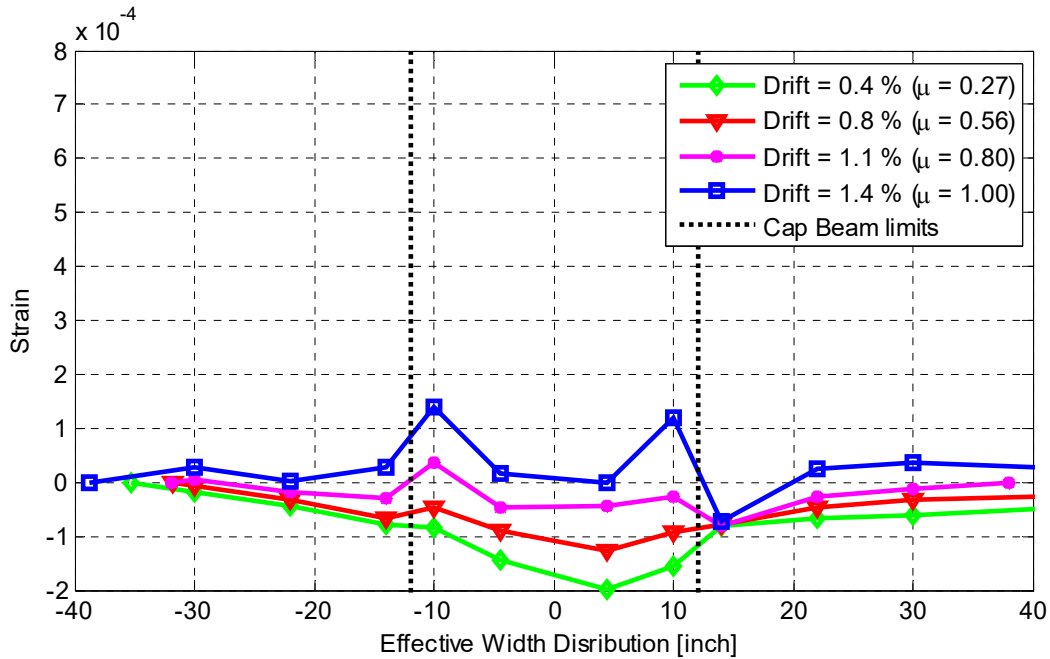


Figure 5.89 Strain distribution along cap beam and box-girder transverse soffit slab reinforcement (compression side) at Section B for different small-level loading cycles (strain values recorded at loading cycle peak when loading is in east direction).

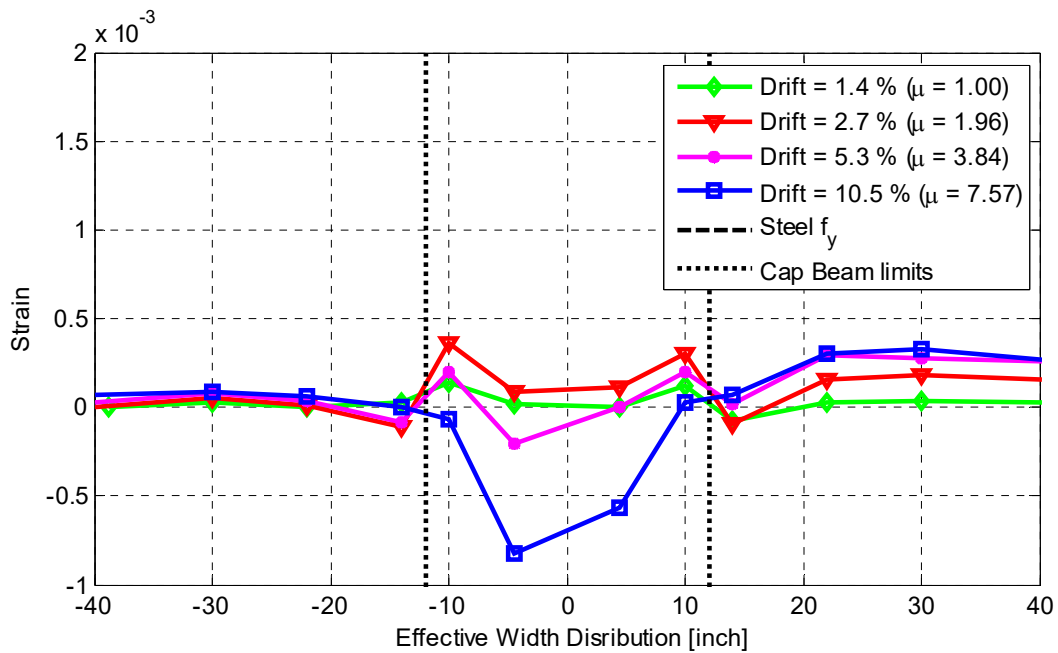


Figure 5.90 Strain distribution along cap beam and box-girder transverse soffit slab reinforcement (compression side) at Section B for different high-level loading cycles (strain values recorded at loading cycle peak when loading is in east direction).

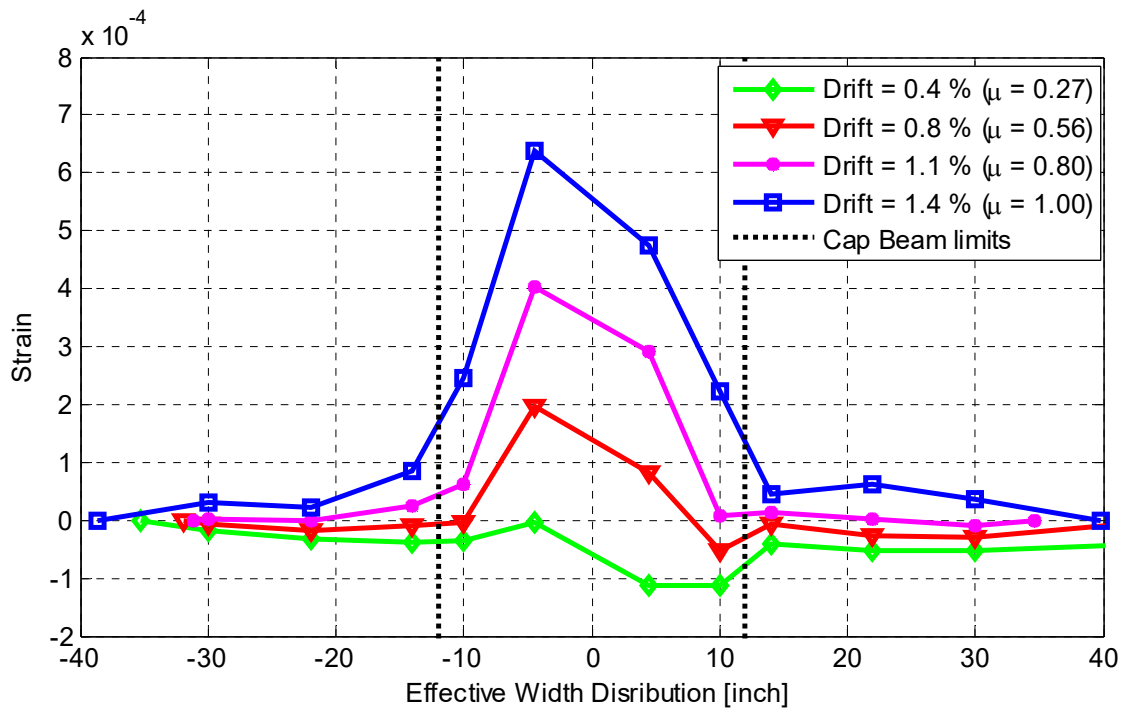


Figure 5.91 Strain distribution along cap beam and box-girder transverse soffit slab reinforcement (compression side) at Section B for different high-level loading cycles (strain values recorded at loading cycle peak when loading is in west direction).

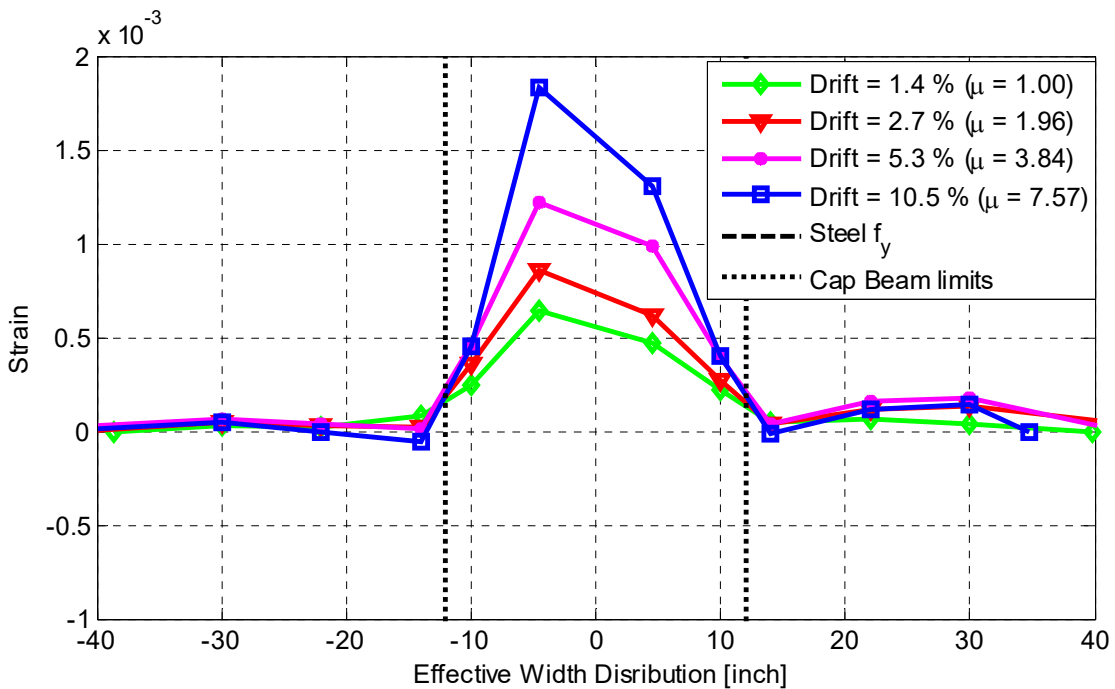


Figure 5.92 Strain distribution along cap beam and box-girder transverse soffit slab reinforcement (compression side) at Section B for different high-level loading cycles (strain values recorded at loading cycle peak when loading is in west direction).

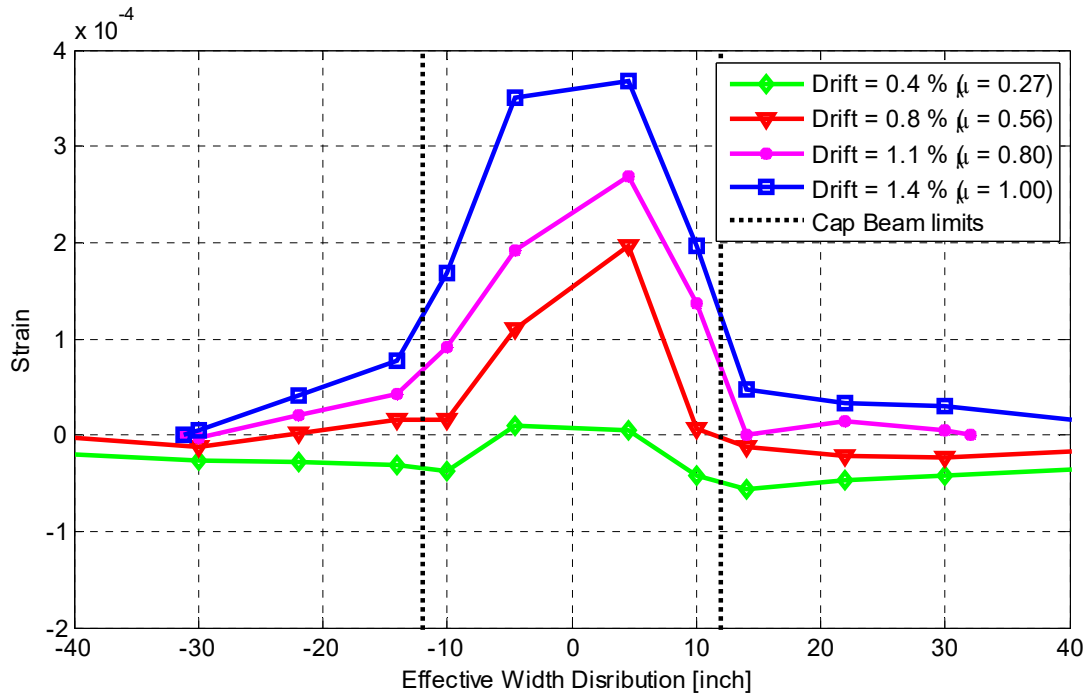


Figure 5.93 Strain distribution along cap beam and box-girder transverse soffit slab reinforcement (compression side) at Section D for different small-level loading cycles (strain values recorded at loading cycle peak when loading is in east direction).

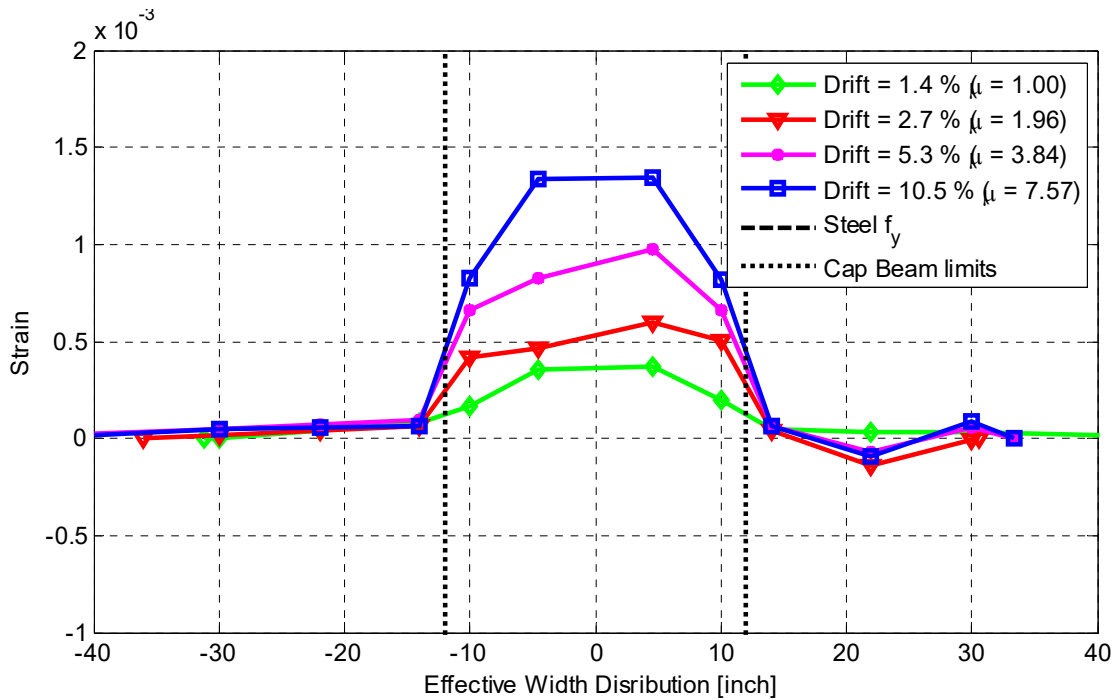


Figure 5.94 Strain distribution along cap beam and box-girder transverse soffit slab reinforcement (compression side) at Section D for different high-level loading cycles (strain values recorded at loading cycle peak when loading is in east direction).

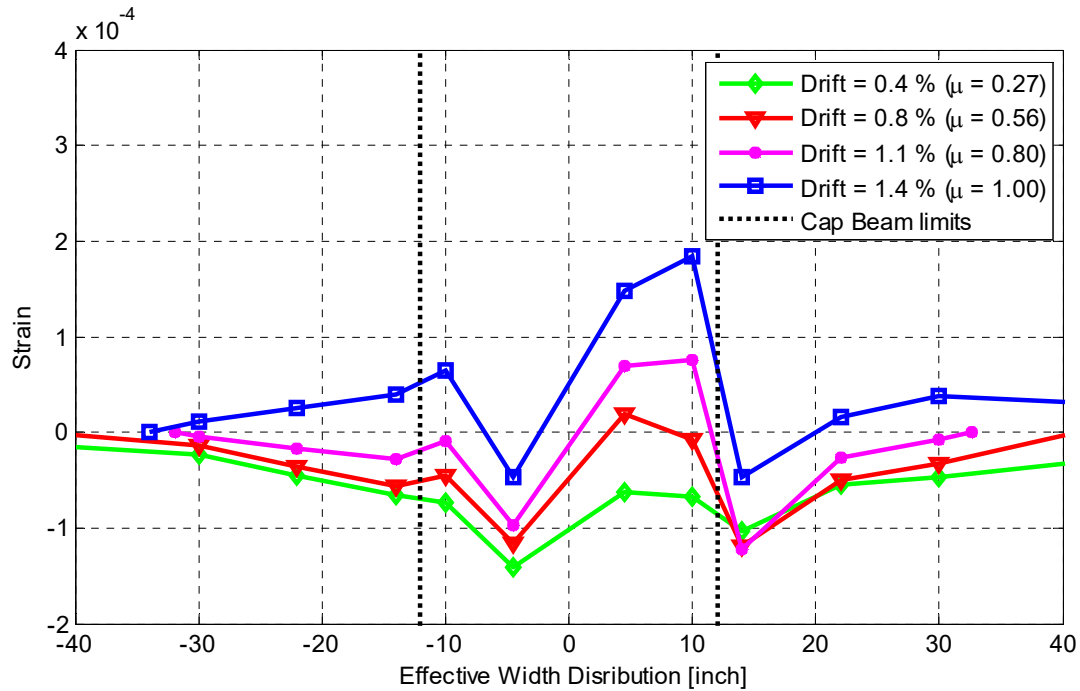


Figure 5.95 Strain distribution along cap beam and box-girder transverse soffit slab reinforcement (compression side) at Section D for different small-level loading cycles (strain values recorded at loading cycle peak when loading is in west direction).

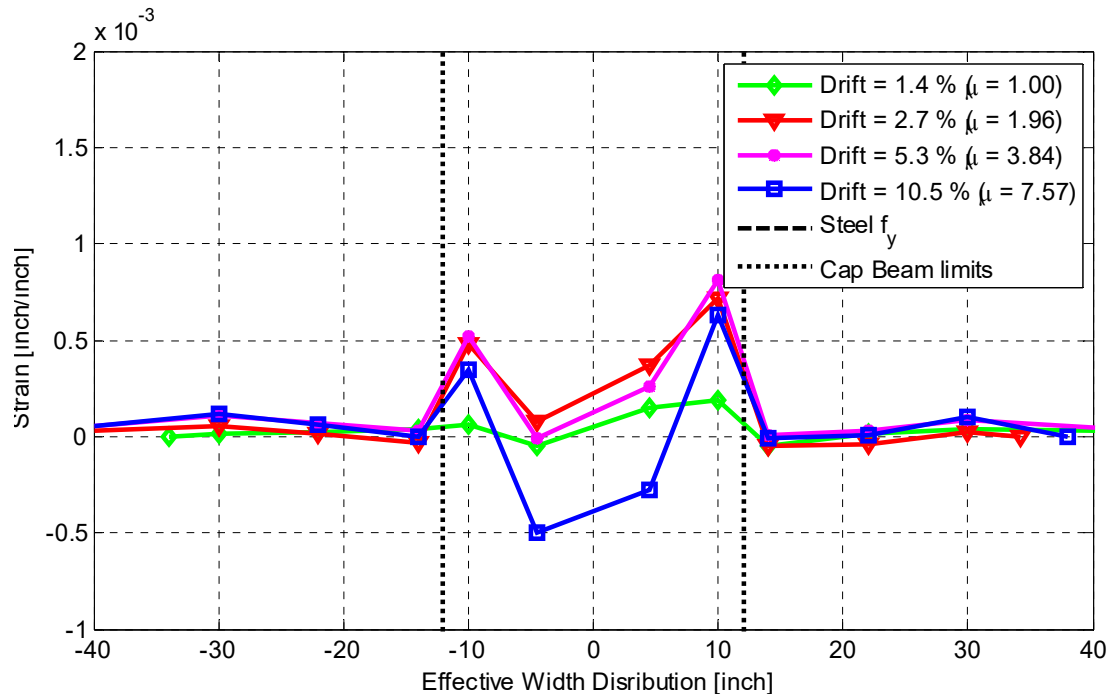


Figure 5.96 Strain distribution along cap beam and box-girder transverse soffit slab reinforcement (compression side) at Section D for different high-level loading cycles (strain values recorded at loading cycle peak when loading is in west direction).

5.6.2 Concrete Gauge Strain Distribution

The strain distribution in the side in compression on the instrumented steel rebars was not conclusive. Estimation of an effective slab width at the compression side was not possible because the measurements were sensitive to the concentrated gravity load. The concrete gauges measurements were even noisier and more sensitive to the concentrated load, and it was not possible to obtain a reasonable strain distribution. Figure 5.97 shows a sample strain history of four embedded concrete gauges at Section B during all the loading cycles. It is obvious from the figure that the concrete gauge reading was noisy and could not accurately capture the different loading cycles and reversals. As a result, a different type of gauge was used for the second phase of testing that involved HS testing of retrofitted Specimen No. 2. This included the use of surface concrete gauges that did not need to be installed during the construction. Surface concrete gauges were attached directly to the surface of the concrete from the soffit slab side where compression was expected. A discussion of the surface concrete gauges sample measurements obtained during the HS test is presented in the companion report.

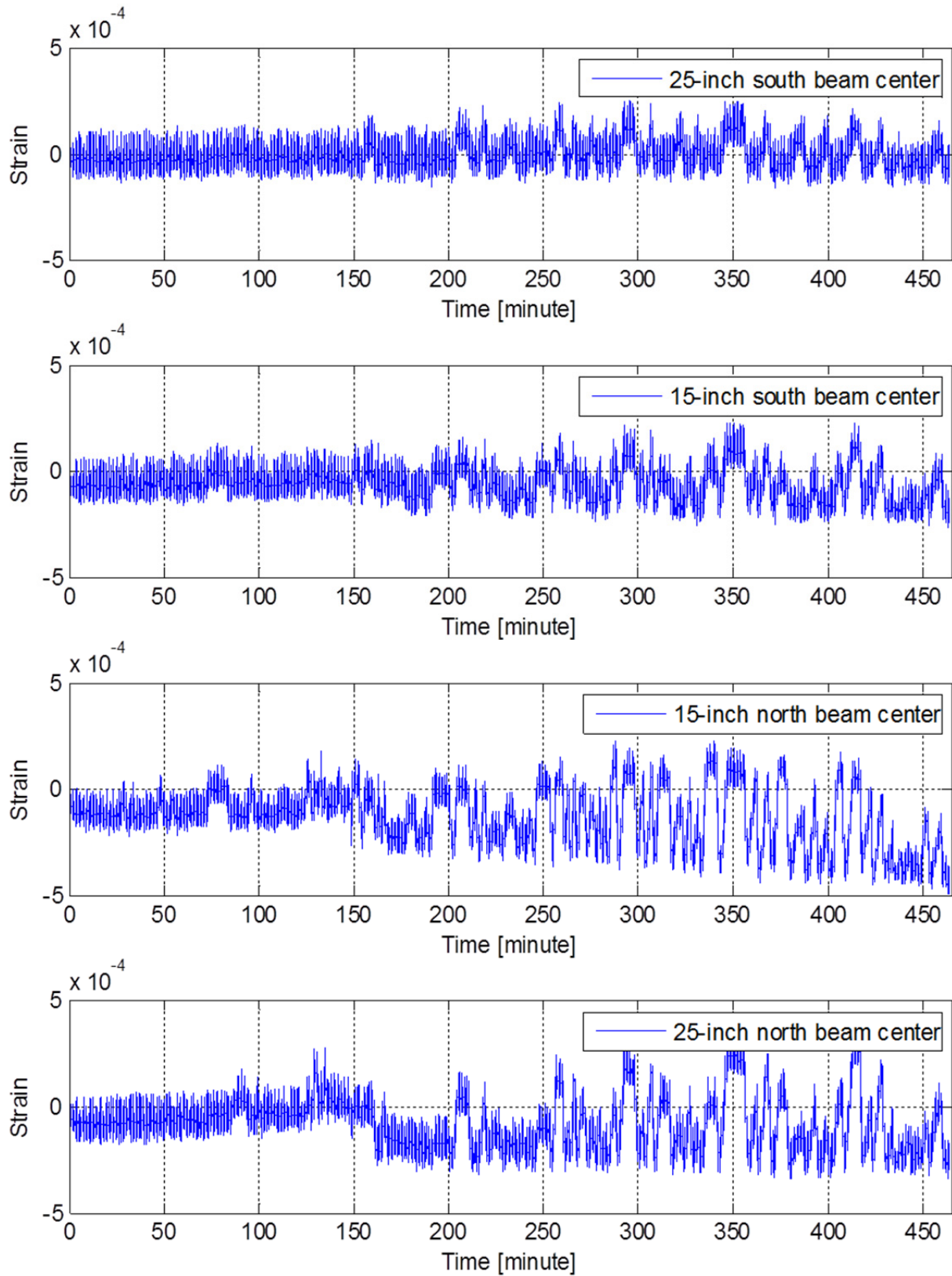


Figure 5.97 Sample of four concrete strain gauges history located at the compression zone from both sides of the bent cap beam at Section B.

5.7 OTHER RESPONSE QUANTITIES

The main focus of the experimental program was to monitor the bent cap beam behavior, the box-girder contribution, and overall system response to combined gravity and bi-directional lateral loading. Complimentary response quantities from the box-girder longitudinal rebars and various transverse shear reinforcement that support the experimental test observations are presented here.

5.7.1 Longitudinal Slab Strain

Cyclic loading tests of as-built Specimen No. 1 consisted of bi-directional lateral loading in both of the transverse and longitudinal directions. Loading in the longitudinal direction caused flexural bending in the box-girder. The strain values in the longitudinal box-girder reinforcing steel were monitored to ensure that the box-girder remained essentially elastic as required by the Caltrans SDC. Figure 5.98 shows the strain history of a longitudinal rebar at two sections in the box-girder deck slab, which was almost aligned with the box-girder center line, at the two sides of the bent cap beam where maximum moments were expected. Figure 5.99 shows the strain history at similar sections but in a different rebar that was aligned with one of the box-girder webs. Both figures show that the yielding strain of 0.0026 observed from material tests was not reached in the longitudinal box-girder rebars. Accordingly, it is safe to conclude that the box-girder remained elastic during the testing as no yielding was observed. Note that these strain values were recorded by the NEFF data acquisition system, which did not record the application of gravity load or the pausing times. Thus, a shorter total testing time was recorded versus the PI data acquisition responses.

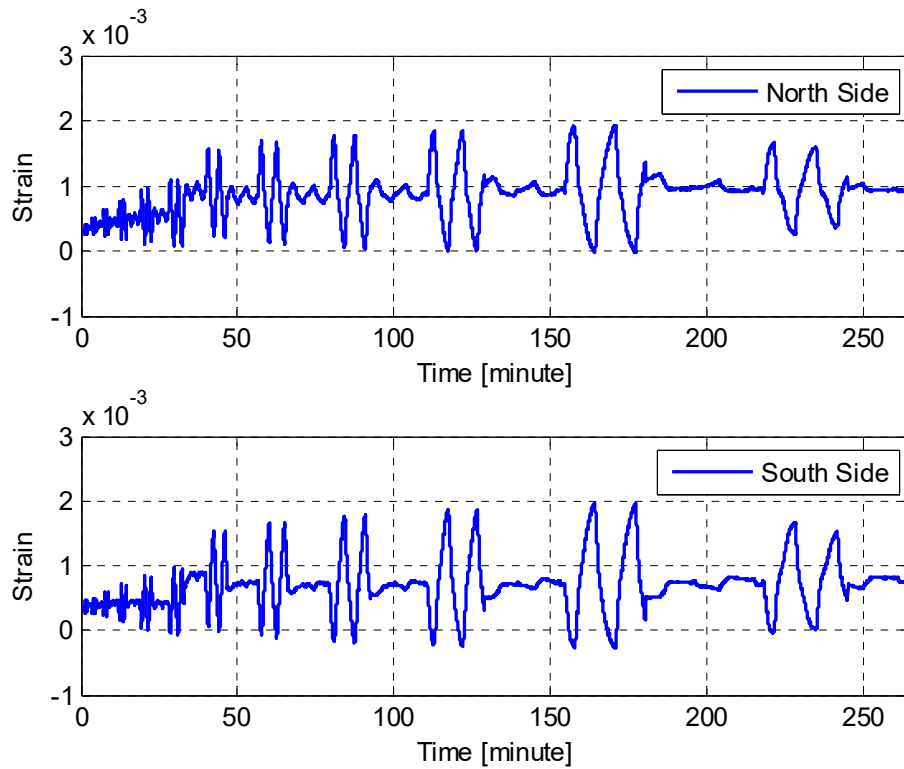


Figure 5.98 History of box-girder deck longitudinal reinforcement strain measured in the rebar at the middle of the box-girder at north and south sides of the column for all cycles.

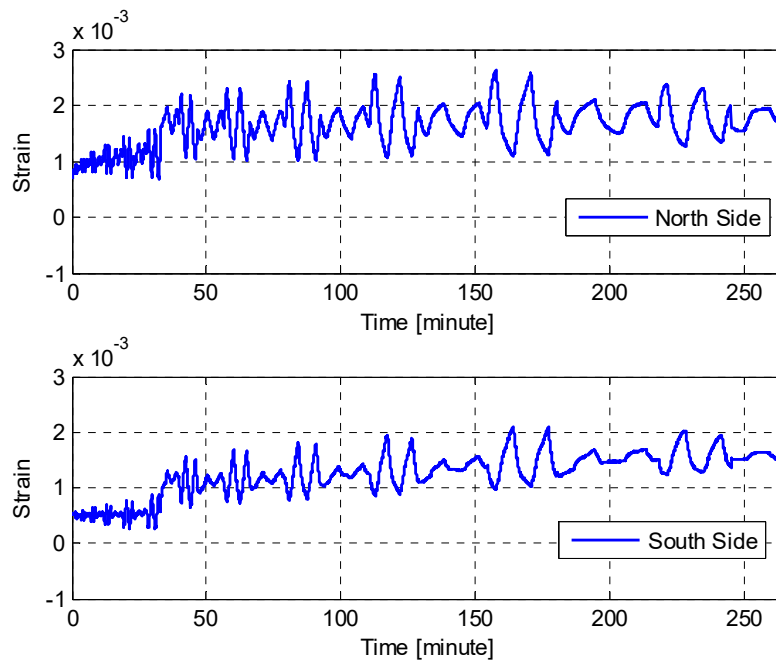


Figure 5.99 History of box-girder deck longitudinal reinforcement strain measured in a rebar aligned with a box-girder web at north and south sides of the column for all cycles.

5.7.2 Box-Girder Web Tie Strain

In addition to monitoring the longitudinal rebars strain in the box-girder, the web tie (transverse) reinforcement strain was monitored as well. The strain at the most critical sections was observed to ensure that no shear yielding took place in any of the box-girder webs. The strains in the ties where the maximum shear forces were expected (the inner and outer box-girder webs, i.e., north and south sides of the column) are plotted in Figures 5.100 and 5.101, respectively. As expected, the shear strain at box-girder webs did not exceed the 0.0026 yield limit of the reinforcement. Note that the capacity design is extended to cover the shear checks for all superstructure components [Caltrans SDC 2013] in addition to the strength check against the column overstrength moments.

5.7.3 Joint Reinforcement Strain

The joint region, one of the most critical regions in the bridge superstructure, must remain essentially elastic in case of extreme earthquake events; brittle shear failure is not allowed according to the Caltrans SDC seismic capacity design approach. As noted earlier, only minor cracks developed in the specimen joint region during cyclic tests of as-built Specimen No. 1. Strains in critical horizontal and vertical joint tie reinforcement were monitored to make sure no yielding took place; see Figure 5.102.

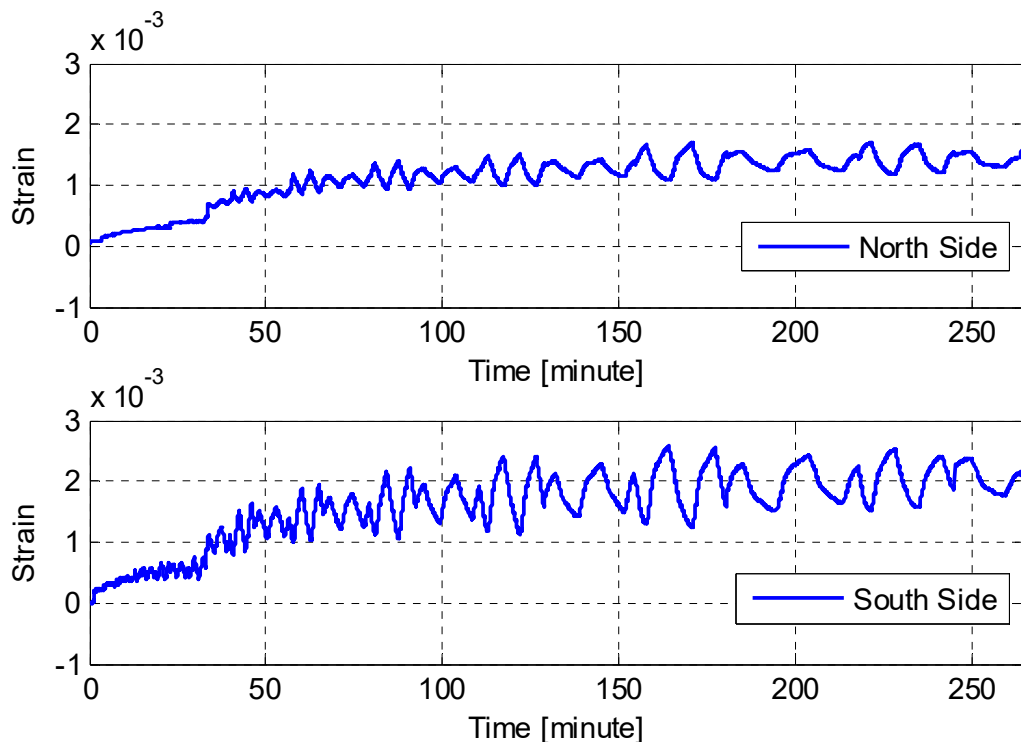


Figure 5.100 History of box-girder web tie reinforcement strain measured at the first tie in an inner web from both the north and south sides of the column for all cycles.

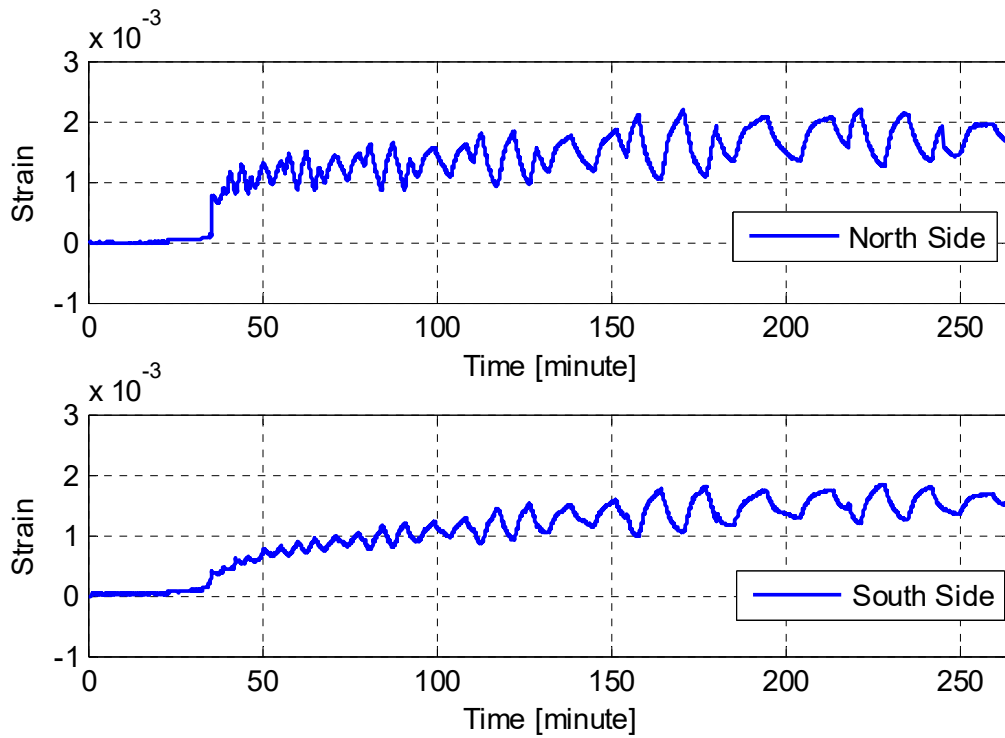


Figure 5.101 History of box-girder web tie reinforcement strain measured at the first tie in an outer web from both the north and south sides of the column for all cycles.

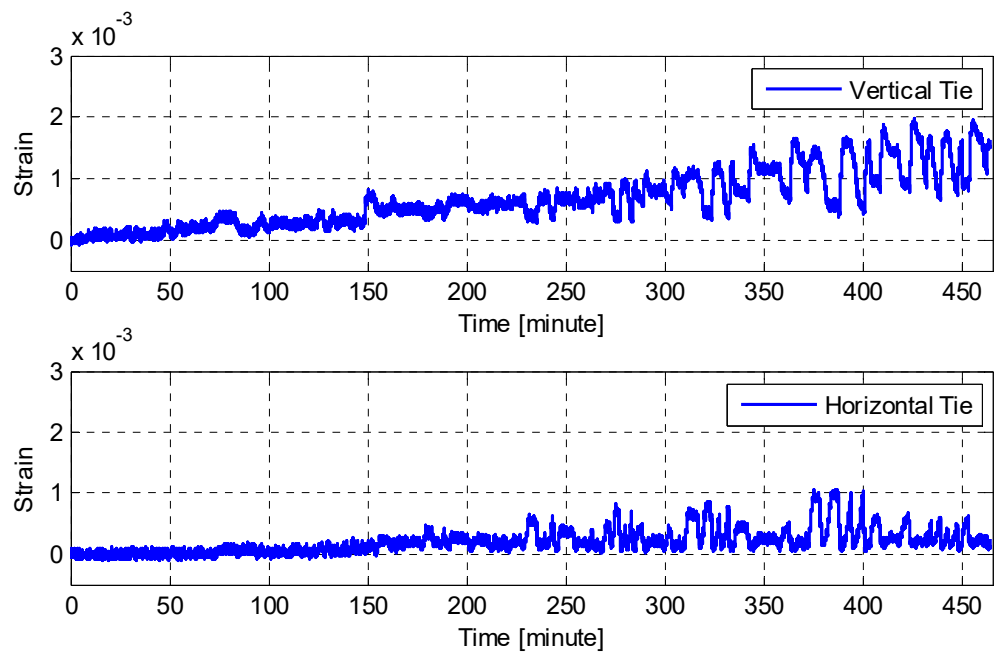


Figure 5.102 Strain history of selected critical joint vertical and horizontal cross-ties.

5.7.4 Cap Beam Stirrups Strain

Shear failure is not allowed in the bent cap beam. For the test specimen's relatively wide cap beam, four-branch stirrups were used for transverse shear reinforcement. as shown in Figure 5.103, The strain exhibited in the inner branches and the outer branches of one of the stirrups at maximum expected shear force location did not reach yield. Thus, it is concluded that all the shear reinforcement in tested Specimen No. 1 did not yield and no brittle shear failure took place.

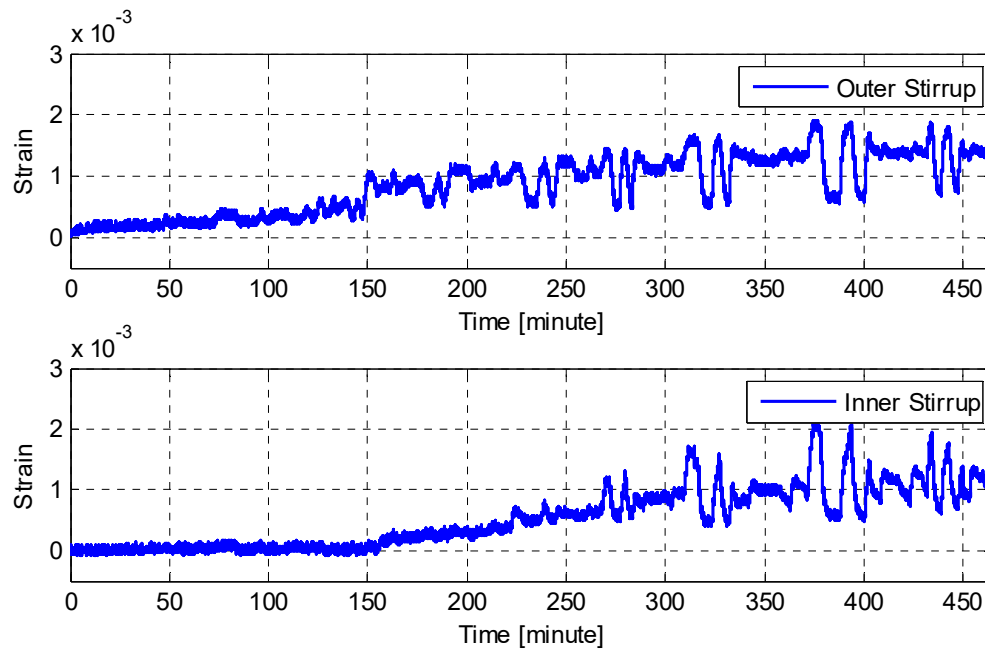


Figure 5.103 Strain history of selected bent cap outer and inner transverse stirrups.

6 Quasi-Static Tests: Repaired Specimen One

As discussed in Chapter 5, Specimen No. 1 was tested as-built in a quasi-static cyclic loading protocol. Specimen No. 1 was repaired and then tested twice; first in a quasi-static test and then for HS trials to validate the newly developed HS communication system. This chapter presents a brief discussions of the undertaken rapid repair procedure and key results from the cyclic loading tests of the repaired Specimen No. 1. The results are compared against the original as-built test for insight regarding the effectiveness of the repair.

6.1 REPAIR PROCEDURE

The damage experienced by Specimen No. 1 after the cyclic tests included extensive concrete spalling, reinforcing steel buckling, and several rupture of several rebar. The repair involved replacing the damaged concrete regions with high-strength mortar, injecting all cracks with high-strength epoxy, adding polymer reinforcing bars next to the ruptured original reinforcing steel bars, and wrapping the column with three layers of unidirectional CFRP layers; see Chapter 3 for more detail on the repair materials. Details of the step-by-step repair procedure are presented below.

The first step required cleaning and hammering out all loose chunks of concrete; see Figure 6.1. The prepared clean plastic hinge region is shown also in the same figure. A drilling machine was used to drill holes along the cracks lines at adequate spacing in the cracked regions to be used for injecting the epoxy. The drilling procedure and final holes pattern viewed from the east side of the column are shown in Figure 6.2. Figure 6.3(a) shows all the drilled holes outfitted with plastic injection ports; the application of a sealant layer of epoxy that covered the cracked zones and around the injection ports to avoid any epoxy leakage during injection. Using a wire brush, the exposed parts of the reinforcing bars were cleaned of any concrete debris and dust that had accumulated from the drilling process. A special type of epoxy for bonding and corrosion protection (BC-020) was used to cover the rebars to enhance the bond with other repair materials. The reinforcing bars after all repairs are shown in Figure 6.3(b). Subsequently, high-strength mortar was used to patch and fill the large voids (wider than 0.75 in.) and cover all the exposed rebars; see Figure 6.4(a).

In a typical repair job following extensive rebars buckling and rupture, the column's cross section is usually increased and new reinforcing steel dowels are implanted. In this study, no new steel rebars were implanted, so that the bent cap or the cap-column joint region were not

altered. This was to confirm that the cap beam remained essentially elastic in its actual condition after the as-built test. In addition, a partial repair ensured that a reasonable enough force capacity remained for the HS test trials. Accordingly, the repair consisted of only restoring the original 18-in.-diameter column and a rapid fabricated on-site form of polymer reinforcing bars. Eight of these polymer reinforcing bars were used and placed next to the ruptured steel rebars. For this purpose, vertical holes that were 8-in. deep were drilled for installing the desired polymer reinforcing bars; see Figure 6.4(b).

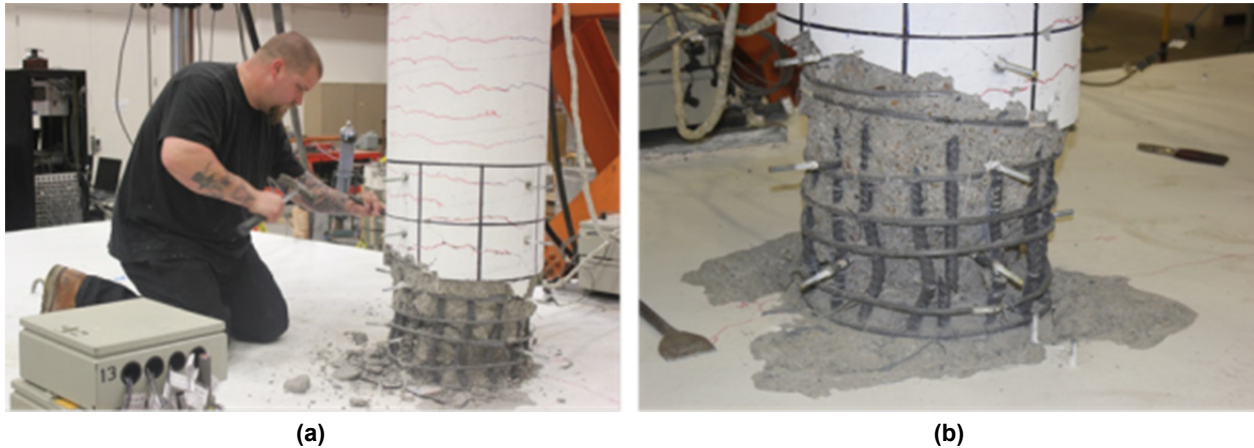


Figure 6.1 (a) Hammering loose concrete in the plastic hinge zone in the tested specimen; and (b) final damaged state of the tested specimen after removal of all loose chunks of concrete.



Figure 6.2 (a) Drilling holes along the cracks for epoxy injection; and (b) final pattern of injection sites for repair with epoxy.



Figure 6.3 (a) Installing the injection ports along the cracks and patching the concrete surface around the ports; and (b) exposed rebars coated with epoxy primer for better bond.



Figure 6.4 (a) Patching the column damaged core with high-strength mortar in the plastic hinge zone; and (b) 8-in.-deep vertical holes to add polymer reinforcing bars.

A typical polymer reinforcing bar was used in the repair procedure consisted of a 20-in.-long strip of the uni-directional carbon fiber sheets that were rolled longitudinally and soaked with epoxy resin; see Figure 6.5(a). Drilled vertical holes were filled with the same epoxy used in soaking the polymer rolled bars before the wet polymer bars were inserted, as shown in Figure 6.5(b). Note that the polymer bars gain their longitudinal tensile strength when they dry. After installation of the CFRP bars, the column–bent cap interface was repaired. This region underwent additional damage and cracking as the vertical holes were drilled. A mix of sand-epoxy paste was used to fill all the voids and to restore a flat bent cap top surface around the column undergoing the repair; see Figure 6.6. After all major voids were patched and the CFRP bars installed, only a final layer of sand-epoxy mixture was needed to compensate for any concrete cover lost in testing and, more importantly, to restore the column’s circular shape to facilitate the application of the CFRP jacket. A sonotube formwork was assembled around the column to restore the 18-in. -diameter column; see Figure 6.7(a). Before any paste was poured inside the sonotube formwork, the injection ports were connected to the epoxy pump. A fluid

RN151 structural epoxy was injected in all cracks through multi-port injection system [see Figure 6.7(b)] at a relatively low pressure to prevent cracks widening or any further damage to the cracked concrete.

After injecting all cracks, installing the added CFRP bars, and patching all damaged parts, the next step was to prepare the column for the CFRP wrapping. A sand-epoxy mixture that was similar to the one used for fixing the column–bent cap interface was poured inside the sonotube formwork; see Figure 6.8(a). One day later the formwork was removed, and all the injection ports that were still in place were removed and the surface was grinded. A view of the column after the sonotube removal and grinding the surface is shown in Figure 6.8(b). Note that the rods sticking out of the column in Figure 6.8 are the instrumentation rods used for installing the LVDTs and are not any remaining injection ports. Figure 6.8(b) also shows that some voids remained as the poured sand-epoxy did not fill all the voids. Therefore, a final layer of the high-strength mortar, previously used in patching the column core damaged parts, was applied to fill any remaining voids and finalize restoration of the column for efficient CFRP wrapping; see Figure 6.9(a). The final surface was then cleaned of any dust or debris, and one coat of RN075 primer was applied to the surface; see Figure 6.9(b). Finally, a total of three layers of FC061 uni-directional carbon fiber sheets were impregnated with RN075 structural epoxy system to form the column CFRP jacket. Each layer was 0.04 in. thick for a 0.12-in.-thick jacket that extended up to the column’s mid-height. Installation of the first layer of the wet carbon fiber sheets at the column lower section and installation of the last layer at the column middle section are shown in Figure 6.10(a) and (b), respectively. Figure 6.11 shows the final repaired column after all CFRP layers were installed.

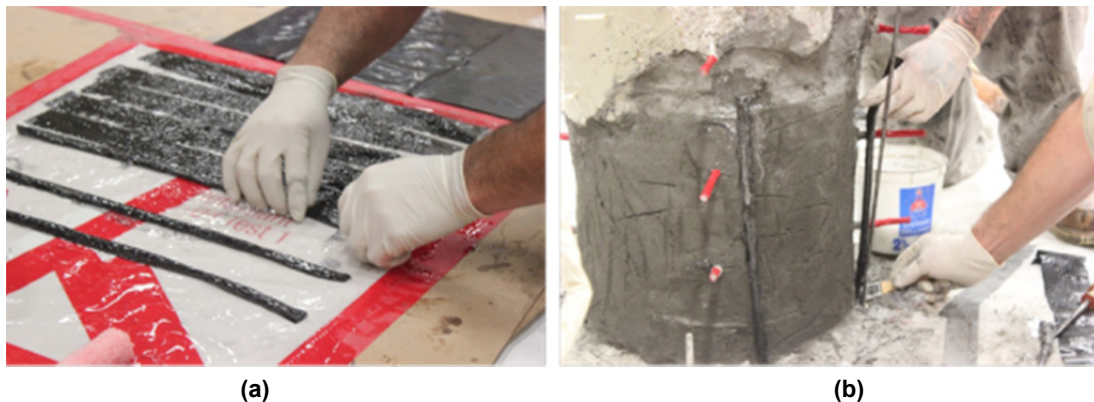


Figure 6.5 (a) Preparation of 20-in.-long CFRP bars using carbon fiber sheets coated with epoxy resin; (b) installing the wet CFRP bars in the holes drilled into the cap beam.



Figure 6.6 (a) Partially fixing the column-bent cap interface using a sand-epoxy mixture; and (b) overview of the partial repaired column after installing all injection ports, CFRP reinforcing bars, and patching the damaged parts in column core and at the column-bent cap interface.



Figure 6.7 (a) Installing the sonotube around the damaged zone to restore the column's circular shape; and (b) injecting fluid epoxy into the cracks using the installed injection ports.



Figure 6.8 (a) Pouring sand-epoxy mixture inside the sonotube formwork to restore the column shape; and (b) view of the partially repaired column after the sonotube was removed.



Figure 6.9 (a) A final layer of high strength mortar was applied to patch any remaining voids; and (b) applying a primer epoxy coat to the surface before applying the CFRP sheets.

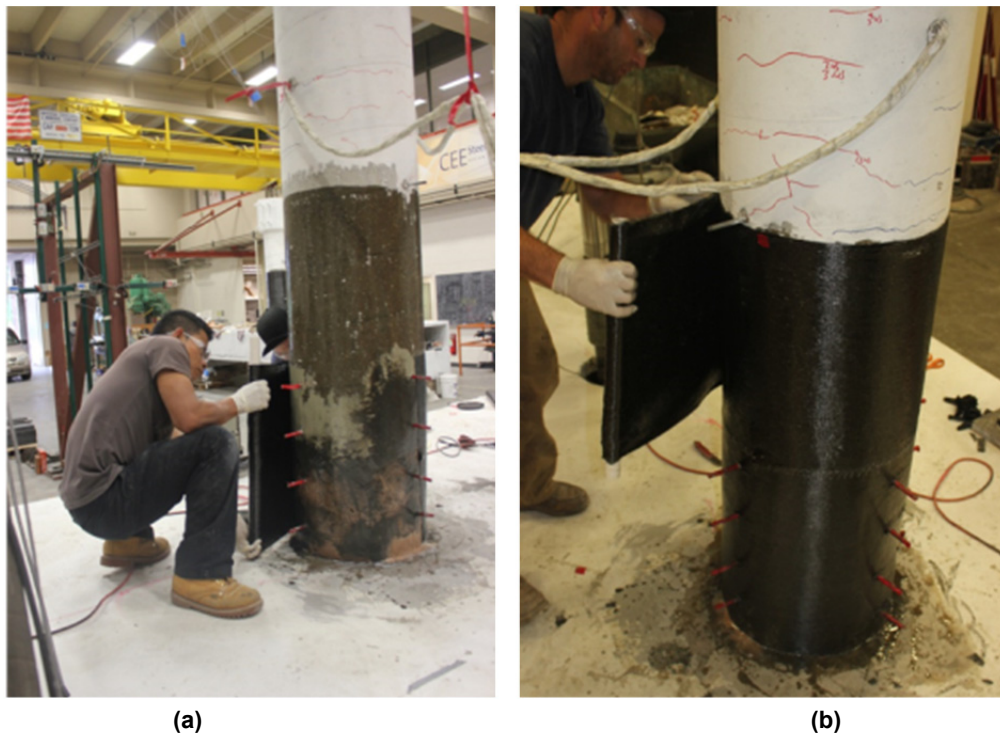


Figure 6.10 (a) Applying the first epoxy-coated CFRP layer at the bottom section of the column; and (b) applying the last CFRP layer at the middle section of the column.



Figure 6.11 Final repaired column after it was wrapped by three CFRP layers.

6.2 PROGRESSION OF TESTING AND DAMAGE

The only difference between as-built Specimen No 1 and repaired Specimen No. 1 was that the cyclic loading tests of the repaired specimen stopped at the 5.44 μ -ductility level. This maintained a minimal force capacity for further HS trial tests but preserved enough cycles at various ductility levels to compare the repaired specimen behavior to the as-built one. The same set-up was used, and a view of the test while transverse and longitudinal loadings were in progress is shown in Figures 6.12 and 6.13, respectively.

Unlike the original unconfined specimen, as a result of the CFRP jacket confinement, no concrete spalling or damage were observed in the repaired specimen tests. Popping sounds of steel reinforcing bars rupture were heard during the tests, indicating that the rebars that had buckled in the previous test had now ruptured. The ruptured steel rebars explain the significant drop in the force capacity observed in both transverse and longitudinal direction, as discussed below. The only visually observed damage was the opening-closing crack at the column-bent cap beam interface as loading progressed. A photograph of the interface cracking that occurred at the peak of the last loading cycle in the transverse direction, corresponding to a 5.44 μ -ductility level, is shown in Figure 6.14.



Figure 6.12 Overview of repaired Specimen No. 1 cyclic loading test set-up when loading is in progress and applied in transverse direction.

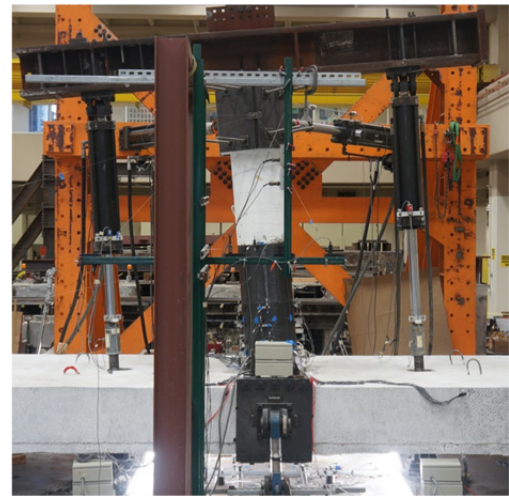


Figure 6.13 Overview of repaired Specimen No. 1 cyclic loading test set-up when loading is in progress and applied in longitudinal direction.

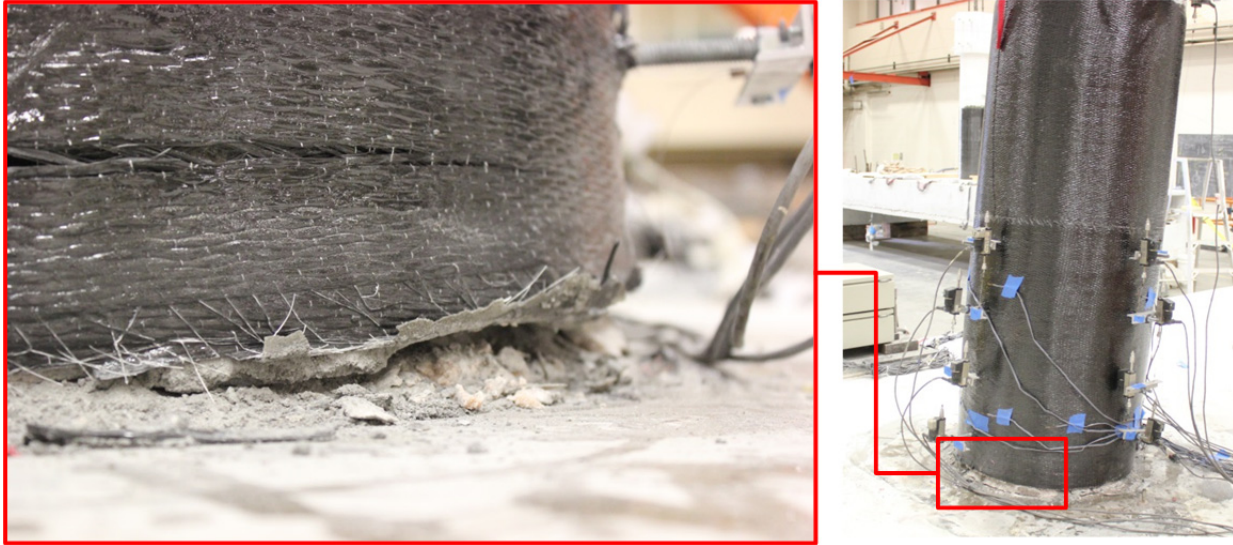


Figure 6.14 Circumferential tear in the CFRP jacket and cracking at the column-bent cap interface as lateral loading progressed.

6.3 GLOBAL BEHAVIOR

An extensive framework for post-processing the data acquired from the as-built Specimen No. 1 cyclic tests was utilized to present the test results and discussion in Chapter 5. For the repaired Specimen No. 1 tests, only selected results that serve the purpose of comparing the behavior of the repaired and as-built specimen are presented and discussed here. This section presents the global forces and displacements obtained from the repaired specimen tests. The computed stiffness in both transverse and longitudinal directions are also discussed. The column and bent cap beam moment-curvature behavior along with selected results of the CFRP jacket strains are presented in the following sections.

The repaired Specimen No. 1 cyclic tests were carried out under a single constant gravity load level of 164 kips, which corresponded to 10% of the axial column capacity. Note that as-built Specimen No. 1 tests were conducted under two levels of gravity load; for repaired Specimen No. 1, only the second level of gravity load was used (10%). The force applied through each of the two vertical actuators along with the total resulting gravity load throughout the full course of repaired Specimen No. 1 cyclic tests is shown in Figure 6.15. The total vertical reactions at the two struts at the ends of the bent cap beam as compared to the total gravity load are shown in Figure 6.16. The total reactions at the struts are almost 70% of the total gravity load (115 kips to 164 kips ratio), i.e., the box-girder ends where the specimen was supported on the two cast-in-place beams attracted the remaining 30% of the gravity load. Note that the total reaction at the two struts is almost constant throughout the transverse and longitudinal lateral loading. This confirms that two equal but opposite reactions always existed at the two struts during the lateral transverse loading. Also, no additional reactions were generated during lateral longitudinal loading because the resulting moment did not occur within the bent cap beam plane and did not generate any vertical reactions at the struts.

Figure 6.17 verifies that the intended load pattern was applied correctly, showing the displacement orbit of all the loading cycles in both transverse and longitudinal directions. The cross-displacement orbit illustrates that both transverse and longitudinal loadings were applied independently, i.e., one direction at a time. However as shown in the figure, at extreme longitudinal displacements, a small transverse displacement was obtained, which was due to the triangular actuator set-up flexibility in the longitudinal direction. The displacement history that reflects the FEMA 461 [2007] load pattern for all repaired Specimen No. 1 cyclic tests in transverse and longitudinal directions is shown in Figure 6.18. Only one cycle of loading was applied in the last group of cycles in both transverse and longitudinal directions. The testing was then stopped to avoid extensive damage to the repaired Specimen No. 1 and maintain a reasonable residual force capacity for the HS trials. The history of the measured forces is shown in Figure 6.19. It is obvious that the force capacity was decreasing significantly as testing proceeded, which could be related to the rupture of the rebar during the test. The test was stopped when the residual force capacity reached about 10 kips in one side and 20 kips in the other. This was considered a reasonable force capacity to preserve for conducting the HS trials.

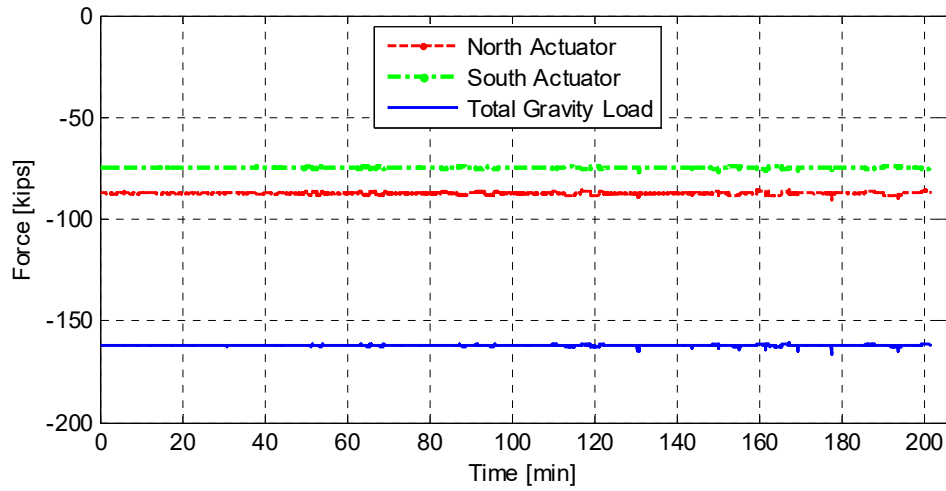


Figure 6.15 Gravity load history at both vertical actuators and total applied gravity load throughout the repaired Specimen No. 1 transverse and longitudinal cyclic loading tests.

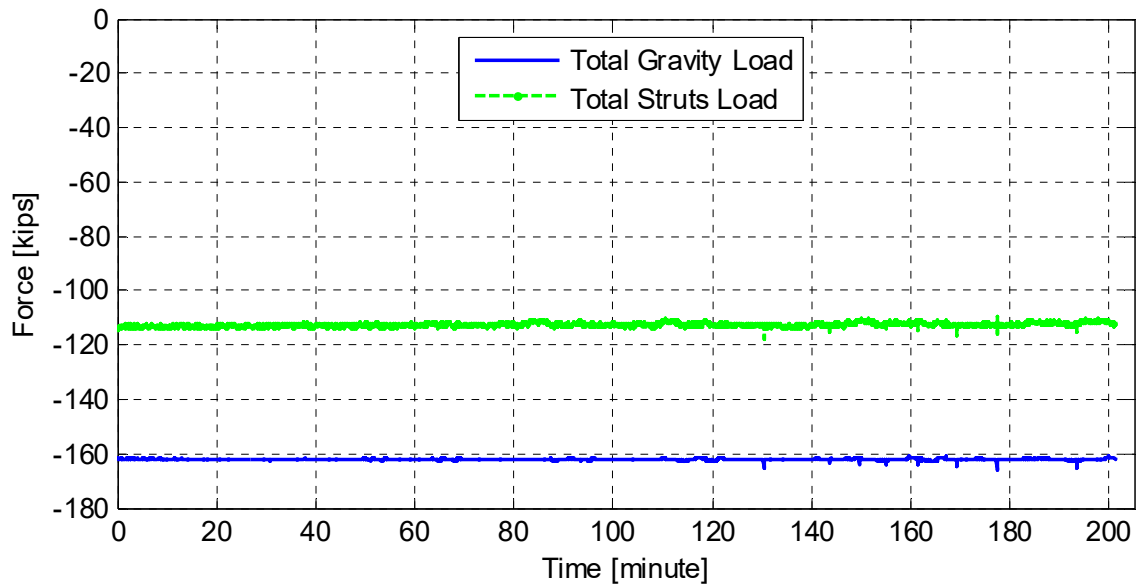


Figure 6.16 Total vertical reaction at the two bent cap end struts versus the total applied gravity load throughout the repaired Specimen No. 1 transverse and longitudinal cyclic loading tests.

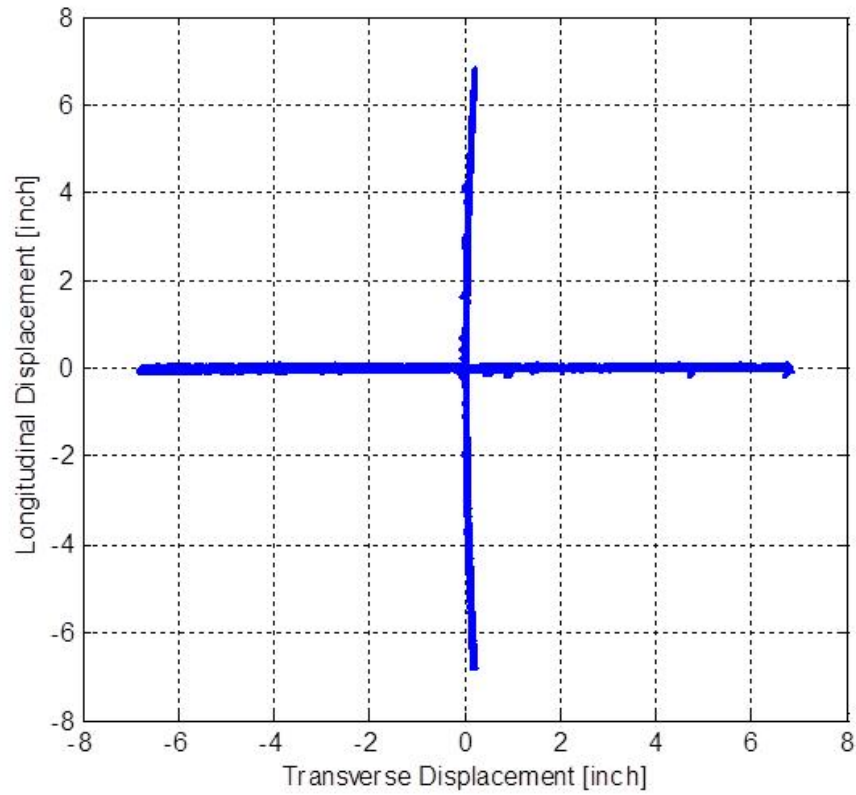


Figure 6.17 Displacement orbit (plan view) of the lateral loading pattern applied to the repaired Specimen No. 1.

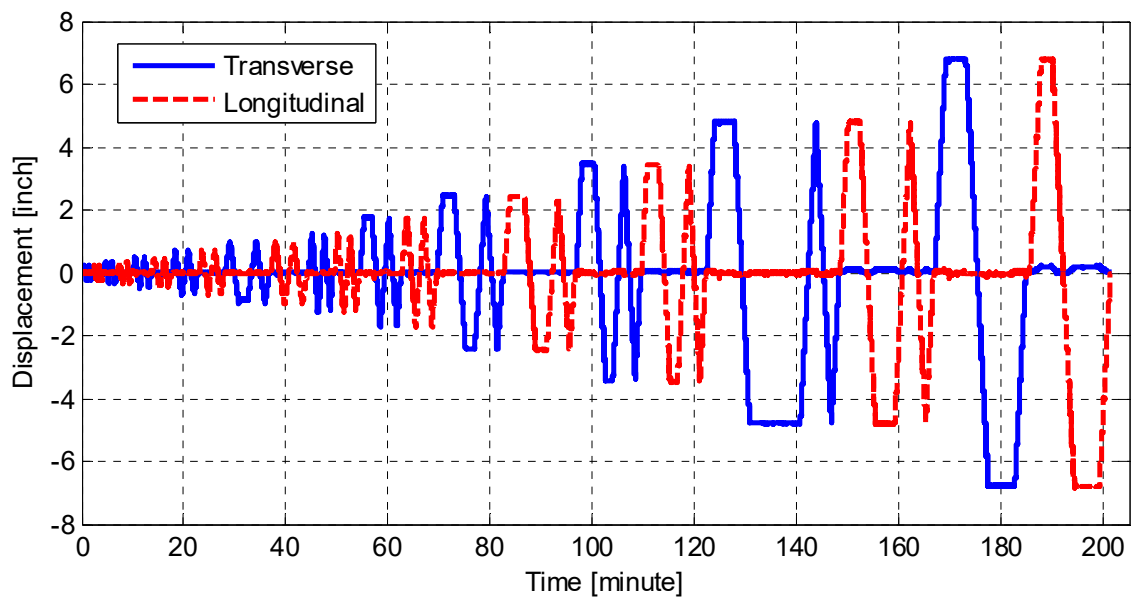


Figure 6.18 Displacement history of the lateral cyclic loading pattern applied during the repaired Specimen No. 1 tests in transverse and longitudinal directions.

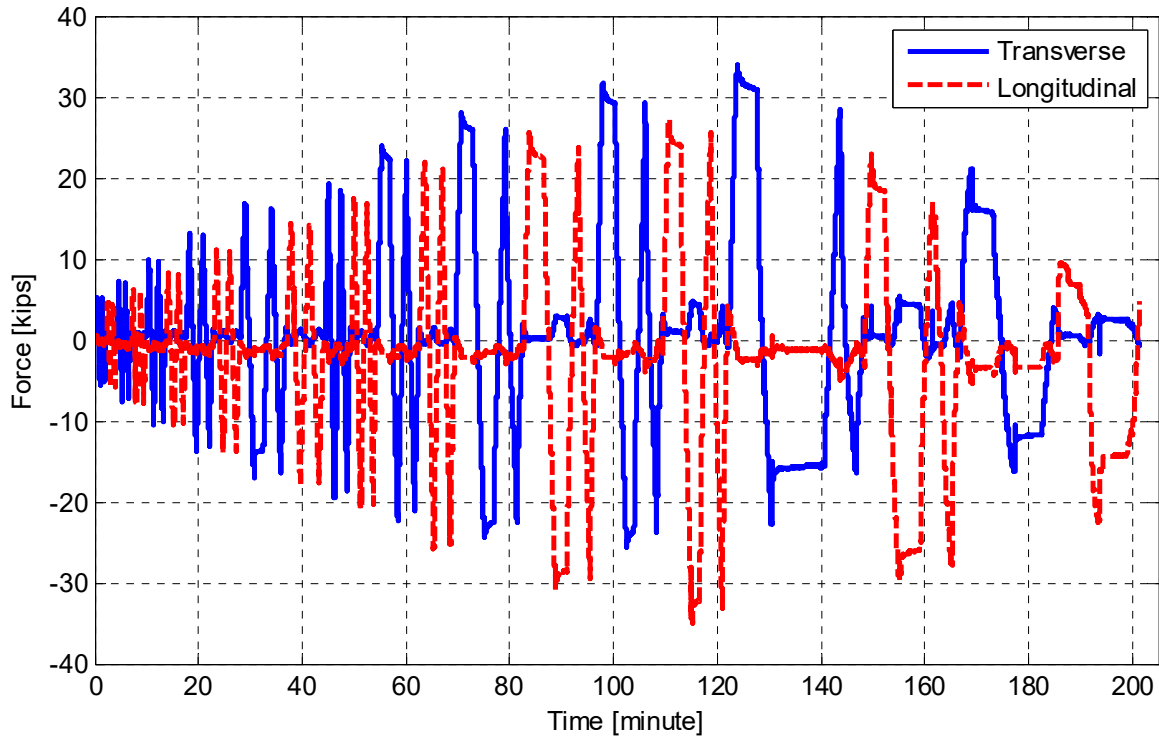


Figure 6.19 Lateral force history measured during testing the repaired Specimen No. 1 under lateral cyclic loading in transverse and longitudinal directions.

To evaluate the effectiveness of the repair procedure, the global and local behaviors for both the as-built and the repaired specimens were compared. For a meaningful comparison, the overall residual force and secant stiffness obtained from the last loading cycle of the as-built specimen were compared to the maximum corresponding quantities from the repaired specimen in both transverse and longitudinal directions. A summary of the as-built and repaired Specimen No. 1 force and stiffness comparison is shown in Table 6.1. The ratio of the increase in the force capacity and secant stiffness from the final as-built state due to the repair is computed and also shown. Figure 6.20 compares the overall force-displacement relationship for all as-built and repaired Specimen No. 1 cyclic loading test runs in both transverse and longitudinal directions. Figure 6.21 compares the stiffness degradation as loading proceeded in both as-built and repaired Specimen No. 1 tests, as represented by the secant stiffness value against the loading cycle ductility level in both transverse and longitudinal directions.

From Table 6.1 and Figure 6.20, it is observed that the repair led to a 22% and 25% increase of the force capacity from the last residual force obtained from the as-built tests when loading progressed in the north longitudinal and west transverse directions, respectively. Meanwhile, the repair did not enhance the force at all or just slightly increased it when the specimen was loaded in the east transverse and south longitudinal directions. This is attributed to the fact that the CFRP reinforcing bars that replaced the ruptured steel reinforcing bars were added mainly in the east and south sides of the column, i.e., when reinforcement is added in one side—the east side—of the column, it enhanced the moment capacity when the column was

pushed in the opposite side, i.e., west side. In addition, the force increase can be attributed to the confinement effect that helped engage the buckled rebars before they ruptured.

While only a maximum of 25% increase in column capacity was obtained in one side, a significant increase of the stiffness was observed due to the repair. It is expected that the moment of inertia and, in turn, the stiffness of the column should increase because the column full cross section was restored and well-confined. Table 6.1 shows a huge improvement in the stiffness—well above 300% of the final soft state—was reached at the end of the as-built tests. As shown in Figure 6.2,1 the initial stiffness obtained from the first loading cycle is slightly higher in the transverse direction than the longitudinal direction; this observation is consistent in both as-built and repaired specimen tests. Note that the final stiffness estimated for the last loading cycle of the repaired specimen tests is lower than what was estimated for the as-built specimen test. This can be tied to the observed crack at the column-bent cap interface that led to this softer behavior at the end of loading; see Figure 6.14.

Table 6.1 Repaired Specimen No. 1's improved force and stiffness relative to the as-built residuals.

Direction of loading		Force (kips)			Stiffness (kip/in.)		
		As-built residual	Repair	Increase ratio (%)	As-built residual	Repair	Increase ratio (%)
Transverse	West	-20.68	-25.91	25.3	5	22.3	346.0
	East	33.63	33.58	-0.1			
Longitudinal	South	-25.06	-26.09	4.1	4.8	20	316.7
	North	24.79	30.35	22.4			

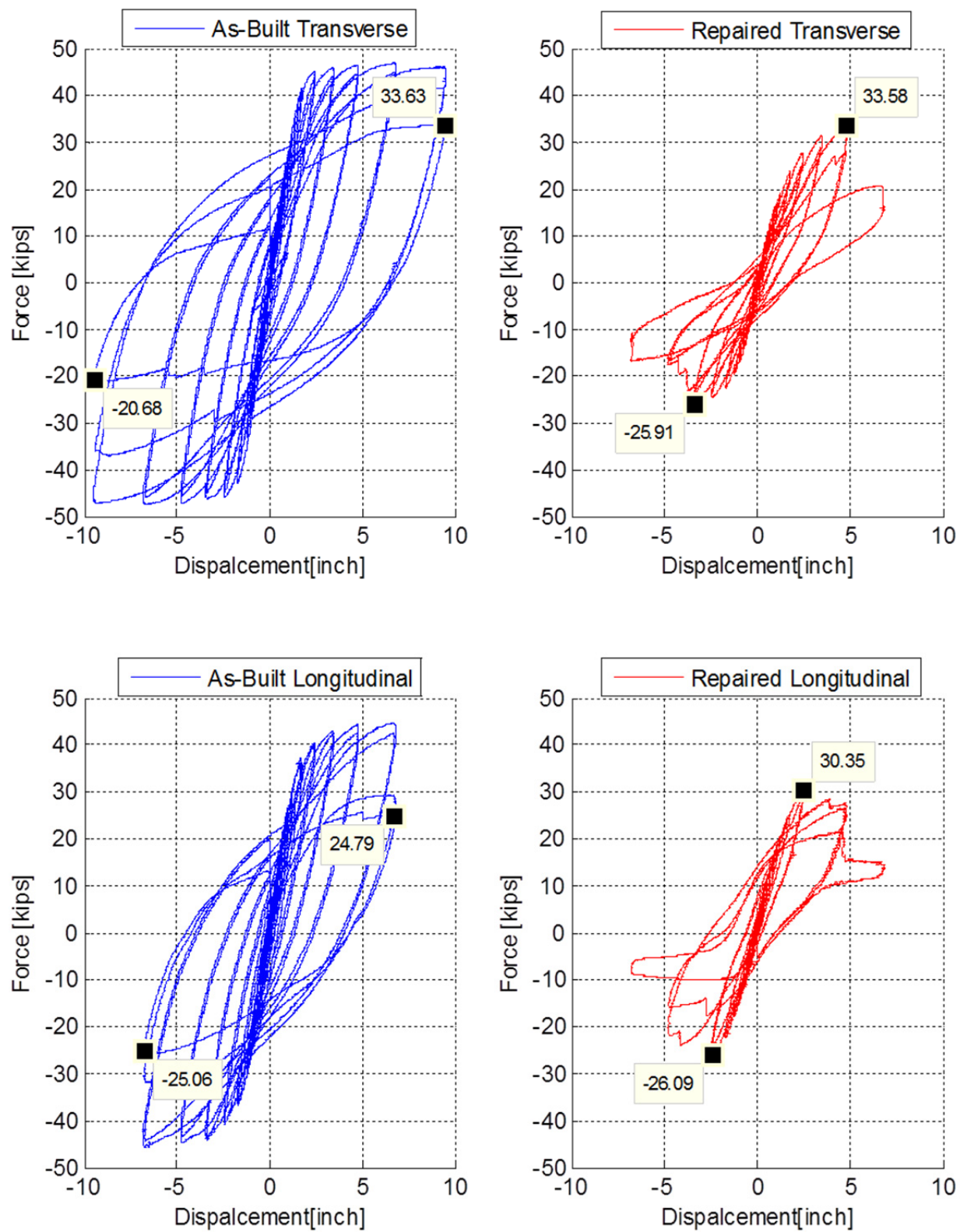


Figure 6.20 Comparison of force-displacement relationships for the as-built and repaired Specimen No. 1 cyclic loading tests in both transverse and longitudinal directions.

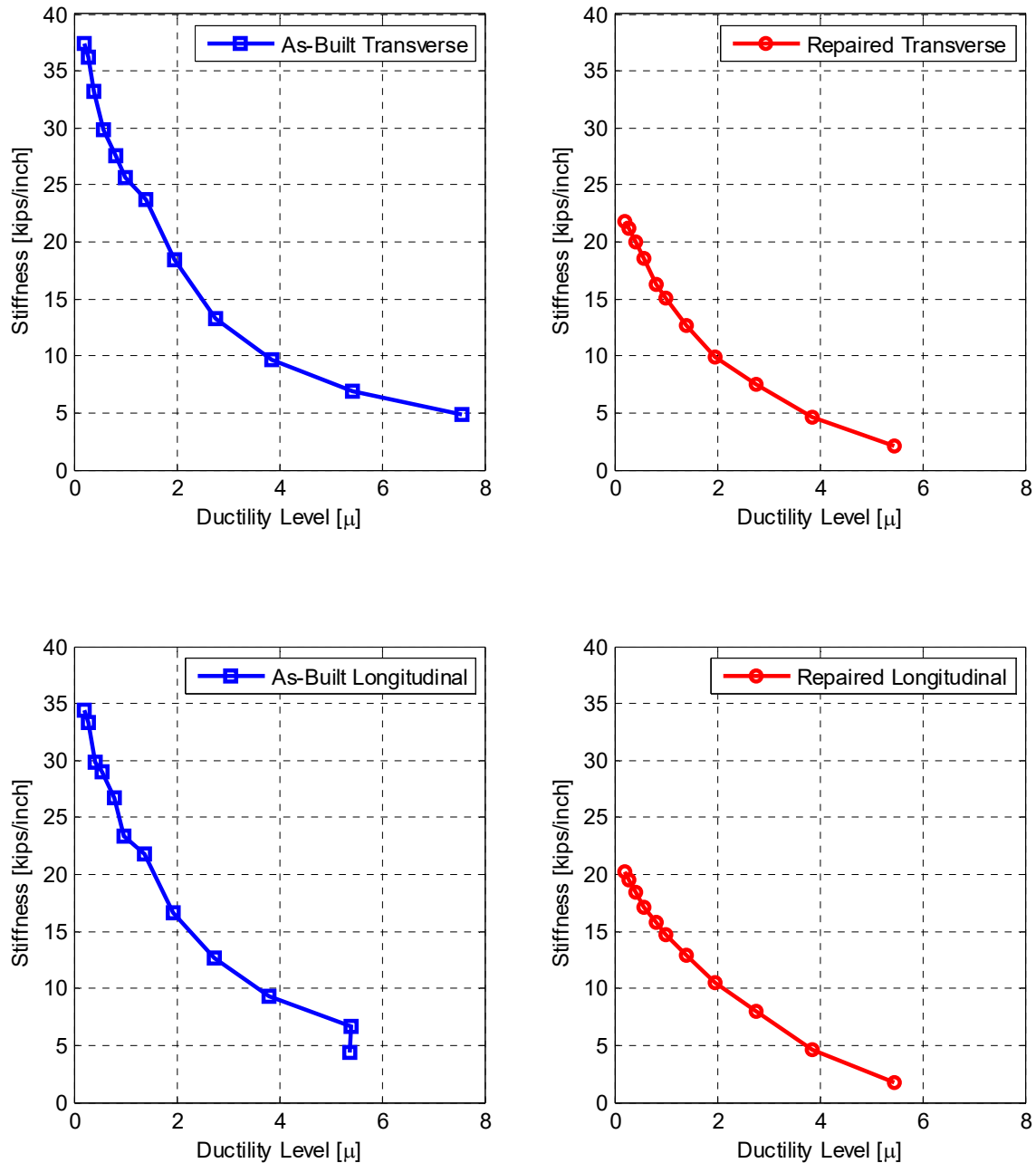


Figure 6.21 Comparison of secant stiffness degradation relative to the ductility levels for the as-built and repaired Specimen No. 1 cyclic tests in both transverse and longitudinal directions.

6.4 COLUMN LOCAL BEHAVIOR

Similar observations can be drawn from the column local behavior and extrapolated into understanding the global behavior. That is because the overall column-cap beam-box girder behavior was mainly governed by the column behavior, which agrees with the Caltrans SDC seismic capacity design objective. Figure 6.22 compares the moment-curvature behavior of the

column for the as-built and repaired specimen tests. The results for the curvature capacity of the as-built test to the results for the repaired specimen are comparable. Note that the residual moment capacity from the as-built tests are not shown in the figure because the last run in both transverse and longitudinal direction of the as-built tests, which were excluded from the plots, experienced extensive spalling and bar ruptures that displaced the LVDTs and led to incorrect curvature estimates. Nevertheless, the increase in the moment capacity is proportional to the increase in the force capacity, as previously discussed.

Worth noting is how the moment-curvature distribution of the columns varied at different height levels inside or outside the plastic hinge zone. The moment-curvature relationships obtained at four different levels are shown in Figures 6.23 and 6.24 for the transverse and longitudinal directions, respectively; see Chapter 3. As shown in both figures, unlike in the as-built case, for repaired Specimen No. 1 all the curvatures were concentrated in level 1, which is nearest to the column-bent cap interface. This implies that in the regular column plastic hinge mode of failure, the damage extended throughout the plastic hinge zone. However, in case of the well-confined repaired specimen column, all the damage was tied to an opening gap and separation that took place at the column-bent cap interface. Thus, the whole repaired column experienced a rigid body rotation, as illustrated in Figure 6.25.

Verification that the rigid column had rotated was done by computing the rotation at the column's base from the estimated curvature and related it to the column's top displacement. The rotation of the column in the last transverse loading cycle was found to be 4.2° . The corresponding displacement at the column's point of loading was roughly estimated using the column's height, as shown in Figure 6.25. A lateral displacement of 6.59 in. was associated to a 4.2° -rigid column rotation, which was compared against the 6.8 in. actual applied displacement for this loading cycle. This 3% difference between the actual displacement and that corresponding to a rigid column rotation supports the experimental observation that the well-confined column limited the damage to its interface with the cap beam.

The rigid column rotation observation can be tied to rocking column behavior exhibited in other bridge configurations. This study tested the column and bridge superstructure in an inverted position, i.e., all the column damage that was observed would be located at the column top in the correct orientation. The specimen's prototype bridge is a three-column bent with pinned pile caps at the supports; therefore, although the column in this study is not a rocking column, useful observations can be extended to rocking columns. In bridge configurations where the pile caps provide full fixation, a CFRP jacket that well-confines the plastic hinge zone of the column at the bottom could promote rocking column behavior. Note that most of the recent studies that have focused on resilient bridge columns have tied resiliency to the rocking behavior that is achieved using different techniques, e.g., self-centering prestressing, hybrid fiber RC, or dual shell (Trono et al. [2014] among others). A CFRP jacket could be another technique to obtain resilient columns and is worth further investigation.

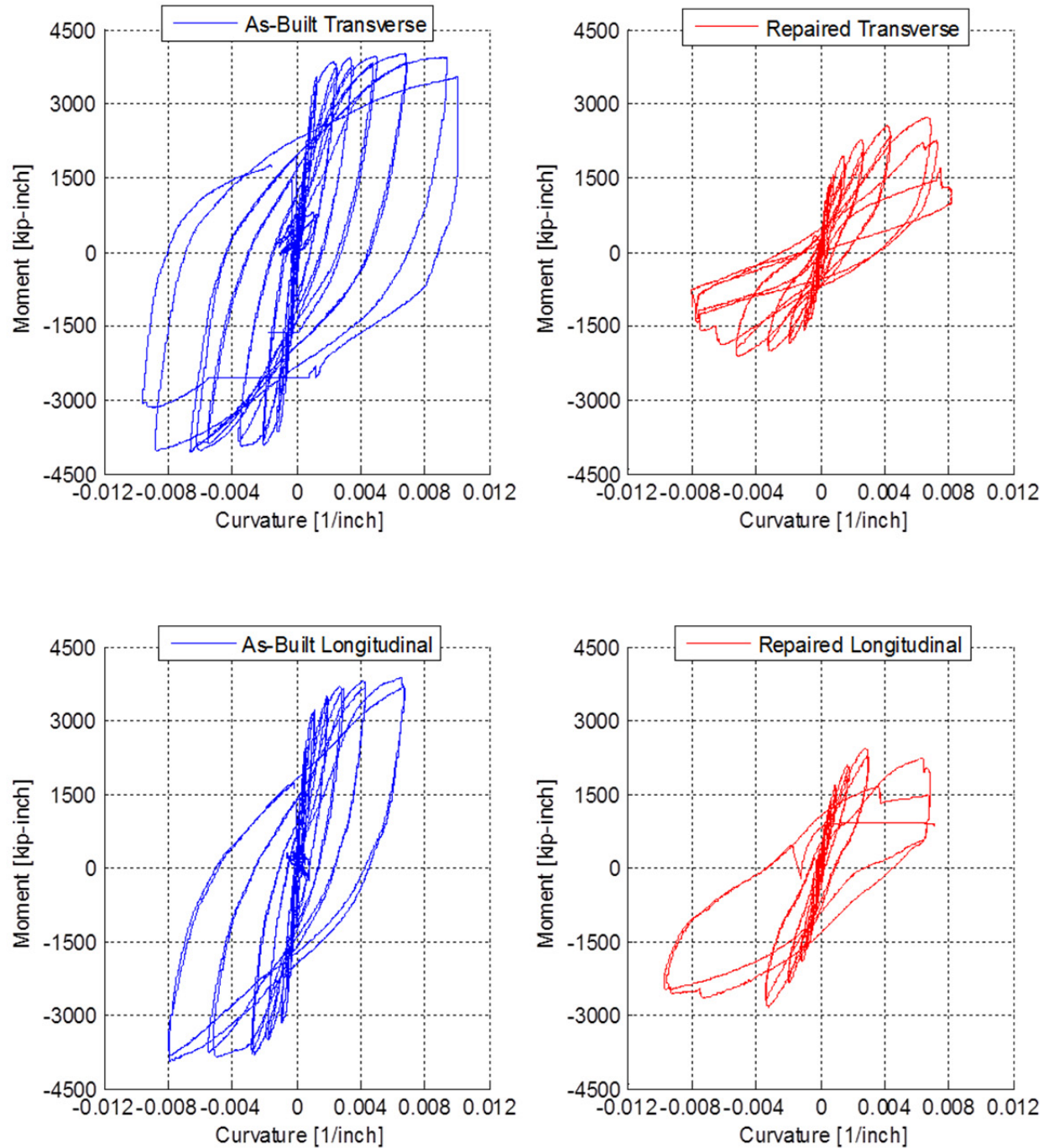


Figure 6.22 Comparison of moment-curvature relationships at the base of the column from the as-built and repaired Specimen No. 1 cyclic loading tests in transverse and longitudinal directions.

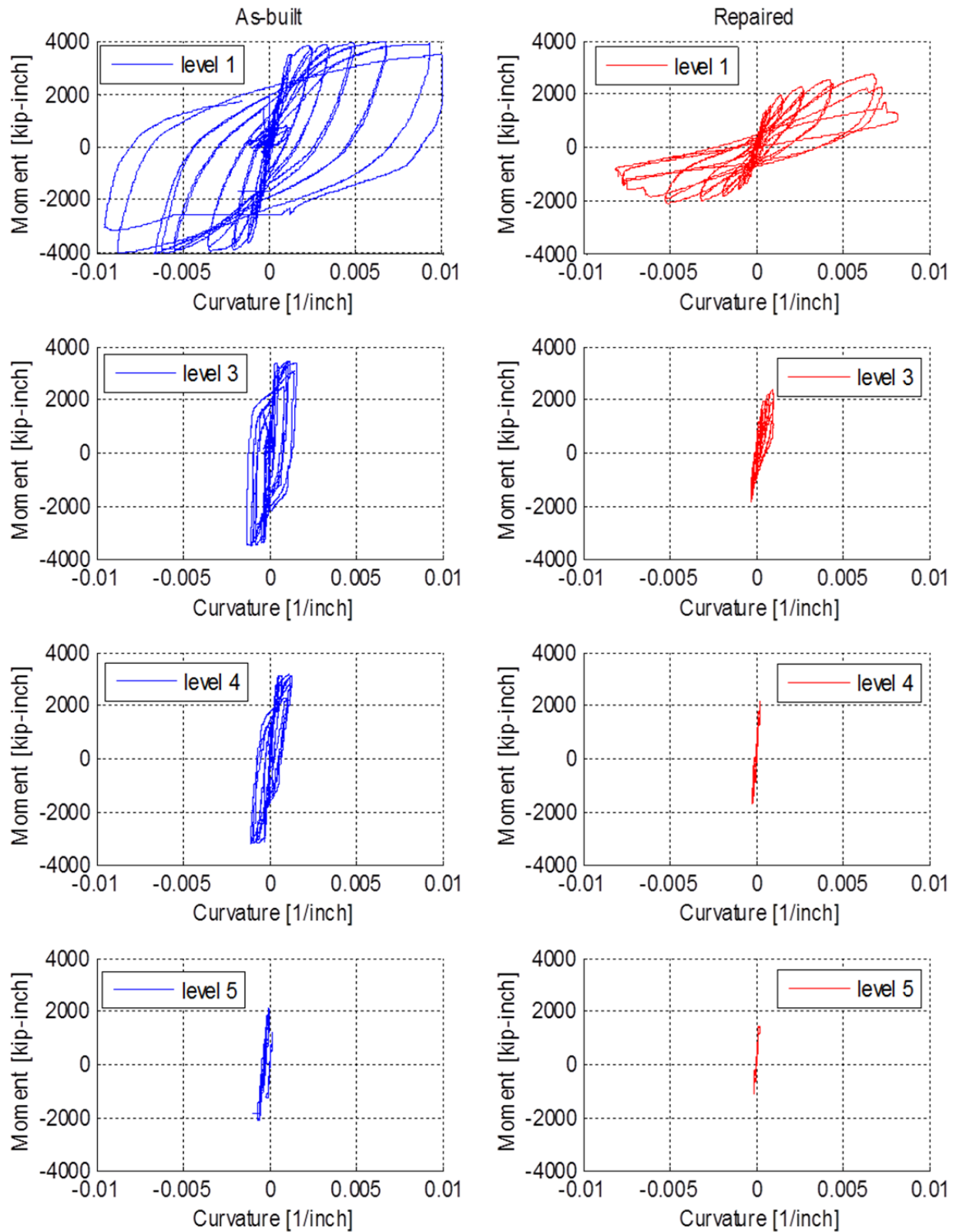


Figure 6.23 Comparison of moment-curvature relationships at different levels of the column from the as-built and repaired Specimen No. 1 cyclic loading tests in transverse direction.

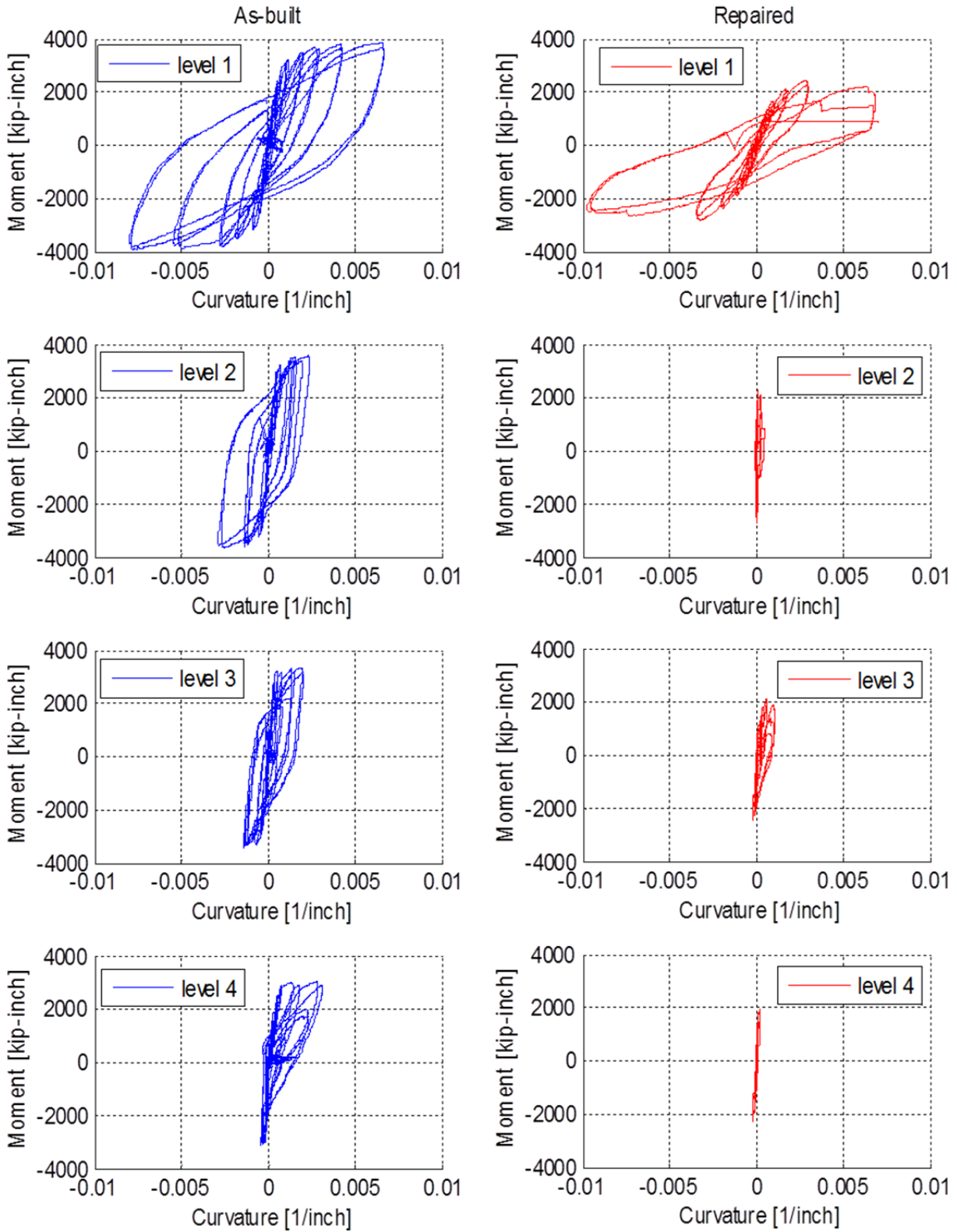


Figure 6.24 Comparison of moment-curvature relationships at different levels of the column from the as-built and repaired Specimen No. 1 cyclic loading tests in longitudinal direction.

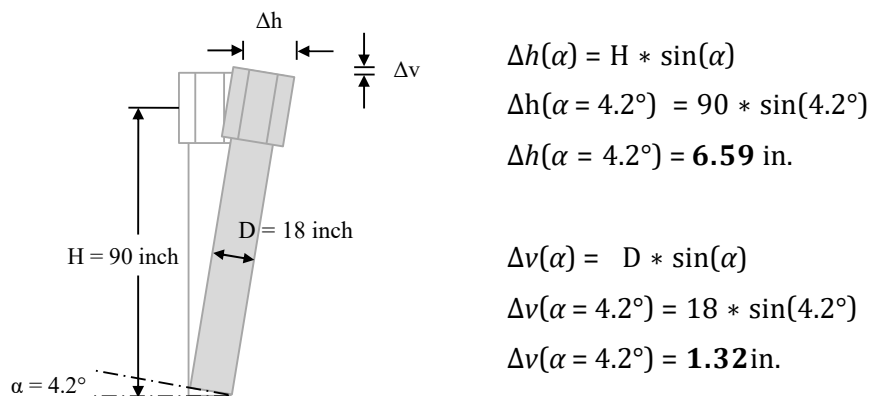


Figure 6.25 Calculation of the column head displacement for rocking as a rigid body around the base.

6.5 CAP BEAM LOCAL BEHAVIOR

One of the main reasons to carry out a set of cyclic loading tests on repaired Specimen No. 1 was to verify the essentially elastic cap beam behavior. It has been mentioned several times that a bridge seismic capacity design approach limits all damage to the column and that the bent cap beam must stay essentially elastic. All the test results and discussion in Chapter 5 shows that the as-built specimen behavior complied with the Caltrans SDC requirements. However, it was desired to further involve the bent cap beam in a second set of cyclic loading to verify whether it remained elastic after the extensive yielding observed from the as-built tests. The reactions observed at the beam end struts were used to calculate the cap beam moments, while the strains measured in the cap beam top and bottom reinforcement were used to estimate the curvature. To verify that the moment values are correct, moment equilibrium at the column-bent cap joint due to lateral loading only was sought. The total cap beam moment from both sides of the joint along with box-girder torsion due to lateral transverse loading should sum up to the column moment. From pre-test analysis, the component from the box-girder torsion, especially for the case of extensively cracked section, was negligible. Thus, the total cap moment should be approximately the same as the column moment, which is verified in Figure 6.26 for repaired Specimen No. 1 and similar to Figure 5.62 for as-built Specimen No. 1. The two individual components that contributed to the total bent cap beam moment, namely the moment at sections B and D, are shown in Figure 6.27.

The obtained cap beam moments from repaired Specimen No. 1 tests were also compared with as-built Specimen No. 1 to verify the essentially-elastic state of the bent cap beam. The moment history for the cap beam at Section B is shown in Figure 6.28 for both as-built and repaired Specimen No. 1 cases. The criterion used to judge whether the cap beam had remained elastic or not is the moment-curvature relationship at different loading levels and reversals. The moment-curvature relationships for the as-built and repaired Specimen No. 1 tests are compared at both Sections B and D in Figures 6.29 and 6.30, respectively. The residual strains from the as-built test were not selected from the start of the repaired specimen test due to possible load relaxation and instrumentation, and data acquisition reset. Thus, the curvature values estimated

from the strains were set to zero as a starting point of plots of the repaired specimen tests; see Figures 6.29 and 6.30. That said, this should not change the way those plots are interpreted. The main objective here was to see how the moment-curvature relationship related as loading progressed and its direction reversed. The figures demonstrate that the cap beam in the repaired specimen tests showed linear elastic behavior at all loading cycles and reversals in both transverse and longitudinal loading directions. In addition, the cap beam experienced less moment demands during the repaired specimen tests and did not reach the yielding moment value. Sample plots of the instrumented bent cap beam reinforcing steel bars strain history at Sections B and D are presented in Figures 6.31 and 6.32, respectively. Given a yielding strain value of 0.0026 ($= 2600 \mu\text{strain}$), the cap beam rebars either slightly yielded or did not yield at all; see Figures 6.31 and 6.32. Although the cap beam extensively yielded during the as-built specimen tests, it did not yield at all in the repaired specimen tests due to reduced demand. Therefore, the behavior of the bent cap beam that was observed in the as-built specimen testing is experimentally verified to be essentially elastic because the cap beam did not yield or show any plastic or residual strain when it was retested in the repaired specimens.

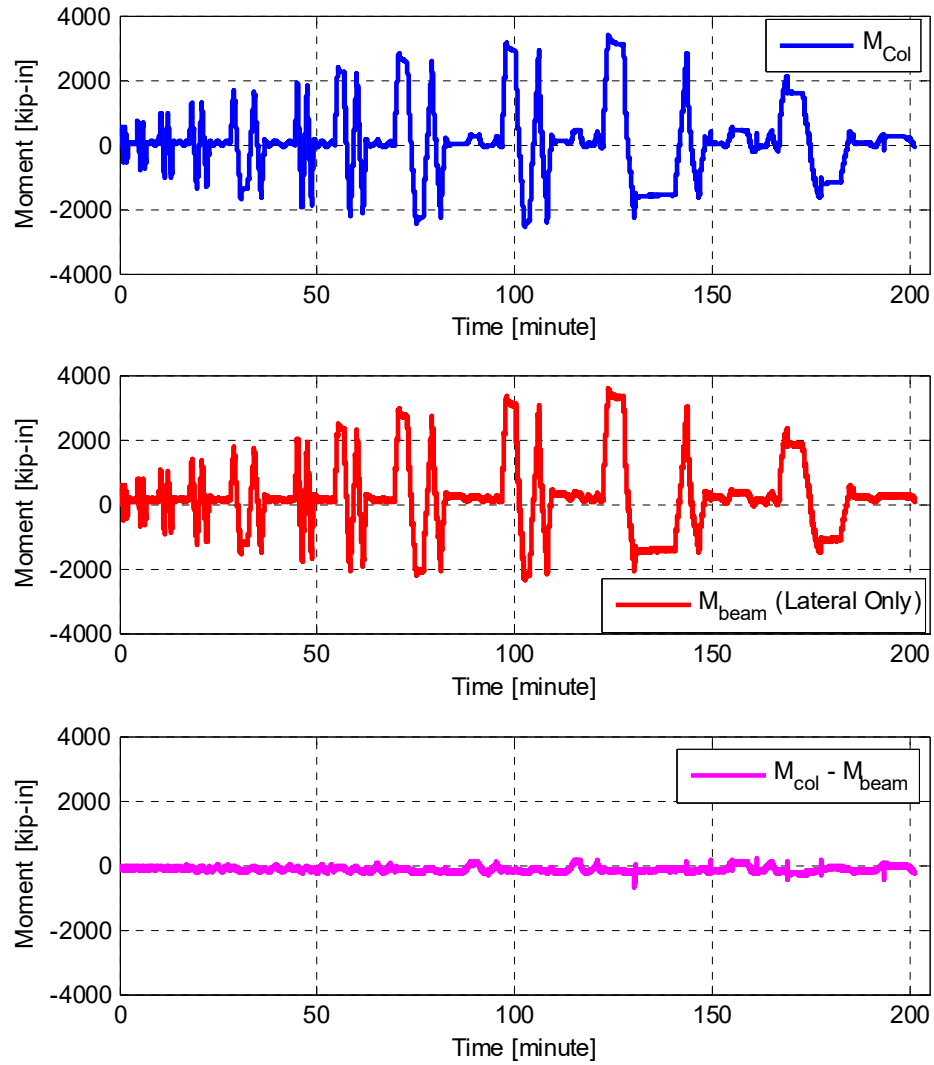


Figure 6.26 Column and total bent cap beam moment history for all repaired Specimen No. 1 cyclic loading tests in both transverse and longitudinal directions.

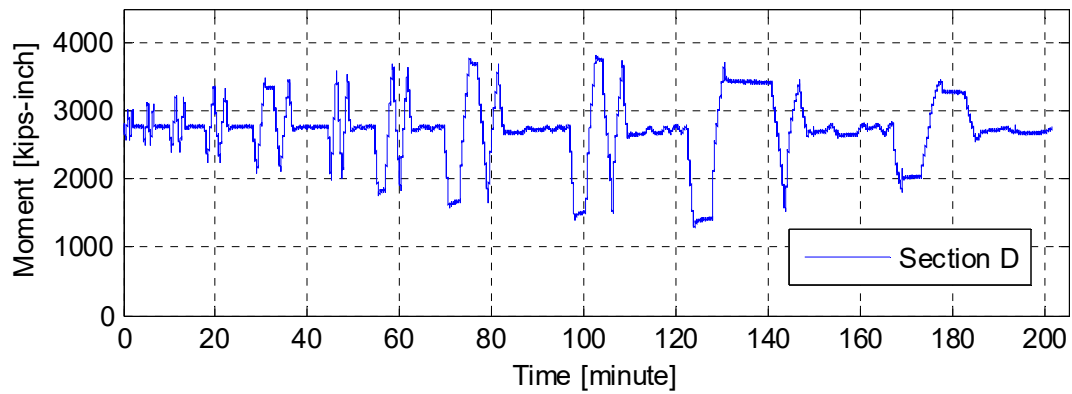
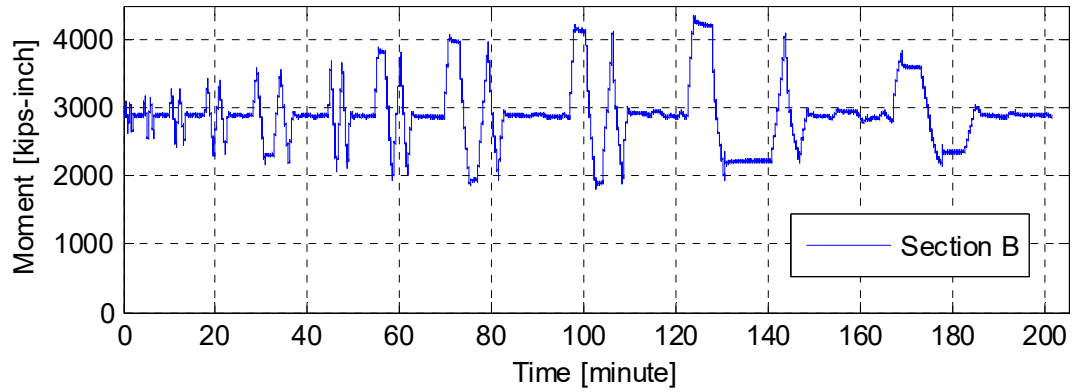


Figure 6.27 Bent cap beam moment history at both Sections B and D for all repaired Specimen No. 1 cyclic loading tests in both transverse and longitudinal directions.

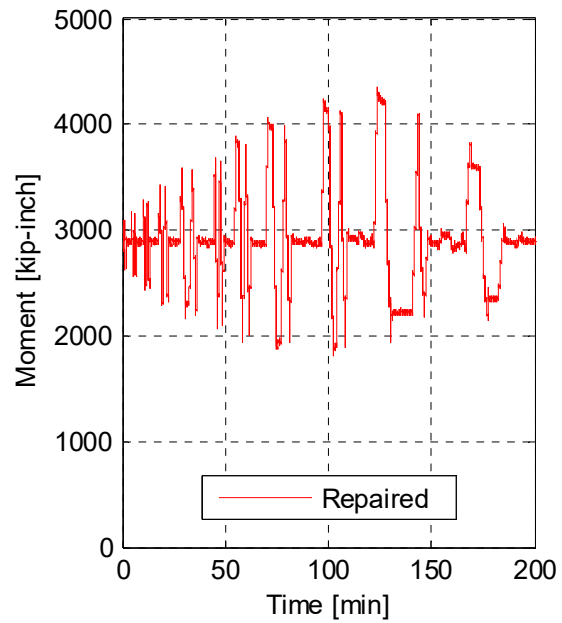
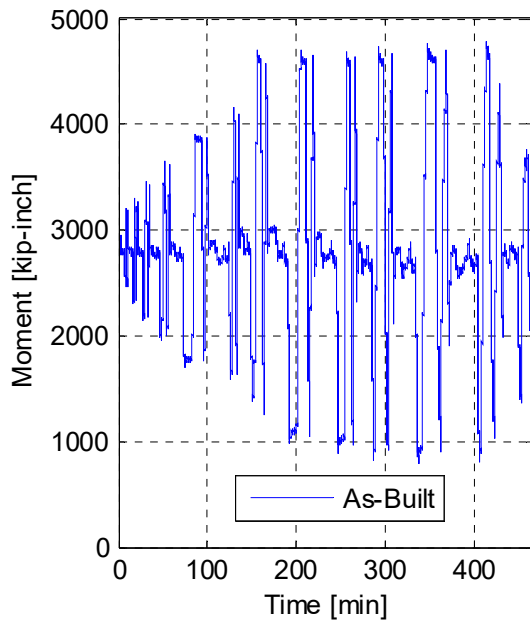


Figure 6.28 Comparison of bent cap beam moment at Section B for all as-built and repaired Specimen No. 1 cyclic loading tests in both transverse and longitudinal directions.

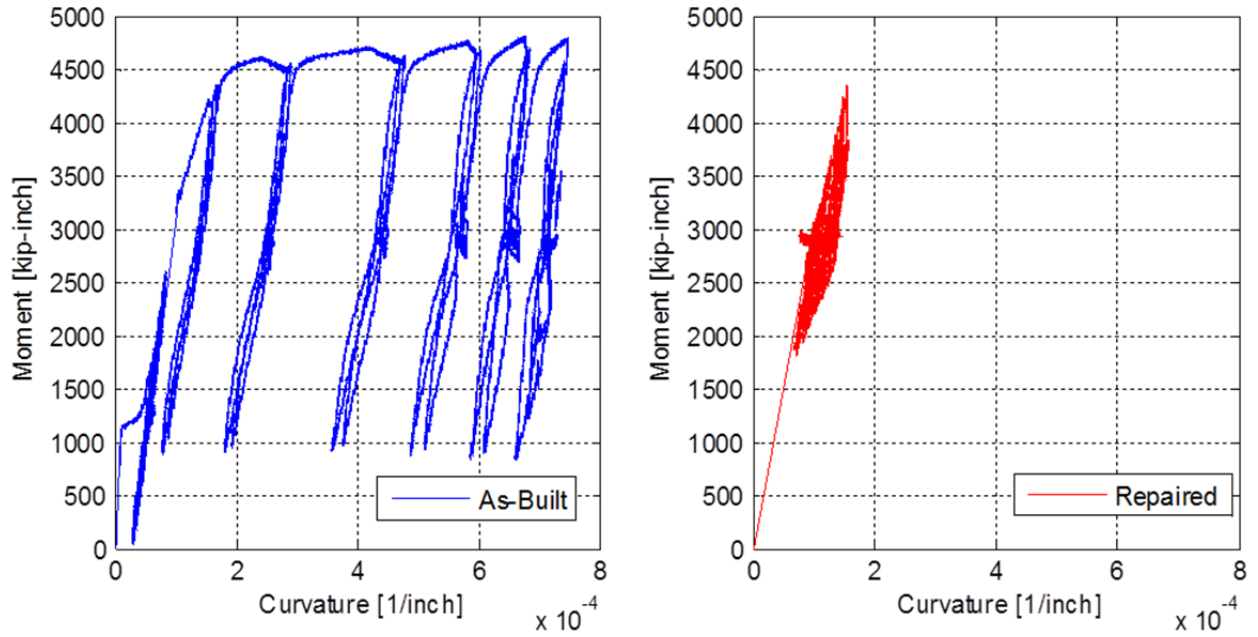


Figure 6.29 Cap beam moment–curvature relationship comparison between Specimen No. 1 as-built and repaired tests at Section B.

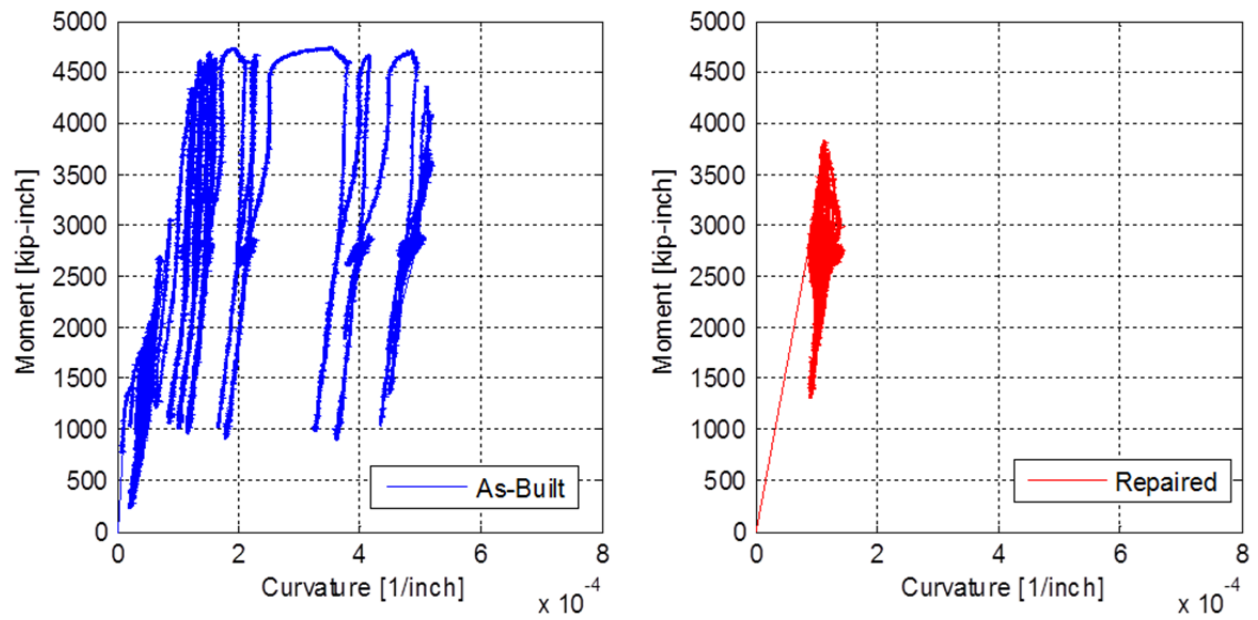


Figure 6.30 Cap beam moment–curvature relationship comparison between Specimen No. 1 as-built and repaired tests at Section D.

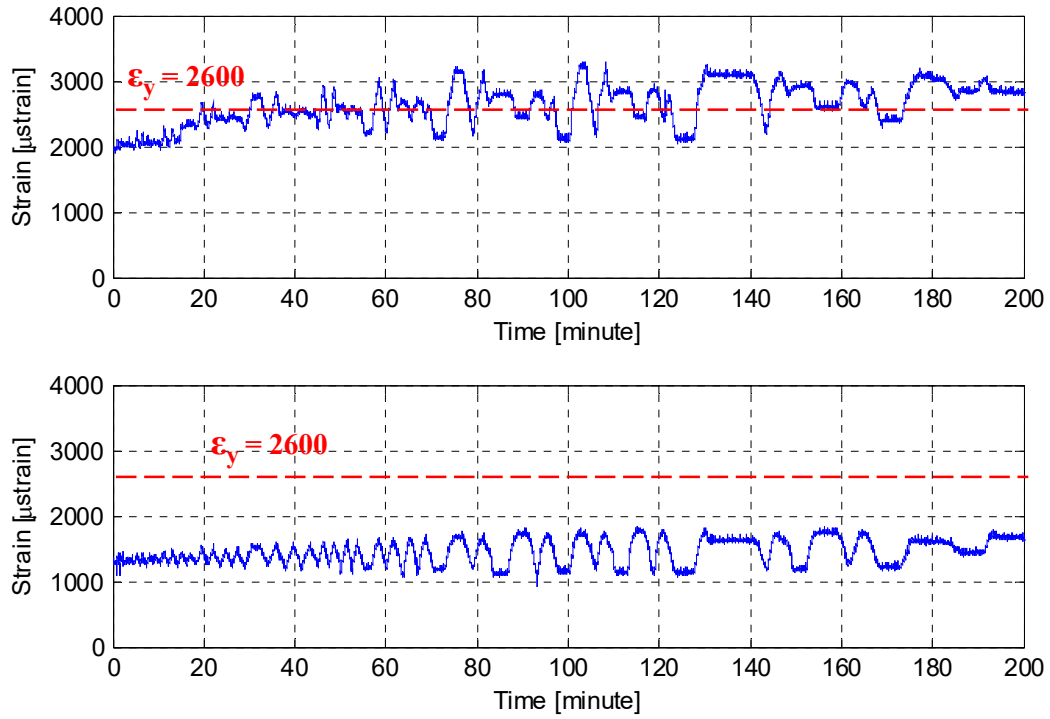


Figure 6.31 Sample of two of the six instrumented cap beam reinforcing bars strain history at Section B for all repaired Specimen No. 1 cyclic tests.

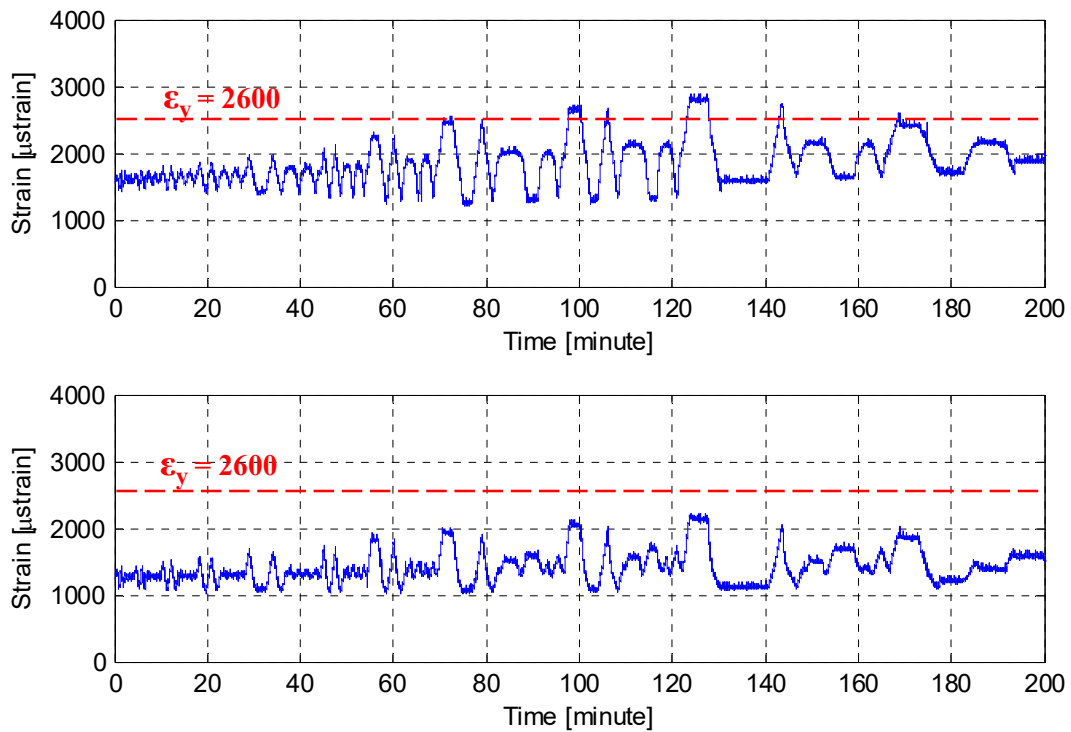


Figure 6.32 Sample of two of the six instrumented cap beam reinforcing bars strain history at Section D for all repaired Specimen No. 1 cyclic tests.

6.6 FRP JACKET STRAIN

One last metric to judge the effectiveness of the CFRP jacket confinement and the repair scheme is the jacket circumferential strain. A progressing circumferential jacket strain typically reflects a dilating column that is resisted by a counter confining action. The dilation is more localized in the compression zone, especially at elevated loading levels, where the reinforcing bars might buckling and displace the concrete cover but are stopped by the confining jacket. To monitor this phenomenon during the repaired specimen cyclic loading tests, strain gauges were installed around the circumference of the CFRP jacket at eight locations. The circumferential strain history at the transverse loading's two principal sides, namely the east and west sides of the column, are shown in Figure 6.33. The figure shows that the strain gauge actively engaging only when loading was aligned with the plane of strain gauges, i.e., transverse loading (east–west in this case). Meanwhile, the circumferential strain was sensitive to the loading and unloading as the load was reversed. When loading was towards the west, only the strain gauge in the west side, where compression occurred, reflected higher strains, while the east side gauge maintained an almost constant strain and vice versa. This confirms that dilation was localized in the compression zone, and, more importantly, the CFRP jacket effectively confined the column, regardless of the extensive damage experienced by the column before the repair.

The recordings of two strain gauges at 45° from transverse loading plane are shown in Figure 6.34. The strain values in this case are much less and not very sensitive to the loading direction, as documented away from the main dilated regions.

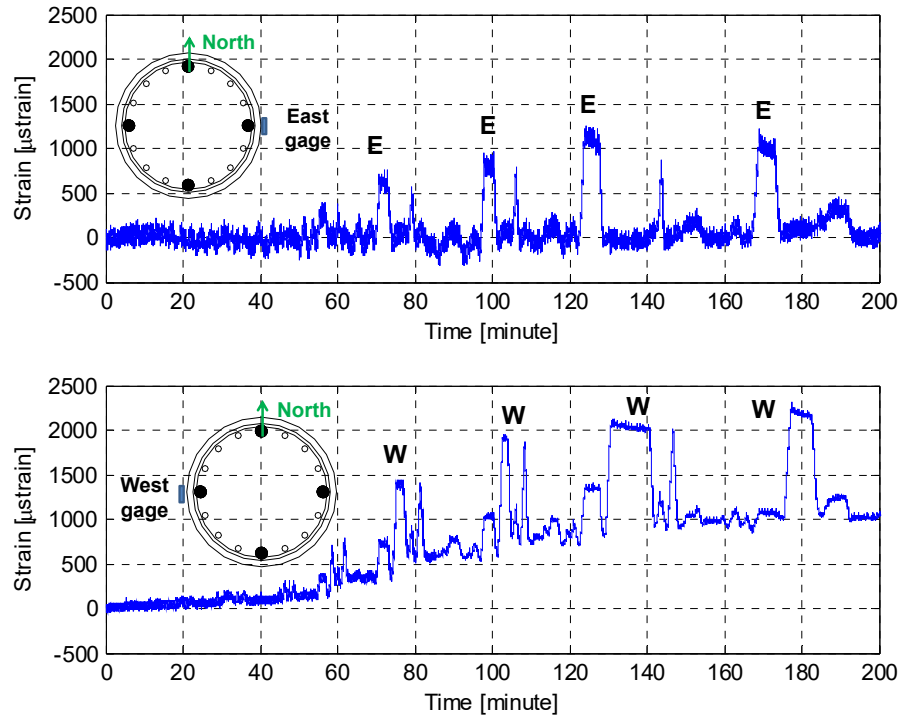


Figure 6.33 Circumferential CFRP jacket strain history in the column east and west sides for all repaired Specimen No. 1 cyclic loading tests in transverse and longitudinal directions.

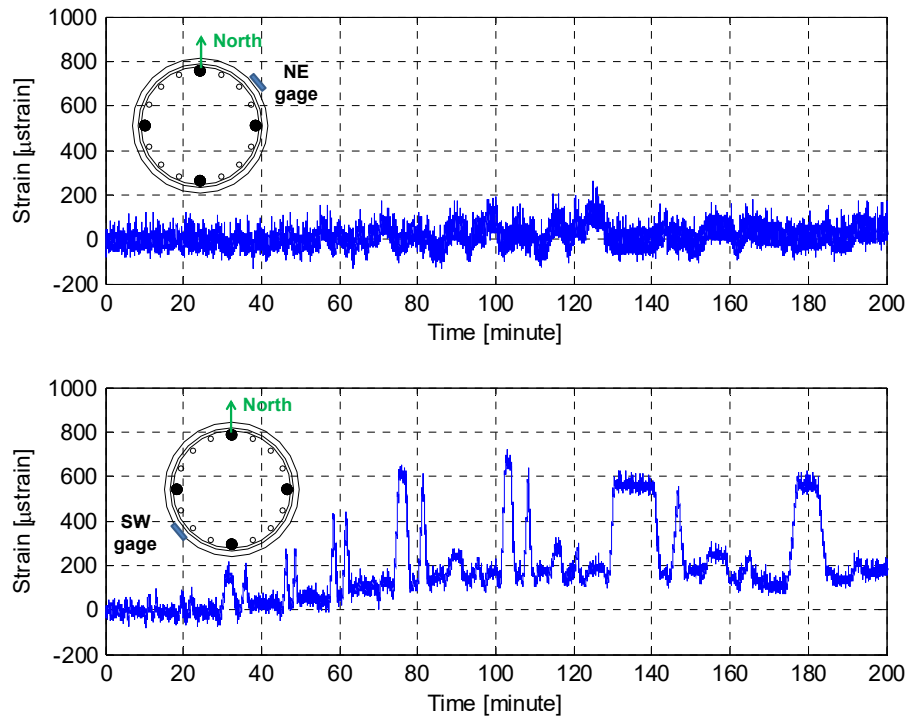


Figure 6.34 Circumferential CFRP jacket strain history in the column north-east (top) and south-west (bottom) sides for all repaired Specimen No. 1 cyclic loading tests in transverse and longitudinal directions.

7 Conclusions

7.1 SUMMARY

This report presents the pre-test analysis, design and construction of test specimens, and the main observations and conclusions drawn from the quasi-static tests of the column-bent cap beam-box girder bridge subassembly specimen, referred to as Specimen No. 1. The hybrid simulation development, tests, post-test analysis, and design implications are presented in the companion report. The reader is referred to this companion report for the full conclusion and overview of the study.

The main objective of this study was to accurately estimate the effective flange width of the bent cap beam due to the box-girder slabs contributions under combined vertical and lateral loads, which directly influence the stiffness and capacity of a bent cap. The part of the study presented in this report focused on investigating the behavior of bridge column–super structure systems in light of the most recent AASHTO and Caltrans SDC provisions. In addition, the bridge system, and particularly the integral cap beam, was investigated in as-built and repaired bridge column scenarios.

Several computational and experimental methods were utilized in this study. For the pre-test analysis, a 1D, 2D, and 3D FE models were developed and used to carry out different types of analyses that varied from linear elastic static analysis to nonlinear time history analysis. Different models were developed for both the full prototype bridge and the test specimen using OpenSees, SAP2000, and DIANA FE packages. The pre-test analysis successfully verified the expected subassembly behavior, provided the input for the final gravity load levels and lateral loading protocol, delivered the expected loads and straining actions for test set-up design, and provided necessary information for instrumentation distribution.

The pre-test analysis was then followed by the experimental program. The first stage of the experimental program involved quasi-static cyclic loading tests of Specimen No. 1 in as-built and repaired conditions. Bi-directional cyclic loading tests in both transverse and longitudinal directions were conducted under constant gravity load. A rapid repair strategy was adopted for the tested Specimen No. 1, which used a three-layer CFRP column jacket. The partial repair aimed at providing minimal capacity for the specimen to be reused for the HS development and trail runs. However, a quasi-static cyclic test similar to the one applied to the as-built specimen was carried out for the repaired specimen for comparison purposes and to verify the essentially

elastic status of the bent cap beam. The second stage of the experimental program and the post-test analysis are presented in the companion report.

7.2 CONCLUSIONS

Several conclusions were drawn from the conducted pre-test analysis and quasi-static cyclic loading tests of the as-built and repaired Specimen No 1 subassembly, and are summarized as follows:

- The preliminary prototype bridge triaxial time history analysis showed that the inclusion of the vertical excitation component can lead to unfavorable damage or failure in the bent cap beams. A large number of near-fault ground motions were used to run time history analysis on the modified Academy Bridge prototype with and without the vertical excitation component. Six out of 88 considered ground motions led to excessive curvature values; plastic hinge damage at different locations of the bent cap beam only occurred when the vertical excitation was included. These six ground motions were concluded to cause highest demands in the bent cap, independently from the column capacity due to the vertical excitations. This observation violates the fundamental design principle of strong-beam–weak-column capacity design concept required by the Caltrans SDC and AASHTO seismic design guidelines. Further investigation is needed.
- The most detailed and accurate 3D DIANA model for the test specimen successfully predicted the subassembly behavior and mode of failure. A lateral force capacity was determined from the DIANA nonlinear pushover analysis to be almost 45 kips, which is only within 5% difference from the 47.5 kips experimentally determined capacity. Different modes of failures were observed from the 3D DIANA model under different gravity load levels combined with the lateral pushover. At the 10% gravity load level, which was used in the large-level cyclic loading tests, the predicted mode of failure from the analysis matched the experimentally observed failure mode of column plastic hinging. The detailed DIANA model was further calibrated and used in post-test analysis and will be discussed further in the companion report.
- The observed as-built Specimen No. 1 behavior satisfied all the Caltrans SDC design objectives. The mode of failure was a fully developed plastic hinge in the subassembly column; the bent cap beam and superstructure remained essentially elastic. The bridge system performed well up to high-performance levels that exceeded the minimum required performance levels set by Caltrans SDC. The bridge subassembly, and particularly its ductile column, successfully achieved a 7.6 ductility level, which corresponded to a 10.5% drift ratio in the transverse direction. A 5.4 ductility level corresponding to 7.5% drift ratio was achieved in the longitudinal direction; however, the

buckled column rebars started to rupture at the 5.4 ductility level loading in the longitudinal direction, leading to capacity loss. The 5.4 ductility level was still superior to the minimum displacement ductility of 4.0 required by Caltrans SDC.

- The bridge subassembly tests showed slightly different stiffness in the transverse and the longitudinal directions. This is attributed to the slightly more flexible column-box girder connection relative to the column–bent cap connection. The stiffness in the longitudinal direction is, however, very sensitive to the soffit and deck slab thicknesses, which govern the box-girder overall stiffness. Therefore, due to construction imperfections, the stiffness can vary, as observed from tests of Specimen No. 2 (discussed in the companion report). The stiffness degradation in both transverse and longitudinal directions was monitored and related to the different ductility levels and drift ratios. At 7.56 ductility level, the transverse stiffness was about 13% of its initial value, while a longitudinal stiffness of almost 10% of the initial value was observed at 5.40 ductility level, i.e., the specimen lost close to 90% of its initial stiffness at the final damaged state.
- The rapid CFRP repair technique successfully achieved its objective of partially restoring the subassembly capacity of Specimen No. 1 and significantly increased the stiffness in both transverse and longitudinal directions. To quantify the repair effectiveness, a maximum increase of 25% in capacity was obtained due to the repair relative to the residual capacity after all column rebars buckled and six of them ruptured. Moreover, the damaged specimen achieved an increase in the stiffness of more than 300% after the repair; however, regardless of the significant increase in the stiffness, the original initial stiffness and strength were not fully achieved. Note that the injection of the cracks prior to the application of the CFRP was the main contributor to this increase in stiffness, not the CFRP jacket itself.
- The bent cap beam experienced yielding throughout the as-built tests of Specimen No. 1 but remained essentially elastic. The essentially elastic state was confirmed by visual evidence that no extensive cracking took place at the tension side nor concrete crushing occurred in the compression side. In addition, the bent cap beam behaved linearly elastic when the subassembly was repaired and retested. A more accurate value for the yield moment of the bent cap beam was determined accordingly. In terms of the effective slab width contribution, the yield moment rendered the recommended Caltrans SDC and AASHTO guideline bent cap beam flanged section conservative.
- A simple procedure was devised to experimentally determine the bent cap beam effective slab width using the equivalent strain block concept from the Specimen No. 1 cyclic tests and Specimen No. 2 HS tests. Two strain values from the different reinforcing steel bars in the bent cap were used for the

equivalent strain block. These were the minimum values and the mean of six instrumented bars at a given cross section. Consequently, the effective slab width was evaluated for all test runs and for different sections, mainly on the tension side. The results from the compression side were not conclusive because the strain measurements were sensitive to the concentrated gravity load. The results for the effective slab width, obtained from the tension side, rendered the $12t_s$ Caltrans SDC and AASHTO code value for effective slab width unnecessarily conservative. The overall mean value for the effective width as determined from all as-built Specimen No. 1 cyclic tests was $13.7t_s$ and $21.2t_s$ when the cap beam mean and minimum strain values were used, respectively. Similar numbers were obtained from the retrofitted Specimen No. 2 HS tests, as discussed in the companion report. Thus, the original $12t_s$ code value was supplemented by a proposed revised value of $18t_s$ for investigating the bent cap beam capacity estimation and design implications.

- The underestimated yield moment from the code-based sectional analysis relative to the experimentally observed value was determined to be a consequence of excluding the tension-side slab reinforcement, and the use of only a $12t_s$ effective slab width. A similar observation for the bent cap beam moment capacity from tests of Specimen No. 2 is discussed in the companion report. Consequently, it is recommended to include the transverse deck and soffit slab tension reinforcement within a revised $18t_s$ effective slab width in the bent cap yield and capacity moment estimation.

7.3 FUTURE WORK

Extending the results of this study and future areas of potential research are as follows:

- A comprehensive study of the effect of the vertical excitation, especially in near-fault regions, on the superstructure, bent caps, and outriggers of bridges should be pursued. The preliminary pre-test analysis conducted in this study demonstrated that the bent cap beam is vulnerable to excessive plastic damage due to vertical excitations. This was observed from the full prototype bridge OpenSees nonlinear dynamic analysis that used triaxial earthquake excitations, i.e., which included the vertical excitation component. A 3D full bridge model should be considered for investigating any possible unfavorable modes of failure or damage due to the lack of proper account for the vertical excitations in bridge design. The 3D modeling is recommended because the vertical forces resulting from vertical excitations are sensitive to the mass distribution of the superstructure. Approximating the lumped mass at selected nodes of the bridge superstructure and bent cap model is not the most accurate method for tackling the issue of the vertical excitations.

- Investigation of the behavior of bent caps in different bridge types beyond the RC box-girder bridges should be considered. Composite steel and RC bridge superstructures that connect to a RC bent cap beam are another type of popular configuration for bridges; a proper investigation of the bent cap behavior should be carried out. The contribution from the RC box-girder slabs is natural in integral bent caps because of the monolithic connections; however, composite girders have a stiffening and strengthening effect as well. Proper bent cap capacity estimates for seismic capacity design checks should be revisited.
- Investigation of the behavior of bent caps in different bridge geometries and configurations is needed. In particular, skew bridges with various skew angles might affect the overall box-girder soffit and deck slab contributions and, more critically, the bent cap beam capacity. Thus, a comprehensive study that relates the bent cap beam behavior, effective slab width, and capacity estimation to the skewness of the bridge would be useful. Currently, the Caltrans SDC and AASHTO guidelines recommend a similar $12t_s$ value for the effective width in a direction orthogonal to the bent cap axis. A revisited value might be strongly dependent on the skew angle and requires further investigation.

REFERENCES

- AASHTO (2007). *LRFD Bridge Design Specification*, American Association of State Highway and Transportation Officials, Washington, D.C.
- AASHTO (2009). *Guide Specifications for LRFD Seismic Bridge Design*, 1st ed., American Association of State Highway and Transportation Officials, Washington, D.C.
- AASHTO (2011). *Guide Specifications for LRFD Seismic Bridge Design*, 2nd ed., American Association of State Highway and Transportation Officials, Washington, D.C.
- ACI Committee 318 (2008). *Building Code Requirements for Structural Concrete and Commentary*, ACI 318-08, American Concrete Institute, Farmington Hills, MI.
- ACI Committee 318 (2011). *Building Code Requirements for Structural Concrete and Commentary*, ACI 318-11, American Concrete Institute, Farmington Hills, MI.
- ACI374.2R-13 (2013). *Guide for Testing Reinforced Concrete Structural Elements under Slowly Applied Simulated Seismic Loads*, American Concrete Institute, Farmington Hill, MI.
- ASCE-41-06 (2006). *Seismic Rehabilitation of Existing Buildings*, American Society of Civil Engineers, Reston, VA.
- ASTM (2005). *Standard Test Method for Compressive Strength of Cylindrical Concrete Specimens: Designation C39/C39M-05*, American Society for Testing Materials, west Conshohocken, PA.
- ASTM (2004a). *Standard Test Method for Splitting Tensile Strength of Cylindrical Concrete Specimens: Designation C496/C496M-04*. American Society for Testing Materials, west Conshohocken, PA.
- ASTM (2004b). *Standard Specification for Low-Alloy Steel Deformed and Plain Bars for Concrete Reinforcement: Designation A706-04*, American Society for Testing Materials, west Conshohocken, PA.
- ASTM (2004c). *Standard Test Methods for Tension Testing of Metallic Materials: Designation E8-04*, American Society of Testing Materials, west Conshohocken, PA.
- ASTM (2007). *Standard Test Method for Flexural Strength of Concrete (Using Simple Beam with Center-Point Loading: Designation C293-07*, American Society for Testing Materials, west Conshohocken, PA.
- ATC-24 (1992). Guidelines for cyclic seismic testing of components of steel structures for buildings, *Report No. ATC-24*, Applied Technology Council, Redwood City, CA.
- Aviram A., Mackie K., Stojadinovic B. (2008). Guidelines for nonlinear analysis of bridge structures in California, *PEER Report 2008/03*, Pacific Earthquake Engineering Research Center, University of California, Berkeley, CA.
- Berry M.P., Eberhard M.O. (2007). Performance modeling strategies for modern reinforced concrete bridge columns, *PEER Report No. 2007/07*, Pacific Earthquake Engineering Research Center, University of California, Berkeley, CA.
- Bas A. (1990). *Behavior of Reinforced Concrete Beam-Column Connections with Floor Slabs under Bi-Directional Loads*, Master's Thesis, Department of Civil Engineering, University of Toronto, Ontario, Canada.
- Bazant Z.P., Planas J. (1998). *Fracture and Size Effect in Concrete and other Quasibrittle Materials*, CRC Press, Boca Raton, FL.
- Bozorgnia Y., Campbell K.W. (2004). The vertical-to-horizontal response spectral ratio and tentative procedures for developing simplified v/h and vertical design spectra, *J. Earthq. Eng.*, 8(2): 175–207.
- Brendel G. (1964). Strength of compression slab of t-beams subjected to simple bending, *J. Am. Concr. Inst., Proceedings*, 61(1): 57–75.
- British Standard Institution (2009). *Eurocode 2: Design of Concrete Structures*, British Standards Institution, London.
- BS-8110 (2008). *Standard Use of Concrete*, British Standards Institute, London.

- Brown W.A., Lehman D.E., Stanton J.F. (2007). Bar buckling in reinforced concrete bridge columns, *PEER Report No. 2007/11*, Pacific Earthquake Engineering Research Center, University of California, Berkeley, CA.
- Calderone A.J., Lehman D.E., Moehle J.P. (2000). Behavior of reinforced concrete bridge columns having varying aspect ratios and varying lengths of confinement, *PEER Report No. 2000/08*, Pacific Earthquake Engineering Research Center, University of California, Berkeley, CA.
- Caltrans (2010). *Seismic Design Criteria version 1.6*, California Department of Transportation, Sacramento, CA.
- Caltrans (2013). *Seismic Design Criteria version 1.7*, California Department of Transportation, Sacramento, CA.
- Campbell K.W., Bozorgnia Y. (2003). Updated near-source ground-motion (attenuation) relations for the horizontal and vertical components of peak ground acceleration and acceleration response spectra, *Bull Seismol. Soc. Am.*, 93(1): 314–331.
- Canadian Standards Association (1974). Design of highway bridges. CSA-S6.
- CEB-FIP Model Code 1990 (1993). Comité Euro-International du Béton.
- Cheung Y.K. (1969). Folded plate structures by finite strip method, ASCE, *J. Struct. Div.*, 95(ST12): 2963–2979.
- Cheung M.S., Chen M.Y.T. (1978). Finite strip evaluation of effective flange width of bridge girders, *Canadian J. Civil Eng.*, 5(2): 174–185.
- Cheung P.C., Paulay T., Park R. (1991). New Zealand tests on full-scale reinforced concrete beam-column-slab subassemblages designed for earthquake resistance, *ACI Special Publication*, 123(1), 37 pgs.
- Chwalla E. (1936). Die Formeln zur Berechnung der "Voll Mittragenden Breite" dinner Gurt-und Rippenplatten, *Stahlbau*, No. 10, p. 73.
- Clark P.W., Frank K., Krawinkler H., Shaw R., (1997). Protocol for Fabrication, Inspection, Testing, and Documentation of Beam-Column Connection Tests and Other Experimental Specimens, SAC Steel Project Background Document. October, *Report No. SAC/BD-97/02*.
- Computers and Structures Inc. (2012). *SAP2000 V14: Integrated Finite Element Analysis and Design of Structures Basic Analysis Reference Manual*, Berkeley, CA.
- Dryden M., Fenves G.L. (2009). The integration of experimental and simulation data in the study of reinforced concrete bridge systems including soil-foundation-structure interaction, *PEER Report No. 2009/03*, Pacific Earthquake Engineering Research Center, University of California, Berkeley, CA.
- Esmaily-Gh. A., Xiao Y. (2002). Seismic behavior of bridge columns subjected to various loading patterns, *PEER Report No. 2002/15*, Pacific Earthquake Engineering Research Center, University of California, Berkeley, CA.
- Federal Republic of Germany. (1955). DIN 1078. Verbundtrager-strabenbrucken; Richtlinien fiir die Berechnung Anudsbildung. Deutschen Normennusschusses, Berlin 30.
- FEMA-416 (2007). *Interim Testing Protocols for Determining the Seismic Performance Characteristics of Structural and Nonstructural Components*, Federal Emergency Management Agency, Washington, D.C.
- French C.W., Moehle J.P. (1991). Effect of floor slab on behavior of slab-beam-column connections, *ACI Special Publication*, 123: 225-358.
- Hachem M.M., Mahin S.A. (2000). Dynamic response of reinforced concrete columns to multidirectional excitations, *Proceedings, 12th World Conference on Earthquake Engineering*, Paper (No. 2446), New Zealand Society for Earthquake Engineering, Upper Hutt, New Zealand.
- Harris H.G., Sabnis G.M. (1999). *Structural Modeling and Experimental Techniques*, 2nd ed., CRC Press, Boca Raton, FL.
- Hose Y.D., Seible F. (1999). Performance evaluation database for concrete bridge components and systems under simulated seismic loads, *PEER Report No. 1999/11*, Pacific Earthquake Engineering Research Center, University of California, Berkeley, CA.
- Hube M.A., Mosalam K.M. (2010). Experimental and computational evaluation of in-span hinges in reinforced concrete box-girder bridges, ASCE, *J. Struct. Eng.*, 137(11): 1245–1253.

- Hube M.A., Mosalam K.M. (2011). Parametric study and design recommendations for in-span hinges in reinforced concrete box-girder bridges, *J. Bridge Eng.*, 17(2): 334–342.
- ICBO (1994). *Uniform Building Code*, International Conference of Building Officials, Whittier, CA.
- Ingham J.M., Priestley M.J.N., Seible F. (1995). Bridge knee joint with headed reinforcement, *Proceedings, Pacific Conference on Earthquake Engineering*, Melbourne, Australia, 3: 217–225.
- ISO (1998). Timber Structures–joints made with mechanical fasteners–quasi-static reversed-cyclic test method, *ISO/TC 165 WD 16670*, International Organization for Standardization, Geneva, Switzerland.
- Ketchum M., Chang V., Shantz T. (2004). *Influence of Design Ground Motion Level on Highway Bridge Costs*, Project No. 6D01, submitted to the Pacific Earthquake Engineering Research Center, University of California, Berkeley, CA.
- Kramer S.L., Arduino P., Shin H. (2008). Using OpenSees for performance-based evaluation of bridges on liquefiable soils, *PEER Report No. 2008/07*, Pacific Earthquake Engineering Research Center, University of California, Berkeley, CA.
- Krawinkler H. (1996). Cyclic loading histories for seismic experimentation on structural components, *Earthq. Spectra*, 12(1): 1–12.
- Krawinkler H. (2009). Loading histories for cyclic tests in support of performance assessment of structural components, *Proceedings, 3rd International Conference on Advances in Experimental Structural Engineering*, San Francisco, CA.
- Krawinkler H., Parisi F., Ibarra L., Ayoub A., Medina R. (2000). Development of a testing protocol for woodframe structures, *CUREE Publication No. W-02*, Consortium of Universities for Research in Earthquake Engineering, Richmond, CA.
- Lee H., Mosalam K.M. (2014). Effect of vertical acceleration on shear strength of reinforced concrete columns, *PEER Report No. 2014/04*, Pacific Earthquake Engineering Research Center, University of California, Berkeley, CA.
- Lee T.-H., Mosalam K.M. (2006). Probabilistic seismic evaluation of reinforced concrete structural components and systems, *PEER Report 2006/04*, Pacific Earthquake Engineering Research Center, University of California, Berkeley, CA.
- Lehman D.E., Moehle J.P. (1998). Seismic performance of well-confined concrete bridge columns, *PEER Report No. 1998/01*, Pacific Earthquake Engineering Research Center, University of California, Berkeley, CA.
- Leon R.T., Deierlein G.G. (1996). Considerations for the use of quasi-static testing, *Earthq. Spectra*, 12(1): 87–109.
- Luo Q.Z., Tang J., Li Q.S. (2001). Negative shear lag effect in box girders with varying depth, *ASCE, J. Struct. Eng.*, 127(10): 1236–1239.
- Mackie K., Stojadinovic B. (2003). Seismic demands for performance-based design of bridges, *PEER Report No. 2003/16*, Pacific Earthquake Engineering Research Center, University of California, Berkeley, CA.
- MacRae G.A., Priestley M.J.N., Seible F. (1994). Santa Monica viaduct retrofit – large- scale column- cap beam joint transverse test, *Preliminary Report to the California Department of Transportation*, Sacramento, CA.
- Mazzoni S. (1997). *Seismic Response of Beam-Column Joints in Double-Deck Reinforced Concrete Bridge Frames*, PhD Dissertation, Department of Civil and Environmental Engineering, University of California, Berkeley, CA.
- McKenna F., Fenves G.L., Scott M.H., Jeremic B. (2000). *Open System for Earthquake Engineering Simulation* (OpenSees), Pacific Earthquake Engineering Research Center, University of California, Berkeley, CA.
- Metzger W. (1929). *Die Mittmgende Breite*, Luftfahrtforschung, P.
- Mitoulis S.A. (2012) Seismic design of bridges with the participation of seat-type abutments, *Eng. Struct.*, 44(2): 222–233.
- Moehle J.P. (2014). *Seismic Design of Reinforced Concrete Buildings*, 1st ed., McGraw-Hill Education.

- Mosalam K.M., Naito C.J., Khaykina S. (2002). Bidirectional cyclic performance of reinforced concrete bridge column-superstructure subassemblies, *Earthq. Spectra*, 18(4): 663–687.
- Moustafa M.A. (2014). *Structural Behavior of Bent Cap Beams in As-built and Retrofitted Reinforced Concrete Box-Girder Bridges*, PhD Dissertation, University of California, Berkeley, CA
- Moustafa M.A., Mosalam K.M. (2015). Seismic response of bent caps in as-built and retrofitted reinforced concrete box-girder bridges. *Eng. Struct.*, 98: 59–73.
- Naito C.J., Moehle J.P., Mosalam K.M. (2001). Experimental and computational evaluation of reinforced concrete bridge beam-column connections for seismic performance, *PEER Report No. 2001/08*, Pacific Earthquake Engineering Research Center, University of California, Berkeley, CA.
- Rots J.G. (2001). Sequentially linear continuum model for concrete fracture. In: R. de Borst, J. Mazars, G. Pijaudier-Cabot and J.G.M. van Mier (eds.), *Fracture Mechanics of Concrete Structures*, pp. 831–839, Rotterdam: Balkema.
- Pantazopoulou S.J., Moehle J.P., Shahrooz B.M. (1988). Simple analytical model for T-beams in flexure, *ASCE, J. Struct. Eng.*, 114(7): 1507–1523.
- Porter D.M., Cherif Z.E. (1987). *Ultimate Shear Strength of Thin Webbed Steel and Concrete Composite Girders*. Elsevier Applied Science Publishers, pp. 55–64.
- RILEM Draft (1985). Determination of the fracture energy of mortar and concrete by means of three-point bend tests on notched beams, *Mat. Struct.*, 18(106): 285–290.
- Selby R.G., Vecchio F.J. (1993). Three-dimensional constitutive relations for reinforced concrete, *Publication No. 93-02*, Department of Civil Engineering, University of Toronto, Ontario, Canada.
- Seible F., Priestley M.J.N., Latham C.T., Terayama T. (1993). Full-scale test on the flexural integrity of cap/column connections with #18 column bars, *Preliminary Report to the California Department of Transportation*, Sacramento, CA.
- Seible F., Priestley M.J.N., Silva P., Gee D. (1994). Full-scale bridge column test of redesigned cap/column connection with #18 column bars, *Preliminary Report to the California Department of Transportation*, Sacramento, CA.
- Terzic V., Stojadinovic B. (2010). Post-earthquake traffic capacity of modern bridges in California, *PEER Report No. 2010/103I*, Pacific Earthquake Engineering Research Center, University of California, Berkeley, CA.
- Thewalt C.R., Stojadinovic B. (1995). Behavior of bridge outrigger knee joint systems, *Earthq. Spectra*, 11(3): 477–509.
- TNO Diana (2014). *User's Manual - Release 9.5*, Delft, Netherlands.
- Trono W., Jen G., Panagiotou M., Schoettler M., Ostertag C.P. (2014) Seismic response of a damage-resistant recentering post-tensioned-HYFRC bridge column, *J. Bridge Eng.*, DOI: 10.1061/(ASCE)BE.1943-5592.0000692.
- TS-500 (1984). Betonarme Yapıların Hesap ve Yapım Kuralları TS500, Türk Standardları Enstitüsü, Nisan 1984.
- Vecchio F.J., Collins M.P. (1986). The modified compression-field theory for reinforced concrete elements subjected to shear, *ACI Journal Proceedings*, 83(2): 219–231.
- Wallace J.W. (1996). Evaluation of UBC-94 provisions for seismic design of RC structural walls, *Earthq. Spectra*, 12(2): 327–348.
- Wight J.K., Sozen M.A. (1975). Shear strength decay of RC columns under shear reversals, *Proceedings*, ASCE, 101(ST5): 1053–1065.

Appendix A Specimen Design

A.1 DESIGN LOADS

For the design of the subassembly reduced-scale specimen, a full-scale model for the modified prototype was used first to compute the loads and straining actions—basically due to dead and live loads—at each relevant structural element. The computed straining actions were then scaled down using the proper similitude relationships and used to design the different specimen sections. The seismic design loads and criteria were considered according to the Caltrans *Seismic Design Criteria* and *AASHTO LRFD Bridge Design Specifications*. Three-dimensional elastic models were developed for the modified prototype; SAP2000 was used to compute the straining actions under different vertical loads.

Box-Girder Straining Actions

For the full scale box-girder having entire bridge width, the bending moments and shear forces are:

Dead Load (self-weight): $M_{DL(-ve)} = -54,016$ kip-ft. ; $M_{DL(+ve)} = 31,738$ kip-ft

Additional Dead Load (wearing surface): $M_{ADL(-ve)} = -8822$ kip-ft; $M_{ADL(+ve)} = 5183$ kip-ft

Live Load (design vehicle – truck load): $M_{LDT(-ve)} = -2290$ kip-ft; $M_{LDT(+ve)} = 1327$ kip-ft

Live Load (design vehicle – lane load): $M_{LDL(-ve)} = -1673$ kip-ft; $M_{LDL(+ve)} = 983$ kip-ft

The ultimate (factored) moments for the full-scale box-girder can be computed according to the AASHTO load combinations as follows:

$$M_{ult} = \sum_i \eta_i \times \gamma_i \times M_i \quad (AASHTO 3.3.1-1)$$

$$M_{ult} = 1.0 \times [1.25 \times M_{DL} + 1.75 \times M_{LL-design} (1 + IM)]$$

$$M_{ult(-ve)} = -1.0 \times [1.25 \times (54016 + 8822) + (1.75 \times 1.33 \times (2290 + 1673))] = -87,771 \text{ kip-ft.}$$

$$M_{ult(+ve)} = 1.0 \times [1.25 \times (31738 + 5183) + (1.75 \times 1.33 \times (1327 + 983))] = 51,528 \text{ kip-ft.}$$

Similarly, the factored shear force for the full-scale box-girder can be computed as follows:

$$V_{ult} = \sum_i \eta_i \times \gamma_i \times V_i \quad (AASHTO 3.3.1-1)$$

$$V_{ult} = 1.0 \times [1.25 \times V_{DL} + 1.75 \times V_{LL-design} (1 + IM)]$$

$$V_{ult} = 1.0 \times [1.25 \times (1960 + 320) + (1.75 \times 1.33 \times (51.6 + 38.2))] = 3059 \text{ kips}$$

Next, the shear and moment for the specimen design can be calculated using the proper similitude and scale factors from “Structural Modeling and Experimental Techniques, Harris and Sabnis [1999]. Since the specimen will have the same materials as the prototype but with reduced geometric scale ($S = 4$), the bending moments are reduced by $1/S^3 = 1/64$ and the Forces are reduced by $1/S^2 = 1/16$. Also the subassembly specimen consists of only 4 webs and 3 cells, while the full prototype box-girder consists of 8 webs and 7 cells. So the straining actions are reduced accordingly. Therefore, the specimen straining actions are calculated as follows:

$$M_{ult(-ve)} = -87771 \times (3/7) \times (1/64) = -587.76 \text{ kip-ft}$$

$$M_{ult(+ve)} = 51528 \times (3/7) \times (1/64) = 345.10 \text{ kip-ft}$$

$$V_{ult/web} = 3059 \times (1/8) \times (1/16) = 23.90 \text{ kips}$$

Bent Cap Beam and Column Straining Actions

A planer two-dimensional elastic SAP2000 model was developed for the three-column and integral cap beam bent. The loads applied to the bent model were adopted from the full bridge model and the components self-weights were also applied. Only factored design straining actions from vertical loads are shown here and the seismic forces considerations are presented in the next section.

- The factored moment for the full-scale cap beam is calculated as follows:

$$M_{ult} = 1.0 \times [1.25 \times M_{DL} + 1.75 \times M_{LL-design} (1 + IM)]$$

$$M_{ult(-ve)} = -1.0 \times [1.25 \times (5174 + 751.5) + (1.75 \times 1.33 \times 1631.4)] = -11,204 \text{ kip-ft}$$

$$M_{ult(+ve)} = 1.0 \times [1.25 \times (3505 + 518) + (1.75 \times 1.33 \times 1883.4)] = 9,412 \text{ kip-ft}$$

- The factored shear for the full-scale cap beam is calculated as follows:

$$V_{ult} = 1.0 \times [1.25 \times V_{DL} + 1.75 \times V_{LL-design} (1 + IM)]$$

$$V_{ult} = 1.0 \times [1.25 \times (907 + 131) + (1.75 \times 1.33 \times 156.3)] = 1661.3 \text{ kips}$$

- The factored axial force for the full-scale middle column is calculated as follows:

$$P_{ult} = 1.0 \times [1.25 \times P_{DL} + 1.75 \times P_{LL-design} (1 + IM)]$$

$$P_{ult} = 1.0 \times [1.25 \times (1814.1 + 261.6) + (1.75 \times 1.33 \times 171.7)] = 2994 \text{ kips}$$

- Thus, the specimen column and beam straining actions are calculated as follows:

$$M_{Bult(-ve)} = -11204 \times (1 / 64) = -175kip - ft$$

$$M_{Bult(+ve)} = 9412 \times (1 / 64) = 147.1kip - ft$$

$$V_{Bult} = 1661.3 \times (1 / 16) = 103.8kips$$

$$P_{Colult} = 2994 \times (1 / 16) = 187.2kips$$

Specimen Lateral (Seismic) Design Loads

The seismic loads are designed to be carried by the bent columns and beams framing action. According to the SDC (Section 3.4), the bent cap beam and box-girder superstructure are capacity protected components that shall be designed flexurally to remain elastic when the column reaches its overstrength capacity. Consequently, the cap beam and box-girder will be designed under vertical loads only, then the designed capacity of the cross sections will be computed and checked to make sure the beam and box-girder remain elastic when column reaches its capacity. The specimen column design is presented first and then followed by the cap beam and box-girder designs and checks.

A.2 DESIGN OF SPECIMEN CROSS SECTIONS

The design of the specimen includes flexural and shear design for the following components:

- Column
- Cap beam
- Column and cap beam joint
- Box girder deck and soffit slabs
- Box girder webs
- Concrete beams (seats) for specimen attachment to lab rigid floor

The design is made according to the following Codes and Standards:

- AASHTO LRFD Bridge Design Specifications, 2007.
- Caltrans Seismic Design Criteria (SDC), 2010.
- ACI Building Committee 318, 2008.

A.2.1 Column Design

Geometry

Scaling Factor, $S = 4.0$

Diameter of column, $D_{col} = 18 \text{ in.}$

Height of column, $H_{col} = 90 \text{ in.}$

Gross cross-section area of column $= A_g = \frac{\pi}{4} (D_{col})^2 = \frac{\pi}{4} \times 18^2 \approx 254.5 \text{ in}^2$.

Material

The nominal material properties to be used in the specimen construction are :

Concrete Compressive Strength, $f'_c = 5 \text{ ksi.}$

Yield strength of steel, $f_y = 60 \text{ ksi.}$

Ultimate strength of steel, $f_u = 80 \text{ ksi.}$

The expected material properties are determined from nominal properties according to Caltrans SDC Section 3.2,

$$f'_{ce} = \text{the greater of : } \begin{cases} 1.3 \times f'_c = 1.3 \times 5000 = 6500 \text{ psi} = 6.5 \text{ ksi} \\ 5000 \text{ psi} = 5.0 \text{ ksi} \end{cases}$$

Expected concrete comp. strength, $f'_{ce} = 6500 \text{ psi.}$

Expected yield strength of Steel, $f_{ye} = 68 \text{ ksi.}$

Expected Ultimate strength of steel, $f_{ue} = 95 \text{ ksi.}$

Column Axial Load

Due to the nature of the test setup that the specimen is inverted upside down, the gravity load will be applied at the column top during the test. The value of the test's gravity load is chosen such that the moments in the specimen column and cap beam joint region are the same as produced by distributed gravity loads in the scaled prototype bridge.

Thus, from an elastic SAP2000 model for the specimen where the moment in the cap beam is:

$$M_{DL-service} = (5085 + 738.4) \times (1/64) = 91 \text{ kip-ft} = 1092 \text{ kip-in.}$$

The column axial load was found to be: $P_{col} = 72 \text{ kips.}$

$$\text{This corresponds to axial load ratio} = \frac{P_{col}}{A_c \times f'_c} = \frac{72}{254 \times 5} = 5.66\%$$

Longitudinal Steel Reinforcement Requirement

According to SDC, the minimum and maximum column reinforcement ratios are:
1.0% and 4.0%, respectively

For the sake of the test aiming at achieving failure in both the cap beam and column,
a longitudinal reinforcement ratio $\rho_l = 2.5\%$ is chosen to start with.

$$\text{Required } A_{s,col} = 0.025 \times A_g = 0.025 \times 254.5 = 6.36 \text{ in}^2.$$

If using longitudinal rebars #6,

$$A_{\#6} = 0.44 \text{ in}^2. \quad \text{and} \quad \phi_{\#6} = 0.75 \text{ in.}$$

$$\text{number of bars} = 6.36 \div 0.44 = 14.5 \rightarrow \text{use } 16 \#6, \quad \rho_l = \frac{16 \times 0.44}{254.5} = 2.77\%$$

Check spacing requirements between bars,

Define D_o as the distance from center of long. rebar to the outer edge of column.

$$D_o = D_{col} - 2 \left(\text{Clear Cover} + \phi_{\#3} + \frac{\phi_{\#6}}{2} \right)$$

For clear cover = 1.0 in. and hoop #3 ($\phi_{\#3} = 0.375 \text{ in.}$),

$$D_o = 18 - 2 \left(1.0 + 0.375 + \frac{0.75}{2} \right) = 14.5 \text{ in.}$$

$$\text{Then, spacing between long. bars, } \delta_l = \frac{\pi D_o}{\text{number of bars} - 1} = \frac{\pi \times 14.5}{15} = 3.04 \text{ in.} < 8 \text{ in. OK}$$

Plastic Hinge Length (equivalent)

$$L_p = 0.08L + 0.15f_{ye}\phi_{\#6} = 0.08 \times 90 + 0.15 \times 68 \times 0.75 = 14.85 \text{ in.}$$

$$L_p \geq 0.3f_{ye}\phi_{\#6} = 0.3 \times 68 \times 0.75 = 15.3 \text{ in.} \rightarrow \text{consider } L_p = 15.3 \text{ in}$$

Plastic Region Extent

$$\left. \begin{aligned} L_{pr} &\geq 1.5D_{col} = 1.5 \times 18 = 27 \text{ in.} \\ L_{pr} &\geq 0.25H_{col} = 0.25 \times 90 = 22.5 \text{ in.} \\ L_{pr} &\geq (\text{length where } M > 0.75M_p) = 0.25H_{col} = 22.5 \text{ in.} \end{aligned} \right\} L_{pr} = 27 \text{ in.}$$

Traverse Steel Reinforcement Requirement

- Determine minimum transverse steel according to AASHTO:

$$\frac{A_v}{s} \geq 0.0316 \times \sqrt{f'_c} \times \frac{b_v}{f_y} \quad (AASHTO, 5.8.2.5-1)$$

$$\frac{A_v}{s} \geq 0.0316 \times \sqrt{5} \times \frac{18}{60}$$

$$\frac{A_v}{s} \geq 0.021 \text{ in}^2 / \text{in}$$

$$\text{If using \#3 hoops, } s_{\text{required}} \leq \frac{0.11}{0.021} \approx 5.2 \text{ in.}$$

- Minimum spacing of transverse steel in compression members:

According to Section 5.10.6.3, The spacing of ties along the longitudinal axis of the compression member shall not exceed the least dimension of the compression member or 12.0 in.

Then, for the scaled specimen,

minimum spacing outside plastic hinge zone = $12 \times (1/4) = 3.0 \text{ in.}$

- Minimum transverse steel in plastic hinge zone for seismic design:

$$\rho_s \geq 0.12 \times \frac{f'_c}{f_y} \quad (AASHTO, 5.10.11.4.1d-1)$$

$$\rho_s \geq 0.12 \times \frac{5}{60} \geq 0.01$$

$$\rho_s = \frac{4A_{sh, \text{required}}}{D's_h} \geq 0.01$$

$$\text{If using \#3 hoops, } s_{h, \text{required}} \leq \frac{4 \times 0.11}{0.01 \times 15.25} \approx 2.8 \text{ in.}$$

Then, minimum stirrups to use: #3 hoop at 2.5 in. center-to-center spacing

The above column design is used to run a moment-curvature analysis using the software XTRACT to calculate the section capacity. The column section capacity will be used consequently to design the specimen cap beam and box-girder cross sections. The confined concrete model parameters can be calculated automatically in XTRACT for the moment-curvature analysis. However, those parameters are calculated manually here to check if different from program values.

Column M - ϕ Analysis and Results (based on Caltrans SDC)

Diameter $D_{col} = 18 \text{ in.}$, length of the column $= 90 \text{ in.}$, 16#6 longitudinal rebars, $P_{axial} = 72 \text{ kips.}$

$f_{ye, \#6} = 68 \text{ ksi}$, $E_s = 29,000 \text{ ksi}$, Clear cover $= 1.0 \text{ in.}$, hoop #3@2.5 in., $f_{ye, \#3} = 68 \text{ ksi}$,

$f'_c = 6.5 \text{ ksi}$, unconfined concrete ultimate (spalling) strain $\epsilon_{sp} = 0.0050$,

Confined Concrete:

$$1. \text{ Confinement effectiveness, } k_e = 1 - \frac{s_h}{D'} = 1 - \frac{2.5}{15.25} \approx 0.84$$

2. Maximum stress capacity of confining reinforcement

$$f_s = E_s \left(0.0025 + 0.21 \sqrt{\frac{k_e \rho_s}{f'_c}} \right) \leq f_{yt} = 60,000$$

$$f_s = 29,000,000 \left(0.0025 + 0.21 \sqrt{\frac{0.84 \times 0.014}{5000}} \right) = 154,406 \text{ psi}$$

Then, use $f_s = 60,000 \text{ psi}$.

$$3. \text{ Effective confinement stress, } f_{1e} = k_e \frac{\rho_s f_s}{2} = 0.84 \times \frac{0.0144 \times 60000}{2} \approx 361.2 \text{ psi}$$

4. Confined concrete strength (using Mander et.al. curves):

$$\frac{f_{1e}}{Cf'_c} = \frac{361.2}{0.85 \times 5000} = 0.085 \xrightarrow{\text{from curves with } f_{1e} = f_{2e}} \frac{f_{cc}}{Cf'_c} \approx 1.50$$

$$f_{cc} = 1.50 \times Cf'_c = 1.50 \times 0.85 \times 5000 = 6375 \text{ psi} \approx 6.38 \text{ ksi}$$

$$5. \text{ Strain at peak stress, } \epsilon_{cc} = \epsilon_0 \left(1 + 5 \left(\frac{f_{cc}}{Cf'_c} - 1 \right) \right)$$

$$\epsilon_0 = \text{strain at peak stress in unconfined concrete} = 0.003, \epsilon_{cc} = 0.003(1 + 5(1.50 - 1)) = 0.0105$$

$$6. \text{ Ultimate strain in confined concrete, } \epsilon_{cu} = 0.004 + 0.25 \frac{f_{emin}}{f'_c} = 0.004 + 0.25 \frac{0.365}{5} \approx 0.0222$$

$$7. \text{ Using Mander Model, } E_c = 57,000 \sqrt{f'_c} = 57,000 \sqrt{5000} = 4030 \text{ ksi}$$

$$r = \frac{E_c}{E_c - \frac{f_{cc}}{\epsilon_{cc}}} = \frac{4030}{4030 - \frac{6.38}{0.0105}} = 1.086, x = \frac{\epsilon_c}{\epsilon_{cc}} = \frac{0.0222}{0.0105} \approx 2.11$$

$$f_c = \frac{f_{cc} x r}{r - 1 + x^r} = \frac{6.38 \times 2.11 \times 1.086}{1.086 - 1 + 2.11^{1.086}} = 6.26 \text{ ksi}$$

Results of $M - \phi$ Analysis

Moment at first yield (XTRACT): $M_y = 2246 \text{ kips-in}$ and curvature: $\phi_y = 0.00022 \text{ rad/in}$.

Effective yield moment (XTRACT): $M'_y = 3244 \text{ kips-in}$ and curvature: $\phi'_y = 0.00031 \text{ rad/in}$.

Ultimate yield moment (XTRACT): $M_u = 3667 \text{ kips-in}$ and curvature: $\phi_u = 0.0045 \text{ rad/in}$

Idealized Caltrans SDC Plastic Moment, $M_p \approx \frac{M'_y + M_u}{2} \approx \frac{3244 + 3667}{2} = 3456 \text{ kips-in}$

$$\phi_Y = \frac{M_p \phi_y}{M_y} = \frac{3456 \times 0.00022}{2246} = 0.000338 \text{ rad/in}$$

$$\text{Curvature ductility, } \mu_{\phi,c} = \frac{\phi_u}{\phi_Y} = \frac{0.0045}{0.000338} = 13.29$$

Calculate and Check the Displacement Ductility Capacity

$$\Delta_Y = \phi_Y \frac{L^2}{3} = 0.000338 \times \frac{90^2}{3} = 0.912 \text{ in}$$

$$\phi_p = \phi_u - \phi_Y = 0.0045 - 0.000338 = 0.00416 \text{ rad/in}$$

$$\theta_p = \phi_p L_p = 0.00416 \times 15.3 = 0.0637 \text{ rad}$$

$$\Delta_p = \theta_p \left(L - \frac{L_p}{2} \right) = 0.0637 \left(90 - \frac{15.3}{2} \right) = 5.244 \text{ in}$$

$$\Delta_u = \Delta_Y + \Delta_p = 0.912 + 5.244 = 6.16 \text{ in}$$

$$\text{Displacement ductility, } \mu_{\Delta,c} = \frac{\Delta_u}{\Delta_Y} = \frac{6.16}{0.91} = 6.75 \geq 4.0 \text{ OK}$$

The SDC also defines overstrength moment M_o to be used at different design aspects.

According to SDC Equation (4.4), $M_o = 1.2 \times M_p = 1.2 \times 3456 = 4147 \text{ kips-in}$

Column Shear Design (SDC Section 3.6)

As per the SDC requirements, the shear capacity for ductile concrete members is given by:

$$\text{Capacity}(\phi_v V_n) \geq \text{Demand}(V_o)$$

It shall also be conservatively based on the nominal material strengths.

$$\text{Overstrength shear, } V_o = \frac{1.2 M_p}{L} = \frac{1.2 \times 3456}{90} = 46.08 \text{ kips}$$

$$\text{Nominal shear capacity, } V_n = \phi_v (V_c + V_s)$$

A.2.2 Cap Beam Design

According to the SDC, the cap beam is considered a capacity protected member. Thus, it is required that the cap beam remains elastic when the column reaches its plastic moment capacity taking into consideration the overstrength factor ($=1.2$). The specimen cap beam will be designed first using the factored moments and shear, then a moment-curvature analysis will be carried out for the designed section using XTRACT to check that beam remains elastic as the column reaches its overstrength moment.

Beam Factored Design Straining Actions

$$M_{Bult(-ve)} = -175 \text{ kip} - \text{ft} = -2100 \text{ kip} - \text{in}$$

$$M_{Bult(+ve)} = 147.1 \text{ kip} - \text{ft} = 1765.2 \text{ kip} - \text{in}$$

$$V_{Bult} = 103.8 \text{ kips}$$

Geometry and Material Properties

beam width, $b = 24 \text{ in}$ and beam height, $h = 20.375 \text{ in}$

clear cover $= 0.75 \text{ in}$

use #5 bars for longitudinal reinforcement ($\phi_{\#5} = 0.625 \text{ in}$, $A_{s,\#5} = 0.31 \text{ in}^2$)

use #3 bars for transverse reinforcement ($\phi_{\#3} = 0.375 \text{ in}$, $A_{s,\#3} = 0.11 \text{ in}^2$)

define distance between upper most compression fiber and tension reinforcement c.g. as " d ",

$$d = h - (\text{clear cover} + \text{stirrup bar diameter} + \frac{1}{2} \times \text{long. bar diameter})$$

$$d = 20.375 - (0.75 + 0.375 + \frac{1}{2} \times 0.625) \approx 18.94 \text{ in}$$

Same materials properties used in column design are also used in beam and other elements design.

Flexural Design

$$\phi_f M_n \geq M_u$$

Start the first beam design trial by neglecting compression steel and assuming a moment arm of "0.90×d" between the tension steel reinforcement c.g. and the compression stress block c.g.

For negative moment :

$$M_{u,-ve} = 2100 \text{ kip-in}$$

$$\phi_f = 0.9 \text{ (according to AASHTO, Section 5.5.4.2)}$$

$$M_n = \text{Tension force in steel} \times \text{moment arm} = A_s \times f_{sy} \times 0.90 \times d$$

then, required reinforcement :

$$A_{s, \text{required}} \geq \frac{M_{u,-ve}}{\phi_f \times f_{sy} \times 0.9 \times d} = \frac{2100}{0.9 \times 60 \times 0.90 \times 18.94} = 2.28 \text{ in}^2$$

$$\text{number of \#5 bars required} = \frac{A_{s, \text{required}}}{A_{s, \#5}} = \frac{2.28}{0.31} = 7.36 \rightarrow \text{use 8 \#5 bars for negative moment}$$

$$C = T = A_s \times f_{sy} = 8 \times 0.31 \times 60 = 148.8 \text{ kips}$$

$$C = c \times b \times \beta_1 \times f'_c, \beta_1 = 0.85 - \frac{0.05}{1000} (f'_c - 4000) = 0.80 \text{ (AASHTO, Section 5.7.2.2)}$$

$$\text{then, } c = \frac{C}{b \times \beta_1 \times f'_c} = \frac{148.8}{24 \times 0.80 \times 5} = 1.55 \text{ in}$$

$$M_n = T \times (d - \frac{a}{2}) = 148.8 \times (18.94 - 0.775) = 2702.9 \text{ kip-in} > \frac{M_u}{\phi_f} = \frac{2100}{0.9} = 2333.3 \text{ kip-in OK}$$

check minimum reinforcement according to AASHTO:

According to AASHTO, Section 5.7.3.3.3, a minimum reinforcement to develop at least 1.2 times the cracking moment of the cross-section is needed.

$$\text{The cracking moment can be given as } M_{cr} = \frac{f_r \times I_g}{y_t}$$

$$f_r = 0.24 \times \sqrt{f'_c} = 0.24 \times \sqrt{5} = 0.537 \text{ ksi}$$

$$I_g \text{ and } y_t \text{ are calculated from section properties, } y_t = 10.42 \text{ in \& } I_g = 18101.9 \text{ in}^4$$

$$\text{then, } M_{cr} = \frac{0.537 \times 18102}{10.42} = 932.9 \text{ kip-in}$$

The required steel to develop such moment can be approximately calculated as follows :

$$A_{s, \text{min}} = \frac{1.2 \times M_{cr}}{\phi \times f_{sy} \times 0.9 \times d} = \frac{1.2 \times 932.9}{0.9 \times 60 \times 0.9 \times 18.94} = 1.22 \text{ in}^2 << 8 \times 0.31 = 2.48 \text{ in}^2 \text{ OK}$$

For positive moment :

$$M_{u,+ve} = 1765.2 \text{ kip-in}$$

$$\phi_f = 0.9 \text{ (according to AASHTO, Section 5.5.4.2)}$$

$$M_n = \text{Tension force in steel} \times \text{moment arm} = A_s \times f_{sy} \times 0.9 \times d$$

then, required reinforcement :

$$A_{s,required} \geq \frac{M_{u,+ve}}{\phi_f \times f_{sy} \times 0.9 \times d} = \frac{1765.2}{0.9 \times 60 \times 0.9 \times 18.94} = 1.92 \text{ in}^2$$

$$\text{number of \#5 bars required} = \frac{A_{s,required}}{A_{s,\#5}} = \frac{1.92}{0.31} = 6.2$$

However, use 8 #5 bars for symmetric section capacity under cyclic and earthquake load reversals.

check bars' center – to – center spacing :

$$s_b = \frac{b - 2 \times (\text{cover} + \phi_{\#3} + \frac{\phi_{\#5}}{2})}{\text{number of bars} - 1} = \frac{24 - 2 \times (0.75 + 0.375 + \frac{0.625}{2})}{8 - 1} \approx 3 \text{ in} \begin{cases} < 8 \text{ in OK} \\ > 1.5 \text{ in OK} \end{cases}$$

Shear Design

According to AASHTO (Section 5.8.2.1), $V_u \leq \phi_s \times V_n$

$$\phi_s = 0.90 \text{ (AASHTO, Section 5.5.4.2.1)}$$

$$V_u = 103.8 \text{ kips}$$

$$V_n = \text{lesser of } (V_c + V_s) \text{ and } (0.25 \times f'_c \times b \times d)$$

$$V_c = 0.0316 \times \beta \times \sqrt{f'_c} \times b \times d \text{ (AASHTO, 5.8.3.3-3), } \beta = 2.0 \text{ (Section 5.8.3.4.1)}$$

$$V_c = 0.0316 \times 2 \times \sqrt{5} \times 24 \times 18.94 = 64.24 \text{ kips}$$

$$\text{then, required } V_s \geq \frac{V_u}{\phi_s} - V_c = \frac{103.8}{0.90} - 64.24 = 51.1 \text{ kips}$$

$$V_s = \frac{A_v \times f_{sy} \times d}{s_h},$$

$$\text{if using \#3 stirrups with 4 branches} \rightarrow A_v = 4 \times A_{s,\#3} = 4 \times 0.11 = 0.44 \text{ in}^2$$

$$\text{then required spacing } s_{h,required} = \frac{A_v \times f_{sy} \times d}{V_s} = \frac{0.44 \times 60 \times 18.94}{51.1} = 9.78 \text{ in}$$

Check Minimum Shear Reinforcement

$$\text{max stirrups spacing (AASHTO Section 5.8.2.7)} = 0.8 \times d = 0.8 \times 18.94 = 15.1 \text{ in} \leq \frac{24}{4} = 6 \text{ in}$$

use 4 branch #3 stirrups at 5 inch spacing

$$A_v \geq 0.0316 \times \sqrt{f'_c} \times \frac{b \times s}{f_y} = 0.0316 \times \sqrt{5} \times \frac{24 \times 5}{60} = 0.141 \text{ in}^2 < 0.44 \text{ in}^2 \text{ OK}$$

Check Cap Beam Design According to SDC

The SDC requires that the cap beam remains elastic when column reaches its overstrength moment. For the considered specimen, a middle bent column is connected to the cap beam forming a T-shape connection. Accordingly, the column overstrength moment is likely splitted equally between the two beam sections at the column right and left sides.

$$\text{Thus, the cap beam is expected to remain elastic up to } \frac{M_o}{2} = \frac{1.2 \times 3456}{2} = 2073.6 \text{ kip-in}$$

From the moment-curvature analysis using XTRACT,

$$\text{Moment at first yield} = 3002 \text{ kip-in} >> 2073.6 \text{ kip-in OK}$$

Check Beam Torsion Design

One way to check if additional torsion reinforcement is needed is using the ACI-318,

"The design criteria for combined torsion and shear"

The specimen cap beam will be exposed to torsion if the column is pushed in the longitudinal direction, thus, the maximum expected torsion (T_u) on cap beam when elastic column moment is equivalent to its capacity was found approximately from SAP2000 model to be 105.4 kips-in

$$\text{Permitted factored Torque to neglect torsion effects } T_p = \phi \times \sqrt{f'_c} \times \frac{A_{cp}^2}{P_{cp}} \text{ (ACI-318, Section 11.5.1)}$$

$$A_{cp} = \text{area enclosed by beam perimeter} = 24 \times 20.375 = 489 \text{ in}^2, \text{ neglect slab contribution}$$

$$P_{co} = \text{beam perimeter} = 2 \times (24 + 20.375) = 88.75 \text{ in}$$

$$T_p = 0.75 \times \sqrt{5000} \times \frac{489^2}{88.75} = 142888 \text{ lb-in} = 142.9 \text{ kip-in}$$

Since $T_u < T_p$, the torsion effects can be neglected on beam

A.2.3 COLUMN-CAP BEAM JOINT DESIGN

The specimen column-beam joint is considered a T-joint and designed according to Section 7.4 in Caltrans SDC. The joint dimensions and proportionality are checked first, then the required reinforcement is calculated.

Check Joint Proportioning

The principal stresses in the joint should not exceed certain limits.

$$A_{jh} = (D_c + D_s) B_{cap} = (18 + 20.375) \times 24 = 921 \text{ in}^2$$

$$f_v = \frac{P_c}{A_{jh}} = \frac{72}{921} = 0.0782 \text{ ksi} = 78.2 \text{ psi}$$

$$A_{jv} = l_{ac} \times B_{cap} = 18 \times 24 = 432 \text{ in}^2$$

$$T_c = \frac{M_o^{col}}{h} = \frac{4147.2}{0.75 \times 18} = 307.2 \text{ kips}$$

$$v_{jv} = \frac{T_c}{A_{jv}} = \frac{307.2}{432} = 0.711 \text{ ksi} = 711 \text{ psi}$$

$$f_h = \frac{P_f}{B_f \times D_f} = 0 \text{ as beam axial force } P_f \text{ is } 0$$

$$\text{then, } p_t = \frac{f_v + f_h}{2} - \sqrt{\left(\frac{f_v + f_h}{2}\right)^2 + v_{jv}^2} = \frac{78.2 + 0}{2} - \sqrt{\left(\frac{78.2 + 0}{2}\right)^2 + 720^2} = 39.1 - 721.1 = -681.96 \text{ psi}$$

$$\text{Check } p_t < 12\sqrt{f'_c} = 12\sqrt{5000} = 848.5 \text{ psi, So } p_t < 848 \text{ psi OK}$$

$$p_c = \frac{f_v + f_h}{2} + \sqrt{\left(\frac{f_v + f_h}{2}\right)^2 + v_{jv}^2} = \frac{78.2 + 0}{2} + \sqrt{\left(\frac{78.2 + 0}{2}\right)^2 + 720^2} = 39.1 + 721.1 = 760.2 \text{ psi}$$

$$\text{Check } p_c < 0.25f'_c = 0.25 \times 5000 = 1250 \text{ psi, Also } p_c < 1250 \text{ psi OK}$$

So joint proportioning is OK

Joint Shear Reinforcement

Check the principle tensile stress for minimum reinforcement

If $p_t < 3.5\sqrt{f'_c} \rightarrow$ minimum joint shear reinforcement is needed

but $p_t = 681.96 \text{ psi} \gg 3.5\sqrt{5000} = 247.5 \text{ psi}$

then, Shear reinforcement is needed!

Vertical Stirrups :

percentage of column reinforcement, $A_s^{iv} = 0.2 \times A_{st} = 0.2 \times 16 \times 0.44 = 1.41 \text{ in}^2$

if using #3 stirrups with 2 legs, number of stirrups needed $= \frac{1.41}{2 \times 0.11} = 6.4$

use #3 stirrups at 4 inch spacing and distributed in a distance $= 2 \times D_c = 36 \text{ in}$

Horizontal Stirrups :

percentage of column reinforcement, $A_s^{ih} = 0.1 \times A_{st} = 0.1 \times 16 \times 0.44 = 0.704 \text{ in}^2$

if using #3 cross ties, number of ties needed $= \frac{0.704}{0.11} = 6.4$

and maximum vertical spacing in the scaled specimen is $18 \times \frac{1}{4} = 4.5 \text{ in}$,

then use total of 9 #3 cross ties at 3 layers

Horizontal Side Reinforcement :

$A_s^{sf} = \text{greater of } 0.1 \times A_{cap}^{top} \text{ and } 0.1 \times A_{cap}^{bot} = 0.1 \times 8 \times 0.31 = 0.248 \text{ in}^2$

if using #3 side bars, number of bars needed $= \frac{0.248}{0.11} = 2.25$

but maximum spacing in the scaled specimen is $12 \times \frac{1}{4} = 3 \text{ in}$, then use 4 #3 equally spaced at each side

Minimum Continuing Column hoops :

$\rho_s = 0.4 \times \frac{A_{st}}{l_{ac}^2} = 0.4 \times \frac{18 \times 0.44}{18^2} = 0.0098 < \rho_s \text{ from design } (0.014)$

then, the column hoops #3 at 2.0 in. spacing continue into the joint

A.2.4 BOX-GIRDER SLABS DESIGN

The scaled design bending moments of the prototype box-girder slabs can be used to design the specimen slabs, but typically, the gravity loads and bridges spans are large enough to be resisted by ordinary reinforced concrete sections. Consequently, box-girder bridges are pre-stressed (post-tensioned) to reduce cross-sections dimensions and required ordinary reinforcement, which is the case in the used Academy bridge prototype.

However, due to the nature of the test and specimen orientation, the specimen box-girder slabs will not be carrying any direct gravity loads during the test. Thus, for practical reasons, no pre-stressing is needed to be applied to the specimen. Instead, enough ordinary reinforcement can be used to satisfy the SDC and AASHTO requirements. That is to keep the box-girder section elastic when the column reaches its overstrength moment since the bridge superstructure, similar to the cap beam, is a capacity protected member.

Longitudinal Steel

According to AASHTO, Section 5.7.3.3.3., a minimum reinforcement to develop at least 1.2 times the cracking moment of the cross-section is needed. Only the longitudinal bars in the soffit and deck slabs are assumed to provide all the required tensile reinforcement and no contribution is considered from the box-girder web longitudinal reinforcement.

The cracking moment for the specimen box-girder is: $M_{cr} = \frac{f_r \times I_g}{y_t}$

$$f_r = 0.24 \times \sqrt{f'_c} = 0.24 \times \sqrt{5} = 0.537 \text{ ksi}$$

I_g and y_t are calculated from section properties, $y_t = 10.47 \text{ in}$ & $I_g = 41104.2 \text{ in}^4$

$$\text{then, } M_{cr} = \frac{0.537 \times 41104}{10.47} = 2106.9 \text{ kip-in}$$

The required steel to develop such moment can be approximately calculated as follows :

$$A_{s, \text{long}, \text{min}} = \frac{1.2 \times M_{cr}}{\phi \times f_{sy} \times 0.9 \times d} = \frac{1.2 \times 2107}{0.9 \times 60 \times 0.9 \times 18.94} = 2.75 \text{ in}^2$$

Because of the slab thickness limitations in the scaled specimen, use only a single #3 layer, and to guarantee the capacity of box – girder is higher than overstrength of moment of column, try #3 bars at 2.5 inch spacing and check the section capacity

$$\text{number of bars} = \frac{102 - 2}{2.5} + 1 = 41 \text{ bars}$$

$$A_{s, \text{long}} = 41 \times 0.11 = 4.51 \text{ in}^2 > A_{s, \text{long}, \text{min}} = 2.72 \text{ in}^2 \text{ OK}$$

$$\rho_{\text{deck}} = \frac{A_{s, \text{long}}}{A_{\text{deck slab}}} = \frac{4.51}{102 \times 2.25} = 1.97\%, \rho_{\text{soffit}} = \frac{A_{s, \text{long}}}{A_{\text{soffit slab}}} = \frac{4.51}{102 \times 2.125} = 2.08\% > \rho_{\text{min}} = 0.4\% \text{ OK}$$

$$\text{also maximum spacing between bars for scaled specimen} = 18 \times \frac{1}{4} = 4.5 \text{ in} > 2 \text{ in OK}$$

The SDC also requires that box-girder remains elastic when column reaches its overstrength capacity. Thus, moment-curvature analysis was carried out for the specimen box-girder section using XTTRACT.

$$\text{The moment at first yield, } M_y^{\text{box}} = 5554 \text{ kip-in} > \frac{M_o^{\text{col}}}{2} = \frac{4156}{2} = 2078 \text{ kip-in OK}$$

Transverse Steel

Similar to longitudinal direction, the minimum reinforcement to develop at least 1.2 times the cracking moment of the cross-section is calculated first. The cracking moment for a 1-foot slice of the specimen

$$\text{box-girder in the transverse direction can be calculated from } M_{cr} = \frac{f_r \times I_g}{y_t}$$

$$f_r = 0.24 \times \sqrt{f'_c} = 0.24 \times \sqrt{5} = 0.537 \text{ ksi}$$

$$I_g \text{ and } y_t \text{ are calculated from slice section properties, } y_t = 10.645 \text{ in \& } I_{g, 1\text{-ft slice}} = 4348.5 \text{ in}^4$$

$$\text{then, } M_{cr} = \frac{0.537 \times 4348.5}{10.645} = 219.4 \text{ kip-in / ft}$$

The calculated M_{cr} per foot length was found larger than the scaled design transverse bending moments from prototype SAP2000 model, and thus the minimum reinforcement from M_{cr} governs the design.

The required steel to develop such moment can be approximately calculated as follows :

$$A_{s, \text{long}} = \frac{1.2 \times M_{cr}}{\phi \times f_{sy} \times 0.9 \times d} = \frac{1.2 \times 219.4}{0.9 \times 60 \times 0.9 \times 18.94} = 0.286 \text{ in}^2 / \text{ft}$$

Because of the slab thickness limitations in the scaled specimen, use only a single #3 layer,

$$\text{required number of bars} = \frac{0.286}{0.11} = 2.59 \text{ i.e. 3\#3 / ft or 1\#3 at 4 inch spacing}$$

then, use 1\#3 at 4 inch spacing in each of the soffit and deck slabs

A.2.5 BOX-GIRDER WEBS SHEAR DESIGN

The scaled design shear force of the prototype box-girder slabs can be used to design the specimen webs. The factored shear force for the entire prototype box-girder section and each web share was found from SAP2000 model as:

$$V_{u,box-girder} = 3059 \text{ kips and } V_{u,web} = 437 \text{ kips}$$

Accordingly, the factored shear/web for specimen design:

$$V_{u,web}^{spec.} = V_{u,web}^{proto} \times \frac{1}{S_l^2} = 437 \times \frac{1}{4^2} = 27.31 \text{ kips}$$

According to AASHTO (Section 5.8.2.1), $V_u \leq \phi_s \times (V_c + V_s)$

$$\phi_s = 0.90 \text{ (AASHTO, Section 5.5.4.2.1)}$$

$$V_c = 0.0316 \times \beta \times \sqrt{f'_c} \times b \times d \text{ (AASHTO, 5.8.3.3-3), } \beta = 2.0 \text{ (Section 5.8.3.4.1)}$$

$$V_c = 0.0316 \times 2 \times \sqrt{5} \times 3 \times 18.94 = 8.03 \text{ kips}$$

$$\text{then, required } V_s \geq \frac{V_u}{\phi_s} - V_c = \frac{27.31}{0.90} - 8.03 = 22.3 \text{ kips}$$

$$V_s = \frac{A_v \times f_{sy} \times d}{s_h},$$

$$\text{Due to the limited web thickness, try \#3 tie with single leg} \rightarrow A_v = 1 \times A_{s,\#3} = 0.11 \text{ in}^2$$

$$\text{then required spacing } s_{h,required} = \frac{A_v \times f_{sy} \times d}{V_s} = \frac{0.11 \times 60 \times 18.94}{22.3} = 5.6 \text{ in}$$

→ use #3 tie at 5 inch spacing

Check Minimum Shear Reinforcement

$$\text{max stirrups spacing (AASHTO Section 5.8.2.7)} = 0.8 \times d = 0.8 \times 18.94 = 15.1 \text{ in} \leq \frac{24}{4} = 6 \text{ in} > 5 \text{ in OK}$$

use 4 branch #3 stirrups at 5 inch spacing

$$A_v \geq 0.0316 \times \sqrt{f'_c} \times \frac{b \times s}{f_y} = 0.0316 \times \sqrt{5} \times \frac{3 \times 5}{60} = 0.018 \text{ in}^2 < 0.11 \text{ in}^2 \text{ OK}$$

A.2.6 SPECIMEN RC SEAT BEAM DESIGN

Geometry

Start with a seat beam with width, $b = 12 \text{ in}$ and height, $h = 19 \text{ in}$

The materials are the same as the specimen since the seat beams will be casted in place with the specimen

Flexural Design

$$\phi_f M_n \geq M_u$$

From the preliminary analysis of the specimen in addition to considering the three prestressing forces per seat to attach the specimen to the laboratory rigid floor, $M_u = 640 \text{ kip-in}$

Start the first beam design trial by neglecting compression steel and assuming a moment arm of " $0.9 \times d$ " between the tension steel reinforcement c.g. and the compression stress block c.g.

$$d = h - \text{cover} - \phi_{\text{stirrup}} - \frac{\phi_{\text{long.bar}}}{2} = 19 - 0.75 - 0.375 - \frac{0.625}{2} = 17.56 \text{ in}$$

$$\phi_f = 0.9$$

$$M_n = \text{Tension force in steel} \times \text{moment arm} = A_s \times f_{sy} \times 0.9 \times d$$

then, required reinforcement :

$$A_{s, \text{required}} \geq \frac{M_u}{\phi_f \times f_{sy} \times 0.9 \times d} = \frac{640}{0.9 \times 60 \times 0.9 \times 17.56} = 0.75 \text{ in}^2$$

$$\text{number of \#5 bars required} = \frac{A_{s, \text{required}}}{A_{s, \#5}} = \frac{0.75}{0.31} = 2.4 \rightarrow \text{use 4 \#5 bars for bottom reinforcement}$$

$$C = T = A_s \times f_{sy} = 4 \times 0.31 \times 60 = 74.4 \text{ kips}$$

$$C = c \times b \times \beta_1 \times f'_c, \beta_1 = 0.85 - \frac{0.05}{1000} (f'_c - 4000) = 0.80 \text{ (AASHTO, Section 5.7.2.2)}$$

$$\text{then, } c = \frac{C}{b \times \beta_1 \times f'_c} = \frac{74.4}{12 \times 0.80 \times 5} = 1.55 \text{ in}$$

$$M_n = T \times (d - \frac{a}{2}) = 74.4 \times (17.56 - 0.775) = 1248.2 \text{ kip-in} > \frac{M_u}{\phi_f} = \frac{640}{0.9} = 711.11 \text{ kip-in OK}$$

check bars' center-to-center spacing :

$$s_b = \frac{b - 2 \times (\text{cover} + \phi_{\#3} + \frac{\phi_{\#5}}{2})}{\text{number of bars} - 1} = \frac{12 - 2 \times (0.75 + 0.375 + \frac{0.625}{2})}{4 - 1} \approx 3 \text{ in} \begin{cases} < 8 \text{ in OK} \\ > 1.5 \text{ in OK} \end{cases}$$

Shear Design

$$V_u \leq \phi_s \times (V_c + V_s)$$

From analysis, $V_u = 84 \text{ kips}$, $\phi_s = 0.90$,

$$V_c = 0.0316 \times \beta \times \sqrt{f'_c} \times b \times d \quad (\text{AASHTO, 5.8.3.3-3}), \quad \beta = 2.0 \text{ (Section 5.8.3.4.1)}$$

$$V_c = 0.0316 \times 2 \times \sqrt{5} \times 12 \times 17.56 = 29.78 \text{ kips}$$

$$\text{then, required } V_s \geq \frac{V_u}{\phi_s} - V_c = \frac{84}{0.90} - 29.8 = 63.5 \text{ kips}$$

$$V_s = \frac{A_v \times f_{sy} \times d}{s_h},$$

$$\text{if using \#3 stirrups with 2 legs} \rightarrow A_v = 2 \times A_{s,\#3} = 2 \times 0.11 = 0.22 \text{ in}^2$$

$$\text{then required spacing } s_{h,\text{required}} = \frac{A_v \times f_{sy} \times d}{V_s} = \frac{0.22 \times 60 \times 17.56}{63.5} = 3.65 \text{ in}$$

$$\text{if using 2 \#3 stirrups with 2 legs each} \rightarrow A_v = 4 \times A_{s,\#3} = 4 \times 0.11 = 0.44 \text{ in}^2$$

$$\text{then required spacing } s_{h,\text{required}} = \frac{A_v \times f_{sy} \times d}{V_s} = \frac{0.44 \times 60 \times 17.56}{63.5} = 7.30 \text{ in}$$

Check minimum shear reinforcement:

$$A_v \geq 0.0316 \times \sqrt{f'_c} \times \frac{b \times s}{f_y} = 0.0316 \times \sqrt{5} \times \frac{12 \times 5}{60} = 0.07 \text{ in}^2 < 0.22 \text{ in}^2 \text{ OK}$$

\rightarrow use 2 #3 stirrups with 2 legs each at 5.0 inch center – to – center spacing

Appendix B Structural and Shop Drawings

The final structural and shop drawings (Figures B.1–B.9, and Tables B-1–B.3) sent out to bid to steel fabricators and the construction contractor to build the test specimens follows.



University of California, Berkeley
Structures Laboratory

Box-Girder and Column Subassembly Test Specimens – Final Bidding Document

Final Test Setup, Specimen Drawings and
Reinforcement Tables

March 2013

NOTES:

Concrete:

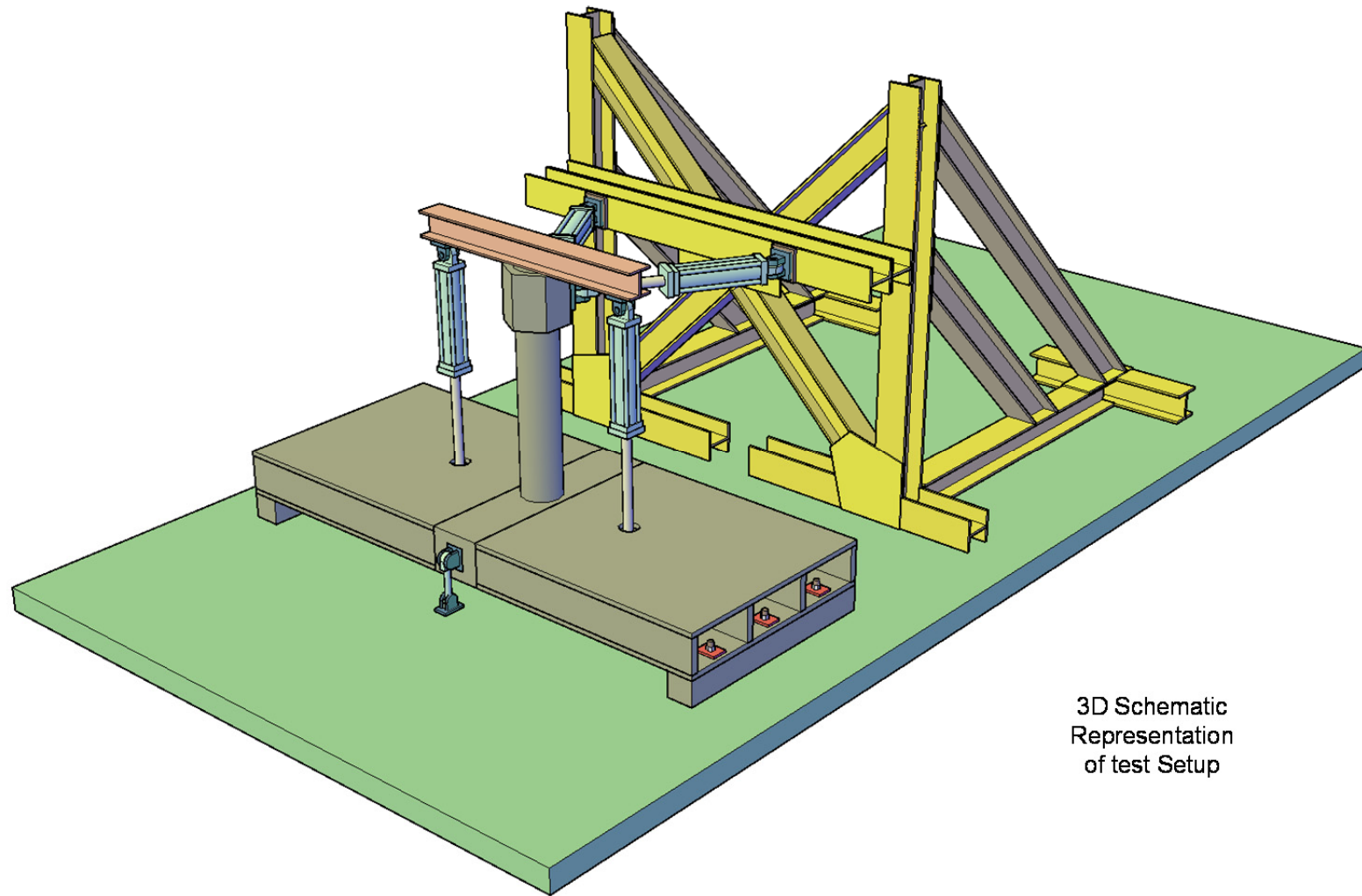
- $f'_c = 5000$ psi at 28th day.
- Maximum aggregate size = 3/8 inch.

Reinforcing steel:

- All ASTM A706 Grade 60 except for stirrups.
- Stirrups can be either A706 Grade 60 or A615 Grade 60.
- Supply all reinforcements made from the same batch such that they have consistent material properties.

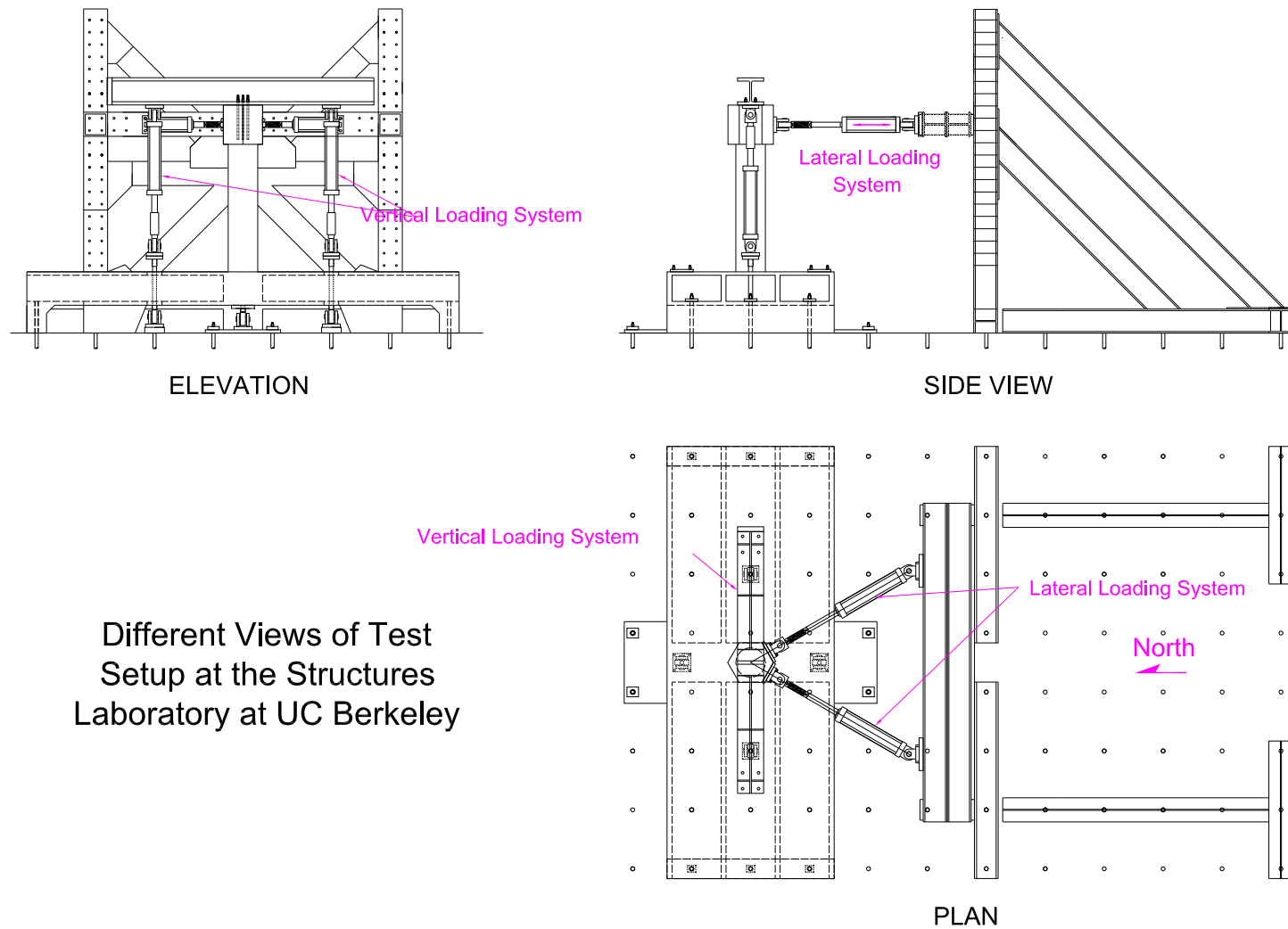
A minimum concrete cover of 3/8" is required for stirrups and ties.

A minimum concrete cover of 3/4" is required for main longitudinal reinforcement.



3D Schematic
Representation
of test Setup

Figure B.1 Schematic representation of the test set-up at the Structures Laboratory at UCB.



Different Views of Test
Setup at the Structures
Laboratory at UC Berkeley

Figure B.2 Different views of the test set-up at the Structures Laboratory at UCB.

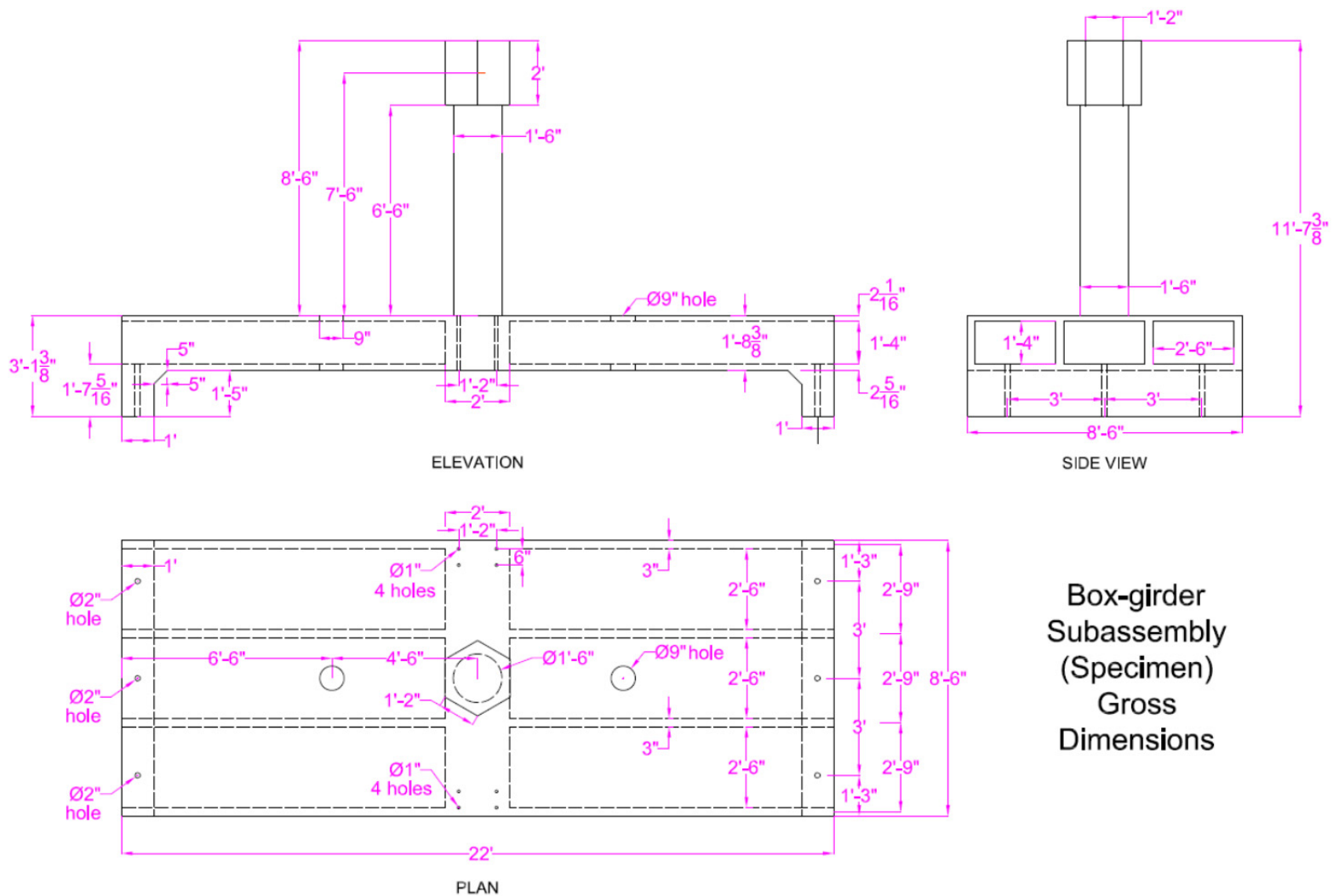


Figure B.3 Different views of the test specimen dimensions.

Construction Stages:

- Concrete quantities shown are for one specimen only.
- For two specimens built concurrently, double the shown concrete quantities will be needed for each pour.

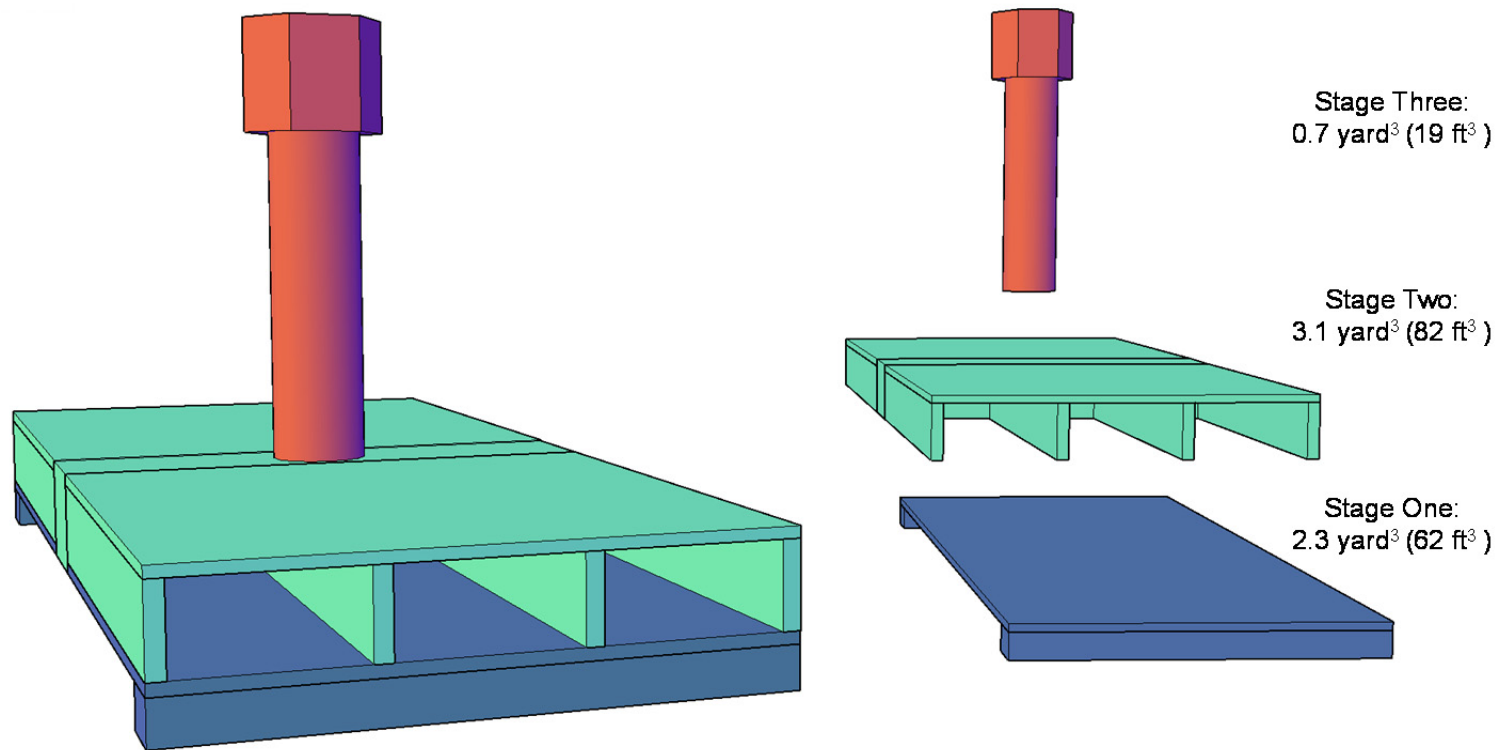
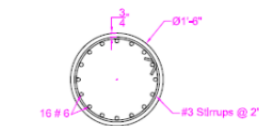
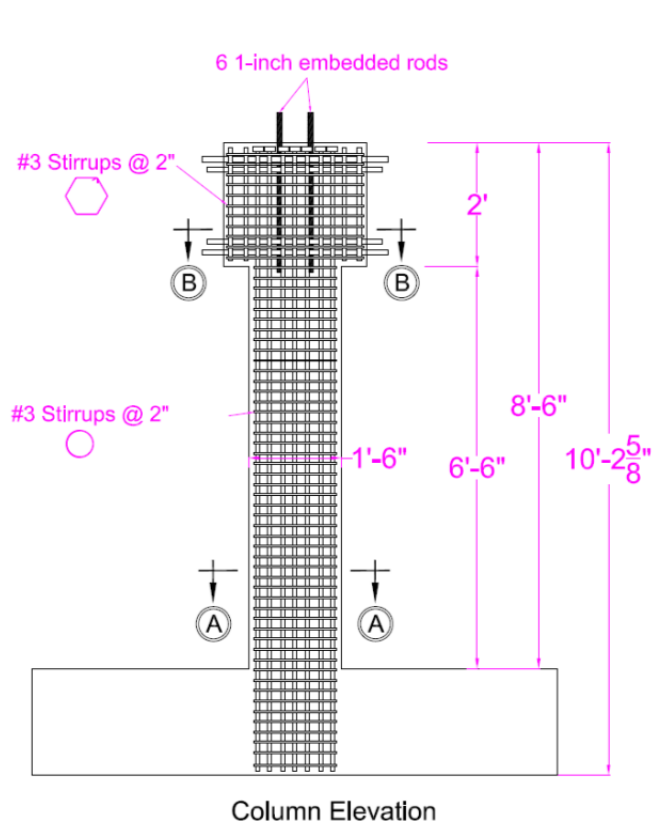
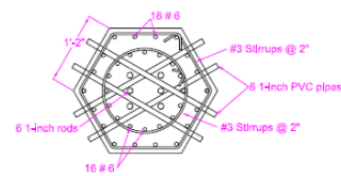


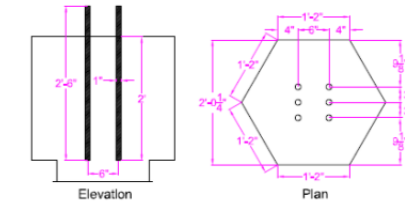
Figure B.4 Three phases and concrete lifts sought for construction of the specimens.



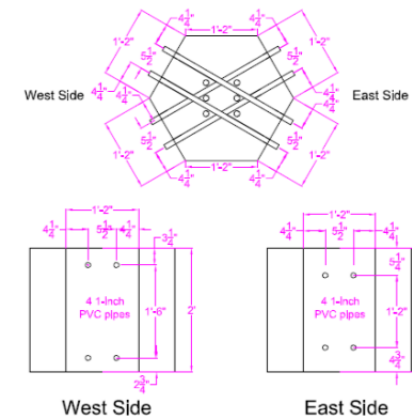
Cross-Section A-A



Cross-Section B-B



Six embedded 1-inch rods locations



Column Head pipes locations
"Total of 8 1-inch through pipes"

Figure B.5 Different views and cross sections of the column reinforcement and location of construction pipes.

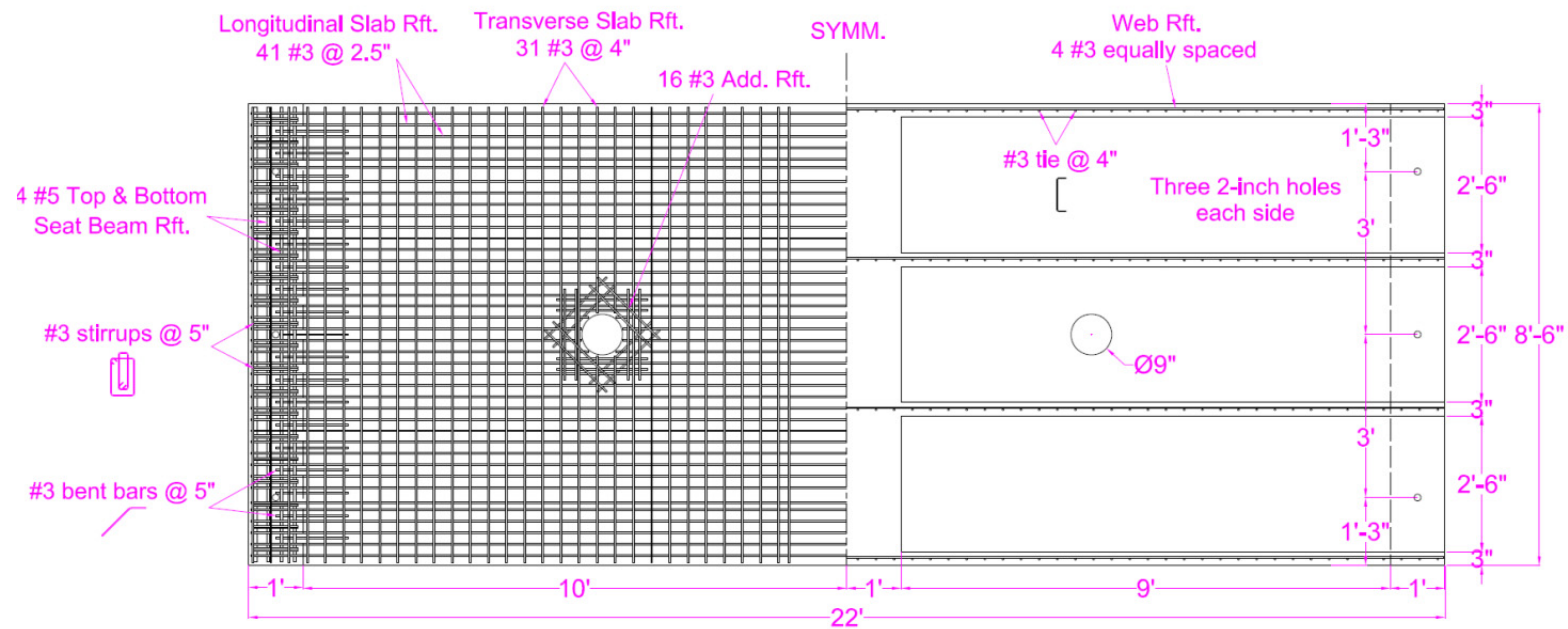


Figure B.6 Deck slab reinforcement and details.

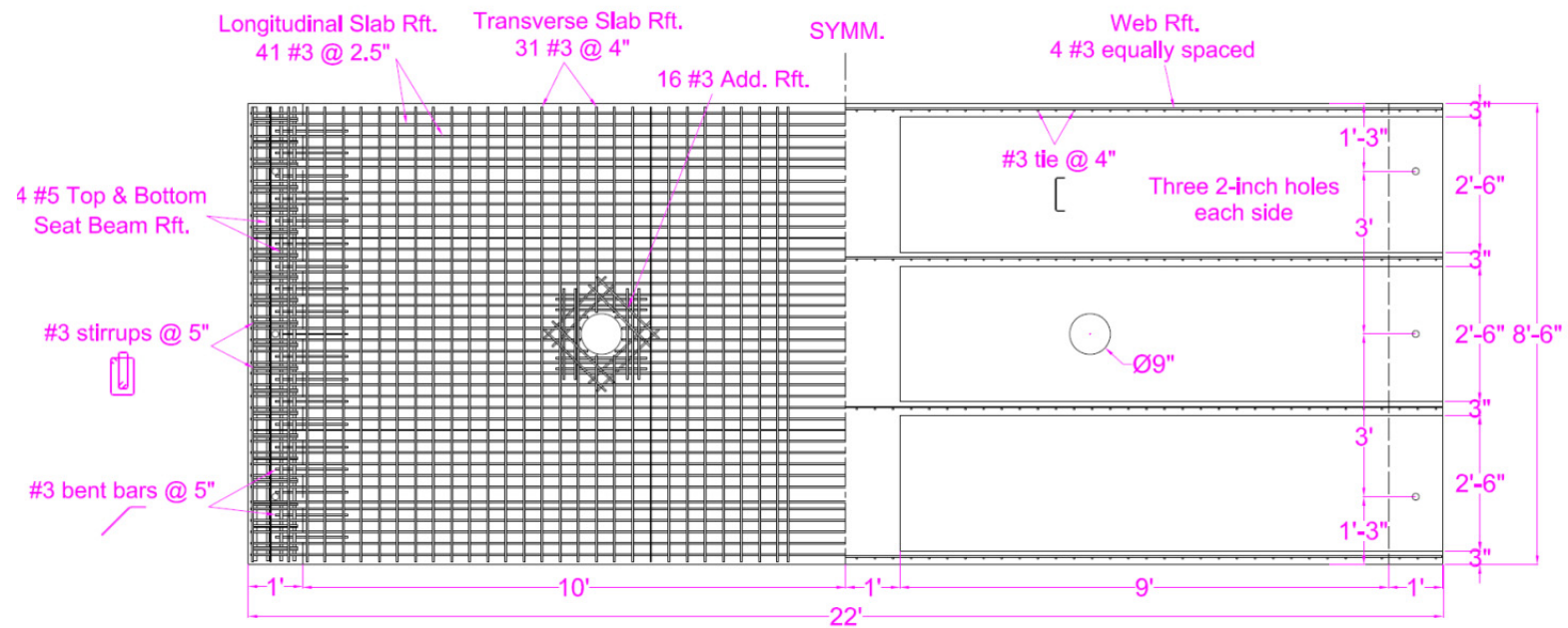


Figure B.7 Soffit slab reinforcement and details.

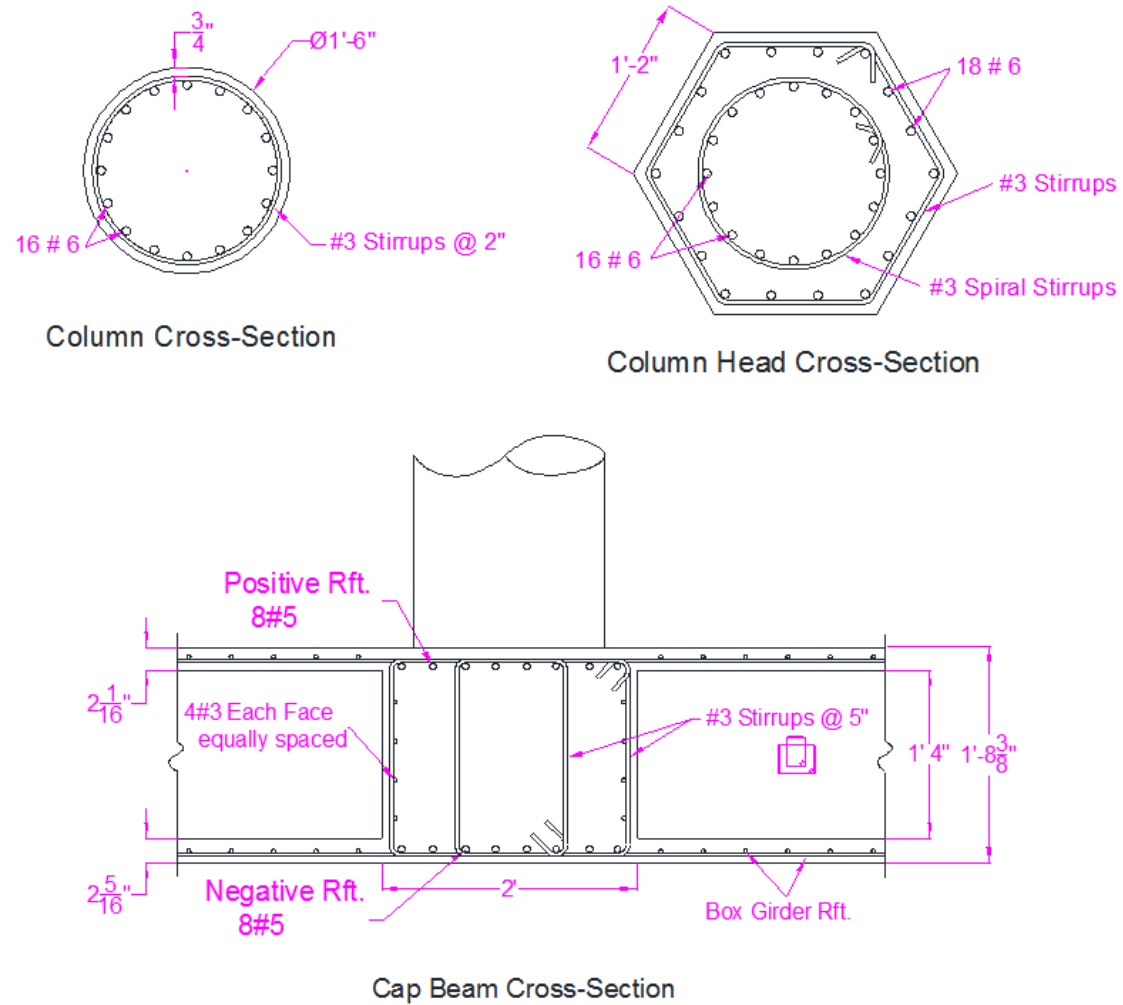


Figure B.8 Details of the longitudinal and transverse reinforcement for the column and cap beam section of the specimens.

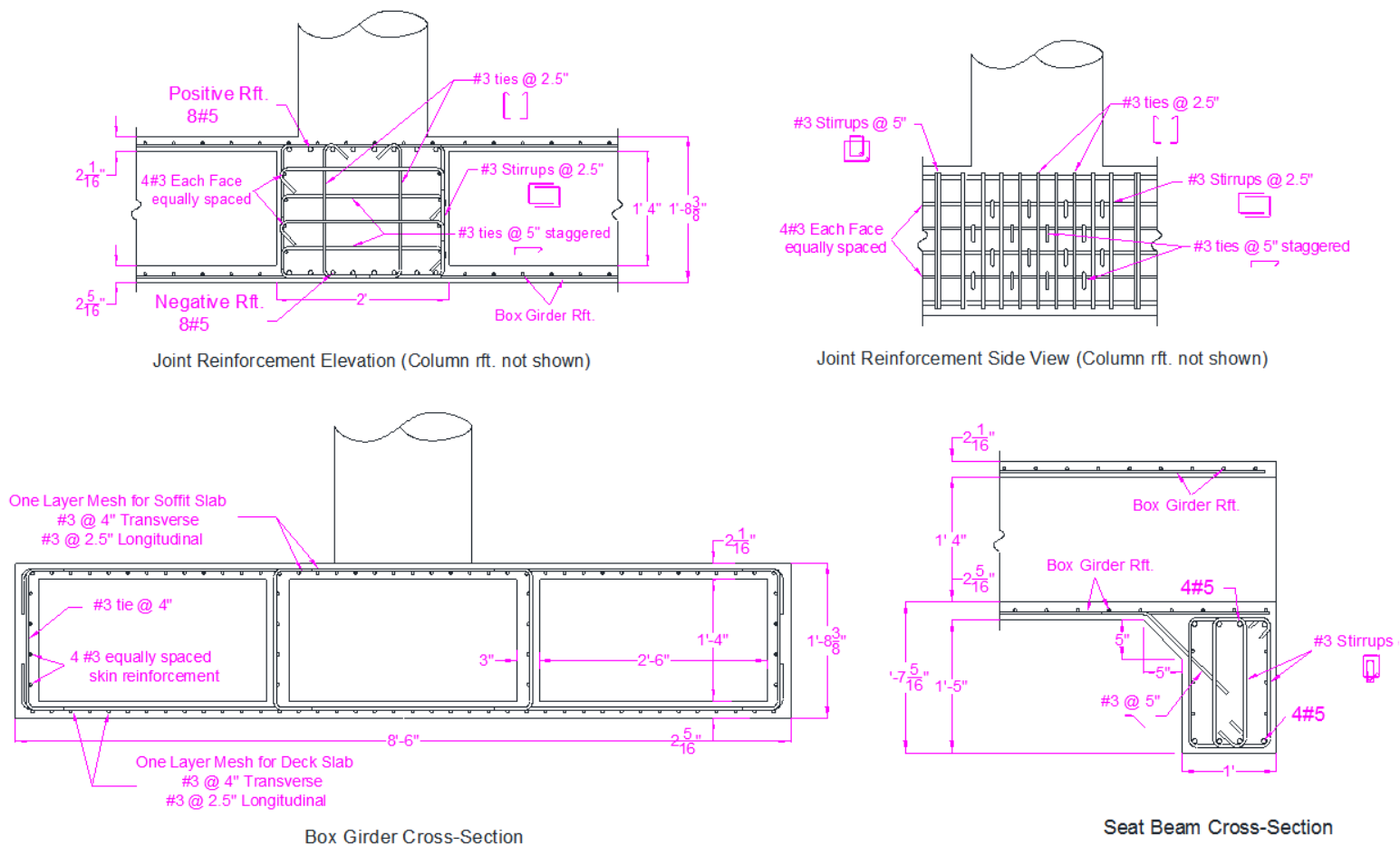


Figure B.9 Details of longitudinal and transverse reinforcement for the specimens' joint, box-girder, and beam section.

Table B.1 Longitudinal reinforcement shop drawing for one specimen (quantity).

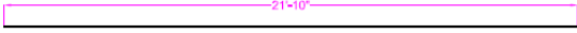
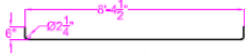
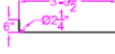
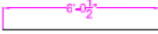
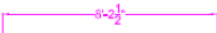

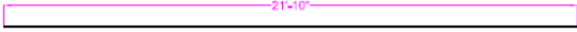
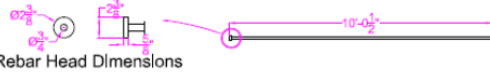
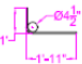
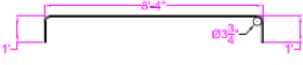
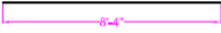

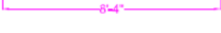
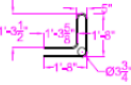

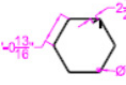
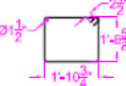
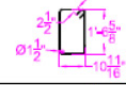




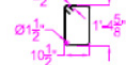
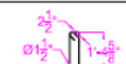
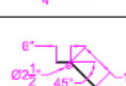
Item Discription		Bar Length	Diameter	Total bar length	Quantity
Soffit & Deck Slabs	Long. Slab Rft.		#3	21' 10"	82
	Transverse Slab Rft.		#3	9' 4.5"	136
	Trans. Rft. @ hole		#3	4' 3.5"	16
	Long. Rft. @ hole (two ends)		#3	6' 0.5"	16
	Long. Rft. @ hole (middle)		#3	8' 2.5"	8
	Rft. around hole		#3	1' 8"	68
Box girder Web Long. Rft.			#3	21' 10"	16
Column Long. Rft. (Headed Rebars)			#6	10' 0.5"	19
Column Head Rft.			#6	2' 11"	18
Cap Beam	Negative & Positive Rft.		#5	10' 4"	18
	Skin Rft.		#3	8' 4"	8
Seat Beams	Negative & Positive Rft.		#5	10' 4"	16
	Skin Rft.		#3	8' 4"	12
Lifting Hook			#5	6' 5"	6

Table B 2 Transverse reinforcement shop drawing for one specimen (quantity and total weights and length).

Item No.	Discription	Bar Length	Diameter	Quantity	Bar weight (lb.)	Total weight (lb.)	Total length (ft.)
1	Long. Slab and web Rft.		#3	98	8.21	673.2	1791
2	Transverse Slab Rft.		#3	136	3.53	479.4	1275
3	Trans. Rft. @ hole		#3	16	1.61	25.8	69
4	Long. Rft. @ hole (two ends)		#3	16	2.27	36.4	97
5	Long. Rft. @ hole (middle)		#3	8	3.09	24.7	66
6	Add. Slab Rft. around hole		#3	68	0.63	42.6	114
7	Column Long. Rft. (headed bars)		#6	19	15.08	286.6	191
8	Column head Long. Rft.		#6	18	4.38	78.9	53
9	Cap and Seat Beams Long. Rft.		#5	34	10.78	366.5	352
10	Cap and Seat Beams Skin Rft.		#3	20	3.13	25.1	67
11	Lifting Hook		#5	6	6.69	40.2	39

Total weight of #3 rebars ~ 1476 lb	Total length of #3 rebars ~ 3926 ft
Total weight of #5 rebars ~ 407 lb	Total length of #5 rebars ~ 390 ft
Total weight of #6 rebars ~ 365 lb	Total length of #6 rebars ~ 244 ft

Table B.3 Longitudinal reinforcement shop drawing for one specimen (Total weight and length).

Item No.	Dimensions	Length (ln.)	Diameter	Quantity	Unit weight (lb.)	Total weight (lb.)	Total length (ft.)
1		57	#3	60	1.79	107.2	285
2		85	#3	11	2.66	29.3	78
3		91	#3	32	2.85	91.2	243
4		67	#3	24	2.10	50.4	134
5		65	#3	18	2.04	36.66	98
6		29	#3	264	0.91	239.9	638
7		28.5	#3	20	0.89	17.9	48
8		32.75	#3	16	1.03	16.4	44
9		62.5	#3	42	1.96	82.3	220
10		50	#3	42	1.57	65.8	175
11		21	#3	42	0.66	27.6	74

All dimensions are outer dimensions, and a minimum 1.5"-diameter bend to be used for hooks and corners

Total weight of #3 stirrups and ties ~ 737 lb

Total length of #3 stirrups and ties ~ 2034 ft

Appendix C Construction of Specimens

Figures C.2–C.17 illustrate the different stages and phases for constructing the formwork of the two test specimens including: fabricating the reinforcement cages, casting the concrete in three different lifts, and removal. all formwork All the construction work took place inside the Structures Laboratory at UCB where the specimens were set-up and tested.

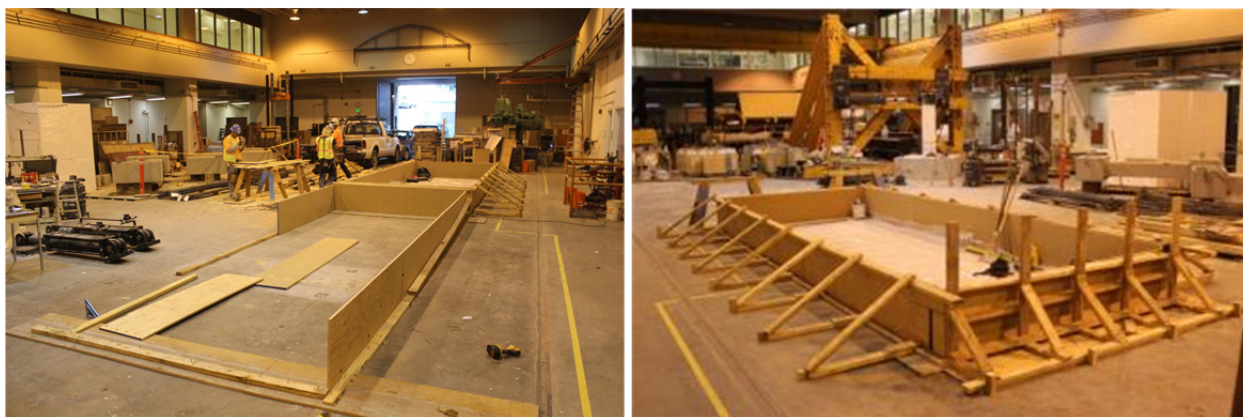


Figure C.1 Laying out the construction space and setting up the formwork for the seat beams of the specimens.

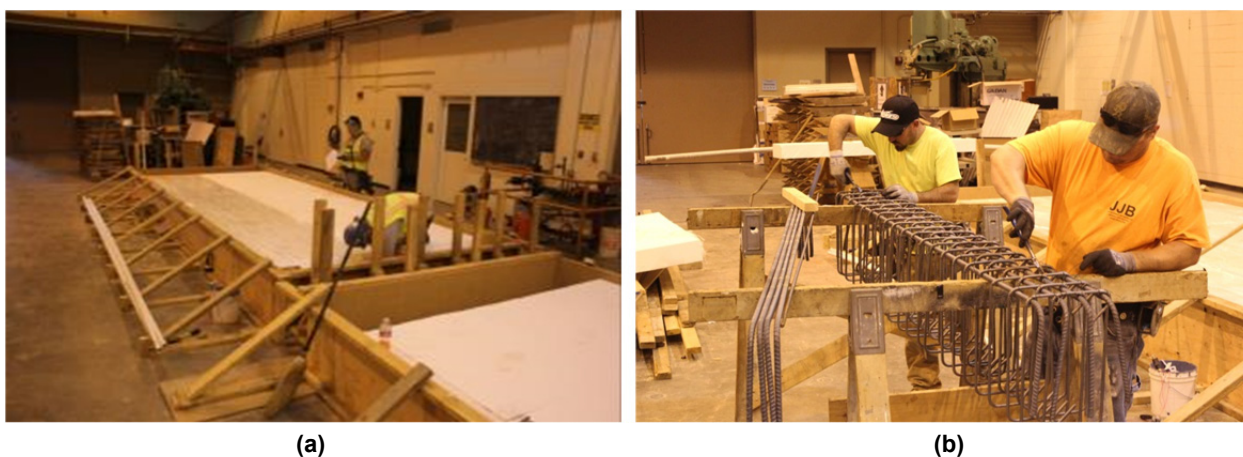


Figure C.2 (a) Preparing styrofoam blocks used to fill the void between seat beams, which were then covered with plastic; and (b) fabricating the reinforcement cage of the seat beams.

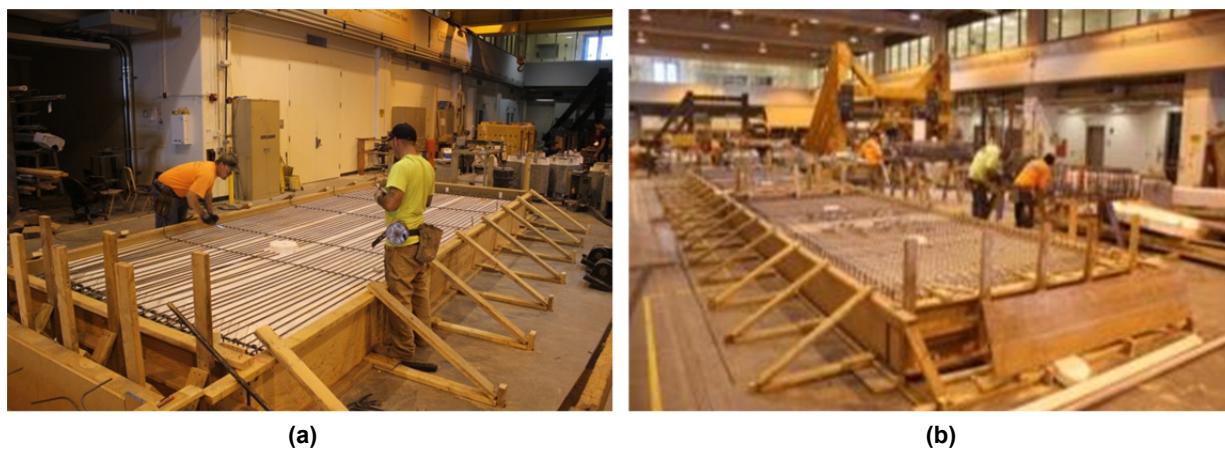
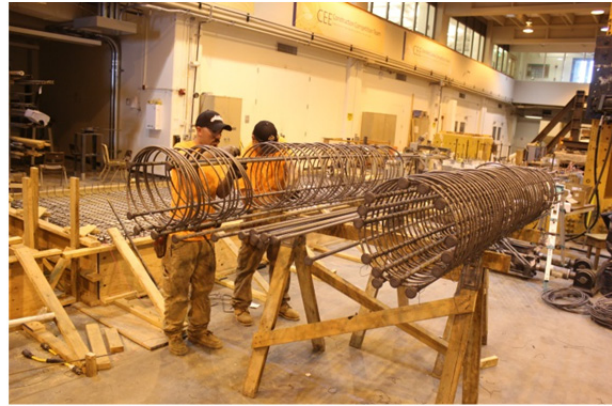


Figure C.3 (a) Laying out the deck slab longitudinal and transverse reinforcement and installing two styrofoam cylinders to construct the 9-in. holes for actuator rods to pass through (left); and (b) final completed deck slab reinforcement mesh.



(a)



(b)

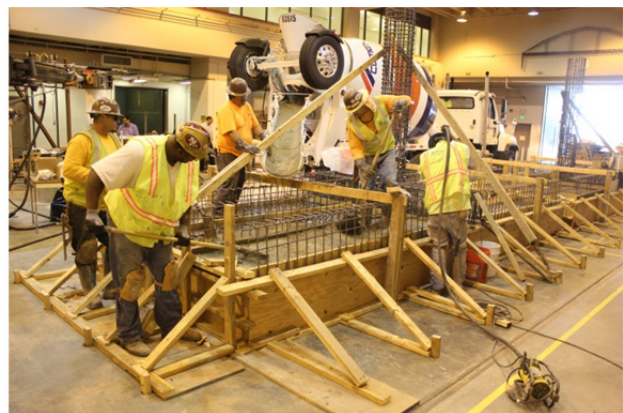
Figure C.4 (a) Fabrication of the bent cap beam and (b) columns cages.



Figure C.5 Different stages of assembling the bent cap beam and column cages then installing the assembly in place using the overhead crane



(a)



(b)

Figure C.6 (a) A view of the complete reinforcement installation for the first construction phase including the box-girder webs reinforcement; and (b) casting the seat beams and box-girder deck slab concrete first lift.



(a)



(b)

Figure C.7 (a) Finishing the concrete surface after first lift; and (b) covering the deck slab fresh concrete with curing blankets to avoid shrinkage cracks.



(a)



(b)

Figure C.8 (a) Setting up the side formwork for the second construction phase to build the box-girder; and (b) installing special custom-made cardboard boxes for the box-section cells.



(a)



(b)

Figure C.9 (a) Laying out the soffit slab reinforcement mesh; and (b) casting the box-girder soffit slab and cap beam second concrete lift.



Figure C.10 (a) Finishing the surface of the second concrete lift; and (b) using curing blankets in addition to the E-CURE to avoid any shrinkage cracks in the soffit slab.

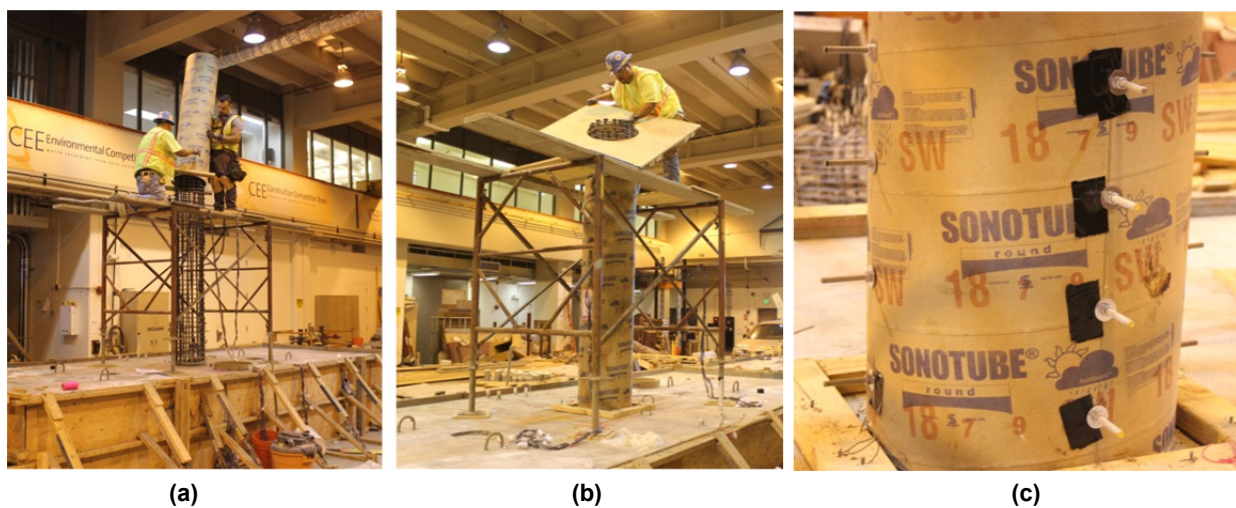


Figure C.11 (a) Installing the column sonotube; (b) building the column head scaffolding; and (c) inserting instrumentation rods into the column formwork.



(a)



(b)

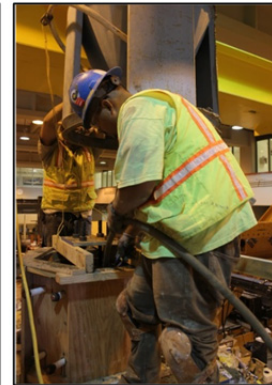
Figure C.12 (a) Special hexagonal formwork for the column head; and (b) overview of the complete formwork and scaffolding for the columns and column heads.



(a)



(b)



(c)

Figure C.13 (a) Placing concrete into an overhead hopper for the third concrete lift; (b) moving the hopper using the overhead crane; and (c) placing and vibrating the concrete of the column and column head.



Figure C.14 Finished construction of the two specimens after three stages and being left to cure for 21 days before removing the formwork.

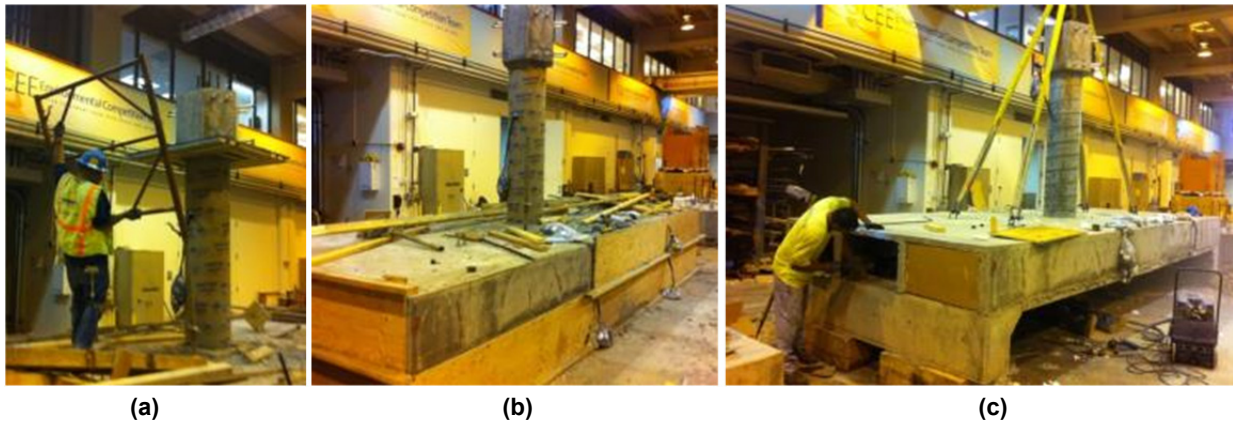


Figure C.15 (a) Removal of column scaffolding, (b) side formwork, and (c) inside cardboard boxes.



Figure C.16 (a) Remnants of the cardboard boxes from inside the box-girder cells; and (b) grinding any styrofoam or plastic wrap stuck to the concrete surface.



Figure C.17 A view of one of the two constructed box-girder subassembly specimens after all formwork removal.

Appendix D: Test Set-Up Procedure

Figures D.1–D.14 illustrate the different stages and phases for setting up and testing of the bridge column-bent cap beam-box girder subassembly specimens at the Structures Laboratory at UCB.



Figure D.1 Reconfiguring the reaction frame and horizontal actuators at the Structures Laboratory at University of California, Berkeley, to match the height of the test specimens.



(a)



(b)

Figure D.2 (a) Preparing the transfer plates where the vertical struts were attached by drilling matching set of holes; and (b) hydrostoning it to the laboratory floor.



(a)



(b)

Figure D.3 (a) Installing the vertical actuators base plates; and (b) an overview of the vertical struts transfer plates and vertical actuators base plates after hydrostoning and prestressing to the rigid floor.



Figure D.4 Moving the first specimen from where it was constructed to where it was tested using the laboratory overhead 10-ton crane.



(a)

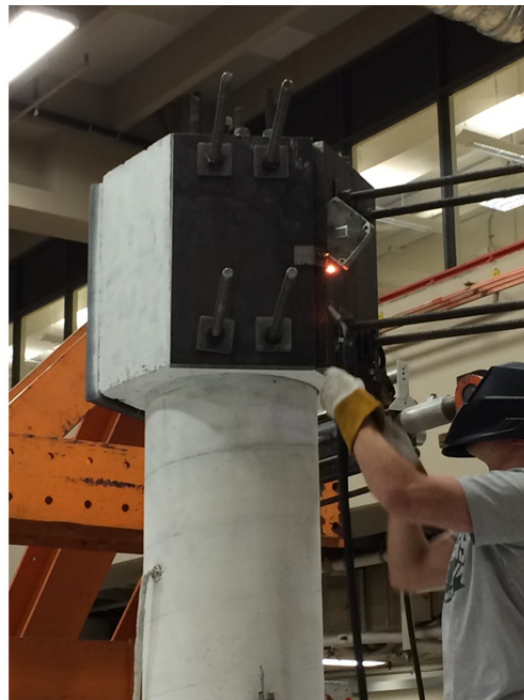


(b)

Figure D.5 (a) Installing the south and (b) east auxiliary instrumentation frames.



(a)



(b)

Figure D.6 (a) Hydrostoning the specimen's seat beams to the rigid floor; and (b) installing the column head plates and instrumentation target eyebolt.



(a)



(b)

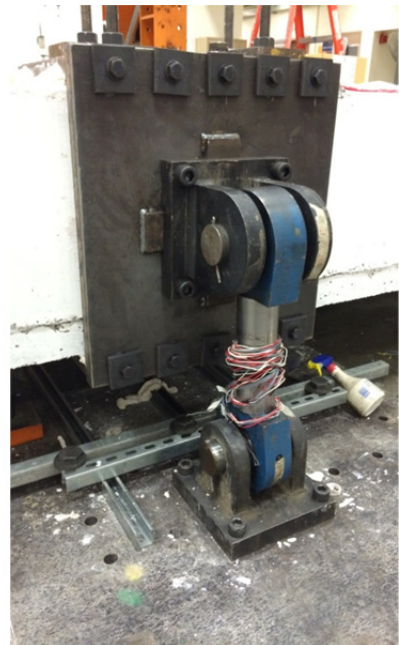
Figure D.7 (a) Installing the top and (b) bottom plates used as part of the vertical strut connection at one of the bent cap beam ends.



(a)



(b)



(c)

Figure D.8 (a) Assembling one of the vertical struts using the instrumented load cell and two clevises; (b) aligning and attaching the side plate used as part of the vertical strut connection; and (c) final vertical strut connection at one of the bent cap beam ends.

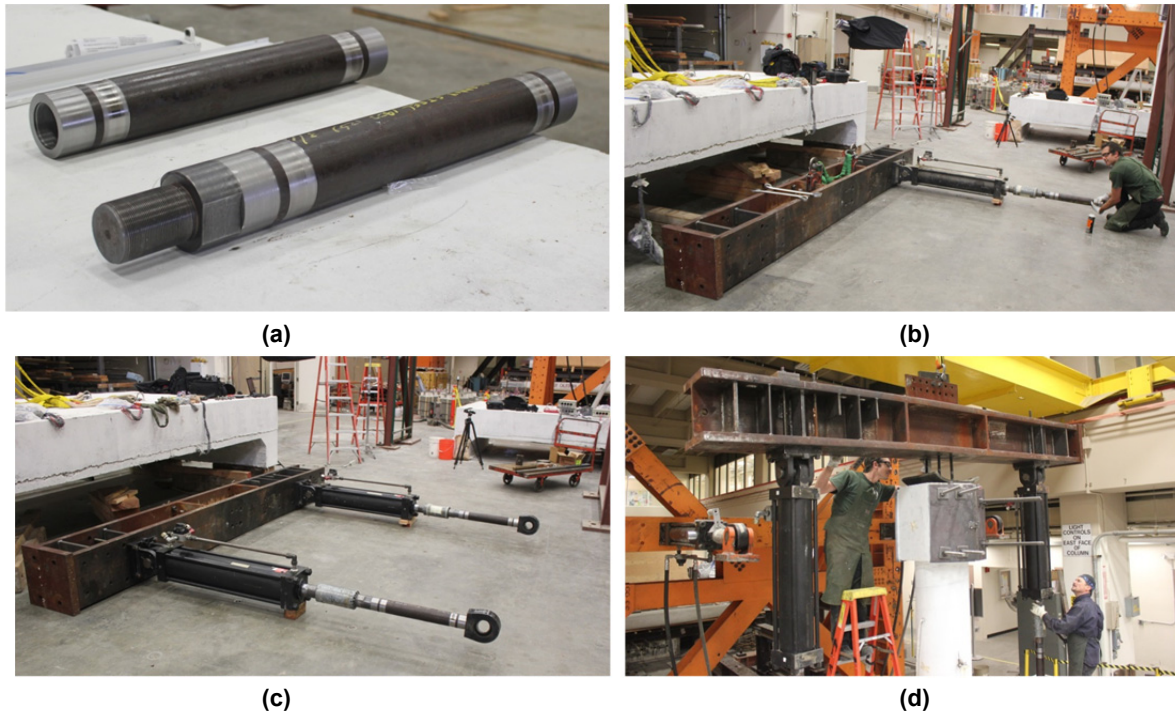


Figure D.9 (a) Different stages of assembling the vertical gravity loading system by assembling the actuators extensions; (b) and (c) attaching the actuators to the spreader beam; and (d) moving the whole gravity loading system by the overhead crane to install it on top of the column.

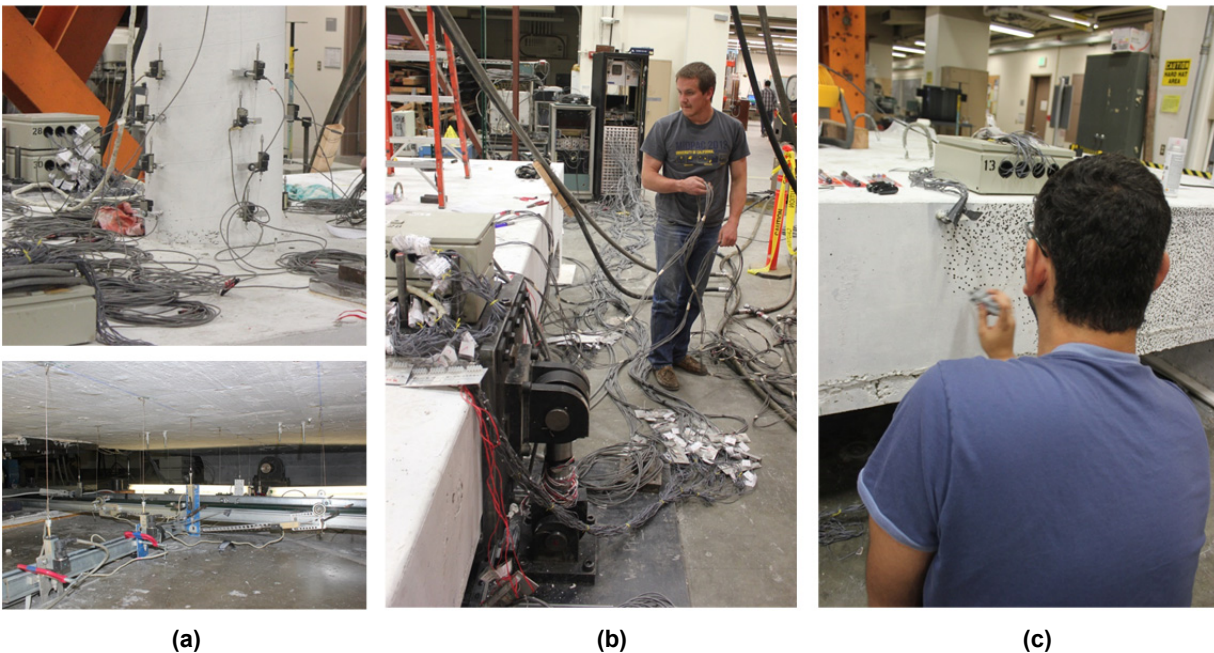


Figure D.10 Different stages of instrumenting the test specimen with LVDTs at (a) the column expected plastic hinge zone (top) and under the specimen (bottom); (b) extending instrumentation cables; and (c) preparing the specimen for digital image correlation advanced monitoring technique.

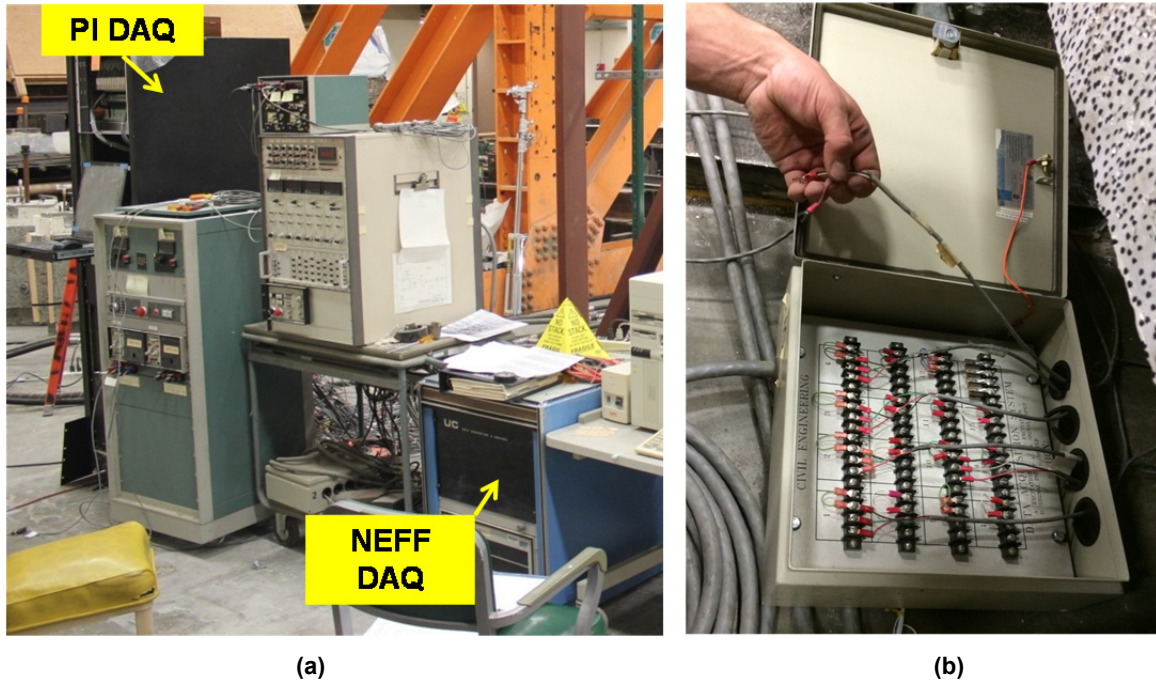


Figure D.11 (a) Two different types of data acquisition system (DAQ) used for collecting over 250 instruments data; and (b) example of connecting instruments cables to one of the NEFF DAQ special connection boxes.



Figure D.12 Attaching the two horizontal actuators to the column head to complete the last step of the test set-up procedure.



Figure D.13 Overview of the test set-up and final cameras and flash light installations.



Figure D.14 Close-up view of the test set-up during testing of Specimen No. 1..

Appendix E: Instrumentations List

More than 250 instruments were used during the course of the experimental program conducted in this study. The instruments were split between two data acquisition systems: Pacific instruments (PI) and NEFF. The list of channels acquired from the PI and NEFF data acquisition systems is shown in Table E.1 and Table E.2, respectively.

Table E.1 List of instrumentation channels connected to the PI data acquisition.

Channel #	Name	Type of Instrument	Unit
1	Time	n/a	microsecond
2	Run	n/a	n/a
3	Pacific - 129 (0:2:0) N lat tem	Tempasonic	in.
4	Pacific - 130 (0:2:1) s lat tem	Tempasonic	in.
5	Pacific - 135 (0:2:6) n grav te	Tempasonic	in.
6	Pacific - 136 (0:2:7) s grav te	Tempasonic	in.
7	Pacific - 131 (0:2:2) n gravity	Load cell	kips
8	Pacific - 132 (0:2:3) s grav lo	Load cell	kips
9	Pacific - 133 (0:2:4) n lat loa	Load cell	kips
10	Pacific - 134 (0:2:5) s lat loa	Load cell	kips
11	Pacific - 137 (0:3:0) bs-out-e1	Strain gauge	microstrain
12	Pacific - 139 (0:3:2) bs-out-e3	Strain gauge	microstrain
13	Pacific - 141 (0:3:4) bs-out-w2	Strain gauge	microstrain
14	Pacific - 142 (0:3:5) bs-out-w3	Strain gauge	microstrain
15	Pacific - 143 (0:3:6) bs-in-e1	Strain gauge	microstrain
16	Pacific - 144 (0:3:7) bs-in-e2	Strain gauge	microstrain
17	Pacific - 145 (0:4:0) bs-in-e3	Strain gauge	microstrain
18	Pacific - 146 (0:4:1) bs-in-w1	Strain gauge	microstrain
19	Pacific - 147 (0:4:2) bs-in-w2	Strain gauge	microstrain
20	Pacific - 148 (0:4:3) bs-in-w3	Strain gauge	microstrain
21	Pacific - 149 (0:4:4) js-out-w1	Strain gauge	microstrain
22	Pacific - 151 (0:4:6) jv-e1	Strain gauge	microstrain
23	Pacific - 152 (0:4:7) jv-e2	Strain gauge	microstrain
24	Pacific - 153 (0:5:0) jv-w2	Strain gauge	microstrain
25	Pacific - 155 (0:5:2) jh-e2	Strain gauge	microstrain
26	Pacific - 156 (0:5:3) jh-w1	Strain gauge	microstrain
27	Pacific - 157 (0:5:4) jh-w2	Strain gauge	microstrain
28	Pacific - 158 (0:5:5) cbt-n1-a	Strain gauge	microstrain
29	Pacific - 159 (0:5:6) cbt-n1-b	Strain gauge	microstrain
30	Pacific - 160 (0:5:7) cbt-n1-d	Strain gauge	microstrain
31	Pacific - 161 (0:6:0) cbt-n1-a	Strain gauge	microstrain
32	Pacific - 162 (0:6:1) cbt-n2-b	Strain gauge	Microstrain
33	Pacific - 163 (0:6:2) cbt-n2-c	Strain gauge	microstrain
34	Pacific - 164 (0:6:3) cbt-n2-d	Strain gauge	microstrain
35	Pacific - 165 (0:6:4) cbt-n2-e	Strain gauge	microstrain
36	Pacific - 166 (0:6:5) cbt-s1-b	Strain gauge	microstrain
37	Pacific - 167 (0:6:6) cbt-s1-d	Strain gauge	microstrain
38	Pacific - 168 (0:6:7) cbt-s1-e	Strain gauge	microstrain
39	Pacific - 169 (0:7:0) cbt-s2-a	Strain gauge	microstrain
40	Pacific - 170 (0:7:1) cbt-s2-b	Strain gauge	microstrain
41	Pacific - 171 (0:7:2) cbt-s2-c	Strain gauge	microstrain
42	Pacific - 172 (0:7:3) cbt-s2-d	Strain gauge	microstrain
43	Pacific - 173 (0:7:4) cbt-s2-e	Strain gauge	microstrain
44	Pacific - 174 (0:7:5) cbb-n1-a	Strain gauge	microstrain
45	Pacific - 175 (0:7:6) cbb-n1-b	Strain gauge	Microstrain
46	Pacific - 176 (0:7:7) cbb-n1-c	Strain gauge	Microstrain
47	Pacific - 177 (0:8:0) cbb-n1-d	Strain gauge	microstrain
48	Pacific - 178 (0:8:1) cbb-n2-a	Strain gauge	microstrain
49	Pacific - 179 (0:8:2) cbb-n2-b	Strain gauge	microstrain
50	Pacific - 181 (0:8:4) cbb-n2-d	Strain gauge	microstrain
51	Pacific - 182 (0:8:5) cbb-n2-e	Strain gauge	microstrain
52	Pacific - 183 (0:8:6) cbb-s1-b	Strain gauge	microstrain
53	Pacific - 184 (0:8:7) cbb-s1-c	Strain gauge	microstrain
54	Pacific - 130 (0:9:1) cbb-s1-e	Strain gauge	microstrain
55	Pacific - 131 (0:9:2) cbb-s2-a	Strain gauge	microstrain
56	Pacific - 132 (0:9:3) cbb-s2-b	Strain gauge	microstrain
57	Pacific - 133 (0:9:4) cbb-s2-c	Strain gauge	microstrain

Table E.1 Continued.

Channel #	Name	Type of Instrument	Unit
58	Pacific - 134 (0:9:5) cbb-s2-d	Strain gauge	microstrain
59	Pacific - 135 (0:9:6) cbb-s2-e	Strain gauge	microstrain
60	Pacific - 136 (0:9:7) cbb-s0-b	Strain gauge	microstrain
61	Pacific - 137 (0:10:0) cbb-n0-b	Strain gauge	microstrain
62	Pacific - 138 (0:10:1) cbb-s0-d	Strain gauge	microstrain
63	Pacific - 139 (0:10:2) cbb-n0-d	Strain gauge	microstrain
64	Pacific - 140 (0:10:3) cg-n1-b	Strain gauge	microstrain
65	Pacific - 141 (0:10:4) cg-n2-b	Strain gauge	microstrain
66	Pacific - 142 (0:10:5) cg-n3-b	Strain gauge	microstrain
67	Pacific - 143 (0:10:6) cg-s1-b	Strain gauge	microstrain
68	Pacific - 144 (0:10:7) cg-s2-b	Strain gauge	microstrain
69	Pacific - 145 (0:11:0) cg-s3-b	Strain gauge	microstrain
70	Pacific - 146 (0:11:1) cg-n1s1-	Strain gauge	microstrain
71	Pacific - 147 (0:11:2) col-n1-a	Strain gauge	microstrain
72	Pacific - 148 (0:11:3) col-s1-a	Strain gauge	microstrain
73	Pacific - 149 (0:11:4) col-s1-b	Strain gauge	microstrain
74	Pacific - 150 (0:11:5) col-e1-a	Strain gauge	microstrain
75	Pacific - 151 (0:11:6) col-e1-b	Strain gauge	microstrain
76	Pacific - 152 (0:11:7) col-w1-a	Strain gauge	microstrain
77	Pacific - 153 (0:12:0) col-w1-b	Strain gauge	microstrain
78	Pacific - 154 (0:12:1) hoop-3-a	Strain gauge	microstrain
79	Pacific - 155 (0:12:2) LCI east	Strain gauge	microstrain
80	Pacific - 156 (0:12:3) Loadcell	Strain gauge	microstrain
81	Pacific - 157 (0:12:4) Loadcell	Strain gauge	Microstrain
82	Pacific - 158 (0:12:5) LC west	Strain gauge	microstrain
83	Pacific - 159 (0:12:6) Loadcell	Strain gauge	microstrain
84	Pacific - 160 (0:12:7) Loacell2	Strain gauge	microstrain
85	Pacific - 161 (0:13:0) Col-N-1	LVDT	in.
86	Pacific - 162 (0:13:1) Col-N-2	LVDT	in.
87	Pacific - 163 (0:13:2) Col-N-3	LVDT	in.
88	Pacific - 164 (0:13:3) Col-N-4	LVDT	in.
89	Pacific - 165 (0:13:4) Col-S-1	LVDT	in.
90	Pacific - 166 (0:13:5) Col-S-2	LVDT	in.
91	Pacific - 167 (0:13:6) Col-S-3	LVDT	in.
92	Pacific - 168 (0:13:7) Col-S-4	LVDT	in.
93	Pacific - 169 (0:14:0) Col-E-1	LVDT	in.
94	Pacific - 170 (0:14:1) Col-E-2	LVDT	in.
95	Pacific - 171 (0:14:2) Col-E-3	LVDT	inch
96	Pacific - 172 (0:14:3) Col-E-4	LVDT	in.
97	Pacific - 173 (0:14:4) Col-E-5	LVDT	in.
98	Pacific - 174 (0:14:5) Col-W-1	LVDT	in.
99	Pacific - 175 (0:14:6) Col-W-2	LVDT	in.
100	Pacific - 176 (0:14:7) Col-W-3	LVDT	in.
101	Pacific - 65 (0:15:0) Col-W-4	LVDT	in.
102	Pacific - 66 (0:15:1) Col-W-5	LVDT	in.
103	Pacific - 67 (0:1:2) WP-FH-H-E	Wire pot	in.
104	Pacific - 68 (0:1:3) WP-FH-A-E	Wire pot	in.
105	Pacific - 69 (0:1:4) WP-FH-H-S	Wire pot	in.
106	Pacific - 70 (0:1:5) WP-FH-A-S	Wire pot	in.
107	Pacific - 71 (0:1:6) WP-MH-A-E	Wire pot	in.
108	Pacific - 72 (0:1:7) WP-MH-H-E	Wire pot	in.
109	Pacific - 177 (0:16:0)WP-MH-S	Wire pot	in.
110	Pacific - 178 (0:16:1)WP-MH-S	Wire pot	in.
111	Pacific - 179 (0:16:2)WP-BH	Wire pot	in.
112	Pacific - 180 (0:16:3)WP-BA	Wire pot	in.
113	Pacific - 181 (0:16:4)WP-fh-AL	Wire pot	in.
114	Pacific - 182 (0:16:5)WP-fh-AS	Wire pot	in.
115	Pacific - 184 (0:16:7) Pulse	electric pulse	volt

Table E.2 List of instrumentation channels connected to the NEFF data acquisition.

Channel #	Name	Type of Instrument	Unit
1	DATE		
2	TIME		
3	CLOCK		millisecond
4	LOG		
5	Top north actuator load	laod cell	kip
6	Top south actuator load	laod cell	kip
7	Gravity north actuator load	laod cell	kip
8	Gravity south actuator load	laod cell	kip
9	Top north actuator tempo disp	temposonic	in.
10	Top south actuator tempo disp	temposonic	in.
11	Gravity north actuator disp	temposonic	in.
12	Gravity south actuator disp	temposonic	in.
13	disp slab a-5	LVDT	in.
14	disp slab c-3	LVDT	in.
15	disp slab c-2	LVDT	in.
16	disp slab b-5	LVDT	in.
17	disp slab b-4	LVDT	in.
18	disp slab c-4	LVDT	in.
19	disp slab d-4	LVDT	in.
20	disp slab c-5	LVDT	in.
21	disp slab e-5	LVDT	in.
22	disp slab d-5	LVDT	in.
23	disp slab c-7	LVDT	in.
24	disp slab c-8	LVDT	in.
25	disp slab d-6	LVDT	in.
26	disp slab c-6	LVDT	in.
27	disp slab b-6	LVDT	in.
28	disp wp-twist	wire pot	in.
29	disp wp-mh-h-e	wire pot	in.
30	disp wp-fh-a-el	wire pot	in.
31	disp wp-mh-a-e	wire pot	in.
32	disp wp-fh-aer	wire pot	in.
33	disp wp-fh-h-e	wire pot	in.
34	disp wp-fh-a-e	wire pot	in.
35	disp wp-mh-a-s	wire pot	in.
36	disp wp-mh-h-s	wire pot	in.
37	disp wp-fh-a-s	wire pot	in.
38	disp wp-fh-h-s	wire pot	in.
39	disp wp-beamh	wire pot	in.
40	disp wp-beama	wire pot	in.
41	tds-s1-b	strain gauge	microstrain
42	tds-s3-c	strain gauge	microstrain
43	tds-s1-a	strain gauge	microstrain
44	lds-s1-a	strain gauge	microstrain
45	lds-s2-b	strain gauge	microstrain
46	tds-s2-a	strain gauge	microstrain
47	tds-s3-b	strain gauge	microstrain
48	tds-s4-b	strain gauge	microstrain
49	tds-s4-c	strain gauge	microstrain
50	cg-s3-a	strain gauge	microstrain
51	cg-s2-a	strain gauge	microstrain
52	cg-s1-a	strain gauge	microstrain
53	col-w1-h	strain gauge	microstrain
54	col-n1-g	strain gauge	microstrain
55	col-n1-e	strain gauge	microstrain
56	col-n1-d	strain gauge	microstrain
56	col-n1-d	strain gauge	microstrain
57	col-w1-g	strain gauge	microstrain

Table E.2 Continued.

Channel #	Name	Type of Instrument	Unit
58	col-n1-c	strain gauge	microstrain
59	hoop-2-c	strain gauge	microstrain
60	hoop-1-c	strain gauge	microstrain
61	col-w1-f	strain gauge	microstrain
62	col-w1-e	strain gauge	microstrain
63	hoop-1-b	strain gauge	microstrain
64	hoop-2-a	strain gauge	microstrain
65	col-w1-d	strain gauge	microstrain
66	col-w1-c	strain gauge	microstrain
67	ws-e1-north	strain gauge	microstrain
68	tds-n3-d	strain gauge	microstrain
69	tds-n1-e	strain gauge	microstrain
70	tds-n2-a	strain gauge	microstrain
71	lds-n2-b	strain gauge	microstrain
72	lds-n4-b	strain gauge	microstrain
73	ws-w1-north	strain gauge	microstrain
74	tds-n1-d	strain gauge	microstrain
75	tds-n2-e	strain gauge	microstrain
76	lds-n1s1-b	strain gauge	microstrain
77	tds-n2-c	strain gauge	microstrain
78	tds-n3-b	strain gauge	microstrain
79	lds-n1-c	strain gauge	microstrain
80	tds-n1-a	strain gauge	microstrain
81	col-s1-g	strain gauge	microstrain
82	hoop-3-c	strain gauge	microstrain
83	col-e1-g	strain gauge	microstrain
84	col-e1-h	strain gauge	microstrain
85	col-s1-e	strain gauge	microstrain
86	hoop-3-b	strain gauge	microstrain
87	col-s1-c	strain gauge	microstrain
88	col-e1-f	strain gauge	microstrain
89	col-e1-d	strain gauge	microstrain
90	col-s1-d	strain gauge	microstrain
91	col-e1-e	strain gauge	microstrain
92	hoop-1-a	strain gauge	microstrain
93	hoop-2-b	strain gauge	microstrain
94	col-e1-c	strain gauge	microstrain
95	tds-n2-d	strain gauge	microstrain
96	tds-n2-b	strain gauge	microstrain
97	tds-n4-c	strain gauge	microstrain
98	tds-n4-d	strain gauge	microstrain
99	tds-n1-c	strain gauge	microstrain
100	tds-n3-c	strain gauge	microstrain
101	lds-n1-b	strain gauge	microstrain
102	tds-n1-b	strain gauge	microstrain
103	lds-n1-a	strain gauge	microstrain
104	cg-n1s1-a	strain gauge	microstrain
105	cg-n3-a	strain gauge	microstrain
106	cg-n2-a	strain gauge	microstrain
107	cg-n1-a	strain gauge	microstrain
108	tss-n3-d	strain gauge	microstrain
109	tss-n1-b	strain gauge	microstrain
110	lss-n1-a	strain gauge	microstrain
111	tss-n2-c	strain gauge	microstrain
112	lss-n1-b	strain gauge	microstrain
113	lss-n2-b	strain gauge	microstrain
114	lss-n1-c	strain gauge	microstrain
115	tss-n1-a	strain gauge	microstrain

Table E.2 Continued.

Channel #	Name	Type of Instrument	Unit
116	tss-n3-c	strain gauge	microstrain
117	tss-n2-b	strain gauge	microstrain
118	tss-n2-d	strain gauge	microstrain
119	tss-n1-c	strain gauge	microstrain
120	tss-n1-e	strain gauge	microstrain
121	tss-n3-b	strain gauge	microstrain
122	tss-n1-d	strain gauge	microstrain
123	tss-s1-c	strain gauge	microstrain
124	lss-s2-b	strain gauge	microstrain
125	tss-s1-a	strain gauge	microstrain
126	tss-s1-d	strain gauge	microstrain
127	tss-s3-b	strain gauge	microstrain
128	tss-s3-d	strain gauge	microstrain
129	tss-s3-c	strain gauge	microstrain
130	lss-s1-a	strain gauge	microstrain
131	lss-s1-c	strain gauge	microstrain
132	tss-s1-b	strain gauge	microstrain
133	lss-s1-b	strain gauge	microstrain
134	tss-s2-d	strain gauge	microstrain
135	tss-s1-e	strain gauge	microstrain
136	tss-s2-c	strain gauge	microstrain
137	tss-s2-b	strain gauge	microstrain
138	lds-n1s1-c	strain gauge	microstrain
139	tds-s1-e	strain gauge	microstrain
140	ws-w1-south	strain gauge	microstrain
141	tds-s2-e	strain gauge	microstrain
142	tds-s1-d	strain gauge	microstrain
143	tds-s2-d	strain gauge	microstrain
144	lds-s1-c	strain gauge	microstrain
145	ws-e1-south	strain gauge	microstrain
146	tds-s2-c	strain gauge	microstrain
147	lds-s1-b	strain gauge	microstrain
148	tds-s1-c	strain gauge	microstrain
149	tds-s4-a	strain gauge	microstrain
150	lds-n1s1-a	strain gauge	microstrain

Appendix F Struts Fabrication and Calibration

This appendix describes the characteristics of the two vertical struts fabricated and instrumented specifically for this study. These struts were fabricated with a target capacity of 250 kip each and were made of AISI 4140 steel. More details about the fabrication, instrumentation, and calibration of the two instrumented strut load cells are presented below.

F.1 FABRICATION AND INSTRUMENTATION

The two struts were meant to provide vertical roller supports at the two ends of the bent cap beam in the test specimen. Two special rods were fabricated with female threaded ends such that two clevises could be attached from the two sides of each of the two rods. Longitudinal and cross sections showing the geometry and dimensions of the typical strut rod are shown in Figure F.1. The rods were fabricated from a hollow AISI 4140 steel cylinder, as shown in Figure F.2. One of the two final fabricated rods and typical strain gauge instrumentation is shown in Figure F.3. For determining the bent cap beam moments in this study, the two vertical struts were instrumented and calibrated to relate the strain readings to the axial force in the strut. Each of the two struts was instrumented with two rosettes and two linear strain gauges. Each rosette comprised two strain gauges that were attached to the strut such that one gauge was aligned with the centerline of the strut, while the other was aligned with the circumference. Meanwhile, the linear strain gauges were aligned with the rod centerline. All the strain gauges had 120 Ω resistance and a gauge length of 0.062 in. The gauges were glued to the struts and were covered with three protective coating layers. For each strut, the four gauges in the two rosettes were connected using a full Wheatstone bridge circuit, while the two linear gauges were connected separately each through a quarter bridge circuit. The layout of the linear and rosettes strain gauges and the Wheatstone bridge connections are schematically shown in Figure F.4. The final instrumented strut attached to the two clevises from the two ends is shown in Figure F.5.

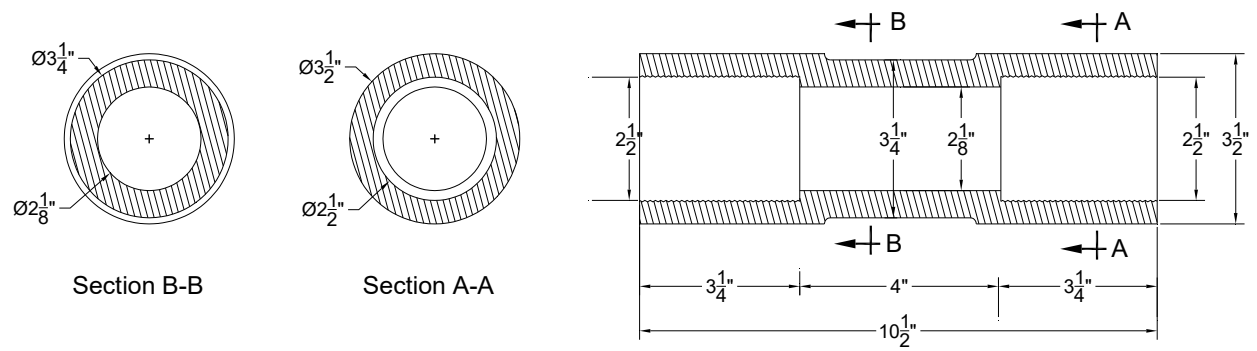


Figure F.1 Longitudinal and cross sections of the fabricated vertical struts.

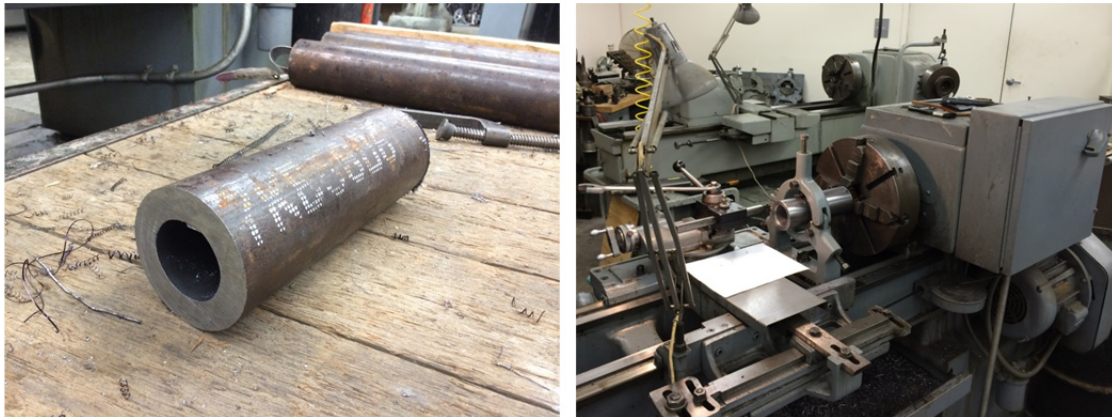


Figure F.2 Fabrication of the struts from raw 4140 steel cylinders using the milling machine at the machine shop at UCB.

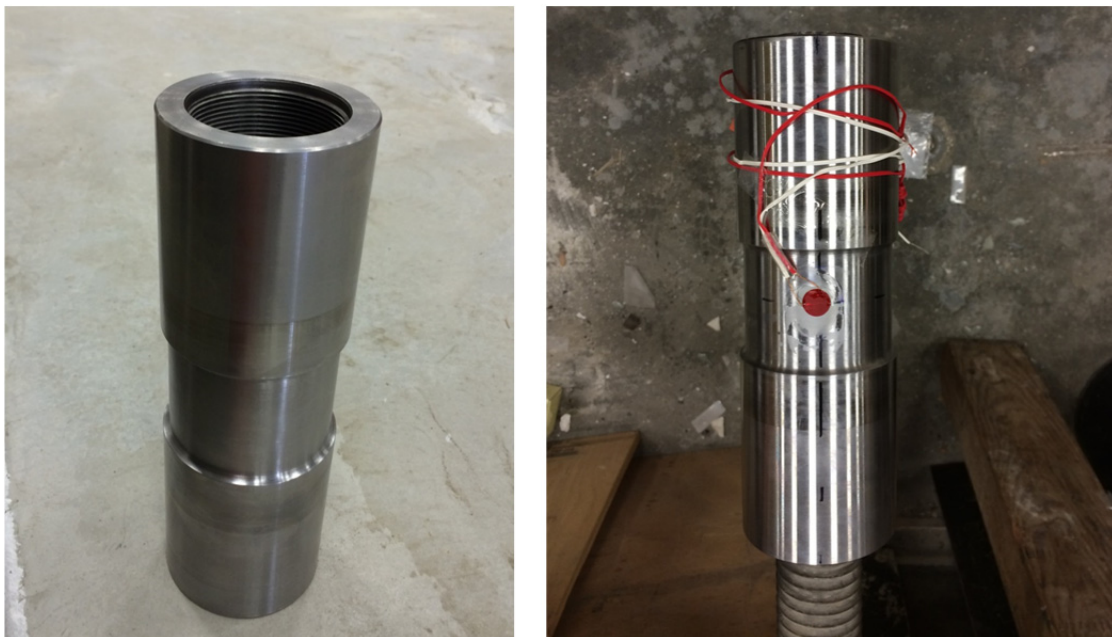


Figure F.3 Final fabricated vertical strut (left) and installing a rosette strain gauge (right).

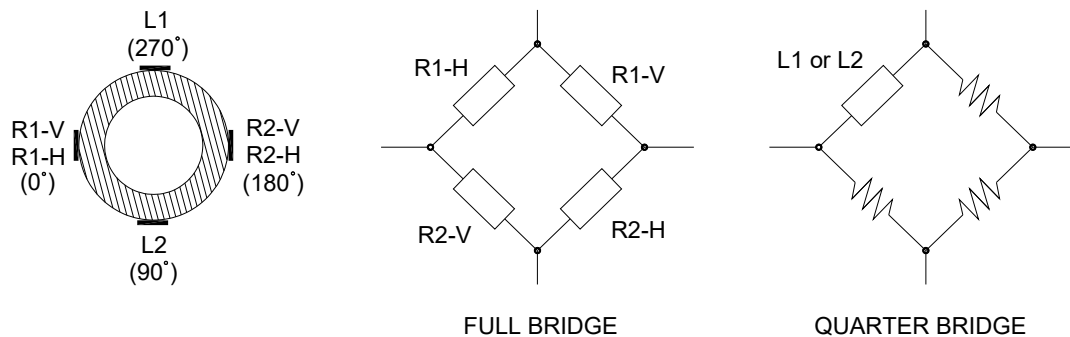


Figure F.4 Lay out of the strut strain gauges and bridge connections for rosettes and linear gauges.

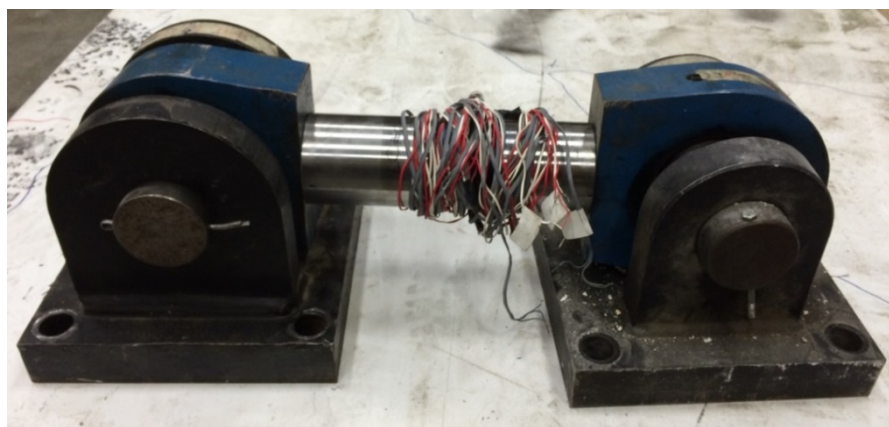


Figure F.5 A fully assembled vertical strut with two clevises at the two ends.

F.2 LOAD CELLS CALIBRATION

The two instrumented load cell struts were calibrated using a Universal Testing Machine with a capacity of 140 kip, as shown in Figure F.6. To perform the calibration, the two struts were loaded up to 120 kips and unloaded several times. The force and different strain gauge readings were acquired continuously through the PI data acquisition system. Meanwhile, the force and the full bridge strain readings were manually recorded at 10-kips increments. The force-strain relationships were plotted using both the rosettes full bridge strain and the linear strain gauges. The data from the full bridge strain were found to be more accurate and less noisy than the linear gauges. A linear slope was the best fit to the force-full bridge strain data for each of the two struts, and the calibration factor was estimated accordingly. Figure F.7 shows the calibration data for one of the struts, which was acquired manually at 10-kip increments; the calibration data from the PI for both struts are shown in Figure F.8. The calibration demonstrates excellent linearity of the load cells during loading and unloading.

The calibration factor is considered the slope of the best fitted linear function. Note that for the same load cell, the slope obtained from the manually collected data is little lower than the more accurate value obtained from the continuously recorded PI data. Meanwhile, the calibration factor for the two load cells is slightly different: 0.0069 for the first strut load cell versus 0.0061

for the second strut load cell. This could be attributed to possible slight differences in fabrication, but it is assumed that it is mainly because of the variation of the strain gauges location and orientation from the two struts.

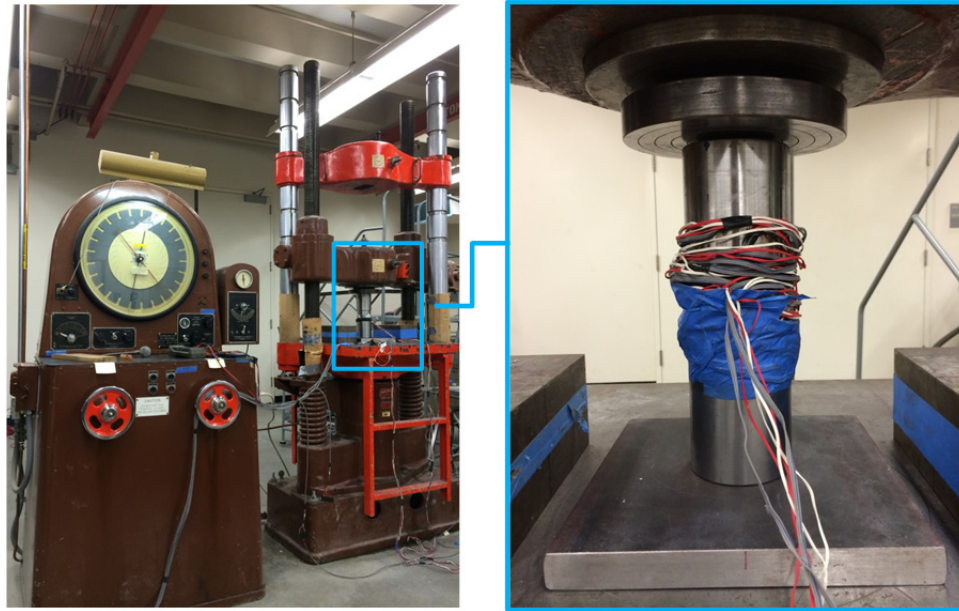


Figure F.6 Vertical struts load cell calibration using Universal Testing Machine.

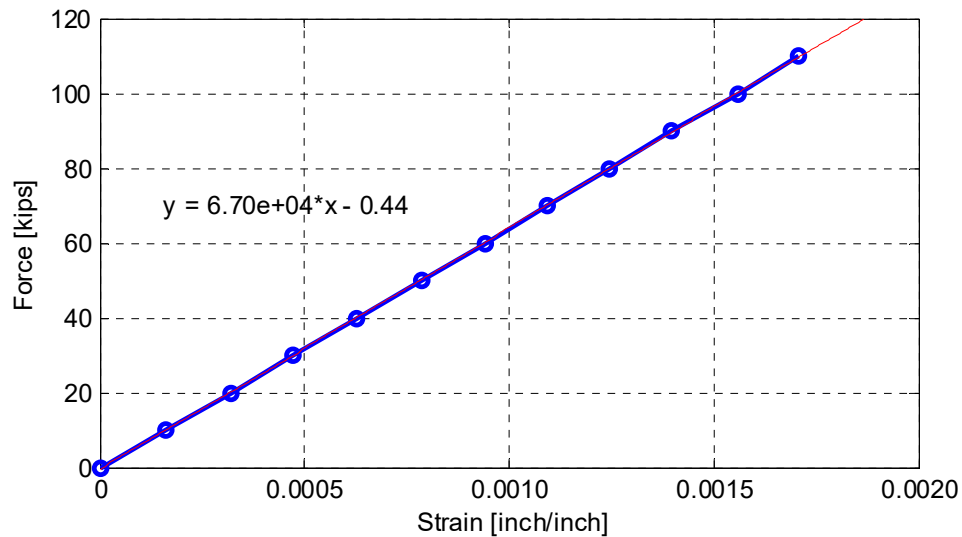


Figure F.7 Force-strain relationship for the first load cell using manually acquired data.

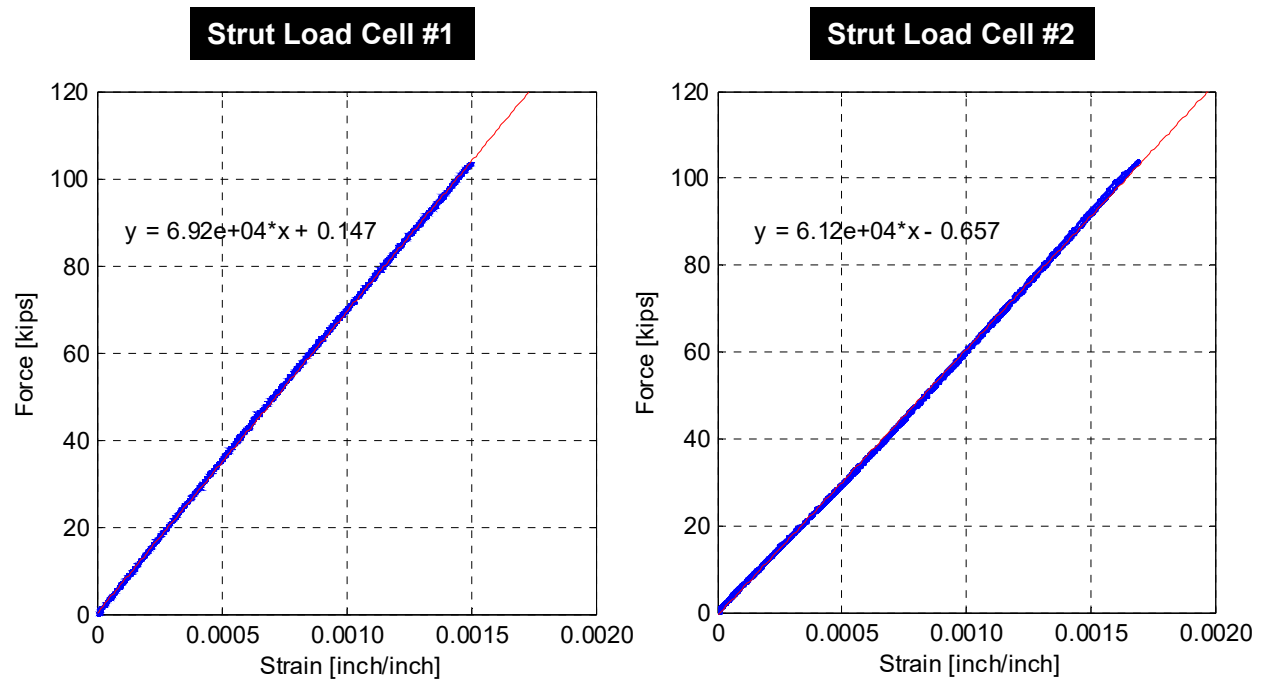


Figure F.8 Force-strain relationship for both load cells using the PI acquired data for the rosettes full bridge strain (the best fit slope resembles the calibration factor and identified on the plots).

PEER REPORTS

PEER reports are available as a free PDF download from http://peer.berkeley.edu/publications/peer_reports_complete.html. Printed hard copies of PEER reports can be ordered directly from our printer by following the instructions at http://peer.berkeley.edu/publications/peer_reports.html. For other related questions about the PEER Report Series, contact the Pacific Earthquake Engineering Research Center, 325 Davis Hall mail code 1792, Berkeley, CA 94720. Tel.: (510) 642-3437; Fax: (510) 665-1655; Email: peer_editor@berkeley.edu

- PEER 2015/09** *Structural Behavior of Column-Bent Cap Beam-Box Girder Systems in Reinforced Concrete Bridges Subjected to Gravity and Seismic Loads. Part I: Pre-Test Analysis and Quasi-Static Experiments.* Mohamed A. Moustafa and Khalid M. Mosalam. September 2015.
- PEER 2015/08** *NGA-East: Adjustments to Median Ground-Motion Models for Center and Eastern North America.* August 2015.
- PEER 2015/07** *NGA-East: Ground-Motion Standard-Deviation Models for Central and Eastern North America.* Linda Al Atik. June 2015.
- PEER 2015/06** *Adjusting Ground-Motion Intensity Measures to a Reference Site for which $V_{S30} = 3000$ m/sec.* David M. Boore. May 2015.
- PEER 2015/05** *Hybrid Simulation of Seismic Isolation Systems Applied to an APR-1400 Nuclear Power Plant.* Andreas H. Schellenberg, Alireza Sarebanha, Matthew J. Schoettler, Gilberto Mosqueda, Gianmario Benzoni, and Stephen A. Mahin. April 2015.
- PEER 2015/04** *NGA-East: Median Ground-Motion Models for the Central and Eastern North America Region.* April 2015.
- PEER 2015/03** *Single Series Solution for the Rectangular Fiber-Reinforced Elastomeric Isolator Compression Modulus.* James M. Kelly and Niel C. Van Engelen. March 2015.
- PEER 2015/02** *A Full-Scale, Single-Column Bridge Bent Tested by Shake-Table Excitation.* Matthew J. Schoettler, José I. Restrepo, Gabriele Guerrini, David E. Duck, and Francesco Carrea. March 2015.
- PEER 2015/01** *Concrete Column Blind Prediction Contest 2010: Outcomes and Observations.* Vesna Terzic, Matthew J. Schoettler, José I. Restrepo, and Stephen A. Mahin. March 2015.
- PEER 2014/20** *Stochastic Modeling and Simulation of Near-Fault Ground Motions for Performance-Based Earthquake Engineering.* Mayssa Dabaghi and Armen Der Kiureghian. December 2014.
- PEER 2014/19** *Seismic Response of a Hybrid Fiber-Reinforced Concrete Bridge Column Detailed for Accelerated Bridge Construction.* Wilson Nguyen, William Trono, Marios Panagiotou, and Claudia P. Ostertag. December 2014.
- PEER 2014/18** *Three-Dimensional Beam-Truss Model for Reinforced Concrete Walls and Slabs Subjected to Cyclic Static or Dynamic Loading.* Yuan Lu, Marios Panagiotou, and Ioannis Koutromanos. December 2014.
- PEER 2014/17** *PEER NGA-East Database.* Christine A. Goulet, Tadahiro Kishida, Timothy D. Ancheta, Chris H. Cramer, Robert B. Darragh, Walter J. Silva, Youssef M.A. Hashash, Joseph Harmon, Jonathan P. Stewart, Katie E. Wooddell, and Robert R. Youngs. October 2014.
- PEER 2014/16** *Guidelines for Performing Hazard-Consistent One-Dimensional Ground Response Analysis for Ground Motion Prediction.* Jonathan P. Stewart, Kioumars Afshari, and Youssef M.A. Hashash. October 2014.
- PEER 2014/15** *NGA-East Regionalization Report: Comparison of Four Crustal Regions within Central and Eastern North America using Waveform Modeling and 5%-Damped Pseudo-Spectral Acceleration Response.* Jennifer Dreiling, Marius P. Isken, Walter D. Mooney, Martin C. Chapman, and Richard W. Godbee. October 2014.
- PEER 2014/14** *Scaling Relations between Seismic Moment and Rupture Area of Earthquakes in Stable Continental Regions.* Paul Somerville. August 2014.
- PEER 2014/13** *PEER Preliminary Notes and Observations on the August 24, 2014, South Napa Earthquake.* Grace S. Kang (Editor), Stephen A. Mahin (Editors). September 2014.
- PEER 2014/12** *Reference-Rock Site Conditions for Central and Eastern North America: Part II – Attenuation (Kappa) Definition.* Kenneth W. Campbell, Youssef M.A. Hashash, Byungmin Kim, Albert R. Kottke, Ellen M. Rathje, Walter J. Silva, and Jonathan P. Stewart. August 2014.
- PEER 2014/11** *Reference-Rock Site Conditions for Central and Eastern North America: Part I - Velocity Definition.* Youssef M.A. Hashash, Albert R. Kottke, Jonathan P. Stewart, Kenneth W. Campbell, Byungmin Kim, Ellen M. Rathje, Walter J. Silva, Sissy Nikolaou, and Cheryl Moss. August 2014.

- PEER 2014/10** *Evaluation of Collapse and Non-Collapse of Parallel Bridges Affected by Liquefaction and Lateral Spreading.* Benjamin Turner, Scott J. Brandenburg, and Jonathan P. Stewart. August 2014.
- PEER 2014/09** *PEER Arizona Strong-Motion Database and GMPEs Evaluation.* Tadahiro Kishida, Robert E. Kayen, Olga-Joan Ktenidou, Walter J. Silva, Robert B. Darragh, and Jennie Watson-Lamprey. June 2014.
- PEER 2014/08** *Unbonded Pretensioned Bridge Columns with Rocking Detail.* Jeffrey A. Schaefer, Bryan Kennedy, Marc O. Eberhard, John F. Stanton. June 2014.
- PEER 2014/07** *Northridge 20 Symposium Summary Report: Impacts, Outcomes, and Next Steps.* May 2014.
- PEER 2014/06** *Report of the Tenth Planning Meeting of NEES/E-Defense Collaborative Research on Earthquake Engineering.* December 2013.
- PEER 2014/05** *Seismic Velocity Site Characterization of Thirty-One Chilean Seismometer Stations by Spectral Analysis of Surface Wave Dispersion.* Robert Kayen, Brad D. Carlin, Skye Corbet, Camilo Pinilla, Allan Ng, Edward Gorbis, and Christine Truong. April 2014.
- PEER 2014/04** *Effect of Vertical Acceleration on Shear Strength of Reinforced Concrete Columns.* Hyerin Lee and Khalid M. Mosalam. April 2014.
- PEER 2014/03** *Retest of Thirty-Year-Old Neoprene Isolation Bearings.* James M. Kelly and Niel C. Van Engelen. March 2014.
- PEER 2014/02** *Theoretical Development of Hybrid Simulation Applied to Plate Structures.* Ahmed A. Bakhaty, Khalid M. Mosalam, and Sanjay Govindjee. January 2014.
- PEER 2014/01** *Performance-Based Seismic Assessment of Skewed Bridges.* Peyman Kaviani, Farzin Zareian, and Ertugrul Taciroglu. January 2014.
- PEER 2013/26** *Urban Earthquake Engineering. Proceedings of the U.S.-Iran Seismic Workshop.* December 2013.
- PEER 2013/25** *Earthquake Engineering for Resilient Communities: 2013 PEER Internship Program Research Report Collection.* Heidi Tremayne (Editor), Stephen A. Mahin (Editor), Jorge Archbold Monterossa, Matt Brosman, Shelly Dean, Katherine deLaveaga, Curtis Fong, Donovan Holder, Rakeeb Khan, Elizabeth Jachens, David Lam, Daniela Martinez Lopez, Mara Minner, Geffen Oren, Julia Pavicic, Melissa Quinonez, Lorena Rodriguez, Sean Salazar, Kelli Slaven, Vivian Steyert, Jenny Taing, and Salvador Tena. December 2013.
- PEER 2013/24** *NGA-West2 Ground Motion Prediction Equations for Vertical Ground Motions.* September 2013.
- PEER 2013/23** *Coordinated Planning and Preparedness for Fire Following Major Earthquakes.* Charles Scawthorn. November 2013.
- PEER 2013/22** *GEM-PEER Task 3 Project: Selection of a Global Set of Ground Motion Prediction Equations.* Jonathan P. Stewart, John Douglas, Mohammad B. Javanbarg, Carola Di Alessandro, Yousef Bozorgnia, Norman A. Abrahamson, David M. Boore, Kenneth W. Campbell, Elise Delavaud, Mustafa Erdik and Peter J. Stafford. December 2013.
- PEER 2013/21** *Seismic Design and Performance of Bridges with Columns on Rocking Foundations.* Grigorios Antonellis and Marios Panagiotou. September 2013.
- PEER 2013/20** *Experimental and Analytical Studies on the Seismic Behavior of Conventional and Hybrid Braced Frames.* Jiun-Wei Lai and Stephen A. Mahin. September 2013.
- PEER 2013/19** *Toward Resilient Communities: A Performance-Based Engineering Framework for Design and Evaluation of the Built Environment.* Michael William Mieler, Bozidar Stojadinovic, Robert J. Budnitz, Stephen A. Mahin and Mary C. Comerio. September 2013.
- PEER 2013/18** *Identification of Site Parameters that Improve Predictions of Site Amplification.* Ellen M. Rathje and Sara Navidi. July 2013.
- PEER 2013/17** *Response Spectrum Analysis of Concrete Gravity Dams Including Dam-Water-Foundation Interaction.* Arnkjell Løkke and Anil K. Chopra. July 2013.
- PEER 2013/16** *Effect of hoop reinforcement spacing on the cyclic response of large reinforced concrete special moment frame beams.* Marios Panagiotou, Tea Visnjic, Grigorios Antonellis, Panagiotis Galanis, and Jack P. Moehle. June 2013.
- PEER 2013/15** *A Probabilistic Framework to Include the Effects of Near-Fault Directivity in Seismic Hazard Assessment.* Shrey Kumar Shahi, Jack W. Baker. October 2013.
- PEER 2013/14** *Hanging-Wall Scaling using Finite-Fault Simulations.* Jennifer L. Donahue and Norman A. Abrahamson. September 2013.
- PEER 2013/13** *Semi-Empirical Nonlinear Site Amplification and its Application in NEHRP Site Factors.* Jonathan P. Stewart and Emel Seyhan. November 2013.

- PEER 2013/12** *Nonlinear Horizontal Site Response for the NGA-West2 Project.* Ronnie Kamai, Norman A. Abramson, Walter J. Silva. May 2013.
- PEER 2013/11** *Epistemic Uncertainty for NGA-West2 Models.* Linda Al Atik and Robert R. Youngs. May 2013.
- PEER 2013/10** *NGA-West 2 Models for Ground-Motion Directionality.* Shrey K. Shahi and Jack W. Baker. May 2013.
- PEER 2013/09** *Final Report of the NGA-West2 Directivity Working Group.* Paul Spudich, Jeffrey R. Bayless, Jack W. Baker, Brian S.J. Chiou, Badie Rowshandel, Shrey Shahi, and Paul Somerville. May 2013.
- PEER 2013/08** *NGA-West2 Model for Estimating Average Horizontal Values of Pseudo-Absolute Spectral Accelerations Generated by Crustal Earthquakes.* I. M. Idriss. May 2013.
- PEER 2013/07** *Update of the Chiou and Youngs NGA Ground Motion Model for Average Horizontal Component of Peak Ground Motion and Response Spectra.* Brian Chiou and Robert Youngs. May 2013.
- PEER 2013/06** *NGA-West2 Campbell-Bozorgnia Ground Motion Model for the Horizontal Components of PGA, PGV, and 5%-Damped Elastic Pseudo-Acceleration Response Spectra for Periods Ranging from 0.01 to 10 sec.* Kenneth W. Campbell and Yousef Bozorgnia. May 2013.
- PEER 2013/05** *NGA-West 2 Equations for Predicting Response Spectral Accelerations for Shallow Crustal Earthquakes.* David M. Boore, Jonathan P. Stewart, Emel Seyhan, Gail M. Atkinson. May 2013.
- PEER 2013/04** *Update of the AS08 Ground-Motion Prediction Equations Based on the NGA-West2 Data Set.* Norman Abrahamson, Walter Silva, and Ronnie Kamai. May 2013.
- PEER 2013/03** *PEER NGA-West2 Database.* Timothy D. Ancheta, Robert B. Darragh, Jonathan P. Stewart, Emel Seyhan, Walter J. Silva, Brian S.J. Chiou, Katie E. Wooddell, Robert W. Graves, Albert R. Kottke, David M. Boore, Tadaihiro Kishida, and Jennifer L. Donahue. May 2013.
- PEER 2013/02** *Hybrid Simulation of the Seismic Response of Squat Reinforced Concrete Shear Walls.* Catherine A. Whyte and Bozidar Stojadinovic. May 2013.
- PEER 2013/01** *Housing Recovery in Chile: A Qualitative Mid-program Review.* Mary C. Comerio. February 2013.
- PEER 2012/08** *Guidelines for Estimation of Shear Wave Velocity.* Bernard R. Wair, Jason T. DeJong, and Thomas Shantz. December 2012.
- PEER 2012/07** *Earthquake Engineering for Resilient Communities: 2012 PEER Internship Program Research Report Collection.* Heidi Tremayne (Editor), Stephen A. Mahin (Editor), Collin Anderson, Dustin Cook, Michael Erceg, Carlos Esparza, Jose Jimenez, Dorian Krausz, Andrew Lo, Stephanie Lopez, Nicole McCurdy, Paul Shipman, Alexander Strum, Eduardo Vega. December 2012.
- PEER 2012/06** *Fragilities for Precarious Rocks at Yucca Mountain.* Matthew D. Purvance, Rasool Anooshehpour, and James N. Brune. December 2012.
- PEER 2012/05** *Development of Simplified Analysis Procedure for Piles in Laterally Spreading Layered Soils.* Christopher R. McGann, Pedro Arduino, and Peter Mackenzie-Helnwein. December 2012.
- PEER 2012/04** *Unbonded Pre-Tensioned Columns for Bridges in Seismic Regions.* Phillip M. Davis, Todd M. Janes, Marc O. Eberhard, and John F. Stanton. December 2012.
- PEER 2012/03** *Experimental and Analytical Studies on Reinforced Concrete Buildings with Seismically Vulnerable Beam-Column Joints.* Sangjoon Park and Khalid M. Mosalam. October 2012.
- PEER 2012/02** *Seismic Performance of Reinforced Concrete Bridges Allowed to Uplift during Multi-Directional Excitation.* Andres Oscar Espinoza and Stephen A. Mahin. July 2012.
- PEER 2012/01** *Spectral Damping Scaling Factors for Shallow Crustal Earthquakes in Active Tectonic Regions.* Sanaz Rezaeian, Yousef Bozorgnia, I. M. Idriss, Kenneth Campbell, Norman Abrahamson, and Walter Silva. July 2012.
- PEER 2011/10** *Earthquake Engineering for Resilient Communities: 2011 PEER Internship Program Research Report Collection.* Eds. Heidi Faison and Stephen A. Mahin. December 2011.
- PEER 2011/09** *Calibration of Semi-Stochastic Procedure for Simulating High-Frequency Ground Motions.* Jonathan P. Stewart, Emel Seyhan, and Robert W. Graves. December 2011.
- PEER 2011/08** *Water Supply in regard to Fire Following Earthquake.* Charles Scawthorn. November 2011.
- PEER 2011/07** *Seismic Risk Management in Urban Areas. Proceedings of a U.S.-Iran-Turkey Seismic Workshop.* September 2011.
- PEER 2011/06** *The Use of Base Isolation Systems to Achieve Complex Seismic Performance Objectives.* Troy A. Morgan and Stephen A. Mahin. July 2011.

- PEER 2011/05** *Case Studies of the Seismic Performance of Tall Buildings Designed by Alternative Means*. Task 12 Report for the Tall Buildings Initiative. Jack Moehle, Yousef Bozorgnia, Nirmal Jayaram, Pierson Jones, Mohsen Rahnama, Nilesh Shome, Zeynep Tuna, John Wallace, Tony Yang, and Farzin Zareian. July 2011.
- PEER 2011/04** *Recommended Design Practice for Pile Foundations in Laterally Spreading Ground*. Scott A. Ashford, Ross W. Boulanger, and Scott J. Brandenburg. June 2011.
- PEER 2011/03** *New Ground Motion Selection Procedures and Selected Motions for the PEER Transportation Research Program*. Jack W. Baker, Ting Lin, Shrey K. Shahi, and Nirmal Jayaram. March 2011.
- PEER 2011/02** *A Bayesian Network Methodology for Infrastructure Seismic Risk Assessment and Decision Support*. Michelle T. Bensi, Armen Der Kiureghian, and Daniel Straub. March 2011.
- PEER 2011/01** *Demand Fragility Surfaces for Bridges in Liquefied and Laterally Spreading Ground*. Scott J. Brandenburg, Jian Zhang, Pirooz Kashighandi, Yili Huo, and Minxing Zhao. March 2011.
- PEER 2010/05** *Guidelines for Performance-Based Seismic Design of Tall Buildings*. Developed by the Tall Buildings Initiative. November 2010.
- PEER 2010/04** *Application Guide for the Design of Flexible and Rigid Bus Connections between Substation Equipment Subjected to Earthquakes*. Jean-Bernard Dastous and Armen Der Kiureghian. September 2010.
- PEER 2010/03** *Shear Wave Velocity as a Statistical Function of Standard Penetration Test Resistance and Vertical Effective Stress at Caltrans Bridge Sites*. Scott J. Brandenburg, Naresh Bellana, and Thomas Shantz. June 2010.
- PEER 2010/02** *Stochastic Modeling and Simulation of Ground Motions for Performance-Based Earthquake Engineering*. Sanaz Rezaeian and Armen Der Kiureghian. June 2010.
- PEER 2010/01** *Structural Response and Cost Characterization of Bridge Construction Using Seismic Performance Enhancement Strategies*. Ady Aviram, Božidar Stojadinović, Gustavo J. Parra-Montesinos, and Kevin R. Mackie. March 2010.
- PEER 2009/03** *The Integration of Experimental and Simulation Data in the Study of Reinforced Concrete Bridge Systems Including Soil-Foundation-Structure Interaction*. Matthew Dryden and Gregory L. Fenves. November 2009.
- PEER 2009/02** *Improving Earthquake Mitigation through Innovations and Applications in Seismic Science, Engineering, Communication, and Response. Proceedings of a U.S.-Iran Seismic Workshop*. October 2009.
- PEER 2009/01** *Evaluation of Ground Motion Selection and Modification Methods: Predicting Median Interstory Drift Response of Buildings*. Curt B. Haselton, Ed. June 2009.
- PEER 2008/10** *Technical Manual for Strata*. Albert R. Kottke and Ellen M. Rathje. February 2009.
- PEER 2008/09** *NGA Model for Average Horizontal Component of Peak Ground Motion and Response Spectra*. Brian S.-J. Chiou and Robert R. Youngs. November 2008.
- PEER 2008/08** *Toward Earthquake-Resistant Design of Concentrically Braced Steel Structures*. Patxi Uriz and Stephen A. Mahin. November 2008.
- PEER 2008/07** *Using OpenSees for Performance-Based Evaluation of Bridges on Liquefiable Soils*. Stephen L. Kramer, Pedro Arduino, and HyungSuk Shin. November 2008.
- PEER 2008/06** *Shaking Table Tests and Numerical Investigation of Self-Centering Reinforced Concrete Bridge Columns*. Hyung IL Jeong, Junichi Sakai, and Stephen A. Mahin. September 2008.
- PEER 2008/05** *Performance-Based Earthquake Engineering Design Evaluation Procedure for Bridge Foundations Undergoing Liquefaction-Induced Lateral Ground Displacement*. Christian A. Ledezma and Jonathan D. Bray. August 2008.
- PEER 2008/04** *Benchmarking of Nonlinear Geotechnical Ground Response Analysis Procedures*. Jonathan P. Stewart, Annie On-Lei Kwok, Youssef M. A. Hashash, Neven Matasovic, Robert Pyke, Zhiliang Wang, and Zhaohui Yang. August 2008.
- PEER 2008/03** *Guidelines for Nonlinear Analysis of Bridge Structures in California*. Ady Aviram, Kevin R. Mackie, and Božidar Stojadinović. August 2008.
- PEER 2008/02** *Treatment of Uncertainties in Seismic-Risk Analysis of Transportation Systems*. Evangelos Stergiou and Anne S. Kiremidjian. July 2008.
- PEER 2008/01** *Seismic Performance Objectives for Tall Buildings*. William T. Holmes, Charles Kircher, William Petak, and Nabih Youssef. August 2008.
- PEER 2007/12** *An Assessment to Benchmark the Seismic Performance of a Code-Conforming Reinforced Concrete Moment-Frame Building*. Curt Haselton, Christine A. Goulet, Judith Mitrani-Reiser, James L. Beck, Gregory G. Deierlein, Keith A. Porter, Jonathan P. Stewart, and Ertugrul Taciroglu. August 2008.
- PEER 2007/11** *Bar Buckling in Reinforced Concrete Bridge Columns*. Wayne A. Brown, Dawn E. Lehman, and John F. Stanton. February 2008.

- PEER 2007/10** *Computational Modeling of Progressive Collapse in Reinforced Concrete Frame Structures.* Mohamed M. Talaat and Khalid M. Mosalam. May 2008.
- PEER 2007/09** *Integrated Probabilistic Performance-Based Evaluation of Benchmark Reinforced Concrete Bridges.* Kevin R. Mackie, John-Michael Wong, and Božidar Stojadinović. January 2008.
- PEER 2007/08** *Assessing Seismic Collapse Safety of Modern Reinforced Concrete Moment-Frame Buildings.* Curt B. Haselton and Gregory G. Deierlein. February 2008.
- PEER 2007/07** *Performance Modeling Strategies for Modern Reinforced Concrete Bridge Columns.* Michael P. Berry and Marc O. Eberhard. April 2008.
- PEER 2007/06** *Development of Improved Procedures for Seismic Design of Buried and Partially Buried Structures.* Linda Al Atik and Nicholas Sitar. June 2007.
- PEER 2007/05** *Uncertainty and Correlation in Seismic Risk Assessment of Transportation Systems.* Renee G. Lee and Anne S. Kiremidjian. July 2007.
- PEER 2007/04** *Numerical Models for Analysis and Performance-Based Design of Shallow Foundations Subjected to Seismic Loading.* Sivapalan Gajan, Tara C. Hutchinson, Bruce L. Kutter, Prishati Raychowdhury, José A. Ugalde, and Jonathan P. Stewart. May 2008.
- PEER 2007/03** *Beam-Column Element Model Calibrated for Predicting Flexural Response Leading to Global Collapse of RC Frame Buildings.* Curt B. Haselton, Abbie B. Liel, Sarah Taylor Lange, and Gregory G. Deierlein. May 2008.
- PEER 2007/02** *Campbell-Bozorgnia NGA Ground Motion Relations for the Geometric Mean Horizontal Component of Peak and Spectral Ground Motion Parameters.* Kenneth W. Campbell and Yousef Bozorgnia. May 2007.
- PEER 2007/01** *Boore-Atkinson NGA Ground Motion Relations for the Geometric Mean Horizontal Component of Peak and Spectral Ground Motion Parameters.* David M. Boore and Gail M. Atkinson. May 2007.
- PEER 2006/12** *Societal Implications of Performance-Based Earthquake Engineering.* Peter J. May. May 2007.
- PEER 2006/11** *Probabilistic Seismic Demand Analysis Using Advanced Ground Motion Intensity Measures, Attenuation Relationships, and Near-Fault Effects.* Polsak Tothong and C. Allin Cornell. March 2007.
- PEER 2006/10** *Application of the PEER PBEE Methodology to the I-880 Viaduct.* Sashi Kunnath. February 2007.
- PEER 2006/09** *Quantifying Economic Losses from Travel Forgone Following a Large Metropolitan Earthquake.* James Moore, Sungbin Cho, Yue Yue Fan, and Stuart Werner. November 2006.
- PEER 2006/08** *Vector-Valued Ground Motion Intensity Measures for Probabilistic Seismic Demand Analysis.* Jack W. Baker and C. Allin Cornell. October 2006.
- PEER 2006/07** *Analytical Modeling of Reinforced Concrete Walls for Predicting Flexural and Coupled-Shear-Flexural Responses.* Kutay Orakcal, Leonardo M. Massone, and John W. Wallace. October 2006.
- PEER 2006/06** *Nonlinear Analysis of a Soil-Drilled Pier System under Static and Dynamic Axial Loading.* Gang Wang and Nicholas Sitar. November 2006.
- PEER 2006/05** *Advanced Seismic Assessment Guidelines.* Paolo Bazzurro, C. Allin Cornell, Charles Menun, Maziar Motahari, and Nicolas Luco. September 2006.
- PEER 2006/04** *Probabilistic Seismic Evaluation of Reinforced Concrete Structural Components and Systems.* Tae Hyung Lee and Khalid M. Mosalam. August 2006.
- PEER 2006/03** *Performance of Lifelines Subjected to Lateral Spreading.* Scott A. Ashford and Teerawat Juirnarongrit. July 2006.
- PEER 2006/02** *Pacific Earthquake Engineering Research Center Highway Demonstration Project.* Anne Kiremidjian, James Moore, Yue Yue Fan, Nesrin Basoz, Ozgur Yazali, and Meredith Williams. April 2006.
- PEER 2006/01** *Bracing Berkeley. A Guide to Seismic Safety on the UC Berkeley Campus.* Mary C. Comerio, Stephen Tobriner, and Ariane Fehrenkamp. January 2006.
- PEER 2005/16** *Seismic Response and Reliability of Electrical Substation Equipment and Systems.* Junho Song, Armen Der Kiureghian, and Jerome L. Sackman. April 2006.
- PEER 2005/15** *CPT-Based Probabilistic Assessment of Seismic Soil Liquefaction Initiation.* R. E. S. Moss, R. B. Seed, R. E. Kayen, J. P. Stewart, and A. Der Kiureghian. April 2006.
- PEER 2005/14** *Workshop on Modeling of Nonlinear Cyclic Load-Deformation Behavior of Shallow Foundations.* Bruce L. Kutter, Geoffrey Martin, Tara Hutchinson, Chad Harden, Sivapalan Gajan, and Justin Phalen. March 2006.
- PEER 2005/13** *Stochastic Characterization and Decision Bases under Time-Dependent Aftershock Risk in Performance-Based Earthquake Engineering.* Gee Liek Yeo and C. Allin Cornell. July 2005.

- PEER 2005/12** *PEER Testbed Study on a Laboratory Building: Exercising Seismic Performance Assessment.* Mary C. Comerio, editor. November 2005.
- PEER 2005/11** *Van Nuys Hotel Building Testbed Report: Exercising Seismic Performance Assessment.* Helmut Krawinkler, editor. October 2005.
- PEER 2005/10** *First NEES/E-Defense Workshop on Collapse Simulation of Reinforced Concrete Building Structures.* September 2005.
- PEER 2005/09** *Test Applications of Advanced Seismic Assessment Guidelines.* Joe Maffei, Karl Telleen, Danya Mohr, William Holmes, and Yuki Nakayama. August 2006.
- PEER 2005/08** *Damage Accumulation in Lightly Confined Reinforced Concrete Bridge Columns.* R. Tyler Ranf, Jared M. Nelson, Zach Price, Marc O. Eberhard, and John F. Stanton. April 2006.
- PEER 2005/07** *Experimental and Analytical Studies on the Seismic Response of Freestanding and Anchored Laboratory Equipment.* Dimitrios Konstantinidis and Nicos Makris. January 2005.
- PEER 2005/06** *Global Collapse of Frame Structures under Seismic Excitations.* Luis F. Ibarra and Helmut Krawinkler. September 2005.
- PEER 2005/05** *Performance Characterization of Bench- and Shelf-Mounted Equipment.* Samit Ray Chaudhuri and Tara C. Hutchinson. May 2006.
- PEER 2005/04** *Numerical Modeling of the Nonlinear Cyclic Response of Shallow Foundations.* Chad Harden, Tara Hutchinson, Geoffrey R. Martin, and Bruce L. Kutter. August 2005.
- PEER 2005/03** *A Taxonomy of Building Components for Performance-Based Earthquake Engineering.* Keith A. Porter. September 2005.
- PEER 2005/02** *Fragility Basis for California Highway Overpass Bridge Seismic Decision Making.* Kevin R. Mackie and Božidar Stojadinović. June 2005.
- PEER 2005/01** *Empirical Characterization of Site Conditions on Strong Ground Motion.* Jonathan P. Stewart, Yoojoong Choi, and Robert W. Graves. June 2005.
- PEER 2004/09** *Electrical Substation Equipment Interaction: Experimental Rigid Conductor Studies.* Christopher Stearns and André Filiatrault. February 2005.
- PEER 2004/08** *Seismic Qualification and Fragility Testing of Line Break 550-kV Disconnect Switches.* Shakhzod M. Takhirov, Gregory L. Fenves, and Eric Fujisaki. January 2005.
- PEER 2004/07** *Ground Motions for Earthquake Simulator Qualification of Electrical Substation Equipment.* Shakhzod M. Takhirov, Gregory L. Fenves, Eric Fujisaki, and Don Clyde. January 2005.
- PEER 2004/06** *Performance-Based Regulation and Regulatory Regimes.* Peter J. May and Chris Koski. September 2004.
- PEER 2004/05** *Performance-Based Seismic Design Concepts and Implementation: Proceedings of an International Workshop.* Peter Fajfar and Helmut Krawinkler, editors. September 2004.
- PEER 2004/04** *Seismic Performance of an Instrumented Tilt-up Wall Building.* James C. Anderson and Vitelmo V. Bertero. July 2004.
- PEER 2004/03** *Evaluation and Application of Concrete Tilt-up Assessment Methodologies.* Timothy Graf and James O. Malley. October 2004.
- PEER 2004/02** *Analytical Investigations of New Methods for Reducing Residual Displacements of Reinforced Concrete Bridge Columns.* Junichi Sakai and Stephen A. Mahin. August 2004.
- PEER 2004/01** *Seismic Performance of Masonry Buildings and Design Implications.* Kerri Anne Taeko Tokoro, James C. Anderson, and Vitelmo V. Bertero. February 2004.
- PEER 2003/18** *Performance Models for Flexural Damage in Reinforced Concrete Columns.* Michael Berry and Marc Eberhard. August 2003.
- PEER 2003/17** *Predicting Earthquake Damage in Older Reinforced Concrete Beam-Column Joints.* Catherine Pagni and Laura Lowes. October 2004.
- PEER 2003/16** *Seismic Demands for Performance-Based Design of Bridges.* Kevin Mackie and Božidar Stojadinović. August 2003.
- PEER 2003/15** *Seismic Demands for Nondeteriorating Frame Structures and Their Dependence on Ground Motions.* Ricardo Antonio Medina and Helmut Krawinkler. May 2004.
- PEER 2003/14** *Finite Element Reliability and Sensitivity Methods for Performance-Based Earthquake Engineering.* Terje Haukaas and Armen Der Kiureghian. April 2004.

- PEER 2003/13** *Effects of Connection Hysteretic Degradation on the Seismic Behavior of Steel Moment-Resisting Frames.* Janise E. Rodgers and Stephen A. Mahin. March 2004.
- PEER 2003/12** *Implementation Manual for the Seismic Protection of Laboratory Contents: Format and Case Studies.* William T. Holmes and Mary C. Comerio. October 2003.
- PEER 2003/11** *Fifth U.S.-Japan Workshop on Performance-Based Earthquake Engineering Methodology for Reinforced Concrete Building Structures.* February 2004.
- PEER 2003/10** *A Beam-Column Joint Model for Simulating the Earthquake Response of Reinforced Concrete Frames.* Laura N. Lowes, Nilanjan Mitra, and Arash Altoontash. February 2004.
- PEER 2003/09** *Sequencing Repairs after an Earthquake: An Economic Approach.* Marco Casari and Simon J. Wilkie. April 2004.
- PEER 2003/08** *A Technical Framework for Probability-Based Demand and Capacity Factor Design (DCFD) Seismic Formats.* Fatemeh Jalayer and C. Allin Cornell. November 2003.
- PEER 2003/07** *Uncertainty Specification and Propagation for Loss Estimation Using FOSM Methods.* Jack W. Baker and C. Allin Cornell. September 2003.
- PEER 2003/06** *Performance of Circular Reinforced Concrete Bridge Columns under Bidirectional Earthquake Loading.* Mahmoud M. Hachem, Stephen A. Mahin, and Jack P. Moehle. February 2003.
- PEER 2003/05** *Response Assessment for Building-Specific Loss Estimation.* Eduardo Miranda and Shahram Taghavi. September 2003.
- PEER 2003/04** *Experimental Assessment of Columns with Short Lap Splices Subjected to Cyclic Loads.* Murat Melek, John W. Wallace, and Joel Conte. April 2003.
- PEER 2003/03** *Probabilistic Response Assessment for Building-Specific Loss Estimation.* Eduardo Miranda and Hesameddin Aslani. September 2003.
- PEER 2003/02** *Software Framework for Collaborative Development of Nonlinear Dynamic Analysis Program.* Jun Peng and Kincho H. Law. September 2003.
- PEER 2003/01** *Shake Table Tests and Analytical Studies on the Gravity Load Collapse of Reinforced Concrete Frames.* Kenneth John Elwood and Jack P. Moehle. November 2003.
- PEER 2002/24** *Performance of Beam to Column Bridge Joints Subjected to a Large Velocity Pulse.* Natalie Gibson, André Filiatrault, and Scott A. Ashford. April 2002.
- PEER 2002/23** *Effects of Large Velocity Pulses on Reinforced Concrete Bridge Columns.* Greg L. Orozco and Scott A. Ashford. April 2002.
- PEER 2002/22** *Characterization of Large Velocity Pulses for Laboratory Testing.* Kenneth E. Cox and Scott A. Ashford. April 2002.
- PEER 2002/21** *Fourth U.S.-Japan Workshop on Performance-Based Earthquake Engineering Methodology for Reinforced Concrete Building Structures.* December 2002.
- PEER 2002/20** *Barriers to Adoption and Implementation of PBEE Innovations.* Peter J. May. August 2002.
- PEER 2002/19** *Economic-Engineered Integrated Models for Earthquakes: Socioeconomic Impacts.* Peter Gordon, James E. Moore II, and Harry W. Richardson. July 2002.
- PEER 2002/18** *Assessment of Reinforced Concrete Building Exterior Joints with Substandard Details.* Chris P. Pantelides, Jon Hansen, Justin Nadauld, and Lawrence D. Reaveley. May 2002.
- PEER 2002/17** *Structural Characterization and Seismic Response Analysis of a Highway Overcrossing Equipped with Elastomeric Bearings and Fluid Dampers: A Case Study.* Nicos Makris and Jian Zhang. November 2002.
- PEER 2002/16** *Estimation of Uncertainty in Geotechnical Properties for Performance-Based Earthquake Engineering.* Allen L. Jones, Steven L. Kramer, and Pedro Arduino. December 2002.
- PEER 2002/15** *Seismic Behavior of Bridge Columns Subjected to Various Loading Patterns.* Asadollah Esmaeily-Gh. and Yan Xiao. December 2002.
- PEER 2002/14** *Inelastic Seismic Response of Extended Pile Shaft Supported Bridge Structures.* T.C. Hutchinson, R.W. Boulanger, Y.H. Chai, and I.M. Idriss. December 2002.
- PEER 2002/13** *Probabilistic Models and Fragility Estimates for Bridge Components and Systems.* Paolo Gardoni, Armen Der Kiureghian, and Khalid M. Mosalam. June 2002.
- PEER 2002/12** *Effects of Fault Dip and Slip Rake on Near-Source Ground Motions: Why Chi-Chi Was a Relatively Mild M7.6 Earthquake.* Brad T. Aagaard, John F. Hall, and Thomas H. Heaton. December 2002.

- PEER 2002/11** *Analytical and Experimental Study of Fiber-Reinforced Strip Isolators.* James M. Kelly and Shakhzod M. Takhirov. September 2002.
- PEER 2002/10** *Centrifuge Modeling of Settlement and Lateral Spreading with Comparisons to Numerical Analyses.* Sivapalan Gajan and Bruce L. Kutter. January 2003.
- PEER 2002/09** *Documentation and Analysis of Field Case Histories of Seismic Compression during the 1994 Northridge, California, Earthquake.* Jonathan P. Stewart, Patrick M. Smith, Daniel H. Whang, and Jonathan D. Bray. October 2002.
- PEER 2002/08** *Component Testing, Stability Analysis and Characterization of Buckling-Restrained Unbonded Braces™.* Cameron Black, Nicos Makris, and Ian Aiken. September 2002.
- PEER 2002/07** *Seismic Performance of Pile-Wharf Connections.* Charles W. Roeder, Robert Graff, Jennifer Soderstrom, and Jun Han Yoo. December 2001.
- PEER 2002/06** *The Use of Benefit-Cost Analysis for Evaluation of Performance-Based Earthquake Engineering Decisions.* Richard O. Zerbe and Anthony Falit-Baiamonte. September 2001.
- PEER 2002/05** *Guidelines, Specifications, and Seismic Performance Characterization of Nonstructural Building Components and Equipment.* André Filiatrault, Constantin Christopoulos, and Christopher Stearns. September 2001.
- PEER 2002/04** *Consortium of Organizations for Strong-Motion Observation Systems and the Pacific Earthquake Engineering Research Center Lifelines Program: Invited Workshop on Archiving and Web Dissemination of Geotechnical Data, 4–5 October 2001.* September 2002.
- PEER 2002/03** *Investigation of Sensitivity of Building Loss Estimates to Major Uncertain Variables for the Van Nuys Testbed.* Keith A. Porter, James L. Beck, and Rustem V. Shaikhutdinov. August 2002.
- PEER 2002/02** *The Third U.S.-Japan Workshop on Performance-Based Earthquake Engineering Methodology for Reinforced Concrete Building Structures.* July 2002.
- PEER 2002/01** *Nonstructural Loss Estimation: The UC Berkeley Case Study.* Mary C. Comerio and John C. Stallmeyer. December 2001.
- PEER 2001/16** *Statistics of SDF-System Estimate of Roof Displacement for Pushover Analysis of Buildings.* Anil K. Chopra, Rakesh K. Goel, and Chatpan Chintanapakdee. December 2001.
- PEER 2001/15** *Damage to Bridges during the 2001 Nisqually Earthquake.* R. Tyler Ranf, Marc O. Eberhard, and Michael P. Berry. November 2001.
- PEER 2001/14** *Rocking Response of Equipment Anchored to a Base Foundation.* Nicos Makris and Cameron J. Black. September 2001.
- PEER 2001/13** *Modeling Soil Liquefaction Hazards for Performance-Based Earthquake Engineering.* Steven L. Kramer and Ahmed-W. Elgamal. February 2001.
- PEER 2001/12** *Development of Geotechnical Capabilities in OpenSees.* Boris Jeremić. September 2001.
- PEER 2001/11** *Analytical and Experimental Study of Fiber-Reinforced Elastomeric Isolators.* James M. Kelly and Shakhzod M. Takhirov. September 2001.
- PEER 2001/10** *Amplification Factors for Spectral Acceleration in Active Regions.* Jonathan P. Stewart, Andrew H. Liu, Yoojoong Choi, and Mehmet B. Baturay. December 2001.
- PEER 2001/09** *Ground Motion Evaluation Procedures for Performance-Based Design.* Jonathan P. Stewart, Shyh-Jeng Chiou, Jonathan D. Bray, Robert W. Graves, Paul G. Somerville, and Norman A. Abrahamson. September 2001.
- PEER 2001/08** *Experimental and Computational Evaluation of Reinforced Concrete Bridge Beam-Column Connections for Seismic Performance.* Clay J. Naito, Jack P. Moehle, and Khalid M. Mosalam. November 2001.
- PEER 2001/07** *The Rocking Spectrum and the Shortcomings of Design Guidelines.* Nicos Makris and Dimitrios Konstantinidis. August 2001.
- PEER 2001/06** *Development of an Electrical Substation Equipment Performance Database for Evaluation of Equipment Fragilities.* Thalia Agnamos. April 1999.
- PEER 2001/05** *Stiffness Analysis of Fiber-Reinforced Elastomeric Isolators.* Hsiang-Chuan Tsai and James M. Kelly. May 2001.
- PEER 2001/04** *Organizational and Societal Considerations for Performance-Based Earthquake Engineering.* Peter J. May. April 2001.
- PEER 2001/03** *A Modal Pushover Analysis Procedure to Estimate Seismic Demands for Buildings: Theory and Preliminary Evaluation.* Anil K. Chopra and Rakesh K. Goel. January 2001.

- PEER 2001/02** *Seismic Response Analysis of Highway Overcrossings Including Soil-Structure Interaction.* Jian Zhang and Nicos Makris. March 2001.
- PEER 2001/01** *Experimental Study of Large Seismic Steel Beam-to-Column Connections.* Egor P. Popov and Shakhzod M. Takhirov. November 2000.
- PEER 2000/10** *The Second U.S.-Japan Workshop on Performance-Based Earthquake Engineering Methodology for Reinforced Concrete Building Structures.* March 2000.
- PEER 2000/09** *Structural Engineering Reconnaissance of the August 17, 1999 Earthquake: Kocaeli (Izmit), Turkey.* Halil Sezen, Kenneth J. Elwood, Andrew S. Whittaker, Khalid Mosalam, John J. Wallace, and John F. Stanton. December 2000.
- PEER 2000/08** *Behavior of Reinforced Concrete Bridge Columns Having Varying Aspect Ratios and Varying Lengths of Confinement.* Anthony J. Calderone, Dawn E. Lehman, and Jack P. Moehle. January 2001.
- PEER 2000/07** *Cover-Plate and Flange-Plate Reinforced Steel Moment-Resisting Connections.* Taejin Kim, Andrew S. Whittaker, Amir S. Gilani, Vitelmo V. Bertero, and Shakhzod M. Takhirov. September 2000.
- PEER 2000/06** *Seismic Evaluation and Analysis of 230-kV Disconnect Switches.* Amir S. J. Gilani, Andrew S. Whittaker, Gregory L. Fenves, Chun-Hao Chen, Henry Ho, and Eric Fujisaki. July 2000.
- PEER 2000/05** *Performance-Based Evaluation of Exterior Reinforced Concrete Building Joints for Seismic Excitation.* Chandra Clyde, Chris P. Pantelides, and Lawrence D. Reaveley. July 2000.
- PEER 2000/04** *An Evaluation of Seismic Energy Demand: An Attenuation Approach.* Chung-Che Chou and Chia-Ming Uang. July 1999.
- PEER 2000/03** *Framing Earthquake Retrofitting Decisions: The Case of Hillside Homes in Los Angeles.* Detlof von Winterfeldt, Nels Roselund, and Alicia Kitsuse. March 2000.
- PEER 2000/02** *U.S.-Japan Workshop on the Effects of Near-Field Earthquake Shaking.* Andrew Whittaker, ed. July 2000.
- PEER 2000/01** *Further Studies on Seismic Interaction in Interconnected Electrical Substation Equipment.* Armen Der Kiureghian, Kee-Jeung Hong, and Jerome L. Sackman. November 1999.
- PEER 1999/14** *Seismic Evaluation and Retrofit of 230-kV Porcelain Transformer Bushings.* Amir S. Gilani, Andrew S. Whittaker, Gregory L. Fenves, and Eric Fujisaki. December 1999.
- PEER 1999/13** *Building Vulnerability Studies: Modeling and Evaluation of Tilt-up and Steel Reinforced Concrete Buildings.* John W. Wallace, Jonathan P. Stewart, and Andrew S. Whittaker, editors. December 1999.
- PEER 1999/12** *Rehabilitation of Nonductile RC Frame Building Using Encasement Plates and Energy-Dissipating Devices.* Mehrdad Sasani, Vitelmo V. Bertero, James C. Anderson. December 1999.
- PEER 1999/11** *Performance Evaluation Database for Concrete Bridge Components and Systems under Simulated Seismic Loads.* Yael D. Hose and Frieder Seible. November 1999.
- PEER 1999/10** *U.S.-Japan Workshop on Performance-Based Earthquake Engineering Methodology for Reinforced Concrete Building Structures.* December 1999.
- PEER 1999/09** *Performance Improvement of Long Period Building Structures Subjected to Severe Pulse-Type Ground Motions.* James C. Anderson, Vitelmo V. Bertero, and Raul Bertero. October 1999.
- PEER 1999/08** *Envelopes for Seismic Response Vectors.* Charles Menun and Armen Der Kiureghian. July 1999.
- PEER 1999/07** *Documentation of Strengths and Weaknesses of Current Computer Analysis Methods for Seismic Performance of Reinforced Concrete Members.* William F. Cofer. November 1999.
- PEER 1999/06** *Rocking Response and Overturning of Anchored Equipment under Seismic Excitations.* Nicos Makris and Jian Zhang. November 1999.
- PEER 1999/05** *Seismic Evaluation of 550 kV Porcelain Transformer Bushings.* Amir S. Gilani, Andrew S. Whittaker, Gregory L. Fenves, and Eric Fujisaki. October 1999.
- PEER 1999/04** *Adoption and Enforcement of Earthquake Risk-Reduction Measures.* Peter J. May, Raymond J. Burby, T. Jens Feeley, and Robert Wood.
- PEER 1999/03** *Task 3 Characterization of Site Response General Site Categories.* Adrian Rodriguez-Marek, Jonathan D. Bray, and Norman Abrahamson. February 1999.
- PEER 1999/02** *Capacity-Demand-Diagram Methods for Estimating Seismic Deformation of Inelastic Structures: SDF Systems.* Anil K. Chopra and Rakesh Goel. April 1999.
- PEER 1999/01** *Interaction in Interconnected Electrical Substation Equipment Subjected to Earthquake Ground Motions.* Armen Der Kiureghian, Jerome L. Sackman, and Kee-Jeung Hong. February 1999.

- PEER 1998/08** *Behavior and Failure Analysis of a Multiple-Frame Highway Bridge in the 1994 Northridge Earthquake.* Gregory L. Fenves and Michael Ellery. December 1998.
- PEER 1998/07** *Empirical Evaluation of Inertial Soil-Structure Interaction Effects.* Jonathan P. Stewart, Raymond B. Seed, and Gregory L. Fenves. November 1998.
- PEER 1998/06** *Effect of Damping Mechanisms on the Response of Seismic Isolated Structures.* Nicos Makris and Shih-Po Chang. November 1998.
- PEER 1998/05** *Rocking Response and Overturning of Equipment under Horizontal Pulse-Type Motions.* Nicos Makris and Yiannis Roussos. October 1998.
- PEER 1998/04** *Pacific Earthquake Engineering Research Invitational Workshop Proceedings, May 14–15, 1998: Defining the Links between Planning, Policy Analysis, Economics and Earthquake Engineering.* Mary Comerio and Peter Gordon. September 1998.
- PEER 1998/03** *Repair/Upgrade Procedures for Welded Beam to Column Connections.* James C. Anderson and Xiaojing Duan. May 1998.
- PEER 1998/02** *Seismic Evaluation of 196 kV Porcelain Transformer Bushings.* Amir S. Gilani, Juan W. Chavez, Gregory L. Fenves, and Andrew S. Whittaker. May 1998.
- PEER 1998/01** *Seismic Performance of Well-Confined Concrete Bridge Columns.* Dawn E. Lehman and Jack P. Moehle. December 2000.

ONLINE PEER REPORTS

The following PEER reports are available by Internet only at http://peer.berkeley.edu/publications/peer_reports_complete.html.

- PEER 2012/103** *Performance-Based Seismic Demand Assessment of Concentrically Braced Steel Frame Buildings*. Chui-Hsin Chen and Stephen A. Mahin. December 2012.
- PEER 2012/102** *Procedure to Restart an Interrupted Hybrid Simulation: Addendum to PEER Report 2010/103*. Vesna Terzic and Bozidar Stojadinovic. October 2012.
- PEER 2012/101** *Mechanics of Fiber Reinforced Bearings*. James M. Kelly and Andrea Calabrese. February 2012.
- PEER 2011/107** *Nonlinear Site Response and Seismic Compression at Vertical Array Strongly Shaken by 2007 Niigata-ken Chuetsu-oki Earthquake*. Eric Yee, Jonathan P. Stewart, and Kohji Tokimatsu. December 2011.
- PEER 2011/106** *Self Compacting Hybrid Fiber Reinforced Concrete Composites for Bridge Columns*. Pardeep Kumar, Gabriel Jen, William Trono, Marios Panagiotou, and Claudia Ostertag. September 2011.
- PEER 2011/105** *Stochastic Dynamic Analysis of Bridges Subjected to Spatially Varying Ground Motions*. Katerina Konakli and Armen Der Kiureghian. August 2011.
- PEER 2011/104** *Design and Instrumentation of the 2010 E-Defense Four-Story Reinforced Concrete and Post-Tensioned Concrete Buildings*. Takuya Nagae, Kenichi Tahara, Taizo Matsumori, Hitoshi Shiohara, Toshimi Kabeyasawa, Susumu Kono, Minehiro Nishiyama (Japanese Research Team) and John Wallace, Wassim Ghanoum, Jack Moehle, Richard Sause, Wesley Keller, Zeynep Tuna (U.S. Research Team). June 2011.
- PEER 2011/103** *In-Situ Monitoring of the Force Output of Fluid Dampers: Experimental Investigation*. Dimitrios Konstantinidis, James M. Kelly, and Nicos Makris. April 2011.
- PEER 2011/102** *Ground-motion prediction equations 1964 - 2010*. John Douglas. April 2011.
- PEER 2011/101** *Report of the Eighth Planning Meeting of NEES/E-Defense Collaborative Research on Earthquake Engineering*. Convened by the Hyogo Earthquake Engineering Research Center (NIED), NEES Consortium, Inc. February 2011.
- PEER 2010/111** *Modeling and Acceptance Criteria for Seismic Design and Analysis of Tall Buildings*. Task 7 Report for the Tall Buildings Initiative - Published jointly by the Applied Technology Council. October 2010.
- PEER 2010/110** *Seismic Performance Assessment and Probabilistic Repair Cost Analysis of Precast Concrete Cladding Systems for Multistory Buildings*. Jeffrey P. Hunt and Božidar Stojadinovic. November 2010.
- PEER 2010/109** *Report of the Seventh Joint Planning Meeting of NEES/E-Defense Collaboration on Earthquake Engineering. Held at the E-Defense, Miki, and Shin-Kobe, Japan, September 18–19, 2009*. August 2010.
- PEER 2010/108** *Probabilistic Tsunami Hazard in California*. Hong Kie Thio, Paul Somerville, and Jascha Polet, preparers. October 2010.
- PEER 2010/107** *Performance and Reliability of Exposed Column Base Plate Connections for Steel Moment-Resisting Frames*. Ady Aviram, Božidar Stojadinovic, and Armen Der Kiureghian. August 2010.
- PEER 2010/106** *Verification of Probabilistic Seismic Hazard Analysis Computer Programs*. Patricia Thomas, Ivan Wong, and Norman Abrahamson. May 2010.
- PEER 2010/105** *Structural Engineering Reconnaissance of the April 6, 2009, Abruzzo, Italy, Earthquake, and Lessons Learned*. M. Selim Günay and Khalid M. Mosalam. April 2010.
- PEER 2010/104** *Simulating the Inelastic Seismic Behavior of Steel Braced Frames, Including the Effects of Low-Cycle Fatigue*. Yuli Huang and Stephen A. Mahin. April 2010.
- PEER 2010/103** *Post-Earthquake Traffic Capacity of Modern Bridges in California*. Vesna Terzic and Božidar Stojadinović. March 2010.
- PEER 2010/102** *Analysis of Cumulative Absolute Velocity (CAV) and JMA Instrumental Seismic Intensity (I_{JMA}) Using the PEER–NGA Strong Motion Database*. Kenneth W. Campbell and Yousef Bozorgnia. February 2010.
- PEER 2010/101** *Rocking Response of Bridges on Shallow Foundations*. Jose A. Ugalde, Bruce L. Kutter, and Boris Jeremic. April 2010.
- PEER 2009/109** *Simulation and Performance-Based Earthquake Engineering Assessment of Self-Centering Post-Tensioned Concrete Bridge Systems*. Won K. Lee and Sarah L. Billington. December 2009.
- PEER 2009/108** *PEER Lifelines Geotechnical Virtual Data Center*. J. Carl Stepp, Daniel J. Ponti, Loren L. Turner, Jennifer N. Swift, Sean Devlin, Yang Zhu, Jean Benoit, and John Bobbitt. September 2009.

- PEER 2009/107** *Experimental and Computational Evaluation of Current and Innovative In-Span Hinge Details in Reinforced Concrete Box-Girder Bridges: Part 2: Post-Test Analysis and Design Recommendations.* Matias A. Hube and Khalid M. Mosalam. December 2009.
- PEER 2009/106** *Shear Strength Models of Exterior Beam-Column Joints without Transverse Reinforcement.* Sangjoon Park and Khalid M. Mosalam. November 2009.
- PEER 2009/105** *Reduced Uncertainty of Ground Motion Prediction Equations through Bayesian Variance Analysis.* Robb Eric S. Moss. November 2009.
- PEER 2009/104** *Advanced Implementation of Hybrid Simulation.* Andreas H. Schellenberg, Stephen A. Mahin, Gregory L. Fenves. November 2009.
- PEER 2009/103** *Performance Evaluation of Innovative Steel Braced Frames.* T. Y. Yang, Jack P. Moehle, and Božidar Stojadinovic. August 2009.
- PEER 2009/102** *Reinvestigation of Liquefaction and Nonliquefaction Case Histories from the 1976 Tangshan Earthquake.* Robb Eric Moss, Robert E. Kayen, Liyuan Tong, Songyu Liu, Guojun Cai, and Jiaer Wu. August 2009.
- PEER 2009/101** *Report of the First Joint Planning Meeting for the Second Phase of NEES/E-Defense Collaborative Research on Earthquake Engineering.* Stephen A. Mahin et al. July 2009.
- PEER 2008/104** *Experimental and Analytical Study of the Seismic Performance of Retaining Structures.* Linda Al Atik and Nicholas Sitar. January 2009.
- PEER 2008/103** *Experimental and Computational Evaluation of Current and Innovative In-Span Hinge Details in Reinforced Concrete Box-Girder Bridges. Part 1: Experimental Findings and Pre-Test Analysis.* Matias A. Hube and Khalid M. Mosalam. January 2009.
- PEER 2008/102** *Modeling of Unreinforced Masonry Infill Walls Considering In-Plane and Out-of-Plane Interaction.* Stephen Kadysiewski and Khalid M. Mosalam. January 2009.
- PEER 2008/101** *Seismic Performance Objectives for Tall Buildings.* William T. Holmes, Charles Kircher, William Petak, and Nabih Youssef. August 2008.
- PEER 2007/101** *Generalized Hybrid Simulation Framework for Structural Systems Subjected to Seismic Loading.* Tarek Elkhoraibi and Khalid M. Mosalam. July 2007.
- PEER 2007/100** *Seismic Evaluation of Reinforced Concrete Buildings Including Effects of Masonry Infill Walls.* Alidad Hashemi and Khalid M. Mosalam. July 2007.

PEER REPORTS

PEER reports are available as a free PDF download from http://peer.berkeley.edu/publications/peer_reports_complete.html. Printed hard copies of PEER reports can be ordered directly from our printer by following the instructions at http://peer.berkeley.edu/publications/peer_reports.html. For other related questions about the PEER Report Series, contact the Pacific Earthquake Engineering Research Center, 325 Davis Hall mail code 1792, Berkeley, CA 94720. Tel.: (510) 642-3437; Fax: (510) 665-1655; Email: peer_editor@berkeley.edu

- PEER 2015/09** *Structural Behavior of Column-Bent Cap Beam-Box Girder Systems in Reinforced Concrete Bridges Subjected to Gravity and Seismic Loads. Part I: Pre-Test Analysis and Quasi-Static Experiments.* Mohamed A. Moustafa and Khalid M. Mosalam. September 2015.
- PEER 2015/08** *NGA-East: Adjustments to Median Ground-Motion Models for Center and Eastern North America.* August 2015.
- PEER 2015/07** *NGA-East: Ground-Motion Standard-Deviation Models for Central and Eastern North America.* Linda Al Atik. June 2015.
- PEER 2015/06** *Adjusting Ground-Motion Intensity Measures to a Reference Site for which $V_{S30} = 3000$ m/sec.* David M. Boore. May 2015.
- PEER 2015/05** *Hybrid Simulation of Seismic Isolation Systems Applied to an APR-1400 Nuclear Power Plant.* Andreas H. Schellenberg, Alireza Sarebanha, Matthew J. Schoettler, Gilberto Mosqueda, Gianmario Benzoni, and Stephen A. Mahin. April 2015.
- PEER 2015/04** *NGA-East: Median Ground-Motion Models for the Central and Eastern North America Region.* April 2015.
- PEER 2015/03** *Single Series Solution for the Rectangular Fiber-Reinforced Elastomeric Isolator Compression Modulus.* James M. Kelly and Niel C. Van Engelen. March 2015.
- PEER 2015/02** *A Full-Scale, Single-Column Bridge Bent Tested by Shake-Table Excitation.* Matthew J. Schoettler, José I. Restrepo, Gabriele Guerrini, David E. Duck, and Francesco Carrea. March 2015.
- PEER 2015/01** *Concrete Column Blind Prediction Contest 2010: Outcomes and Observations.* Vesna Terzic, Matthew J. Schoettler, José I. Restrepo, and Stephen A. Mahin. March 2015.
- PEER 2014/20** *Stochastic Modeling and Simulation of Near-Fault Ground Motions for Performance-Based Earthquake Engineering.* Mayssa Dabaghi and Armen Der Kiureghian. December 2014.
- PEER 2014/19** *Seismic Response of a Hybrid Fiber-Reinforced Concrete Bridge Column Detailed for Accelerated Bridge Construction.* Wilson Nguyen, William Trono, Marios Panagiotou, and Claudia P. Ostertag. December 2014.
- PEER 2014/18** *Three-Dimensional Beam-Truss Model for Reinforced Concrete Walls and Slabs Subjected to Cyclic Static or Dynamic Loading.* Yuan Lu, Marios Panagiotou, and Ioannis Koutromanos. December 2014.
- PEER 2014/17** *PEER NGA-East Database.* Christine A. Goulet, Tadahiro Kishida, Timothy D. Ancheta, Chris H. Cramer, Robert B. Darragh, Walter J. Silva, Youssef M.A. Hashash, Joseph Harmon, Jonathan P. Stewart, Katie E. Wooddell, and Robert R. Youngs. October 2014.
- PEER 2014/16** *Guidelines for Performing Hazard-Consistent One-Dimensional Ground Response Analysis for Ground Motion Prediction.* Jonathan P. Stewart, Kioumars Afshari, and Youssef M.A. Hashash. October 2014.
- PEER 2014/15** *NGA-East Regionalization Report: Comparison of Four Crustal Regions within Central and Eastern North America using Waveform Modeling and 5%-Damped Pseudo-Spectral Acceleration Response.* Jennifer Dreiling, Marius P. Isken, Walter D. Mooney, Martin C. Chapman, and Richard W. Godbee. October 2014.
- PEER 2014/14** *Scaling Relations between Seismic Moment and Rupture Area of Earthquakes in Stable Continental Regions.* Paul Somerville. August 2014.
- PEER 2014/13** *PEER Preliminary Notes and Observations on the August 24, 2014, South Napa Earthquake.* Grace S. Kang (Editor), Stephen A. Mahin (Editors). September 2014.
- PEER 2014/12** *Reference-Rock Site Conditions for Central and Eastern North America: Part II – Attenuation (Kappa) Definition.* Kenneth W. Campbell, Youssef M.A. Hashash, Byungmin Kim, Albert R. Kottke, Ellen M. Rathje, Walter J. Silva, and Jonathan P. Stewart. August 2014.
- PEER 2014/11** *Reference-Rock Site Conditions for Central and Eastern North America: Part I - Velocity Definition.* Youssef M.A. Hashash, Albert R. Kottke, Jonathan P. Stewart, Kenneth W. Campbell, Byungmin Kim, Ellen M. Rathje, Walter J. Silva, Sissy Nikolaou, and Cheryl Moss. August 2014.

- PEER 2014/10** *Evaluation of Collapse and Non-Collapse of Parallel Bridges Affected by Liquefaction and Lateral Spreading.* Benjamin Turner, Scott J. Brandenburg, and Jonathan P. Stewart. August 2014.
- PEER 2014/09** *PEER Arizona Strong-Motion Database and GMPEs Evaluation.* Tadahiro Kishida, Robert E. Kayen, Olga-Joan Ktenidou, Walter J. Silva, Robert B. Darragh, and Jennie Watson-Lamprey. June 2014.
- PEER 2014/08** *Unbonded Pretensioned Bridge Columns with Rocking Detail.* Jeffrey A. Schaefer, Bryan Kennedy, Marc O. Eberhard, John F. Stanton. June 2014.
- PEER 2014/07** *Northridge 20 Symposium Summary Report: Impacts, Outcomes, and Next Steps.* May 2014.
- PEER 2014/06** *Report of the Tenth Planning Meeting of NEES/E-Defense Collaborative Research on Earthquake Engineering.* December 2013.
- PEER 2014/05** *Seismic Velocity Site Characterization of Thirty-One Chilean Seismometer Stations by Spectral Analysis of Surface Wave Dispersion.* Robert Kayen, Brad D. Carlin, Skye Corbet, Camilo Pinilla, Allan Ng, Edward Gorbis, and Christine Truong. April 2014.
- PEER 2014/04** *Effect of Vertical Acceleration on Shear Strength of Reinforced Concrete Columns.* Hyerin Lee and Khalid M. Mosalam. April 2014.
- PEER 2014/03** *Retest of Thirty-Year-Old Neoprene Isolation Bearings.* James M. Kelly and Niel C. Van Engelen. March 2014.
- PEER 2014/02** *Theoretical Development of Hybrid Simulation Applied to Plate Structures.* Ahmed A. Bakhaty, Khalid M. Mosalam, and Sanjay Govindjee. January 2014.
- PEER 2014/01** *Performance-Based Seismic Assessment of Skewed Bridges.* Peyman Kaviani, Farzin Zareian, and Ertugrul Taciroglu. January 2014.
- PEER 2013/26** *Urban Earthquake Engineering. Proceedings of the U.S.-Iran Seismic Workshop.* December 2013.
- PEER 2013/25** *Earthquake Engineering for Resilient Communities: 2013 PEER Internship Program Research Report Collection.* Heidi Tremayne (Editor), Stephen A. Mahin (Editor), Jorge Archbold Monterossa, Matt Brosman, Shelly Dean, Katherine deLaveaga, Curtis Fong, Donovan Holder, Rakeeb Khan, Elizabeth Jachens, David Lam, Daniela Martinez Lopez, Mara Minner, Geffen Oren, Julia Pavicic, Melissa Quinonez, Lorena Rodriguez, Sean Salazar, Kelli Slaven, Vivian Steyert, Jenny Taing, and Salvador Tena. December 2013.
- PEER 2013/24** *NGA-West2 Ground Motion Prediction Equations for Vertical Ground Motions.* September 2013.
- PEER 2013/23** *Coordinated Planning and Preparedness for Fire Following Major Earthquakes.* Charles Scawthorn. November 2013.
- PEER 2013/22** *GEM-PEER Task 3 Project: Selection of a Global Set of Ground Motion Prediction Equations.* Jonathan P. Stewart, John Douglas, Mohammad B. Javanbarg, Carola Di Alessandro, Yousef Bozorgnia, Norman A. Abrahamson, David M. Boore, Kenneth W. Campbell, Elise Delavaud, Mustafa Erdik and Peter J. Stafford. December 2013.
- PEER 2013/21** *Seismic Design and Performance of Bridges with Columns on Rocking Foundations.* Grigorios Antonellis and Marios Panagiotou. September 2013.
- PEER 2013/20** *Experimental and Analytical Studies on the Seismic Behavior of Conventional and Hybrid Braced Frames.* Jiun-Wei Lai and Stephen A. Mahin. September 2013.
- PEER 2013/19** *Toward Resilient Communities: A Performance-Based Engineering Framework for Design and Evaluation of the Built Environment.* Michael William Mieler, Bozidar Stojadinovic, Robert J. Budnitz, Stephen A. Mahin and Mary C. Comerio. September 2013.
- PEER 2013/18** *Identification of Site Parameters that Improve Predictions of Site Amplification.* Ellen M. Rathje and Sara Navidi. July 2013.
- PEER 2013/17** *Response Spectrum Analysis of Concrete Gravity Dams Including Dam-Water-Foundation Interaction.* Arnkjell Løkke and Anil K. Chopra. July 2013.
- PEER 2013/16** *Effect of hoop reinforcement spacing on the cyclic response of large reinforced concrete special moment frame beams.* Marios Panagiotou, Tea Visnjic, Grigorios Antonellis, Panagiotis Galanis, and Jack P. Moehle. June 2013.
- PEER 2013/15** *A Probabilistic Framework to Include the Effects of Near-Fault Directivity in Seismic Hazard Assessment.* Shrey Kumar Shahi, Jack W. Baker. October 2013.
- PEER 2013/14** *Hanging-Wall Scaling using Finite-Fault Simulations.* Jennifer L. Donahue and Norman A. Abrahamson. September 2013.
- PEER 2013/13** *Semi-Empirical Nonlinear Site Amplification and its Application in NEHRP Site Factors.* Jonathan P. Stewart and Emel Seyhan. November 2013.

- PEER 2013/12** *Nonlinear Horizontal Site Response for the NGA-West2 Project.* Ronnie Kamai, Norman A. Abramson, Walter J. Silva. May 2013.
- PEER 2013/11** *Epistemic Uncertainty for NGA-West2 Models.* Linda Al Atik and Robert R. Youngs. May 2013.
- PEER 2013/10** *NGA-West 2 Models for Ground-Motion Directionality.* Shrey K. Shahi and Jack W. Baker. May 2013.
- PEER 2013/09** *Final Report of the NGA-West2 Directivity Working Group.* Paul Spudich, Jeffrey R. Bayless, Jack W. Baker, Brian S.J. Chiou, Badie Rowshandel, Shrey Shahi, and Paul Somerville. May 2013.
- PEER 2013/08** *NGA-West2 Model for Estimating Average Horizontal Values of Pseudo-Absolute Spectral Accelerations Generated by Crustal Earthquakes.* I. M. Idriss. May 2013.
- PEER 2013/07** *Update of the Chiou and Youngs NGA Ground Motion Model for Average Horizontal Component of Peak Ground Motion and Response Spectra.* Brian Chiou and Robert Youngs. May 2013.
- PEER 2013/06** *NGA-West2 Campbell-Bozorgnia Ground Motion Model for the Horizontal Components of PGA, PGV, and 5%-Damped Elastic Pseudo-Acceleration Response Spectra for Periods Ranging from 0.01 to 10 sec.* Kenneth W. Campbell and Yousef Bozorgnia. May 2013.
- PEER 2013/05** *NGA-West 2 Equations for Predicting Response Spectral Accelerations for Shallow Crustal Earthquakes.* David M. Boore, Jonathan P. Stewart, Emel Seyhan, Gail M. Atkinson. May 2013.
- PEER 2013/04** *Update of the AS08 Ground-Motion Prediction Equations Based on the NGA-West2 Data Set.* Norman Abrahamson, Walter Silva, and Ronnie Kamai. May 2013.
- PEER 2013/03** *PEER NGA-West2 Database.* Timothy D. Ancheta, Robert B. Darragh, Jonathan P. Stewart, Emel Seyhan, Walter J. Silva, Brian S.J. Chiou, Katie E. Wooddell, Robert W. Graves, Albert R. Kottke, David M. Boore, Tadaihiro Kishida, and Jennifer L. Donahue. May 2013.
- PEER 2013/02** *Hybrid Simulation of the Seismic Response of Squat Reinforced Concrete Shear Walls.* Catherine A. Whyte and Bozidar Stojadinovic. May 2013.
- PEER 2013/01** *Housing Recovery in Chile: A Qualitative Mid-program Review.* Mary C. Comerio. February 2013.
- PEER 2012/08** *Guidelines for Estimation of Shear Wave Velocity.* Bernard R. Wair, Jason T. DeJong, and Thomas Shantz. December 2012.
- PEER 2012/07** *Earthquake Engineering for Resilient Communities: 2012 PEER Internship Program Research Report Collection.* Heidi Tremayne (Editor), Stephen A. Mahin (Editor), Collin Anderson, Dustin Cook, Michael Erceg, Carlos Esparza, Jose Jimenez, Dorian Krausz, Andrew Lo, Stephanie Lopez, Nicole McCurdy, Paul Shipman, Alexander Strum, Eduardo Vega. December 2012.
- PEER 2012/06** *Fragilities for Precarious Rocks at Yucca Mountain.* Matthew D. Purvance, Rasool Anooshehpour, and James N. Brune. December 2012.
- PEER 2012/05** *Development of Simplified Analysis Procedure for Piles in Laterally Spreading Layered Soils.* Christopher R. McGann, Pedro Arduino, and Peter Mackenzie-Helnwein. December 2012.
- PEER 2012/04** *Unbonded Pre-Tensioned Columns for Bridges in Seismic Regions.* Phillip M. Davis, Todd M. Janes, Marc O. Eberhard, and John F. Stanton. December 2012.
- PEER 2012/03** *Experimental and Analytical Studies on Reinforced Concrete Buildings with Seismically Vulnerable Beam-Column Joints.* Sangjoon Park and Khalid M. Mosalam. October 2012.
- PEER 2012/02** *Seismic Performance of Reinforced Concrete Bridges Allowed to Uplift during Multi-Directional Excitation.* Andres Oscar Espinoza and Stephen A. Mahin. July 2012.
- PEER 2012/01** *Spectral Damping Scaling Factors for Shallow Crustal Earthquakes in Active Tectonic Regions.* Sanaz Rezaeian, Yousef Bozorgnia, I. M. Idriss, Kenneth Campbell, Norman Abrahamson, and Walter Silva. July 2012.
- PEER 2011/10** *Earthquake Engineering for Resilient Communities: 2011 PEER Internship Program Research Report Collection.* Eds. Heidi Faison and Stephen A. Mahin. December 2011.
- PEER 2011/09** *Calibration of Semi-Stochastic Procedure for Simulating High-Frequency Ground Motions.* Jonathan P. Stewart, Emel Seyhan, and Robert W. Graves. December 2011.
- PEER 2011/08** *Water Supply in regard to Fire Following Earthquake.* Charles Scawthorn. November 2011.
- PEER 2011/07** *Seismic Risk Management in Urban Areas. Proceedings of a U.S.-Iran-Turkey Seismic Workshop.* September 2011.
- PEER 2011/06** *The Use of Base Isolation Systems to Achieve Complex Seismic Performance Objectives.* Troy A. Morgan and Stephen A. Mahin. July 2011.

- PEER 2011/05** *Case Studies of the Seismic Performance of Tall Buildings Designed by Alternative Means*. Task 12 Report for the Tall Buildings Initiative. Jack Moehle, Yousef Bozorgnia, Nirmal Jayaram, Pierson Jones, Mohsen Rahnama, Niles Shome, Zeynep Tuna, John Wallace, Tony Yang, and Farzin Zareian. July 2011.
- PEER 2011/04** *Recommended Design Practice for Pile Foundations in Laterally Spreading Ground*. Scott A. Ashford, Ross W. Boulanger, and Scott J. Brandenburg. June 2011.
- PEER 2011/03** *New Ground Motion Selection Procedures and Selected Motions for the PEER Transportation Research Program*. Jack W. Baker, Ting Lin, Shrey K. Shahi, and Nirmal Jayaram. March 2011.
- PEER 2011/02** *A Bayesian Network Methodology for Infrastructure Seismic Risk Assessment and Decision Support*. Michelle T. Bensi, Armen Der Kiureghian, and Daniel Straub. March 2011.
- PEER 2011/01** *Demand Fragility Surfaces for Bridges in Liquefied and Laterally Spreading Ground*. Scott J. Brandenburg, Jian Zhang, Pirooz Kashighandi, Yili Huo, and Minxing Zhao. March 2011.
- PEER 2010/05** *Guidelines for Performance-Based Seismic Design of Tall Buildings*. Developed by the Tall Buildings Initiative. November 2010.
- PEER 2010/04** *Application Guide for the Design of Flexible and Rigid Bus Connections between Substation Equipment Subjected to Earthquakes*. Jean-Bernard Dastous and Armen Der Kiureghian. September 2010.
- PEER 2010/03** *Shear Wave Velocity as a Statistical Function of Standard Penetration Test Resistance and Vertical Effective Stress at Caltrans Bridge Sites*. Scott J. Brandenburg, Naresh Bellana, and Thomas Shantz. June 2010.
- PEER 2010/02** *Stochastic Modeling and Simulation of Ground Motions for Performance-Based Earthquake Engineering*. Sanaz Rezaeian and Armen Der Kiureghian. June 2010.
- PEER 2010/01** *Structural Response and Cost Characterization of Bridge Construction Using Seismic Performance Enhancement Strategies*. Ady Aviram, Božidar Stojadinović, Gustavo J. Parra-Montesinos, and Kevin R. Mackie. March 2010.
- PEER 2009/03** *The Integration of Experimental and Simulation Data in the Study of Reinforced Concrete Bridge Systems Including Soil-Foundation-Structure Interaction*. Matthew Dryden and Gregory L. Fenves. November 2009.
- PEER 2009/02** *Improving Earthquake Mitigation through Innovations and Applications in Seismic Science, Engineering, Communication, and Response. Proceedings of a U.S.-Iran Seismic Workshop*. October 2009.
- PEER 2009/01** *Evaluation of Ground Motion Selection and Modification Methods: Predicting Median Interstory Drift Response of Buildings*. Curt B. Haselton, Ed. June 2009.
- PEER 2008/10** *Technical Manual for Strata*. Albert R. Kottke and Ellen M. Rathje. February 2009.
- PEER 2008/09** *NGA Model for Average Horizontal Component of Peak Ground Motion and Response Spectra*. Brian S.-J. Chiou and Robert R. Youngs. November 2008.
- PEER 2008/08** *Toward Earthquake-Resistant Design of Concentrically Braced Steel Structures*. Patxi Uriz and Stephen A. Mahin. November 2008.
- PEER 2008/07** *Using OpenSees for Performance-Based Evaluation of Bridges on Liquefiable Soils*. Stephen L. Kramer, Pedro Arduino, and HyungSuk Shin. November 2008.
- PEER 2008/06** *Shaking Table Tests and Numerical Investigation of Self-Centering Reinforced Concrete Bridge Columns*. Hyung IL Jeong, Junichi Sakai, and Stephen A. Mahin. September 2008.
- PEER 2008/05** *Performance-Based Earthquake Engineering Design Evaluation Procedure for Bridge Foundations Undergoing Liquefaction-Induced Lateral Ground Displacement*. Christian A. Ledezma and Jonathan D. Bray. August 2008.
- PEER 2008/04** *Benchmarking of Nonlinear Geotechnical Ground Response Analysis Procedures*. Jonathan P. Stewart, Annie On-Lei Kwok, Youssef M. A. Hashash, Neven Matasovic, Robert Pyke, Zhiliang Wang, and Zhaohui Yang. August 2008.
- PEER 2008/03** *Guidelines for Nonlinear Analysis of Bridge Structures in California*. Ady Aviram, Kevin R. Mackie, and Božidar Stojadinović. August 2008.
- PEER 2008/02** *Treatment of Uncertainties in Seismic-Risk Analysis of Transportation Systems*. Evangelos Stergiou and Anne S. Kiremidjian. July 2008.
- PEER 2008/01** *Seismic Performance Objectives for Tall Buildings*. William T. Holmes, Charles Kircher, William Petak, and Nabih Youssef. August 2008.
- PEER 2007/12** *An Assessment to Benchmark the Seismic Performance of a Code-Conforming Reinforced Concrete Moment-Frame Building*. Curt Haselton, Christine A. Goulet, Judith Mitrani-Reiser, James L. Beck, Gregory G. Deierlein, Keith A. Porter, Jonathan P. Stewart, and Ertugrul Taciroglu. August 2008.
- PEER 2007/11** *Bar Buckling in Reinforced Concrete Bridge Columns*. Wayne A. Brown, Dawn E. Lehman, and John F. Stanton. February 2008.

- PEER 2007/10** *Computational Modeling of Progressive Collapse in Reinforced Concrete Frame Structures.* Mohamed M. Talaat and Khalid M. Mosalam. May 2008.
- PEER 2007/09** *Integrated Probabilistic Performance-Based Evaluation of Benchmark Reinforced Concrete Bridges.* Kevin R. Mackie, John-Michael Wong, and Božidar Stojadinović. January 2008.
- PEER 2007/08** *Assessing Seismic Collapse Safety of Modern Reinforced Concrete Moment-Frame Buildings.* Curt B. Haselton and Gregory G. Deierlein. February 2008.
- PEER 2007/07** *Performance Modeling Strategies for Modern Reinforced Concrete Bridge Columns.* Michael P. Berry and Marc O. Eberhard. April 2008.
- PEER 2007/06** *Development of Improved Procedures for Seismic Design of Buried and Partially Buried Structures.* Linda Al Atik and Nicholas Sitar. June 2007.
- PEER 2007/05** *Uncertainty and Correlation in Seismic Risk Assessment of Transportation Systems.* Renee G. Lee and Anne S. Kiremidjian. July 2007.
- PEER 2007/04** *Numerical Models for Analysis and Performance-Based Design of Shallow Foundations Subjected to Seismic Loading.* Sivapalan Gajan, Tara C. Hutchinson, Bruce L. Kutter, Prishati Raychowdhury, José A. Ugalde, and Jonathan P. Stewart. May 2008.
- PEER 2007/03** *Beam-Column Element Model Calibrated for Predicting Flexural Response Leading to Global Collapse of RC Frame Buildings.* Curt B. Haselton, Abbie B. Liel, Sarah Taylor Lange, and Gregory G. Deierlein. May 2008.
- PEER 2007/02** *Campbell-Bozorgnia NGA Ground Motion Relations for the Geometric Mean Horizontal Component of Peak and Spectral Ground Motion Parameters.* Kenneth W. Campbell and Yousef Bozorgnia. May 2007.
- PEER 2007/01** *Boore-Atkinson NGA Ground Motion Relations for the Geometric Mean Horizontal Component of Peak and Spectral Ground Motion Parameters.* David M. Boore and Gail M. Atkinson. May 2007.
- PEER 2006/12** *Societal Implications of Performance-Based Earthquake Engineering.* Peter J. May. May 2007.
- PEER 2006/11** *Probabilistic Seismic Demand Analysis Using Advanced Ground Motion Intensity Measures, Attenuation Relationships, and Near-Fault Effects.* Polsak Tothong and C. Allin Cornell. March 2007.
- PEER 2006/10** *Application of the PEER PBEE Methodology to the I-880 Viaduct.* Sashi Kunnath. February 2007.
- PEER 2006/09** *Quantifying Economic Losses from Travel Forgone Following a Large Metropolitan Earthquake.* James Moore, Sungbin Cho, Yue Yue Fan, and Stuart Werner. November 2006.
- PEER 2006/08** *Vector-Valued Ground Motion Intensity Measures for Probabilistic Seismic Demand Analysis.* Jack W. Baker and C. Allin Cornell. October 2006.
- PEER 2006/07** *Analytical Modeling of Reinforced Concrete Walls for Predicting Flexural and Coupled-Shear-Flexural Responses.* Kutay Orakcal, Leonardo M. Massone, and John W. Wallace. October 2006.
- PEER 2006/06** *Nonlinear Analysis of a Soil-Drilled Pier System under Static and Dynamic Axial Loading.* Gang Wang and Nicholas Sitar. November 2006.
- PEER 2006/05** *Advanced Seismic Assessment Guidelines.* Paolo Bazzurro, C. Allin Cornell, Charles Menun, Maziar Motahari, and Nicolas Luco. September 2006.
- PEER 2006/04** *Probabilistic Seismic Evaluation of Reinforced Concrete Structural Components and Systems.* Tae Hyung Lee and Khalid M. Mosalam. August 2006.
- PEER 2006/03** *Performance of Lifelines Subjected to Lateral Spreading.* Scott A. Ashford and Teerawat Juirnarongrit. July 2006.
- PEER 2006/02** *Pacific Earthquake Engineering Research Center Highway Demonstration Project.* Anne Kiremidjian, James Moore, Yue Yue Fan, Nesrin Basoz, Ozgur Yazali, and Meredith Williams. April 2006.
- PEER 2006/01** *Bracing Berkeley. A Guide to Seismic Safety on the UC Berkeley Campus.* Mary C. Comerio, Stephen Tobriner, and Ariane Fehrenkamp. January 2006.
- PEER 2005/16** *Seismic Response and Reliability of Electrical Substation Equipment and Systems.* Junho Song, Armen Der Kiureghian, and Jerome L. Sackman. April 2006.
- PEER 2005/15** *CPT-Based Probabilistic Assessment of Seismic Soil Liquefaction Initiation.* R. E. S. Moss, R. B. Seed, R. E. Kayen, J. P. Stewart, and A. Der Kiureghian. April 2006.
- PEER 2005/14** *Workshop on Modeling of Nonlinear Cyclic Load-Deformation Behavior of Shallow Foundations.* Bruce L. Kutter, Geoffrey Martin, Tara Hutchinson, Chad Harden, Sivapalan Gajan, and Justin Phalen. March 2006.
- PEER 2005/13** *Stochastic Characterization and Decision Bases under Time-Dependent Aftershock Risk in Performance-Based Earthquake Engineering.* Gee Liek Yeo and C. Allin Cornell. July 2005.

- PEER 2005/12** *PEER Testbed Study on a Laboratory Building: Exercising Seismic Performance Assessment.* Mary C. Comerio, editor. November 2005.
- PEER 2005/11** *Van Nuys Hotel Building Testbed Report: Exercising Seismic Performance Assessment.* Helmut Krawinkler, editor. October 2005.
- PEER 2005/10** *First NEES/E-Defense Workshop on Collapse Simulation of Reinforced Concrete Building Structures.* September 2005.
- PEER 2005/09** *Test Applications of Advanced Seismic Assessment Guidelines.* Joe Maffei, Karl Telleen, Danya Mohr, William Holmes, and Yuki Nakayama. August 2006.
- PEER 2005/08** *Damage Accumulation in Lightly Confined Reinforced Concrete Bridge Columns.* R. Tyler Ranf, Jared M. Nelson, Zach Price, Marc O. Eberhard, and John F. Stanton. April 2006.
- PEER 2005/07** *Experimental and Analytical Studies on the Seismic Response of Freestanding and Anchored Laboratory Equipment.* Dimitrios Konstantinidis and Nicos Makris. January 2005.
- PEER 2005/06** *Global Collapse of Frame Structures under Seismic Excitations.* Luis F. Ibarra and Helmut Krawinkler. September 2005.
- PEER 2005/05** *Performance Characterization of Bench- and Shelf-Mounted Equipment.* Samit Ray Chaudhuri and Tara C. Hutchinson. May 2006.
- PEER 2005/04** *Numerical Modeling of the Nonlinear Cyclic Response of Shallow Foundations.* Chad Harden, Tara Hutchinson, Geoffrey R. Martin, and Bruce L. Kutter. August 2005.
- PEER 2005/03** *A Taxonomy of Building Components for Performance-Based Earthquake Engineering.* Keith A. Porter. September 2005.
- PEER 2005/02** *Fragility Basis for California Highway Overpass Bridge Seismic Decision Making.* Kevin R. Mackie and Božidar Stojadinović. June 2005.
- PEER 2005/01** *Empirical Characterization of Site Conditions on Strong Ground Motion.* Jonathan P. Stewart, Yoojoong Choi, and Robert W. Graves. June 2005.
- PEER 2004/09** *Electrical Substation Equipment Interaction: Experimental Rigid Conductor Studies.* Christopher Stearns and André Filiatrault. February 2005.
- PEER 2004/08** *Seismic Qualification and Fragility Testing of Line Break 550-kV Disconnect Switches.* Shakhzod M. Takhirov, Gregory L. Fenves, and Eric Fujisaki. January 2005.
- PEER 2004/07** *Ground Motions for Earthquake Simulator Qualification of Electrical Substation Equipment.* Shakhzod M. Takhirov, Gregory L. Fenves, Eric Fujisaki, and Don Clyde. January 2005.
- PEER 2004/06** *Performance-Based Regulation and Regulatory Regimes.* Peter J. May and Chris Koski. September 2004.
- PEER 2004/05** *Performance-Based Seismic Design Concepts and Implementation: Proceedings of an International Workshop.* Peter Fajfar and Helmut Krawinkler, editors. September 2004.
- PEER 2004/04** *Seismic Performance of an Instrumented Tilt-up Wall Building.* James C. Anderson and Vitelmo V. Bertero. July 2004.
- PEER 2004/03** *Evaluation and Application of Concrete Tilt-up Assessment Methodologies.* Timothy Graf and James O. Malley. October 2004.
- PEER 2004/02** *Analytical Investigations of New Methods for Reducing Residual Displacements of Reinforced Concrete Bridge Columns.* Junichi Sakai and Stephen A. Mahin. August 2004.
- PEER 2004/01** *Seismic Performance of Masonry Buildings and Design Implications.* Kerri Anne Taeko Tokoro, James C. Anderson, and Vitelmo V. Bertero. February 2004.
- PEER 2003/18** *Performance Models for Flexural Damage in Reinforced Concrete Columns.* Michael Berry and Marc Eberhard. August 2003.
- PEER 2003/17** *Predicting Earthquake Damage in Older Reinforced Concrete Beam-Column Joints.* Catherine Pagni and Laura Lowes. October 2004.
- PEER 2003/16** *Seismic Demands for Performance-Based Design of Bridges.* Kevin Mackie and Božidar Stojadinović. August 2003.
- PEER 2003/15** *Seismic Demands for Nondeteriorating Frame Structures and Their Dependence on Ground Motions.* Ricardo Antonio Medina and Helmut Krawinkler. May 2004.
- PEER 2003/14** *Finite Element Reliability and Sensitivity Methods for Performance-Based Earthquake Engineering.* Terje Haukaas and Armen Der Kiureghian. April 2004.

- PEER 2003/13** *Effects of Connection Hysteretic Degradation on the Seismic Behavior of Steel Moment-Resisting Frames.* Janise E. Rodgers and Stephen A. Mahin. March 2004.
- PEER 2003/12** *Implementation Manual for the Seismic Protection of Laboratory Contents: Format and Case Studies.* William T. Holmes and Mary C. Comerio. October 2003.
- PEER 2003/11** *Fifth U.S.-Japan Workshop on Performance-Based Earthquake Engineering Methodology for Reinforced Concrete Building Structures.* February 2004.
- PEER 2003/10** *A Beam-Column Joint Model for Simulating the Earthquake Response of Reinforced Concrete Frames.* Laura N. Lowes, Nilanjan Mitra, and Arash Altoontash. February 2004.
- PEER 2003/09** *Sequencing Repairs after an Earthquake: An Economic Approach.* Marco Casari and Simon J. Wilkie. April 2004.
- PEER 2003/08** *A Technical Framework for Probability-Based Demand and Capacity Factor Design (DCFD) Seismic Formats.* Fatemeh Jalayer and C. Allin Cornell. November 2003.
- PEER 2003/07** *Uncertainty Specification and Propagation for Loss Estimation Using FOSM Methods.* Jack W. Baker and C. Allin Cornell. September 2003.
- PEER 2003/06** *Performance of Circular Reinforced Concrete Bridge Columns under Bidirectional Earthquake Loading.* Mahmoud M. Hachem, Stephen A. Mahin, and Jack P. Moehle. February 2003.
- PEER 2003/05** *Response Assessment for Building-Specific Loss Estimation.* Eduardo Miranda and Shahram Taghavi. September 2003.
- PEER 2003/04** *Experimental Assessment of Columns with Short Lap Splices Subjected to Cyclic Loads.* Murat Melek, John W. Wallace, and Joel Conte. April 2003.
- PEER 2003/03** *Probabilistic Response Assessment for Building-Specific Loss Estimation.* Eduardo Miranda and Hesameddin Aslani. September 2003.
- PEER 2003/02** *Software Framework for Collaborative Development of Nonlinear Dynamic Analysis Program.* Jun Peng and Kincho H. Law. September 2003.
- PEER 2003/01** *Shake Table Tests and Analytical Studies on the Gravity Load Collapse of Reinforced Concrete Frames.* Kenneth John Elwood and Jack P. Moehle. November 2003.
- PEER 2002/24** *Performance of Beam to Column Bridge Joints Subjected to a Large Velocity Pulse.* Natalie Gibson, André Filiatrault, and Scott A. Ashford. April 2002.
- PEER 2002/23** *Effects of Large Velocity Pulses on Reinforced Concrete Bridge Columns.* Greg L. Orozco and Scott A. Ashford. April 2002.
- PEER 2002/22** *Characterization of Large Velocity Pulses for Laboratory Testing.* Kenneth E. Cox and Scott A. Ashford. April 2002.
- PEER 2002/21** *Fourth U.S.-Japan Workshop on Performance-Based Earthquake Engineering Methodology for Reinforced Concrete Building Structures.* December 2002.
- PEER 2002/20** *Barriers to Adoption and Implementation of PBEE Innovations.* Peter J. May. August 2002.
- PEER 2002/19** *Economic-Engineered Integrated Models for Earthquakes: Socioeconomic Impacts.* Peter Gordon, James E. Moore II, and Harry W. Richardson. July 2002.
- PEER 2002/18** *Assessment of Reinforced Concrete Building Exterior Joints with Substandard Details.* Chris P. Pantelides, Jon Hansen, Justin Nadauld, and Lawrence D. Reaveley. May 2002.
- PEER 2002/17** *Structural Characterization and Seismic Response Analysis of a Highway Overcrossing Equipped with Elastomeric Bearings and Fluid Dampers: A Case Study.* Nicos Makris and Jian Zhang. November 2002.
- PEER 2002/16** *Estimation of Uncertainty in Geotechnical Properties for Performance-Based Earthquake Engineering.* Allen L. Jones, Steven L. Kramer, and Pedro Arduino. December 2002.
- PEER 2002/15** *Seismic Behavior of Bridge Columns Subjected to Various Loading Patterns.* Asadollah Esmaeily-Gh. and Yan Xiao. December 2002.
- PEER 2002/14** *Inelastic Seismic Response of Extended Pile Shaft Supported Bridge Structures.* T.C. Hutchinson, R.W. Boulanger, Y.H. Chai, and I.M. Idriss. December 2002.
- PEER 2002/13** *Probabilistic Models and Fragility Estimates for Bridge Components and Systems.* Paolo Gardoni, Armen Der Kiureghian, and Khalid M. Mosalam. June 2002.
- PEER 2002/12** *Effects of Fault Dip and Slip Rake on Near-Source Ground Motions: Why Chi-Chi Was a Relatively Mild M7.6 Earthquake.* Brad T. Aagaard, John F. Hall, and Thomas H. Heaton. December 2002.

- PEER 2002/11** *Analytical and Experimental Study of Fiber-Reinforced Strip Isolators.* James M. Kelly and Shakhzod M. Takhirov. September 2002.
- PEER 2002/10** *Centrifuge Modeling of Settlement and Lateral Spreading with Comparisons to Numerical Analyses.* Sivapalan Gajan and Bruce L. Kutter. January 2003.
- PEER 2002/09** *Documentation and Analysis of Field Case Histories of Seismic Compression during the 1994 Northridge, California, Earthquake.* Jonathan P. Stewart, Patrick M. Smith, Daniel H. Whang, and Jonathan D. Bray. October 2002.
- PEER 2002/08** *Component Testing, Stability Analysis and Characterization of Buckling-Restrained Unbonded Braces™.* Cameron Black, Nicos Makris, and Ian Aiken. September 2002.
- PEER 2002/07** *Seismic Performance of Pile-Wharf Connections.* Charles W. Roeder, Robert Graff, Jennifer Soderstrom, and Jun Han Yoo. December 2001.
- PEER 2002/06** *The Use of Benefit-Cost Analysis for Evaluation of Performance-Based Earthquake Engineering Decisions.* Richard O. Zerbe and Anthony Falit-Baiamonte. September 2001.
- PEER 2002/05** *Guidelines, Specifications, and Seismic Performance Characterization of Nonstructural Building Components and Equipment.* André Filiatrault, Constantin Christopoulos, and Christopher Stearns. September 2001.
- PEER 2002/04** *Consortium of Organizations for Strong-Motion Observation Systems and the Pacific Earthquake Engineering Research Center Lifelines Program: Invited Workshop on Archiving and Web Dissemination of Geotechnical Data, 4–5 October 2001.* September 2002.
- PEER 2002/03** *Investigation of Sensitivity of Building Loss Estimates to Major Uncertain Variables for the Van Nuys Testbed.* Keith A. Porter, James L. Beck, and Rustem V. Shaikhutdinov. August 2002.
- PEER 2002/02** *The Third U.S.-Japan Workshop on Performance-Based Earthquake Engineering Methodology for Reinforced Concrete Building Structures.* July 2002.
- PEER 2002/01** *Nonstructural Loss Estimation: The UC Berkeley Case Study.* Mary C. Comerio and John C. Stallmeyer. December 2001.
- PEER 2001/16** *Statistics of SDF-System Estimate of Roof Displacement for Pushover Analysis of Buildings.* Anil K. Chopra, Rakesh K. Goel, and Chatpan Chintanapakdee. December 2001.
- PEER 2001/15** *Damage to Bridges during the 2001 Nisqually Earthquake.* R. Tyler Ranf, Marc O. Eberhard, and Michael P. Berry. November 2001.
- PEER 2001/14** *Rocking Response of Equipment Anchored to a Base Foundation.* Nicos Makris and Cameron J. Black. September 2001.
- PEER 2001/13** *Modeling Soil Liquefaction Hazards for Performance-Based Earthquake Engineering.* Steven L. Kramer and Ahmed-W. Elgamal. February 2001.
- PEER 2001/12** *Development of Geotechnical Capabilities in OpenSees.* Boris Jeremić. September 2001.
- PEER 2001/11** *Analytical and Experimental Study of Fiber-Reinforced Elastomeric Isolators.* James M. Kelly and Shakhzod M. Takhirov. September 2001.
- PEER 2001/10** *Amplification Factors for Spectral Acceleration in Active Regions.* Jonathan P. Stewart, Andrew H. Liu, Yoojoong Choi, and Mehmet B. Baturay. December 2001.
- PEER 2001/09** *Ground Motion Evaluation Procedures for Performance-Based Design.* Jonathan P. Stewart, Shyh-Jeng Chiou, Jonathan D. Bray, Robert W. Graves, Paul G. Somerville, and Norman A. Abrahamson. September 2001.
- PEER 2001/08** *Experimental and Computational Evaluation of Reinforced Concrete Bridge Beam-Column Connections for Seismic Performance.* Clay J. Naito, Jack P. Moehle, and Khalid M. Mosalam. November 2001.
- PEER 2001/07** *The Rocking Spectrum and the Shortcomings of Design Guidelines.* Nicos Makris and Dimitrios Konstantinidis. August 2001.
- PEER 2001/06** *Development of an Electrical Substation Equipment Performance Database for Evaluation of Equipment Fragilities.* Thalia Agnanos. April 1999.
- PEER 2001/05** *Stiffness Analysis of Fiber-Reinforced Elastomeric Isolators.* Hsiang-Chuan Tsai and James M. Kelly. May 2001.
- PEER 2001/04** *Organizational and Societal Considerations for Performance-Based Earthquake Engineering.* Peter J. May. April 2001.
- PEER 2001/03** *A Modal Pushover Analysis Procedure to Estimate Seismic Demands for Buildings: Theory and Preliminary Evaluation.* Anil K. Chopra and Rakesh K. Goel. January 2001.

- PEER 2001/02** *Seismic Response Analysis of Highway Overcrossings Including Soil-Structure Interaction.* Jian Zhang and Nicos Makris. March 2001.
- PEER 2001/01** *Experimental Study of Large Seismic Steel Beam-to-Column Connections.* Egor P. Popov and Shakhzod M. Takhirov. November 2000.
- PEER 2000/10** *The Second U.S.-Japan Workshop on Performance-Based Earthquake Engineering Methodology for Reinforced Concrete Building Structures.* March 2000.
- PEER 2000/09** *Structural Engineering Reconnaissance of the August 17, 1999 Earthquake: Kocaeli (Izmit), Turkey.* Halil Sezen, Kenneth J. Elwood, Andrew S. Whittaker, Khalid Mosalam, John J. Wallace, and John F. Stanton. December 2000.
- PEER 2000/08** *Behavior of Reinforced Concrete Bridge Columns Having Varying Aspect Ratios and Varying Lengths of Confinement.* Anthony J. Calderone, Dawn E. Lehman, and Jack P. Moehle. January 2001.
- PEER 2000/07** *Cover-Plate and Flange-Plate Reinforced Steel Moment-Resisting Connections.* Taejin Kim, Andrew S. Whittaker, Amir S. Gilani, Vitelmo V. Bertero, and Shakhzod M. Takhirov. September 2000.
- PEER 2000/06** *Seismic Evaluation and Analysis of 230-kV Disconnect Switches.* Amir S. J. Gilani, Andrew S. Whittaker, Gregory L. Fenves, Chun-Hao Chen, Henry Ho, and Eric Fujisaki. July 2000.
- PEER 2000/05** *Performance-Based Evaluation of Exterior Reinforced Concrete Building Joints for Seismic Excitation.* Chandra Clyde, Chris P. Pantelides, and Lawrence D. Reaveley. July 2000.
- PEER 2000/04** *An Evaluation of Seismic Energy Demand: An Attenuation Approach.* Chung-Che Chou and Chia-Ming Uang. July 1999.
- PEER 2000/03** *Framing Earthquake Retrofitting Decisions: The Case of Hillside Homes in Los Angeles.* Detlof von Winterfeldt, Nels Roselund, and Alicia Kitsuse. March 2000.
- PEER 2000/02** *U.S.-Japan Workshop on the Effects of Near-Field Earthquake Shaking.* Andrew Whittaker, ed. July 2000.
- PEER 2000/01** *Further Studies on Seismic Interaction in Interconnected Electrical Substation Equipment.* Armen Der Kiureghian, Kee-Jeung Hong, and Jerome L. Sackman. November 1999.
- PEER 1999/14** *Seismic Evaluation and Retrofit of 230-kV Porcelain Transformer Bushings.* Amir S. Gilani, Andrew S. Whittaker, Gregory L. Fenves, and Eric Fujisaki. December 1999.
- PEER 1999/13** *Building Vulnerability Studies: Modeling and Evaluation of Tilt-up and Steel Reinforced Concrete Buildings.* John W. Wallace, Jonathan P. Stewart, and Andrew S. Whittaker, editors. December 1999.
- PEER 1999/12** *Rehabilitation of Nonductile RC Frame Building Using Encasement Plates and Energy-Dissipating Devices.* Mehrdad Sasani, Vitelmo V. Bertero, James C. Anderson. December 1999.
- PEER 1999/11** *Performance Evaluation Database for Concrete Bridge Components and Systems under Simulated Seismic Loads.* Yael D. Hose and Frieder Seible. November 1999.
- PEER 1999/10** *U.S.-Japan Workshop on Performance-Based Earthquake Engineering Methodology for Reinforced Concrete Building Structures.* December 1999.
- PEER 1999/09** *Performance Improvement of Long Period Building Structures Subjected to Severe Pulse-Type Ground Motions.* James C. Anderson, Vitelmo V. Bertero, and Raul Bertero. October 1999.
- PEER 1999/08** *Envelopes for Seismic Response Vectors.* Charles Menun and Armen Der Kiureghian. July 1999.
- PEER 1999/07** *Documentation of Strengths and Weaknesses of Current Computer Analysis Methods for Seismic Performance of Reinforced Concrete Members.* William F. Cofer. November 1999.
- PEER 1999/06** *Rocking Response and Overturning of Anchored Equipment under Seismic Excitations.* Nicos Makris and Jian Zhang. November 1999.
- PEER 1999/05** *Seismic Evaluation of 550 kV Porcelain Transformer Bushings.* Amir S. Gilani, Andrew S. Whittaker, Gregory L. Fenves, and Eric Fujisaki. October 1999.
- PEER 1999/04** *Adoption and Enforcement of Earthquake Risk-Reduction Measures.* Peter J. May, Raymond J. Burby, T. Jens Feeley, and Robert Wood.
- PEER 1999/03** *Task 3 Characterization of Site Response General Site Categories.* Adrian Rodriguez-Marek, Jonathan D. Bray, and Norman Abrahamson. February 1999.
- PEER 1999/02** *Capacity-Demand-Diagram Methods for Estimating Seismic Deformation of Inelastic Structures: SDF Systems.* Anil K. Chopra and Rakesh Goel. April 1999.
- PEER 1999/01** *Interaction in Interconnected Electrical Substation Equipment Subjected to Earthquake Ground Motions.* Armen Der Kiureghian, Jerome L. Sackman, and Kee-Jeung Hong. February 1999.

- PEER 1998/08** *Behavior and Failure Analysis of a Multiple-Frame Highway Bridge in the 1994 Northridge Earthquake.* Gregory L. Fenves and Michael Ellery. December 1998.
- PEER 1998/07** *Empirical Evaluation of Inertial Soil-Structure Interaction Effects.* Jonathan P. Stewart, Raymond B. Seed, and Gregory L. Fenves. November 1998.
- PEER 1998/06** *Effect of Damping Mechanisms on the Response of Seismic Isolated Structures.* Nicos Makris and Shih-Po Chang. November 1998.
- PEER 1998/05** *Rocking Response and Overturning of Equipment under Horizontal Pulse-Type Motions.* Nicos Makris and Yiannis Roussos. October 1998.
- PEER 1998/04** *Pacific Earthquake Engineering Research Invitational Workshop Proceedings, May 14–15, 1998: Defining the Links between Planning, Policy Analysis, Economics and Earthquake Engineering.* Mary Comerio and Peter Gordon. September 1998.
- PEER 1998/03** *Repair/Upgrade Procedures for Welded Beam to Column Connections.* James C. Anderson and Xiaojing Duan. May 1998.
- PEER 1998/02** *Seismic Evaluation of 196 kV Porcelain Transformer Bushings.* Amir S. Gilani, Juan W. Chavez, Gregory L. Fenves, and Andrew S. Whittaker. May 1998.
- PEER 1998/01** *Seismic Performance of Well-Confined Concrete Bridge Columns.* Dawn E. Lehman and Jack P. Moehle. December 2000.

ONLINE PEER REPORTS

The following PEER reports are available by Internet only at http://peer.berkeley.edu/publications/peer_reports_complete.html.

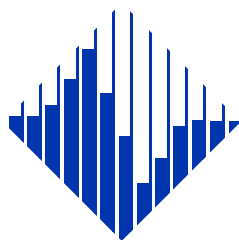
- PEER 2012/103** *Performance-Based Seismic Demand Assessment of Concentrically Braced Steel Frame Buildings*. Chui-Hsin Chen and Stephen A. Mahin. December 2012.
- PEER 2012/102** *Procedure to Restart an Interrupted Hybrid Simulation: Addendum to PEER Report 2010/103*. Vesna Terzic and Božidar Stojadinovic. October 2012.
- PEER 2012/101** *Mechanics of Fiber Reinforced Bearings*. James M. Kelly and Andrea Calabrese. February 2012.
- PEER 2011/107** *Nonlinear Site Response and Seismic Compression at Vertical Array Strongly Shaken by 2007 Niigata-ken Chuetsu-oki Earthquake*. Eric Yee, Jonathan P. Stewart, and Kohji Tokimatsu. December 2011.
- PEER 2011/106** *Self Compacting Hybrid Fiber Reinforced Concrete Composites for Bridge Columns*. Pardeep Kumar, Gabriel Jen, William Trono, Marios Panagiotou, and Claudia Ostertag. September 2011.
- PEER 2011/105** *Stochastic Dynamic Analysis of Bridges Subjected to Spatially Varying Ground Motions*. Katerina Konakli and Armen Der Kiureghian. August 2011.
- PEER 2011/104** *Design and Instrumentation of the 2010 E-Defense Four-Story Reinforced Concrete and Post-Tensioned Concrete Buildings*. Takuya Nagae, Kenichi Tahara, Taizo Matsumori, Hitoshi Shiohara, Toshimi Kabeyasawa, Susumu Kono, Minehiro Nishiyama (Japanese Research Team) and John Wallace, Wassim Ghannoum, Jack Moehle, Richard Sause, Wesley Keller, Zeynep Tuna (U.S. Research Team). June 2011.
- PEER 2011/103** *In-Situ Monitoring of the Force Output of Fluid Dampers: Experimental Investigation*. Dimitrios Konstantinidis, James M. Kelly, and Nicos Makris. April 2011.
- PEER 2011/102** *Ground-motion prediction equations 1964 - 2010*. John Douglas. April 2011.
- PEER 2011/101** *Report of the Eighth Planning Meeting of NEES/E-Defense Collaborative Research on Earthquake Engineering*. Convened by the Hyogo Earthquake Engineering Research Center (NIED), NEES Consortium, Inc. February 2011.
- PEER 2010/111** *Modeling and Acceptance Criteria for Seismic Design and Analysis of Tall Buildings*. Task 7 Report for the Tall Buildings Initiative - Published jointly by the Applied Technology Council. October 2010.
- PEER 2010/110** *Seismic Performance Assessment and Probabilistic Repair Cost Analysis of Precast Concrete Cladding Systems for Multistory Buildings*. Jeffrey P. Hunt and Božidar Stojadinovic. November 2010.
- PEER 2010/109** *Report of the Seventh Joint Planning Meeting of NEES/E-Defense Collaboration on Earthquake Engineering. Held at the E-Defense, Miki, and Shin-Kobe, Japan, September 18–19, 2009*. August 2010.
- PEER 2010/108** *Probabilistic Tsunami Hazard in California*. Hong Kie Thio, Paul Somerville, and Jascha Polet, preparers. October 2010.
- PEER 2010/107** *Performance and Reliability of Exposed Column Base Plate Connections for Steel Moment-Resisting Frames*. Ady Aviram, Božidar Stojadinovic, and Armen Der Kiureghian. August 2010.
- PEER 2010/106** *Verification of Probabilistic Seismic Hazard Analysis Computer Programs*. Patricia Thomas, Ivan Wong, and Norman Abrahamson. May 2010.
- PEER 2010/105** *Structural Engineering Reconnaissance of the April 6, 2009, Abruzzo, Italy, Earthquake, and Lessons Learned*. M. Selim Günay and Khalid M. Mosalam. April 2010.
- PEER 2010/104** *Simulating the Inelastic Seismic Behavior of Steel Braced Frames, Including the Effects of Low-Cycle Fatigue*. Yuli Huang and Stephen A. Mahin. April 2010.
- PEER 2010/103** *Post-Earthquake Traffic Capacity of Modern Bridges in California*. Vesna Terzic and Božidar Stojadinović. March 2010.
- PEER 2010/102** *Analysis of Cumulative Absolute Velocity (CAV) and JMA Instrumental Seismic Intensity (I_{JMA}) Using the PEER–NGA Strong Motion Database*. Kenneth W. Campbell and Yousef Bozorgnia. February 2010.
- PEER 2010/101** *Rocking Response of Bridges on Shallow Foundations*. Jose A. Ugalde, Bruce L. Kutter, and Boris Jeremic. April 2010.
- PEER 2009/109** *Simulation and Performance-Based Earthquake Engineering Assessment of Self-Centering Post-Tensioned Concrete Bridge Systems*. Won K. Lee and Sarah L. Billington. December 2009.
- PEER 2009/108** *PEER Lifelines Geotechnical Virtual Data Center*. J. Carl Stepp, Daniel J. Ponti, Loren L. Turner, Jennifer N. Swift, Sean Devlin, Yang Zhu, Jean Benoit, and John Bobbitt. September 2009.

- PEER 2009/107** *Experimental and Computational Evaluation of Current and Innovative In-Span Hinge Details in Reinforced Concrete Box-Girder Bridges: Part 2: Post-Test Analysis and Design Recommendations.* Matias A. Hube and Khalid M. Mosalam. December 2009.
- PEER 2009/106** *Shear Strength Models of Exterior Beam-Column Joints without Transverse Reinforcement.* Sangjoon Park and Khalid M. Mosalam. November 2009.
- PEER 2009/105** *Reduced Uncertainty of Ground Motion Prediction Equations through Bayesian Variance Analysis.* Robb Eric S. Moss. November 2009.
- PEER 2009/104** *Advanced Implementation of Hybrid Simulation.* Andreas H. Schellenberg, Stephen A. Mahin, Gregory L. Fenves. November 2009.
- PEER 2009/103** *Performance Evaluation of Innovative Steel Braced Frames.* T. Y. Yang, Jack P. Moehle, and Božidar Stojadinovic. August 2009.
- PEER 2009/102** *Reinvestigation of Liquefaction and Nonliquefaction Case Histories from the 1976 Tangshan Earthquake.* Robb Eric Moss, Robert E. Kayen, Liyuan Tong, Songyu Liu, Guojun Cai, and Jiaer Wu. August 2009.
- PEER 2009/101** *Report of the First Joint Planning Meeting for the Second Phase of NEES/E-Defense Collaborative Research on Earthquake Engineering.* Stephen A. Mahin et al. July 2009.
- PEER 2008/104** *Experimental and Analytical Study of the Seismic Performance of Retaining Structures.* Linda Al Atik and Nicholas Sitar. January 2009.
- PEER 2008/103** *Experimental and Computational Evaluation of Current and Innovative In-Span Hinge Details in Reinforced Concrete Box-Girder Bridges. Part 1: Experimental Findings and Pre-Test Analysis.* Matias A. Hube and Khalid M. Mosalam. January 2009.
- PEER 2008/102** *Modeling of Unreinforced Masonry Infill Walls Considering In-Plane and Out-of-Plane Interaction.* Stephen Kadysiewski and Khalid M. Mosalam. January 2009.
- PEER 2008/101** *Seismic Performance Objectives for Tall Buildings.* William T. Holmes, Charles Kircher, William Petak, and Nabih Youssef. August 2008.
- PEER 2007/101** *Generalized Hybrid Simulation Framework for Structural Systems Subjected to Seismic Loading.* Tarek Elkhoraibi and Khalid M. Mosalam. July 2007.
- PEER 2007/100** *Seismic Evaluation of Reinforced Concrete Buildings Including Effects of Masonry Infill Walls.* Alidad Hashemi and Khalid M. Mosalam. July 2007.

The Pacific Earthquake Engineering Research Center (PEER) is a multi-institutional research and education center with headquarters at the University of California, Berkeley. Investigators from over 20 universities, several consulting companies, and researchers at various state and federal government agencies contribute to research programs focused on performance-based earthquake engineering.

These research programs aim to identify and reduce the risks from major earthquakes to life safety and to the economy by including research in a wide variety of disciplines including structural and geotechnical engineering, geology/seismology, lifelines, transportation, architecture, economics, risk management, and public policy.

PEER is supported by federal, state, local, and regional agencies, together with industry partners.



PEER Core Institutions:
University of California, Berkeley (Lead Institution)
California Institute of Technology
Oregon State University
Stanford University
University of California, Davis
University of California, Irvine
University of California, Los Angeles
University of California, San Diego
University of Southern California
University of Washington

PEER reports can be ordered at http://peer.berkeley.edu/publications/peer_reports.html or by contacting

Pacific Earthquake Engineering Research Center
University of California, Berkeley
325 Davis Hall, mail code 1792
Berkeley, CA 94720-1792
Tel: 510-642-3437
Fax: 510-642-1655
Email: peer_editor@berkeley.edu

ISSN 1547-0587X